Ministry of Science and Higher Education of the Russian Federation
ITMO University

ISSN 2220-8054

NANOSYSTEMS:

PHYSICS, CHEMISTRY, MATHEMATICS

2024, volume 15(6)

Наносистемы: физика, химия, математика

2024, том 15, № 6

NANOSYSTEMS:

PHYSICS, CHEMISTRY, MATHEMATICS

ADVISORY BOARD MEMBERS

Chairman: V.N. Vasiliev *(St. Petersburg, Russia)*,
V.M. Buznik *(Moscow, Russia)*; V.M. Ievlev *(Voronezh, Russia)*, P.S. Kop’ev*(St. Petersburg, Russia)*, V.N. Parmon *(Novosibirsk, Russia)*, A.I. Rusanov *(St. Petersburg, Russia)*,

EDITORIAL BOARD

Editor-in-Chief: I.Yu. Popov *(St. Petersburg, Russia)*

Section Co-Editors:
Physics – V.M. Uzdin *(St. Petersburg, Russia)*,
Material science – V.V. Gusarov *(St. Petersburg, Russia);* O.V. Al’myasheva *(St. Petersburg, Russia)*;
Chemistry – V.K. Ivanov *(Moscow, Russia)*,
Mathematics – I.Yu. Popov *(St. Petersburg, Russia).*

Editorial Board Members:
V.M. Adamyan *(Odessa, Ukraine)*; A.P. Alodjants *(St. Petersburg, Russia)*; S. Bechta *(Stockholm, Sweden)*; J. Behrndt *(Graz, Austria)*; A. Chatterjee (*Hyderabad, India)*; A.V. Chizhov *(Dubna, Russia)*; A.N. Enyashin *(Ekaterinburg, Russia)*, P.P. Fedorov *(Moscow, Russia)*; E.A. Gudilin *(Moscow, Russia)*; H. Jónsson *(Reykjavik, Iceland)*; A.A. Kiselev *(Durham, USA)*; Yu.S. Kivshar *(Canberra, Australia)*; S.A. Kozlov *(St. Petersburg, Russia)*; P.A. Kurasov *(Stockholm, Sweden)*; A.V. Lukashin *(Moscow, Russia)*; G.P. Miroshnichenko *(St. Petersburg, Russia)*; I.Ya. Mittova *(Voronezh, Russia)*; H. Najar *(Monastir, Tunisia),* Nguyen Anh Tien *(Ho Chi Minh, Vietnam)*; V.V. Pankov *(Minsk, Belarus)*; K. Pankrashkin *(Orsay, France)*; A.V. Ragulya *(Kiev, Ukraine)*; V. Rajendran *(Tamil Nadu, India)*; A.A. Rempel *(Ekaterinburg, Russia)*; A.A. Rogachev *(Minsk, Belarus)*; V.Ya. Rudyak *(Novosibirsk, Russia)*; H.M. Sedighi (*Ahvaz, Iran*); D Shoikhet *(Karmiel, Israel)*; M.N.Smirnova *(Moscow, Russia)*; P. Stovicek *(Prague, Czech Republic)*; V.M. Talanov *(Novocherkassk, Russia)*; A.Ya. Vul’ *(St. Petersburg, Russia)*; A.V. Yakimansky (*St. Petersburg, Russia*), V.A. Zagrebnov *(Marseille, France)*.

Editors:
I.V. Blinova; A.I. Popov; A.I. Trifanov; E.S. Trifanova *(St. Petersburg, Russia),*
R. Simoneaux *(Philadelphia, Pennsylvania, USA)*.

Address: ITMO University, Kronverkskiy pr., 49, St. Petersburg 197101, Russia.
Phone: +7(812)607-02-54, **Journal site:** http://nanojournal.ifmo.ru/,
E-mail: nanojournal.ifmo@gmail.com

AIM AND SCOPE

The scope of the journal includes all areas of nano-sciences. Papers devoted to basic problems of physics, chemistry, material science and mathematics inspired by nanosystems investigations are welcomed. Both theoretical and experimental works concerning the properties and behavior of nanosystems, problems of its creation and application, mathematical methods of nanosystem studies are considered.

The journal publishes scientific reviews (up to 30 journal pages), research papers (up to 15 pages) and letters (up to 5 pages). All manuscripts are peer-reviewed. Authors are informed about the referee opinion and the Editorial decision.

CONTENT

MATHEMATICS

CHEMISTRY AND MATERIAL SCIENCE

Obituary

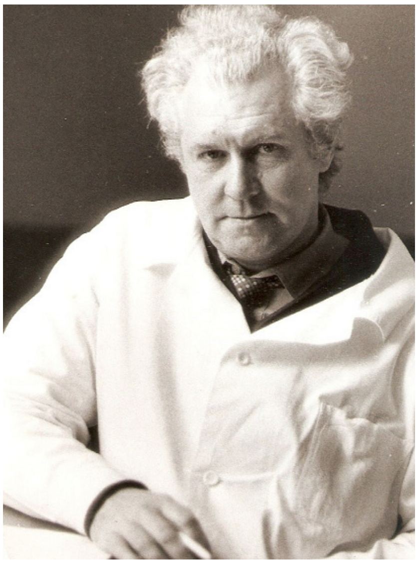

Melikhov Igor Vitalievich
9.11.1932 – 12.10.2024

Igor Vitalyevich Melikhov, a member of the Editorial Board of our journal, Corresponding Member of the Russian Academy of Sciences, a leading chemist, and Doctor of Chemical Sciences, has passed away. Melikhov I.V. is a specialist in the field of physical chemistry and radiochemistry. In 1955 he graduated from the Chemistry Department of Lomonosov Moscow State University and since 1956 he worked at this department. In 1968 he defended his dissertation for the degree of Doctor of Chemical Sciences, in 1984 he was awarded the academic title of professor, and on 30.05.1997 he was elected a Corresponding Member of the Russian Academy of Sciences, Department of Physical Chemistry and Technology of Inorganic Materials, specializing in the chemistry and technology of inorganic substances. Igor Vitalievich's scientific interests were focused on the kinetics of phase formation and sorption, nanochemistry and production of functional materials, optimization of technologies for obtaining dispersed substances with specified properties, radiochemistry and radionuclide diagnostics.

Since 1983, Igor Vitalievich headed the laboratory of heterogeneous processes at the Chemistry Department of Moscow State University. Since 2006, he has been a chief researcher at the Chemistry Department of Moscow State University. Melikhov I.V. was a member of the scientific councils of the Chemistry Department of Moscow State University and the Institute of Physical Chemistry and Electrochemistry of the Russian Academy of Sciences, deputy chairman of the Scientific Council of the Russian Academy of Sciences for the scientific foundations of chemical technology and a member of the Scientific Council of the Russian Academy of Sciences for the chemistry of high-purity substances, a member of the editorial boards of the journals «Achievements of Chemistry», «Theoretical Foundations of Chemical Technology», and «Chemical Technology». He taught not only at Moscow State University, but also at the Sofia, Belgrade, Havana, and Texas Universities.

I.V. Melikhov is the author and co-author of three monographs, a textbook and more than 500 scientific articles, including the monographs «Cocrystallization» (1975) and «Physicochemical Evolution of Solid Matter» (2006). Igor Vitalievich has been a member of the Editorial Board of the Journal since its foundation. Igor Vitalievich’s support for the development of the Journal, especially at the initial stage, was extremely important for the Journal.

We express our deepest condolences to the family and all those close to Igor Vitalievich. The memory of Igor Vitalievich Melikhov, as well as his great contribution to world science, will remain with us forever.

NANOSYSTEMS:
PHYSICS, CHEMISTRY, MATHEMATICS

Original article

Popov I.Y., et al. *Nanosystems: Phys. Chem. Math.*, 2024, **15** (6), 736–741.
http://nanojournal.ifmo.ru
DOI 10.17586/2220-8054-2024-15-6-736-741

Boundary composed of small Helmholtz resonators: asymptotic approach

Igor Y. Popov[1,a], Ekaterina S. Trifanova[1,b], Alexander S. Bagmutov[1,c], Alexander A. Lytaev[1,2,d]

[1]ITMO University, St. Petersburg, Russia
[2]Institute for Problems in Mechanical Engineering of the Russian Academy of Sciences, St. Petersburg, Russia

[a]popov1955@gmail.com, [b]etrifanova@gmail.com, [c]bagmutov94@mail.ru, [d]sas-lyt@ya.ru

Corresponding author: I. Y. Popov, popov1955@gmail.com

PACS 73.23.Ra, 73.63.Nm

ABSTRACT We consider the solution of the two-dimensional Neumann problem for the Helmholtz equation in a complex region composed of a square resonator with large number of smaller square resonators connected to it through small apertures along one side. The sizes of the apertures and distances between the neighbour apertures tend to zero. We use the method of matching of asymptotic expansions of solutions. By directing the number of attached small resonators to infinity, we obtain a problem for the Laplacian in the main square with energy-dependent boundary condition.

KEYWORDS eigenfunction, Helmholtz equation, boundary problem, asymptotics

ACKNOWLEDGEMENTS This work was partially financially supported by Russian Science Foundation (grant 24-21-00107, https://rscf.ru/en/project/24-21-00107/).

FOR CITATION Popov I.Y., Trifanova E.S., Bagmutov A.S., Lytaev A.A. Boundary composed of small Helmholtz resonators: asymptotic approach. *Nanosystems: Phys. Chem. Math.*, 2024, **15** (6), 736–741.

1. Introduction

Changes of the Laplacian spectrum under small perturbation of the domain is important and widely studied problem. It is well-known that sufficiently regular perturbation leads to the situation when $n-$th eigenvalue of the perturbed operator tends to $n-$th eigenvalue of the unperturbed operator if the perturbation decreases [1, 2]. However, if the perturbation is not so regular the situation becomes more complicated [3, 4]. An interesting case takes place if one consider a domain (resonator) with small coupled resonator or several resonators [5]. This is especially interesting if the number of coupled resonators tends to infinity simultaneously with the reducing of its sizes. Under these assumptions, the problem is analogous to homogenization problem [6–15]. This situation was studied from variational point of view in [16]. As a limiting result, one obtains the problem in main domain with a specific energy-dependent boundary condition (such conditions are interesting both from mathematical and physical points of view [17]). The result depends on the details of the limiting procedure (relation between ”rooms” and ”passages” (resonators and coupling channels)). A particular case of the problem was considered in [18] in the framework of the operator extensions theory model for coupled resonators. The role of the coupling windows shape was described in [19]. Numerical results are in [20]. Two close windows were considered in [21, 22] in the framework of the point-like window model. In the present paper, we consider the problem for the system shown in Fig. 1. We deal with asymptotics of the solution of the boundary problem in respect to two small parameters: apertures width and distance between neighbour apertures. Matching of asymptotic expansions of solutions (see, e.g., [23, 24] is used.

Recently, an additional interest to the problem was inspired by investigations towards creation of acoustic metamaterials, i.e. a form of man-made materials that can be specifically developed to have a sub-wavelength periodic structures with extraordinary characteristics not found in nature [25]. Physicists try to find such structures using the Helmholtz resonators, membrane-type structures, locally resonant and space-coiled structures. The particular question in the field is as follows: Can one create an unusual boundary condition by a specific geometry of the boundary? For example, physicists construct different combinations of small acoustic resonators (see, e.g., [26]).

2. The model

We consider the Laplace operator in the two-dimensional domain composed of a square (main resonator) Ω^- (the length of edge equals d) and a chain of N identical square resonators $\Omega_i^+, i = 1, 2, ...N$, coupled to one edge of the square through small apertures of widths $2ad$, where a is a dimensionless small parameter (see Fig. 1). In this domain, we deal with the Laplace operator $-\Delta$ defined on functions from the Sobolev space $W_2^2(\Omega)$, $\Omega = \Omega^- \cup \Omega_1^+ \cup \Omega_2^+ \cup ... \cup \Omega_N^+$, satisfying the Neumann boundary conditions at $\partial\Omega$ and the Meixner condition at edge points of the apertures (to ensure

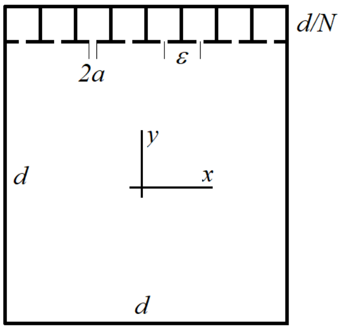

FIG. 1. Geometry of the system

the uniqueness of the solution). Correspondingly, in spectral problem one has the Helmholtz equation with the Neumann boundary conditions:

$$\Delta\psi + k^2\psi = 0, \quad \frac{\partial\psi}{\partial n}\bigg|_{\partial\Omega} = 0. \tag{1}$$

The Green function for the Helmholtz operator for the square having side d) with the Neumann boundary condition has the form:

$$G(X, X', k) = \sum_{n=0}^{\infty}\sum_{m=0}^{\infty} \frac{\chi_{nm}(x,y)\chi_{nm}(x',y')}{\left(k^2 - \frac{\pi^2 n^2}{d^2} - \frac{\pi^2 m^2}{d^2}\right)(\delta_{nm}+1)}, \tag{2}$$

where $X = (x, y)$, $X' = (x', y')$, δ_{nm} is the Kronecker symbol ($\delta_{nm} = 1$ if $n^2 + m^2 = 0$, else $\delta_{nm} = 0$),

$$\chi_{nm}(x,y) = \frac{2}{d}\cos\frac{\pi n x}{d}\cos\frac{\pi m y}{d}. \tag{3}$$

The Green function allows one to transform equation (1) in the main square to the following form:

$$\psi(X) = \int\limits_{\partial\Omega^-} G(X, X', k)\frac{\partial\psi}{\partial n}(X')dX'. \tag{4}$$

The analogous presentation is valid for each small coupled resonator.

We will seek the eigenvalue k^2 close to $\sqrt{2}\pi/d$. The term corresponding to $n = m = 1$ in (2) gives a singularity in respect to the spectral parameter of the Green function. We use the method of matching asymptotic expansions of solutions [23, 24]. In the present paper, we deal with the problem containing two small parameters. We consider asymptotic expansions in small parameter a, that corresponds to the apertures radius and $a \to 0$. However, at the same time, the number of resonators attached tends to infinity ($N \to \infty$) so that the ε (distance between adjacent holes) tends to zero. We assume that these two small parameters are related in accordance with the following formula:

$$\varepsilon = |x_i - x_{i-1}| = ma^\delta = \frac{d}{N}, \quad \delta \in (0,1). \tag{5}$$

Keeping in mind that the integrand in (4) vanishes on the part of the boundary outside the apertures, one can see that the integral is over apertures only. Correspondingly, one can find the main terms of the asymptotics in a in the following form which is analogous to that in [23]. Particularly, the solution of equation (1) near i-th aperture has the form:

$$\psi(X) = \begin{cases} \left(k^2 - \dfrac{2\pi^2}{d^2}\right)\alpha_i G_i^+(X, (x_i, 0), k), & X \in \Omega^+ \setminus S((x_i,0), r(a)); \\ v_0^i(x/a) + v_1^i(x/a)\ln^{-1}a + o(\ln^{-1}a), & X \in S((x_1, 0), 2r(a)); \\ -\left(k^2 - \dfrac{2\pi^2}{d^2}\right)\displaystyle\sum_{j=1}^{N}\alpha_j G^-(X, (x_j, 0), k), & X \in \Omega^- \setminus S((x_i, 0), r(a)), \end{cases} \tag{6}$$

where $S(X, r)$ is sphere with center X and radius r, radius $r(a)$ is chosen in such a way that

$$ad < r(a) < 2r(a) < \varepsilon/2.$$

The asymptotic expansion for the deviation of k^2 from $\dfrac{2\pi^2}{d^2}$ is chosen in accordance with the following formula ($a \to 0$):

$$k^2 - \frac{2\pi^2}{d^2} = \tau_1 \ln^{-1} a + \tau_2 \ln^{-2} a + o\left(\ln^{-2} a\right). \tag{7}$$

Here coefficients τ_1, τ_2 are to be determined.

3. Matching of asymptotic expansions

3.1. Asymptotics of solution for coupled resonators

The asymptotic behavior (when $X \to (x_i, 0)$) of the Green function for each small coupled resonator is as follows:

$$G_N^+((x,0),(x_i,0),k) = \\ -\frac{1}{\pi}\ln a + \frac{4N^2\cos(N\pi x_i/d)\cos(N\pi x/d)}{d^2\left(k^2 - 2N^2\pi^2/d^2\right)} + g_1^+(X) - \frac{1}{\pi}\ln|\xi| = \\ = -\frac{1}{\pi}\ln a + \frac{4\cos(\pi x_i/\varepsilon)\cos(\pi x/\varepsilon)}{k^2\varepsilon^2 - 2\pi^2} + g_1^+(X) - \frac{1}{\pi}\ln|\xi|, \quad (8)$$

where $X = (x, y)$, $\xi = \dfrac{x}{a}$, g_1^+ is bounded function. Note that the second term is bounded for small ε. Therefore, we attach it to the function $g_1^+(X)$ and call it g^+:

$$G_N^+((x,0),(x_i,0),k) = -\frac{1}{\pi}\ln a + g^+(X) - \frac{1}{\pi}\ln|\xi|, \quad (9)$$

where g^+ is bounded function.

Taking into account (7), one comes to the following lemma

Lemma 1. *The first terms of the asymptotic expansion of the solution (6) in the upper i-th resonator has the form:*

$$\psi^+(x,0) = \alpha_i\left(k^2 - \frac{2\pi^2}{d^2}\right)\left[-\frac{1}{\pi}\ln a + g^+(X) - \frac{1}{\pi}\ln\xi\right] = -\frac{1}{\pi}\alpha_i\tau_1 + o(1), \quad (10)$$

where $x \to x_i$, $a \to 0$.

3.2. Asymptotics of solution for the main resonator

For the main cavity, if $N \to \infty$, then each aperture contracts and, simultaneously, the apertures are getting closer to each other (correspondingly, the number of coupled resonators increases). Hence, in addition to the asymptotics of the solution for $a \to 0$, one must also take into account the asymptotics of it for $\varepsilon = |x_i - x_{i-1}| \to 0$. The asymptotics of the Green function near the i-th hole for $X \to (x_i, 0)$ is analogous to that for the coupled resonators (9). The asymptotic behavior of the Green function near the hole (when $\varepsilon \to 0$) depends on the speed of approaching of the holes. Particularly, for the chosen relation (5) it has a conventional form:

$$G^-((x,0),(x_i,0),k) = -\frac{1}{\pi}\ln\varepsilon + \frac{4\cos(\pi x/d)\cos(\pi x_i/d)}{d^2\left(k^2 - \frac{2\pi^2}{d^2}\right)} + h^-(x - x_i) - \frac{1}{\pi}\ln|\xi|, \quad (11)$$

where h^- is bounded function depending on (5). For the main resonator, the asymptotic behavior of the solution (6) near the i-th aperture has the form:

$$\psi^-(x,0) = \\ -\alpha_i\left[-\frac{\tau_1}{\pi} + \frac{4\cos^2(\pi x/d)}{d^2}\right] - \alpha_i\ln^{-1}a\left[-\frac{\tau_2}{\pi} + \tau_1\left(g^-(X) - \frac{1}{\pi}\ln|\xi|\right)\right] - \\ -\left(k^2 - \frac{2\pi^2}{d^2}\right)\sum_{j=1,j\neq i}^{N}\alpha_j\left[-\frac{\delta}{\pi}\ln a + \frac{4\cos(\pi x_j/d)\cos(\pi x_i/d)}{d^2(k^2 - 2\pi^2/d^2)} + h^-(x - x_j)\right] + o(1). \quad (12)$$

Keeping in mind that $x \to x_i$, one comes to the following lemma

Lemma 2. *The asymptotics of the solution to (6) in the main resonator has the following form:*

$$\psi^-(X) = -\alpha_i\left[-\frac{\tau_1}{\pi} + \frac{4}{d^2}\cos^2(\pi x_i/d)\right] - \sum_{j=1,j\neq i}^{N}\alpha_j\left[\frac{4}{d^2}\cos(\pi x_i/d)\cos(\pi x_j/d) - \frac{\delta\tau_1}{\pi} +\right] + o(1). \quad (13)$$

3.3. Matching

To ensure the consistency of the asymptotic expansions in the both regions (6), the coincidence of the zero-order terms is necessary. Correspondingly, the matching function $v_0^i(x/a)$ can be chosen as a constant. Equating the terms of order a^0, one obtains:

$$-\alpha_i\frac{\tau_1}{\pi} = -\alpha_i\left[-\frac{\tau_1}{\pi} + \frac{4}{d^2}\cos^2(\pi x_i/d)\right] - \sum_{j=1,j\neq i}^{N}\alpha_j\left[\frac{4}{d^2}\cos(\pi x_i/d)\cos(\pi x_j/d) - \frac{\delta\tau_1}{\pi}\right]. \quad (14)$$

One has such relation for each aperture. Hence, we obtain the system of linear equations for α_i:

$$\alpha_i \left[-\frac{2\tau_1}{\pi} + \frac{4}{d^2}\cos^2(\pi x_i/d) \right] - \sum_{j=1, j\neq i}^{N} \alpha_j \left[\frac{4}{d^2}\cos(\pi x_i/d)\cos(\pi x_j/d) - \frac{\delta\tau_1}{\pi} \right] = 0, \quad i = 1, 2, \ldots N. \tag{15}$$

Let us make designations for the convenience of calculating the determinant of the system. Then we get the following system of linear equations:

$$\alpha_i \left(\cos^2 x_i' - \beta \right) + \sum_{j=1, j\neq i}^{N} \alpha_j \left(\cos x_i' \cos x_j' - \delta' \beta \right) = 0, \tag{16}$$

where $\beta = d^2\tau_1/2\pi$, $x_i' = \pi x_i/d$, $\delta' = -\delta/2$.

The system (16) has a nontrivial solution if its determinant is zero. Calculation of the determinant (see, e.g., [27,28]) gives one the following relation:

$$\det \begin{pmatrix} \cos^2 x_1 - \beta & \cos x_1 \cos x_2 & \cos x_1 \cos x_3 & \ldots & \cos x_1 \cos x_N \\ \cos x_2 \cos x_1 & \cos^2 x_2 - \beta & \cos x_2 \cos x_3 & \ldots & \cos x_2 \cos x_N \\ \ldots & & & & \\ \cos x_N \cos x_1 & \cos x_N \cos x_2 & \cos x_N \cos x_3 & \ldots & \cos^2 x_N - \beta \end{pmatrix} =$$

$$= \beta^{N-1}(1+\delta')^{N-2}\delta' N \left[-\frac{1}{2}N + (1+\delta')\beta + o(1) \right] = 0, \tag{17}$$

whence we get

$$\beta = \frac{N}{2+\delta} + o(N), \quad N \to \infty. \tag{18}$$

Then we can get the first coefficient in the expansion (7) for k^2.

Lemma 3.

$$\tau_1 = \frac{2\pi}{d^2(2-\delta)}N + o(N). \tag{19}$$

Let us express α_i from each equality (15) and substitute the expression to (6). We obtain an expression for ψ in the main cavity using (19) and (15):

$$\psi^-(x,0) = -\left(k^2 - \frac{2\pi^2}{d^2}\right) \sum_{i=1}^{N} G^-((x,0),(x_i,0),k) \left[\frac{d^2\tau_1}{2\pi} - \cos^2\left(\frac{\pi x_i}{d}\right) \right]^{-1} \times$$
$$\sum_{j=1, j\neq i}^{N} \alpha_j \left(\cos(\pi x_i/d)\cos(\pi x_j/d) - \frac{d^2\delta\tau_1}{4\pi} \right) =$$
$$-\left(k^2 - \frac{2\pi^2}{d^2}\right) \frac{2-\delta}{N} \sum_{i=1}^{N} G^-((x,0),(x_i,0),k) \left[\frac{\alpha_i}{2(2-\delta)}N - \frac{d^2}{4}\psi^-(x_i,0) + o(1) \right] =$$
$$\frac{1}{2}\psi^-(x,0) + \frac{d}{4}(2-\delta)\left(k^2 - \frac{2\pi^2}{d^2}\right) \sum_{i=1}^{N} G^-((x,0),(x_i,0),k)\big(\psi^-(x_i) + o(1)\big) \cdot \frac{d}{N}. \tag{20}$$

Finally for $\psi^-(x)$ one obtains the following expression:

$$\psi^-(x) = \frac{d}{2}(2-\delta)\left(k^2 - \frac{2\pi^2}{d^2}\right) \sum_{i=1}^{N} G^-((x,0),(x_i,0),k)\big(\psi^-(x_i) + o(1)\big) \cdot \frac{d}{N} \tag{21}$$

which presents the integral sum. Performing the limiting transition for $N \to \infty$, one obtains the integral equation for the eigenfunction ψ.

Lemma 4. *Eigenfunction for the limit problem satisfies the following integral equation:*

$$\psi^-(X) = \frac{d}{2}(2-\delta)\left(k^2 - \frac{2\pi^2}{d^2}\right) \int_{\Gamma} G^-(X, X', k)\psi^-(X')dX'. \tag{22}$$

4. Conclusion

Taking into account (4), one can determine the boundary condition corresponding to the obtained integral eq. (22).

Theorem 4.1. *Eigenfunctions of the Laplacian corresponding to eigenvalue close to* $\dfrac{2\pi^2}{d^2}$ *for the system with many coupled resonators converges to the eigenfunctions of the Laplacian with the following boundary condition on the edge of the main square:*

$$\frac{\partial\psi}{\partial n}\Big|_{\partial\Omega} = \frac{d}{2}(2-\delta)\left(k^2 - \frac{2\pi^2}{d^2}\right)\psi\Big|_{\partial\Omega}. \tag{23}$$

The dependence of the boundary condition on the spectral parameter correlates with the results of [16]. We considered the eigenvalue close to one of the eigenvalues of the Neumann Laplacian in the square. Evidently, the same can be made for any eigenvalue. Square domain was taken for simplicity only. Really, we use only the fact that the part of the boundary with coupled resonators is straight. The result can be generalized to the case of any smooth boundary.

References

[1] Courant R., Hilbert D. *Methods of Mathematical Physics. Vol. 1*, New York: Wiley-Interscience, 1953.

[2] Sanchez-Palencia E. *Nonhomogeneous Media and Vibration Theory*, Berlin - New York: Springer-Verlag, 1980.

[3] Chechkin G.A., Friedman A., Piatnitski A.L. The boundary-value problem in domains with very rapidly oscillating boundary. *J. Math. Anal. Appl.*, 1999, **231**, P. 213–234.

[4] Jimbo S. The singularity perturbed domain and the characterization for the eigenfunctions with Neumann boundary condition. *J. Differential Equations*, 1989, **77**, P. 322–350.

[5] Arrieta J.M., Hale J.K., Han Q. Eigenvalue problems for non-smoothly perturbed domains, *J. Differential Equations*, 1991, **91**, P. 24–52.

[6] Birman M.Sh., Suslina T.A. Homogenization with corrector term for periodic elliptic differential operators. *St. Petersburg Math. J.*, 2006, **17**, P. 897–973.

[7] Borisov D., Bunoiu R., Cardone G. Homogenization and asymptotics for a waveguide with an in
nite number of closely located small windows. *J. Math. Sci.*, 2011, **176**, P. 774–785.

[8] Briet Ph. A model of sheared nanoribbons. *Nanosystems: Phys. Chem. Math.*, 2022, **13**(1), P. 12–16.

[9] Brizzi R., Chalot J.-P. Boundary homogenization and Neumann boundary value problem, *Ricerche Mat*, 1997, **46**, P. 341–387.

[10] Cardone G., Durante T. Asymptotic analysis of a planar waveguide perturbed by a non periodic perforation. *Nanosystems: Phys. Chem. Math.*, 2022, **13**, P. 5–11.

[11] Griso G. Error estimate and unfolding for periodic homogenization. *Asymptot. Anal.*, 2004, **40**, P. 269–286.

[12] Kenig C.E., Lin F., Shen Z. Periodic homogenization of Green and Neumann functions. *Comm. Pure Appl. Math.*, 2014, **67**, P. 1219–1262.

[13] Khrabustovskyi A. Homogenization of eigenvalue problem for Laplace-Beltrami operator on Riemannian manifold with complicated ”bubble-like” microstructure, *Math. Methods Appl. Sci.*, 2009, **32**, P. 2123–2137.

[14] Suslina T.A. Homogenization of elliptic operators with periodic coefficients depending on the spectral parameter. *St. Petersburg Math. J.*, 2016, **27**(4), P. 651–708.

[15] Zhikov V.V. Spectral method in homogenization theory. *Proc. Steklov Inst. Math.*, 2005, **250**, P. 85-94.

[16] Cardone G. and Khrabustovskyi A. Neumann spectral problem in a domain with very corrugated boundary. *Journal of Differential Equations*, 2015, **259**(6), P. 2333–2367.

[17] Behrndt J. Elliptic boundary value problems with k-dependent boundary conditions. *J Differential Equations*, 2010, **249**, P. 2663–2687.

[18] Popov I.Y., Blinova I.V., Popov A.I. A model of a boundary composed of the Helmholtz resonators. *Complex Variables and Elliptic Equations*, 2021, **66**(8), P. 1256–1263.

[19] Bagmutov A.S., Najar H., Melikhov I.F., Popov I.Y. On the discrete spectrum of a quantum waveguide with Neumann windows in presence of exterior field. *Nanosystems: Phys. Chem. Math.*, 2022, **13**(2), P. 156–164.

[20] Bagmutov A.S., Trifanova E.S., Popov I.Y. Resonator with a corrugated boundary: Numerical results. *Physics of Particles and Nuclei Letters*, 2023, **20**(2), P. 96–99.

[21] Belolipetskaia A.G., Boitsev A.A., Fassari S., Popov I.Y., Rinaldi F. Two-dimensional Helmholtz resonator with two close point-like windows: regularization for the Neumann case. *Methods of Functional Analysis and Topology*, 2022, **28**(2), P. 95–104.

[22] Belolipetskaya A.G., Boitsev A.A., Fassari S. and Popov I.Y. 3D Helmholtz resonator with two close point-like windows: Regularisation for Dirichlet case. *International Journal of Geometric Methods in Modern Physics*, 2021, **18**(10), P. 2150153.

[23] Gadyl’shin R.R. Existence and asymptotics of poles with small imaginary part for the Helmholtz resonator. *Russian Mathematical Surveys*, 1997, **52**(1), P. 1–72.

[24] Il’in A.M. *Matching of Asymptotic Expansions of Solutions of Boundary Value Problems*, Moscow: Nauka, 1989 [in Russian]; English transl. (Transl. Math. Monographs, **102**), Providence: Amer. Math. Soc., 1992.

[25] Gulcan Aydin, Sait Eren San, Breaking the limits of acoustic science: A review of acoustic metamaterials,*Materials Science and Engineering: B*, 2024, **305**, P. 117384.

[26] Ni X., Chen K., Weiner M., Apigo D.J., Prodan C., Alu A., Prodan E., Khanikaev A.B. Observation of Hofstadter butterfly and topological edge states in reconfigurable quasi-periodic acoustic crystals. *Commun. Phys.*, 2019, **2**, P. 55.

[27] Proskuryakov I.V. *Problems In Linear Algebra. English translation*, Moscow: Mir Publishers, 1978.

[28] Vorobiev A.M., Bagmutov A.S., Popov A.I. On formal asymptotic expansion of resonance for quantum waveguide with perforated semitransparent barrier. *Nanosystems: Phys. Chem. Math.*, 2019, **10**(4), P. 415–419.

Submitted 13 July 2024; revised 10 October 2024; accepted 20 October 2024

Information about the author:

Igor Y. Popov – Center of Mathematics, ITMO University, Kroverkskiy, 49, St. Petersburg, 197101, Russia; ORCID 0000-0002-5251-5327; popov1955@gmail.com

Ekaterina S. Trifanova – Center of Mathematics, ITMO University, Kroverkskiy, 49, St. Petersburg, 197101, Russia; etrifanova@gmail.com

Alexander S. Bagmutov – Center of Mathematics, ITMO University, Kroverkskiy, 49, St. Petersburg, 197101, Russia; bagmutov94@mail.ru

Alexander A. Lytaev – Center of Mathematics, ITMO University, Kroverkskiy, 49, St. Petersburg, 197101, Russia; Institute for Problems in Mechanical Engineering of the Russian Academy of Sciences, Vasilievskiy island, Bolshoi av., 61, St. Petersburg, 199178, Russia; sas-lyt@ya.ru

Conflict of interest: the authors declare no conflict of interest.

NANOSYSTEMS:
PHYSICS, CHEMISTRY, MATHEMATICS

Original article

Muminov S., et al. *Nanosystems:
Phys. Chem. Math.*, 2024, **15** (6), 742–748.
http://nanojournal.ifmo.ru
DOI 10.17586/2220-8054-2024-15-6-742-748

Qualitative properties of the mathematical model of nonlinear cross-diffusion processes

Sokhibjan Muminov[1,2,a], Praveen Agarwal[3,4,5,b], Dildora Muhamediyeva[6,c]

[1]Mamun university, Khiva, Uzbekistan

[2]Urgench state university, Urgench, Uzbekistan

[3]Nonlinear Dynamics Research Center (NDRC), Ajman University, Ajman, UAE

[4]Department of Mathematics, Anand International College of Engineering, Jaipur, India

[5]International Center for Basic and Applied Sciences, Jaipur, India

[6]Department of Software of Information Technologies, Tashkent University of information technologies named after Muhammad Al-Khwarizmi, Tashkent, Uzbekistan

[a]sokhibjan.muminov@mamunedu.uz, [b]praveen.agarwal@anandice.ac.in, [c]matematichka@inbox.ru

Corresponding author: S. Muminov, sokhibjan.muminov@mamunedu.uz

PACS 35A01, 35B44, 35K57, 35K65

ABSTRACT The work is devoted to developing a self-similar solution for a system of nonlinear differential equations that describe diffusion processes. Various techniques are used to examine the capacity for generating self-similar solutions that can estimate and predict system behavior under diffusion conditions. The focus is on developing and applying numerical algorithms, as well as using theoretical tools such as asymptotic analysis, to obtain more accurate and reliable results. The study's results can be applied to various scientific and technical fields, such as physics, chemistry, biology, and engineering, where diffusion processes play an essential role. The development of self-similar solutions for systems of nonlinear differential equations related to diffusion opens novel opportunities for modeling and analyzing complex systems and enhancing diffusion processes in various fields.

KEYWORDS nonlinear system, diffusion, self-similar solution, flow, model, algorithm, parabolic differential equation.

FOR CITATION Muminov S., Agarwal P., Muhamediyeva D. Qualitative properties of the mathematical model of nonlinear cross-diffusion processes. *Nanosystems: Phys. Chem. Math.*, 2024, **15** (6), 742–748.

1. Introduction

The scientific community is actively studying self-similar solutions of nonlinear differential equations related to mutual diffusion. Interdiffusion refers to the movement of substances within a medium where components interact through diffusion flow. Analytical solutions to such systems are complicated due to nonlinearities. Therefore, self-similar methods are an effective tool for constructing approximate solutions and analysis of such systems.

Various methods for simulating systems of nonlinear differential equations that describe mutual diffusion are explored. The article is focused on the problem of finding weak solutions and analyzing the asymptotic properties of these equations. Particular attention is given to the study of regular, unbounded, and finite solutions to gain a more complete understanding of the system's behavior. Such models can be applied across various scientific and technical fields where mutual diffusion is essential. Understanding and modeling interdiffusion are of practical importance in biology, ecology, chemistry, and physics. The complexity of the analytical solution of systems of nonlinear differential equations describing mutual diffusion requires the development of effective numerical methods. The self-similar methods are considered as a practical approach for obtaining approximate solutions with complex interactions between components and diffusion conditions. This method makes it possible to apply numerical methods to solve the current type of nonlinear differential equations and provides the ability to simulate diffusion processes. Applying self-similar solutions in the prediction and analysis of mutual diffusion systems is extensive. They can be used to optimize processes, manage resources, prevent the spread of harmful substances and diseases, and understand fundamental principles.

Exploring the category of nonlinear differential equations and systems, particularly those that include the desired function and its derivative in power form, is intriguing in the study of real physical processes. These nonlinearities are commonly observed in reaction-diffusion, interdiffusion, and biological population problems [1–3].

Finding an analytical solution to nonlinear boundary value problems is challenging. Determining the new properties of the solution requires a significant energy and time. Their solving faces with several difficulties. The works of A.A.

Samarsky, V.A. Galaktionov, A.S. Kalashnikov, L.K. Martinson, R. Kershner, G.I. Barenblatt, B.F. Knerr, Chen Xingfu, Yu.W. Qi, J.S. Guo, I. Kombe, T. Kusano, T. Tanigawa, S.N. Dimov, M.M. Aripov, and A.T. Khaidarov are devoted to the study of the properties of solving the above problems. Sh.A. Sadullaeva et al. have shown the significance of self-similar solutions corresponding to specific parameter values [4–18], The critical curves of a degenerate parabolic equation were studied in the work of M.Aripov and J.Raimbekov [19].

Cross-diffusion processes are significant in many areas of nanoscience, and a deeper study of these processes contributes to the development of advanced technologies. For example, in nanoelectronics, the interdiffusion of atoms and particles in semiconductors significantly influences electronic devices' performance characteristics and reliability. Diffusion processes in the field of nanomaterials play a decisive role in the formation of nanostructures of materials and the optimization of their mechanical, optical, and electrical properties. In nano-optics and plasmonics, the propagation of light and collective oscillations of electrons in nanostructured materials depends on the diffusion processes, which expands the possibilities of light control and redirection. In nanomedicine and biomaterials, cross-diffusion in drug delivery systems ensures efficient distribution of drugs within cells and tissues, increasing treatment effectiveness. In nanocatalysis, the interdiffusion of reactants on the catalyst surface is a critical factor in controlling the rate and selectivity of chemical reactions. Also, diffusion processes in nanocomputer technologies affect the ability of nano-sized memory elements to store and process information. Thus, the study of mutual diffusion processes contributes to a deeper understanding of the physicochemical behavior of substances at the nanoscale and is also of fundamental importance in developing new materials and devices.

In article [20], the formation processes of Liesegang structures are studied using the Keller-Rubinow model. Liesegang structures are periodic layered structures formed by chemical reactions from diffusion and precipitation. The article examines a mathematical analysis of these processes using the Keller-Rubinow model, and the modeling results clearly show the main features of the formation of Liesegang structures. The research results are essential in creating nanoscale structures and understanding their formation mechanisms.

The article [21] examines the characteristics of the oriented ring of neurons based on the FitzHugh-Nagumo model. The FitzHugh-Nagumo model is widely used for mathematical modeling of neuronal activity dynamics and represents the transmission processes of nerve impulses. This study analyzes an oriented neuron loop's steady states and dynamic behavior. The article shows the interactions between neurons in the ring, the conditions of signal propagation, and the effect of these processes on the functional activity of neural networks. The research findings are important for understanding neurobiological systems and their modeling in artificial intelligence systems.

These articles [20, 21] cover the mathematical and physical approaches needed for modeling and analysis in nanotechnology and neurobiology and act as a bridge between theoretical research and experimental practice. This work is devoted to the study of constructing a self-similar solution to a system of nonlinear differential equations representing mutual diffusion problems.

2. Methods and models

We consider the following problem in a specified spatial region $\Omega = \{(x,t) : x \in \mathbb{R},\ t \in (0;T)\}$

$$\begin{cases} \dfrac{\partial u}{\partial t} = \dfrac{\partial}{\partial x}\left(u^{\sigma_1}\dfrac{\partial u}{\partial x}\right) - v^{\beta_1}\left|\dfrac{\partial u}{\partial x}\right|^{P_1}, \\ \dfrac{\partial v}{\partial t} = \dfrac{\partial}{\partial x}\left(v^{\sigma_2}\dfrac{\partial v}{\partial x}\right) - u^{\beta_2}\left|\dfrac{\partial v}{\partial x}\right|^{P_2}, \end{cases} \tag{1}$$

with initial conditions

$$u\left(x,0\right) = u_0\left(x\right),\ v\left(x,0\right) = v_0\left(x\right),\ x \in \mathbb{R}, \tag{2}$$

and boundary conditions

$$u(0,t) = u_1(t),\ v(0,t) = v_1(t),\ 0 \le t \le T, \tag{3a}$$

$$u(1,t) = u_2(t),\ v(1,t) = v_2(t),\ 0 \leqslant t \leqslant T, \tag{3b}$$

where σ_1, σ_2, β_1, β_2, p_1, p_2 are real numbers which specified surrounding and front parameters.

The equations of the system characterize the migration of salt or dust taking into account humidity and change in humidity taking into account the migration of salt or dust, respectively.

We represent the solution of the system (1) in the following form

$$u\left(t,x\right) = \left(T+t\right)^{n_1}\left(t\right) w_1\left(\tau,x\right), \tag{4}$$

$$v\left(t,x\right) = \left(T+t\right)^{n_2}\left(t\right) w_2\left(\tau,x\right), \tag{5}$$

where $\tau(t)$ is function of time. Using equations (4),(5) we find n_1 and n_2:

$$\begin{aligned} n_1 &= \frac{(p_1-2)(2p_2-p_2\sigma_2-2)-2\beta_1(p_2-2)}{(2p_1-p_1\sigma_1-2)(2p_2-p_2\sigma_2-2)-4\beta_1\beta_2}, \\ n_2 &= \frac{(p_2-2)(2p_1-p_1\sigma_1-2)-2\beta_2(p_1-2)}{(2p_1-p_1\sigma_1-2)(2p_2-p_2\sigma_2-2)-4\beta_1\beta_2}. \end{aligned} \tag{6}$$

We will assume that the functions $w_1(x,\tau)$ and $w_2(x,\tau)$ are representable in the form $w_1(x,\tau)=f_1(\xi)$, $w_2(x,\tau)=f_2(\xi)$, where $\xi=\dfrac{x}{\sqrt{\tau}}$.

Now system (1) can be represented as

$$\begin{cases} -\dfrac{\xi}{2}\dfrac{df_1}{d\xi}=\dfrac{d}{d\xi}({f_1}^{\sigma_1}\dfrac{df_1}{d\xi})-(n_1\sigma_1+1)^{\frac{p_1-2}{2}}\cdot {f_2}^{\beta_1}\left|\dfrac{df_1}{d\xi}\right|^{p_1}-\dfrac{n_1}{n_1\sigma_1+1}\cdot f_1, \\ -\dfrac{\xi}{2}\dfrac{df_2}{d\xi}=\dfrac{d}{d\xi}({f_2}^{\sigma_2}\dfrac{df_2}{d\xi})-(n_2\sigma_2+1)^{\frac{p_2-2}{2}}\cdot {f_1}^{\beta_2}\left|\dfrac{df_2}{d\xi}\right|^{p_2}-\dfrac{n_2}{n_2\sigma_2+1}\cdot f_2. \end{cases} \tag{7}$$

Where the functions f_1 and f_2 are chosen in the form

$$f_1=(a+\xi)^{\gamma_1},\ f_2=(a+\xi)^{\gamma_2}. \tag{8}$$

Then we find that the parameters of system (7) must satisfy the following conditions

$$\begin{cases} \gamma_1(\sigma_1\gamma_1+\gamma_1-1)=(n_1\sigma_1+1)^{\frac{p_1-2}{2}}|\gamma_1|^{p_1}, \\ \gamma_2(\sigma_2\gamma_2+\gamma_2-1)=(n_2\sigma_2+1)^{\frac{p_2-2}{2}}|\gamma_1|^{p_1}, \end{cases} \tag{9}$$

$$(\sigma_i\gamma_i+\gamma_i-1)>0, \quad i=\overline{1,2}$$

Now, let us calculate the values γ_1 and γ_2. We obtain that

$$\gamma_1=\frac{(\delta_2-p_2+1)(2-p_1)+\beta_1(2-p_2)}{(\delta_1-p_1+1)(\delta_2-p_2+1)-\beta_1\beta_2};\quad \gamma_2=\frac{(\delta_1-p_1+1)(2-p_2)+\beta_2(2-p_1)}{(\delta_1-p_1+1)(\delta_2-p_2+1)-\beta_1\beta_2}.$$

The following theorem holds for the upper bound of the solutions obtained.

Theorem. Let

1) $\sigma_1\geq 0;\quad \sigma_2\geq 0;$

2) $a^{\frac{\beta_1}{\sigma_2}+\frac{(1-\sigma_1)p_1-1}{\sigma_1}+\frac{p_1}{2}}\geq\dfrac{(\frac{n_1}{n_1\sigma_1+1}+\frac{1}{2})}{(n_1\sigma_1+1)^{\frac{p_1-1}{2}}}$ and $a^{\frac{\beta_2}{\sigma_1}+\frac{(1-\sigma_2)p_2-1}{\sigma_2}+\frac{p_2}{2}}\geq\dfrac{(\frac{n_2}{n_2\sigma_2+1}+\frac{1}{2})}{(n_2\sigma_2+1)^{\frac{p_2-1}{2}}}$;

3) $u(t,0)\leq u_+(t,0),\ v(t,0)\leq v_+(t,0),\ x\in\mathbb{R}$.

Then there is a global solution to problem (1)-(3) and the following conditions are valid:

$$u(x,t)\leq u_+(x,t)=(T+t)^{n_1}f_1(\xi),\ v(x,t)\leq v_+(x,t)=(T+t)^{n_2}f_2(\xi). \tag{10}$$

Proof: To prove the theorem, we use the comparison [1]. We choose the following function as a comparison function

$$u(x,t)=(T+t)^{n_1}\cdot f_1(\xi),\ v(x,t)=(T+t)^{n_2}\cdot f_2(\xi). \tag{11}$$

Substituting (11) into system (1), we obtain the following system

$$\begin{cases} \dfrac{\xi}{2}\dfrac{df_1}{d\xi}+\dfrac{d}{d\xi}({f_1}^{\sigma_1}\dfrac{df_1}{d\xi})-(n_1\sigma_1+1)^{\frac{p_1-1}{2}}\cdot {f_2}^{\beta_1}\left|\dfrac{df_1}{d\xi}\right|^{p_1}-\dfrac{n_1}{n_1\sigma_1+1}\cdot f_1\leqslant 0, \\ \dfrac{\xi}{2}\dfrac{df_2}{d\xi}+\dfrac{d}{d\xi}({f_2}^{\sigma_2}\dfrac{df_2}{d\xi})-(n_2\sigma_2+1)^{\frac{p_2-1}{2}}\cdot {f_1}^{\beta_2}\left|\dfrac{df_2}{d\xi}\right|^{p_2}-\dfrac{n_2}{n_2\sigma_2+1}\cdot f_2\leqslant 0, \end{cases} \tag{12}$$

$$\begin{cases} \dfrac{d}{d\xi}({f_1}^{\sigma_1}\dfrac{df_1}{d\xi})+\dfrac{\xi}{2}\dfrac{df_1}{d\xi}+\dfrac{f_1}{2}-\dfrac{f_1}{2}-(n_1\sigma_1+1)^{\frac{p_1-1}{2}}\cdot {f_2}^{\beta_1}\left|\dfrac{df_1}{d\xi}\right|^{p_1}-\dfrac{n_1}{n_1\sigma_1+1}\cdot f_1\leqslant 0, \\ \dfrac{d}{d\xi}({f_2}^{\sigma_2}\dfrac{df_2}{d\xi})+\dfrac{\xi}{2}\dfrac{df_2}{d\xi}+\dfrac{f_2}{2}-\dfrac{f_2}{2}-(n_2\sigma_2+1)^{\frac{p_2-1}{2}}\cdot {f_1}^{\beta_2}\left|\dfrac{df_2}{d\xi}\right|^{p_2}-\dfrac{n_2}{n_2\sigma_2+1}\cdot f_2\leqslant 0, \end{cases}$$

$$\frac{d}{d\xi}({f_1}^{\sigma_1}\frac{df_1}{d\xi})=-\frac{d(\xi f_1)}{2d\xi},\quad \frac{d}{d\xi}({f_2}^{\sigma_2}\frac{df_2}{d\xi})=-\frac{d(\xi f_2)}{2d\xi}. \tag{13}$$

If equality (12) holds, then relation (13) holds.

If the condition $\sigma_1\geq 0;\quad \sigma_2\geq 0;$ in the theorem holds, then, we will have the following system

$$\begin{cases} -(n_1\sigma_1+1)^{\frac{p_1-1}{2}}\cdot {f_2}^{\beta_1}\left|\dfrac{df_1}{d\xi}\right|^{p_1}-(\dfrac{n_1}{n_1\sigma_1+1}+\dfrac{1}{2})f_1\leq 0, \\ -(n_2\sigma_2+1)^{\frac{p_2-1}{2}}\cdot {f_1}^{\beta_2}\left|\dfrac{df_2}{d\xi}\right|^{p_2}-(\dfrac{n_2}{n_2\sigma_2+1}+\dfrac{1}{2})f_2\leq 0, \end{cases}$$

$$\begin{cases} -(n_1\sigma_1+1)^{\frac{p_1-1}{2}}\cdot(a-\frac{\sigma_2}{4}\xi^2)^{\frac{\beta_1}{\sigma_2}}\left|(a-\frac{\sigma_1}{4}\xi^2)^{\frac{1-\sigma_1}{\sigma_1}}\frac{\xi}{2}\right|^{p_1}-(a-\frac{\sigma_1}{4}\xi^2)^{\frac{1}{\sigma_1}}(\frac{n_1}{n_1\sigma_1+1}+\frac{1}{2})\leqslant 0, \\ -(n_2\sigma_2+1)^{\frac{p_2-1}{2}}\cdot(a-\frac{\sigma_1}{4}\xi^2)^{\frac{\beta_2}{\sigma_1}}\left|(a-\frac{\sigma_1}{4}\xi^2)^{\frac{1-\sigma_2}{\sigma_2}}\frac{\xi}{2}\right|^{p_2}-(a-\frac{\sigma_2}{4}\xi^2)^{\frac{1}{\sigma_2}}(\frac{n_2}{n_2\sigma_2+1}+\frac{1}{2})\leqslant 0. \end{cases}$$

Here $\xi=2\sqrt{\frac{a}{\sigma_1}}$ evaluate and expand the first expression

$$-(n_1\sigma_1+1)^{\frac{p_1-1}{2}}a^{\frac{\beta_1}{\sigma_2}}a^{\frac{(1-\sigma_1)p_1}{\sigma_1}}\left(\sqrt{\frac{a}{\sigma_1}}\right)^{p_1}-a^{\frac{1}{\sigma_1}}(\frac{n_1}{n_1\sigma_1+1}+\frac{1}{2})\leqslant 0,$$

$$-(n_2\sigma_2+1)^{\frac{p_2-1}{2}}a^{\frac{\beta_2}{\sigma_1}}a^{\frac{(1-\sigma_2)p_2}{\sigma_2}}\left(\sqrt{\frac{a}{\sigma_2}}\right)^{p_2}-a^{\frac{1}{\sigma_2}}(\frac{n_2}{n_2\sigma_2+1}+\frac{1}{2})\leqslant 0,$$

$$\frac{-(n_1\sigma_1+1)^{\frac{p_1-1}{2}}a^{\frac{\beta_1}{\sigma_2}+\frac{(1-\sigma_1)p_1-1}{\sigma_1}}a^{\frac{p_1}{2}}}{\sigma_1{}^{\frac{p_1}{2}}}\leqslant(\frac{n_1}{n_1\sigma_1+1}+\frac{1}{2}),$$

$$\frac{-(n_2\sigma_2+1)^{\frac{p_2-1}{2}}a^{\frac{\beta_2}{\sigma_1}+\frac{(1-\sigma_2)p_2-1}{\sigma_2}}a^{\frac{p_2}{2}}}{\sigma_1{}^{\frac{p_1}{2}}}\leqslant(\frac{n_2}{n_2\sigma_2+1}+\frac{1}{2}),$$

$$a^{\frac{\beta_1}{\sigma_2}+\frac{(1-\sigma_1)p_1-1}{\sigma_1}+\frac{p_1}{2}}\geqslant\frac{(\frac{n_1}{n_1\sigma_1+1}+\frac{1}{2})}{(n_1\sigma_1+1)^{\frac{p_1-1}{2}}}.$$

As for the second inequality of system (12), if the corresponding operations are carried out

$$a^{\frac{\beta_2}{\sigma_1}+\frac{(1-\sigma_2)p_2-1}{\sigma_2}+\frac{p_2}{2}}\geqslant\frac{(\frac{n_2}{n_2\sigma_2+1}+\frac{1}{2})}{(n_2\sigma_2+1)^{\frac{p_2-1}{2}}},$$

it follows that condition 2 in the theorem is valid.

Therefore, according to the hypotheses of the theorem and the principle of comparison, the following relations are valid: $u(t,x)\le u_+(t,x)$; $v(t,x)\le v_+(t,x)$. **The theorem is proven.**

Thus, it was found that the self-similar solution for system (1) can be represented in the form:

$$\begin{aligned} u(x,t)&=(T+t)^{n_1}\cdot f_1(\xi)=(T+t)^{n_1}\cdot(a-\xi)^{\gamma_1}, \\ v(x,t)&=(T+t)^{n_2}\cdot f_2(\xi)=(T+t)^{n_2}\cdot(a-\xi)^{\gamma_2}. \end{aligned} \tag{14}$$

3. Calculation results

Using self-similar solutions (14) of system (1) - (3), the iteration or sweep method, numerical solutions were found, the graphs of which are given below. (The graphs presented have a horizontal axis representing the values of the variable x and a vertical axis intended to represent the values of the functions u and v.)

Graphs of solutions to the mutual diffusion problem: The results of studies of the processes of mutual diffusion for parameters $\sigma_1,\ \sigma_2,\ \beta_1,\ \beta_2,\ p_1,\ p_2,\ a$ are described and graphs are presented for analysing changes in moisture (u) and the content of salt and dust particles (v) under different conditions.

In Fig. 1, the results for the following values of the parameters are shown: $\sigma_1=4,\ \sigma_2=5,\ \beta_1=2.5,\ \beta_2=2.1,\ p_1=2.25,\ p_2=3.8,\ a=0.5$

In Fig. 2, the parameters indicated are as follows: $\sigma_1=4,\ \sigma_2=5,\ \beta_1=2.2,\ \beta_2=2.1,\ p_1=2.87,\ p_2=3.76,\ a=3.5$

The graphs of v-salt-dust migration for cases in steps are given in different colors.

Under the influence of certain parameters, the movement of moisture and salt (or dust) occurs “almost evenly” over a “short time interval”. This suggests that the diffusion under consideration is likely rapid. Rapid diffusion is characterized by concentration gradients becoming uniform over short intervals, which corresponds to the description of significant acceleration of diffusion processes and minimal concentration variations over time.

In Fig. 3, the diffusion process for the followimg parameter values: $\sigma_1=4,\ \sigma_2=5,\ \beta_1=1.7,\ \beta_2=2.1,\ p_1=3.1,\ p_2=3.2,\ a=0.5$, is shown, where changes in humidity occur almost identically to the migration of salt-dust particles.

In Fig. 3, the changes in moisture and salt-dust content are shown depending on environmental parameters. It can be seen that the initial phases of the diffusion processes differ, but later the changes become almost uniform.

In Fig. 4, the diffusion process for the parameter values is presented: $\sigma_1=4,\ \sigma_2=7,\ \beta_1=2.91,\ \beta_2=2.22,\ p_1=3.8,\ p_2=2.5,\ a=2.5$.

In Figs. 3 and 4, the results for various values of $\sigma_2,\ \beta_2$ are shown. It is evident that with an increase in σ_2 , the process accelerates, and the concentration gradients equalize more quickly.

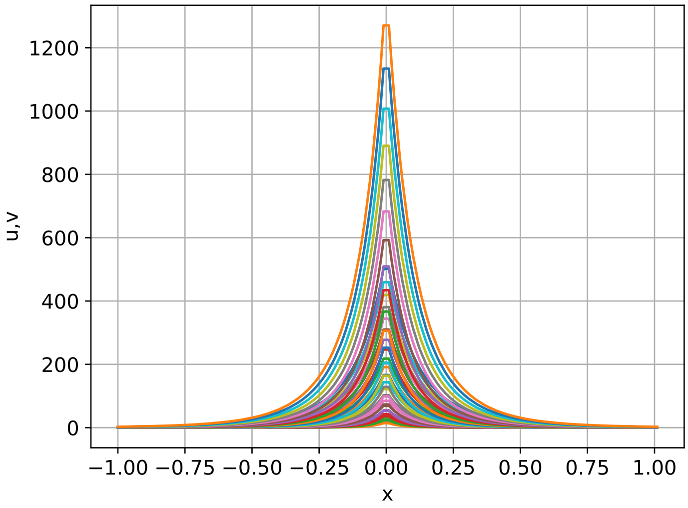

FIG. 1. Solutions of the system of equations representing the mutual diffusion process

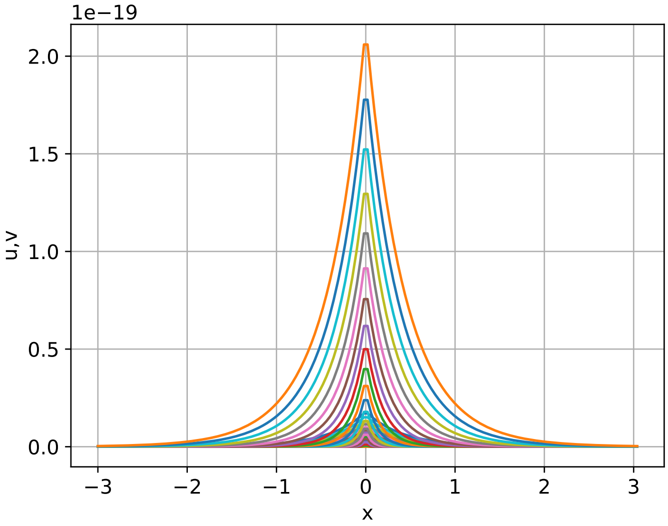

FIG. 2. Graphical representation of moisture and salt-dust diffusion process

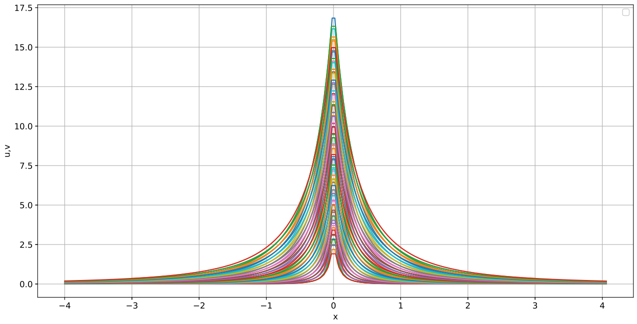

FIG. 3. Solutions of the diffusion problem corresponding to the given values of the parameters

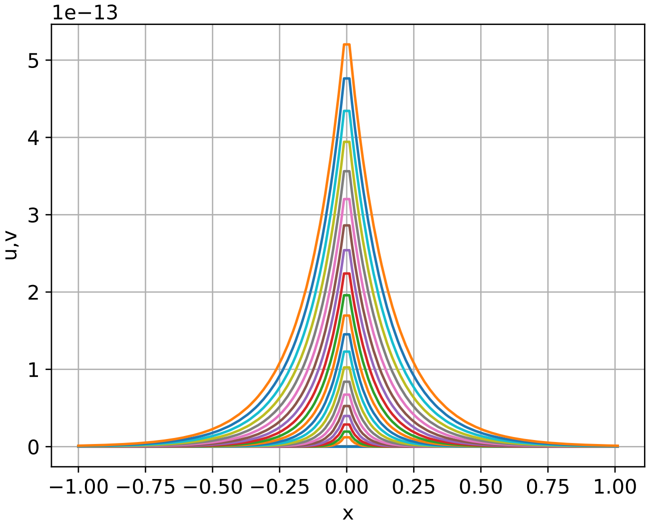

FIG. 4. Solutions of the diffusion problem corresponding to the given values of the parameters

Changes in parameters lead to an acceleration or deceleration of the mutual diffusion processes. At certain values, the concentration of moisture and salt-dust particles equalizes more quickly, reducing fluctuations. Changes in moisture (u) and salt-dust content (v) indicate that, depending on environmental parameter values, in some cases, changes in moisture occur almost identically to the migration of salt-dust particles. In system (1), representing cross-diffusion processes, under conditions of rapid diffusion, the movement of moisture and salt (or dust) changes almost uniformly over a short time interval. With the proper selection of parameter values, these changes asymptotically approach an infinitely small value. This means that due to significant acceleration of diffusion processes, the concentration gradients of moisture and salt become almost uniform throughout the system, leading to minimal concentration changes over time.

The figures show that, depending on the medium and front parameter values, the diffusion process begins differently and then changes almost uniformly.

u-moisture change, V-salt-dust content change, in which depending on the change of parameter values, in some cases it can be seen that the moisture changes almost identically with the salt-dust migration.

In the system (1) representing cross-diffusion processes, under conditions of rapid diffusion, the movement of moisture and salt (or dust) changes almost uniformly over a short time interval. As the parameter values are chosen appropriately, these changes asymptotically approach an infinitesimally small amount. This implies that due to the significant acceleration of the diffusion processes, the concentration gradients of moisture and salt become nearly uniform across the entire system, leading to minimal variations in concentration over time.

4. Conclusion

The method for developing a self-similar solution for a system of nonlinear differential equations that explain mutual diffusion processes in a one-dimensional spatial approximation is investigated. The results have clear practical implications when considering the Cauchy problem for equations with variable coefficients. An approach to approximation of the solution of a second-order nonlinear problem is described and supported. Based on the impacts of the finiteness of the disturbances' propagation speed and spatial localization, asymptotes of regular, finite, and unbounded solutions are derived. The observed results allow us to build an iterative procedure for the numerical solution of the mutual diffusion issue to acquire an initial approximation. These mathematical models can be used to solve many practical problems, including biological population issues, epidemic spread, and numerical modeling of various diffusion processes.

References

[1] Samarsky A.A., Mikhailov A.P. *Mathematical Modeling*, Fizmatlib, Moscow, 2001, 320 p.
[2] Aripov M.M. *Methods of Reference Equations for Solving Nonlinear Boundary Value Problems.*, Fan, Tashkent, 1988, 136 p.
[3] Aripov M.M., Sadullaeva Sh.A. *Computer Modeling of Nonlinear Diffusion Processes.* University, Tashkent, 2020, 656 p.
[4] Aripov M.M., Matyakubov A.S., Imomnazarov B.Kh. The cauchy problem for a nonlinear degenerate parabolic system in non-divergence form. *Mathematical Notes of NEFU*, 2020, **27**(3), P. 27–38.
[5] Matyakubov A.S., Raupov D. On some properties of the blow-up solutions of a nonlinear parabolic system non-divergent form with cross-diffusion. *Lec. Notes in Civil Engineering*, 2022, **180**, P. 289–301.
[6] Aripov M.M., Matyakubov A.S., Xasanov J.O. To the qualitative properties of self-similar solutions of a cross-diffusion parabolic system not in divergence form with a source. *AIP Conf. Proc.*, 2023, **2781**.

[7] Aripov M.M., Matyakubov A.S., Khasanov J.O., Bobokandov M.M. Mathematical modeling of double nonlinear problem of reaction diffusion in not divergent form with a source and variable density. *J. Phys. : Conf. Ser.*, 2021, **2131**(3).

[8] Muhamediyeva D.K. Properties of self similar solutions of reaction-diffusion systems of quasilinear equations. *Int. J. of Mech. and Prod. Eng. Research and Development*, 2018, **36**(8), P. 555–566.

[9] Muhamediyeva D.K. Qualitative properties of wave solutions of the equation of reaction-diffusion of a biological population. Conference proceedings of "2020 International Conference on Information Science and Communications Technologies (ICISCT)", Tashkent, Uzbekistan, 04-06 November 2020.

[10] Muhamediyeva D.K., Nurumova A.Y, Muminov S.Y. Fuzzy evaluation of cotton varieties in the natural climatic. In IOP Conf. Ser.: Earth and Environmental Science, 2022, **1076**, P. 012043.

[11] Muhamediyeva D.K., Madrakhimov A.Kh., Kodirov Z.Z. Construction of a system of differential equations taking into account convective transfer. Proceedings of "Computer applications for management and sustainable development of production and industry (CMSD2022)". Dushanbe, Tajikistan, 21-23 December 2022.

[12] Muhamediyeva D.K., Muminov S.Y., Shaazizova M.E., Hidirova Ch., and Bahromova Yu. Limited different schemes for mutual diffusion problems. *E3S Web of Conf*, 2023, **401**, P. 05057.

[13] Muhamediyeva D.K., Nurumova A.Y, Muminov S.Y. Numerical modeling of cross-diffusion processes. *E3S Web of Conf*, 2023, **401**, P. 05060.

[14] Muhamediyeva D.K., Nurumova A.Y., Muminov S.Y. Cauchy problem and boundary-value problems for multicomponent cross-diffusion systems. Proceedings of "Int. Conf. on Inf. Sci. and Comm. Tech.". Tashkent 2021. 01-05.

[15] Muminov S.Y. Construction of self-similar solutions of the system of nonlinear differential equations of cross-diffusion. Proceedings of "The int. Sci. and Prac. Conf.", China 2023. 57–60.

[16] Rakhmonov Z.R., Alimov A.A. Properties of solutions for a nonlinear diffusion problem with a gradient nonlinearity. *Int. J. App. Math.*, 2023, **36**(3), P. 1–20.

[17] Yang Liu, Yanwei Du, Hong Li, Jichun Li, and Siriguleng He. A two-grid mixed finite element method for a nonlinear fourth-order reaction-diffusion problem with time-fractional derivative. *Comp. and Math. with Appl.*, 2015, **70**(10), P. 2474–2492.

[18] Farina A., Gianni R. Self-similar solutions for the heat equation with a positive non-Lipschitz continuous, semilinear source term. *Nonl. Anal.: Real World Appl.*, 2024, **79**.

[19] Aripov M.M., Raimbekov J.R. The critical curves of a doubly nonlinear parabolic equation in non-divergent form with a source and nonlinear boundary flux. *J. Sib. Fed. Univ. - Math. and Phys.*, 2019, **12**(1), P. 112–124.

[20] Topaev T.N., Popov A.I., Popov I.Yu. On Keller-Rubinow model for Liesegang structure formation. *Nanosystems: physics, chemistry, mathematics*, 2022, **13**(4), P. 365–371.

[21] Fedorov E.G. Properties of an oriented ring of neurons with the Fitzhugh-Nagumo model. *Nanosystems: physics, chemistry, mathematics*, 2021, **12**(5), P. 553–562.

Submitted 7 August 2024; revised 28 October 2024, 12 November 2024; accepted 13 November 2024

Information about the authors:

Sokhibjan Muminov – Mamun university, Bolkhovuz street 2, Khiva 220900, Uzbekistan; Urgench state university, Khamid Alimjan street 14, Urgench 220100, Uzbekistan; ORCID 0000-0003-2471-4836; sokhibjan.muminov@mamunedu.uz

Praveen Agarwal – Nonlinear Dynamics Research Center (NDRC), Ajman University, Ajman, UAE; Department of Mathematics, Anand International College of Engineering, Jaipur 303012, India; International Center for Basic and Applied Sciences, Jaipur-302029, India; ORCID 0000-0001-7556-8942; praveen.agarwal@anandice.ac.in

Dildora Muhamediyeva – Department of Software of Information Technologies, Tashkent University of information technologies named after Muhammad Al-Khwarizmi, Amir Temur Avenue 108, Tashkent 100084, Uzbekistan; ORCID 0000-0003-2154-4157; matematichka@inbox.ru

Conflict of interest: the authors declare no conflict of interest.

NANOSYSTEMS:
PHYSICS, CHEMISTRY, MATHEMATICS

Original article

Kuo-Shou Chiu, et al. *Nanosystems: Phys. Chem. Math.*, 2024, **15** (6), 749–754.
http://nanojournal.ifmo.ru
DOI 10.17586/2220-8054-2024-15-6-749-754

Some conditions for the existence of 4-periodic solutions in non-homogeneous differential equations involving piecewise alternately advanced and retarded arguments

Kuo-Shou Chiu[1,a], Fernando Cordova-Lepe[2]

[1]Departamento de Matemática, Facultad de Ciencias Básicas, Universidad Metropolitana de Ciencias de la Educación, José Pedro Alessandri 774, Santiago, Chile

[2]Departamento de Matemática, Física y Estadística, Universidad Católica del Maule, Talca, Chile

[a]kschiu@umce.cl

Corresponding author: Kuo-Shou Chiu, kschiu@umce.cl

ABSTRACT The manuscript introduces a method to characterize 4-periodic solutions in first-order non- homogeneous differential equations involving piecewise alternately advanced and retarded argument. It systematically delineates the prerequisites for these solutions to exist and furnishes precise methodologies for their determination. Additionally, the paper includes the illustrative example, including scenarios with infinitely many solutions, to demonstrate the effectiveness of the proposed approach.

KEYWORDS Piecewise alternately advanced and retarded argument, Periodic solution.

ACKNOWLEDGEMENTS This research was in part supported by ANID FONDECYT N°1231256 and DIUMCE 09-2023-SAC.

FOR CITATION Kuo-Shou Chiu, Fernando Cordova-Lepe Some conditions for the existence of 4-periodic solutions in non-homogeneous differential equations involving piecewise alternately advanced and retarded arguments. *Nanosystems: Phys. Chem. Math.*, 2024, **15** (6), 749–754.

1. Introduction

A differential equation with piecewise alternately advanced and retarded argument (DEPCA) is represented by the following equation:

$$x'(t) = f\left(t, x(t), x\left(2\left[\frac{t+1}{2}\right]\right)\right), \tag{1.1}$$

where $[\cdot]$ denotes the greatest integer function, and f is continuous on $\mathbb{R} \times \mathbb{R} \times \mathbb{R}$. DEPCAs are hybrid equations that amalgamate features of discrete equations and continuous systems. They bear significant relevance in applications pertaining to biomedical dynamics and physical phenomena (refer to [1, 2] and the associated references [3–7]).

Recent publications [8–17] have investigated particular formulations of the DEPCA. Authors in [18–22] have streamlined the problem of n-periodic solvability to a set of n linear equations. Leveraging established properties of linear systems in algebra, they systematically delineated all conditions necessary for the existence of n-periodic solutions and furnished explicit formulas for solving these equations.

In 2024, M.I. Muminov and T.A. Radjabov [22] examined the existence conditions for 2-periodic solutions of first order differential equations with piecewise constant delay:

$$T'(t) = a(t)T(t) + b(t)T([t]) + f(t).$$

The authors developed a method for identifying 2-periodic solutions, thoroughly outlined the existence conditions, and presented explicit formulas for these solutions.

To the best of our knowledge, only one study has addressed the existence of infinitely many periodic solutions related to the DEPCA [22]. However, none of the available works have provided clear criteria for determining the existence of such solutions in differential equations with piecewise alternately advanced and retarded arguments.

In this paper, we examine a non-homogeneous differential equation involving piecewise alternately advanced and retarded arguments, given by

$$y'(t) = a(t)y(t) + b(t)y\left(2\left[\frac{t+1}{2}\right]\right) + g(t), \quad t \geq 1, \tag{1.2}$$

where the functions $a(t)$, $b(t)$, and $g(t)$ are continuous and nonzero on $[1, \infty)$. The general case of this problem was previously examined in [23, 24], where the authors established conditions for solution existence and demonstrated a Gronwall's type integral inequality as an application. This note is dedicated to elucidating the conditions necessary for the existence of 4-periodic solutions to this initial value problem. We present an example that illustrates an equation with an infinite number of 4-periodic solutions, thus offering additional insights to complement the uniqueness assertions made in prior studies focusing on homogeneous cases.

2. Alternately advanced and retarded differential equation

Let us define the solution for DEPCA (1.2). A function y is considered a solution of DEPCA (1.2) on $[1,\infty)$ if the following conditions are met: i) y is continuous on $[1,\infty)$. ii) The derivative $y'(t)$ exists at each point $t\in[1,\infty)$, except possibly at points $t=2n-1$ for $n\in\mathbb{N}$, where one-sided derivatives exist. iii) The DEPCA (1.2) is satisfied by y on each interval $(2n-1,2n+1)$ for $n\in\mathbb{N}$, and it holds for the right-hand derivative at the points $2n-1$ for $n\in\mathbb{N}$.

To determine the solution of DEPCA (1.2), following the approach outlined in [25], we integrate DEPCA (1.2) and obtain the following result:

$$\begin{aligned} y(t) &= e^{\int_2^t a(s)ds} y(2) + \int_2^t b(s) y\left(2\left[\frac{s+1}{2}\right]\right) e^{\int_s^t a(r)dr} ds \\ &+ \int_2^t g(s) e^{\int_s^t a(r)dr} ds, \quad t\in[1,3). \end{aligned}$$

We define

$$\lambda(t,s) := e^{\int_s^t a(n)dn} + \int_s^t e^{\int_u^t a(n)dn} b(u)du,$$

$$\Psi(t,s) = \lambda\left(t, 2\left[\frac{t+1}{2}\right]\right) \prod_{j=\left[\frac{s+1}{2}\right]+1}^{\left[\frac{t+1}{2}\right]} \frac{\lambda(2j-1,2j-2)}{\lambda(2j-1,2j)}, \quad t\geq s,$$

$$G(t,s) = \int_s^t e^{\int_u^t a(\kappa)d\kappa} g(u)du,$$

where $t,s\in[1,\infty)$, $\lambda(2j-1,2j)\neq 0$, $j\in\mathbb{N}$.

Theorem 2.1. *If $\lambda(2j-1,2j)\neq 0$ for $j\in\mathbb{N}$, then $y(t)$ represents the unique solution to DEPCA (1.2) for $t\geq 1$ if and only if $y(t)$ is expressed as*

$$\begin{aligned} y(t) &= \Psi(t,1)y(1) + \sum_{k=1}^{[(t+1)/2]} \int_{2k-1}^{2k} \Psi(t,2k-1) G(2k-1,s)ds \\ &+ \sum_{k=1}^{[(t+1)/2]-1} \int_{2k}^{2k+1} \Psi(t,2k+1) G(2k+1,s)ds \qquad (2.1) \\ &+ G(t, 2[(t+1)/2]). \end{aligned}$$

The demonstration of the theorem closely resembles the proof provided for Theorem 1 in [25] and Theorem 2.1 in [23].

3. 4-periodic solutions

In this section, we present a methodology for identifying 4-periodic solutions of DEPCA (1.2) in scenarios where $a(\cdot)$, $b(\cdot)$, and $g(\cdot)$ are continuous functions defined on the interval $[1,\infty)$ and demonstrate a pattern of 4-periodic behavior.

Integrating DEPCA (1.2), we obtain:

$$y(t) = \lambda(t,2n)y(2n) + G(t,2n), \quad 2n-1\leq t<2n+1,$$

where $G(t,2n) = \int_{2n}^t g(s) e^{\int_s^t a(r)dr} ds$ and $n\in\mathbb{N}$. Let $y(t)$ be 4-periodic on $[1,\infty)$. The function $y(t)$ on $[1,5)$ can be represented as:

$$y(t) = \begin{cases} \dfrac{\lambda(t,2)}{\lambda(1,2)}(y(1)-G(1,2)) + G(t,2), & t\in[1,3), \\ \dfrac{\lambda(t,4)}{\lambda(3,4)}(y(3)-G(3,4)) + G(t,4), & t\in[3,5). \end{cases} \qquad (3.1)$$

This indicates that the expression on the right-hand side of (3.1) is solely dependent on the unknowns $y_1 = y(1)$ and $y_3 = y(3)$. Utilizing the continuity of $y(\cdot)$, we define y_1 and y_3 as $y(3) = \lim\limits_{t\to 3^-} y(t)$ for $t \in [1,3)$ and $y_5 = y(5) = \lim\limits_{t\to 5^-} y(t)$ for $t \in [3,5)$. Given the continuity and periodicity of $y(\cdot)$, it follows that $y(1) = y(5)$. To determine $y_1 = y_5$ from (3.1), we obtain the system of equations:

$$\begin{aligned} \frac{\lambda(3,2)}{\lambda(1,2)} y(1) - y(3) &= \frac{\lambda(3,2)}{\lambda(1,2)} G(1,2) - G(3,2), \\ y(1) - \frac{\lambda(5,4)}{\lambda(3,4)} y(3) &= -\frac{\lambda(5,4)}{\lambda(3,4)} G(3,4) + G(5,4). \end{aligned} \tag{3.2}$$

Let Δ denote the determinant of the matrix $\mathcal{M}$, where

$$\mathcal{M} = \begin{pmatrix} \dfrac{\lambda(3,2)}{\lambda(1,2)} & -1 \\ 1 & -\dfrac{\lambda(5,4)}{\lambda(3,4)} \end{pmatrix}.$$

We then obtain the following theorem for the existence of 4-periodic solutions to the DEPCA (1.2).

Theorem 3.1. *Let $a(\cdot)$, $b(\cdot)$, and $g(\cdot)$ be 4-periodic continuous functions.*

(a) *If $\Delta \neq 0$, then DEPCA* (1.2) *possesses a unique 4-periodic solution presented in* (3.1)*, where (y_1, y_3) denotes the exclusive solution of the system* (3.2)*.*

(b) *If $\Delta = 0$ and $G(1,2) = G(3,2) = G(3,4) = G(5,4) = 0$, then DEPCA* (1.2) *possesses an infinite number of 4-periodic solutions as detailed below:*

$$y(t) = \begin{cases} \alpha \dfrac{\lambda(t,2)}{\lambda(1,2)} \left(y(1) - G(1,2)\right) + G(t,2), & t \in [1,3), \\ \alpha \dfrac{\lambda(t,4)}{\lambda(3,4)} \left(y(3) - G(3,4)\right) + G(t,4), & t \in [3,5). \end{cases}$$

Here, (y_1, y_3) denotes an eigenvector of $\mathcal{M}$ associated with the eigenvalue 0, while α represents a real number.

(c) *If $\Delta = 0$ and the rank $\mathcal{M}$ is less than the rank of $(\mathcal{M}|b)$, where*

$$b = \left(\frac{\lambda(3,2)}{\lambda(1,2)} G(1,2) - G(3,2)\ ,\ -\frac{\lambda(5,4)}{\lambda(3,4)} G(3,4) + G(5,4) \right)^T,$$

then the DEPCA (1.2) *does not admit a 4-periodic solution.*

Proof. (a) Suppose $y(t)$ represents a 4-periodic solution to DEPCA (1.2). This solution can be described using (3.1), where (y_1, y_3) is the solution of (3.2). The solvability of the linear system (3.2) depends on the condition $\Delta \neq 0$. Therefore, it must hold that $\Delta \neq 0$. Conversely, if $\Delta \neq 0$, DEPCA (3.2) admits a unique solution (y_1, y_3). It can be shown that the function $y(\cdot)$, expressed as in (3.1), constitutes the periodic solution to DEPCA (1.2).

(b) The values of G at points $(1,2)$, $(3,2)$, $(3,4)$, and $(5,4)$ are all zero. Consequently, Equation (3.2) simplifies to a homogeneous form. A non-trivial solution to this equation exists if and only if Δ equals zero. The pair of non-zero solutions (y_1, y_3) represents an eigenvector of $\mathcal{M}$ associated with the eigenvalue 0. Thus, $(\alpha y_1, \alpha y_3)$ constitutes a non-trivial solution to Equation (3.2), where α denotes any non-zero scalar. Consequently, the 4-periodic function

$$y(t) = \begin{cases} \alpha \dfrac{\lambda(t,2)}{\lambda(1,2)} \left(y(1) - G(1,2)\right) + G(t,2), & t \in [1,3), \\ \alpha \dfrac{\lambda(t,4)}{\lambda(3,4)} \left(y(3) - G(3,4)\right) + G(t,4), & t \in [3,5), \end{cases}$$

satisfies DEPCA (1.2), where α can take any value.

(c) If $\Delta = 0$ and the rank $\mathcal{M}$ is less than the rank of $(\mathcal{M} \mid b)$, where

$$b = \left(\frac{\lambda(3,2)}{\lambda(1,2)} G(1,2) - G(3,2)\ ,\ -\frac{\lambda(5,4)}{\lambda(3,4)} G(3,4) + G(5,4) \right)^T,$$

then Eq. (3.2) has no solution. Consequently, DEPCA (1.2) does not possess a 4-periodic solution. This concludes the proof.

□

4. Illustrative example

In this section, we present a relevant example to illustrate the practical applicability of our theory. We examine the following scalar equations with piecewise alternately advanced and retarded argument.

$$y'(t) = b(t)y\left(2\left[\frac{t+1}{2}\right]\right) + \sin(2\pi t) + \cos(2\pi t), \quad t \geq 1, \tag{4.1}$$

where

$$b(t) = \begin{cases} b_1(t), & t \in [4k+1, 4k+2)\,, \\ b_2(t), & t \in [4k+2, 4k+3)\,, \\ -\cos\left(\frac{\pi}{2}t\right) + \dfrac{\pi^2 - 4}{\pi^2 - 2\pi}, & t \in [4k+3, 4k+4)\,, \\ \dfrac{2-3\pi}{2}\cos\left(\frac{\pi}{2}t\right) + 1 - \dfrac{2}{\pi}, & t \in [4k+4, 4k+5)\,, \end{cases}$$

where $b_1(t) = \dfrac{2\pi^4 + 8\pi^3 - 48\pi^2 + 32\pi + 32}{-2\pi^4 + 16\pi^3 - 40\pi^2 + 32\pi}\sin\left(\dfrac{\pi}{2}t\right) + \dfrac{4\pi^4 - 12\pi^3 + 24\pi^2 - 80\pi + 96}{2\pi^4 - 16\pi^3 + 40\pi^2 - 32\pi}$,
$b_2(t) = \dfrac{\pi^4 - 12\pi^3 + 16\pi^2 + 16\pi - 16}{2\pi^3 - 12\pi^2 + 16\pi}\cos\left(\dfrac{\pi}{2}t\right) + \dfrac{\pi^2 - 4}{\pi^2 - 2\pi}$ and $k \in \mathbb{N} \cup \{0\}$.
DEPCA (4.1) is a specific instance of DEPCA (1.2) with $a = 0$ and $g(t) = \sin(2\pi t) + \cos(2\pi t)$. It is straightforward to verify that $G(1,2) = G(3,2) = G(3,4) = G(5,4) = 0$, and the matrix corresponding to the linear system of equations involving the variables y_1 and y_3 is as follows:

$$\mathcal{M} = \begin{pmatrix} \dfrac{\lambda(3,2)}{\lambda(1,2)} & -1 \\ 1 & -\dfrac{\lambda(5,4)}{\lambda(3,4)} \end{pmatrix} = \begin{pmatrix} -1 & -1 \\ 1 & 1 \end{pmatrix}.$$

The determinant $\mathcal{M}$ is zero and $(1,1)$ is an eigenvector of $\mathcal{M}$ associated with the eigenvalue 0. By Theorem 3.1(b), the solution of DEPCA

$$y_\alpha(t) = \begin{cases} \alpha\lambda(t,2)y(1) + \dfrac{1 + \sin(2\pi t) - \cos(2\pi t)}{2\pi}, & t \in [1,3), \\ \alpha\lambda(t,4)y(3) + \dfrac{1 + \sin(2\pi t) - \cos(2\pi t)}{2\pi}, & t \in [3,5), \end{cases}$$

is a 4-periodic solution for any value of α.

The graphs of $y_\alpha(t)$ for $\alpha = 2$ and $\alpha = -3$ are presented in Figs. 1 and 2, respectively.

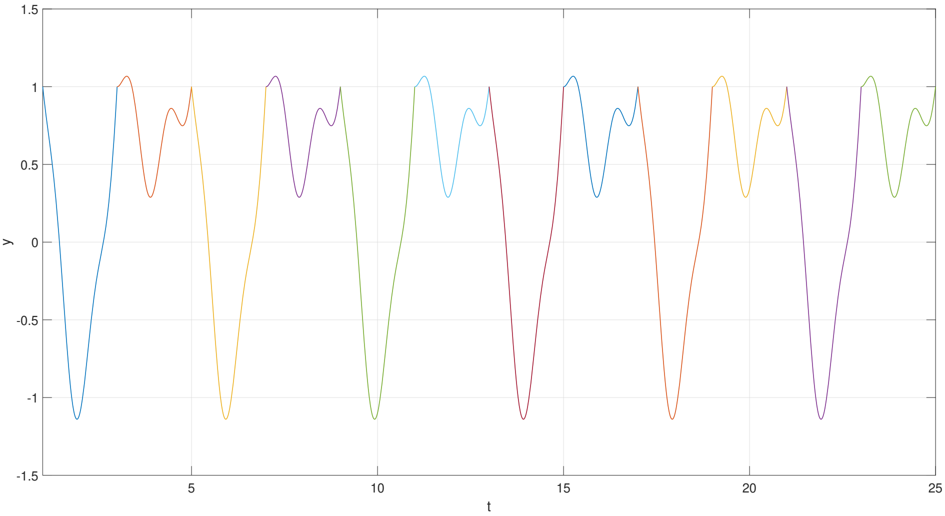

Fig. 1. 4-periodic solution of DEPCA (4.1) when $\alpha = 2$.

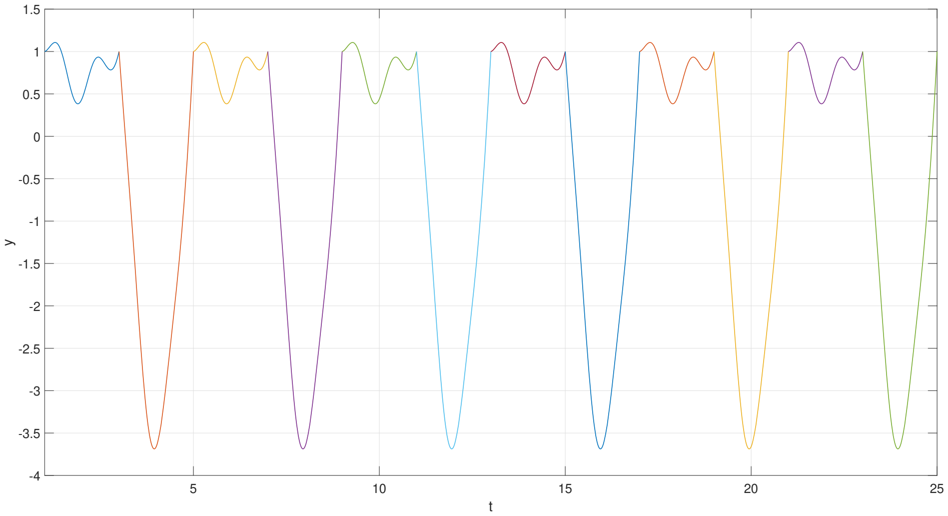

Fig. 2. 4-periodic solution of DEPCA (4.1) when $\alpha = -3$.

It is noteworthy that the parameters of the equation in this example adhere to the conditions delineated in the primary findings of papers [9]. Example 4.1 improves upon the findings of Theorem 4.4 in [9], which assert the uniqueness of the solution to DEPCA (1.2).

5. Conclusion and perspectives

This article investigates the existence of infinitely many periodic solutions for first-order differential equations involving piecewise alternately advanced and retarded arguments. We have established several theorems that ensure both the existence and uniqueness of solutions for the DEPCA with these types of arguments. By employing methods inspired by [22], we have derived sufficient conditions that guarantee the existence of infinitely many periodic solutions under suitable assumptions. Furthermore, we have provided a variety of numerical examples and simulations to illustrate the practical applicability of our findings.

Looking forward, several open problems warrant further investigation:

1. Examination of the existence of infinitely many periodic solutions for generalized types of DEPCA with piecewise alternately advanced and retarded arguments.
2. In-depth study of the asymptotic behavior and the existence of infinitely many periodic solutions for second-order DEPCA.
3. Comparative analysis of the asymptotic and periodic properties of first-order neutral differential equations with piecewise alternately advanced and retarded arguments, along with a comparison to equations incorporating linearly transformed arguments.

References

[1] Busenberg S., Cooke K.L. Models of vertically transmitted diseases with sequential-continuous dynamics. *Nonlinear Phenomena in Mathematical Sciences*, Academic Press, New York, 1982, P. 179–187.

[2] Dai L. *Nonlinear dynamics of piecewise constant systems and implementation of piecewise constant arguments*, World Scientific, Singapore, 2008.

[3] Chiu K.-S. Global exponential stability of bidirectional associative memory neural networks model with piecewise alternately advanced and retarded argument. *Comp. Appl. Math.*, 2021, **40**, P. 263.

[4] Chiu K.-S., Li T. New stability results for bidirectional associative memory neural networks model involving generalized piecewise constant delay. *Math. Comput. Simul.*, 2022, **194**, P. 719–743.

[5] Chiu K.-S. Existence and global exponential stability of periodic solution for Cohen-Grossberg neural networks model with piecewise constant argument. *Hacettepe J. Math. Stat.*, 2022, **51**(5), P. 1219–1236.

[6] Karakoc F. Asymptotic behaviour of a population model with piecewise constant argument. *Appl. Math. Lett.*, 2017, **70**, P. 7–13.

[7] Lafci M. Behavior of the solutions of a single-species population model with piecewise constant argument. *Iran. J. Math. Sci. Inform.*, 2024, **19**(2), P. 111–117.

[8] Aftabizadeh A.R., Wiener J. Oscillatory and periodic solutions of an equation alternately of retarded and advanced type. *Appl. Anal.*, 1986, **23**, P. 219–231.

[9] Chiu K.-S., Pinto M. Oscillatory and periodic solutions in alternately advanced and delayed differential equations. *Carpathian J. Math.*, 2013, **29**(2), P. 149–158.

[10] Chiu K.-S. Green's function for periodic solutions in alternately advanced and delayed differential systems. *Acta Math. Appl. Sin. Engl. Ser.*, 2020, **36**, P. 936–951.

[11] Chiu K.-S. Green's function for impulsive periodic solutions in alternately advanced and delayed differential systems and applications. *Commun. Fac. Sci. Univ. Ank. Ser. A1 Math. Stat.*, 2021, **70**(1), P. 15–37.

[12] Chiu K.-S. Periodic solutions of impulsive differential equations with piecewise alternately advanced and retarded argument of generalized type. *Rocky Mountain J. Math.*, 2022, **52**, P. 87–103.

[13] Chiu K.-S. Numerical-analytic successive approximation method for the investigation of periodic solutions of nonlinear integro-differential systems with piecewise constant argument of generalized type. *Hacettepe J. Math. Stat.*, 2024, **53**(5), P. 1272–1290.

[14] Karakoc F., H. Bereketoglu H., Seyhan G. Oscillatory and periodic solutions of impulsive differential equations with piecewise constant argument. Acta Appl. Math., 2010, **110**, P. 499–510.

[15] Karakoc F., Unal A., Bereketoglu H. Oscillation of a nonlinear impulsive differential equation system with piecewise constant argument. *Adv. Differ. Equ.*, 2018, **99**.

[16] Oztepe G.S., Karakoc F., Bereketoglu H. Oscillation and periodicity of a second order impulsive delay differential equation with a piecewise constant argument. *Communications in Mathematics*, 2017, **25**, P. 89–98.

[17] Wang G.-Q. Periodic solutions of a neutral differential equation with piecewise constant arguments. *J. Math. Anal. Appl.*, 2007, **326**, P. 736–747.

[18] Muminov M.I. On the method of finding periodic solutions of second-order neutral differential equations with piecewise constant arguments. *Adv. Differ. Equ.*, 2017, **336**.

[19] Muminov M.I., Ali H.M. Existence conditions for periodic solutions of second-order neutral delay differential equations with piecewise constant arguments. *Open Math.*, 2020, **18**(1), P. 93–105.

[20] Muminov M.I., Jumaev Z.Z. Exact periodic solutions of second-order differential equations with piecewise constant arguments. *Advances in Mathematics: Scientific Journal*, 2021, **10**(9), P. 3113–3128.

[21] Muminov M.I., Radjabov T.A. On existence conditions for periodic solutions to a differential equation with constant argument. *Nanosystems: Phys. Chem. Math.*, 2022, **13**(5), P. 491–497.

[22] Muminov M.I., Radjabov T.A. Existence conditions for 2-periodic solutions to a non-homogeneous differential equations with piecewise constant argument. *Examples and Counterexamples*, 2024, **5**, P. 100145.

[23] Chiu K.-S., Pinto M. Variation of parameters formula and Gronwall inequality for differential equations with a general piecewise constant argument. *Acta Math. Appl. Sin. Engl. Ser.*, 2011, **27**(4), P. 561–568.

[24] Chiu K.-S., Berna I. Nonautonomous impulsive differential equations of alternately advanced and retarded type. *Filomat*, 2023, **37**(23), P. 7813–7829.

[25] Jayasree K.N., Deo S.G. Variation of parameters formula for the equation of Cooke and Wiener. *Proc. Am. Math. Soc.*, 1991, **112**(1), P. 75–80.

Submitted 16 October 2024; revised 24 October 2024; accepted 25 October 2024

Information about the authors:

Kuo-Shou Chiu – Departamento de Matemática, Facultad de Ciencias Básicas, Universidad Metropolitana de Ciencias de la Educación, José Pedro Alessandri 774, Santiago, Chile; ORCID 0000-0002-3823-5898; kschiu@umce.cl

Fernando Cordova-Lepe – Departamento de Matemática, Física y Estadística, Universidad Católica del Maule, Talca, Chile; ORCID 0000-0001-6515-6880

Conflict of interest: the authors declare no conflict of interest.

NANOSYSTEMS:
PHYSICS, CHEMISTRY, MATHEMATICS

Almjasheva O.V. *Nanosystems: Phys. Chem. Math.*, 2024, **15** (6), 755–767.
http://nanojournal.ifmo.ru
DOI 10.17586/2220-8054-2024-15-6-755-767

Review

The role of non-autonomous phases in the formation and transformation of solid-phase oxide systems

Oksana V. Almjasheva[1,a]

[1]Branch of Petersburg Nuclear Physics Institute named by B.P. Konstantinov of National Research Centre "Kurchatov Institute" – Institute of Silicate Chemistry, St. Petersburg, Russia

[a]almjasheva@mail.ru

Corresponding author: O. V. Almjasheva, almjasheva@mail.ru

PACS 05.70.Np; 82.65.+r

ABSTRACT It is shown that the nature of processes in oxide solid-phase systems, primarily in nanosized ones, is determined by the behavior of the substance in a non-autonomous state. The composition of non-autonomous phases, the temperature of transition of non-autonomous phases to a liquid-like state, the equilibrium (locally equilibrium) and metastable thickness of non-autonomous phases, and the viscosity of the liquid-like non-autonomous phase are considered as the main parameters of non-autonomous phases.

KEYWORDS oxides, nanosystems, non-autonomous phase, melting point of the non-autonomous phase.

ACKNOWLEDGEMENTS The work was supported by state assignment No. 1023032900322-9-1.4.3

FOR CITATION Almjasheva O.V. The role of non-autonomous phases in the formation and transformation of solid-phase oxide systems. *Nanosystems: Phys. Chem. Math.*, 2024, **15** (6), 755–767.

1. Introduction

According to the definition given in the works of Defay and Prigogine [1, 2], surface phases, as well as phase and grain boundaries in polycrystalline systems are considered in a number of works as non-autonomous phases [4–46]. Such a definition has a number of advantages due to its more general nature. In this regard, the present paper employs this particular terminology.

A large number of both original works and reviews have been and are devoted to the formation and transformation of solid-phase oxides [46–66]. It should be noted that in the majority of the works on this topic, which have become classic, the main attention is paid to the influence, which the diffusion of components in bulk (autonomous) phases has on the processes occurring in the systems based on solid phases [61–66]. However, recent decades have shown an increased interest in studying the features of phase formation processes in nanopowders [47–61]. The volume fraction of non-autonomous phases in nanocrystalline systems, including those based on oxide nanocrystals, can be very significant [9]. This, apparently, should be taken into account in experimental studies, when determining the mechanisms and kinetics of the processes of phase formation and transformation, and when constructing physicochemical models of chemical and structural transformations in nanocrystalline systems. By now, there are no works that would analyze studies on the influence of the composition, structure, and properties of the non-autonomous phases on processes in solid-phase systems and, in the first place, in nanocrystalline systems. Of particular interest is the study of phase formation and phase transformation processes in materials based on oxide systems, since this is apparently the class of materials most widely represented in nature and in technology [65–73].

In relation to the listed reasons, this work is aimed at analyzing the results available in the literature, which are related to the determination of the properties and behavior of non-autonomous phases in polycrystalline systems and their influence on the course of phase formation processes and structural transformations, mainly in oxide phases.

2. Non-autonomous phases in polycrystals: composition, structure, properties

Conclusions that the composition, structure and surface properties of solid substances differ from their bulk properties were made on the basis of empirical data already in the works of 19th century scientists [74–76]. The works of Gibbs [77] theoretically consider some features of the behavior and properties of the surface of substances (interphase regions) from a thermodynamic standpoint. A detailed thermodynamic description of the regions between bulk (autonomous) phases as non-autonomous phases was given in [1–3]. These works considered the non-autonomous phases as regions between the coexisting (bordering on each other) autonomous phases, having a finite thickness, composition and structure, and changing from one autonomous phase to another.

It was shown in [4, 78–80] that such a description of non-autonomous phases is equivalent from the thermodynamic point of view to such a consideration of surface phases, in which all their 'excessive' properties are attributed to some two-dimensional surface, as was proposed in [1–3]. This statement is absolutely true when the volume fraction of non-autonomous phases is negligibly small compared to the volume fraction of autonomous phases, i.e. for the case of macrocrystalline systems. When the particle (crystallite) sizes decrease to nanometer values, the volume fraction of non-autonomous phases increases sharply [11, 15]. In this case, it is no longer possible to ignore the thickness of non-autonomous phases. It is especially important to know the sizes and behavioral features of non-autonomous phases when considering the kinetics of processes in solid-phase systems [15].

The work [81] shows a certain similarity in the behavior of substance at the boundaries of different autonomous phases and at the boundaries of grains of one phase. That is why further on, as is shown in [81], non-autonomous phases can be understood as layers of finite thickness also in the autonomous phases contact area and at the boundaries of grains of the same phase, if these layers have not formed their own autonomous phase.

A detailed analysis of experimental data and the construction of calculation models, carried out in [81], showed that in the case of high-angle boundaries of grains of the same autonomous phase of variable composition, components redistribution between the autonomous and non-autonomous phases can be described in the first approximation by a dependency shown in Fig. 1. This result was obtained assuming that the non-autonomous phases formed at high-angle boundaries of the autonomous phase grains contain a thin layer of amorphous substance (Fig. 2). Naturally, a dependency similar to that shown in Fig. 1 cannot be expected in cases with low-angle and special boundaries of grains.

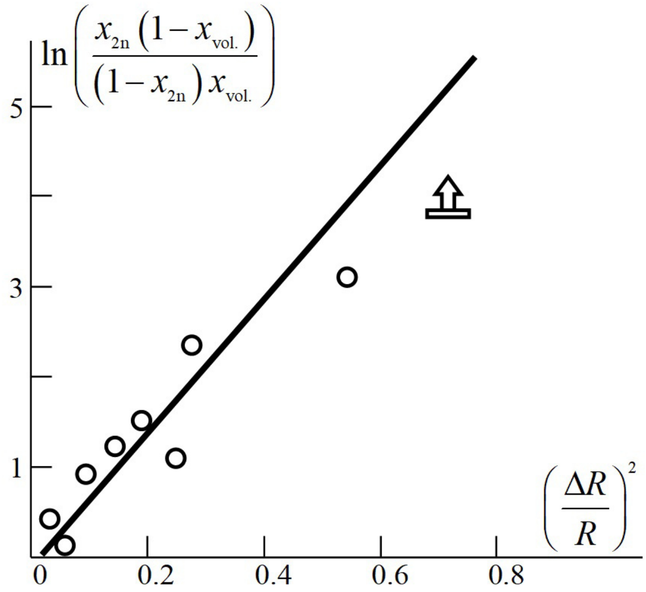

FIG. 1. Dependence of the impurity component distribution between the autonomous and non-autonomous phases [81]

It should be noted that the described effect of components redistribution between the autonomous and non-autonomous phases in particles based on crystalline autonomous phases can lead to the formation of structures of the core-shell type. In these structures, the shell appears due to the segregation of some components located on the particles surface in the non-autonomous phase. This effect is most noticeable when obtaining nanocrystalline particles. To date, a large number of examples of such structures formation are known [82–87]. A variant of the mechanism for the core-shell nanoparticles formation is described in [87]. However, apparently, this is only a special case of such nanostructures formation, and this area will be expanded subsequently.

When different solid autonomous phases are in contact, then the composition of the corresponding non-autonomous phase at temperatures not much different from the eutectic temperature will be close to the eutectic composition [81]. It should be noted that this result allows for describing the phenomenon of eutectic melting from positions different from the traditional ones [88].

Another case where it is convenient to use the term 'non-autonomous phase', or more precisely, the 'non-autonomous state of substance', is the state of substance under conditions of spatial limitations, when the amount of substance is insufficient for the formation of an autonomous phase with a composition and structure characteristic of the specified temperature and pressure. Such states may be exemplified by nanoparticles of certain sizes, thin surface layers, as well as the substance in micropores, in nanochannels, and in the matrices of composites with inclusions of nanoparticles at a certain placement density [89–106]. In this case, when the spatial restrictions are chemically inert, a substance, being in a non-autonomous state, will be unable to change the initially specified composition, but will have a structure different from that of the autonomous phase of the same composition at the same temperature and pressure.

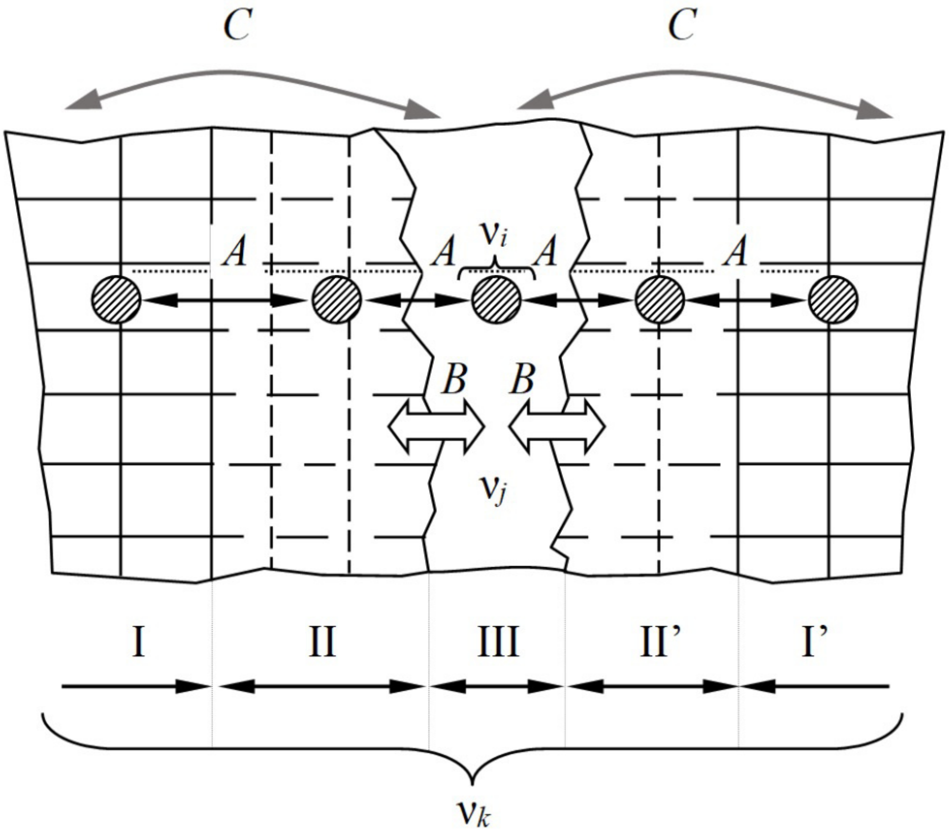

FIG. 2. Schematic representation of a 2-D non-autonomous phase (regions II, II', III) and relaxation processes in a polycrystalline system [81]. **Regions**: ν_i – inside autonomous (I, I'), structured (II,II') and amorphized (III) zones of the non-autonomous phase; ν_j – region coinciding with the amorphized zone of the 2-D non-autonomous phase; ν_k – two grains in contact with each other together with the intergranular formation. **Processes**: A – establishment of the locally equilibrium state in regions ν_i by introducing corresponding changes in the structure and composition; B – establishment of the locally equilibrium thickness of region III without mutual turning of grains; C – turning and shift of grains until the crystal sublattices completely coincide – for polycrystals based on one autonomous phase, or until the energy of translational mismatch is minimized – for systems consisting of different phases

The possibility of a liquid phase appearance at the boundary of solids at a temperature below their melting point was exemplified by ice already in [74, 75], but the quantitative relationship between the melting temperatures of the surface and bulk of solids was revealed only after an of experimental series by Tammann et al. [107]. It should be noted that despite the establishment of a quantitative relationship between the solid phase melting point and the so-called Tammann temperature (T_T) in these works (Table 1), the discovered phenomenon was interpreted incorrectly. For instance, the authors of [107] believed that volume diffusion processes are activated at the Tammann temperature. Only after a series of similar experiments, it was concluded in [108] that the T_T value in processes described in [107] determines the temperature, above which mass transfer is activated at the boundaries of solid phase particles.

TABLE 1. Tammann temperature for different materials

Materials	Tammann temperature	References
Metals	~ 0.33 T$_m$	[107]
Oxide	~ 0.57 T$_m$	
Metals	~ 0.3 T$_m$	[108]

Based on the analysis of [109], the work [110–112] presents the generalized data on the temperature dependency of the diffusion in the crystalline (autonomous) phase, on the surface, and at the boundaries of grains, i.e. in non-autonomous phases. Taking into account the results of [107,108], as well as the dependency of the surface phase thickness on temperature [11], these results can be illustrated by Fig. 3. The data presented in Fig. 3 allow concluding that the substance in the non-autonomous phase is found in the liquid (liquid-like) state at temperatures above T_T.

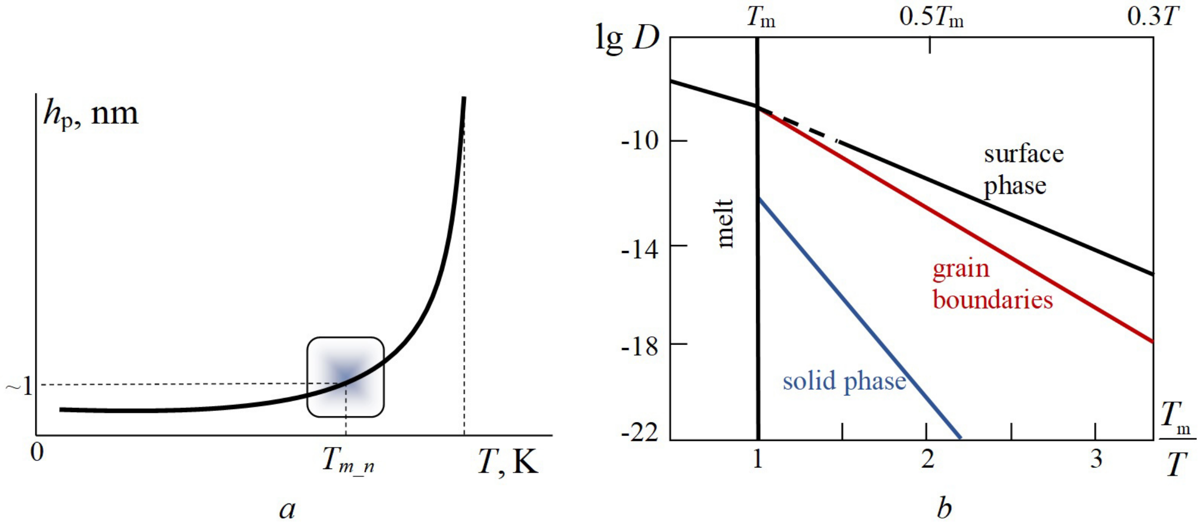

FIG. 3. Temperature dependences of the surface phase thickness (a) and the diffusion coefficients of the substance (b). For case (b), the solid lines are from [81], the dashed line is an extrapolation of the dependence presented in [81]

By now, a significant number of experimental and theoretical works analyze the transition of non-autonomous phases to the liquid (liquid-like) state [113–131]. A detailed thermodynamic analysis of the relationship between the melting temperatures of autonomous and non-autonomous phases was made in [81]. It was shown in [11] that in cases when non-autonomous phases contain a thin amorphous layer of substance, the dependency between the melting temperatures of the autonomous and non-autonomous phases can be represented by the expression

$$T_{m\_n} \approx \frac{1-\alpha_H}{1-\alpha_S} T_m, \tag{1}$$

where $\alpha_H = \Delta H_{am}/\Delta H_m$; $\alpha_S = \Delta S_{am}/\Delta S_m$; T_m – is the autonomous phase melting temperature, K; T_{m_n} – is the melting temperature of the non-autonomous phase of the same composition, K; ΔH_{am} – is the amorphization enthalpy; ΔH_m – is the melting enthalpy; ΔS_{am} – is the amorphization entropy; ΔS_m – is the melting entropy.

Further on, expression (1) was analyzed in [18] for a number of oxide substances, and the limits of variation of the non-autonomous phase melting temperature were determined as a function of the autonomous phase melting temperature for this class of compounds:

$$T_{m\_n} = \gamma T_m, \tag{2}$$

where γ – is a dimensionless parameter that takes values from 0.55 to 0.75, but most often 0.65.

A comparison of expression (2) with that for the Tammann temperature given in Table 1 shows their good agreement. This result once again confirms that in physical sense the empirical dependency of the Tammann temperature on the substances melting point reflects the dependency of the temperature of the non-autonomous phase transition into the liquid (liquid-like) state on the melting point of the autonomous phase of the corresponding composition. It should be noted that, as was analyzed in [81], the temperature of the non-autonomous phase transition into the liquid-like state depends on the phase structure. For example, in cases of the coherent grain intergrowth, this temperature approaches the autonomous phase melting point [81].

Another important parameter for the analysis of high-temperature processes in polycrystalline systems is the thickness of non-autonomous phases. From the mid-20th century to the present, a large number of experimental, theoretical papers and reviews have been devoted to the problem of determining the thickness and structure of non-autonomous phases. The works [2,115,116,122,126–132] can be cited as an example. An important component of these works is the determination of the dependency of the non-autonomous phase thickness on temperature. The most well-known expressions for the non-autonomous phase thickness as a function of temperature are presented in Table 2. Among the expressions given in this Table, it is possible to single out the dependency described in [81], which differs from the others by two factors. First, this dependency changes at the non-autonomous phase melting point, which was not reflected in other formulas (Table 2). Second, when approaching the melting point of the solid phase, its thickness does not tend to infinity, as in other expressions, but remains a finite (albeit large) value. In this case, the crystal sizes decrease, apparently, to nanometer values. Physically, this means, as was indicated in [81], that the melting of solids can be considered as the autonomization of the liquid non-autonomous phase with the transition of the crystalline (autonomous) phase to non-autonomous nanoclusters in the melt. To confirm the possibility of such a consideration of the melting process, the work [81] cited [135–144], in which various experimental data and theoretical calculations allowed making conclusions that solid (crystalline) clusters are observed in the melt near the melting point. The existence of nanosized solid clusters above the melting point of the substance, demonstrated in these works, allowed constructing in [145–154] a model of nanofluid flow in nanochannels, which under certain conditions predicts an unusually high flow rate due to the effect of solid clusters slipping along the nanochannel walls. Along with that, the cases where the channel dimensions were smaller than those of the nanoclusters, the effect of sharp deceleration of such liquids flow was described [146].

TABLE 2. Dependence of the thickness of the non-autonomous phase on temperature

Formula	References
$h_p = \alpha \ln(\frac{\beta}{T_m - T} + \delta)$	[113]
$h_p = \frac{C}{(T_k - T)^{\frac{1}{6}}}$	[4]
$h_p = \frac{a}{(T_m - T)^{\frac{1}{24}}}$	[115]
$h_p = \xi \ln(\gamma T)$	[116]
$h_p = \frac{a}{(T_m - T)^{\frac{1}{3}}}$	[119]
$h_p = \frac{\alpha}{(T_m - T + (T_{m2n} - T)H(T_{m2n} - T)\beta + \delta)^{\frac{1}{3}}}$	[11]

The dependencies of the non-autonomous phase thickness on temperature given in Table 2 describe the equilibrium (locally equilibrium) value of its thickness. However, the dimensional parameters of the particles of a substance in the non-autonomous state may turn out to be larger than those described by these expressions. In such cases, this non-autonomous state can be regarded as metastable, associated with the existence of some spatial or other limitations for mass transfer, described, for instance, in [155]. These limitations on the amount of substance in the system do not allow the formation of an autonomous phase, i.e. a solid phase with a structure that it would have at the given temperature and pressure if the said limitations did not exist. A substance in the metastable non-autonomous state can stably exist in the amorphous or crystalline state, but its crystalline structure will differ from that of the equilibrium (autonomous) phase. Similar cases of metastable non-autonomous states of substance have been experimentally discovered and theoretically described for a large number of oxide compounds and some other substances [94–106]. It should be noted that the thermodynamic estimate of the particle sizes of a substance in some metastable non-autonomous state may differ from the actually observed sizes [89, 156]. This is connected not only with the evaluative nature of the calculated data, but also with the role of kinetic factors, which can play a decisive role at temperatures below the melting point of non-autonomous phases [156].

Another important characteristic of non-autonomous phases for the analysis of interaction processes in solid polycrystalline systems is the viscosity of the liquid (liquid-like) non-autonomous phase. It was shown in [157] that by assuming that the viscosity of a liquid non-autonomous phase at a certain temperature can be calculated by extrapolating the dependency of the viscosity of the molten autonomous phase of the same composition on a given temperature, it is possible to obtain a quantitative match between the experimental and calculated data for the rate of particles migration through ice. Such an approach to predicting the non-autonomous phase viscosity is also corroborated by the temperature dependency of the diffusion coefficients of the substance in it (Fig. 3), since these values are closely related to each other [158]. Based on the above-mentioned nature of the dependency of the non-autonomous phase viscosity on temperature, some phenomena that can be observed during the liquid non-autonomous phase flow in polycrystalline systems were theoretically predicted in [12, 81, 159, 160].

Of considerable interest from the point of view of understanding the structural features of non-autonomous phases are the results of an experimental study of the nature of the viscous behavior of the surface layer (surface – non-autonomous phase) of the crystalline phase, given in [126]. It was experimentally shown in this work that the nature of the viscous behavior of the surface layer at relatively high values of the homologous temperature can only be described if this layer is imagined as inhomogeneous, consisting of a liquid phase with inclusions of solid particles of very small size. It can be noted that essentially this result is close to the conclusions made in [81, 138, 139], in which melting was considered as developing in a rather narrow, but still certain temperature range, as a transition of solid autonomous phase particles to a non-autonomous state, and of the non-autonomous liquid phase to the autonomous one. Another conclusion, apparently very important for understanding the features of the liquid-like non-autonomous phase behavior at high temperatures, is an experimentally derived conclusion that the thickness of these phases is several times greater compared to the values presented in conclusions of works [161–164].

So to date many basic questions related to the structure and properties of non-autonomous phases remain open. Moreover, this applies both to the region of high values of the homologous temperature, and to the region of temperatures below the melting point of the non-autonomous phase. In the latter case, this is due to the 'frozen' state of the non-autonomous phase, which complicates studies of the processes of approaching this state to equilibrium.

3. Solid-phase reactions and sintering of materials

The experimental works of Tammann and co-authors [107] were aimed at determining the temperature of the onset of active sintering of particles of different composition (T_T). The further studies, which interpreted the effect discovered in these works as associated with the transition of phase boundaries and grains (non-autonomous phases) into the liquid-like state [119], began considering the Tammann temperature (T_T) as a boundary temperature, upon reaching or exceeding which any processes of solid particles interaction, including solid-phase reactions, start [61]. Along with that, the mechanisms and models of solid-phase chemical reactions, the rate of which was determined by the mass transfer between components, were described as those limited by the rate of diffusion in the solid phase [61, 65]. This situation was apparently due to the fact that the volume fraction of non-autonomous phases in these works was significantly smaller than the fraction of solid (autonomous) phases. The transition of a non-autonomous phase to the liquid-like state could increase only the rate of reagent particles agglomeration. This led to a noticeable increase in the contact area of the interacting particles. In addition, point contacts of solid particles were replaced by areas with a liquid-like interlayer. An increase in the rate of components diffusion through the liquid-like non-autonomous phase in the case of interaction of relatively large particles of micron and even submicron sizes could not significantly affect the total mass transfer rate due to the extremely small proportion of non-autonomous phases in such reaction systems.

The situation changed dramatically when chemical reactions began to take place between nanosized reagent particles. For example, it was shown in [166–169] that in nanosized layers obtained by molecular layering [169–173], no interaction between reagents resulting in formation of solid-phase compounds is observed at temperatures below the non-autonomous phase melting point, and upon reaching this temperature, the synthesis proceeds at such a high rate, which cannot be described as that limited by solid-phase diffusion. A similar situation is observed in the case of synthesizing solid-phase compounds from nanosized reagent powders [174–178]. An analysis of the processes of solid-phase compounds synthesis in oxide compositions consisting of nanosized reagent particles in [179] yields a somewhat paradoxical conclusion that all solid-phase chemical reactions occurring at a high or simply noticeable rate are liquid-phase to some extent, i.e. a liquid-like non-autonomous phase must first form in the reaction system for such reactions to start. The role of non-autonomous phases in the processes of solid particles interaction was considered in more detail in [15]. Numerous examples of the influence of liquid-like non-autonomous phases on mass transfer in solid-phase systems and on the synthesis of solid-phase compounds are given in [28–34, 36, 180].

Other processes in solid-phase systems that start only after the transition of the non-autonomous phases to the liquid-like state, as was shown, e.g. in [81, 107, 108], are the processes of sintering and inelastic deformation of ceramics by the mechanism of high-temperature creep. It should be noted that the role of liquid-like non-autonomous phases can consist not only in increasing the rate of particles agglomeration due to the facilitation of their sliding relative to each other due to the appearance of a liquid-like non-autonomous phase, but, as was shown in [9, 10, 12, 81], also by the transformation-transport mechanism of solid-phase particles interaction. Such interactions are schematically illustrated in Fig. 4a,b. It was shown in [81] that proceeding from a more general model relationship and variation of the expressions for the non-autonomous phase viscosity, the transformation-transport mechanism makes it possible to obtain practically the same dependencies as a set of known models of sintering and inelastic deformation of materials obtained by applying different mechanisms. The corresponding comparison of models is given in Table 3.

An important role in solid-phase chemical reactions, in the processes of sintering and inelastic deformation of ceramics, can be played by small additives of relatively fusible solid-phase substances, even in cases where they are chemically inert to other components of the solid-phase system. It was shown in [5, 81, 182] that such additives get quickly distributed over the surface of other components at a temperature equal to or higher than the melting point of the non-autonomous phase based on such additives. This, in turn, promotes agglomeration of particles of the solid-phase system and, as a consequence, an increase in the rate of solid-phase synthesis and sintering of ceramics.

Another area for which the transition of non-autonomous phases to the liquid-like state is important is the construction of phase equilibrium diagrams in solid-phase systems. For instance, while the approach to the equilibrium state in oxide solid-phase systems at high temperatures requires hours, tens or hundreds of hours [185], the process of approaching equilibrium in the low-temperature region can take a year or more [185], or even geological epochs. In this regard, the analysis of characteristic values of the diffusion rate in solid phases in [185] resulted in proposing the time criterion as a criterion for dividing into high-temperature and low-temperature processes. When the time of approaching the equilibrium state in a solid-phase system is a year and more, then it is proposed to define such systems as low-temperature ones [185]. However, the above analysis of the role of non-autonomous phases in the behavior of solid-phase systems allows proposing another criterion for dividing solid-phase processes into high-temperature and low-temperature ones.

TABLE 3. Parametric dependence of shrinkage during sintering and hot pressing of materials

Model	Time, t	Average particle radius $\hat{R}=\frac{d}{2}$	Mechanical force per square of the average particle radius, $f=\frac{F}{\hat{R}}$
Transformation-transport mechanism (approximation without taking into account the contribution of dislocation tubes to transport processes)			
Asymptotic equation of the initial stage of sintering [81]	t^1	$\hat{R}^{-1}$	–
Equation of sintering limited by mass transfer of a substance through a liquid non-autonomous phase [81]	$t^{\frac{2}{3}\cdot\frac{n}{1+n}}$	$\hat{R}^{-\frac{2}{3}\cdot\frac{1+2n}{1+n}}$	$f^{\frac{2}{3}\cdot\frac{1}{1+n}}$
n=0.5	$t^{\frac{1}{2}}$	$\hat{R}^{-\frac{8}{9}}$	$f^{\frac{4}{9}}$
n=1 (Newtonian fluid)	$t^{\frac{1}{3}}$	$\hat{R}^{-1}$	$f^{\frac{1}{3}}$
n=2	$t^{\frac{4}{9}}$	$\hat{R}^{-\frac{10}{9}}$	$f^{\frac{2}{9}}$
n=3	$t^{\frac{1}{2}}$	$\hat{R}^{-\frac{7}{6}}$	$f^{\frac{1}{6}}$
n$\to\infty$	$t^{\frac{2}{3}}$	$\hat{R}^{-\frac{4}{3}}$	f^0
Compaction due to redistribution of particles in the liquid phase [183]	t^{1+x}	$\hat{R}^0$	f^1
Volume diffusion			
[182]	$t^{0.49}$	$\hat{R}^{-0.98}$	$f^{0.49}$
[183]	$t^{0.4}$	$\hat{R}^{-0.8}$	$f^{0.40}$
[184]	$t^{\frac{1}{2}}$	$\hat{R}^{-1}$	$f^{\frac{1}{2}}$
[182]	$t^{0.46}$	$\hat{R}^{-0.92}$	$f^{0.46}$
[116]	$t^{0.48}$	$\hat{R}^{-0.96}$	$f^{0.48}$
Volume diffusion to grain boundaries and spherical surface of particles [184]	$t^{0.53}$	$\hat{R}^{-1.06}$	$f^{0.53}$
Grain boundaries diffusion			
[182]	$t^{\frac{1}{3}}$	$\hat{R}^{-1}$	$f^{\frac{1}{3}}$
[184]	$t^{\frac{1}{3}}$	$\hat{R}^{-1}$	$f^{\frac{1}{3}}$
[184]	$t^{0.31}$	$\hat{R}^{-0.93}$	$f^{0.32}$
[116]	$t^{0.32}$	$\hat{R}^{-0.96}$	$f^{0.31}$
Limited dissolution of the solid phase in the liquid and diffusion-viscous flow of the liquid phase [183]	$t^{\frac{1}{3}}$	$\hat{R}^{-1}$	$f^{\frac{1}{3}}$

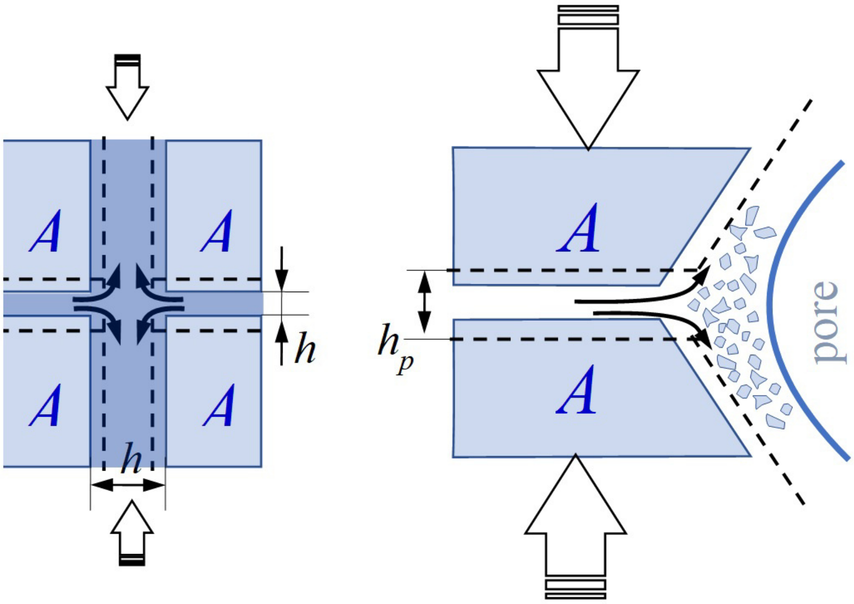

FIG. 4. Schematic representation of the transformation-transport mechanism of solid phase particles interaction

Apparently, it makes more physical sense to use the temperature of the non-autonomous phases transition to the liquid-like state as such a criterion. The corresponding division of processes in solid-phase systems into high-temperature and low-temperature ones is schematically shown in Fig. 5. It should be noted that in terms of the real division of solid-phase systems, the proposed boundary does not differ much from that proposed in [185], but is more justified in physical sense.

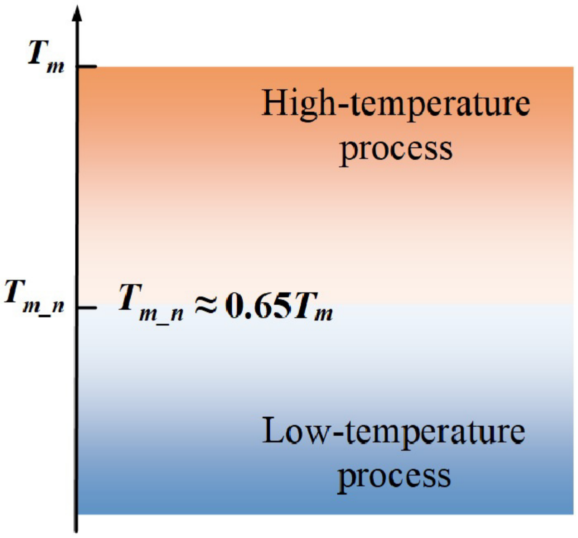

FIG. 5. Scheme of processes division in solid-phase systems into high-temperature and low-temperature

4. Conclusion

An analysis of the literature data on the nature of processes in oxide solid-phase systems demonstrated that the decisive role in them is played by the behavior of the substance in the non-autonomous state. A particularly great influence the non-autonomous phases have on the behavior of nanosized systems. The main parameters of the non-autonomous phases that determine the properties and behavior of the solid-phase, especially nanocrystalline ones, are the composition of the non-autonomous phases, the temperature of the non-autonomous phase transition to the liquid-like state, the equilibrium (locally-equilibrium) and metastable thickness of non-autonomous phases, and the viscosity of the liquid-like non-autonomous phase.

The data available in the literature show that there are still a large number of open questions both on the structure and properties of the substance in the non-autonomous state, and on the influence of the non-autonomous state on the behavior and properties of solid-phase systems, which indicates the prospects for further research in this area.

References

[1] Defay R. *Etude thermodinamique de la tension superficielle*. Gauntier-Vellarg and Cie, Paris, 1934, 372 p.

[2] Defay R., Prigogin I. *Tension superficielle et adsorption*. Edition Desoer., Liege, 1951, 295 p.

[3] Defay R. Prigogin I. Sanfelg A Surface Termodynamics. *J. Colloid Interface Sci*, 1977, **58**(3), P. 498–510.

[4] Rusanov A.I. *Phase equilibria and surface phenomena*. Chemistry, Leningrad, 1967, 234 p. (in Russian)

[5] Gusarov V.V., Egorov F.K., Ekimov S.P., Suvorov S.A. Mössbauer study of the kinetics of formation of film states during the interaction of magnesium and iron oxides. *Rus. J. Phys. Chem. of the USSR*, 1987, **61**(6), P. 1652–1654.

[6] Gusarov V.V., Suvorov S.A. Autocatalytic solid-phase reaction of chrysoberyl formation. *J. General Chem. of the USSR*, 1988, **58**(4), P. 932–934.

[7] Gusarov V.V., Suvorov S.A. Melting-point of locally equilibrium surface phases in polycrystallibe systems based on a single volume phase. *J. Appl. Chem. of the USSR*, 1990, **63**(8), P. 1560–1565.

[8] Gusarov V.V., Suvorov S.A. Self-accelerating processes of development of solid-phase systems (synthesis and functioning). Promising directions of chemistry and chemical technology. *Chemistry, Leningrad*. 1991, P. 153–158.

[9] Gusarov V.V., Suvorov S.A. Transformation of non-autonomous phases and compaction of polycrystalline systems. *J. Appl. Chem. of the USSR*, 1992, **65**(7), P. 1478–1488.

[10] Gusarov V.V., Suvorov S.A. Transformation-transport processes in polycrystalline systems and creep of materials. *J. Appl. Chem. of the USSR*, 1992, **65**(10), P. 2377–2380.

[11] Gusarov V.V., Suvorov S.A. Thickness of 2-dimensional non-autonomous phases in locally equilibrium polycrystalline systems based on one bulk phase. *J. Appl. Chem. of the USSR*, 1993, **66**(7), P. 1529–1534.

[12] Gusarov V.V., Popov I.Yu., Gugel Yu.V. Transformation-transport processes of formation of dynamic structures in 2-dimensional non-autonomous phases during thermomechanical processing of oxide and polycrystalline systems. *J. Appl. Chem. of the USSR*, 1994, **67**(7), P. 1116–1120.

[13] Smirnova Zh.N., Gusarov V.V., Malkov A.A., Malygin A.A., Suvorov S.S. Stabilization of the γ-form of aluminum oxide in the $AlO_{1.5}$–SiO_2 system with different levels of spatial conjugation of components. *J. Appl. Chem. of the USSR*, 1995, **68**(12), P. 1950–1954.

[14] Gusarov V.V., Malkov A.A., Malygin A.A., Suvorov S.A. Thermally stimulated transformations of 2-dimensional non-autonomous phases and compaction of oxide polycrystalline materials. *Inorg. Mater.*, 1995, **31**(3), P. 346–350.

[15] Gusarov V.V., Almjasheva O.V. The role of non-autonomous state of matter in the formation of structure and properties of nanomaterials. Chapter 13 in the book Nanomaterials: properties and promising applications. Ed A.B. Yaroslavtsev. Scientific World Publishing House, Moscow, 2014, P. 378–403. (in Russian)]

[16] Gusarov V.V. Statics and dynamics of polycrystalline systems based on refractory oxides. Abstract of diss. Doctor of Chemical Sciences. St. Petersburg, 1996, 44 p.

[17] Sanfeld A. *Introdaction to the thermodynamics of charged and polarized layers*. Wiley, N.Y., 1969, 258 p.

[18] Gusarov V.V. The thermal effect of melting in polycrystalline systems. *Thermochim. Acta*, 1995, **256**(2), P. 467–472.

[19] Sanfeld A., Steinchen A. Surface stress of isotropic solid under irreversible condition. *Comptes Rendus Chimie*, 2003, **6**(7), P. 677–682.

[20] Urusov V.S., Tauson V.L., Akimov V.V. Geochemistry of solids. GEOS, Moscow, 1997, 500 p. (in Russian)

[21] Tauson V.L., Parkhomenko I.Yu., Smagunov N.V., Babkin D.N., Menshikov V.I. Non-autonomous surface phases in the synthesis of sulfides and their geochemical role. Electronic scientific and information journal "Bulletin of the Department of Earth Sciences of the Russian Academy of Sciences", 2003, **1**(21).

[22] Tauson V.L., Akimov V.V., Lipko S.V., Loginov B.A. Nonautonomous phases as potential sources of incompatible elements. *Doklady Earth Sciences*, 2006, **407**(2), P. 280–283.

[23] Tauson V.L., Babkin D.N., Lipko S.V., Kravtsova R.G., Grebenshchikova V.I., Lustenberg E.E. Nonautonomous nanophases on a hydrothermal pyrite surface and its geochemical significance. *Doklady Earth Sciences*, 2008, **423**(2), P. 1501–1506.

[24] Akimov V.V., Gerasimov I.N., Tauson V.L., Loginov B.A. Mucrostructure and chemical composition of nonautonomous surface phases in crystals of pirrohotine ($Fe_{1-x}S$). *Bulletin of the Russian Academy of Sciences: Physics.*, 2006, **70**(7), P. 1051–1054.

[25] Glavatskiy K. *Multicomponent Interfacial Transport*, Springer, Berlin Heidelberg, 2011.

[26] Sanfeld A. Ordering induced by chemical, thermal and mechanical constraints at solid interfaces. *Pure and Appl. Chem.*, 1984, **56**(12), P. 1727–1738.

[27] Novoselov A.R. Point contact and linear interfaces as non-autonomous phases, their role in wetting and heterogeneous condensation processes. *Russ. J. Phys. Chem.*, 1991, **65**(2), P. 459–463.

[28] Lipko S.V. Non-autonomous phases on the surface of mineral and inorganic crystals and their role in the concentration of impurity elements. Abstract of diss. ... candidate of chemical sciences, Irkutsk, 2010, 18 p. (in Russian)

[29] Neiman A.Ya., Trafieva M.F., Kostikov Yu.P. Chemistry and mass transfer routes during formation of phases of the V_2O_5-MoO_3 system. *Russ. J. Inorg. Chem.*, 2005, **50**(10), P. 1582–1595.

[30] Neiman A.Ya., Uvarov N.F., Pestereva N.N. Solid state surface and interface spreading: An experimental study. *Solid State Ionics*, 2007, **177**(39-40), P. 3361–3369.

[31] Neiman A.Ya., Guseva A.F., Trifonova M.V., Sukhankina I.V. Surface reaction diffusion in the synthesis of molybdates and tungstates: the role of the phase composition of the products. *Russ. J. Inorg. Chem.*, 2005, **50**(3), P. 367–372.

[32] Neiman A.Ya., Kulikova T.E. Electrochemistry of solid-phase reactions: Phase formation in the In_2O_3-WO_3 system. Processes at the $WO_3|In_2O_3$ and $WO_3|In_6WO_{12}$ interfaces. *Russ. J. Electrochem.*, 2007, **43**(6), P. 682–694.

[33] Neiman, A.Y., Pestereva, N.N. Tsipis, E.V. Surface diffusion, migration, and conjugated processes at heterophase interfaces between WO_3 and $MeWO_4$ (Me = Ca, Sr, Ba). *Russ. J. Electrochem.*, 2007, **43**(6), P. 672–681.

[34] Pervov V.S., Makhonina E.V., Zotova A.E., Kireeva N.V., Kedrinsky I.-M.A. New possibilities to obtain ceramic nanoheterostructures with enhanced ionic conductivity. *Nanotechnol Russia*, 2014, **14**(9), P. 347–355.

[35] Krasnenko T.I., Rothermel M.V. Conditions for the formation of a non-autonomous phase during chemical and thermal deformations of complex oxides. In the book: Solid State Chemistry and Functional Materials – 2018. Thermodynamics and Materials Science. Abstracts of the Russian Conference with International Participation and the 12-th Russian Symposium with International Participation. edited by V.V. Gusarov, 2018, P. 21. (in Rassian).

[36] Tauson V.L., Lipko S.V., Arsent'ev K.Y., Smagunov N.V. Crystal growth through the medium of nonautonomous phase: Implications for element partitioning in ore systems. *Crystallogr. Rep.*, 2019, **64**(3), P. 496–507.

[37] Krasnenko T.I., Rotermel M.V., Samigullina, R.F. Stabilizing the associated non-autonomous phase upon thermal expansion of $Zn_2V_2O_7$. *Russ. J. Inorg. Chem.*, 2017, **62**(4), P. 413–417.

[38] Gerasimov I.N. Modeling of non-autonomous phase formation on the surface of inorganic mineral substances. Dissertation for the degree of candidate of chemical sciences. Irkutsk State University. Irkutsk, 2010. (in Russian).

[39] Samsonov V.M., Bazulev A.N., Sdobnyakov N.Yu. On surface non-tension of small objects. Chemistry and computer modeling. *Butlerov communications*, 2002, **10**, P. 267–271. Supplement to special issue. (in Russian).

[40] Luo J., Chiang Y.-M. Existence and stability of nanometer-thick disordered films on oxide. *Acta Materialia*, 2000, **48**(18–19), P. 4501–4515.

[41] Kaul A.R., Gorbenko O.Yu., Kamenev A.A. The role of heteroepitaxy in the development of new thin-film oxide-based functional materials. *Russ. Chem. Rev.*, 2004, **73**(9), P. 861–880.

[42] Magomedov M.N. On the dependence of surface energy on the size and shape of a nanocrystal. *Physics of the Solid State*, 2004, **46**(5), P. 924–937. (in Russian).

[43] Zhang H., Banfield J.F. Thermodynamic analysis of phase stability of nanocrystalline titania *J. Mater. Chem.*, 1998, **8**(9), P. 2073–2076.

[44] Samsonov V.M., Khashin V.A. Thermodynamic approaches to the problem of phase state of nanoparticles. *Condensed matter and interphases*, 2007, **9**(4), P. 387–391. (in Russian).

[45] Rempel A.W., Wettlaufer J.S., Grae M. Worster Premelting dynamics in a continuum model of frost heave. *Journal of Fluid Mechanics*, 2004, **498**, P. 227–244.

[46] Batsanov S.S. Features of solid-phase transformations induced by shock compression. *Russ. Chem. Rev.*, 2006, **75**(7), P. 601–616.

[47] Ogbezode J.E., Offia-Kalu N.E., Bello A., Anye V. Ch, Onwalu P.A. Phase structure transformation and growth mechanism for iron oxide nanoparticles synthesized by mechanochemical method: A mini-review. *J.Alloys and Metallurgical Systems*, 2024, **7**, P. 100103

[48] Kozlova T.O., Sheichenko E.D., Vasilyeva D.N., Kozlov D.A., Kolesnik I.V., Tronev I.V., Teplonogova M.A., Baranchikov A.E., Ivanov V.K. Ultrasonic-assisted hydrothermal synthesis of nanoscale double ceric phosphates. *Nanosyst.: Pysh., Chem., Math.*, 2024, **15**(2), P. 215-223.

[49] Kozlova T.O., Vasilyeva D.N., Kozlov D.A., Kolesnik I.V., Teplonogova M. A., Tronev I.V., Sheichenko E.D., Protsenko M.R., Kolmanovich D.D., Ivanova O.S., Baranchikov A.E., Ivanov V.K. A Comparative study of cerium(III) and cerium(IV) phosphates for sunscreens. *Molecules*, 2024, **29**(9), P. 2157–2157.

[50] Al'myasheva O.V., Korytkova E.N., Maslov A.V., Gusarov V.V. Preparation of nanocrystalline alumina under hydrothermal conditions. *Inorg. Mater.*, 2005, **41**(5), P. 460–467.

[51] Korytkova, E.N., Maslov, A.V., Pivovarova, L.N. et al. Synthesis of nanotubular $\mathrm{Mg_3Si_2O_5(OH)_4}$-$\mathrm{Ni_3Si_2O_5(OH)_4}$ silicates at elevated temperatures and pressures. *Inorg Mater.*, 2005, **41**(7), P. 743–749.

[52] Enikeeva M.O., Proskurina O.V., Motaylo E.S., Danilovich D.P., Gusarov V.V. The influence of conditions of the monazite structured $\mathrm{La_{0.9}Y_{0.1}PO_4}$ nanocrystas sintering on thermal and mechanical properties of the material. *Nanosyst.: Phys. Chem. Math.*, 2021, **12**(6), P. 799–807.

[53] Lomanova N.A., Tomkovich M.V., Osipov A.V., Ugolkov V.L., Panchuk V.V., Semenov V.G., Gusarov V.V. Formation of $\mathrm{Bi}_{m+1}\mathrm{Fe}_{m-3}\mathrm{Ti_3O}_{3m+3}$ (m = 4–9) nanocrystals upon thermal decomposition of coprecipitated hydroxides. *Russ. J. Inorg. Chem.*, 2021, **66**(5), P. 755–764.

[54] Gyrdasova O.I., Samigullina R.F., Vladimirova E.V., Medyankina I.S., Buldakova L.Yu., Yanchenko M.Yu., Pasechnik L.A. Precursor method for the synthesis of highly dispersed $\mathrm{ZrO_2}$ doped with scandium. *Mendeleev Communications*, 2024, **34**(5), P. 640–642.

[55] Zhang K., Ma Ch., Paul S., Zaffran J. Unveiling the phenol direct carboxylation reaction mechanism at $\mathrm{ZrO_2}$ surface. *Molecular Catalysis*, 2024, **569**, P. 114606.

[56] Boykobilov D., Thakur S., Samiev A., Nasimov A., Turaev K., Nurmanov S. Prakash J., Ruzimuradov O. Electrochemical synthesis and modification of novel $\mathrm{TiO_2}$ nanotubes: Chemistry and role of key synthesis parameters for photocatalytic applications in energy and environment. *Inorganic Chemistry Communications*, 2024, **170**(3), P. 113419.

[57] Sozarukova M.M., Proskurnina E.V., Baranchikov A.E., Ivanov V.K. $\mathrm{CeO_2}$ nanoparticles as free radical regulators in biological systems. *Nanosyst.: Phys. Chem. Math.*, 2020, **11**(3), P. 324–332.

[58] Popova N.R., Shekunova T.O., Popov A.L., Selezneva I.I., Ivanov V.K. Cerium oxide nanoparticles provide radioprotective effects upon X-ray irradiation by modulation of gene expression. *Nanosyst.: Phys. Chem. Math.*, 2019, **10**(5), P. 564–572.

[59] Qi Junnan, Liu Huimin, Liu Guihong, Chen Yao Innovation of TiO_{2-x} nanomaterials in the biomedical field: synthesis, properties, and application prospects. *Chemical Engineering Journal*, 2024, **491**, P. 151773.

[60] Priya Dhuria, Satnam Singh Bhamra Influence of LTSSR and TSSR synthesis methods on the structural properties of $\mathrm{YFeO_3}$ orthoferrite. *Materials Science and Engineering: B*, 2022, **285**, P. 115960.

[61] Tretyakov Yu.D. *Solid-phase reactions*. Chemistry, Moscow, 1978, 360 p. (in Russian)

[62] West A.R. *Solid State Chemistry and Its Applications*. Wiley India Pvt. Limited, 2007, 744 p.

[63] Rao C.N.R., Gopalakrishnan J. *New directions in solid state chemistry*. Nauka, Moscow, 1990, 520 p. (in Russian)

[64] Schmalzried H. *Chemical Kinetics of Solids*. Weinheim, VCH, 1995, 700 p.

[65] Guseva A.F., Neiman A.Ya. New data on the mechanism of mass transfer in solid-phase reactions: 1. Reactions in an electric field. *Kinetics and catalysis*, 1994, **35**(1), P. 1–7

[66] Chebotin V.M. *Chemical diffusion in solids*. Science, Moscow, 1989, 208 p.

[67] Andrievsky R.A. Fundamentals of nanostructured materials science. Possibilities and problems. *Laboratoriya znaniy*, Moscow, 2029, 228 p. (in Russian)

[68] Suzdalev I.P. Multifunctional nanomaterials. *Russ. Chem. Rev.*, 2009, **78**(3), P. 249–282. (in Russian)

[69] Eliseev A.A., Lukashin A.V. *Functional nanomaterials, Fizmatlit*, Moscow, 2010, 456 p. (in Russian).

[70] Guozhong Cao, Ying Wang. *Nanostructures and Nanomaterials: Synthesis, Properties, and Applications*. World Scientific, 2011, 581 p.

[71] Aaga G.F. Zinc oxide and its engineered derivative nanomaterials: Insight into energy, environmental, medical, agricultural, and food applications. *Materials Today Sustainability*, 2024, **28**, P. 101051.

[72] Karmakar D., Karmakar S., Ghosh A., Jana D. A comparative overview of the recent progress of some novel metal oxide and sulfide nanomaterials-based photocatalyst. *Materials Today Communications*, 2024, **40**, P. 110115.

[73] Sadykov V.A., Eremeev N.F., Shlyakhtina A.V., Pikalova E.Yu, Advances in alternative metal oxide materials of various structures for electrochemical and catalytic applications. *International Journal of Hydrogen Energy*, 2024, **94**, P. 179–208.

[74] Faraday M. On certain conditions of freezing water. *Athenaeum*, 1850, **1181**, P. 640–641.

[75] Faraday M. XXIV. On Regelation, and on the Conservation of Force, *Philos. Mag., Ser.*, **417**, 1859, 162 p.

[76] Mendeleev D.I. On the influence of touch on the course of chemical transformations. *ZhRHO*, 1886, **18**(8). (in Russian)

[77] Gibbs D. *Thermodynamic works*. GITTL, Moscow-Leningrad. 1950, 492 p. (in Russian)

[78] Rusanov A.I., Shchukin E.D., Rebinder P.A. On the theory of dispersion. I. Thermodynamics of monodisperse systems *Colloidal journal*, 1968, **30**(5), P. 573–580.

[79] Kuni F.M., Rusanov A.I. Statistical theory of aggregative equilibrium. *Theor. Math. Phys*, 1970, **2**(2), P. 192–206.

[80] Kligman F.I., Rusanov A.I. On the thermodynamic equilibrium states of disperse systems with suspended particles. *Koll. Zh.*, 1977, **39**(1), P. 44–47. (in Russian)

[81] Gusarov V.V. Statics and dynamics of polycrystalline systems based on refractory oxides: dis. Doctor of Chemical Sciences: 02.00.04. St. Petersburg, 1996, 598 p.

[82] Tomkovich M.V., Andrievskaya E.R., Gusarov V.V. Formation under hydrothermal conditions and structural features of nanoparticles based on the ZrO_2–Gd_2O_3 system. *Nanosyst.: Phys., Chem., Math.*, 2011, **2**(2), P. 6–14.

[83] Smirnov A.V., Fedorov B.A., Tomkovich M.V., Almjasheva O.V., Gusarov V.V. Core-shell nanoparticles forming in the ZrO_2-Gd_2O_3-H_2O system under hydrothermal conditions. *Doklady Physical Chemistry*, 2014, **456**(1), P. 71–73.

[84] Almjasheva O.V., Smirnov A.V., Fedorov B.A., Tomkovich M.V., V.V. Gusarov. Structural features of ZrO_2-Y_2O_3 and ZrO_2-Gd_2O_3 nanoparticles formed under hydrothermal conditions. *Russ. J. Gen. Chem.*, 2014, **84**(5), P. 804–809.

[85] Eshmakov R., Sherstobitov A.V., Filatova D., Konstantinova E., Rumyantseva M. SnO_2/MnO_x composite systems as VOCs sensors: Influence of manganese chemical state and distribution on functional performances. *Materials Chemistry and Physics*, 2024, **328**, P. 129992

[86] Shaposhnik A.V., Shaposhnik D.A., Turishchev S.Y., Chuvenkova O.A., Ryabtsev S.V., Vasiliev A.A., Vilanova X., Hernandez-Ramirez F., Morante J.R. Gas sensing properties of individual SnO_2 nanowires and SnO_2 sol–gel nanocomposites. *Beilstein J. Nanotechnol*, 2019, **10**, P. 1380–1390.

[87] Almjasheva O.V., Krasilin A.A., Gusarov V.V. Formation mechanism of core-shell nanocrystals obtained via dehydration of coprecipitated hydroxides at hydrothermal conditions. *Nanosyst.: Phys., Chem., Mathem.*, 2018, **9**(4), P. 568–572.

[88] Voronin G.F. Fundamentals of Thermodynamics Publishing House, Moscow, Moscow University, 1987, 192 p.

[89] Almjasheva O.V. Formation and structural transformations of nanoparticles in the TiO_2–H_2O system. *Nanosyst.: Phys., Chem., Math.*, 2016, **7**(6), P. 1031–1049.

[90] Dzhevaga E.V., Chebanenko M.I., Martinson K.D., Lobinsky A.A., Popkov V.I. One-step combustion synthesis of undoped c-ZrO_2 for Cr(VI) removal form aqueous solutions. *Nanotechnology*, 2022, **33**(41), P. 415601.

[91] Proskurina O.V., Sokolova A.N., Sirotkin A.A., Abiev R.S., Gusarov V.V. Role of hydroxide precipitation conditions in the formation of nanocrystalline $BiFeO_3$. *Russ. J. Inorg. Chem.*, 2021, **66**(2), P. 163–169.

[92] Gusarov V.V., Malkov A.A., Malygin A.A., Polyakova E.V., Khabibova S.V., Petrova L.I., Suvorov S.A. Evolution of $AlO_{1.5}$–TiO_2 systems with different prehistories. *Russ. J. Applied Chemistry*, 1991, **64**(5), P. 1134–1135.

[93] Eliseev A.A., Falaleev N.S., Verbitskiy N.I., Volykhov A.A., Yashina L.V., Kumskov A/, Zhigalina V.G., Vasiliev A.L., Lukashin A.V., Sloan J. Size-dependent structure relations between nanotube and encapsulated nanocrystal. *Nano Letters*, 2017, **17**, P. 805–810.

[94] Popkov V.I., Martinson K.D., Kondrashkova I.S., Enikeeva M.O., Nevedomskiy V.N., Panchuk V.V., Semenov V.G., Volkov M.P., Pleshakov I.V. SCS-assisted production of $EuFeO_3$ core-shell nanoparticles: formation process, structural features and magnetic behavior. *J. Alloys and Compounds*, 2021, **859**, P. 157812.

[95] Koroleva E., Naberezhnov A., Rysiakiewicz-Pasek E., Vakhrushev S., Sysoeva A., Kumzerov Yu. Dielectric response of potassium nitrate in a restricted geometry. *Composites Part B: Engineering*, 2016, **94**, P. 322–326.

[96] Alekseeva O.A., Naberezhnov A.A., Fokin A.V. Effect of restricted geometry on phase transitions in nanostructured sodium nitrate. *Physica B: Condensed Matter*, 2025, **696**, P. 416676.

[97] Alekseeva O.A., Enikeeva M.O., Naberezhnov A.A., Sysoeva A.A. Stabilization of the monoclinic phase of KH_2PO_4 under limited geometry conditions. *Technical Physics Letters*, 2024, **50**(11), P. 7–10.

[98] Naberezhnov A.A., Alekseeva O.A., Kudryavtseva A.V., Chernyshov D.Yu., Vergentiev T.Yu., Fokin A.V. Structural transition and temperature dependences of thermal expansion coefficients of $NaNO_3$ embedded in non-pressurized glass. *Physics of the Solid State*, 2022, **64**(3), P. 365–370.

[99] Mikhailin N.Y., Shamshur D.V., Parfen'ev R.V., Kozub V.I., Gal'perin Y.M., Kumzerov Y.A., Fokin A.V. Size dependences of the magnetic properties of superconducting lead-porous glass nanostructures. *Physics of the Solid State*, 2018, **60**(6), P. 1068–1072.

[100] Belotitskii V.I., Kumzerov Y.A., Kalmykov A.E., Kirilenko D.A., Romanov S.G., Sorokin L.M., Sysoeva A.A., Peschel U., Zhuromskyy O. Optical properties of metal nanoparticles in chrysotile channels, *Technical Physics Letters*, 2016, **42**(6), P. 656–658.

[101] Kumzerov Y.A., Naberezhnov A.A. Effect of restricted geometry on the superconducting properties of low-melting metals (review article). *Low Temperature Physics*, 2016, **42**(11), P. 1028–1040.

[102] Gatina E.N., Maslennikova T.P. Formation of chrysotile nanotubes with titania in the internal channel. *Nanosyst: Phys, Chem, Math.*, 2024, **15**(3), P. 380–387.

[103] Almjashev O.V., Gusarov V.V. Effect of ZrO_2 nanocrystals on the stabilization of the amorphous state of alumina and silica in the ZrO_2–Al_2O_3 and ZrO_2–SiO_2 systems. *Glass Physics and Chemistry*, 2006, **32**(2), P. 162–166.

[104] Al'myasheva O.V., Gusarov V.V. Nucleation in media in which nanoparticles of another phase are distributed. *Doklady Physical Chemistry*, 2009, **424**(2), P. 43–45.

[105] Al'myashev O.V., Gusarov V.V. Features of the phase formation in the nanocomposites. *Russ. J. Gen. Chem.*, 2010, **80**(3), P. 385–390.

[106] Zlobin V.V., Krasilin A.A., Almjasheva O.V. Effect of heterogeneous inclusions on the formation of TiO_2 nanocrystals in hydrothermal conditions. *Nanosyst.: Phys., Chem., Mathem.*, 2019, **10**(6), P. 733–739.

[107] Tammann G, Mansuri Q.A. Metallographische mitteilungen aus dem Institut für physikalische chemie der universität göttingen CXIII. Zur Rekristallisation von Metallen und Salzen. Zeitschrift für anorganische und allgemeine Chemie, 1923, **126**, 119 p.

[108] Hüttig G.F., Theimer H., Breuer W. Über reaktionen fester stoffe: 126. Mitteilung. Über die entgasung fester stoffe. Zeitschrift für anorganische und allgemeine Chemie, 1942, **249**(2), P. 134–145.

[109] Kaur I., Gust W. Fundamentals of grain and interphase boundary diffusion. Stuttgart: Ziegler Press, 1989, 422 p. (Russ. ed.: Kaur, I., Gust, W. Diffuziya po granitsam zeren i faz. Moscow: Mashinostroenie, 1991, 446 p.)

[110] Hwang J.C.M., Ho P.S., Lews J.E., Campbell D.R. Grain boundary diffusion of aluminum in polycrystalline silicon films. *J. Appl. Phys.* 1980, **51**(3), P. 1576–1581.

[111] Hwang J.C.M., Amos D.E., Nelson G.C. Analysis of grain-boundary diffusion in thin films: Chromium in gold. *J. Appl. Phys.*, 1976, **47**(9), P. 3769–3775.

[112] Wuttig M., Brinbaum H.K. Self-Diffusion along edge dislocations in nickel. *Phys. Rev.*, 1966, **147**, P. 495.

[113] Fletcher N.H. The Chemical Physics of Ice Cambridge Univ. Press. 1970, 271 p.

[114] Barer S.S., Klividze V.I., Kurzaev A.B., Sobolev V.D., Churaev N.V. Thickness and viscosity of thin non-freezing layers between the surface of ice and quartz. *Doklady USSR Academy of Sciences*, 1977, **235**(3), P. 601. (in Russian)

[115] Gilpin R.R. A model for the prediction of ice lensing and frost heave in soils. *Water Resour. Res.*, 1980, **16**(5), P. 918.

[116] Clarke D.R. On the equilibrium thickness of intergranular glass phases in ceramic materials. *J. Am. Seram. Soc.*, 1987, **70**(1), P. 15–25.

[117] Kikuchi R., Cahn J.W. Grain-boundary melting transition in a two-dimension lattice-gas model. *Phys. Rev. B.*, 1980, **21**(5), P. 1893.

[118] Mizuno Y. Hanafusa N. Studies of surface properties of ice using nuclear magnetic resonance. *J. Phys. Colloques*, 1987, **48**, P. C1-511–C1-517.

[119] Dash J.G. Surface melting. *Contemp. Phys.*, 1989, **30**(2), P. 89.

[120] Elbaum M., Schick M. Application of the theory of dispersion forces to the surface melting of ice. *Phys. Rev. Lett.*, 1991, **66**(13), P. 1713.

[121] Elbaum M., Lipson S.G., Dash J.G. Optical study of surface melting on ice. *J. Cryst. Growth.*, 1993, **129**, P. 491.

[122] Dash, J.G., Haiying Fu, Wettlaufer, J.S. The premelting of ice and its environmental consequences. *Reports Prog. Phys.*, 1995, **58**, P. 115.

[123] Wettlaufer J.S., Worster M.G., Wilen L.A., Dash J.G. A theory of premelting dynamics for all power law forces. *Phys. Rev. Lett.*, 1996, **76**, P. 3602

[124] Shultz M.J. Ice surfaces. *Annu. Rev. Phys. Chem.*, 2017, **68**, P. 285.

[125] Slater B., Michaelides A. Surface premelting of water ice. *Nat Rev Chem*, 2019,**3**, P. 172–188.

[126] Canale L., Comtet J., Nigu'es A., Cohen C., Clanet C., SiriaA., Bocquet L. Nanorheology of interfacial water during ice gliding. *Phys. Rev.*, 2019, **X9**, P. 041025.

[127] Richhariya V., Tripathy A., Carvalho O., Nine J., Losic D., Silva F.S. Unravelling the physics and mechanisms behind slips and falls on icy surfaces: A comprehensive review and nature-inspired solutions. *Materials & Design*, 2023, **234**, P. 112335.

[128] Boxe C.S., Saiz-Lopez A. Influence of thin liquid films on polar ice chemistry: Implications for Earth and planetary science. *Polar Science*, 2009, **3**, P. 73–81.

[129] Pavlovska A., Dobrev D., Bauer E. Orientation dependence of the quasi-liquid layer on tin and indium crystals. *Surface Science*, 1994, **314**, P. 341–352.

[130] Smit W.J., Bakker H.J. The Surface of Ice Is Like Supercooled Liquid Water. *Angew. Chem.*, 2017, **129**, P. 15746–15750.

[131] Bluhm H., Ogletree D.F., Fadley C.S., Hussain, Z., Salmeron M. The premelting of ice studied with photoelectron spectroscopy. *J. Phys. Condens. Matter.*, 2002, **14**, P. L227–L233.

[132] Conde M. M., Vega C. Patrykiejew A. The thickness of a liquid layer on the free surface of ice as obtained from computer simulation. *J. Chem. Phys.*, 2008, **129**, P. 014702.

[133] Pickering I., Paleico M., Sirkin Y.A.P., Scherlis D.A., Factorovich M.H. Grand canonical investigation of the quasi-liquid layer of ice: is it liquid? *J. Phys. Chem. B*, 2018, **122**, P. 4880–4890.

[134] Dosch H., Lied A. & Bilgram J.H. Glancing-angle X-ray scattering studies of the premelting of ice surfaces. *Surf. Sci.*, 1995, **327**, P. 145–164.

[135] Frenkel Ya.I. Liquid state and theory of melting. I. Continuity of solid and liquid states. Collection of selected works. Scientific articles. Publishing house of the USSR Academy of Sciences, Moscow-Leningrad, 1958, Vol. 2, P. 269–279. (in Russian)

[136] Frenkel Ya.I. Liquid state and theory of melting. II. Theory of melting and crystallization. Collection of selected works. Scientific articles. Publishing house of the USSR Academy of Sciences, Moscow-Leningrad, 1958, Vol. 2, P. 269–279. (in Russian)

[137] Ubbelode A. The Molten State of Matter. London University, London, 1978, 384 p.

[138] Ubbelode A. Melting and Crystal Structure. Clarendon Press, 1965, 325 p. M, Mir, 1969, 420 p.

[139] Pastukhov E.A., Vatolin N.A., List V.L., Detsov V.M., Kachin S.V. Diffraction studies of the structure of high-temperature melts. Ekaterinburg; Ural Branch of the Russian Academy of Sciences, 2003, 353 p. (in Russian).

[140] Ladyanov V.I., Logunov S.V., Kuzminykh E.V. On the viscosity of micro-inhomogeneous liquid metals. *Metalls*, 1997, **4**, P. 22. (in Russian).

[141] Ladyanov V.I., Novokhatsky I.A., Logunov S.V. Estimation of the lifetime of clusters in liquid metals. *Metalls*, 1995, **2**, P. 13. (in Rissian).

[142] Psarev V.I., Ivanov A.L. On the pre-crystallization structural state of supercooled selenium melt. *Russ. J. Phis. Chem.*, 1992, **66**(3), P. 788–790. (in Russian)

[143] Skripov V.P., Koverda V.P. Spontaneous crystallization of liquids. Nauka, Moscow, 1984, 232 p. (iv Russian).

[144] Filippov E.S. Structure, chemistry and physics of metallurgical melts. *Metallurgy*, Moscow, 1995, 303 p. (in Russian)

[145] Chivilikhin S.A., Gusarov V.V., Popov I.Yu., Svitenkov A.I. Model of fluid flow in a nano-channel. *Russ. J. Math. Phys.*, 2008, **15**(3), P. 409–411.

[146] Popov I.Y., Rodygina O.A., Chivilikhin S.A., Gusarov V.V. Soliton in a nanotube wall and stokes flow in the nanotube. *Tech. Phys. Lett.*, 2010, **36**(9), P. 852–855.

[147] Ershova A.A., Popov I.Y., Chivilikhin S.A., Gusarov V.V. Waveguide modes and adhesion conditions for flow in a nanochannel. *Dokl. Phys.*, 2010, **55**(6), P. 271–273.

[148] Popov I.Yu., Chivilikhin S.A., Gusarov V.V. Model of fluid flow in nanotube: Classical and quantum features. *J. Phys.: Conf. Ser.*, **248**, 2010, Art. No 012006.

[149] Chivilikhin S.A., Popov I.Yu., Gusarov V.V. Planar flows in nanoscale regions. *Nanosyst.: Phys., Chem., Math.*, 2011, **2**(3), P. 49-52.

[150] Chivilikhin S.A., Popov I.Yu., Aryslanova E.M., Vavulin D.N., Gusarov V.V. Liquid flow in nanotubes. *J. Phys.: Conf. Ser.*, 2012, **345**, Art. No 012036.

[151] Chivilikhin S.A., Gusarov V.V., Popov I.Yu. Flows in nanostructures: hybrid classical-quantum models. *Nanosyst.: Phys., Chem., Math.,* 2012, **3**(1), P. 7–26.

[152] Belonenko M.B., Chivilikhin S.A., Gusarov V.V., Popov I.Yu., Rodygina O.A. Soliton-induced flow in carbon nanotube. *Europhysics Letters.*, 2013, **101**(6), P. 66001.

[153] Rodygina O.A., Chivilikhin S.A., Popov I.Yu., Gusarov V.V. Crystallite model for flow in nanotube caused by wall soliton. *Nanosyst.: Phys., Chem., Math.*, 2014, **5**(3), P. 400–404.

[154] Chivilikhin S.A., Gusarov V.V., Popov I.Yu. Charge pumping in nanotube filled with electrolyte. *Chinese J. Phys.*, 2018, **56**(5), P. 2531–2537.

[155] Almjasheva O.V., Popkov V.I., Proskurina O.V., Gusarov V.V. Phase formation under conditions of self-organization of particle growth restrictions in the reaction system. *Nanosyst.: Phys., Chem., Math.*, 2022, **13**(2), P. 164–180.

[156] Almiasheva O.V. Formation of oxide nanocrystals and nanocomposites under hydrothermal conditions, structure and properties of materials based on them: dis. Doctor of Chemical Sciences: 02.00.21. Moscow, 2018, 362 p.

[157] Gilpin R.R. A Model of the "Liquid-Like" layer between ice and a substrate with applications to wire regelation and particle migration. *J. Colloid and Interface Science*, 1979, **68**(2), P. 235–251.

[158] Frenkel J. The Liquid State and the Theory of Fusion. *Acta Physicochimica URSS*, 1935, **3**, P. 633–648.

[159] Gusarov V.V., Popov I.Yu. Dynamic structure formation during high-temperature deformation of polycrystalline oxides. *Izvestiya Universiteta. Physics.*, 1995, **38**(8), P. 69–75.

[160] Gusarov V.V., Popov I.Yu. Flows in two-dimensional nonautonomous phases in polycrystalline system. *Nuovo Cimento della Societa Italiana di Fisica D.*, 1996. **18D**(7), P. 799–805.

[161] Döppenschmidt A., Butt H.J. Measuring the thickness of the Liquid-like layer on ice surfaces with atomic force microscopy. *Langmuir*, 2000, **16**, P. 6709.

[162] Kornienko M.E., Sheiko N.L., Kornienko O.M., Nikolaienko T.Y. Discrete properties of quasi-liquid water film in the ice premelting range. 1. Temperature dependences of water nanofilm thickness and viscoelastic properties of polycrystalline ice. *Ukr. J. Phys.*, 2013, **58**, P. 151.

[163] Conde M.M., Vega C., Patrykiejew A. The thickness of a liquid layer on the free surface of ice as obtained from computer simulation. *J. Chem. Phys.*, 2008, **129**, P. 014702.

[164] Wettlaufer J.S. Ice surfaces: Macroscopic effects of microscopic structure. *Phil. Trans. R. Soc. A*, 1999, **357**, P. 3403.

[165] Schmalzried H. Chemical kinetics of solids. Weinheim: VCH, 1995, 700 p.

[166] Gusarov V.V., Ishutina Z.N., Malkov A.A., Malygin A.A. Peculiarities of the solid-phase chemical reaction in formation of mullite in the nanosize film composition. *Doklady Akademii Nauk.*, 1997, **357**(2), P. 203–205. (In Russian)]

[167] Smirnova Zh.N., Gusarov V.V., Malkov A.A., Firsanova T.V., Malygin A.A., Suvorov S.A. High-speed synthesis of mullite. *Russ. J. Gen. Chem.*, 1995, **65**(2), P. 199–204.

[168] Gusarov V.V., Malkov A.A., Ishutina Zh.N., Malygin A.A. Phase formation in a nanosized silicon oxide film on the surface of aluminum oxide. *Tech. Phys. Lett.*, 1998, **24**(1), P. 3–8.

[169] Kol'tsov S.I., Aleskovskii V.B. Effect of degree of dehydration of silica gel on mechanism of hydrolysis of adsorbed titanium tetrachloride. *Russ. J. Phys. Chem.*, 1968, **42**(5), P. 630–632.

[170] Aleskovskii V.B. Chemistry and technology of solids. *J. Appl. Chem. of the USSR*, 1974, **47**(10), P. 2207–2217.

[171] Malygin A.A. Molecular Layering Nanotechnology. *Nanotechnologies in Russia (Rossiiskie Nanotekhnologii)*, 2007, **2**(3-4), P. 87–100. (In Russian)

[172] Malygin A.A., Drozd V.E., Malkov A.A., Smirnov V.M. From V.B. Aleskovskii's "Framework" hypothesis to the method of molecular layering/atomic layer deposition. *Chemical Vapor Deposition*, 2015, **21**, P. 216–240.

[173] Sosnov E.A., Malkov A.A., Malygin A.A. Nanotechnology of Molecular Layering in Production of Inorganic and Hybrid Materials for Various Functional Purposes (a Review): I. History of the Development of the Molecular Layering Method. *Russ. J. Appl. Chem.*, 2021, **94**(8), P. 1022–1037.

[174] Almjasheva O.V., Gusarov V.V. Effect of ZrO_2 nanocrystals on the stabilization of the amorphous state of alumina and silica in the ZrO_2-$Al_2O_3$and ZrO_2-SiO_2 systems. *Glass Physics and Chemistry*, 2006, **32**(2), P. 162–166

[175] Bachina A., Almajasheva O.V., Danilovich D.P., Popkov V.I. Synthesis, crystal structure and thermophysical properties of $ZrTiO_4$ nanoceramics. *Russ. J. Phys. Chem. A: Focus on Chemistry*, 2021, **95**(8), P. 1529–1536.

[176] Artamonova O.V., Almyasheva O.V., Mittova I.Ya., Gusarov V.V. Sintering of nanopowders and properties of ceramics in the ZrO_2–In_2O_3 system. *Advanced Materials*, 2009, **1**, P. 91–94.

[177] Khadidja Laziri, Amar Djemli, Djaida Redaoui, Foudil Sahnoune, Essebti Dhahri, S.F. Hassan, Nouari Saheb. Kinetics of formation, microstructure, and properties of monolithic forsterite (Mg_2SiO_4) produced through solid-state reaction of nano-powders of MgO and SiO_2. *Ceramics International*, 2024, **50**(22), Part A, P. 45179–45188.

[178] Zargar H.R., Bayati M.R., Rezaie H.R., Golestani-Fard F., Molaei R., Zanganeh S., Kajbafvala A. Influence of nano boehmite on solid state reaction of alumina and magnesia, *J. Alloys and Compounds*, 2010, **507**(2), P. 443–447.

[179] Gusarov V.V. Fast Solid-Phase Chemical Reactions. *Russ. J. Gen. Chem.*, 1997, **67**(12), P. 1846–1851.

[180] Kirillova S.A., Panchuk V.V., Semenov V.G., Almjasheva O.V. Solid-phase interaction in the ZrO_2–Fe_2O_3 nanocrystalline system. *Nanosys.: Phys., Chem., Math.*, 2018, **9**(6), P. 763–769.

[181] Kingery W.D. Regelation, surface diffusion and ice sintering. *J. Appl. Phys.*, 1960, **31**(5), P. 883–838.

[182] Jonson D.L. New method of obtaining volume, grain-boundary and surface diffusion coefficient from sintering data *J. Appl. Phys.*, 1969, **40**(1), P. 192–200.

[183] Kingery W.D., Berg M. Study of initial stages of sintering solids by viscous flow, evaporation – condensation end self-diffusion. *J. Appl. Phys.*, 1955, **26**(10), P. 1205–1212.

[184] Coble R.L. Diffusion model for hot pressing with surface energy and pressure effect as driving forces. *J. Appl. Phys.*, 1970, **41**(12), P. 4798–4807.

[185] Fedorov P.P. Determination of annealing duration in the study of phase equilibria in the solid state of binary systems. *Russ. J. Inorg. Chem.*, 1992, **37**(8), P. 1891–1894. (in Russian).

Submitted 15 September 2024; accepted 28 November 2024

Information about the authors:

Oksana V. Almjasheva – Branch of Petersburg Nuclear Physics Institute named by B.P. Konstantinov of National Research Centre "Kurchatov Institute" – Institute of Silicate Chemistry, 199034, St. Petersburg, Russia; ORCID 0000-0002-6132-4178; almjasheva@mail.ru

Conflict of interest: the authors declare no conflict of interest.

NANOSYSTEMS:
PHYSICS, CHEMISTRY, MATHEMATICS

Original article

Pasechnik L.A., et al. *Nanosystems: Phys. Chem. Math.*, 2024, **15** (6), 768–773.
http://nanojournal.ifmo.ru
DOI 10.17586/2220-8054-2024-15-6-768-773

Scandium modified zirconia extracted from red mud as a waste of alumina production

Liliya A. Pasechnik, Irina S. Medyankina, Danil I. Pereverzev, Alexander Yu. Chufarov, Alexey Yu. Suntsov

Institute of Solid State Chemistry UB RAS, Ekaterinburg, Russia

Corresponding author: L.A. Pasechnik, pasechnik@ihim.uran.ru

ABSTRACT The total or partial utilization or recycling of bauxite processing waste (red mud) has the potential to reduce the harmful effect on the environment while simultaneously extracting the most valuable ingredient, scandium which is currently underutilized due to its high cost. The new efficient carbonation technology promises an assured supply of scandium and zirconium at a significantly reduced cost. Here, scandium-zirconium concentrate, extracted by hydrolysis from leachate after carbonate treatment of red mud, was subjected to sintering by ceramic technology at 1100 °C to produce scandia-stabilised zirconia (ScSZ). The XRD patterns demonstrate the successful doping of scandium into the zirconia lattice through the hydrolytic precipitation method. The ratio between the essential components of the functional ceramics Zr and Sc is approximately 4, which correlates with the doping level of ScSZ up to $Zr_{0.8}Sc_{0.2}O_{1.9}$.

KEYWORDS zirconia oxide, Sc–Zr concentrate, ScSZ, zirconium ceramics, thermal expansion, red mud

ACKNOWLEDGEMENTS The work was supported by RCF and Government of the Sverdlovsk region, project No. 24-29-20278, https://rscf.ru/en/project/24-29-20278/

FOR CITATION Pasechnik L.A., Medyankina I.S., Pereverzev D.I., Chufarov A.Yu., Suntsov A.Yu. Scandium modified zirconia extracted from red mud as a waste of alumina production. *Nanosystems: Phys. Chem. Math.*, 2024, **15** (6), 768–773.

1. Introduction

Zirconium oxide and ceramic materials based on it are widely employed in engineering and medicine due to their high refractory properties, strength, chemical inertness, superionic oxygen conductivity, as well as their biocompatibility and catalytic activity [1–5]. Yttrium-stabilized zirconia (YSZ) is commonly used material in solid oxide fuel cells (SOFC) for high temperature applications [6]. Scandia stabilized zirconia (ScSZ) exhibits conductivity that is 1.5 – 3 times superior to that of YSZ, due to its distinctive crystal structure [7]. At the same time Sc-containing materials are not commonly used as functional ceramic due to high cost but small additives appear to be effective for the increased ionic conductivity, structural and thermodynamic stability.

It is known that not only the type and amount of additives the size of the initial powders have a significant impact on the process of their sintering, and, as a consequence, on the structure and mechanical properties of ceramics [8,9]. Studies have shown that with the decrease in particle sizes, the physicochemical properties like strength, thermal conductivity, high-temperature resistance, toughness and specific surface area improve, comparing micron-ZrO_2 to nano-ZrO_2 [10,11]. On the other hand, the physical and mechanical properties change significantly depending on the sintering temperature and the holding time at maximum temperature [12].

At present most widespread methods for preparing initial zirconia particles with a narrow particle size distribution are emulsion method [13], sol-gel combustion [14], spray-drying and spray-pyrolysis [15], solvothermal synthesis [16] and other [17]. In many instances, the raw materials are either costly and toxic organometallic compounds or solutions of inorganic salts utilized for the execution of solvothermal processes with simultaneous or subsequent heat treatment at selected temperatures. A controlled double-jet precipitation is believed to be a rather simple method enabling to govern size, shape and porosity of hydrous zirconia particles maintaining a narrow size distribution of zirconia particles after drying and calcination [18]. A similar relatively simple deposition process of a carbonate-hydrocarbonate solution can be implemented to produce scandium-containing zirconia from red mud – residue from bauxite processing [19]. However, industrial raw materials contain impurities of other metals along with the specified elements [20, 21]. Their presence can be both beneficial to the sintering process and detrimental to the properties of the final material. In this work, the direct cheap creation of ceramics based on scandium-stabilized zirconia (ScSZ) and the assessment of its thermochemical properties are of interest.

2. Experimental

2.1. Extraction of zirconia concentrate

Sc-doped zirconia oxide was produced by hydrolysis of carbonate-hydrocarbonate solution after the carbonation leaching of red mud derived from an alumina plant located in the Ural region (Russia). The detailed description of carbonation processing of red mud with 10 % $NaHCO_3$ solution or using sintering furnaces (7 – 20 % CO_2) and precipitation of Sc–Zr concentrate are provided earlier [19, 22]. Supplying of carbon dioxide promotes the synthesis of soluble carbonate complexes $[Sc(CO_3)_4]^{5-}$ and $[(ZrTi)(CO_3)_4]^{4-}$ and starts neutralization processes of alkali from red mud and alkali resulted from the hydrolysis of aluminates, titanates, etc. The carbonate-bicarbonate filtrate at pH = 8 – 9, separated from the insoluble mass of carbonized red mud, contains up to 30 – 50 g/m^3 Sc and 250 – 350 g/m^3 Zr. Concentrate from the clarified solution was precipitated by sodium hydroxide at heating and holding for 4 or 24 hours to coagulate the precipitate. In this work, the hydrolysis of a carbonate-bicarbonate solution was carried out at 90 – 100 °C to pH 12.5 for 24 h. Before control of the chemical composition both initial red mud and Sc–Zr concentrate were further dried at 125 °C for 24 h (initial moisture content was about 20 – 30 wt %) and comminuted. The respective compositions of initial red mud and the concentrate obtained from hydrochemical branch of the plant are listed in Table 1.

TABLE 1. The compositions of initial red mud and Sc–Zr concentrate

Component	Red mud, % wt.	Sc–Zr concentrate, % wt.
Fe_2O_3	41.0	7.52
Al_2O_3	15.4	0.94
CaO	9.0	4.09
MgO	0.4	2.17
TiO_2	5.5	8.37
SiO_2	7.5	1.05
Na_2O	5.6	5.89
K_2O	0.4	0.41
ZrO_2	**0.04**	**58.87**
Sc_2O_3	**0.012**	**10.46**

2.2. Methods of characterization

The element content in Sc–Zr concentrate after drying at 125 °C was determined by inductively coupled plasma atomic emission spectroscopy (ICP-AES) using a spectrometer Elan9000 (PerkinElmer).

In order to obtain polycrystalline powders dried concentrates were thoroughly grinded and mixed up in jasper mortar then pressed into disk shape bar and annealed at 600, 800, 1000 and 1100 °C in air during 10 – 12 hours. XRD patterns were collected at room temperature on a Shimadzu XRD–7000 diffractometer using CuKα radiation in the 2θ range 10° to 70° with a step of 0.03° and exposition 3 s. Polycrystalline silicon ($a = 5.43075(5)$ Å) was used as an external standard. The PDF2 database (ICDD, USA, Release 2016) was applied for phase analysis and the identification of c-ZrO_2 (card No. 00-054-1136). Polythermal dependencies were recorded at temperature scan rate of 10 °C/min up to 800 °C, with alumina as a standard.

Microstructure was analyzed by means of scanning electron microscopy method with the use of scanning electron microscope (SEM) VEGA 3 LMH (TESCAN) equipped with energy dispersive analyzer INCA Energy 350/X-max 80 (Oxford Instruments) used for the study of atomic distribution and a scanning electron microscope JEOL-JSM LA 6390 equipped with a JEOL JED-2300 detector.

Thermal expansion was studied on rectangular bar with a section of 5 × 5 mm cut from the sintered sample. Data on linear elongation was collected using L75 (Linseis) dilatometer at heating mode with the rate 3 °/min in air.

3. Results and discussion

The typical SEM-image of the Sc–Zr concentrate produced directly from red mud shown in Fig. 1a reveals that sample consists of homogeneously dispersed very fine near spherical shaped particles with easily crushed micrometer-sized agglomerates. The results of EDX analysis (Fig. 1b) correlate with the concentrations of elements obtained from ICP–AES analysis as shown in Table 1.

The pattern of initial Sc–Zr concentrate with a wide hump between 20° and 40° 2θ indicates an amorphous nature or nanocrystalline structure of the sample. Calcination at 200 °C to constant mass shows adsorbed and structured moisture of about 25 – 30 wt. %, which is typical of amorphous hydroxide phases with a highly developed surface. The thermal

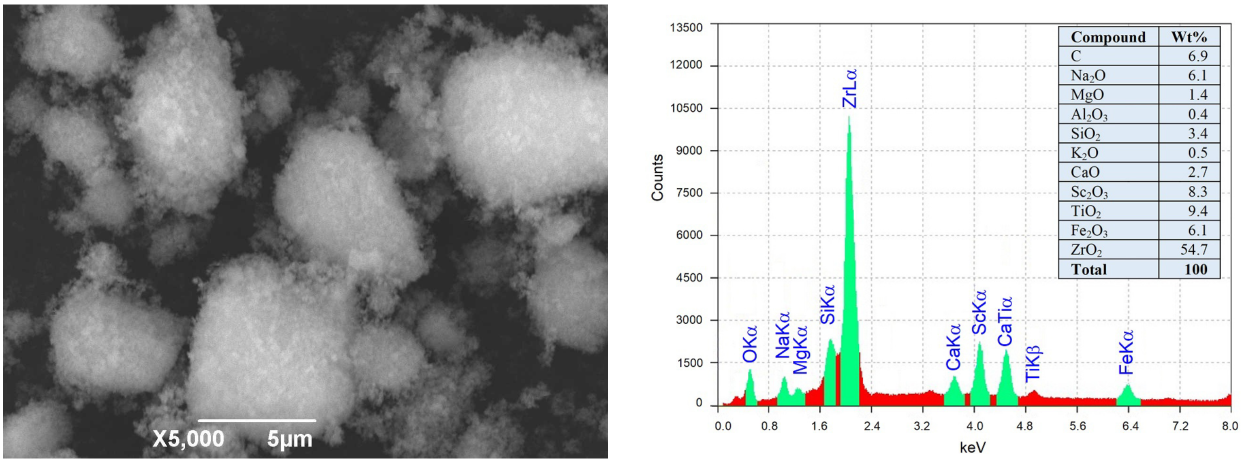

Compound	Wt%
C	6.9
Na_2O	6.1
MgO	1.4
Al_2O_3	0.4
SiO_2	3.4
K_2O	0.5
CaO	2.7
Sc_2O_3	8.3
TiO_2	9.4
Fe_2O_3	6.1
ZrO_2	54.7
Total	**100**

(a) (b)

FIG. 1. SEM images (a) and EDX-analysis (b) of initial Sc–Zr concentrate

behavior of Sc–Zr concentrate after heating at 200 °C is shown in Fig. 2a. The total mass loss is pretty much finished after annealing at 600 °C. The rest 1 – 2 % of the mass are lost during the further 9 h of annealing from 600 to 800 °C with the exposition at 800 °C. The calcination of the initial Sc–Zr concentrate for 4 h at 600 °C corresponds to complete decomposition of amorphous hydroxide and carbonate compounds ($ScCO_3OH$, $TiO(OH)_2$, $ZrO(OH)_2$, $Sc(OH)_3$, $Ti(OH)_4$, $Zr(OH)_4$, etc.). From the XRD patterns of calcined samples (Fig. 2b) it is clear that a nanosized composite of the solid solution based on c-ZrO_2 (cubic) structure (ICDD Card No. 00-054-1136, pr. gr. $\mathrm{Fm\overline{3}m}$) was obtained [23], with no apparent diffraction peaks corresponding to the m-ZrO_2 (monoclinic) phase. The lattice parameters of the fluorite structure c-ZrO_2 powders in Table 2 were estimated by the Rietveld refinements. The observed narrowing of the X-ray lines indicates an increase in the size of zirconia particles doped with scandium ions when samples annealed from 600 to 1100 °C. The average value of the crystallite size (d) was calculated from X-ray line broadening using Scherrer.

TABLE 2. Variation of the lattice parameters and crystallite size of c-ZrO_2 with the calcination temperature

T, °C	Lattice parameter		d, nm
	a, Å	V, cm^3	
600	5.04(1)	128.0(5)	9
800	5.058(6)	129.4(2)	74
1000	5.053(3)	129.0(1)	98
1100	5.074(1)	130.63(3)	>100

Except for orthorombic perovskite $CaTiO_3$, no Sc_2O_3 or other impurities were found by X-ray diffraction. These results show that scandium was successfully incorporates into the zirconia lattice by the hydrolysis so-precipitation method. At the same time other components such as iron, alumina and magnesium may also act as dopant in ScSZ for crystal structure stabilization and created functional properties [24–26]. For example, in a compositions with oxides of aluminum, chromium and iron, which are not, in the conventional sense, stabilizers of the c-ZrO_2 phase, the formation of 100 % of the cubic phase was establish [27].

For the evaluation of functional properties, the obtained Sc–Zr product was uniaxially pressed and sintered at 1100 °C. Fig. 3a presents the fractured surface morphology of sintered ScSZ ceramic, which shows that some micro pores were uniformly distributed in the area of SEM-image. As seen from Fig. 3b in BEC regime, the grain size is 1 – 3 μm for bulk Sc–Zr product.

Figure 3c demonstrates overall EDS-mapping and partial chemical components of the ceramic samples obtained by splitting. By analyzing Fig. 3c one can see that the most cations are distributed fairly evenly over the surface. It is important that this also applies to key components forming ScSZ. It is worth noting that there are some elements form separate areas, for example, iron and calcium. However, given the low concentration of most components, their presence in the selected pictures allows us to suggest that the cations are statistically distributed throughout the sample bulk.

Table 3 demonstrates compositions determined from EDX analysis (in % at.). As can be seen main component is zirconium. It is important to pay attention to the ratio of Zr and Sc as key components of the functional ceramics. This parameter lies about the value 4 that corresponds to doping state of ScSZ up to $Zr_{0.8}Sc_{0.2}O_{1.9}$. The obtained result is in

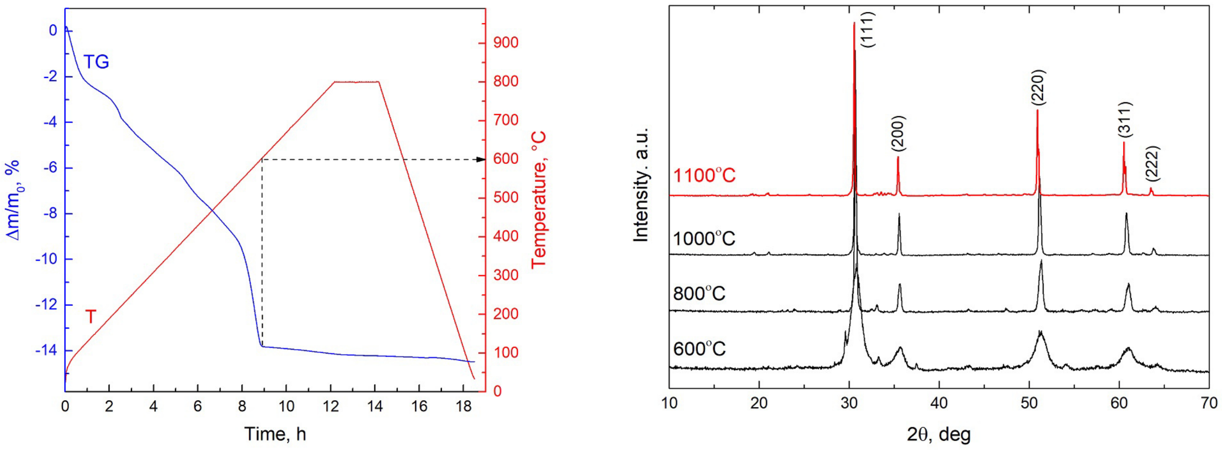

(a) (b)

FIG. 2. TG curve (a) and temperature dependent changes of XRD patterns (b) of Sc–Zr powders

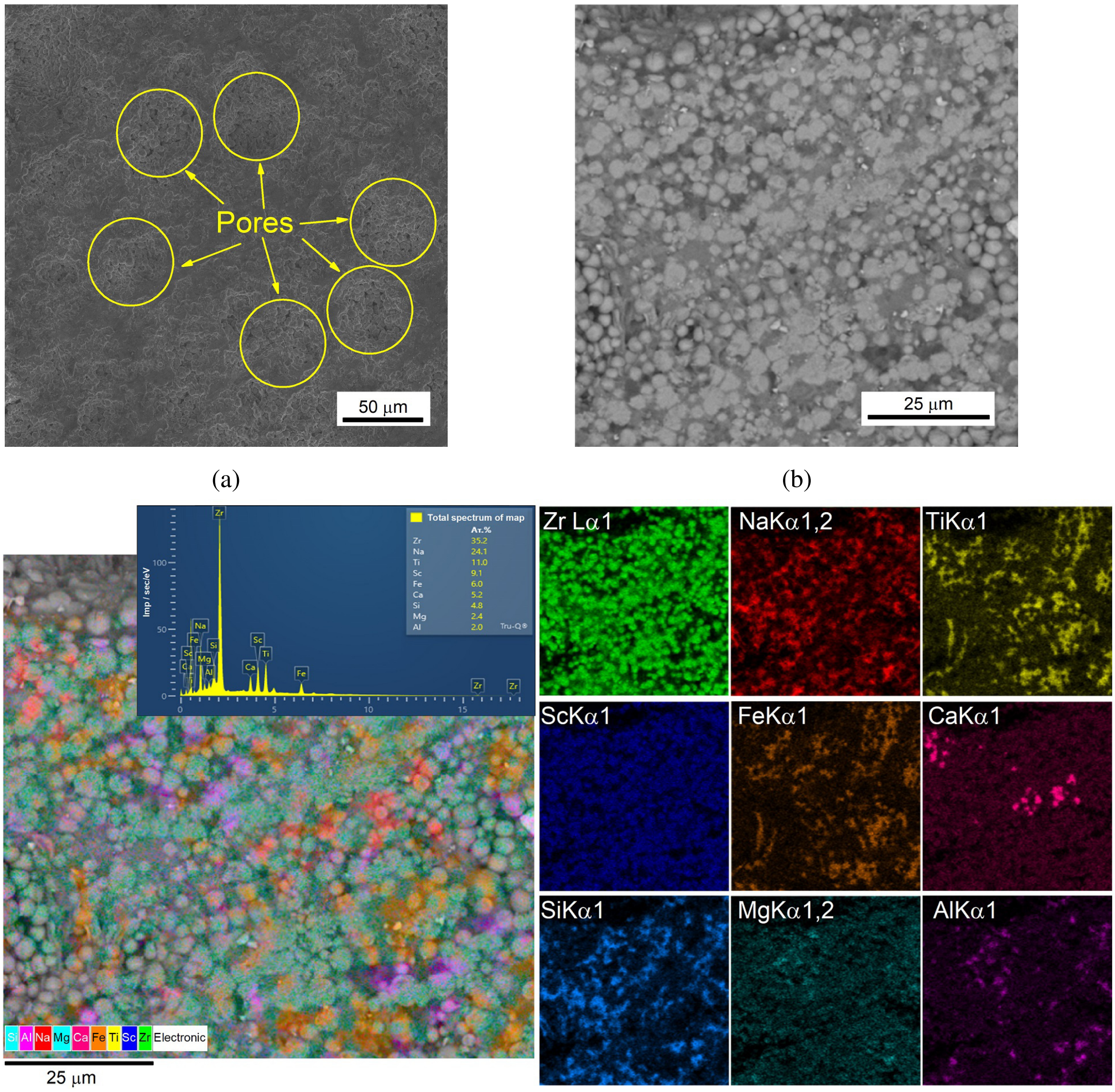

Total spectrum of map

	Aт.%
Zr	35.2
Na	24.1
Ti	11.0
Sc	9.1
Fe	6.0
Ca	5.2
Si	4.8
Mg	2.4
Al	2.0

(a) (b)

(c)

FIG. 3. Surface SEM image of the sintered bulk ScSZ material in regimes SEI (a) and BEC (b) and (c) EDX mapping with corresponding partial cationic distributions over the chipped ceramic obtained from the Sc–Zr concentrate

good agreement with XRD data and is strongly supported by work [23] where a formation of cubic fluorite ScSZ in these doping limits was distinguished as preferable. Accordingly, the applied conditions were found to permit the production of well-sintered ceramics, thereby facilitating subsequent analysis of functional properties. It is assumed that sum quantity of oxide components can act as sintering aids for zirconia ceramics (Al_2O_3, CaO, MgO, etc) [28, 29], which are used, either individually or in combination, to optimize the properties of ceramic thermal barrier coatings [30, 31].

The change for linear elongations of the studied Sc–Zr ceramics with temperature is represented in Table 4. Additionally, the values of the thermal expansion coefficients for every point k were calculated in accordance with the following formulae:

$$a_{\text{phys}}(k) = \frac{1}{L_0}\frac{d(\Delta L_k)}{dT} \quad \text{and} \quad a_{\text{tech}}(k) = \frac{1}{L_0}\frac{\Delta L_k - \Delta L_0}{T_k - T_0} \quad \text{for } (k = 1 \dots n),$$

where L_0 is the sample length at 20 °C, ΔL_k is the length change at T_k, ΔL_0 is the change in length at 20 °C (linear extrapolated out of the first data point).

TABLE 3. Chemical composition of sintered Sc–Zr ceramics obtained from EDX analysis (at %)

Element	Zr	Sc	Zr/Sc	Na	Ti	Fe	Ca	Si	Mg	Al
Content	35.2	9.1	3.89	24.1	11.0	6.0	5.2	4.8	2.4	2.0

TABLE 4. Thermal expansion coefficient values of the Sc–Zr ceramic materials

T, °C	Ceramic on $Zr_{0.8}Sc_{0.2}O_{1.9}$		14Sc_1YSZ (mol %) bulk material [32]	8Sc_1YSZ (wt %) coating [33]
	$\alpha_{\text{tech}} \cdot 10^6$, K^{-1}	$\alpha_{\text{phys}} \cdot 10^6$, K^{-1}		
500	10.78	11.91	9.7	10.65
600	10.86	11.98	9.8	10.75
700	11.37	13.11	10.05	10.80
800	11.76	14.53	10.17	10.85
900	11.93	10.55	10.30	10.80

The values of α selected at 500 – 900 °C for comparison with available literature data are provided. It should be noticed that the value of expansion coefficient is in the best coincidences with Sc doped YSZ ceramics both in the coating and in the bulk material. Thus, the present impurity components co-precipitated from the carbonate-bicarbonate solution and the phases formed during sintering did not significantly affect the thermal behavior of Sc–Zr ceramics in the studied temperature range.

4. Conclusion

Sc–Zr ceramics were obtained by ceramic technology from Sc–Zr concentrate produced by co-precipitation method after carbonation of red mud pulp. Scandium oxide was not detected as a single phase, but successfully stabilized the c-ZrO_2 structure (pr. gr. $\mathrm{Fm\overline{3}m}$) by substitution during sintering of Sc–Zr concentrate. Despite the fact that the main mass loss practically was finished at temperatures above 600 °C the crystallization of scandium-stabilized zirconia continues up to 1100 °C. Analysis of Sc–Zr ceramic has shown that the scandium distribution along the surface is homogeneous and the Sc_2O_3 amount regarding zirconia is almost identical to its content in the concentrate. In conclusion, we have shown that the thermal expansion coefficient values of the ceramic on $Zr_{0.8}Sc_{0.2}O_{1.9}$ phase in the temperature range of 500 – 900 °C are much like to the values for materials from co-doped Sc and Y zirconia. The impurities did not significantly affect the phase composition and thermal behavior of Sc–Zr ceramics obtained by a simple and inexpensive way from the metallurgical waste.

References

[1] Liu Q., Huang, S., He, A. Composite ceramics thermal barrier coatings of yttria stabilized zirconia for aero-engines. *J. Mater. Sci. Technol*, 2019, **35**, P. 2814–2823.

[2] Vinchhi P., et al. Recent advances on electrolyte materials for SOFC: A review. *Inorg. Chem. Commun.*, 2023, **152**, 110724.

[3] Soon G., et al. Review of zirconia-based bioceramic: Surface modification and cellular response. *Ceram. Int.*, 2016, **42**, P. 12543–12555.

[4] Basahel S.N., et al. Influence of crystal structure of nanosized ZrO_2 on photocatalytic degradation of methyl orange. *Nanoscale Res. Lett.*, 2015, **10**, 73.

[5] Pushpalatha S., et al. Green synthesis of cellulose/ZrO_2 nanocomposite: assessment of antibacterial and photocatalytic activity. *Biomass Convers. Biorefinery*, 2024.

[6] Chitoria A.K., Mir A., Shah M.A. A review of ZrO_2 nanoparticles applications and recent advancements. *Ceram. Int.*, 2023, **49**, P. 32343–32358.

[7] Arifin N.A., et al. Characteristic and challenges of scandia stabilized zirconia as solid oxide fuel cell material – In depth review. *Solid State Ion.*, 2023, **399**, 116302.

[8] Zamudio-García J., et al. Exploring alkali metal doping in solid oxide cells materials: A comprehensive review. *Chem. Eng. J.*, 2024, **493**, 152832.

[9] Danilenko I., et al. Do smaller oxide particles sinter worse? Paradoxes of the initial stages of sintering of zirconia nanoparticles. *Results Phys.*, **42**, 2022, 106027.

[10] Du Z., et al. Size effects and shape memory properties in ZrO_2 ceramic micro- and nano-pillars. *Scr. Mater.*, 2015, **101**, P. 40–43.

[11] Wang Y., et al. Failure analysis of fine-lamellar structured YSZ based thermal barrier coatings with submicro/nano-grains. *Surf. Coat. Technol.*, 2017, **319**, P. 95–103.

[12] Sodeoka S., et al. Thermal and mechanical properties of ZrO_2–CeO_2 plasma-sprayed coatings. *J. Therm. Spray Technol.*, 1997, **6**, P. 361–367.

[13] Chatterjee M., Naskar M.K., Ganguli D. Sol-emulsion-gel synthesis of alumina-zirconia composite microspheres. *J. Sol-Gel Sci. Technol.*, 2003, **28**, P. 217–225.

[14] Liang S., et al. Scalable preparation of hollow ZrO_2 microspheres through a liquid-liquid phase reunion assisted sol-gel method. *Ceram. Int.*, 2020, **46**, P. 14188–14194.

[15] Falcony C., Aguilar-Frutis M.A., García-Hipólito M. Spray pyrolysis technique; high-k dielectric films and luminescent materials: A Review. *Micromachines*, 2018, **9**, 414.

[16] Liu L., et al. Supercritical hydrothermal synthesis of nano-ZrO_2: Influence of technological parameters and mechanism. *J. Alloys Compd.*, 2022, **898**, 162878.

[17] Mosavari M., Khajehhaghverdi A., Mehdinavaz Aghdam R. Nano-ZrO_2: A review on synthesis methodologies. *Inorg. Chem. Commun.*, 2023, **157**, 111293.

[18] Buinachev S., et al. A new approach for the synthesis of monodisperse zirconia powders with controlled particle size. *Int. J. Hydrog. Energy*, 2021, **46**, P. 16878–16887.

[19] Pasechnik L.A., et al. High purity scandium extraction from red mud by novel simple technology. *Hydrometallurgy*, **202**, 2021, 105597.

[20] Chanturia V.A., Samusev A.L., Minenko V.G., Kozhevnikov G.A. Rare metal and rare earth recovery from silica gel-eudialyte concentrate leaching product. *J. Min. Sci.*, **57**, 2021, P. 1006–1013.

[21] Vobenkaul D., et al. Hydrometallurgical processing of eudialyte bearing concentrates to recover rare earth elements via low-temperature dry digestion to prevent the silica gel formation. *J. Sustain. Metall.*, 2017, **3**, P. 79–89.

[22] Pyagay I.N., et al. Carbonization processing of bauxite residue as an alternative rare metal recovery process. *Tsvetnye Met.*, 2020, P. 56–63.

[23] Xue Q., et al. Effects of Sc doping on phase stability of $Zr_{1-x}Sc_xO_2$ and phase transition mechanism: First-principles calculations and Rietveld refinement. *Mater. Des.*, 2017, **114**, P. 297–302.

[24] Nakajima H., et al. Effects of Fe doping on crystalline and optical properties of yttria-stabilized zirconia. *J. Phys. Chem. Solids*, 2007, **68**, P. 1946–1950.

[25] Hassan A.A.E., et al. Influence of alumina dopant on the properties of yttria-stabilized zirconia for SOFC applications. *J. Mater. Sci.*, 2002, **37**, P. 3467–3475.

[26] Rong T.J., et al. State of magnesia in magnesia (10.4 mol %)-doped zirconia powder prepared from coprecipitation. *J. Am. Ceram. Soc.*, 2002, **85**, P. 1324–1326.

[27] Danilenko I., et al. Determination of the nature of the co-doping effect on the structure, mechanical properties and ionic conductivity of SOFC electrolyte based on YSZ. *Solid State Ion.*, 2024, **412**, 116581.

[28] Flegler A.J., et al. Cubic yttria stabilized zirconia sintering additive impacts: A comparative study. *Ceram. Int.*, 2014, **40**, P. 16323–16335.

[29] Hbaieb K., et al. Reducing sintering temperature of yttria stabilized zirconia through addition of lithium nitrate and alumina. *Ceram. Int.*, 2012, **38**, P. 4159–4164.

[30] Zhang X., et al. Structural evolution of Al-modified PS-PVD 7YSZ TBCs in thermal cycling. *Ceram. Int.*, 2019, **45** (6), P. 7560–7567.

[31] Zhu D., et al. Furnace cyclic oxidation behavior of multicomponent low conductivity thermal barrier coatings. *J. Therm. Spray Technol.*, 2004, **13**, P. 84–92.

[32] Fan W., et al. Improved properties of scandia and yttria co-doped zirconia as a potential thermal barrier material for high temperature applications. *J. Eur. Ceram. Soc.*, 2018, **38**, P. 4502–4511.

[33] Zu J.H., et al. Preparation and high-temperature performance of Sc_2O_3–Y_2O_3 co-stabilized ZrO_2 thermal barrier coatings. *Ceram. Int.*, 2024, **50**, P. 20460–20472.

Submitted 13 September 2024; accepted 17 October 2024

Information about the authors:

Liliya A. Pasechnik – Institute of Solid State Chemistry UB RAS, Pervomayskaya, 91 Ekaterinburg 620108, Russia; ORCID 0000-0002-0631-5287; pasechnik@ihim.uran.ru

Irina S. Medyankina – Institute of Solid State Chemistry UB RAS, Pervomayskaya, 91 Ekaterinburg 620108, Russia; ORCID 0000-0002-8636-3755; lysira90@mail.ru

Danil I. Pereverzev – Institute of Solid State Chemistry UB RAS, Pervomayskaya, 91 Ekaterinburg 620108, Russia; ORCID 0000-0002-5678-4970; danil_per@mail.ru

Alexander Yu. Chufarov – Institute of Solid State Chemistry UB RAS, Pervomayskaya, 91 Ekaterinburg 620108, Russia; ORCID 0000-0003-3667-144X; circulchufa@gmail.com

Alexey Yu. Suntsov – Institute of Solid State Chemistry UB RAS, Pervomayskaya, 91 Ekaterinburg 620108, Russia; ORCID 0000-0002-3488-1454; suntsov@ihim.uran.ru

Conflict of interest: the authors declare no conflict of interest.

NANOSYSTEMS:
PHYSICS, CHEMISTRY, MATHEMATICS

Original article

Guskov A.V., et al. *Nanosystems: Phys. Chem. Math.*, 2024, **15** (6), 774–780.
http://nanojournal.ifmo.ru
DOI 10.17586/2220-8054-2024-15-6-774-780

Synthesis of gadolinium titanate based nanocrystalline multicomponent rare earth oxides

Anton V. Guskov, Pavel G. Gagarin , Vladimir N. Guskov, Konstsntin S. Gavrichev

Kurnakov Institute General and Inorganic Chemistry Russian Academy of Sciences, Moscow, Russia

Corresponding author: V.N. Guskov, guskov@igic.ras.ru

ABSTRACT Optimal conditions for the synthesis of single-phase crystalline and nanocrystalline multicomponent oxides based on pyrochlore structure gadolinium titanate have been determined. The parameters of cubic lattices were determined and the morphology of the surface of RE titanates was studied.

KEYWORDS retitanates, synthesis, nanocrystalline pyrochlore

ACKNOWLEDGEMENTS This study was carried out in the frameworks of research project “Solving the actual problems using charged particle beams of the NICA complex” (State assignment No. 1024050300012-6-1.4.2)

FOR CITATION Guskov A.V., Gagarin P.G., Guskov V.N., Gavrichev K.S. Synthesis of gadolinium titanate based nanocrystalline multicomponent rare earth oxides. *Nanosystems: Phys. Chem. Math.*, 2024, **15** (6), 774–780.

1. Introduction

Mixed oxides of composition $RE_2B_2O_7$ (RE=rare-earth elements, B=Ti, Zr, Hf) with pyrochlore structure type (*Fd3m*) are characterized by a high melting point and absence of structural phase transitions in a wide temperature range of existence, with the exception of disordering occurring at temperatures above 1800 °C and transformation into a phase of defective fluorite (*Fm3m*) [1–3]. High chemical and thermal stability of these substances, as well as low thermal conductivity, allows them to be considered as materials for thermal barrier coatings [4, 5], solid electrolytes for SOFC [6], as well as scintillators, phosphors and dielectrics [7, 8]. In addition, pyrochlores are recognized as the most promising materials for the immobilization of actinides in the nuclear fuel cycle due to their low solubility in acids and water and resistance to radiation exposure [9–11]. Actinides (3+) are able to replace the rare earth element in the RE position, while (4+) actinides can be placed in the B position. In any case, the internal decay of radionuclides leads to the transition of the matrix to an amorphous state as defects accumulate [12], which can lead to the actinides release. Radiation damage modeling and determination of maximum doses are carried out based on the results of irradiation with heavy ion beams [13]. These studies have demonstrated that the effects of radiation depend both on the ratio of the radii of r(RE^{3+})/r(B^{4+}) cations, since the probability of amorphization increases with its increase, and on the nature of cation B, since replacing Ti^{+4} with Zr^{+4} increases radiation resistance [14–16].

At the same time, zirconates of “heavy” lanthanides having the structure of defective fluorite, i.e. $Er_2O_3 \cdot 2ZrO_2$, retain their crystalline structure at higher doses of radiation and turn out to be more radiation-resistant materials than pyrochlores. (Here it should be noted that zirconates and hafnates of “heavy” lanthanides and yttrium are solid solutions with a wide homogeneity range based on cubic zirconium dioxide and should be represented as $(1-x)RE_2O_3 \cdot 2xZrO_2$, $x \sim 0.4 - 1.0$, and the writing $RE_2Zr_2O_7$ adopted in a number of articles for Ln=Tb–Lu and Y, i.e. $x = 0.5$, is in fact not correct [17].)

Modeling of defect formation under the action of ionizing radiation confirms the general concept of the relative stability of pyrochlores, but does not take into account such phenomena as dynamic annealing, migration and recombination of defects under the action of radiation, and also does not explain the influence of the size of the RE^{+3} cation and the type of crystal structure [14]. The influence of the degree of crystallinity of the material is also unknown. The studies carried out in [16] showed the existence of a critical amorphization temperature T_c, above which rapid recrystallization of radiation damage occurs, and amorphization of the sample is not proceed due to kinetic reasons. An important consequence of the work [16] results is that the critical temperature of amorphization increases with an increase in the mass of a heavy ion, creating a larger cascade of damage. Titanates of rare earth elements are convenient objects for studying the effects of heavy ion beams due to their cubic structure, relatively wide area of homogeneity and satisfactory response to radiation exposure [18]. In [14], a systematic determination of the amorphization temperature of a number of single-crystal lanthanide (Sm–Lu) and yttrium titanates of the pyrochlore structural type was performed under the action of a Kr^+ beam with an energy of 1 MeV. It was found that gadolinium titanate ($T_c = 1120$ K) has the highest amorphization temperature, which decreases both with an increase in the radius of the rare earth element to samarium titanate ($T_c = 1045$ K) and with a decrease in the radius of RE^{+3} during the transition from gadolinium to lutetium titanate ($T_c = 480$ K). A decrease in the critical temperature of amorphization means an increase in resistance to radiation damage. From this fact, it was concluded in [14] that pyrochlores, which are closer to the ideal structure of fluorite, are also more resistant to ion beam amorphization. The authors [14] attribute the unusual behavior of T_c in a series of titanates not only to a change in RE^{3+} radius, but also to a change in the nature of the chemical bond, which, as stated, depends on the degree of filling of the $4f$ electron shell: in gadolinium, it is half filled, and in lutetium it is completely filled. Determination of the enthalpy of formation of lanthanide titanates and yttrium $RE_2Ti_2O_7$ [19] by the measuring of enthalpy of dissolution in oxide melt showed that with a decrease in the radius of the RE^{3+} ion, the enthalpy stability of titanates with respect to simple oxides decreases and correlates with the amorphization temperatures given in [14]. Recently, special attention has been paid to new materials based on multicomponent solid solutions of oxides for use in extreme conditions, including for the immobilization of radioactive waste, since the introduction of several various cations leads to defects of the crystal lattice that prevent the accumulation of damage in materials and stop the spread of 1-D defects [20]. An increase in the stability of such materials is achieved by reducing the Gibbs free energy owing to an increase in the configuration entropy due to an increase in the number of components of the solid solution. At the same time, varying the number and ratio of components allows you to control the functional properties of materials, limit grain growth, reduce thermal conductivity due to phonon scattering, and increase thermal and radiation stability. Traditionally, three- and four-component solid solutions are considered to be "middle entropy", and five- and higher – "highentropy" [21]. In [22], the effect of a 3 MeV beam of Au^{2+} ions on medium- and multicomponent pyrochlores based on gadolinium titanate was studied and it was found that with an increase in the dose load, the structure of pyrochlore turns into defective fluorite, and then amorphization occurs, and high entropy pyrochlore $(GdDyHoErYb)_{2/5}Ti_2O_7$ showed the minimum tendency to amorphization. Authors concluded that the greatest influence on depreciation is exerted not by the entropy factor, but by the ratio of the radii of $r(RE^{3+})/r(B^{4+})$ cations. The effects of heavy ion beams on the nanocrystalline structures of simple and complex titanates remained outside the scope of the studies considered, although nanocrystalline substances are characterized by increased Gibbs energy, and, therefore, should have a reduced amorphization temperature T_c of relatively well-crystallized oxides, moreover, it is unknown whether irradiation will lead to amorphization of nanocrystalline matter or, conversely, to recrystallization, according to at least at the initial stage.

The goal of this study was to develop a method for the synthesis of "high-entropy titanates" for subsequent experiments to study amorphization under the action of a high-energy heavy ion beams conducted within the framework of the ARIADNA project: applied Research at the NICA complex.

2. Experimental

To carry out such research, it is necessary to determine the optimal method for the synthesis of nanocrystalline titanates. As is known, during the synthesis of lanthanide zirconates or hafnates by "reverse" deposition followed by annealing at a high temperature (800 – 1300 °C), a nanoscale fluorite-like phase is formed, and calcination at temperatures > 1500 °C is required for the complete interaction of the components and the formation of crystalline pyrochlores [17, 23, 24]. The method is convenient because it allows you to control the synthesis at all stages – from the synthesis of a hydroxide precursor of a given composition to the intermediate stages of heat treatment.

The $TiOSO_4 \cdot xH_2O$ (Sigma-Aldrich 99.99 wt.%), Gd_2O_3 (99.998 wt. %), Sm_2O_3 (99.998 wt. %), Dy_2O_3 (99.998 wt. %) and Tb_2O_3 (99.998 wt. %) LANHIT, Y_2O_3 (99.998 wt. %), hydrochloric acid (35 – 38 wt. % HCl, Os. Ch. qualification) and ammonia solution (25 – 28 wt. % NH_4OH) produced by KHIMMED were used as starting materials for the synthesis of gadolinium titanate-based samples. A simultaneous thermal analysis unit STA 449F1 Jupiter (NETZSCH-Gerätebaug GmbH) was used for thermal analysis using the DSC/TG method, and X-ray phase analysis was performed using a diffractometer D8 Advance (CuKa, $\lambda = 1.5418$ Å, Ni filter, LYNXEYE detector, reflection geometry) in the angle range $2\theta = 10° – 80°$. The morphology of the samples was studied using a TESCAN AMBER electron microscope with a Bright Beam non-immersion column and an ultra-high resolution of 1.3 nm at an accelerating voltage of 1 kV. The data [25] were used to calculate the molar masses of the samples, and average radii of the cations were estimated using the recommended in [26] values.

3. Results and discussion

Multicomponent oxides based on gadolinium titanate, samarium, terbium and dysprosium, as well as yttrium, were selected for the research (Table 1), in contrast to the work [22], where additional elements to gadolinium were Dy, Ho, Er, Yb and Nd. The choice of additional elements in this study, as in [22], is quite arbitrary, however, it must satisfy the condition $1.46 < r(RE^{3+})/r(B^{4+}) < 1.78$ for the implementation of the *Fd3m* pyrochlore structure [1]. Low values (<1.46) are typical for the structural type of defective fluorite *Fm3m*, and higher values (>1.78) are typical for the monoclinic perovskite lattice *P21*.

To carry out the synthesis, titanyl sulfate was dissolved in water, and oxides of rare earths were dissolved in hydrochloric acid. The molal concentration of metals in solutions in terms of oxides were determined by the weight method, precipitating metal hydroxides with an aqueous solution of ammonia, followed by drying and calcination to a temperature of 1000 °C. The weight method of initial solutions mixing allows you to more accurately obtain the stoichiometric ratio of metals. (The use of molal concentrations, firstly, is due to the possibility of using more concentrated solutions due to the fact that the accuracy of weighing significantly exceeds the accuracy of determining volume, and, secondly,

TABLE 1. Composition of studied specimens, molar mass, middle ionic radius RE^{3+} (CN=8), ratio of cationic radiir (RE^{3+})/r(B^{4+}), calculated and experimental unit cell parameters of pyrochlore structure (a) and maximum temperatures of transition in DSC curves

Composition	Molar mass, g-mol	Middle radius r(RE^{+3}), Å	r(RE^{+3})/ r(Ti^{+4})	Lattice parameter a, Å		DSC $t_{\max}$, °C
				Calc. from [27]	Experiment	
$Gd_2Ti_2O_7$	522.2298	1.053	1.74	10.1838(2)	10.185(1)	838
$GdSmTi_2O_7$	515.3398	1.066	1.76	10.2074	10.198(3)	824
$Gd_{2/3}Sm_{2/3}Y_{2/3}Ti_2O_7$	472.0737	1.050	1.74	10.1698	10.169(9)	813
$Gd_{1/2}Sm_{1/2}Y_{1/2}Dy_{1/2}Ti_2O_7$	487.23773	1.044	1.73	10.1607	10.162(7)	806
$Gd_{2/5}Sm_{2/5}Y_{2/5}Dy_{2/5}Tb_{2/5}Ti_2O_7$	494.90628	1.043	1.72	10.1588	10.159(1)	809

molal concentrations are temperature independent). The prepared solution was added dropwise with intensive stirring to a concentrated ammonia solution taken in excess. The sediment was washed, centrifuged and dried at 90 °C for 72 hours. Samples of the obtained substances were studied by DSC/TG analysis to determine the temperature stages of formation of crystalline pyrochlores from pre-dried hydroxides, Fig. 1.

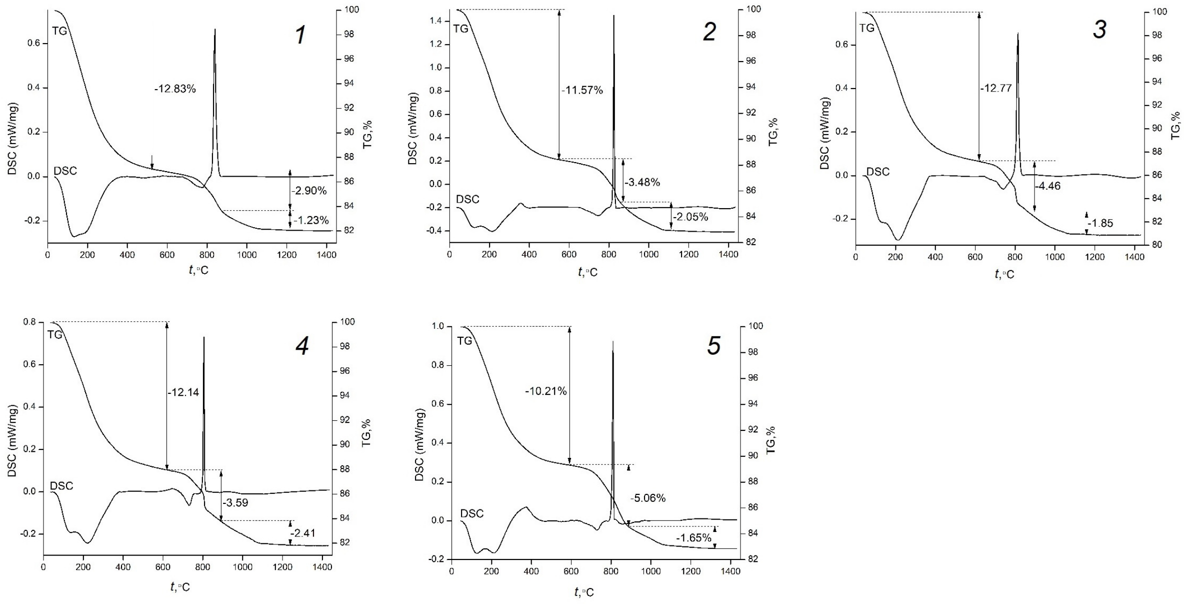

FIG. 1. DSC/TG curves of dried hydroxide precursors: 1) $Gd_2Ti_2O_7$, 2) $GdSmTi_2O_7$, 3) $Gd_{2/3}Sm_{2/3}Y_{2/3}Ti_2O_7$, 4) $Gd_{1/2}Sm_{1/2}Y_{1/2}Dy_{1/2}Ti_2O_7$, 5) $Gd_{2/5}Sm_{2/5}Y_{2/5}Dy_{2/5}Tb_{2/5}Ti_2O_7$

The common view of the DSC/TG heating curves (Fig. 1) for all 5 samples is similar and can be subdivided into 3 stages: at the first stage of heating (75 – 500 °C), an endothermic effect is observed, which is accompanied by a loss of mass corresponding to $\sim$ 2.5 – 3 water molecules per mole of the substance. Further heating (the second stage) from 500 to 900 °C is accompanied by dehydroxylation with a loss of $\sim$ 1.5 – 2 H_2O, while in the region of 800 – 850 °C there is a sharp exothermic effect corresponding to the formation of hydroxylated pyrochlore of the probable composition $RE_2Ti_2O_6 \cdot 5OH$, and the temperature of the maximum $t_{\max}$ of transformation decreases slightly with an increase in the number of RE-elements (Table 1). The residual hydroxyl group is revealed only at the third stage in the range of $\sim$ 900 – 1000 °C to form compounds of the structural type of pyrochlore $RE_2Ti_2O_7$. Unlike the RE_2O_3–ZrO_2 and RE_2O_3–HfO_2 systems, in which, with this synthesis method and these temperatures, a nanoscale metastable phase of the structural type of disordered fluorite is formed [17,23,24], in the Gd_2O_3–TiO_2 system, a fluorite-like phase is not found either in a stable or metastable state [28]. To determine the sequence of processes occurring during the heating of precursors, samples of dried precursors were calcinated for 2 hours at 700, 1000 and 1500 °C, and were studied by X-ray diffraction phase analysis. Fig. 2 shows XRD patterns of the annealed $Gd_2Ti_2O_7$ sample. As can be seen, at 700 °C (curve 1), a pattern typical for the amorphous state of the sample is observed. Calcination of the samples above the component interaction temperature (1000 °C, curve 2) leads to the formation of a sample of the structural type of pyrochlore, as evidenced by the characteristic diffraction reflections 111, 311, 331 and 511. At the same time, the size of the crystallites (according to the results of the Debye–Scherrer evaluation) is about 35 nm, which corresponds to the range of nanoscales ($<$ 100 nm). And finally, annealing at 1500 °C (curve 3) leads to a significant change in diffractograms, associated with the formation of narrower and more pronounced reflexes, which indicates satisfactory crystallization of the sample and on the size of the crystallites beyond the nanoscale region.

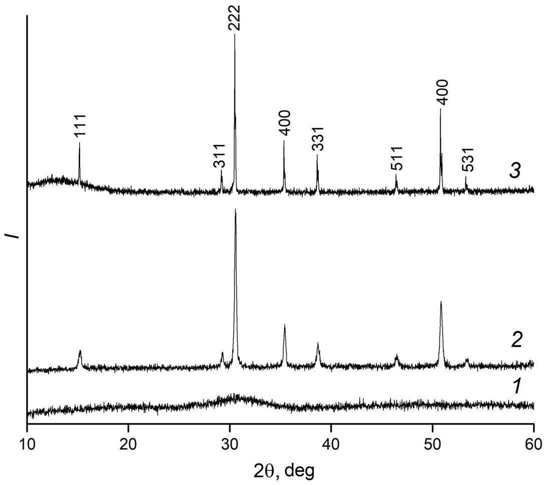

FIG. 2. XRD patterns of $Gd_2Ti_2O_7$ precursor annealed at 1 –700 °C, 2 – 1000 °C, 3 – 1500 °C

Diffraction studies performed for all samples of solid solutions of RE titanates prepared at a temperature of 1000 °C are shown in Fig. 3. They confirm the formation of single-phase crystalline compounds of the pyrochlore structural type. It must be note that in the case of multicomponent compounds and solid solutions, it is not possible to use the Debye–Scherrer approximation to estimate the size of coherent scattering regions due to distortions of the crystal lattice leading to broadening of diffraction reflections. A comparison of these results with the diffractograms shown in Fig. 4 of samples well crystallized by annealing at 1500 °C indicates a possible nanoscale particle size of specimens obtained at 1000 °C. It is possible to confirm the size of synthesized samples by conducting scanning electron microscopy (SEM) studies. Scanning microscopy of the surface of powdered samples annealed at 1000 °C (Fig. 5), even with the maximum magnification available for these substances of 80,000× does not allow to assess the size of the crystallites due to the nanoscale state of the samples, whereas after annealing at a temperature of 1500 °C, larger particles ($>$ 100 nm) form a monolithic (and, probably, gas-tight) surface structure (Fig. 6).

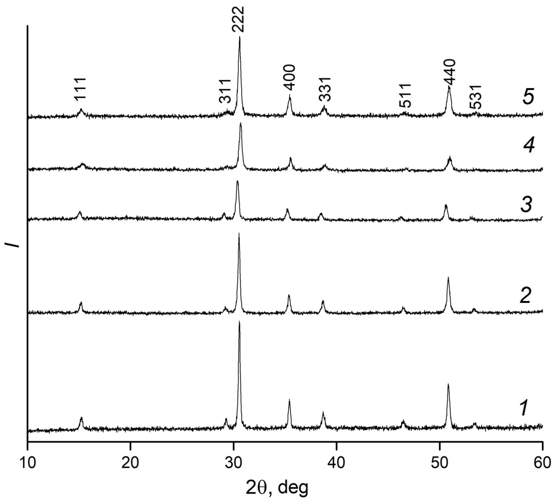

FIG. 3. XRD patterns for annealed at 1000 °C RE titanates: 1) $Gd_2Ti_2O_7$, 2) $GdSmTi_2O_7$, 3) $Gd_{2/3}Sm_{2/3}Y_{2/3}Ti_2O_7$, 4) $Gd_{1/2}Sm_{1/2}Y_{1/2}Dy_{1/2}Ti_2O_7$, 5) $Gd_{2/5}Sm_{2/5}Y_{2/5}Dy_{2/5}Tb_{2/5}Ti_2O_7$

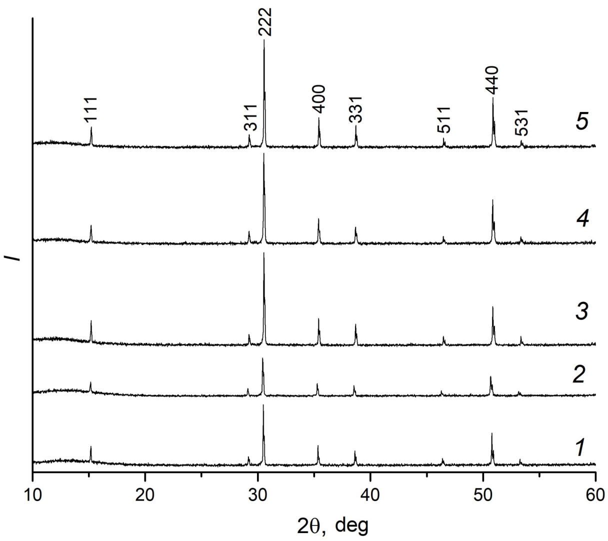

FIG. 4. XRD patterns of RE titanates annealed at 1500 °C: 1) $Gd_2Ti_2O_7$, 2) $GdSmTi_2O_7$, 3) $Gd_{2/3}Sm_{2/3}Y_{2/3}Ti_2O_7$, 4) $Gd_{1/2}Sm_{1/2}Y_{1/2}Dy_{1/2}Ti_2O_7$, 5) $Gd_{2/5}Sm_{2/5}Y_{2/5}Dy_{2/5}Tb_{2/5}Ti_2O_7$

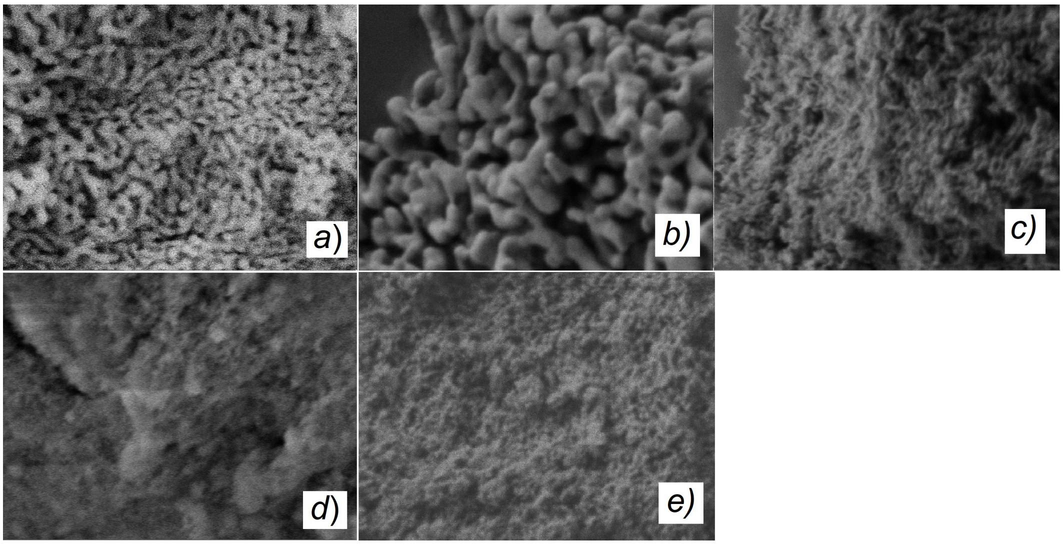

FIG. 5. Surface morphology of specimens annealed at 1000 °C: a) $Gd_2Ti_2O_7$, b) $GdSmTi_2O_7$, c) $Gd_{2/3}Sm_{2/3}Y_{2/3}Ti_2O_7$, d) $Gd_{1/2}Sm_{1/2}Y_{1/2}Dy_{1/2}Ti_2O_7$, e) $Gd_{2/5}Sm_{2/5}Y_{2/5}Dy_{2/5}Tb_{2/5}Ti_2O_7$, ×80 000

4. Conclusions

The sequence of phase transformations during the formation of nanoscale gadolinium titanate based multicomponent oxides of rare earth elements with a pyrochlore structure was determined as a result of the conducted investigations. The temperature ranges of separate stages of process of their formation were determined.

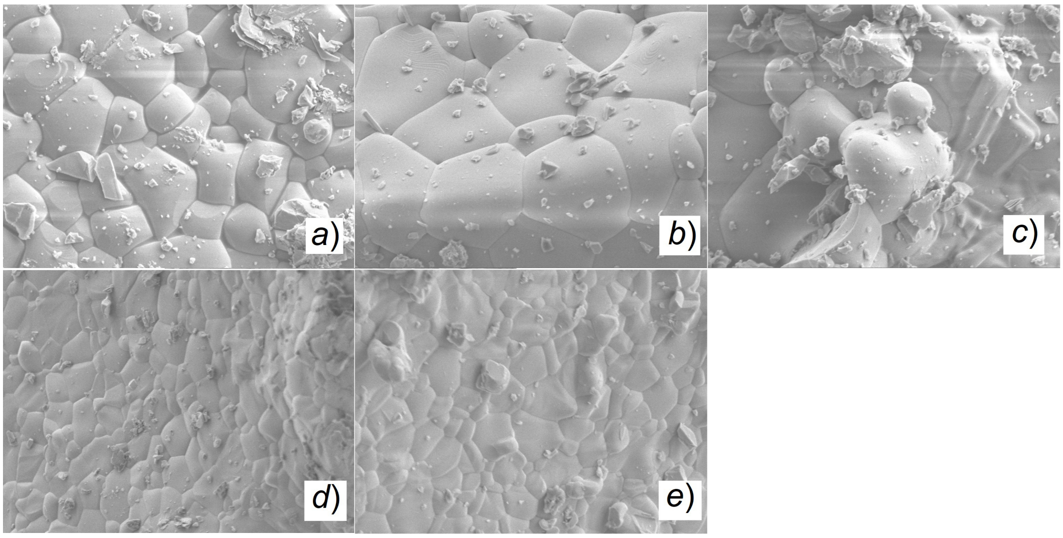

FIG. 6. Surface morphology of specimens annealed at 1500 °C: a) $Gd_2Ti_2O_7$, b) $GdSmTi_2O_7$, c) $Gd_{2/3}Sm_{2/3}Y_{2/3}Ti_2O_7$, d) $Gd_{1/2}Sm_{1/2}Y_{1/2}Dy_{1/2}Ti_2O_7$, e) $Gd_{2/5}Sm_{2/5}Y_{2/5}Dy_{2/5}Tb_{2/5}Ti_2O_7$, ×30 000

References

[1] Andrievskaya E.R. Phase equilibria in the refractory oxide systems of zirconia, hafnia and yttria with rare-earth oxides. *J. Europ. Ceram. Soc.*, 2008, **28**, P. 2363–2388.

[2] Komissarova L.N., Shatsky V.M., Pushkina G.Ya, Scherbakova L.G., Mamsurova L.G., Sukhanova G.E. *Rare-earth compounds. Carbonates, oxalates, nitrates, titanates*. Nauka Publ. Co. 1984. 235 p.

[3] Subramanian M.A., Aravamudan G., Subba Rao G.V. Oxide pyrochlores—A review. *Prog. Solid State Chem.*, 1983, **15**, P. 55–143 .

[4] Clarke D. R., Phillpot S. R. Thermal barrier coating materials. *Materials Today*, 2005, **8**, P. 22–29.

[5] Vaßen R., Jarligo M.O., Steinke T., Mack D.E., Stöver D. Overview on advanced thermal barrier coatings. *Surf. Coat. Tech.*, 2010, **205**, P. 938–942.

[6] Yamamura H. Electrical conductivity anomaly around fluorite-pyrochlore phase boundary. *Solid State Ionics*, 2003, **158**, P. 359–365.

[7] Brixner L.H. Structural and luminescent properties of the $Ln_2Hf_2O_7$-type rare earth hafnates. *Mater. Res. Bull.*, 1984, **19**, P. 143–149.

[8] Ji Y., Jiang D., Shi J. $La_2Hf_2O_7$:Ti^{4+} ceramic scintillator for X-ray imaging. *J. Mater. Res.*, 2005, **20**, P. 567–570.

[9] Ewing R.C., Weber W.J., Lian J. Nuclear waste disposa lpyrochlore ($A_2B_2O_7$): nuclear waste form for the immobilization of plutonium and “minor” actinides. *J. Appl. Phys.*, 2004, **95**, P. 5949–5971.

[10] McMaster S.A., Ram R., Faris N., Powenceby M.I. Radionuclide disposal using the pyrochlore supergroup of minerals as a host matrix. A review. *J. Hazard Mater.*, 2018, **360**, P. 257–269.

[11] Wang Y., Jing C., Ding Z.Y., Zhang Y.Z., Wei T., Quang J.H., Liu Z.G., Wang Y.-J., Wang Y.-M. The structure, property, and ion irradiation effects of pyrochlores: a comprehensive review. *Crystals*, 2003, **13**.

[12] Weber W.J., Ewing R.C., Plutonium immobilizationand radiation effects. *Science*, 2000, **289** (5787), P. 2051–2052.

[13] Lu X., Shu X., Wang L., Shao D., Zhang H., Zhang K., Xie Y. Heavy-ion irradiation effects on $Gd_2Zr_2O_7$ ceramics bearing complex nuclear waste. *J. Alloys Compd.*, 2019, **771**, P. 973–979.

[14] Lian J., Chen J., Wang L.M., Ewing R.C. Radiation-induced amorphization of rare-earh titanate pyrochlores. *Phys. Rev. B*, 2003, **68**, 134107.

[15] Sickafu K.E., Minervini I. Grimes R.W., Valdez J.A., Ishimaru M., Li F., McClellan K.J. Radiation tolerance of complex oxides. *Science*, 2000, **289** (5480), P. 748–751.

[16] Wang S.X., Wang L.M., Ewing R.C., Govindan Kutti K.V. Ion irradiation effects for two pyrochlore compositions: $Gd_2Ti_2O_7$ and $Gd_2Zr_2O_7$. *Mat. Res. Soc. Symp. Proc.*, 1998, **540**, P. 355–360.

[17] Guskov V.N., Gavrichev K.S., Gagarin P.G., Guskov A.V. Thermodynamic function of complex zirconia based lanthanide oxides-pyrochlores $Ln_2Zr_2O_7$ (Ln=La, Pr, Sm, Eu, Gd) and fluorites $Ln_2O_3 \cdot 2ZrO_2$ (Ln=Tb, Ho, Er, Tm). *Russ. J. Inorg. Chem.*, 2019, **64**, P. 1265–1281.

[18] Yang D.Y., Xu C.P., Fu C.G., Zhang K.Q., Wang Y.Q., Li Y.H. Structure and radiation effect of Er-stuffed pyrochlore $Er_2(Ti_{2-x}Er_x)O_{7-x/2}$ ($x = 0 - 0.667$). *Nucl. Instr. Meth. Phys. Res B*, 2015, **356–357**, P. 69–74.

[19] Helean K.B., Ushakov S.V., Brown C.E., Navrotsky A., Lian J., Ewing R.C., Farmer J.M., Boatner L.A. Formation enthalpies of rare earth titanate pyrochlores. *J. Sol. State Chem.*, 2004, **177**, P. 1858–1866.

[20] Ward T.Z., Wilkerson R.P., Muziko B.L., Foley A., Brahleg M., Weber W.J., Sickafus K.E., Mazza A.R. High entropy ceramics for applications in extreme environments. *J. Phys.: Mater.*, 2024, **7**, 021001.

[21] Yeh J.W., Chen S.K., Lin S.J., Gan J.Y., Chin T.S., Shun T.T., Tsau C.H. Nanostructured high-entropy alloys with multiple principale: novel alloy design concepts and outcomes. *Advance Eng. Mater.*, 2004, **6**, P. 299–303.

[22] Guo H., Zhang K., Li Y. Heavy-ion irradiation effects of high-entropy $A_2Ti_2O_7$ pyrochlore with multi-elements at site. *Ceram. Int.*, 2024, **50**, P. 21859–21868.

[23] Gagarin P.G., Tyurin A.V., Guskov V.N., Khoroshilov A.V., Nikiforova G.E., Gavrichev K.S. Thermodynamic properties of p-$Sm_2Zr_2O_7$. *Inorgan. Mater.*, 2017, **53**, P. 619–625.

[24] Guskov A.V. Gagarin P.G., Guskov V.N., Khoroshilov A.V., Gavrichev K.S. Thermal properties of solid solutions $Ln_2O_3 \cdot 2HfO_2$ (Ln = Dy, Ho, Er, Tm, Yb, Lu) at 300 – 1300 K. *Ceram. Int.*, 2021, **47**, P. 28004–28007.

[25] Prohaska T., Irrgeher J., Benefield J., Böhlke J.K., Chesson L.A., Coplen T.B., Ding T., Dunn P. J.H., Gröning M., Holden N.E., Meijer H. A. J., Moossen H., Possolo A., Takahashi Y., Vogl J., Walczyk T., Wang J., Wieser M.E., Yoneda S., Zhu X.-K, Meija J. Standard atomic weights of the elements 2021 (IUPAC Technical Report). *Pure and Applied Chemistry*, 2022, **94**, P. 573–600.

[26] Shannon R.D. Revised effective ionic radii and systematic studies of interatomic distances in halides and chalcogenides. *Acta Crystallogr. Sect. A: Cryst. Phys. Diffr. Theor. Gen. Crystallogr.*, 1976, **32**, P. 751–767.
[27] ICDD PDF Database, https://www.icdd.com/
[28] Waring J.L., Schneider S.J. Phase equilibrium relationships in the system Gd_2O_3–TiO_2. *J. Res. Nat. Bur. Stand. A*, 1965, **69**, P. 255–261.

Submitted 30 July 2024; revised 13 October 2024; accepted 16 October 2024

Information about the authors:

Anton V. Guskov – Kurnakov Institute General and Inorganic Chemistry Russian Academy of Sciences, 119991, Leninsky pr. 31, Moscow, Russia; ORCID 0000-0003-00826-5495; a.gus@igic.ras.ru

Pavel G. Gagarin – Kurnakov Institute General and Inorganic Chemistry Russian Academy of Sciences, 119991, Leninsky pr. 31, Moscow, Russia; ORCID 0000-0001-6450-3959; gagarin@igic.ras.ru

Vladimir N. Guskov – Kurnakov Institute General and Inorganic Chemistry Russian Academy of Sciences, 119991, Leninsky pr. 31, Moscow, Russia; ORCID 0000-0003-0425-8618; guskov@igic.ras.ru

Konstsntin S. Gavrichev – Kurnakov Institute General and Inorganic Chemistry Russian Academy of Sciences, 119991, Leninsky pr. 31, Moscow, Russia; ORCID 0000-0001-5304-3555; gavrich@igic.ras.ru

Conflict of interest: the authors declare no conflict of interest.

NANOSYSTEMS:
PHYSICS, CHEMISTRY, MATHEMATICS

Enikeeva M.O., et al. *Nanosystems: Phys. Chem. Math.*, 2024, **15** (6), 781–792.
http://nanojournal.ifmo.ru
DOI 10.17586/2220-8054-2024-15-6-781-792

Original article

Phase formation and thermal analysis in the $LaPO_4$–$GdPO_4$–H_2O system

Maria O. Enikeeva[1,2,a], Kseniya A. Zhidomorova[2,3,b], Dmitriy P. Danilovich[3,c],
Vladimir N. Nevedomskiy [1,d], Olga V. Proskurina[1,3,e], Victor V. Gusarov[1,f]

[1]Ioffe Institute, St. Petersburg, Russia
[2]Branch of Petersburg Nuclear Physics Institute named after B.P. Konstantinov of National Research Centre "Kurchatov Institute" – Institute of Silicate Chemistry, St. Petersburg, Russia
[3]St. Petersburg State Institute of Technology, St. Petersburg, Russia

[a]i@odin2tri.ru, [b]zhidomorovak@gmail.com, [c]dmitrydanilovich@gmail.com,
[d] nevedom@mail.ioffe.ru, [e]proskurinaov@mail.ru, [f]gusarov@mail.ioffe.ru

Corresponding author: M. O. Enikeeva, i@odin2tri.ru

Abstract Structural transformations of nanocrystals in the $LaPO_4$–$GdPO_4$–(H_2O) system under hydrothermal conditions at 230 °C were studied depending on the duration of isothermal holding (2 hours, 3 days, and 5 days). It has been shown that a phase with the rhabdophane-like structure, $La_{1-x}Gd_xPO_4 \cdot nH_2O$ ($0.00 \leq x \leq 1.00$), exhibits a weighted average crystallite size of 4–7 nm and crystallizes in the system prior to hydrothermal treatment. As a result of hydrothermal treatment, samples in the $LaPO_4$–$GdPO_4$–(H_2O) system are completely transformed into a phase with a monazite structure within five days, with the slowest transformation observed for gadolinium orthophosphate. It was found that nanoparticles with a rhabdophane structure, $GdPO_4 \cdot nH_2O$, possess a single-crystal structure. The thermal analysis data indicated that the samples obtained via the precipitation method contain an X-ray amorphous phase and impurity compounds. The onset temperature of the structural transformation from rhabdophane to monazite, as well as the number of water molecules in the rhabdophane-like structure, depends on the chemical composition of the compound, particularly with regard to the isomorphic substitution of lanthanum cations with gadolinium cations.

Keywords solid solution, rhabdophane structure, thermal analysis, structural transformations.

Acknowledgements X-ray diffraction studies were carried out in the laboratory of new inorganic materials (Ioffe Institute). Scanning electron microscopy and DTA/TG studies were carried out on the instruments of the Engineering department of the Saint Petersburg State Institute of Technology (Technical University). The work of M.O.E. was carried out with the support of the Russian Science Foundation project No. 24-13-00445.

For citation Enikeeva M.O., Zhidomorova K.A., Danilovich D.P., Nevedomskiy V.N., Proskurina O.V., Gusarov V.V. Phase formation and thermal analysis in the $LaPO_4$–$GdPO_4$–H_2O system. *Nanosystems: Phys. Chem. Math.*, 2024, **15** (6), 781–792.

1. Introduction

Orthophosphates of rare earth elements (REE), represented as $REEPO_4$, include elements ranging from lanthanum to lutetium, as well as yttrium and scandium. These materials are of significant interest in modern materials science due to their potential applications in non-carbon energy fields such as catalysis [1–4], immobilization of radioactive waste [5–8], various types of luminescence [9–13], and thermal barrier coatings [14–17]. Compounds with monazite and xenotime structures exhibit high chemical and radiation resistance [18–23], a high melting point [24–26], and a diverse chemical composition [27–31]. In addition to the anhydrous phases with monazite and xenotime structures, REE orthophosphates can form hydrated structures – rhabdophane and churchite, which are often considered precursor phases to the anhydrous compounds [32–35]. Compounds with the churchite structure, $HREEPO_4 \cdot 2H_2O$, are layered orthophosphates of heavy rare earth elements (HREE: elements from gadolinium to lutetium and yttrium). In the churchite structure, each layer comprises a two-dimensional framework of yttrium atoms coordinated to phosphate groups through oxygen atoms, with water molecules coordinated to the yttrium atoms and located on the outer sides of the layers. The churchite structure contains two water molecules per formula unit, as confirmed by thermal analysis studies [33, 36], and serves as a structural analogue of gypsum ($CaSO_4 \cdot 2H_2O$) [37, 38].

The structure of rhabdophane ($REEPO_4 \cdot nH_2O$) is known to contain quasi-one-dimensional channels that include water molecules. Compounds with the rhabdophane-like structure are typically synthesized in a single step using soft chemistry methods, such as precipitation [27, 34, 39] and hydrothermal treatment [34, 40–43]. Early X-ray structural analysis indicated that the structure of rhabdophane ($REEPO_4 \cdot nH_2O$) for REE = La, Ce, and Nd could be described as having hexagonal symmetry in the space group $P6_222$ (180) [44, 45]. However, this description does not account for the presence of water molecules within the unit cell. Subsequent analysis [41, 46] prompted a revision of the space group for rhabdophane, changing it from hexagonal $P6_222$ to monoclinic $C2$ (5) for the hydrated compound, and to trigonal $P3_121$ (152) for the anhydrous form [41]. The monoclinic model describing rhabdophane in the space group $C2$ contains channels oriented along the [101] direction, which are formed by the contact between the edges of the REE polyhedra and PO_4 tetrahedra. This structural description assumes the presence of channels within the unit cell, rather than at the boundaries, as indicated by the hexagonal model. The determined values for the number of water molecules in the rhabdophane structure (C2) are n=2/3≈0.67 or n =1/2≈0.50 per formula unit of the compound, and the crystal chemical structure resembles $CaSO_4 \cdot 0.5H_2O$ [47]. It should be noted separately that refining the number of water molecules in the rhabdophane structure using electron diffraction does not yield exact answers regarding their quantity, positional occupancy, or atomic coordinates.

Electron single-crystal diffraction data for a single crystal of $DyPO_4 \cdot nH_2O$ with the rhabdophane-like structure indicate that the hydrated structure can be described using a trigonal lattice of space group $P3_121$, exhibiting an effective doubling of the unit cell compared to the original Mooney description in [44, 45]. Moreover, there is a significant shift in the ion positions within the unit cell [48]. In the work [41], it is suggested that the channel size of the rhabdophane structure depends on the ionic radius of the rare earth element (REE) and affects the amount of structurally bound water: the smaller the ionic radius, the lower the unit cell volume and, consequently, the lower the water content in the structure. Additionally, the role of water in stabilizing the rhabdophane structure is discussed, with the assumption that water present in the channels helps stabilize the structure; its loss can lead to a monotropic transition to the monazite structure [42, 49]. A primary challenge in describing the structure of rhabdophane arises from the water molecules that are part of the compound; these molecules are not easily localized within the unit cell, and their locations can vary randomly among several equivalent positions in the structure [48].

One of the approaches for quantitatively describing the water content in the rhabdophane structure involves thermal analysis methods such as DTA/DSC/TG. Despite the uncertainties inherent in thermal analysis data – such as the superposition of various stages of mass loss, thermal effects associated with the removal of adsorbed water or water from structural channels, and the decomposition of reaction by-products and surfactants [50–53], these methods are widely applicable in the study of hydrated compounds [33, 42, 54, 55]. Data on the thermal behavior of the rhabdophane structure are presented in references [42, 53, 56, 57] and pertain to the determination of the thermodynamic characteristics of individual compounds, with less frequent studies on phases of variable composition [43, 46]. Furthermore, investigating the rhabdophane structure with variable composition could contribute to developing a unified concept of "the role of water in hydrated compounds with the rhabdophane-like structure", which would be valuable for the creation of new functional materials.

To obtain hydrated phases and investigate the phase formation of complex oxide systems, various soft chemistry approaches are employed [58]. This group of methods enables phase formation processes to occur at relatively low temperatures, making it particularly applicable to hydrated compounds and often utilized for the synthesis of nanomaterials [59–61].

As a result, the present work aims to study the formation process of nanocrystalline orthophosphates with variable composition in the $LaPO_4$–$GdPO_4$–H_2O system using soft chemistry methods. Additionally, it seeks to examine the thermal behavior of the resulting compounds composed of nanocrystalline particles with a rhabdophane-like structure.

2. Materials and methods

For the synthesis of $La_{1-x}Gd_xPO_4 \cdot (nH_2O)$ samples (x=0.00, 0.20, 0.50, 0.75, 0.85, 1.00), hexahydrate nitrates of rare earth elements (chemically pure) and ammonium dihydrogen phosphate (chemically pure) were used. Precipitation was carried out by adding an aqueous solution of $NH_4H_2PO_4$ to an aqueous solution of REE nitrates while continuously stirring at a temperature of 25±5 °C. The resulting white suspension with a pH of 1 was stirred for 15 minutes.

For synthesis under hydrothermal conditions, the suspension obtained by precipitation was placed in a Teflon ampoule of a laboratory autoclave (fill factor 0.7) and treated hydrothermally at 230 °C and ∼10 MPa, with isothermal holding times of 2 hours, 3 days, and 5 days.

All samples obtained were washed with distilled water until a pH of 7 was achieved, precipitated by centrifugation (10,000 rpm), dried at 75–80 °C for 24 hours, and milled in an agate mortar.

SEM images and elemental composition of the samples were obtained using a Tescan Vega 3 SBH scanning electron microscope (Tescan, Czech Republic) equipped with an Oxford Instruments INCA x-act attachment (Oxford Instruments, UK). The images of the samples were recorded using secondary electron detectors. Composition analysis was performed on 4–5 different areas, averaging the obtained values.

The study of the crystal structure and microstructure of the samples was conducted using transmission electron microscopy (TEM) on a JEM-2100F microscope (JEOL Ltd., Akishima, Tokyo, Japan) operating at an accelerating voltage of 200 kV.

Diffraction studies were carried out using a DRON-8N X-ray powder diffractometer (Bourevestnik, JSC, Russia) under Bragg-Brentano geometry conditions and an X-ray tube with a copper anode (K_α doublet) equipped with Goebel parabolic mirrors at the primary beam output. Data collection was performed for the Bragg angle (2θ) ranging from 10 to

90° with a step of 0.01° in exposure mode with a shutter speed of 7 s. Phase analysis of the samples was conducted using PDF-2 and CCDC databases. Full-profile phase analysis was performed using SmartLab Studio II v4.4.241.0 software (Rigaku Corporation, Japan) using the Rietveld method [62]. The weighted average values of crystallite sizes were calculated in accordance with the lognormal distribution law for non-overlapping reflections of each phase: reflection 200 was used for the phase with the monazite-like structure and reflection $11\bar{1}$ for the phase with the rhabdophane-like structure.

Differential thermal analysis and thermogravimetry (DTA/TG) was performed using a Shimadzu DTG-60 (Shimadzu, Japan) with a heating rate of 10 °C/min in air. The first part of the experiment was conducted on all $La_{1-x}Gd_xPO_4 \cdot nH_2O$ samples (x=0.00, 0.20, 0.50, 0.75, 0.85, 1.00) obtained by precipitation, covering a temperature range from 25 to 1000 °C.

In the second part, the samples underwent preliminary heat treatment in a muffle furnace at the same heating rate: for 3 minutes at 300 °C for the $LaPO_4 \cdot nH_2O$ sample and for 10 minutes at 400 °C for the $GdPO_4 \cdot nH_2O$ sample. After isothermal holding, the samples were removed from the furnace, allowed to cool spontaneously to room temperature, ground again in an agate mortar, and then examined by X-ray diffraction to determine the phase composition. Following this procedure, DTA/TG of the samples was conducted at a heating rate of 10 °C/min in dynamic mode over the range from 25 to 1000 °C, as well as in quasi-static mode from 25 to 500 °C. The temperature steps for the quasi-isothermal mode were chosen to initiate the dehydration of the rhabdophane-like structure at each temperature step.

3. Results and discussion

3.1. Phase formation in $LaPO_4$–$GdPO_4$–H_2O system

Based on the results of energy dispersive X-ray, the ratio (La + Gd) : P was found to be approximately 1:1, which corresponds to the stoichiometry of REE orthophosphate. The experimentally determined molar fraction of gadolinium orthophosphate (x) in the compound $La_{1-x}Gd_xPO_4 \cdot (nH_2O)$ is used to designate the samples. The results of the elemental analysis, which reflect the content of $GdPO_4$ in the system, are presented in Table S1.

The X-ray diffraction patterns of the samples obtained via the precipitation method are shown in Fig. 1. All samples crystallize in the rhabdophane-like structure (space group $C2$). The X-ray diffraction patterns for the samples produced using hydrothermal treatment are presented in figs. S1–S3 in the Supplementary Materials. The results of quantitative phase analysis for samples synthesized under hydrothermal conditions for 2 hours and 3 days are shown in Fig. 2. After 2 hours of isothermal holding in the hydrothermal fluid, the phase with the rhabdophane-like structure was completely transformed into the monazite-like structure for the sample with x=0.00 (Fig. 2a). Samples containing 0.20 to 0.75 mol. fr. of $GdPO_4$ transformed into the monazite phase more slowly and exhibited a mixture of phases with both monazite-like and rhabdophane-like structures. In contrast, samples x=0.85 and x=1.00 retained the rhabdophane structure. As illustrated in Fig. 2b, increasing the isothermal holding time to three days results in the formation of a wide homogeneity region of the monazite-like structure based on $La_{1-x}Gd_xPO_4$, for x from 0.00 to 0.85. Only gadolinium orthophosphate (x=1.00) contains approximately 19% of the monazite phase. After five days of isothermal holding, all samples crystallized in the monazite phase.

Fig. 3 illustrates the dependencies of the unit cell volumes of the phases with monazite and rhabdophane structures, normalized to one formula unit (V/z), for samples obtained through precipitation and hydrothermal treatment. In the samples obtained via the precipitation method, a phase of variable composition with the rhabdophane-like structure forms across the entire concentration range (Fig. 3a). As shown in Fig. 3b, after hydrothermal treatment for 2 hours, two solid solutions: one with the rhabdophane-like structure and another with the monazite-like structure are observed in the system. Notably, the transformation from the rhabdophane structure to the monazite structure appears to occur without changing the cation ratio, as indicated by the linear dependence of the V/z parameter for the rhabdophane structure on composition. The absence of data for the monazite structure in the sample x=0.75 in Fig. 3b is attributed to the small amount of the monazite phase, which are less than 5% and makes it impossible to determine the precise parameters of the unit cell. After hydrothermal treatment for 3 and 5 days (Fig. 3c,d), the chemical composition of the monazite-like phase are the same, indicating complete isomorphic substitution of cations in the $LaPO_4$–$GdPO_4$–(H_2O) system.

The dependences of the weighted average value of crystallite sizes on the composition are shown in Fig. 4 for the samples obtained by precipitation and hydrothermal treatment with different durations of isothermal holding. The precipitation method was used to obtain nanocrystalline powders with an average value of crystallite sizes of 4–7 nm for $La_{1-x}Gd_xPO_4 \cdot nH_2O$ (x=0.00–1.00) with a rhabdophane-like structure (Fig. 4a). As shown in Fig.4b, during the structural transformation in a hydrothermal fluid after 2hours of isothermal holding, the weighted average values of the crystallite sizes of the monazite structure are about 15 nm and coincide with the weighted average values of the crystallite sizes of the rhabdophane structure in the two-phase region (x=0.20–0.50). In the $La_{1-x}Gd_xPO_4 \cdot nH_2O$ (x=0.20–1.00) samples, a close to exponential nature of the dependence of the weighted average value of the crystallite sizes of the rhabdophane structure on the concentration of $GdPO_4$ in the $LaPO_4$–$GdPO_4$–H_2O system is noted. A similar dependence $D(x)$ was determined in the work devoted to the $LaPO_4$–YPO_4–H_2O system [34]. Thus, the substitution of La^{3+} ((C.N.=9) 1.216 Å) in orthophosphate for REE with a smaller ionic radius Y^{3+} ((C.N.=9) 1.075 Å) or Gd^{3+} ((C.N.=9)

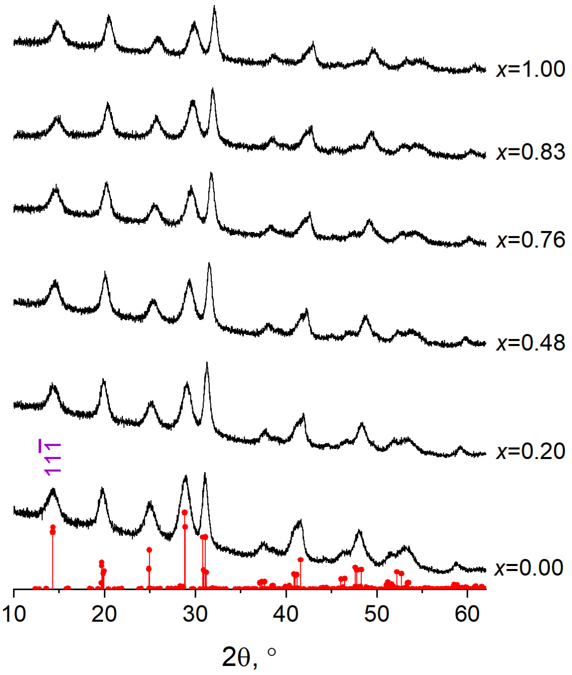

FIG. 1. Diffraction patterns of $La_{1-x}Gd_xPO_4 \cdot nH_2O$ samples obtained by precipitation. The vertical lines accompany rhabdophane-like structure (space group $C2$ [46])

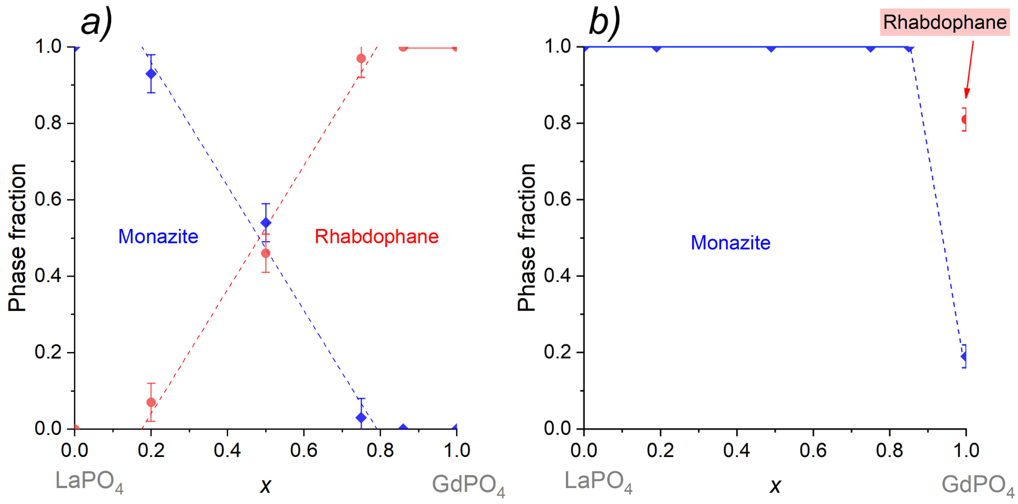

FIG. 2. The phase ratio in the system for $La_{1-x}Gd_xPO_4 \cdot (nH_2O)$ samples: a) after 2 hours of isothermal holding, b) after 3 days of isothermal holding

1.107 Å), leads to a slowdown in the rhabdophane $\rightarrow$ monazite structural transformation and to an increase in the crystallite sizes of the rhabdophane structure due to recrystallization in a hydrothermal fluid. As shown in Fig. 4c, the weighted average value of the crystallite sizes of the monazite structure after 3 days of isothermal holding varies from 19±10 nm for the x=0.00 sample to 145±10 nm for the x=1.00 sample. The weighted average value of the crystallite sizes of the rhabdophane structure in the sample x=1.00 is about 100 nm, which is slightly lower than the value for the monazite structure in the same sample. This effect is probably associated with the process of transformation of the phase with the rhabdophane structure into the phase with the monazite structure, when the increase in the crystallite sizes is caused by the slow rate of structural transformation compared to the samples $0.00 \leq x \leq 0.85$. The data on the weighted average values of the crystallite sizes of the samples with the monazite structure obtained after 5 days of isothermal holding are shown in Fig. 4d, which, within the error, coincide with the crystallite sizes obtained after 3 days of hydrothermal treatment; the nature of the $D(x)$ dependence remains close to exponential.

Fig. 5 shows images of nanoparticles with the composition x=1.00 obtained by precipitation followed by heat treatment for 5 minutes at 400 °C (Fig. 5a-c) and after hydrothermal treatment for 2 hours (Fig. 5d-f). Their electron diffraction patterns are shown in Fig. 5g,h. The nanoparticles with the rhabdophane-like structure exhibit a quasi-one-dimensional

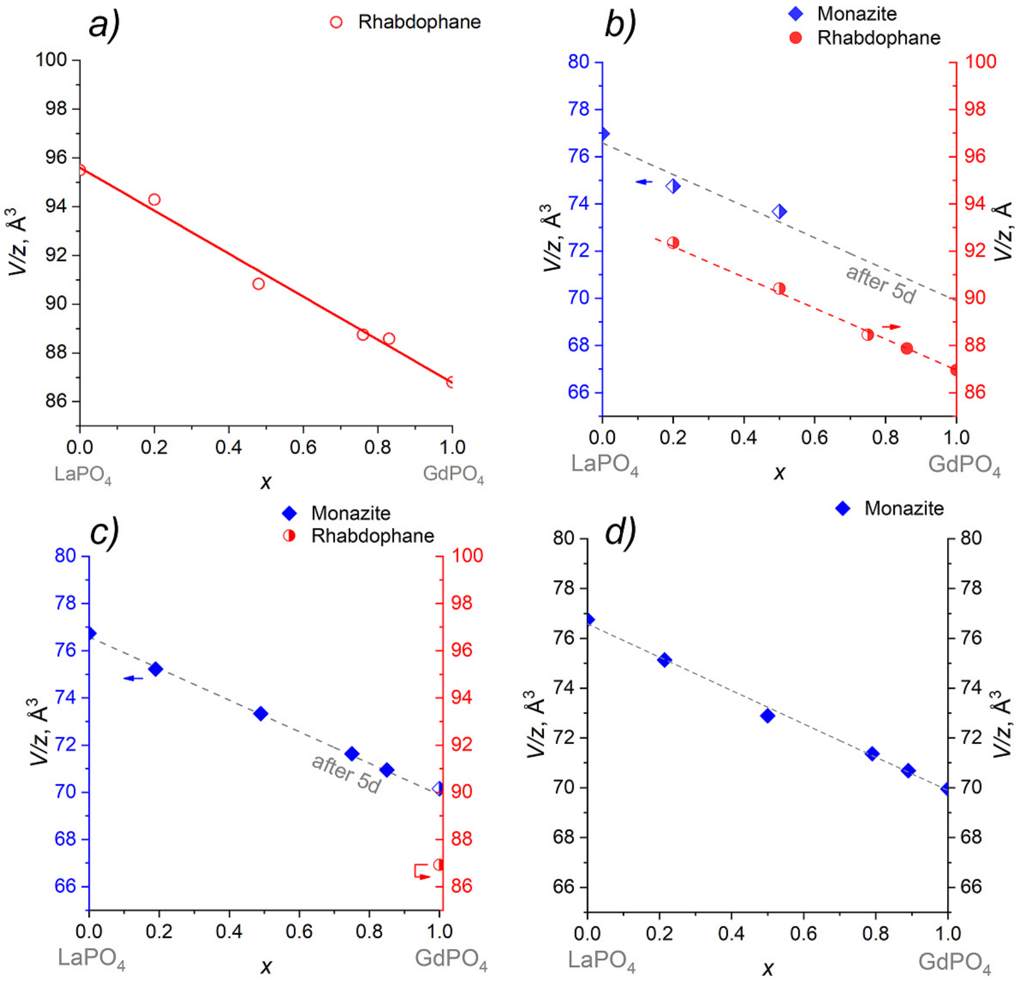

FIG. 3. Dependences of the unit cell volumes, normalized to one formula unit (V/z), on the composition of the system for phases with rhabdophane-like and monazite-like structures are presented as follows: a) precipitation, b) hydrothermal treatment for 2 hours, c) hydrothermal treatment for 3 days, d) hydrothermal treatment for 5 days

morphology. The average thickness of nanoparticles obtained by precipitation is 9±2 nm, while after hydrothermal treatment, it is 40±12 nm. The average thickness of nanoparticles in the samples correlates well with the weighted average values of crystallite sizes (Fig. 4a,b): D=6±2 nm and D=55±35 nm for the samples before and after hydrothermal treatment, respectively. The dark-field TEM images (Fig. 5b,e) indicate that the nanoparticles of the samples possess a single-crystal structure, meeting the Bragg reflection condition. Therefore, it can be concluded that the rhabdophane-like particles are single crystals. The high-resolution TEM images (Fig. 5c,f) display the average interplanar distances (d), which coincide within the margin of error with the X-ray diffraction data and are associated with the rhabdophane-like structure (space group $C2$ [41, 46]). According to the electron diffraction data, the interplanar distances for the samples with x = 1.00, obtained via the deposition method (Fig. 5g) and after hydrothermal treatment (Fig. 5h), differ slightly: the interplanar distances in the sample obtained by deposition followed by heat treatment for 5 minutes at 400 °C are smaller than those in the sample obtained after hydrothermal treatment. Since both samples crystallize in the same rhabdophane-like structure, the difference in d values may be attributed to the varying water content in the structure.

3.2. DTA/TG studies of samples obtained by precipitation method

Fig. 6a-f presents the DTA/TG data for the entire series of samples with x=0.00–1.00 obtained via the precipitation method. Based on changes in the slope of the tangent to the TG curve, four steps of mass loss associated with the removal of water from the samples were identified: the zero step from 25 °C to approximately 125 °C is p presumably related to the removal of water from the surface of the nanoparticles (adsorbed water), while the first, second, and third steps are associated with the removal of water from the rhabdophane-like structure. An analysis of the obtained data is presented in Table S2 and Fig. 7a,b as a function of the number of water molecules (n) in the rhabdophane structure per formula unit of the compound, as well as a dependence of the temperatures at which mass loss begins for steps 1–3 on the composition of the compound, expressed in ionic radii of the 9-coordinated REE^{3+} ion. The studied samples can be divided into two

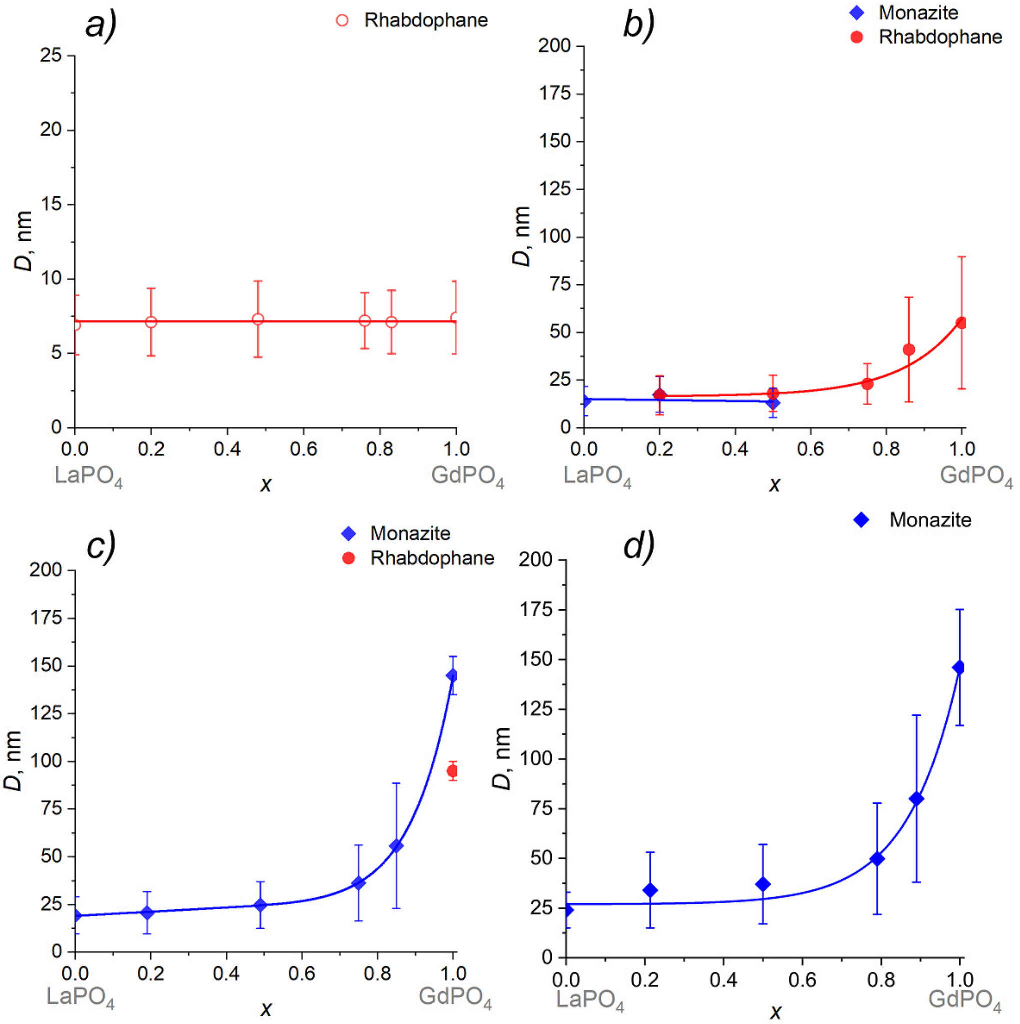

FIG. 4. Dependences of the weighted average crystallite sizes on the composition of the system for phases with rhabdophane-like and monazite-like structures in the $La_{1-x}Gd_xPO_4 \cdot (nH_2O)$ system: *a*) precipitation, *b*) hydrothermal treatment for 2 hours, *c*) hydrothermal treatment for 3 days, *d*) hydrothermal treatment for 5 days

groups: those obtained by precipitation without heat treatment [27, 43, 53, 63, 64] and those obtained using hydrothermal methods [42, 43, 65, 66]. The mass loss for the $La_{1-x}Gd_xPO_4 \cdot nH_2O$ x=0.00–1.00 samples is approximately 10%. The temperature at which the first stage of mass loss begins is close to 125 °C for all samples, and the number of water molecules leaving the channels of the structure at this stage varies from 0.16 to 0.29, depending on the composition of the compound. It is worth noting that accurately determining the temperature at which the first stage begins is challenging due to the superposition of endothermic effects in the range from 25 °C to ~200 °C.

The second step of mass loss is the most clearly distinguished for all samples, which is also evident in the samples obtained under hydrothermal conditions [40, 42, 43, 65]. The temperature at the onset of the second step shows a linear dependence on the composition of the compound, increasing from approximately 160 °C for sample x=1.00 to approximately 200 °C for sample x=0.00 (Fig. 7b). During the second step, approximately n=0.47 molecule of water leaves channels of the structure. Moreover, analysis of data [42] obtained for individual REE orthophosphates with the rhabdophane structure demonstrates a close match between the value of $n \approx 0.47$ molecule H_2O at the second step of mass loss and the literature data.

The third stage of mass loss in all compounds corresponds to an exothermic effect on the DTA curve. It appears that, during this step, in addition to the removal of water from the rhabdophane-like structure, the decomposition of impurity compounds (for example, hydroxides) and the crystallization of the X-ray amorphous phase occur. The temperature at the onset of the third step of mass loss is related to the second step and follows a linear dependence, exhibiting lower values when $LaPO_4$ is replaced with $GdPO_4$. Based on these data, it was determined that the water content in the rhabdophane-like structure for samples obtained by precipitation depends on the composition of the compounds and decreases with a reduction in the ionic radius of the REE. The TG curves show a distinguishable third step [27, 43, 51, 63, 64], associated with the removal of water from the rhabdophane-like structure, in contrast to the samples obtained through

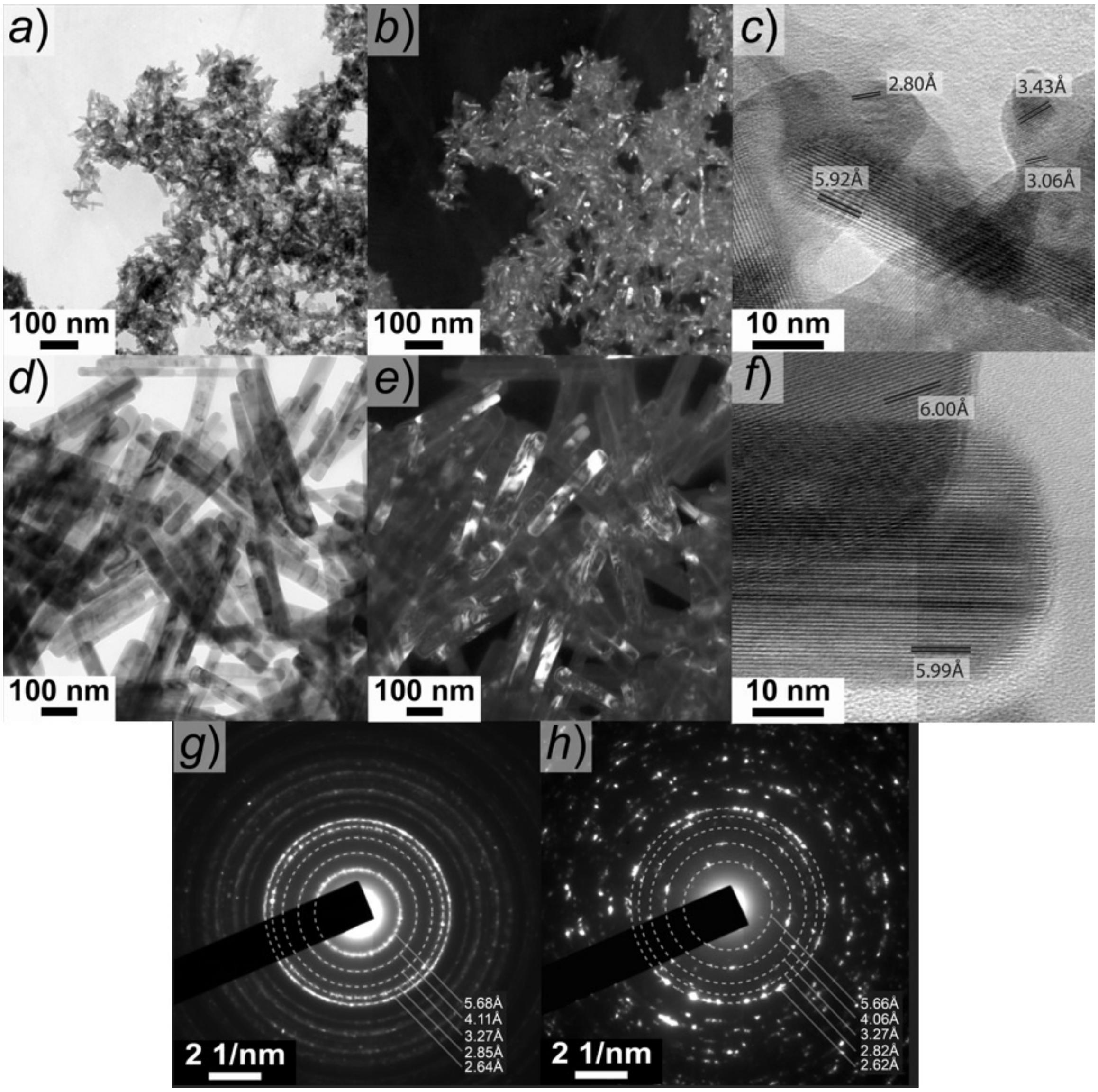

FIG. 5. Bright-field, dark-field, and high-resolution TEM images of the x=1.00 samples are presented as follows: (*a–c*) samples obtained by the precipitation, (*d–f*) samples obtained under hydrothermal conditions for 2 hours, (g) electron diffraction of the x=1.00 sample obtained by the precipitation, and (*h*) electron diffraction of the x=1.00 sample obtained under hydrothermal conditions for 2 hours

hydrothermal treatment. The onset temperature of the exothermic effect, occurring at $T \geq 600$ °C, is connected to the transition of the rhabdophane-like phase to the monazite-like phase. As lanthanum phosphate is substituted by gadolinium phosphate in the solid solution series $La_{1-x}Gd_xPO_4 \cdot nH_2O$, the onset transformation temperature increases from 601 °C to 733 °C, indicating that the thermal stability of $GdPO_4 \cdot nH_2O$ with the rhabdophane-like structure is greater than that of $LaPO_4 \cdot nH_2O$. A similar dependence of the transformation temperature on ionic radius in the rhabdophane-like structure is noted in references [42,43].

The results of the TG study of samples x=0.00 and x=1.00, which were calcined at 300–400 °C for 5 minutes, in both dynamic and quasi-isothermal modes, are shown in Fig. 6a,b. Three steps of mass loss are evident on the TG curves obtained under dynamic heating conditions. At the first stage, $n \approx 0.20$ water molecules per formula unit are lost for both samples; at the second stage, $n \approx 0.30$ water molecules are lost. These values are slightly lower than those for the samples without heat treatment (Table S2), which is likely due to the absence of impurity compounds in the heat-treated samples. The third step of mass loss in samples x=0.00 and x=1.00 differs slightly. In this regard, the boundary between the second and third steps for sample x=1.00 (Fig. 8b) is more distinctly defined than for sample x=0.00 (Fig. 8a). The number of water molecules released from the rhabdophane-like structure during the heating process in the third stage varies between the two compounds: n=0.35 for lanthanum orthophosphate (Fig. 8a) and n=0.21 for gadolinium orthophosphate (Fig. 8b). The total amount of water in the rhabdophane structure is n=0.88 for $LaPO_4 \cdot nH_2O$ and n=0.72 for $GdPO_4 \cdot nH_2O$, which

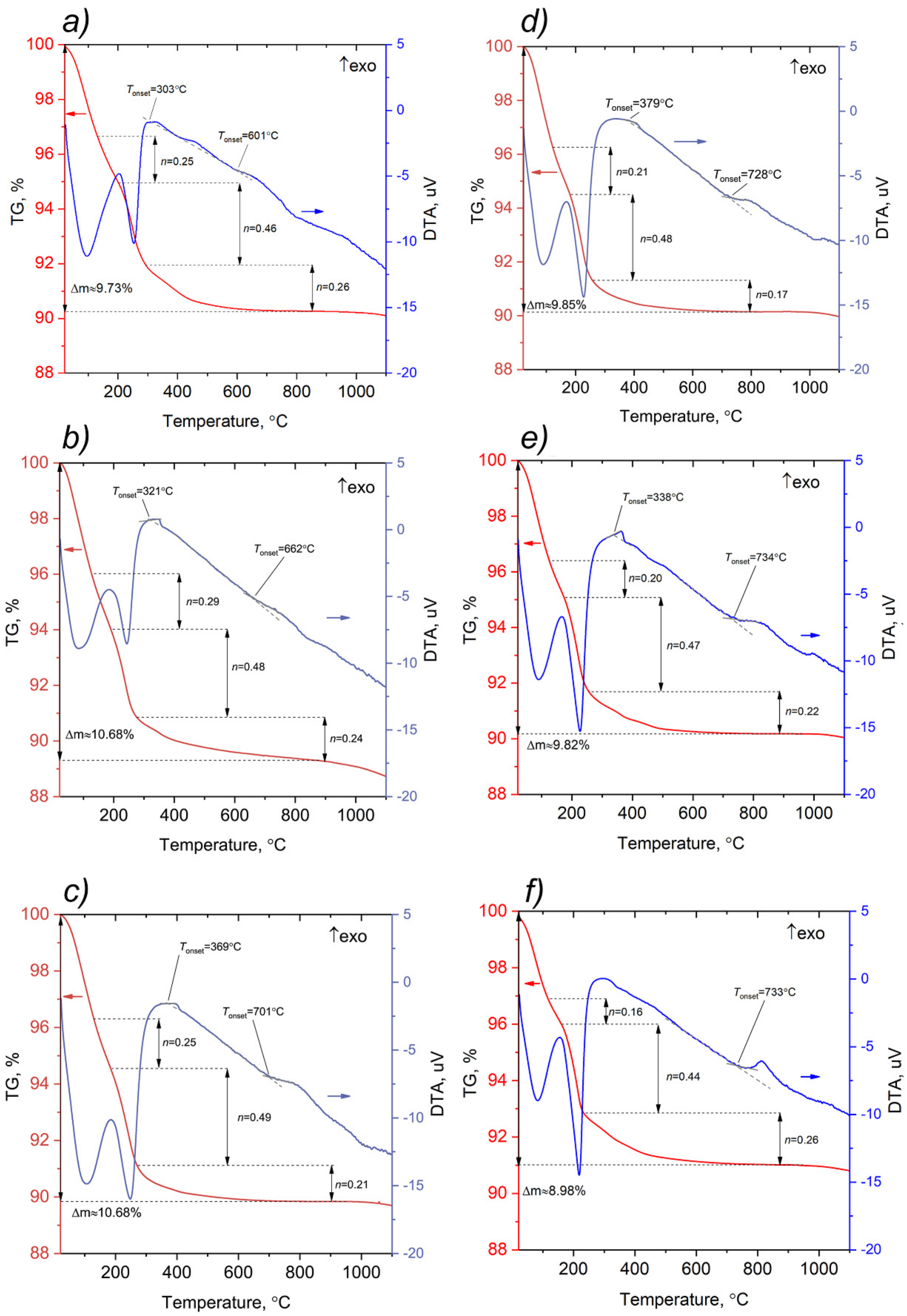

FIG. 6. DTA/TG study of samples in the $La_{1-x}Gd_xPO_4 \cdot nH_2O$ system with the rhabdophane-like structure, obtained by the precipitation method: *a*)x=0.00, *b*)x=0.20, *c*)x=0.48, *d*)x=0.76, *e*)x=0.83, *f*)x=1.00

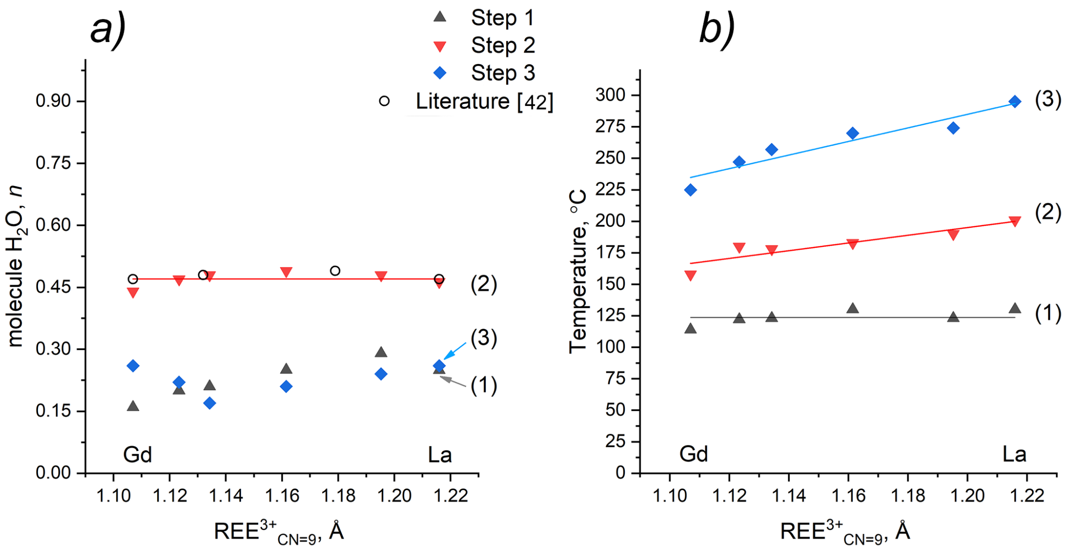

FIG. 7. *a*) The number of water molecules (n) in the rhabdophane structure, determined from the mass loss at each step and *b*) The temperature at which each step of mass loss begins, depending on the composition

correlates with the trend presented in Table S2, a decrease in the ionic radius of the REE leads to a reduction in the amount of water in the structure for samples obtained by the precipitation method.

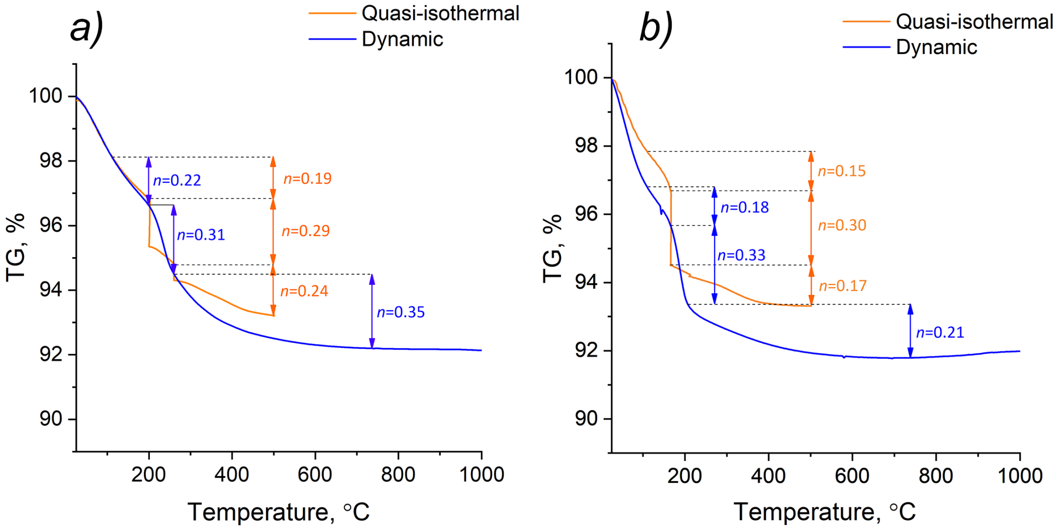

FIG. 8. DTA/TG data obtained in quasi-isothermal and dynamic modes for samples: *a*) x=0.00, *b*) x=1.00

When studying the samples with the rhabdophane-like structure at x=0.00 and x=1.00 in quasi-isothermal mode, it was found that isothermal holding at 200 °C for the x=0.00 sample and at 160 °C for the x=1.00 sample results in a sharp mass loss. This mass loss, when recalculated for the formula unit of the compounds, is approximately 0.30 molecule of water. After this loss, the mass of the samples reaches a plateau. The obtained values are in good agreement with data from the dynamic mode. Subsequently, the samples were continuously heated to the temperature at which the third step of mass loss begins (Table S2): T=260 °C for the x=0.00 sample and T=210 °C for the x=1.00 sample. Increasing the temperature at a constant rate to these specified values results in a decrease in the mass of the samples with the structure of rhabdophane-like, while quasi-isothermal holding at the same temperatures does not affect the mass change. Further heating of the samples to 500 °C after the isothermal stage (T=260 °C for the x=0.00 sample and T =210 °C for the x=1.00) is characterized by a mass loss.

These observations indicate that the third step of mass loss is initiated by an increase in sample temperature and is associated with the characteristics of the chemical bonding of water molecules in the rhabdophane structure. The number of water molecules lost per formula unit during the third step is n=0.24 for the x=0.00 sample and n=0.17 for the x=1.00 sample. According to the quasi-isothermal TG mode, the total number of water molecules in the rhabdophane structure for $LaPO_4 \cdot nH_2O$ and $GdPO_4 \cdot nH_2O$ is n=0.72 and n=0.62, respectively. These values are lower than those determined in the dynamic heating mode, likely due to incomplete removal of water from the rhabdophane structure, as the water removal process can extend up to 600–650 °C.

Based on the data obtained from DTA/TG and TEM, it can be inferred that the samples with the rhabdophane-like structure synthesized by precipitation may contain a different number of water molecules compared to those synthesized under hydrothermal conditions. This inference is supported by the distinct shapes of the TG curves for the samples before and after hydrothermal treatment. For the samples obtained through precipitation, at least three stages of mass loss were identified, which are associated with the removal of water molecules from the channels of structure. In contrast, compounds with the rhabdophane structure that were synthesized under hydrothermal conditions primarily exhibit two stages of mass loss. The first of these stages corresponds to the loss of adsorbed water on the surface of nanoparticles. As mentioned earlier, the samples with the rhabdophane-like structure, $LaPO_4 \cdot nH_2O$ and $GdPO_4 \cdot nH_2O$, obtained via the precipitation method can contain at least 0.62 water molecules per formula unit (excluding the adsorbed water), whereas the hydrothermally synthesized samples contain approximately 0.48–0.50 water molecules (also excluding surface-bound water). Additionally, TEM studies reveal slight differences in interplanar distances for $GdPO_4 \cdot nH_2O$ samples obtained by the precipitation method compared to those subjected to hydrothermal treatment. This difference may be related to structural rearrangements caused by the varying amounts of water incorporated within the structure.

4. Conclusion

It is demonstrated that a continuous series of $La_{1-x}Gd_xPO_4 \cdot nH_2O$ ($0.00 \leq x \leq 1.00$) solid solutions with a rhabdophane-like structure and crystallite sizes ranging from 4 to 7 nm can be synthesized by precipitation in the $LaPO_4$–$GdPO_4$–H_2O system. According to TEM data, the average thickness of nanoparticles with the rhabdophane structure for the sample with x=1.00 correlates well with the weighted average crystallite sizes obtained both before and after hydrothermal treatment, indicating that these particles exhibit a single-crystal structure.

After hydrothermal treatment at 230 °C for 2 hours, phases containing both monazite-like and rhabdophane-like structures are formed within the system. In the two-phase region of phase coexistence ($0.20 \leq x \leq 0.75$), the weighted average values of the crystallite sizes and the chemical compositions of both phases are found to be consistent. It is noteworthy that the structural transformation occurs more slowly for compounds with a higher $GdPO_4$ content. The transformation from the rhabdophane phase to the monazite phase in the $LaPO_4$–$GdPO_4$–H_2O system occurs under hydrothermal conditions at 230 °C over a period of 5 days of isothermal holding. DTA/TG indicates that the samples obtained through the precipitation method contain approximately 1.5% of an X-ray amorphous phase along with impurity compounds.

Furthermore, it is shown that the onset temperature for the structural transformation from rhabdophane to monazite, as well as the onset temperature for each stage of mass loss (dehydration of the rhabdophane structure), and the number of water molecules in the rhabdophane-like structure, are dependent on the chemical composition of the compound. Notably, the thermal stability of $GdPO_4 \cdot nH_2O$ with the rhabdophane structure is higher than that of $LaPO_4 \cdot nH_2O$ (~733 °C versus ~601 °C). However, the onset temperature for the dehydration of $GdPO_4 \cdot nH_2O$ at the second stage of mass loss is lower than that of $LaPO_4 \cdot nH_2O$ (~160 °C versus ~200 °C), and the number of water molecules per formula unit is greater in $LaPO_4 \cdot nH_2O$ (n=0.72) than in $GdPO_4 \cdot nH_2O$ (n=0.62).

References

[1] Feng R., Qi Y., Liu S., Cui L., Dai Q., Bai C. Production of renewable 1,3-pentadiene over $LaPO_4$ via dehydration of 2,3-pentanediol derived from 2,3-pentanedione. *Applied Catalysis A: General*, 2022, **633**, P. 118514.

[2] Lohmann R., Cousins I.T., DeWitt J.C., Glüge J., Goldenman G., Herzke D., Lindstrom A.B., Miller M.F., Ng C.A., Patton S., Scheringer M., Trier X., Wang Z. Are Fluoropolymers Really of Low Concern for Human and Environmental Health and Separate from Other PFAS? *Environmental Science & Technology*, 2020, **54**(20), P. 12820–12828.

[3] Zhang Y.F., Dai B., Zhao D., Zhang D.H., Xu M.X., He X.H., Chen C. Promotion Effect of $PrPO_4$ for Hydrogenation Transformation of Biomass-derived Compounds over Pr-Ni-P Composites. *Materials Advances*, 2021, **2**(12), P. 3927–3939.

[4] Majhi K.C., Yadav M. Facile hydrothermal synthesis of rare earth phosphate for boosting hydrogen evolution reaction. *International Journal of Hydrogen Energy*, 2022, **47**(30), P. 14092–14103.

[5] Liu D., Wang J., Wang J., Liu K., Wen J., Xu J., Jiang P. Temperature dependences of phase composition, densification, and thermal/chemical stability of $Sr_{0.5}Zr_2(PO_4)_3$-$Nd_{0.5}Sm_{0.5}PO_4$ composite ceramics for nuclear waste form. *Journal of the European Ceramic Society*, 2024, **44**(16), P. 116806.

[6] Vance E.R., Zhang Y., McLeod T., Davis J. Actinide valences in xenotime and monazite. *Journal of Nuclear Materials*, 2011, **409**(3), P. 221–224.

[7] Thust A., Hirsch A., Haussühl E., Schrodt N., Loison L., Schott P., Peters L., Roth G., Winkler B. Physical properties and microstructures of $La_{1-x}Pr_xPO_4$ monazite-ceramics. *Physics and Chemistry of Minerals*, 2018, **45**, P. 323–332.

[8] Burakov B.E., Yagovkina M.A., Zamoryanskaya M.V., Petrova M.A., Domracheva Y.V., Kolesnikova E.V., Nikolaeva L.D., Garbuzov V.M., Kitsay A.A., Zirlin V.A. *Behavior of Actinide Host-Phases Under Self-irradiation: Zircon, Pyrochlore, Monazite, and Cubic Zirconia Doped with Pu-238.* In: Krivovichev, S.V. (eds) Minerals as Advanced Materials I. Springer, Berlin, Heidelberg, 2008.

[9] Bermudez S., Rojas J.V. Tunable X-ray-induced luminescence in lanthanide-doped $LaPO_4$ nanoparticles. *Ceramics International*, 2024, **50**(9) Part 1, P. 16076–16087.

[10] Wu J., Wu B., Wang Q., Liu Z., Hu Y., Feng F., Li J., Zhang X., Xie R. Tuning and high temperature fluorescence properties of $LaPO_4$:Sm^{3+} nanophosphors. *Optical Materials*, 2024, **153**, P. 115556.

[11] Ouertani G., Maciejewska K., Piotrowski W., Horchani-Naifer K., Marciniak L., Ferhi M. High thermal stability of warm white emitting single phase $GdPO_4$: Dy^{3+}/ Sm^{3+} phosphor for UV excited wLEDs. *Journal of Luminescence*, 2024, **265**, P. 120228.

[12] Orekhova K., Burakov B., Silantieva E., Kitsay A., Popova T., Yagovkina M., Zamoryanskaya M. Synthesis and cathodoluminescence of YPO_4 and $LuPO_4$ single crystals activated with Er^{3+}. *Journal of Alloys and Compounds*, 2023, **968**, P. 171961.

[13] Correcher V., Boronat C., Garcia-Guinea J., Benavente J.F., Rivera-Montalvo T. Thermoluminescence characterization of natural and synthetic irradiated Ce-monazites. *Journal of Rare Earths*, 2024, **42**(4), P. 643–650.

[14] Hikichi Y., Ota T., Hattori T. Thermal, mechanical and chemical properties of sintered monazite-(La, Ce, Nd or Sm). *Mineralogical Journal*, 1997, **19**(3), P. 123–130.

[15] Zhao Z., Chen H., Xiang H., Dai F.-Z., Wang X., Peng Z., Zhou Y. $(La_{0.2}Ce_{0.2}Nd_{0.2}Sm_{0.2}Eu_{0.2})PO_4$: A high-entropy rare-earth phosphate monazite ceramic with low thermal conductivity and good compatibility with Al_2O_3. *Journal of Materials Science & Technology*, 2019, **35**(12), P. 2892–2896.

[16] Du A., Wan C., Qu Z., Wu R., Pan W. Effects of Texture on the Thermal Conductivity of the $LaPO_4$ Monazite. *Journal of the American Ceramic Society*, 2010, **93**(9), P. 2822–2827.

[17] Enikeeva M.O., Proskurina O.V., Motaylo E.S., Gusarov V.V. The influence of condition of the monazite structured $La_{0.9}Y_{0.1}PO_4$ nanocrystals sintering on thermal and mechanical properties of the material. *Nanosystems: physics, chemistry, mathematics*, 2021, **12**(6), P. 799–807.

[18] Dacheux N., Clavier N., Podor R. Versatile Monazite: Resolving geological records and solving challenges in materials science. Monazite as a promising long-term radioactive waste matrix: Benefits of high-structural flexibility and chemical durability. *American Mineralogist*, 2013, **98**(5-6), P. 833–847.

[19] Van Hoozen C.J., Gysi A.P., Harlov D.E. The solubility of monazite ($LaPO_4$, $PrPO_4$, $NdPO_4$, and $EuPO_4$) endmembers in aqueous solutions from 100 to 250? ° C. *Geochimica et Cosmochimica Acta*, 2020, **280**, P. 302–316.

[20] Mikhailov D.A., Potanina E.A., Orlova A.I., Nokhrin A.V., Boldin M.S., Belkin O.A., Sakharov N.V., Skuratov V.A., Kirilkin N.S., Chuvil'deev V.N. Radiation Resistance and Hydrolytic Stability of $Y_{0.95}Gd_{0.05}PO_4$-Based Ceramics with the Xenotime Structure. *Inorganic Materials*, 2021, **57**, P. 760–765.

[21] Gysi A.P., Harlov D. Hydrothermal solubility of $TbPO_4$, $HoPO_4$, $TmPO_4$, and $LuPO_4$ xenotime endmembers at pH of 2 and temperatures between 100 and 250 °C. *Chemical Geology*, 2021, **567**, P. 120072.

[22] Lender T., Murphy G., Bazarkina E., Bukaemskiy A., Gilson S., Henkes M., Hennig C., Kaspor A., Marquardt J., Nießen J., Peters L., Poonoosamy J., Rossberg A., Svitlyk V., Kvashnina K.O., Huittinen N. Investigation of Radiation Damage in the Monazite-Type Solid Solution $La_{1-x}Ce_xPO_4$. *Inorganic Chemistry*, 2024, **63**(38), P. 17525–17535.

[23] Nasdala L., Akhmadaliev S., Burakov B.E., Chanmuang N C., Škoda R. The absence of metamictisation in natural monazite. *Scientific Reports*, 2020, **10**, P. 14676.

[24] Hikichi Y., Nomura T. Melting Temperatures of Monazite and Xenotime. *Journal of the American Ceramic Society*, 1987, **70**(10), P. 252–253.

[25] Bondar I.A., Mezentseva L.P. Single crystals of rare-earth oxides: Constitution and properties. *Progress in Crystal Growth and Characterization*, 1988, **16**, P. 81–141.

[26] Enikeeva M.O., Proskurina O.V., Gusarov V.V. Phase Diagram and Metastable Phases in the $LaPO_4$–YPO_4–(H_2O) System. *Russian Journal of Inorganic Chemistry*, 2024.

[27] Gysi A.P., Hurtig N.C., Juan Han H., Kindall E.C., Guo X., Kulik D.A., Dan Miron G. Reaction calorimetry and structural crystal properties of non-ideal binary rhabdophane solid solutions ($Ce_{1-x}REE_xPO_4 \cdot nH_2O$). *Geochimica et Cosmochimica Acta*, 2024.

[28] Qin D., Mesbah A., Gausse C., Szenknect S., Dacheux N., Clavier N. Incorporation of thorium in the rhabdophane structure: Synthesis and characterization of $Pr_{1-2x}Ca_xTh_xPO_4{\cdot}nH_2O$ solid solutions. *Journal of Nuclear Materials*, 2017, **492**, P. 88–96.

[29] Monjid A.El., Szenknect S., Mesbah A., Hunault M.O.J.Y., Menut D., Clavier N., Dacheux N. Incorporation of U(iv) in monazite–cheralite ceramics under oxidizing and inert atmospheres. *Dalton Transactions*, 2024, **53**, P. 2252–2264.

[30] Zhao X., Wang W., Teng Y., Li Y., Ma X., Liu Y., Ahuja R., Luo W., Zhang Z. Incorporation of Th^{4+} and Sr^{2+} into Rhabdophane/Monazite by Wet Chemistry: Structure and Phase Stability. *Inorganic Chemistry*, 2023, **62**(38), P. 15605–15615.

[31] Chong S., J. Riley B., Lu X., Du J., Mahadevan T., Hegdec V. Synthesis and properties of anhydrous rare-earth phosphates, monazite and xenotime: a review. *RSC Advances*, 2024, **14**, P. 18978–19000.

[32] Rafiuddin M.R., Guo S., Donato G., Grosvenor A.P., Dacheux N., Cava R.J., Mesbah A. Structural and magnetic properties of churchite-type $REPO_4{\cdot}2H_2O$ materials. *Journal of Solid State Chemistry*, 2022, **312**, P. 123261.

[33] Rafiuddin M.R., Tyagi C., Haq M.A. Synthesis and structural investigation of churchite-type $REPO_4{\cdot}2H_2O$ (RE = Y, Gd, Dy) nanocrystals. *Journal of Solid State Chemistry*, 2022, **311**, P. 123150.

[34] Enikeeva M.O., Proskurina O.V., Gerasimov E.Yu., Nevedomskiy V.N., Gusarov V.V. Synthesis under hydrothermal conditions and structural transformations of nanocrystals in the $LaPO_4$-YPO_4-(H_2O) system. *Nanosystems: physics, chemistry, mathematics*, 2023, **14**(6), P. 660–671.

[35] Bamforth T.G., Xia F., Putnis A., Brugger J., Hu S.-Y., Roberts M.P., Suvorova A., Pring A. Hydrothermal mineral replacement in the apatite-rhabdophane-monazite system: Experiments, reaction mechanisms and geological implications. *Chemical Geology*, 2024, **666**, P. 122307.

[36] Subramani T., Rafiuddin M.R., Shelyug A., Ushakov S., Mesbah A., Clavier N., Qin D., Szenknect S., Elkaim E., Dacheux N., Navrotsky A. Synthesis, Crystal Structure, and Enthalpies of Formation of Churchite-type $REPO_4{\cdot}2H_2O$ (RE = Gd to Lu) Materials. *Crystal Growth & Design*, 2019, **19**(8), P. 4641–4649.

[37] Kohlmann M., Sowa H., Reithmayer K., Schulz H., Krüger R.-R., Abriel W. Structure of a $Y_{1-x}(Gd,Dy,Er)_xPO_4{\cdot}2H_2O$ microcrystal using synchrotron radiation. *Acta Crystallographica section C*, 1994, C**50**, P. 1651–1652.

[38] Ivashkevich L.S., Lyakhov A.S., Selevich A.F. Preparation and structure of the yttrium phosphate dihydrate $YPO_4{\cdot}2H_2O$. *Phosphorus Research Bulletin*, 2013, **28**, P. 45–50.

[39] Roncal-Herrero T., Rodríguez-Blanco J.D., Oelkers E.H., Benning L.G. The direct precipitation of rhabdophane ($REEPO_4 \cdot nH_2O$) nano-rods from acidic aqueous solutions at 5–100 °C. *Journal of Nanoparticle Research*, 2011, **13**, P. 4049–4062.

[40] Khalili R., Larsson A.-C., Telkki V.-V., Lantto P., Kantola A.M. Local structures of rare earth phosphate minerals by NMR. *Journal of Solid State Chemistry*, 2022, **311**, P. 123097.

[41] Mesbah A., Clavier N., Elkaim E., Gausse C., Ben Kacem I., Szenknect S., Dacheux N. Monoclinic Form of the Rhabdophane Compounds: $REEPO4{\cdot}0.667H_2O$. Crystal Growth & Design, 2014, **14**(10), P. 5090–5098.

[42] Shelyug A., Mesbah A., Szenknect S., Clavier N., Dacheux N., Navrotsky A. Thermodynamics and Stability of Rhabdophanes, Hydrated Rare Earth Phosphates $REPO_4{\cdot}nH_2O$. *Frontiers in Chemistry*, 2018, **6**(604), P. 1–25.

[43] Enikeeva M.O., Yakovleva A.A., Proskurina O.V., Nevedomskiy V.N., Gusarov V.V. Phase formation under hydrothermal conditions and thermal transformations in the $GdPO_4$-YPO_4-H_2O system. *Inorganic Chemistry Communications*, 2024, **159**, P. 111777.

[44] Mooney R.C.L. Crystal Structures of a Series of Rare Earth Phosphates. *Journal of Chemical Physics*, 1948, **16**, P. 1003.

[45] Mooney R.C.L. X-ray diffraction study of cerous phosphate and related crystals. I. Hexagonal modification. *Acta Crystallographica*, 1950, **3**, P. 337–340.

[46] Enikeeva M.O., Proskurina O.V., Levin A.A., Smirnov A.V., Nevedomskiy V.N., Gusarov V.V. Structure of $Y_{0.75}La_{0.25}PO_4{\cdot}0.67H_2O$ rhabdophane nanoparticles synthesized by the hydrothermal microwave method. *Journal of Solid State Chemistry*, 2023, **319**, P. 123829.

[47] Weiss H., Bräu M. F. How Much Water Does Calcined Gypsum Contain? *Angewandte Chemie International Edition*, 2009, **48**(19), P. 3520–3524.

[48] Duran E.C., Rafiuddin M.R., Shen Y., Hunt S.A., Haq Mirc A., Eggemana A.S. 3D electron diffraction studies of synthetic rhabdophane ($DyPO_4 \cdot nH_2O$). *Acta Crystallographica section C*, 2024, **81**, Part 10, P. 612–619.

[49] Hikichi Y., Murayama K., Ohsato H., Nomura T. Thermal Changes of Rare Earth Phosphate Minerals. *Journal of the Mineralogical Society of Japan*, 1990, **19**(3), P. 117–126.

[50] Hikichi Y., Ota T., Hattori T., Imaeda T. Synthesis and thermal reactions of rhabdophane-(Y). *Mineralogical Journal*, 1996, **18**(3), P. 87–96.

[51] Boakye E.E., Mogilevsky P., Hay R.S. Synthesis of Nanosized Spherical Rhabdophane Particles. *Journal of the American Ceramic Society*, 2005, **88**(10), P. 2740–2746.

[52] Vanetsev A.S., Samsonova E.V., Gaitko O.M., Keevend K., Popov A.V., Mäeorg U., Mändar H., Sildos I., Orlovskii Yu.V. Phase composition and morphology of nanoparticles of yttrium orthophosphates synthesized by microwave-hydrothermal treatment: The influence of synthetic conditions. *Journal of Alloys and Compounds*, 2015, **639**, P. 415–421.

[53] Kijkowska R. Thermal decomposition of lanthanide orthophosphates synthesized through crystallisation from phosphoric acid solution. *Thermochimica Acta*, 2003, **404**(1-2), P. 81–88.

[54] Lucas S., Champion E., Bernache-Assollant D., Leroy G. Rare earth phosphate powders $RePO_4 \cdot nH_2O$ (Re=La, Ce or Y) II. Thermal behavior. *Journal of Solid State Chemistry*, 2004, **177**(4-5), P. 1312–1320.

[55] Jonasson R.G., Vance E.R. DTA study of the rhabdophane to monazite transformation in rare earth (La-Dy) phosphates. *Thermochimica Acta*, 1986, **108**, P. 65–72.

[56] Ochiai A., Utsunomiya S. Crystal Chemistry and Stability of Hydrated Rare-Earth Phosphates Formed at Room Temperature. *Minerals*, 2017, **7**(5), P. 84.

[57] Mesbah A., Clavier N., Elkaim E., Szenknect S., Dacheux N. In pursuit of the rhabdophane crystal structure: from the hydrated monoclinic $LnPO_4^{\cdot}0.667H_2O$ to the hexagonal $LnPO_4$ (Ln = Nd, Sm, Gd, Eu and Dy). *Journal of Solid State Chemistry*, 2017, **249**, P. 221–227.

[58] J. Livage, "Vers une chimie écologique. Quand l'air et l'eau remplacent le pétrole", Le Monde, 1977.

[59] Skogareva L.S., Kottsov S.Yu., Shekunova T.O., Baranchikov A.E., Ivanova O.S., Yapryntsev A.D., Ivanov V.K. Selective precipitation of rare earth orthophosphates with hydrogen peroxide from phosphoric acid solutions. *Russian Journal of Inorganic Chemistry*, 2017, **62**, P. 1141–1146.

[60] Elovikov D.P., Nikiforova K.O., Tomkovich M.V., Proskurina O.V., Gusarov V.V. The pH value influence on the waylandite-structured $BiAl_3(PO_4)_2(OH)_6$ compound formation under hydrothermal conditions. *Inorganica Chimica Acta*, 2024, **561**, P. 121856.

[61] Khrapova E.K., Ivanova A.A., Kirilenko D.A., Levin A.A., Bert N.A., Ugolkov V.L., Krasilin A.A. Phase transformations of $(Co_xMg_{1-x})_3Si_2O_5(OH)_4$ phyllosilicate nanoscrolls upon heating in Ar, O_2 and H_2 containing atmospheres. *Applied Clay Science*, 2024, **250**, P. 107282.

[62] Rietveld H.M. A profile refinement method for nuclear and magnetic structures. *Journal of Applied Crystallography*, 1969, **2**, P. 65–71.

[63] Anfimova T., Li Q., Jensen J.O., Bjerrum N.J. Thermal Stability and Proton Conductivity of Rare Earth Orthophosphate Hydrates. *International Journal of Electrochemical Science*, 2014, **9**(5), P. 2285-2300.

[64] Maslennikova T.P., Osipov A.V., Mezentseva L.P., Drozdova I.A., Kuchaeva S.K., Ugolkov V.L., Gusarov V.V. Synthesis, mutual solubility, and thermal behavior of nanocrystals in the $LaPO_4$-YPO_4-H_2O system. *Glass Physics and Chemistry*, 2010, **36**, P. 351–357.

[65] Patra C.R., Gabashvili A., Patra S., Jacob D.S., Gedanken A., Landaua A., Gofer Y. Microwave approach for the synthesis of rhabdophane-type lanthanide orthophosphate (Ln = La, Ce, Nd, Sm, Eu, Gd and Tb) nanorods under solvothermal conditions. *New Journal of Chemistry*, 2005. **29**(5), P. 733–739.

[66] Zhao X., Teng Y., Li Y., Zheng X., Zheng Q., Ma R., Liu G., Liu Y., Ahuja R., Luo W. Response of Nd^{3+} and Sm^{3+} precipitating into rhabdophane and the leaching mechanism of associated monazite ceramics. *Journal of the American Ceramic Society*, 2022, **106**(2), P. 1287–1298.

Submitted 30 September 2024; revised 11 November 2024; accepted 25 November 2024

Information about the authors:

Maria O. Enikeeva – Ioffe Institute, 194021 St. Petersburg, Russia; Branch of Petersburg Nuclear Physics Institute named after B.Ṗ. Konstantinov of National Research Centre "Kurchatov Institute" – Institute of Silicate Chemistry, 199034, St. Petersburg, Russia; ORCID 0000-0002-9633-4421; i@odin2tri.ru

Kseniya A. Zhidomorova – Branch of Petersburg Nuclear Physics Institute named after B.Ṗ. Konstantinov of National Research Centre "Kurchatov Institute" – Institute of Silicate Chemistry, 199034, St. Petersburg, Russia; St. Petersburg State Institute of Technology, 190013, St. Petersburg, Russia; ORCID 0009-0007-6447-7341; zhidomorovak@gmail.com

Dmitriy P. Danilovich – St. Petersburg State Institute of Technology, 190013, St. Petersburg, Russia; ORCID 0000-0001-7110-557X; dmitrydanilovich@gmail.com

Vladimir N. Nevedomskiy – Ioffe Institute, 194021 St. Petersburg, Russia; ORCID 0000-0002-7661-9155; nevedom@mail.ioffe.ru

Olga V. Proskurina – Ioffe Institute, 194021 St. Petersburg, Russia; St. Petersburg State Institute of Technology, 190013, St. Petersburg, Russia; ORCID 0000-0002-2807-375X; proskurinaov@mail.ru

Victor V. Gusarov – Ioffe Institute, 194021 St. Petersburg, Russia; ORCID 0000-0003-4375-6388; gusarov@mail.ioffe.ru

Conflict of interest: the authors declare no conflict of interest.

NANOSYSTEMS:
PHYSICS, CHEMISTRY, MATHEMATICS

Jebisha S., et al. *Nanosystems: Phys. Chem. Math.*, 2024, **15** (6), 793–805.
http://nanojournal.ifmo.ru
DOI 10.17586/2220-8054-2024-15-6-793-805

Original article

$(CdO)_{1-x}(Mn_3O_4)_x$ ($x = 0.0/0.25/ 0.50/0.75/1.0$) nanocrystals: preparation by a facile method, physicochemical properties and applications

Selvaraj Jebisha[1], Ganesan Deepa[2], Jesumarian Johnson[3], Chelliah K. Mahadevan[4]

[1]M.S. University, Tirunelveli, Tholayavattam-629167, Tamil Nadu, India
[2]Pioneer Kumaraswamy College, Nagercoil-629003, Tamil Nadu, India
[3]Annai Velankanni College, Tholayavattam-629167, Tamil Nadu, India
[4]Bharathidasan University, Tiruchirappalli-620024, Tamil Nadu, India

Corresponding author: G. Deepa, gdeepavinod@ymail.com; C. K. Mahadevan, mahadevan58@yahoo.co.in

ABSTRACT High phase pure $(CdO)_{1-x}(Mn_3O_4)_x$ ($x = 0.0/0.25/0.50/0.75/1.0$) nanocrystals (including multi-phased nanocomposites) were prepared by using a simple microwave-assisted solvothermal method, and characterized structurally, chemically, optically and electrically by carrying out X-ray diffraction, electron microscopic (SEM/TEM), energy dispersive X-ray absorption spectral, optical (UV-Vis) absorption spectral and AC electrical (at various temperatures and frequencies) measurements. Samples prepared exhibit crystalline nature, high chemical purity, nearly uniform spherical morphology, considerable particle sizes (within 47 nm), higher optical band gap energies (4.0 – 5.3 eV) and normal dielectric behavior. Studies were made to understand their capability in photocatalytic degradation (evaluated using Methylene Blue (MB) dye under UV-visible irradiation) and antimicrobial activity against gram positive Bacillus Subtilis (BS), gram negative Escherichia Coli (EC) and fungal Candida Albicans (CA). Results indicate a higher photocatalytic degradation with MB dye for the three multi-phased $(CdO)_{1-x}(Mn_3O_4)_x$ nanocomposites (with $x = 0.25/0.50/0.75$) prepared (with light of wavelength around 665 nm), and a higher antimicrobial activity with the bacteria (BS and EC) than with the fungus (CA); however, the phase pure Mn_3O_4 (with $x = 1.0$) nanocrystal has been found to be more active with all the three microbes considered.

KEYWORDS transition metal oxides nanocomposites, microwave-assisted solvothermal method, physicochemical properties, photocatalytic degradation, antimicrobial activity

ACKNOWLEDGEMENTS Authors are thanful to the Department of Physics and Research Centre of Annai Velankanni College, Tholayavattam, for providing AU 2603 UV-VIS Double Beam Spectrometer and Muffle furnace.

FOR CITATION Jebisha S., Deepa G., Johnson J., Mahadevan C.K. $(CdO)_{1-x}(Mn_3O_4)_x$ ($x = 0.0/0.25/ 0.50/0.75/1.0$) nanocrystals: preparation by a facile method, physicochemical properties and applications. *Nanosystems: Phys. Chem. Math.*, 2024, **15** (6), 793–805.

1. Introduction

Mn is a complex (but interesting) transition metal that may exist in a variety of oxidation states and can create a variety of oxides (including MnO, Mn_2O_3, Mn_3O_4 and MnO_2), which have a wide range of engineering applications. Cadmium oxide, crystallizing in a cubic rocksalt lattice (with anion centers and octahedral cation), due to its propensity to develop fault structures brought on by anion vacancies, it is uncommon in that it can be found in a variety of hues. The transition metal oxides (TMOs) such as cadmium oxide (CdO) and trimanganese tetraoxide (Mn_3O_4) have been found to be very interesting and highly useful in many applications when they are in nanocrystalline state. The CdO and Mn_3O_4 nanocrystals (nanoparticles) have been prepared in several ways with different morphologies; the crystallite (particle) size depends on the methods of preparation [1].

Nanocrystalline CdO (brown in color, an n-type semiconductor) has low electrical resistivity, high mobility and large refractive index, and has wide range of applications in cadmium plating baths, solar cells, electrodes for storage batteries, *etc*; also, it shows interesting photocatalytic degradation with methylene blue (MB) dye and antimicrobial activity [2–7]. There are several methods to prepare CdO nanoparticlessuch as solvothermal method, chemical method, hydrothermal method, sonochemical method, electrochemical method, microwave combustion method, thermal evaporation method, *etc.*; and they have been found to have excellent morphologies like nanocubes, nanoclusters, rhombus, nanowires, nanotubes and nanorods [1–7].

Somasundaram *et al.* [5] have recently reported the hydrothermal synthesis of cubic CdO nanocrystals with crystallite size of about 40 nm. Christuraj *et al.* [6] have reported the prepartion of pure and Mn doped CdO nanoparticles, calcined at 400 °C by co-precipitation method. Very recently, Alaa Munshi *et al.* [8] have reported their comparative investigation of physicochemical properties of CdO nanoparticles synthesized utilizing urea-assisted auto-combustion and microwave combustion methods. They have found the phase and crystallite size of CdO nanoparticles modified, indicating the influence of heat treatment (at 350 °C) and synthesis procedure.

Nanocrystalline Mn_3O_4 (having higher potential than MnO) is a mixed oxide possessing high capacity, low toxicity, low current density and large surface area; and its spinel structure has Mn^{2+} and Mn^{3+} ions occupying the tetrahedral and octahedral sites respectively [9, 10]. Mn_3O_4 nanoparticles prepared by microwave assisted method have excellent performance as supercapacitors [11]. Atique Ullah *et al.* [12] have successfully synthesized Mn_3O_4 nanoparticles and studied the degradation of MB dye using it. Rafi Shaik *et al.* [13] have obtained the antimicrobial activity against cancer cells using Mn_3O_4 nanoparticles. Kalaiselvan *et al.* [14] have shown that the difference in particle sizes has considerable impact on toxicity, magnetic anisotropy constant and other cubic spinel structure properties, which are the main factors for biomedical applications. Tiny nanoparticles have peculiar physical and chemical properties than their bulk counterparts; and many emerging technologies (including solar energy conversion, optical devices, optical imaging and biomedical detection and therapy) need hybrid nanomaterials with improved optical and electronic properties [15]. Moreover, multi-phased nanocomposites reveal some interesting charactreistics than mono-phased nanomaterials; $CdCO_3$–Mn_3O_4 [15], ZnO/In_2O_3 [16], ZnO/CdO/CeO_2 [17] and Mn_3O_4/ZnO/Eu_2O_3 [18] are examples. Sundar *et al.* [19] have prepared the two-component $Zn_xCd_{1-x}O$ (with $x = 0.0/0.2/0.4/0.6/0.8/1.0$) nanocrystals by the microwave-assisted solvothermal technique (using a domestic microwave oven) and found that the optical bandgap energy changes from 2.24 – 3.06 eV when x is changed from 0.0 to 1.0; the phase purity occurred after annealing the as-prepared samples at 450 °C for 30 min. Nallendran *et al.* [20] have reported the photoconductive and photocatalytic properties of CdO–NiO nanocomposites synthesized by a cost-effective chemical method.

As nanocrystalline CdO and Mn_3O_4 are found to be very interesting, in order to discover new materials, an attempt has been made to prepare (by using the simple microwave-assisted solvothermal procedure, and easily available chemicals as precursors and solvent) and characterize (by determining their physicochemical properties using the available standard techniques) the two-component CdO-Mn_3O_4 (in different compositions) nanocrystals. As CdO and Mn_3O_4 are not isomorphous systems, it may not be possible for us to get lattice mixing sufficiently for the formation of mono-phased solid solutions with them. However, it is already known that creating a multi-component nanocomposite, whether it be mono or multi-phased, may result in the development of novel, intriguing features.

Earlier, Deepa and Mahadevan [21] have attempted to prepare the $(CdCO_3)_{0.5}(Mn_3O_4)_{0.5}$ nanocomposite (using cadmium acetate, manganese acetate and urea as the precursors, and ethylene glycol as the solvent) by a simple microwave-assisted solvothermal method using a domestic microwave oven; they found that the as-prepared sample (understood as $CdCO_3$–Mn_3O_4) has to be annealed at 300 °C to get the nanocomposite (two-phased) with higher phase purity, reduced crystallite size and homogeneity. Later, the same authors [15] have reported the synthesis and properties of un-doped and S^{2-} doped $(CdCO_3)_{1-x}(Mn_3O_4)_x$ nanocomposites (with $x = 0.0$, 0.25, 0.50, 0.75 and 1.0); the results of their thermal analysis have shown that when the as-prepared samples are annealed at more than 600 °C, two-phased nanocomposites (solid solutions) of $(CdO)_{1-x}(Mn_3O_4)_x$ (with $x = 0.0$, 0.25, 0.50, 0.75 and 1.0) can be prepared with high phase purity. So, in the present study, the $(CdO)_{1-x}(Mn_3O_4)_x$ (with $x = 0.0$, 0.25, 0.50, 0.75 and 1.0) nanocrystals (including multi-phased nanocomposites) were prepared by following the method adopted by Deepa and Mahadevan [15] along with annealing the prepared (As-prepared) samples at 650 °C, and then characterized structurally, chemically, optically and electrically. Moreover, photocatalytic degradation (evaluated using MB dye under UV-visible light irradiation) and antimicrobial activity (against gram positive Bacillus Subtilis, gram negative Escherichia Coli and fungus Candida Albicans) have been studied for the As-prepared (un-annealed) and annealed samples. The details are reported herein.

2. Experimental techniques

2.1. Materials

Analytical reagent (AR) grade precursors used in the present study arecadmium acetate dihydrate ($(CH_3COO)_2Cd{\cdot}2H_2O$), manganese acetate tetrahydrate ($(CH_3COO)_2Mn{\cdot}4H_2O$) and urea ($CH_4N_2O$); the solvent utilized was ethylene glycol. All the chemicals considered have beenused without any further purification.

2.2. Sample preparation

Method adopted by Deepa and Mahadevan [15] was used (along with annealing at 650 °C) to synthesise the proposed $(CdO)_{1-x}(Mn_3O_4)_x$ (with $x = 0.0$, 0.25, 0.50, 0.75 and 1.0) nanocrystals (a total of 5 samples). To create homogeneous solution, appropriate composition (x) of cadmium acetate dihydrate and manganese acetate tetrahydrate was dissolved in ethylene glycol (in a beaker); this solution was combined in a 1:3 molal ratio with urea and dissolved for 30 minutes with slight heating and strong stirring. The above solution (taken in a borosil bowl with lid) was microwave irradiated for about 15 – 20 min (till the formation of a colloidal precipitate) utilizing a domestic microwave oven (with 800 W power and 2.45 GHz frequency).

The resultant colloidal precipitate was cooled, washed with acetone three times, and then several times with double distilled water to eliminate any remaining organic contaminates, if any. This washed precipitate was filtered with whatman filter paper and dried in open air atmosphere to get the As-prepared (un-annealed) sample. Finally, the five un-annealed samples obtained were annealed at 650 °C for 2 hin a muffle furnace to obtain the proposed $(\mathrm{CdO})_{1-x}(\mathrm{Mn_3O_4})_x$ (with $x = 0.0, 0.25, 0.50, 0.75$ and 1.0) nanocrystals. By using 2 ton hydraulic pressure, disk shaped pellets of 13 mm diameter (that were needed for some characterization investigations) were created from the powder samples.

The proposed powder samples prepared can be stored for a long time in self-locked covers. Fig. 1(a) shows a photograph of the five powder samples prepared [A1 ($x = 0.0$, CdO), A2 ($x = 0.25$, $(\mathrm{CdO})_{0.75}(\mathrm{Mn_3O_4})_{0.25}$), A3 ($x = 0.5$, $(\mathrm{CdO})_{0.5}(\mathrm{Mn_3O_4})_{0.5}$), A4 ($x = 0.75$, $(\mathrm{CdO})_{0.25}(\mathrm{Mn_3O_4})_{0.75}$) and A5 ($x = 1.0$, $\mathrm{Mn_3O_4}$]. The As-prepared samples are represented here as U1, U2, U3, U4 and U5, respectively. The color of the As-prepared samples have been found to be intensified on annealing at 650 °C.

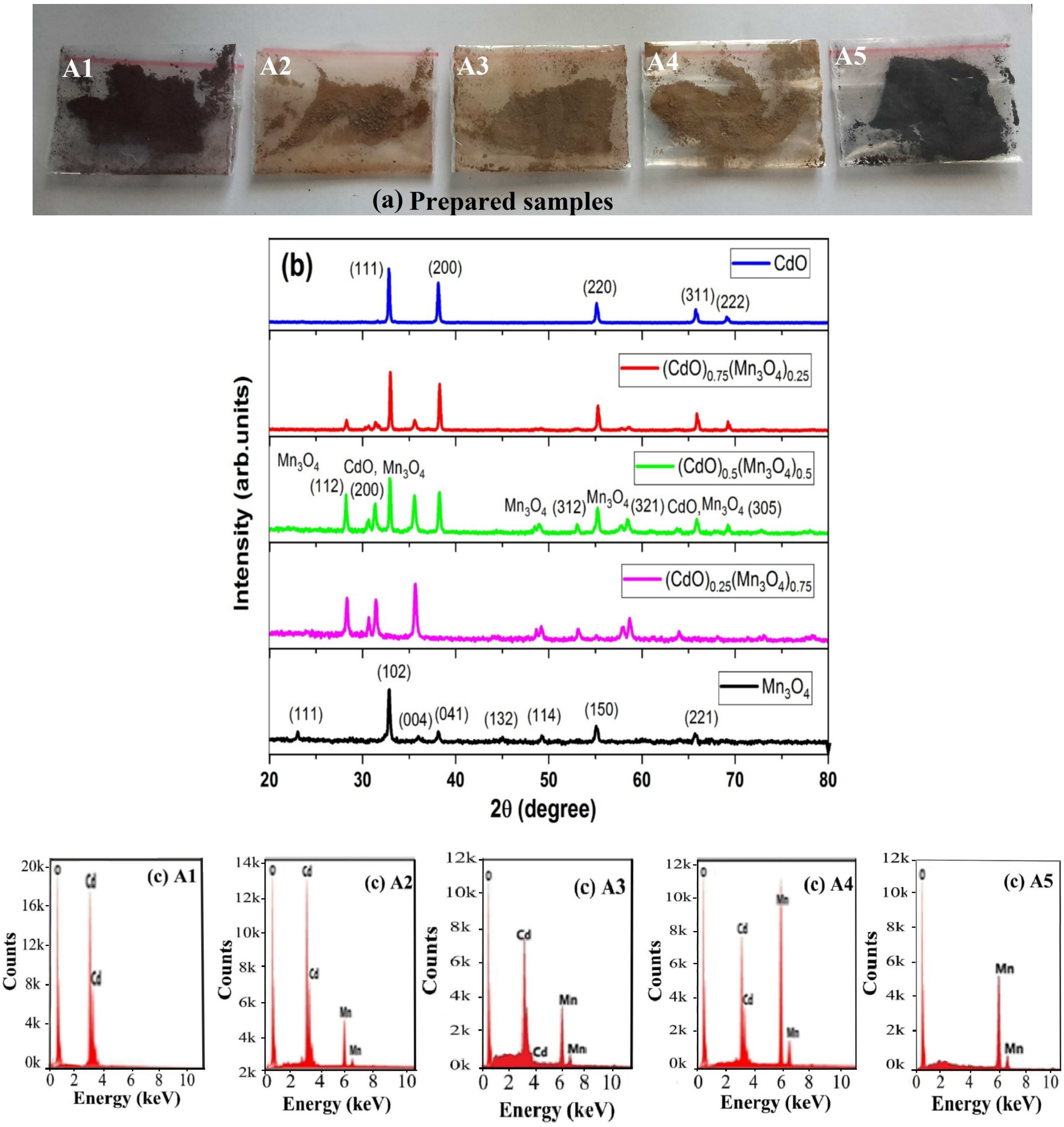

FIG. 1. A photograph showing the proposed powder samples prepared (a); The XRD patterns observed for the $(\mathrm{CdO})_{1-x}(\mathrm{Mn_3O_4})_x$ nanocrystals prepared (b); The EDX spectra observed for the $(\mathrm{CdO})_{1-x}(\mathrm{Mn_3O_4})_x$ nanocrystals prepared (c)

2.3. Characterization

All the five $(CdO)_{1-x}(Mn_3O_4)_x$ nanocrystals (A1, A2, A3, A4 and A5) prepared were characterized by determining their physicochemical properties using the available standard techniques. X-ray diffraction (XRD) patterns were made for all the five nanocrystals prepared using an XPERT-PRO X-ray diffractometer with monochromated CuKα ($\lambda = 1.54060$ Å) radiation in the 2θ range of 20 – 80°, with a scan speed of 2 °/min.

Scanning electron microscopic (SEM) images and energy dispersive X-ray absorption (EDX) spectra were recorded for all the five nanocrystals prepared using a JEOL SEM model, JSM5600LV scanning electron microscope with EDX attachment. Transmission electron microscopic (TEM) images were obtained for all the five nanocrystals prepared by using a JEOL 2011 transmission electron microscope, operating with a voltage of 200 kV; small area electron diffraction (SAED) pattern was also recorded for the sample A3.

The UV-V is (optical) absorption spectrum were captured in the wavelength range of 200 – 800 nm using a PerkinElmer UV-visible spectrophotometer (Lambda 35). The dielectric mesurements were carried out (within ± 2 % accuracy) by the parallel plate capacitor method [15] on pelletised samples using an LCR meter (Agilent 4284A) with five various applied field frequencies (100 Hz, 1 kHz, 10 kHz, 100 kHz and 1 MHz), and at twelve various temperatures between 40 – 150 °C (in step of 10 °C).

In order to understand the application potential of the samples prepared, evaluation of photocatalytic degradation (using MB dye under UV-visible light irradiation, with Xenon lamp) and antimicrobial activity against Bacillus Subtilis (+ive), Escherichia Coli (−ive) and Candida Albicans (fungal) was carried out for all the five annealed samples (CdO–Mn_3O_4). The study has been extended to three un-annealed samples ($CdCO_3$–Mn_3O_4 nanocomposites) also: U2 ($x = 0.25$, $(CdCO_3)_{0.75}(Mn_3O_4)_{0.25}$), U3 ($x = 0.5$, $(CdCO_3)_{0.5}(Mn_3O_4)_{0.5}$) and U4 ($x = 0.75$, $(CdCO_3)_{0.25}(Mn_3O_4)_{0.75}$).

3. Results and discussion

3.1. XRD analysis

Figure 1(b) displays the indexed XRD measurements observed for the $(CdO)_{1-x}(Mn_3O_4)_x$ nanocrystals (A1, A2, A3, A4 and A5) prepared. All the five patterns contain no peaks related to any impurity (other than peaks related to CdO and Mn_3O_4), which confirms the high phase purity of the samples prepared. Also, the sharp peaks are an indication of good crystallinity with reduced strain. The peaks observed for sample A1 at angles 32.84, 38.13, 55.11, 65.74 and 69.08° (corresponding to the crystal planes (111), (200), (220), (311) and (222), respectively) match well with the JCPDS card pattern for the CdO [JCPDS card No. 73-2245], and also with that reported earlier for CdO nanowires [22]. Also, the CdO nanocrystal is found to have the face centered cubic structure with space group Fm$\overline{3}$m, and the estimated lattice constant (a) is found to be 4.699 Å. The peaks observed for sample A5 at angles 23.05, 32.85, 38.13, 49.30, 55.03 and 65.73° (corresponding to the crystal planes (111), (102), (041), (114), (150) and (221), respectively) match well with the JCPDS card pattern for the Mn_3O_4 [JCPDS card No. 75-0765]. The Mn_3O_4 nanocrystal is found to have the orthorhombic structure with space group Pbcm, and the estimated lattice parameters are found to be: $a = 3.042$, $b = 9.682$ and $c = 9.571$ Å.

The PXRD patterns observed for the samples A2, A3 and A4 contain peaks corresponding to both CdO and Mn_3O_4 phases, which indicates that these samples are multi-phased $(CdO)_{1-x}(Mn_3O_4)_x$ nanocomposites. Changes observed in the XRD patterns for these nanocomposites with all of the end members (A1 and A5) indicate that mixing/alloying has taken place in them (A2, A3 and A4). However, few peaks appearingrelated to XRD of Mn_3O_4 in the middle composition match with that for the body-centered tetragonal phase of Mn_3O_4[JCPDS card No. 24-0734]; this is in agreement with that observed by Bousqet–Berthelin and Stuerga [23] for the Mn_3O_4 nanoparticles.

The average crystallite/particle size (D) values of the samples were estimated using the Scherrer's relation: $D = K\lambda/(\beta\cos\theta)$ [28], where λ refers wavelength of X-rays ($= 1.54060$ Å), θ is the Bragg angle of the major peak(s), $K = 0.9$ displays Scherrer's constant, and β is the full width (in radian) at half of maximum intensity of the major peak(s). The estimated D values are 45.2, 41.8, 40.4, 38.6 and 44.7 nm for the samples A1, A2, A3, A4 and A5, respectively. The D value is found to decrease with the increase in Mn concentration. However, for the Mn_3O_4, the value increases and becomes nearly equal to that for the CdO. Moreover, when compared with the un-annealed $[(CdCO_3)_{1-x}(Mn_3O_4)_x]$ nanocrystals (the D values vary from 6.6 to 21.0 nm, increasing as the Mn concentration increases) [15], the particle sizes of the annealed $[(CdO)_{1-x}(Mn_3O_4)_x]$ nanocrystals have increased more significantly along with improved crystallinity. However, the average crystallite sizes found in the present work compare well with that reported (40 nm) for the cubic CdO nanocrystals prepared by the hydrothermal method [5].

3.2. EDX spectral analysis

The observed EDX spectra for all the five $(CdO)_{1-x}(Mn_3O_4)_x$ nanocrystals prepared are shown in Fig. 1(c). The spectrum observed for CdO (A1) shows only Cd and O peaks and the spectrum observed for Mn_3O_4 (A5) shows only Mn and O peaks; and the spectra observed for the nanocomposites (A2, A3 and A4) show only Cd, Mn and O peaks. This shows the higher chemical purity of the nanocrystals prepared, and this result is in agreement with that observed through XRD analysis; also, formation of mixed nanocomposites is confirmed in the case of A2, A3 and A4 samples. It can be seen that, for the mixed nanocomposites, the Cd content decreases nearly in proportion with the increase in x value; that is, the nanocomposites are properly formed as proposed.

3.3. SEM analysis

Figure 2(a) displays the SEM images obtained for all the five nanocrystals prepared; the SEM images reveal that most of the nanoparticles are agglomerated with spherical shape of different sizes. The end members (A1 and A5) are found to have regular and irregular spherical shapes. The nanocomposites (A2, A3 and A4) exhibit agglomerated spherical shape and cluster like patterns. In Fig. 2(a), it was observed that the average particle size from the SEM images varies between 40 – 65 nm [24, 25]. The average crystallite sizes observed from the XRD analysis for all the five nanocrystals prepared are found to be nearly two-third of the average particle sizes obtained through SEM analysis.

3.4. TEM and SAED analysis

The TEM imagesobtained for all the nanocrystals prepared (A1, A2, A3, A4 and A5), and the SAED pattern observed (as an illustration) for the sample A3 are shown respectively in Fig. 2(b,c). The TEM images indicate that the majority of particles appear to be agglomerated in spherical shape.The average particle sizes of the nanoparticles were found to be in the range from 50 – 90 nm [26, 27]. As with the SEM analysis, these are also found to be nearly two times of that obtained through XRD analysis. Furthermore, the TEM images observed have given similar results (regarding the shape of the particles) with that given by the SEM images observed. This shows that the average crystallite sizes obtained through XRD analysis (more valid for spherical and cubic shaped nanocrystals) can be considered as the average individual particle sizes.

The SAED pattern corresponding to the thin rings indicate the plane values such as (112), (211) and (325). The selected area electron diffraction (SAED) pattern observed for the sample A3 shows bright diffraction spots, which indicates a good crystallinity with polycrystalline aggregation [28]; the other samples can also be understood to have (in line with A3) better and good crystalline nature with polycrystalline aggregation.

3.5. UV-visible absorption spectral analysis

The UV-visible absorption spectra recorded in the present study are displayed in Fig. 3; the sharp and maximum absorption intensity peak (absorption band) appears in the UV region (within the wavelength range 230 – 310 nm) for all the five nanocrystals studied. Karthik *et al.* [2] have observed the absorption band for the CdO nanoparticle at around 225 nm. The intense absorption peaks observed in the UV region can be attributed mainly to the allowed charge transfer transitions, O^{2-} to Mn^{2+} and O^{2-} to Mn^{3+} [15]. The optical bandgap energy (E_g) values have been estimated from the absorption edges using the Planck's relation: $E_g = hc/\lambda$, where h specifies the Planck's constant, c refers velocity of light and λ refers wavelength of light (absorption edge). The E_g values obtained are 4.0 eV for A1, 4.7 eV for A2, 4.9 eV for A3, 5.3 eV for A4 and 4.6 eV for A5.

The E_g values observed are found to (nearly) depend on the average particle sizes of the samples; as the particle size increases the E_g value decreases [28]. The E_g value varies from 4.0 eV (for sample A1) to 5.3 eV (for sample A4); correspondingly, the D value varies from 45.26 nm (for sample A1) to 38.64 nm (for sample A4), which indicates that the absorption edge gets blue shifted. Morover, the E_g value increases with the rise in Mn content (x) in the case of nanocomposites (A2, A3 and A4) prepared. For the un-annealed samples [(CdCO$_3$)$_{1-x}$(Mn$_3$O$_4$)$_x$], particularly for the nanocomposites (with $x = 0.25$, 0.50 and 0.75), the spectra contain multiple absorption bands and E_g values [15]. It can be understood that the difference in optical absorption properties between the un-annealed [15] and annealed [present study] samples could be due to the differences in crystallinity, crystallite size, chemical difference, chemical phase purity, etc.

3.6. Dielectric properties

The dielectric measurements were performed on all the five pelletised samples prepared at twelve various temperatures and with five various frequencies by the parallel plate capacitor method. The dielectric constant (ε_r) and AC electrical conductivity (σ_{ac}) values were calculated from the measured capacitance (C) and dielectric loss factor ($\tan\delta$) values by using the relations: (1) $\varepsilon_r = (C/C_{\text{air}})$ and (2) $\sigma_{ac} = (\varepsilon_0)(\varepsilon_r)(\omega)(\tan\delta)$, where C_{air} is the air capacitance, (ε_0) is the permitivity of free space ($= 8.85 \cdot 10^{-12}$ C^{2}N^{-1}M^{-2}), ω refers the angular frequency ($= 2\pi f$), and f implies the frequency of the applied AC electric field.

The temperature dependences of dielectric constant, dielectric loss factor and AC electrical conductivity observed for all the five nanocrystals prepared are displayed in Fig. 4(a,b,c), respectively. The values ε_r and $\tan\delta$ values are observed to increase with increasing temperature, and fall with increasing frequency; the σ_{ac} value is found to increase with both temperature and frequency. This shows that all the five nanocrystals studied exhibit a normal dielectric behavior; however, sample A5 is found to have maximum dielectric constants among all the five samples considered.

The energy that a solid substance has accumulated from an applied AC electric field is known as the ε_r with increase of temperature can essentially be due to the temperature dependency of polarizability due to ionic, dipolar, electronic and space charge contributions; the higher ε_r values found at lower frequencies can be attributed to the space charge,

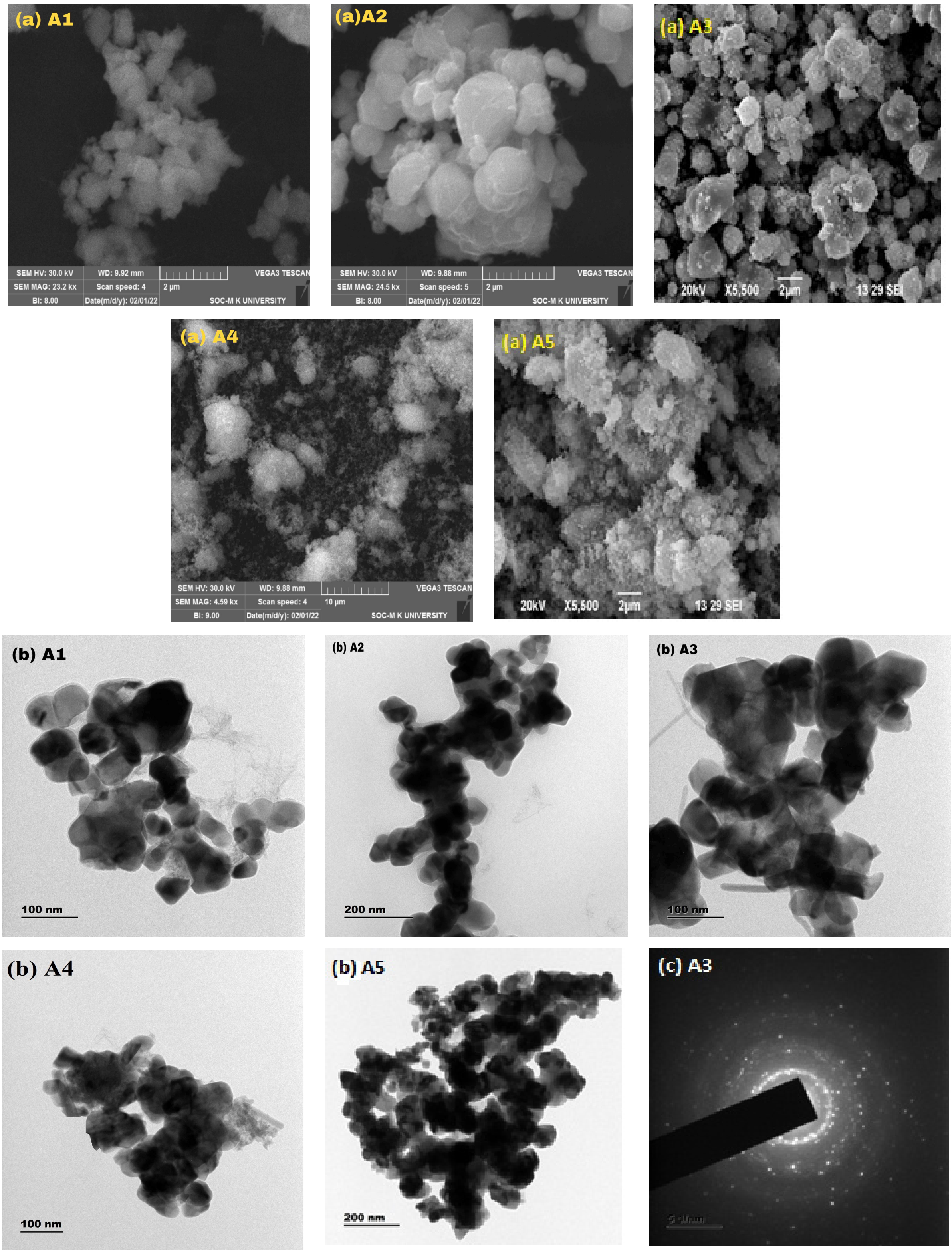

FIG. 2. The SEM images obtained for the $(CdO)_{1-x}(Mn_3O_4)_x$ nanocrystals prepared (a); The TEM images observed for all the five $(CdO)_{1-x}(Mn_3O_4)_x$ nanocrystals, and the SAED pattern for the sample A3 prepared (b,c)

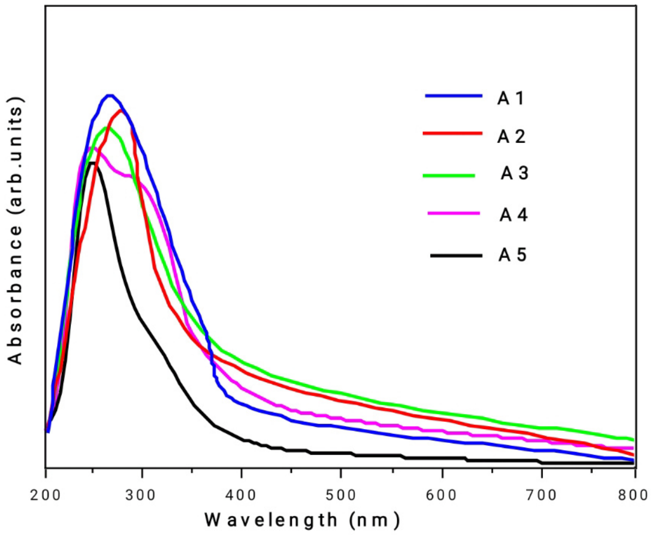

FIG. 3. The UV-visible absorption spectra observed for the $(CdO)_{1-x}(Mn_3O_4)_x$ nanocrystals prepared

crystal grain, crystal grain boundary, ionic, dipolar and electronic contributions to the polarizability [28]. The purity of the nanomaterials under consideration affects the space charge polarization; and the dielectric loss usually takes place due to the absorption of current.

Among the nanocomposites prepared, sample A4 has higher values for the dielectric parameters (ε_r, $\tan\delta$ and σ_{ac}); the D value is minimum for this. The dielectric parameters are found not to vary systematically with the mixed composition (x) in the case of nanocomposites prepared; this results from increased charge carrier and vacancy diffusion along crystal grain boundaries. It is conceivable that the non-synstematic variation of dielectric properties observed as a result of mixing may be caused by non-homogeneity between the crystal grains and crystal grain boundary regions as well as the reduction of movable charges [28].

3.7. Photodegradation of MB dye

The $(CdO)_{1-x}(Mn_3O_4)_x$ samples (A1, A2, A3, A4 and A5) have been investigated with the degradation of Methylene Blue (MB) dye under UV-visible light irradiation and the outcomes obtained are displayed in Fig. 5(a). The photocatalytic activity normally depends on the particle size, optical bandgap energy and particulate surface area of the prepared samples [29]; and this photocatalysis reaction has been used in many medical and environmental applications [30]. In the present study, 100 ml of MB dye solution was added with 50 mg of the prepared sample and stirred for 20 min; the maximum UV-visible light absorption occurred at the wavelength 665 nm and the absorbance decreased as the irradiation time increased (0, 15, 30, 45, 60, 75 and 90 min are the irradiation times used).

The degradation rate was determined by using the pseudo first order kinetic mode,as expressed in Eq. (1) [31]:

$$\log(C_t/C_0) = \log(A_t/A_0) = -k_{\text{app}}t, \tag{1}$$

where C_0 is the intial concentration of MB dye at time 0 (min), k_{app} is the apparent first order rate constant (considered to be the degradation rate in min^{-1} unit), C_t is the final concentration of MB dye at time t (min) and A_0 and A_t are the absorbances at times 0 and t min. The k_{app} values obtained for the samples A1, A2, A3, A4 and A5 are 0.019, 0.152, 0.760, 0.981 and 0.044 min^{-1}, respectively. The k_{app} values observed for the nanocomposites (A2, A3 and A4) are significantly larger than that observed for the end members (A1 and A5); also, for the nanocomposites, the k_{app} value is found to increase with the decrease in x value, which can also be related to the decrease of D value. Karthik *et al.* [2] have found a k_{app} value of 0.0167 min^{-1} for the photocatalytic activity of CdO nanoparticle with MB dye degradation under UV-visible light irradiation; this is in agreement with that found in the present work. Eq. (2) can be used to estimate the degradation percentages:

$$\text{Degradation (\%)} = (A_0 - A_t/A_0) \times 100. \tag{2}$$

The degradation percentages obtained are 62, 85, 88, 95 and 73 %, respectively, for the samples A1, A2, A3, A4 and A5 (with A4 having the maximum degrading efficiency). It has been found that the sample $(CdO)_{0.25}(Mn_3O_4)_{0.75}$ (A4) reacts as a good photocatalyst and better degrades the MB dye under UV-visible light irradiation. Further, Fig. 5(a) shows nearly linear variation of $\log(A_t/A_0)$ with time (t); the recombination of e$^-$/h$^+$ pairs has given easier responses for the degradation [5].

Photocatalytic activity of the un-annealed samples [$(CdCO_3)_{1-x}(Mn_3O_4)_x$ nanocomposites, U2, U3 and U4] has also been studied under UV-visible light irradiation for the degradation of MB dye (0, 10, 25, 40, 55 and 70 min are the irradiation times used), and the results obtained are shown in Fig. 5(b). The maximum absorbance of MB dyeis found to

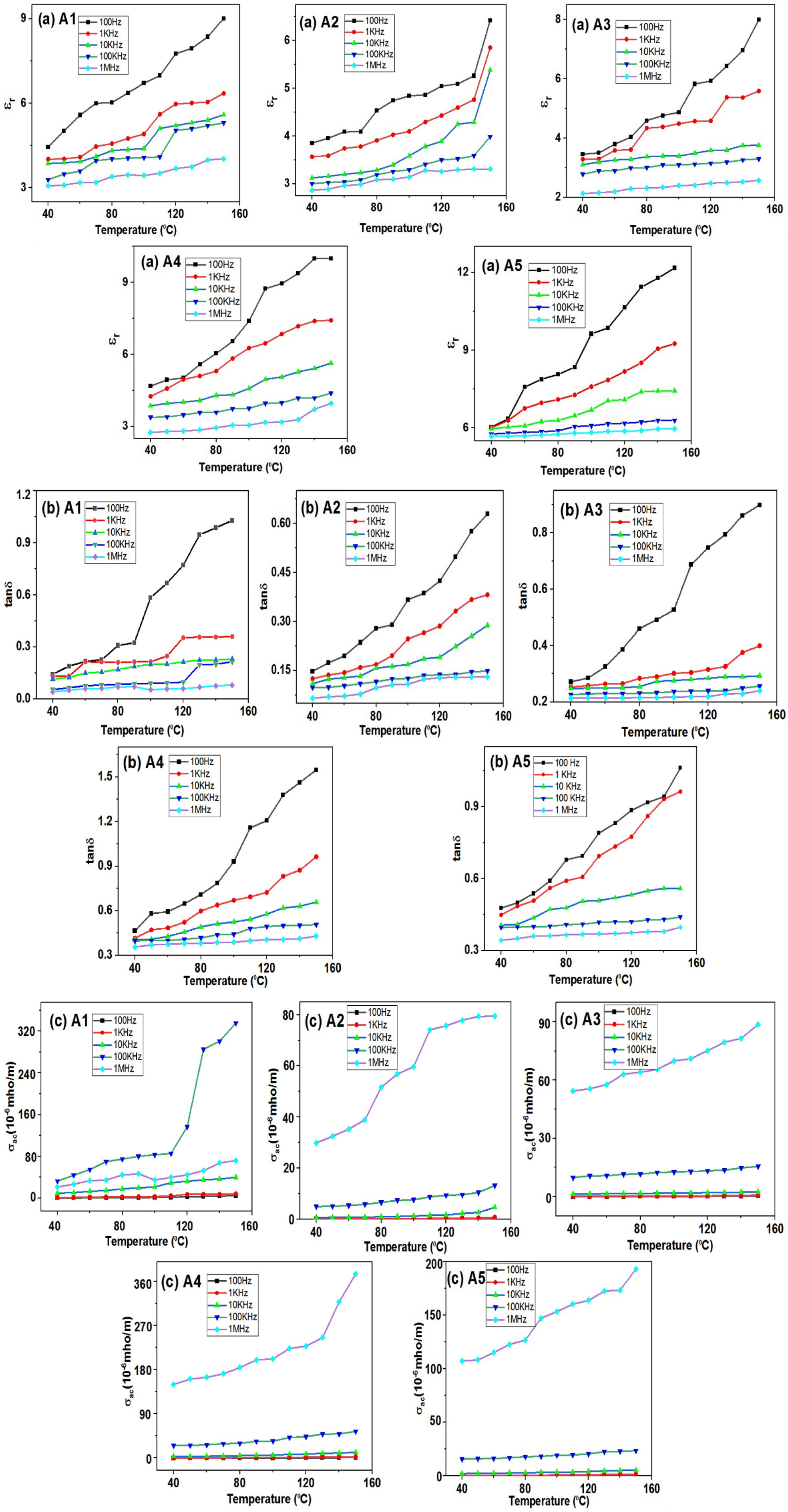

FIG. 4. Temperature dependence of the dielectric constant (ε_r) (a); the dielectric loss factor ($\tan\delta$) (b) and the AC electrical conductivity (σ_{ac}) (c) for the $(CdO)_{1-x}(Mn_3O_4)_x$ nanocrystals prepared

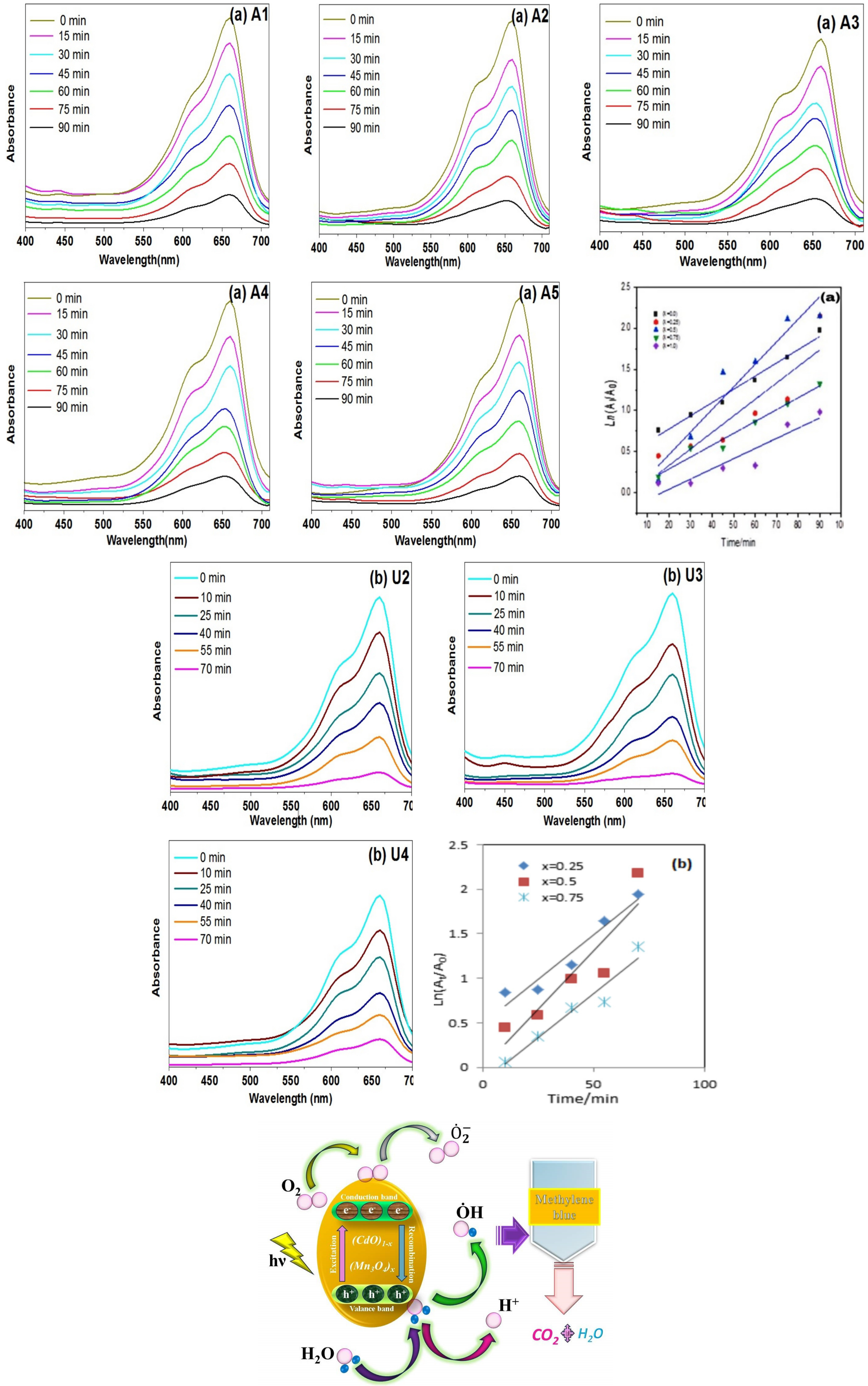

FIG. 5. Photocatalytic degradation curves and the linear plots of $\log(A_t/A_0)$ versus reaction time obtained for the annealed (a) and the un-annealed (b) (CdO)$_{1-x}$(Mn$_3$O$_4$)$_x$ nanocrystals prepared. A schematic diagram of the possible mechanism for the degradation of MB dye over the nanocrystals prepared in the present study (c)

be at 660 nm, and the irradiation time increases with the increasing absorbance. The k_{app} values obtained are 0.011, 0.013 and 0.015, respectively, for the samples U2, U3 and U4; and the photodegradation percentages obtained for the samples U2, U3 and U4 are 44, 49 and 65 % (with U4 having the maximum degrading efficiency), respectively. Fig. 5(b) shows a nearly linear relationship of $\log(A_t/A_0)$ with time (t), which is in line with that observed for the samples A1, A2, A3, A4 and A5.

From the above results, it can be understood that the $(\text{CdO})_{1-x}(\text{Mn}_3\text{O}_4)_x$ nanocomposites (A2, A3 and A4) exhibit significantly higher photocatalytic activity (photodegradation percentages are in the range of 85 – 95 % in about 90 min) than that exhibited by the $(\text{CdCO}_3)_{1-x}(\text{Mn}_3\text{O}_4)_x$ nanocomposites (U2, U3 and U4) (photodegradation percentages are in the range of 44 – 65 % in about 70 min). The present study indicates that all the three multi-phased $(\text{CdO})_{1-x}(\text{Mn}_3\text{O}_4)_x$ nanocomposites preapared (A2, A3 and A4) can very well be used to degrade MB dye irradiated with viible light of wavelength around 665 nm for about 90 min. Representation of the band structure and a possible mechanism for the degradation of MB dye over the nanocrystals prepared irradiated with visible light are shown schematically in Fig. 5(c).

On irradiation with light the photogenerated electrons (e^-) are excited from the valence band (VB) to the conduction band (CB) in the photocatalytic oxidation process, while the photogenerated holes (h^+) remain in the valence band. During the process of recombination, the CB electrons and the VB holes can be reduced as shown in Eq. (3).

$$(\text{CdO})_{1-x}(\text{Mn}_3\text{O}_4)_x + h\nu \rightarrow (\text{CdO})_{1-x}(\text{Mn}_3\text{O}_4)_x(e^-_{\text{CB}} + h^+_{\text{VB}}). \tag{3}$$

Consequently, the photogenerated holes of VB can interact with water molecules and produce hydroxyl radicals (OH*). Similarly, the photogenerated electrons of CB can also interact with oxygen to produce superoxide radicals ($\text{O}_2{*}^-$) as shown in Eqs. (4) and (5).

$$h + +\text{H}_2\text{O} \rightarrow \text{OH}^* + \text{H}^+, \tag{4}$$

$$e - +\text{O}_2 \rightarrow \text{O}_2^{*-}. \tag{5}$$

The hydroxyl and superoxide radicals are considered to be strong oxidation agents [32]. The anions O_2^{*-} do not further contribute to the oxidation process but respond with H^+ for producing HO_2* and e^- for producing OH* radical.

$$\text{O}_2^{*-} + \text{H}^+ \rightarrow \text{HO}_2^*, \tag{6}$$

$$\text{HO}_2^* + e^- \rightarrow \text{OH}^*, \tag{7}$$

$$\text{MB dye} + (\text{O}_2^{*-},\ \text{OH}^*) \rightarrow \text{CO}_2 + \text{H}_2\text{O (Degradation product)}. \tag{8}$$

Therefore, the electrons and hole (e^-, h^+) pairs have fast recombination for the degradation process. In the present study, the results obtained are found to be highly stable in degradation photocatalytic performance.

3.8. Antimicrobial activity

Investigation on the antimicrobial activities of the annealed samples (A1, A2, A3, A4 and A5) [$(\text{CdO})_{1-x}(\text{Mn}_3\text{O}_4)_x$ (with $x = 0.0, 0.25, 0.50, 0.75$ and 1.0) nanocrystals] (photographs shown in Fig. 6(a)) and the un-annealed samples (U2, U3 and U4) [$(\text{CdO})_{1-x}(\text{Mn}_3\text{O}_4)_x$ (with $x = 0.25, 0.50$ and 0.75) nanocrystals] (photographs shown in Fig. 6(b)) have been carried out by the disc diffusion method using Muller Hinton agar against two bacterial pathogens like Gram positive (Bacillus Subtilis, BS), and Gram negative (Escherichia Coli, EC) and the fungus (Candida Albicans, CA). The annealed $(\text{CdO})_{1-x}(\text{Mn}_3\text{O}_4)_x$ nanocrystals A1, A2, A3, A4 and A5 are marked as RJ1, RJ2, RJ3, RJ4 and RJ5, respectively; the un-annealed $(\text{CdCO}_3)_{1-x}(\text{Mn}_3\text{O}_4)_x$ nanocrystals U2, U3 and U4 are marked as RJ7, RJ8 and RJ9, respectively; The antimicrobial efficiency of nanomaterials commonly depend on the particular surface area, size and morphology [2].

People are exposed to EC from contaminated water and food items, and EC causes urinary infection and traveller's diarrhoea; the BS causes infections such as endocarditis, pneumonia, bacteremia and septicemia. The mechanism of antimicrobial activity involves the nanocrystal prepared as positively charged and the microbe as negatively charged; the thin layer of peptidoglycan is EC, and the thick layer of peptidoglycan is BS [33]. The ROS (Reactive Oxygen Species) penetrates through the cell wall and causes DNA damage and cell death; the great antimicrobial activity of nanomaterials is based on the oxygen species and high oxygen vacancies [34]. Moreover, the antimicrobial activity depends on the zone of inhibition [31].

The zones of inhibition (ZOIs) observed with all the three microbes considered (BS, EC and CA) for the annealed (A1, A2, A3, A4 and A5) and un-annealed (U2, U3 and U4) nanocrystals are shown in Fig. 6(c). Somasundaram *et al.* [5] have reported the antimicrobial activity of CdO with ZOIs observed as 9 and 8 mm, respectively, for the microbes BS and EC. The bacterial activity has been exhibited by the CdO nanocrystal prepared in the present study with ZOIs observed as 22 and 20 mm respectively for BS and EC. For all the eight nanocrystals considered for the study, in general, the ZOIs have been found to be higher with the bacteria (ranging from 16 to 22 mm with BS and 15 to 23 mm with EC) than with the fungus (ranging from 9 to 20 mm with CA); however, the A5 nanocrystal has been found to be more active with all the three microbes considered (18, 23 and 20 mm with BS, EC and CA, respectively). The activities of A3 and A4 have been found to be nearly the same as that of U3 and U4; however, the activity of A2 has been found to be significantly higher than that of U2.

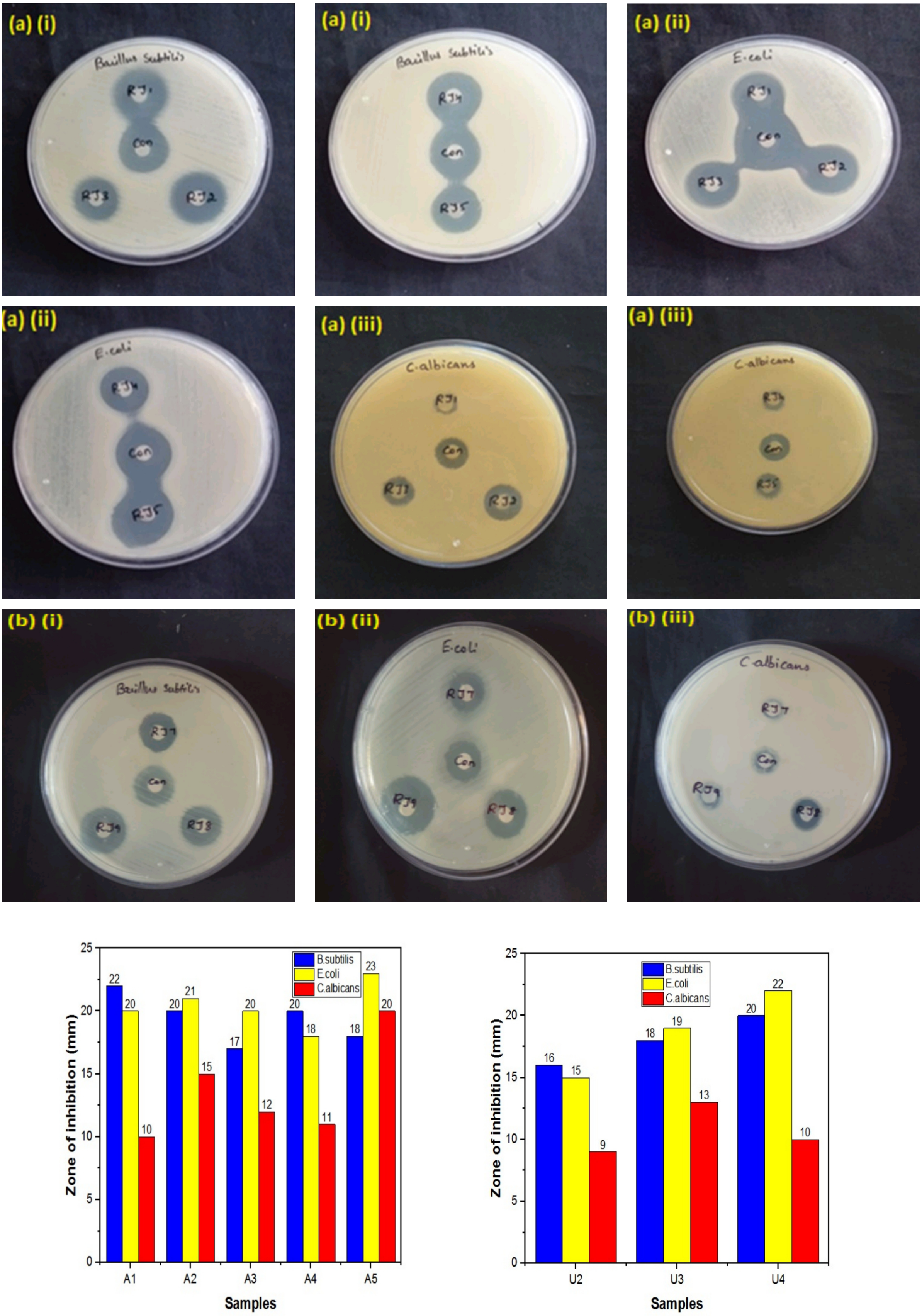

FIG. 6. (a) Observation of ZOIs for the $(CdO)_{1-x}(Mn_3O_4)_x$ nanocrystals (A1, A2, A3, A4 and A5) with: (a)(i) Bacillus Subtilis, (a)(ii) Escherichia Coli and (a)(iii) Candida Albicans. (b) Observation of ZOIs for the $(CdCO_3)_{1-x}(Mn_3O_4)_x$ nanocrystals (U2, U3 and U4) with: (b)(i) Bacillus Subtilis, (b)(ii) Escherichia Coli and (b)(iii) Candida Albicans. (c) Bar graphs showing the ZOIs observed for the $(CdO)_{1-x}(Mn_3O_4)_x$ (A1, A2, A3, A4 and A5) and $(CdCO)_{1-x}(Mn_3O_4)_x$ (U2, U3 and U4) nanocrstals.

4. Conclusion

Nanocrystalline (CdO)$_{1-x}$(Mn$_3$O$_4$)$_x$ (with $x = 0.0$, 0.25, 0.50, 0.75 and 1.0) composites have been successfully prepared by using a simple, fast and low-cost solvothermal technique (using a microwave oven). XRD analysis has revealed phase purity for all the five nanocrystals (A1, A2, A3, A4 and A5) prepared along with revealing the multi-phased composite nature for the three mixed compositions (A2, A3 and A4); the D values obtained are within 38 and 45 nm. EDX spectra have also revealed the high chemical purity and the existence of Cd, Mn and O components in the prepared nanocomposites. SEM and TEM images have indicated nearly spherical morphologies with agglomeration, and SAED pattern shows the polycrystalline nature of the prepared samples. E_g values obtiained from UV-visible spectra are within 4.0 and 5.3 eV; the dielectric measurements at various temperatures and with different frequencies have indicated a normal dielectric behavior for all the five nanocrystals (A1, A2, A3, A4 and A5) studied.

The (CdO)$_{1-x}$(Mn$_3$O$_4$)$_x$ nanocomposites (A2, A3 and A4) have been found to exhibit significantly higher photocatalytic activity than that exhibited by the (CdCO$_3$)$_{1-x}$(Mn$_3$O$_4$)$_x$ nanocomposites (U2, U3 and U4); results obtained have indicated that the three multi-phased (CdO)$_{1-x}$(Mn$_3$O$_4$)$_x$ nanocomposites preapared can very well be used to degrade MB dye irradiated with light of wavelength around 665 nm. The higher zones of inhibition obtained for all the eight nanocrystals (A1, A2, A3, A4, A5, U2, U3 and U4) studied have indicated a higher antimicrobial activity with the bacteria (BS and EC) than with the fungus (CA); however, the A5 (phase pure Mn$_3$O$_4$) nanocrystal has been found to be more active with all the three microbes considered (BS, EC and CA).

References

[1] Yathisa R.O., Arthoba Nayaka Y., Manjunatha P., Vinay M., Purushotham H.T. Effect of doping on the structural, optical and electrical properties of Ni^{2+} doped CdO nanoparticles prepared by microwave combustion route. *Microchemical J.*, 2018, **145** (3), P. 630–641.

[2] Karthik K., Dhanuskodi S., Gobinath C., Prabukumar S., Sivaramakrishnan S. Photocatalytic and antibacterial activities of hydrothermally prepared CdO nanoparticles. *J. Mater. Sci.: Mater. Electron.*, 2017, **28** (15), P. 11420–11429.

[3] Charan Kumar H.C., Rajegowda Shilpa, Sanniaha Ananda. Synthesis of cadmium oxide nanoparticles by electrochemical method: Its photodegradative effects on carboxylic acids and antibacterial behaviours. *J. of Nanoscience and Technology*, 2019, **5** (5), P. 840–845.

[4] Lokanatha Reddy P., Kalim Deshmukh, Chidambaram K., Basheer Ahamed, Kumar Sadasivumi K., Deepalekshmi Ponnamma, Rajasekhar Lakshmipathy, Desagani Dayananda, Khadheer Pasha S.K. Effect of ethylene glycol (PEG) on structural, thermal and photoluminescence properties of CdO nanoparticles for optoelectronics applications. *Materials Today: Proceedings*, 2019, **9**, P. 175–183.

[5] Somasundaram G., Rajan J., Sangaiya P., Dilip R. Hydrothermal synthesis of CdO nanoparticles for photocatalytic and antimicrobial activities. *Results in Materials*, 2019, **4**, 100044.

[6] Christuraj P., Dinesh Raja M., Pari S., Satheesh Kumar G., Uma Shankar V. Synthesis of Mn doped CdO nanoparticles by co-precipitation method for supercapacitor applications. *Materials Today: Proceedings*, 2020, **50** (17), P. 2679–2682.

[7] Krishnaraj S., Anitha R. Photocatalytic degradation analysis of methylene blue aluminium doped cadmium oxide nanoparticles. *J. Advanced Scientic Research*, 2021, **12** (1), P. 75–80.

[8] Munshi A., Prakash T., Ranjith Kumar E., Balamurugan A., Habeebullah T.M., Bawazeer T.M., Abdel-Hafey S.H., El-MetwalyN.M., Indumathi T. Comparative investigation of physicochemical properties of cadmium oxide nanoparticles. *Ceramics International*, 2022, **48** (11), P. 4134–4140.

[9] Xinli Hao, Jinzhe Zhao, Yuehong Song and Zhifang Huang. Synthesis and oxidizability study on Mn$_3$O$_4$ nanoparticles. *J. of Nano Research*, 2017, **48**, P. 138–147.

[10] Tanaswini Patra, Jagannath Panda, Tapas Ranjan Sahoo. Synthesis of Mn$_3$O$_4$ nanoparticles via microwave combustion route for electrochemical energy storage application. *Materials Today: Proceedings*, 2021, **41**, P. 247–250.

[11] Xiao She, Xinmin Zhang, Jingya Liu, Liang Li, Xianghua Yu, Zhiliang Huang, Songmin Shang. Microwave assisted synthesis of Mn$_3$O$_4$ nanoparticles @ reduced graphene oxide nanocomposites for high performance supercapacitors. *Mater. Res. Bulletin*, 2015, **70**, P. 945–950.

[12] Atique Ullah A.K.M., Fazle Kibria A.K.M., Akter M., Khan M.N.I., Tareq A.R.M., Firoz S.H. Oxidative degradation of methylene blue using Mn$_3$O$_4$ nanoparticles. *Water Conservation Sci. Eng.*, 2017, **1** (4), P. 249–256.

[13] Rafi Shaik M., Rabbani Syed, Farooq Adil S., Mufsir Kuniyil, Mujeeb Khan, Alqahtani M.S., Shaik J.P., Siddqui M.R.H., Al-Warthan A., Sharaf M.A.F., Abdelgawad, Mahrous Awwad E. Mn$_3$O$_4$ nanoparticles: Synthesis, characterization and their antimicrobial and anticancer activity against A549 and MCF-7 cell lines. *Saudi J. Biological Science*, 2021, **28**, P. 1196–1202.

[14] Kalaiselvan C.R., Laha S.S., Somvanshi S.B., Tabish T.A., Thorat N.D., Sahu N.K. Manganese ferrite (MnFe$_2$O$_4$) nanostructures for cancer theranostics. *Coord. Chem. Reviews*, 2022, **473**, 214809.

[15] Deepa G., Mahadevan C.K. Nanocrystalline composites based on CdCO$_3$ and Mn$_3$O$_4$: Synthesis and properties. *J. of Alloys and Compounds*, 2018, **763**, P. 935–950.

[16] Zhen-Yu Yuan, Fan Yang, Hong-Min-Zhu, Fan-Li-Meng, Medhat Ibrahim. High-response n-butanol gas sensor based on ZnO/In$_2$O$_3$ heterostructure. *Rare Metals*, 2023, **42** (24), P. 198–209.

[17] Ishfaq M., Hassan W., Sabir M., Somaily H.H., Hachim S.K., Jawad Kadhim Z., Lafta H.A., Alnassar Y.S., Mahdi Rheima A., Rabia Ejaz S., Aadil M. Wet-chemical synthesis of ZnO/CdO/CeO$_2$ heterostructure: A novel material for environmental remediation application. *Ceramics International*, 2022, **48** (23), P. 34590–34601.

[18] Pranesh Shubha J., Shivappa Savitha H., Farooq Adil S., Mujeeb Khan, Rafe Hatshan M., Kavalli K., Shaik B. Straightforward synthesis of Mn$_3$O$_4$/ZnO/Eu$_2$O$_3$-based ternary heterostructure nano-photocatalyst and its application for the photodegradation of methyle orange and methylene blue dyes. *Molecules*, 2021, **26** (15), 4661.

[19] Sundar S.M., Mahadevan C.K., Ramanathan P. On the preparation of ZnO–CdO nanocomposites. *Mater. Manuf. Processes*, 2007, **22** (3), P. 400–403.

[20] Nallendran R., Selvan G., Balu A.R. Photoconductive and photocatalytic properties of CdO–NiO nanocomposites synthesized by a cost effective chemical method. *J. Mater. Sci.: Mater. Electron.*, 2018, **29** (13), P. 11384–11393.

[21] Deepa G., Mahadevan C.K. A facile method to prepare CdO–Mn$_3$O$_4$ nanocomposites. *IOSR J. Applied Physics*, 2013, **5** (1), P. 15–18.

[22] Kumar S., Ojha A.K. Synthesis, characterizations and antimicrobial activities of well dispersed ultra-long CdO nanowires. *AIP Advances*, 2013, **3** (5), 052109.

[23] Bousqet-Berthelin C., Stuerga D. Flash microwave synthesis of Mn_3O_4-hausmannite nanoparticles. *J. Mater. Sci.*, 2005, **40** (1), P. 253–255.

[24] Prammitha Rajaram, Ambrose Rejo Jeice, Kumarasamy Jayakumar. Influences of calcination temperature on titanium dioxide nanoparticles synthesized using Averrhoa carambola leaf extract: in vitro antimicrobial activity and UV-lightvcatalyzed degradation of textile wastewater. *Biomass Conversion and Biorefinery*, 2023, **14** (17).

[25] Krasilin A.A., Bodalyov I.S., Malkov A.A., Khrapova E.K., Maslennikova T.P., Malygin A.A. On an adsorption/photocatalytic performance of nanotubular $Mg_3Si_2O_5(OH)_4/TiO_2$ composite. *Nanosystems: Physics, Chemistry, Mathematics*, 2018, **9** (3), P. 410–416.

[26] Kurilenko K.A., Petukhov D.I., Garshev A.V., Shlyakhtin O.A. Anionic redox effect on the electrochemical performance of LLNMC–CeO_2–C nanocomposites. *Nanosystems: Physics, Chemistry, Mathematics*, 2018, **9** (6), P. 775–782.

[27] Nguyen Anh Tien, Chau Hong Diem, Nguyen Thi Truc Linh, Mittova V.O., Do Tra Huong, Mittova I.Ya. Structural and magnetic properties of $YFe_{1-x}Co_xO_3$ ($0.1 \leq x \leq 0.5$) perovskite nanomaterials synthesized by co-precipitation method. *Nanosystems: Physics, Chemistry, Mathematics*, 2018, **9** (3), P. 424–429.

[28] Raja S., Mahadevan C.K. Nanocrystalline solid slabs of pure and CdS added KCl-KBr for energy storage application: Preparation and properties. *Nano-Structures & Nano-Objects*, 2023, **33**, 100938.

[29] Prammitha Rajaram, Yesuvadian Samson, Ambrose Rejo Jeice. Synthesis of $Cd(OH)_2$–CdO nanoparticles using veldt grape leaf extract: Enhanced dye degradation and microbial resistance. *BioNanoScience*, 2023, **13**, P. 1289–1307.

[30] Hosny N.M., Othman E., Dossoki F.I.EI. $[Cd(Anthranilate)_2]H_2O$ as a precursor of CdO nanoparticles. *J. of Molecular Structure*, 2019, **1195**, P. 723–732.

[31] Bessy T.C., Bindhu M.R., Johnson J., Shen-Ming Chen, Tse-Wei Chen, Almaary K.S. UV light assisted photocatalytic degradation of textile waste water by $Mg_{0.8-X}Zn_XFe_2O_4$ synthesized by combustion method and in-vitro antimicrobial activities. *Environmetal Research*, 2022, **204** (1), 111917.

[32] Vasiljevic Z.Z., Dojcinovic M.P., Vujancevic J.D., Jankovic-Castvan I., Ognjanovic M., Tadic N.B., Stojadinovic S., Brankovic G.O., Nikolic M.V. Photocatalytic degradation of methylene blue under natural sunlight using iron titanate nanoparticles prepared by modified sol-gel method. *Royal Society Open Science*, 2020, **7** (9), 200708.

[33] Aravind M., Amalanathan M., Sony Michael Mary M. Synthesis of TiO_2 nanoparticles by chemical and green synthesis methods and their multifaceted properties. *SN Applied Sciences*, 2021, **3** (4), 409.

[34] Ancy K., Bindhu M.R., Sunitha Bai J., Gatasheh Mansour K., Atef Hatamleh A., Ilavenil S. Photocatalytic degradation of organic synthetic dyes and textile dyeing waste water by Al and F co-doped TiO_2 nanoparticles. *Environmental Research*, 2022, **206** (12), 112492.

Submitted 6 June 2024; revised 4 September 2024; accepted 8 November 2024

Information about the authors:

Selvaraj Jebisha – Ph.D. Scholar of M.S. University, Tirunelveli, Department of Physics, Annai Velankanni College, Tholayavattam-629167, Tamil Nadu, India; ORCID 0009-0002-0394-697X;

Ganesan Deepa – Departmentof Physics, Pioneer Kumaraswamy College, Nagercoil-629003, Tamil Nadu, India; ORCID 0000-0001-9727-8110; gdeepavinod@ymail.com

Jesumarian Johnson – Department of Physics, Annai Velankanni College, Tholayavattam-629167, Tamil Nadu, India; ORCID 0009-0007-7921-3488;

Chelliah Kamalakshiammal Mahadevan – CSIR Emeritus Scientist, Department of Physics, Bharathidasan University, Tiruchirappalli-620024, Tamil Nadu, India; ORCID 0000-0002-3769-4662; mahadevan58@yahoo.co.in

Conflict of interest: The authors declare that they have no known competing financial interests or personal relationships that could have appeared to influence the work reported in this paper.

Funding: The authors declare that this research did not receive any specific grant from funding agencies in the public, commercial, or not-for-profit sectors.

Author contribution:
S. Jebisha: conceptualization, methodology, investigation, data curation, formal analysis, writing – original draft;
G. Deepa: conceptualization, methodology, validation, supervision, writing – original draft, review and editing;
J. Johnson: methodology, supervision;
C. K. Mahadevan: conceptualization, methodology, validation, writing – original draft, review and editing.

NANOSYSTEMS:
PHYSICS, CHEMISTRY, MATHEMATICS

Anannikov E.S., et al. *Nanosystems: Phys. Chem. Math.*, 2024, **15** (6), 806–813.
http://nanojournal.ifmo.ru
DOI 10.17586/2220-8054-2024-15-6-806-813

Original article

Synthesis and research of physical and chemical properties of $InGaZn_2O_5$ prepared by nitrate-glycolate gel decomposition method

Egor S. Anannikov[1], Timofey A. Markin[1], Ibrohimi A. Solizoda[1,2,4], Gleb M. Zirnik[1], Daniil A. Uchaev[3], Alexander S. Chernukha[1,2,3], Svetlana A. Gudkova[1,2], Denis A. Vinnik[1,2,3]

[1]Moscow Institute of Physics and Technology, Dolgoprudny, Russia
[2]St. Petersburg State University, St. Petersburg, Russia
[3]South Ural State University, Chelyabinsk, Russia
[4]Tajik National University, Dushanbe, Tajikistan

Corresponding author: Denis A. Vinnik, vinnik.da@mipt.ru

ABSTRACT Indium-gallium-zinc oxide $InGaZn_2O_5$ was synthesized by nitrate-glycolate gel decomposition method using ethylene glycol as a complexing and chelating agent. In this work, SEM, EDS and UV-vis-diffusion spectra of IGZO were obtained. $InGaZn_2O_5$ optical band gap was found using Kubelka–Munk transformation. The morphology of the particles was examined: at low sintering temperatures many micro-meter particles are observed, the sample is heterogeneous in crystalline state. At annealing temperatures above 800 °C a single-phase crystalline structure is observed.

KEYWORDS indium-gallium-zinc oxide, IGZO, $InGaZn_2O_5$, nitrate-glycolate gel, chelating reagent, ethylene glycol, chelate-nitrate method

ACKNOWLEDGEMENTS The research is supported by the Ministry of Science and Higher Education of the Russian Federation (state assignment) No. 075-03-2024-117, project number FSMG-2024-0028.

FOR CITATION Anannikov E.S., Markin T.A., Solizoda I.A., Zirnik G.M., Uchaev D.A., Chernukha A.S., Gudkova S.A., Vinnik D.A. Synthesis and research of physical and chemical properties of $InGaZn_2O_5$ prepared by nitrate-glycolate gel decomposition method. *Nanosystems: Phys. Chem. Math.*, 2024, **15** (6), 806–813.

1. Introduction

Research in electronics focuses on several areas. There are fields of semiconductor oxides research due to the potential for their usage in various devices such as memristors [1] and thin-film field-effect transistors (TFT) [2, 3]. TFT find the application in the production of modern displays and monitors [4–6]. At present, oxide semiconductor materials cannot completely replace silicon, but it is possible to use them as materials for flexible microelectronics, which is a new development direction for these materials. [7–9]. Among oxides, indium-gallium-zinc oxide (IGZO) is one of the most widely studied [10–13]. Amorphous indium-gallium-zinc oxide used for thin-film transistors (a-IGZO TFTs) have garnered significant interest due to their high electron mobility, straightforward fabrication process, cost-effectiveness, and excellent uniformity [11].

Additionally, IGZO exhibits great optical transparency and in order of magnitude, it can reaches higher than other materials on/off current ratio about 10^8 [10], which are advantageous for display technologies and optoelectronic applications. Its crystallinity also allows for uniform large-area deposition, enhancing scalability and enabling the development of high-resolution, energy-efficient electronic devices. The unique properties of IGZO make it highly suitable for applications in hybrid and microelectronic systems, where high-performance and stable materials are essential [4]. Its compatibility with flexible substrates and potential for integration into low-temperature processing make IGZO a promising candidate for next-generation electronic devices [5]. First, the single-crystal IGZO-based materials were investigated, later it was found that IGZO amorphous thin films also have great potentials for flexible electronics [13–15].

The first synthesized compound for TFT production was $InGaZn_5O_8$ [16], later, studies of IGZO with other concentrations began. Later, the most common studies were of the $InGaZnO_4$ composition (xIn:xGa:xZn = 1:1:1) [17–20]. Further works varied the ion ratio to study the whole concentration triangle [3, 17, 21, 22]. Despite this, the system has not been completely examined yet. For example, in [21], compositions with fixed stoichiometric ratio of Ga and Zn were studied and the amount of In was varied, while in [23], the amount of Ga was varied with fixed In and Zn [24, 25]. At the same time for the In–Ga–Zn–O system in the amorphous state, it is possible to vary the concentration of each element separately within a sufficiently wide range. Thus, by changing the concentration of an element, the properties of the device can also be changed. Unfortunately, this approach is well realizable for the amorphous IGZO only. In the crystalline state, the IGZO homogeneity area is strongly reduced (even at temperatures around 1350 °C [24, 25] and is limited to clearly defined chemical compositions $(In_{1-x}Ga_xO_3)_n(ZnO)_m$, where $x \neq 0$, $x \neq 1$, at strictly defined n and m.

In the process of using IGZO thin films in transistors, a large number of evaluation criteria have been obtained, including stability and degradation characteristics of these semiconductor devices [38–41]. Physical and chemical properties of IGZO such as charge carrier mobility, grain size, threshold voltage, and other characteristics directly depend on the method of synthesis and chemical composition of the final product. For example, increasing the content of In in the oxide increases the mobility of charge carriers [34, 35], and varying the amount of Ga leads to a change in the threshold voltage [22]. The synthesis conditions also affect the semiconductor properties. The annealing temperature affects the charge carriers concentration and mobility, the phase composition and sample morphology of the TFT [3, 18]. As shown in [36, 37], the electrical and optical properties of IGZO thin films depend on the degree of their crystallinity (or amorphous state).

One of the main research areas is the creation of thin semiconductor films. A lot of experimental material for obtaining the TFs and TFTs has been accumulated in [3,17–20,25–27]. Such methods as chemical/physical vapor deposition, pulsed laser deposition, molecular beam and epitaxy, atomic layer deposition, and magnetron sputtering are successfully applied to obtain IGZO-films. Recently, new methods of thin film synthesis, including spin-coating [28, 29] and microplotter-print [30, 31], have been improved. Advantages over classical methods include scalability and cheap implementation [3, 18, 32, 33].

As described above, IGZO has a huge potential for use in flexible electronics, including using the printing technologies. IGZO-based printing technology will allow one to expand the potential application area due to the use of thermally unstable, but extremely cheap and available plastic and paper substrates. To develop this concept, it is necessary to obtain extremely pure (X-ray clean) IGZO powders for their further use. In this case, there is few works devoted to InGaZn$_2$O$_5$ nanoparticles obtaining [42, 43]. Most often, they are obtained by the chelate-nitrate (sol-gel or self-combustion) method due to easy scaling and cheapness of the process. In our work, an oxide of InGaZn$_2$O$_5$ composition was obtained for the first time using ethylene glycol as a complexing agent; previously, it was prepared only with polyvinyl alcohol [44]. The dependence of the morphology of the samples on their sintering temperature was also investigated.

2. Methodology of experimental research

Nitrate-glycolate gel decomposition method was used for InGaZn$_2$O$_5$ synthesis according previous work [45]. Indium nitrate 4.5-aqueous [In(NO$_3$)$_3 \cdot 4.5$H$_2$O ("c.p.")], gallium nitrate 9-aqueous [Ga(NO$_3$)$_3 \cdot 9$H$_2$O ("c.p.")], zinc nitrate 6-aqueous [Zn(NO$_3$)$_2 \cdot 6$H$_2$O ("c.p.")], and ethylene glycol ("p.a.") were used as reagent without further purification. All metal nitrates used in the synthesis were gravimetrically treated by calcination (800 °C, 12 h), so that the practical masses of nitrate-hydroxide salts were corrected according to the gravimetric data. The ratio of precursors was selected to obtain indium-gallium-zinc oxide with the ratio of In:Ga:Zn atoms = 1:1:2 in the product. The reagents were selected on a FA2204N balance. The solutions were stirred, heated, and evaporated in a magnetic stirrer with heating IKA® C-MAG HS7. Afterwards, the residual water in the gel was removed by holding it in a muffle furnace (Plavka.Pro PM-5 muffle furnace) in a ceramic cup. During the holding process, a self-combustion reaction occurred producing a solid substance. The solution after pouring into a ceramic cup was heated in the furnace from room temperature to 300 °C at a rate of 100 °C/hour, followed by isothermal holding for 6 hours. The samples were cooled to room temperature after passing through the self-combustion stage. Afterwards, the sample was divided into pieces and sintered in powdered form in alumina crucibles at temperatures from 400 to 1100 °C in 100 °C increments for 6 hours.

X-ray diffraction (XRD) was performed on a Drawell DW-XRD-2700A powder diffractometer (CuKα, 40 kV, 30 mA; $\lambda = 0.15406$ nm, Ni filter) in the range of 2θ angles from 5 to 95 ° at a rate of 5 ° per min at room temperature. Powder XRD pattern was used for lattice parameters calculation using the Jade 6.5 software package (Table 1).

The microstructure of samples was studied by scanning electron microscopy (SEM Jeol JSM-7001F, accelerating voltage 20 kV). In addition, the elemental composition was investigated and elemental distribution maps were drawn by EDX-spectroscopy (Oxford INCA X-max 80 EDS spectrometer, 20 kV electron beam energy). Due to the significantly higher energy value of the indium K-line compared to the K-lines of other elements in the studied samples, the indium content was calculated by the L-line, and for Zn, Ga and O by the K-line.

The crystal structure of the particles was studied by transmission electron microscopy (Jeol JSM-2100, accelerating voltage 160 kV). The morphology of the particles and their crystal structure state in the nanometer range were investigated.

Diffuse reflectance spectra were obtained for samples sintered at 500, 700, 900 and 1100 °C in the range from 250 to 800 nm at a recording rate of 1 nm/sec on a Shimadzu UV-2700 UV-Visible spectrophotometer. The background calibration was performed for pure barium sulfate BaSO$_4$ tablet. The sample was also applied to a barium sulfate tablet. The source of radiation in the near UV diapason was a deuterium lamp and in the near IR region was a tungsten filament halogen lamp. Switching between the light sources was done automatically when passing through the 320 nm wavelength. Diffuse reflection spectra were used to determine samples energy gap by the Kubelka–Munk transformation method. In Tauc-plot for the expression "$\alpha(h\nu)^n - h\nu$" n was equal to 2 for indirect allowed transitions.

3. Results and discussion

The XRD patterns of $InGaZn_2O_5$ samples annealed at different temperatures are presented in Fig. 1. The vertical red lines (dashed lines) show the allowed reflexes of $InGaZn_2O_5$ [46]. It was observed that at temperatures between 300 and 600 °C, broad maximums of the diffraction pattern are observed, which is responsible for the amorphous structure. In the range of 700 – 800 °C, the sample is in a weakly crystallized state. At annealing temperatures above 800 °C a single-phase crystalline structure is observed. No other reflexes (In_2O_3, ZnO etc.) were observed in the XRD patterns.

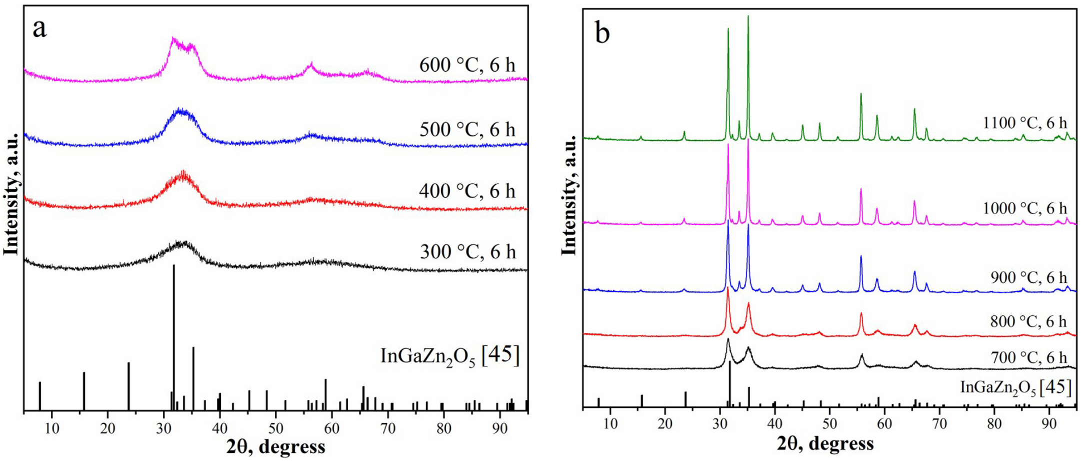

FIG. 1. XRD pattern of $InGaZn_2O_5$ samples annealing at 300 – 600 °C (a); 700 – 1100 °C (b). The dashed diagram shows the $InGaZn_2O_5$ phase [46]

The cell parameters were calculated only for the samples sintered at 700 – 1100 °C, the results are presented in Table 1. The given data are in correspondence with those obtained earlier [46].

TABLE 1. Calculated $InGaZn_2O_5$ lattice constants

No.	**Sample**	**Unit cell parameters**		
		***a*, Å**	***c*, Å**	**V, Å^3**
Sintering temperature, °C				
1	**700**	3.297±0.001	22.589±0.007	212.72±0.22
2	**800**	3.297±0.001	22.584±0.006	212.58±0.18
3	**900**	3.298±0.001	22.588±0.005	212.80±0.13
4	**1000**	3.298±0.001	22.591±0.005	212.84±0.12
5	**1100**	3.297±0.001	22.587±0.006	212.64±0.14
6	**[46]**	3.297±0.001	22.587±0.006	212.64±0.14

Figure 2 shows SEM images (in secondary electrons) of the $InGaZn_2O_5$ samples. Samples sintered at 500 and 700 °C (Fig. 2(a,b)) show many small particles with sizes 1 – 2 μm of abnormal shape. In Fig. 2(c,d), however, individual small particles become significantly smaller. As the annealing temperature increases, clearly faceted surface areas appear, which correlates with the XRD results, since the sample sintered at 1100 °C has a high degree of crystallization. At ×30000 zoom (Fig. 2(g,h)), it can be seen that the sample is an agglomerate of micro- and nanometer-sized crystallites.

The chemical composition of the samples was calculated using EDX-spectroscopy data. The distribution maps of the main elements are presented in Fig. 3. Their distribution is homogeneous throughout the sample for all temperatures of sintering (including 700 and 900 °C). This allows us to state the absence of amorphous regions of impurity phases and, thus, the presence of the sample in a single-phase state throughout the entire presented temperature range.

The chemical composition was calculated basis on the EDX-data. The relevant brutto formulas are presented in Table 2. The obtained data indicate the deviation from the specified composition within the error range (1 – 2 %).

Transmission electron microscopy (TEM) images are presented in Fig. 4. It shows $InGaZn_2O_5$ sample sintered at 500 °C. It can be seen that small particles are grouped together either in several pieces (Fig. 4a) or in large clusters (Fig. 4c). Large agglomerates of particles with different degrees of crystallization in sections are observed – both highly

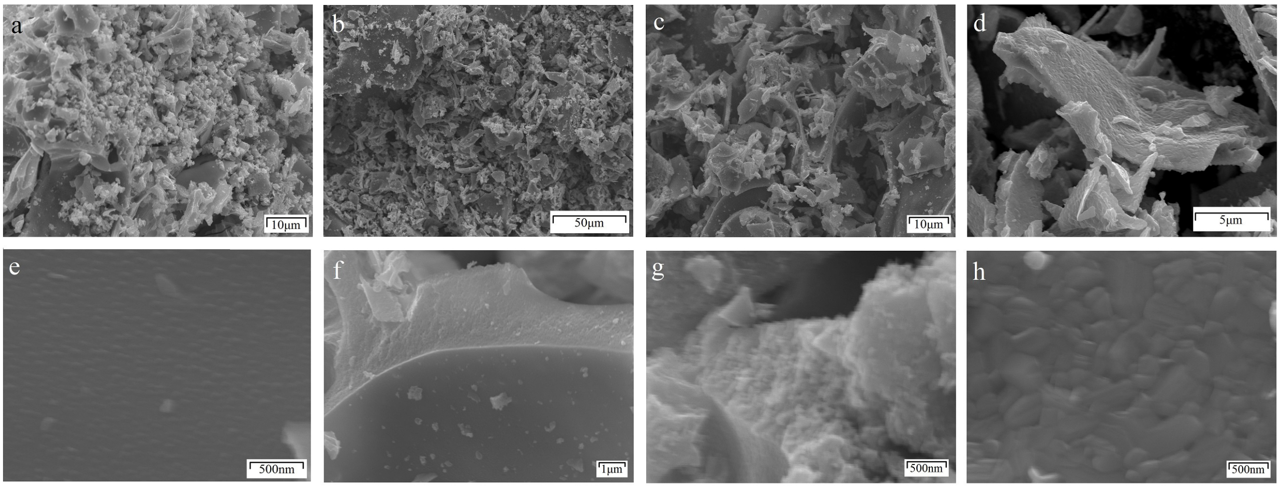

FIG. 2. SEM images of $InGaZn_2O_5$ samples sintered at 500 °C (a, e), 700 °C (b, f), 900 °C (c, g), 1100 °C (d, h) with various magnifications. The scale bar is indicated on the micrograph

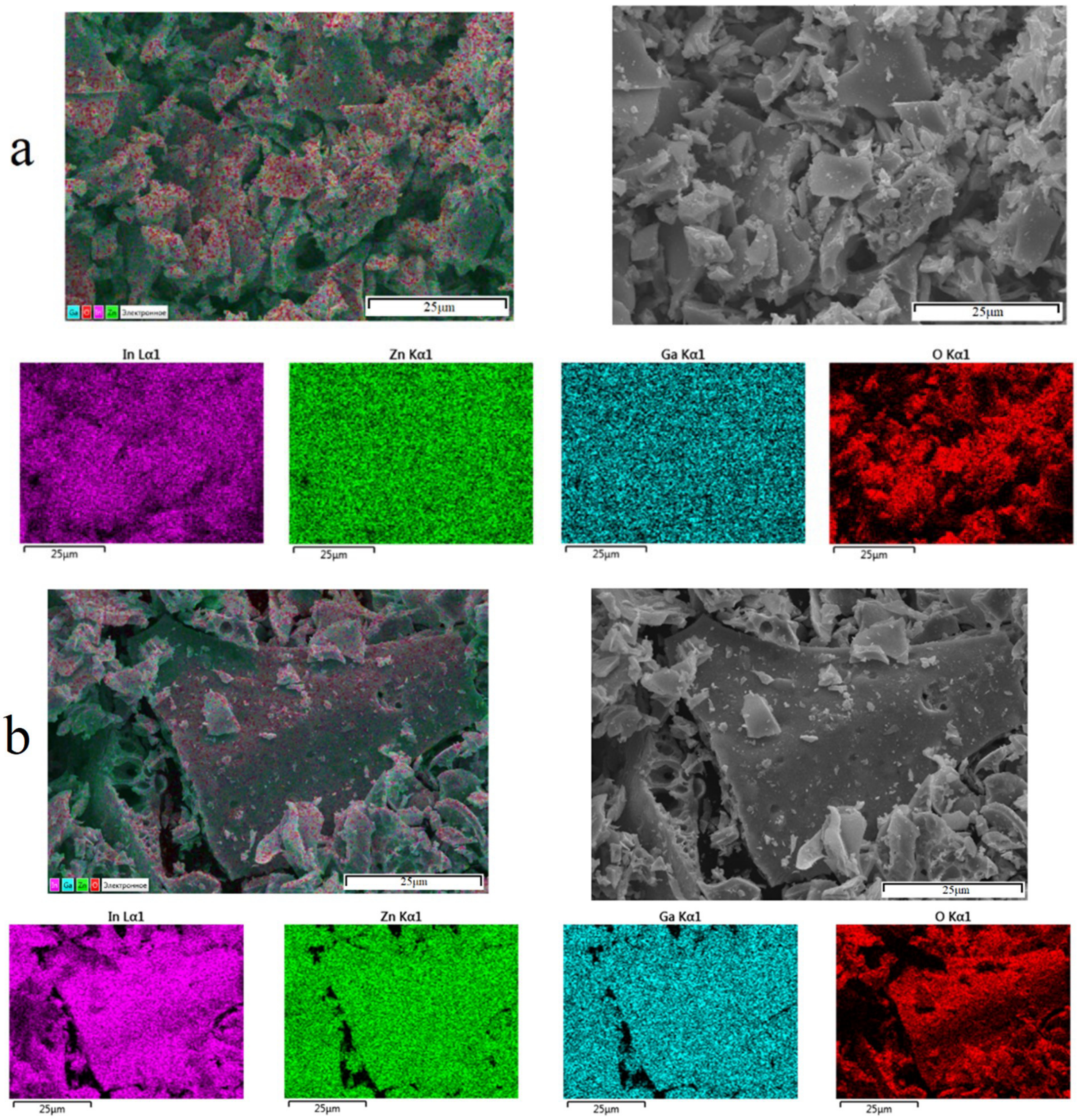

FIG. 3. SEM-images, multilayer EDX map and individual element map distribution (In – pink, Zn – green, Ga – blue, O – red) at sintering temperatures: a) 500 °C; b) 1100 °C. The scale bar is 25 μm for both samples

TABLE 2. Gross formula for $InGaZn_2O_5$ obtained at different temperatures

Annealing temperature	500 °C	700 °C	900 °C	1100 °C
Brutto formula	$In_{0.98}Ga_{0.98}Zn_{2.04}O_5$	$In_{1.02}Ga_{0.97}Zn_{2.01}O_5$	$In_{1.01}Ga_{0.97}Zn_{2.02}O_5$	$In_{1.00}Ga_{0.98}Zn_{2.02}O_5$

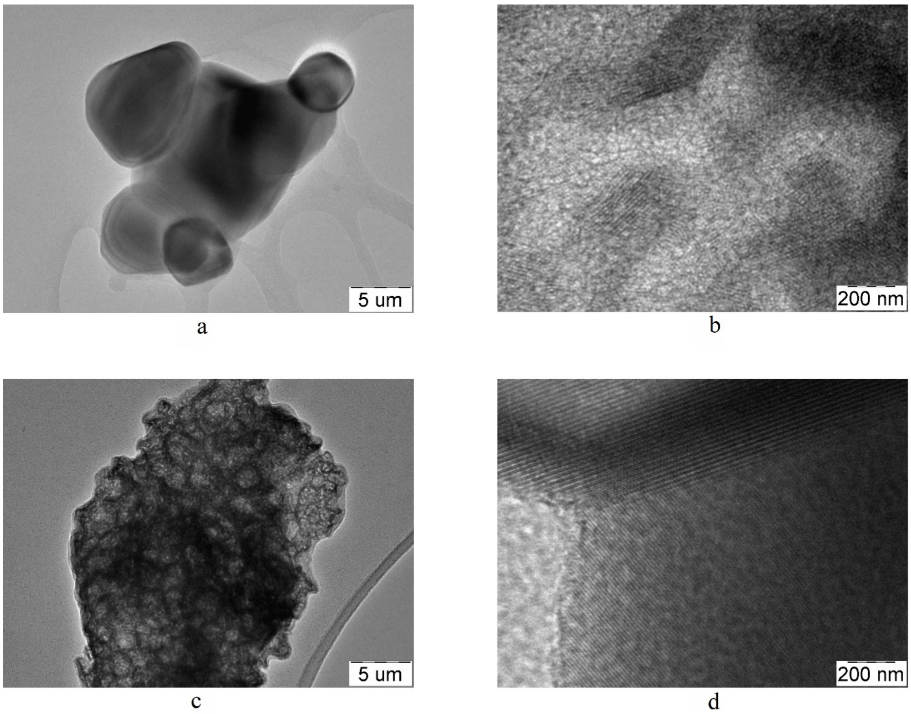

FIG. 4. TEM images of $InGaZn_2O_5$ samples at sintered temperature of 500 °C with different scale bar

crystallized (distinct bands in Fig. 4d) and low-crystallized (Fig. 4b). However, as can be seen, there is no way to calculate d-spacing because high resolution could not be achieved.

The UV-vis-spectroscopy results of the $InGaZn_2O_5$ samples are shown in Fig. 5. The sample does not have absorption peaks in the visible region. The band gaps calculation is given in Table 3, our results correlate with work published earlier [47]. $InGaZn_2O_5$ has a rather wide band gap, and it varies within the error during sintering in the temperature range from 500 to 1000 °C. This explains the fact that the band gap does not depend on the IGZO crystallinity and morphology.

TABLE 3. Band gap for $InGaZn_2O_5$ samples sintered at different temperatures

Annealing temperature, °C	500	700	900	1100	[47]
Band gap, eV	3.159	3.170	3.180	3.159	3.225

4. Conclusions

The nitrate-glycolate gel decomposition method was successfully applied to synthesize $InGaZn_2O_5$ samples. At temperatures from 300 to 600 °C an amorphous structure is observed, at 700 – 800 °C the sample is in a weakly crystallized state, and at annealing temperatures above 800 °C, a high crystalline structure is observed. The morphology of the samples is as follows: at low sintering temperatures many micro-meter particles are observed, the sample is heterogeneous in crystalline state. This is confirmed by TEM images. When the annealing temperature is increased, the particles are organized into clearly faceted structures. The bandgap width of IGZO is 3.17 eV, which correlates with literature data. The obtained data indicate that it is possible to obtain $InGaZn_2O_5$ using the nitrate-glycol method, which creates a scientific basis for using materials to obtain colloidal solutions (ink) and their use in printing technologies in the field of electronics.

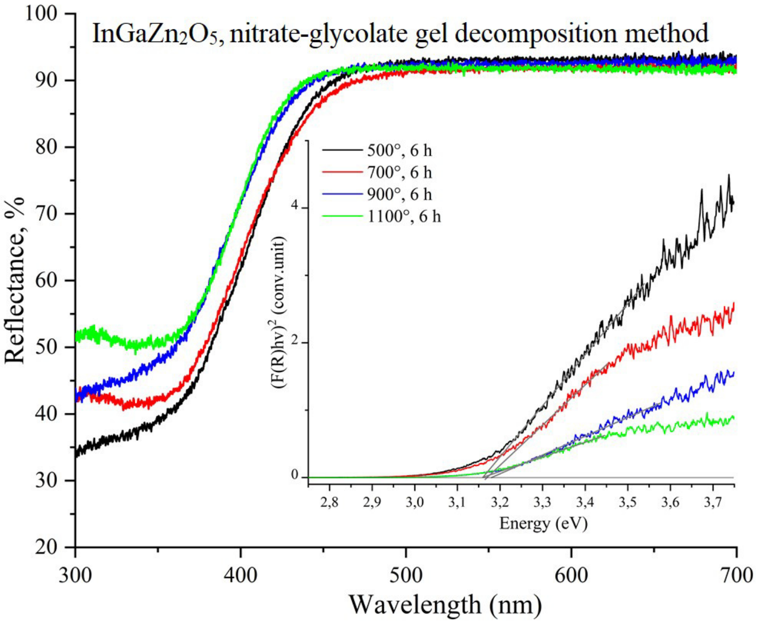

FIG. 5. UV-vis spectra of $InGaZn_2O_5$ for different sintering temperatures. Tauc-plot is presented in the inset

References

[1] Jang J.T., Min J., Hwang Y., Choi S.J., Kim D.M., Kim H., Kim D.H. Digital and Analog Switching Characteristics of InGaZnO Memristor Depending on Top Electrode Material for Neuromorphic System. *IEEE Access*, 2020, **8**, P. 192304–192311.

[2] Sporea R.A., Niang K.M., Flewitt A.J., Silva S.R.P. Novel Tunnel-Contact-Controlled IGZO Thin-Film Transistors with High Tolerance to Geometrical Variability. *J. Adv. Mater.*, 2019, **31** (36), 1902551.

[3] Olziersky A., Barquinha P., Vilà A., Magaña C., Fortunato E., Morante J.R., Martins R. Role of Ga_2O_3–In_2O_3–ZnO channel composition on the electrical performance of thin-film transistors. *Mater. Chem. Phys.*, 2011, **131** (1–2), P. 512–518.

[4] Kataoka Y., Imai H., Nakata Y., Daitoh T., Kimura T.M.N., Nakano T., Mizuno Y., Oketani T., Takahashi M., Tsubuku M., Miyake H., Hirakata T.I.Y, Koyama J., Yamazaki S., Koezuka J., Okazaki K. Development of IGZO-TFT and Creation of New Devices Using IGZO-TFT. *SID Symposium Digest of Technical Papers*, 2013, **44** (1), P. 771–774.

[5] Hendy I., Brewer J., Muir S. Development of High?Performance IGZO Backplanes for Displays. *Inf. Disp.*, 2022, **38** (5), P. 60–68.

[6] Hong T., Kim Y.S., Choi S.H., Lim J.H., Park J.S. Exploration of Chemical Composition of In–Ga–Zn–O System via PEALD Technique for Optimal Physical and Electrical Properties. *Adv. Electron. Mater.*, 2023, **9** (4), 2201208.

[7] Bhatti G., Agrawal Y., Palaparthy V., Mummaneni K., Agrawal M. Flexible Electronics: A Critical Review. In: Agrawal, Y., Mummaneni, K., Sathyakam, P.U. (eds) Interconnect Technologies for Integrated Circuits and Flexible Electronics. *Springer Tracts in Electrical and Electronics Engineering*, Singapore, 2024, P. 221–248.

[8] Bi S., Gao B., Han X., He Z., Metts J., Jiang C., Asare-Yeboah K. Recent progress in printing flexible electronics: A review. *Sci. China Technol. Sci.*, 2024, **67**, P. 2363–2386.

[9] Benwadih M., Coppard R., Bonrad K., Klyszcz A., Vuillaume D. High Mobility Flexible Amorphous IGZO Thin-Film Transistors with a Low Thermal Budget Ultra-Violet Pulsed Light Process. *ACS Appl. Mater. Interfaces*, 2016, **8** (50), P. 34513–34519.

[10] Xu X., He G., Wang L., Wang W., Jiang S., Fang Z. Optimization of electrical performance and stability of fully solution-driven α-InGaZnO thin-film transistors by graphene quantum dots. *J. Mater. Sci. Technol.*, 2023, **141**. P. 100–109.

[11] Xie Y., Cai K., Jian H., Huang Y., Weng J., Wang W. Study on Amorphous InGaZnO Thin-Film Transistor Modeling Method Based on Artificial Neural Network. *IEEE J. Electron Devices Soc.*, 2023, **11**, P. 717–725.

[12] Meléndrez Z.A.L., Durán A., Brown F., Negrete O.H., Paredes J.H., Montano V.E.A. Design of High-Entropy Ceramics with IGZO-Based Compounds for Electroceramics Applications. *Advances in Powder and Ceramic Materials Science 2023*, 2023, P. 3–10.

[13] Han Y., Lee D.H., Cho E.S., Kwon S.J., Yoo H. Argon and Oxygen Gas Flow Rate Dependency of Sputtering-Based Indium-Gallium-Zinc Oxide Thin-Film Transistors. *Micromachines*, 2023, **14** (7), P. 1394–1404.

[14] Lee Y.W., Choi S.H., Lee J.S., Kwon J.Y., Han M.K. Investigation of Amorphous IGZO TFT Employing Ti/Cu Source/Drain and SiNx Passivation. *MRS Online Proceedings Library*, 2011, **1321** (1906), P. 247–252.

[15] Lu Q., Huang X., Li F., Xin H., Huang H. Fabrication and Properties of Amorphous IGZO-TFT. *Proceedings of the 4th Workshop on Advanced Research and Technology in Industry (WARTIA 2018)*, 2018, **173**, P. 279–282.

[16] Nomura K., Ohta H., Ueda K., Kamiya T., Hirano M., Hosono H. Thin-Film Transistor Fabricated in Single-Crystalline Transparent Oxide Semiconductor. *Science*, 2003, **300** (5623), P. 1269–1272.

[17] Nomura K., Takagi A., Kamiya T., Ohta H., Hirano M., Hosono H. Amorphous Oxide Semiconductors for High-Performance Flexible Thin-Film Transistors. *Jpn. J. Appl. Phys.*, 2006, **45** (5B), P. 4303–4308.

[18] Xie Y., Wang D., Fong H.H. High-Performance Solution-Processed Amorphous InGaZnO Thin Film Transistors with a Metal–Organic Decomposition Method. *J. Nanomater.*, 2018, **2018** (1), P. 1–7.

[19] Liao P.-Y., Chang T.-C., Hsieh T.-Y., Tsai M.-Y., Chen B.-W., Tu Y.-H., Chu A.-K., Chou C.-H., Chang J.-F. Investigation of carrier transport behavior in amorphous indium–gallium–zinc oxide thin film transistors. *Jpn. J. Appl. Phys.*, 2015, **54** (9), 094101.

[20] Mohammadian N., Das B.C., Majewski L.A. Low-Voltage IGZO TFTs Using Solution-Deposited OTS-Modified Ta_2O_5 Dielectric. *IEEE Trans. Electron. Devices*, 2020, **67** (4), P. 1625–1631.

[21] Tari A., Lee C.-H., Wong W.S. Electrical dependence on the chemical composition of the gate dielectric in indium gallium zinc oxide thin-film transistors. *Appl. Phys. Lett.*, 2015, **107** (2), 023501.

[22] Lee D.-H., Park S.-M., Kim D.-K., Lim Y.-S., Yi M. Effects of Ga Composition Ratio and Annealing Temperature on the Electrical Characteristics of Solution-processed IGZO Thin-film Transistors. *JSTS*, 2014, **14** (2), P. 163–168.

[23] Nakamura M., Kimizuka N., Mohri T. The phase relations in the In_2O_3–Ga_2ZnO_4–ZnO system at 1350 °C. *J. Solid State Chem.*, 1991, **93** (2), P. 298–315.

[24] Yamazaki S., Kimizuka N. *Physics and Technology of Crystalline Oxide Semiconductor CAAC-IGZO: Fundamentals*. Wiley, New York, 2016. 310 p.

[25] Yang C.S., Huang S.J., Kao Y.C., Chen G.H., Chou W.-C. Physical properties of $InGaO_3(ZnO)$ with various content ratio grown by PAMBE. *J. Cryst. Growth*, 2015, **425**, P. 258–261.

[26] Lee J.-Y., Heo K.-J., Choi S.-G., Ryu H.G., Koh J.-H., Kim S.-J. Effects of Oxygen Injection Rates on a-IGZO Thin-film Transistors with Oxygen Plasma Treatment. *JSTS*, 2021, **21** (3), P. 189–198.

[27] Liu S.-J., Fang H.-W., Hsieh J.-H., Juang J.-Y. Physical properties of amorphous Mo-doped In–Ga–Zn–O films grown by magnetron co-sputtering technique. *Mater. Res. Bull.*, 2012, **47** (6), P. 1568–1571.

[28] Jo E., Ahn J.H., Ha T.E., Kim E., Im H., Kim Y.-S. A Study of Spin Coated a-IGZO TFT with Y-doped ZrO_2 Gate Insulators. *Proceedings of the International Display Workshops*, 2022, **29**, P. 354–357.

[29] Zalte M.B., Naik T.R., Alka A., Ravikanth M., Rao V.R., Baghini M.S. Passivation of Solution-Processed a-IGZO Thin-Film Transistor by Solution Processable Zinc Porphyrin Self-Assembled Monolayer. *IEEE Trans. Electron Devices*, 2021, **68** (11), P. 5920–5924.

[30] Yan X., Li B., Zhang Y., Wang Y., Wang C., Chi Y., Yang X. Effect of Channel Shape on Performance of Printed Indium Gallium Zinc Oxide Thin-Film Transistors. *Micromachines*, 2023, **14** (11), P. 2121.

[31] Zhang L., Guo Q., Tan Q., Fan Z., Xiong J. High Performance Amorphous IGZO Thin-Film Transistor Based on Alumina Ceramic. *IEEE Access*, 2019, **7**, P. 184312–184319.

[32] Chang J.S., Facchetti A.F., Reuss R. A Circuits and Systems Perspective of Organic/Printed Electronics: Review, Challenges, and Contemporary and Emerging Design Approaches. *IEEE J. Emerg. Sel. Top Circuits Syst.*, 2017, **7** (1), P. 7–26.

[33] Sanctis S., Hoffmann R.C., Bruns M., Schneider J.J. Direct Photopatterning of Solution–Processed Amorphous Indium Zinc Oxide and Zinc Tin Oxide Semiconductors – A Chimie Douce Molecular Precursor Approach to Thin Film Electronic Oxides. *Adv. Mater. Interfaces*, 2018, **5** (15), 1800324.

[34] Kimura M., Kamiya T., Nakanishi T., Nomura K., Hosono H. Intrinsic carrier mobility in amorphous In–Ga–Zn–O thin-film transistors determined by combined field-effect technique. *Appl. Phys. Lett.*, 2010, **96** (26), 262105.

[35] Kamiya T., Hosono H. Material characteristics and applications of transparent amorphous oxide semiconductors. *NPG Asia Mater.*, 2010, **2** (1), P. 15–22.

[36] Takagi A., Nomura K., Ohta H., Yanagi H., Kamiya T., Hirano M., Hosono H. Carrier transport and electronic structure in amorphous oxide semiconductor, a-$InGaZnO_4$. *Thin Solid Films*, 2005, **486**(1–2), P. 38–41.

[37] Nomura K., Kamiya T., Ohta H., Shimizu K., Hirano M., Hosono H. Relationship between non-localized tail states and carrier transport in amorphous oxide semiconductor, In–Ga–Zn–O. *Physica Status Solidi (A)*, 2008, **205** (8), P. 1910–1914.

[38] Chen T.-C., Chang T.-C., Hsieh T.-Y., Tsai C.-T., Chen S.-C., Lin C.-S., Hung M.-C., Tu C.-H., Chang J.-J., Chen P.-L. Light-induced instability of an InGaZnO thin film transistor with and without SiOx passivation layer formed by plasma-enhanced-chemical-vapor-deposition. *Appl. Phys. Lett.*, 2010, **97** (19), 192103.

[39] Hsieh T.-Y., Chang T.-C., Chen T.-C., Chen Y.-T., Tsai M.-Y., Chu A.-K., Chung Y.-C., Ting H.-C., Chen C.-Y. Self-Heating-Effect-Induced Degradation Behaviors in a-InGaZnO Thin-Film Transistors. *IEEE Electron Device Lett.*, 2013, **34** (1), P. 63–65.

[40] Hsieh T.-Y., Chang T.-C., Chen T.-C., Tsai M.-Y., Chen Y.-T., Jian F.-Y., Chung Y.-C., Tung H.-C., Chen C.-Y. Investigating the Drain-Bias-Induced Degradation Behavior Under Light Illumination for InGaZnO Thin-Film Transistors. *IEEE Electron Device Lett.*, 2012, **33** (7), P. 1000–1002.

[41] Chen T.-C., Chang T.-C., Hsieh T.-Y., Lu W.-S., Jian F.-Y., Tsai C.-T., Huang S.-Y., Lin C.-S. Investigating the degradation behavior caused by charge trapping effect under DC and AC gate-bias stress for InGaZnO thin film transistor. *Appl. Phys. Lett.*, 2011, **99** (2), 022104.

[42] Wu M.-C., Hsiao K.-C., Lu H.-C. Synthesis of $InGaZnO_4$ nanoparticles using low temperature multistep co-precipitation method. *Mater. Chem. Phys.*, 2015, **162**, P. 386–391.

[43] Fukuda N., Watanabe Y., Uemura S., Yoshida Y., Nakamura T., Ushijima H. In–Ga–Zn oxide nanoparticles acting as an oxide semiconductor material synthesized via a coprecipitation-based method. *J. Mater. Chem. C*, 2014, **2** (13), P. 2448–2454.

[44] Kondrat'eva O.N., Smirnova M.N., Nikiforova G.E., Razumov M.I., Khoroshilov A.V. Layered ceramics based on $InGaO_3(ZnO)_2$: Preparation and experimental investigation of high-temperature heat capacity and thermal conductivity. *J. Eur. Ceram. Soc.*, 2021, **41** (13), P. 6559–6566.

[45] Zirnik G.M., Chernukha A.S., Uchaev D.A., Solizoda I.A., Gudkova S.A., Nekorysnova N.S., Vinnik D.A. Phase formation of nanosized $InGaZnO_4$ obtained by the sol-gel method with different chelating agents. *Nanosystems: Phys. Chem. Math.*, 2024, **15** (4), P. 520–529.

[46] Kimizuka N., Mohri T., Matsui Y., Siratori K. Homologous compounds, $InFeO_3(ZnO)_m$ $(m = 1 - 9)$. *J. Solid State Chem.*, 1988, **74** (1), P. 98–109.

[47] Préaud S., Byl C., Brisset F., Berardan D. SPS?assisted synthesis of $InGaO_3(ZnO)_m$ ceramics, and influence of m on the band gap and the thermal conductivity. *JACerS*, 2020, **103** (5), P. 3030–3038.

Submitted 9 October 2024; revised 12 November 2024; accepted 13 November 2024

Information about the authors:

Egor S. Anannikov – Moscow Institute of Physics and Technology, Institutsky lane, 9, Dolgoprudny, 141701, Russia; ORCID 0009-0003-2012-406X; anannikov.es@phystech.edu

Timofey A. Markin – Moscow Institute of Physics and Technology, Institutsky lane, 9, Dolgoprudny, 141701, Russia; ORCID 0009-0008-0598-1676; markin.ta@phystech.edu

Ibrohimi A. Solizoda – Moscow Institute of Physics and Technology, Institutsky lane, 9, Dolgoprudny, 141701, Russia; St. Petersburg State University, Universitetskaya embankment, 7–9, 199034, St. Petersburg, Russia; Tajik National University, Rudaki Av., 17, Dushanbe, 734025, Tajikistan; ORCID 0000-0001-6973-4633; solizoda.ia@mipt.ru

Gleb M. Zirnik – Moscow Institute of Physics and Technology, Institutsky lane, 9, Dolgoprudny, 141701, Russia; ORCID 0009-0008-4546-1368; glebanaz@mail.ru

Daniil A. Uchaev – South Ural State University, Lenin Av., 76, Chelyabinsk, 454080, Russia; ORCID 0000-0002-8623-4769; uchaevda@susu.ru

Alexander S. Chernukha – Moscow Institute of Physics and Technology, Institutsky lane, 9, Dolgoprudny, 141701, Russia; St. Petersburg State University, Universitetskaya embankment, 7–9, 199034, St. Petersburg, Russia; South Ural State University, Lenin Av., 76, Chelyabinsk, 454080, Russia; ORCID 0000-0002-1272-1628; chernukha.as@mipt.ru

Svetlana A. Gudkova – Moscow Institute of Physics and Technology, Institutsky lane, 9, Dolgoprudny, 141701, Russia; St. Petersburg State University, Universitetskaya embankment, 7–9, 199034, St. Petersburg, Russia; ORCID 0000-0002-3028-947X; svetlanagudkova@yandex.ru

Denis A. Vinnik – Moscow Institute of Physics and Technology, Institutsky lane, 9, Dolgoprudny, 141701, Russia; St. Petersburg State University, Universitetskaya embankment, 7–9, 199034, St. Petersburg, Russia; South Ural State University, Lenin Av., 76, Chelyabinsk, 454080, Russia; ORCID 0000-0002-5190-9834; vinnik.da@mipt.ru

Conflict of interest: the authors declare no conflict of interest.

NANOSYSTEMS:
PHYSICS, CHEMISTRY, MATHEMATICS

Original article

Martinson K.D., et al. *Nanosystems: Phys. Chem. Math.*, 2024, **15** (6), 814–820.
http://nanojournal.ifmo.ru
DOI 10.17586/2220-8054-2024-15-6-814-820

Solution combustion approach to the phase pure nanocrystalline lithium ferrite ($Li_{0.5}Fe_{2.5}O_4$) with spinel structure and magnetically soft behavior

Kirill D. Martinson[1,a], Vadim I. Popkov[1,b]

[1]Ioffe Institute, Politekhnicheskaya st., 26, Saint Petersburg, 194064, Russia

[a]martinsonkirill@mail.ru, [b]vip-07@yandex.ru

Corresponding author: K. D. Martinson, martinsonkirill@mail.ru

---

PACS 61.46Df, 75.50.Gg, 75.75.Fk

ABSTRACT Lithium ferrite nanoparticles ($Li_{0.5}Fe_{2.5}O_4$) were synthesized via the solution combustion method with a substantial deficiency of organic fuel (glycine, f = 0.05), followed by heat treatment of X-ray amorphous combustion products at temperatures ranging from 500 to 750 °C. Comprehensive characterization was performed using scanning electron microscopy (SEM), energy-dispersive spectroscopy (EDS), atomic absorption spectrometry (AAS), powder X-ray diffraction (XRD), and vibrating sample magnetometry (VSM). The results indicate significant morphological and structural changes in the nanopowders depending on the heat treatment temperature. Average particle sizes ranged from 14.2 to 59.5 nm, while crystallinity varied from 89.4% to 62.8%. Magnetic properties also varied, with coercivity (H_c) between 58.4 and 102.4 Oe, residual magnetization (M_r) from 5.2 to 15.4 emu/g, and saturation magnetization (M_s) from 35.1 to 60.7 emu/g. These findings demonstrate that pure lithium ferrite nanoparticles, free from impurity oxide phases, can be produced through controlled heat treatment of X-ray amorphous combustion products. Furthermore, the magnetic properties of the nanoparticles are highly sensitive to the specific heat treatment temperature, indicating that thermal processing conditions play a crucial role in determining their magnetic behavior.

KEYWORDS solution combustion synthesis, lithium ferrite, spinel ferrites, nanocrystals, soft magnetics

ACKNOWLEDGEMENTS The authors of the article express their gratitude to the Institute of Applied Materials Science of the Joint-Stock Company “Almaz Antej - Obuhovskij zavod” for assistance in conducting the study of morphology and structure. This work was supported by the Ministry of Science and Higher Education within the framework of a State Assignment of the Ioffe Institute, Russian Academy of Sciences, project no. FFUG-2024-0036.

FOR CITATION Martinson K.D., Popkov V.I. Solution combustion approach to the phase pure nanocrystalline lithium ferrite ($Li_{0.5}Fe_{2.5}O_4$) with spinel structure and magnetically soft behavior. *Nanosystems: Phys. Chem. Math.*, 2024, **15** (6), 814–820.

---

1. Introduction

Spinel ferrites are a class of oxide materials known for their unique magnetic properties, which arise from their crystalline structure. These materials are characterized by the general chemical formula AFe_2O_4, where A represents metal cations (e.g., Li, Zn, Mn, Mg, Co, Ni), Fe denotes iron cations, and O represents oxygen anions. In ferrites, the cationic role is typically played by iron ions in conjunction with divalent or trivalent metals, such as zinc, magnesium, nickel, cobalt, or manganese [1–3].

The spinel crystal structure consists of a cubic close-packed arrangement of oxygen ions, with metal cations occupying interstitial sites in either tetrahedral or octahedral voids. The distribution of cations within these positions – whether normal, inverted, or random – profoundly influences the magnetic and electrical properties of the material [4]. In a normal spinel, A cations occupy tetrahedral sites, while B cations fill octahedral sites. In an inverted spinel, half of the B cations occupy tetrahedral sites, with the remaining B cations and all A cations positioned in octahedral sites [5].

The magnetic properties of spinel ferrites are primarily due to the interaction between the electron spins of cations in different coordination environments. These materials typically exhibit ferrimagnetism, where the magnetic moments of cations on distinct sublattices are oppositely aligned but do not fully cancel each other, resulting in a net magnetic moment [6]. This makes spinel ferrites invaluable in the production of magnetic cores, transformers, inductors, and other electronic components [7]. Their applications are wide-ranging and include radio electronics, telecommunications, and electrical engineering [8]. Frequently, they serve as electromagnetic wave absorbers, filters, antennas, and magnetic information carriers [9].

Among the various spinel ferrites, lithium ferrite stands out for its practical applications, particularly in microwave electronics, where it maintains a prominent position [10]. The chemical formula of lithium ferrite is typically expressed as $LiFe_5O_8$ or $Li_{0.5}Fe_{2.5}O_4$, depending on the stoichiometry and ionic distribution within the structure. Lithium ferrite's structure is a variant of the spinel, featuring a cubic close-packed array of oxygen ions, with lithium and iron cations occupying the intervening spaces. Lithium cations can reside in both tetrahedral and octahedral sites, while iron cations are distributed between octahedral and tetrahedral sublattices. This distribution significantly influences the functional properties of lithium ferrite [11].

Lithium ferrite exhibits ferrimagnetic behavior, characterized by high coercivity and remanence. Its magnetic properties stem from the interaction of the magnetic moments of iron ions, which are not fully compensated due to their specific distribution within the crystal lattice. Lithium ferrite exhibits high magnetic permeability, especially at elevated frequencies, making it ideal for microwave (ultra-high frequency) applications, such as telecommunications and radar systems. High permeability allows the material to efficiently support magnetic fields, reducing energy loss in components like microwave filters and isolators [12]. Additionally, lithium ferrite's high electrical resistivity minimizes eddy current losses during high-frequency operation. Eddy currents, which cause energy dissipation as heat, are suppressed due to the material's resistivity and crystal structure, which create barriers to charge movement. This property enhances performance in devices that require efficient energy transfer and low heat generation, such as transformers and inductors [13].

Because of these properties – high magnetic permeability and low eddy current losses – lithium ferrite is widely employed in the production of antennas and electromagnetic wave absorbers. These materials enhance antenna performance and mitigate electromagnetic interference, which is crucial in densely populated radio frequency environments and wireless communication systems [14]. Multicomponent lithium ferrites, such as lithium-zinc-manganese and lithium-zinc-titanium-manganese variants, are widely used in the manufacture of microwave electronic devices [15, 16]. The advent of nanostructured material production technologies has expanded the applications of lithium ferrite nanopowders to new fields, such as sensor and detector fabrication [17], lithium-ion batteries [18], and even medical applications [19].

Numerous studies have reported the synthesis of lithium ferrite using various production methods, with the most common techniques including solid-state synthesis [20], sol-gel methods [21], solution combustion [22], and hydrothermal synthesis [23]. In recent years, the sol-gel auto-combustion method [24] and direct solution combustion methods using different organic fuels (e.g., glycine, urea, citric acid) [25–27] have been explored extensively. However, as several studies have shown [25,26], including the author's previous work [27], the direct solution combustion method often fails to yield pure α-$Li_{0.5}Fe_{2.5}O_4$, with impurity phases such as β-$Li_{0.5}Fe_{2.5}O_4$ and γ-$Li_{0.5}Fe_{2.5}O_4$ commonly present.

This work builds upon the author's previous study [27], which employed the direct solution combustion method to synthesize lithium ferrite nanopowders. In the present study, a two-stage synthesis technique is introduced for the first time. This approach involves preparing the initial sample using the solution combustion method with a significant deficiency of glycine (f = 0.05), followed by heat treatment in the temperature range of 500–750 °C, with 50 °C increments. The choice of such a low glycine concentration was made because, under these conditions, the resulting powder is almost entirely X-ray amorphous.

2. Experimental

The following reagents were used to synthesize the initial X-ray amorphous powder: lithium nitrate ($LiNO_3 \cdot 3H_2O$, puriss., NevaReactiv), iron nitrate ($Fe(NO_3)_3 \cdot 9H_2O$, puriss., NevaReactiv), glycine (CH_2NH_2COOH, puriss., NevaReactiv), nitric acid (HNO_3, puriss., NevaReactiv), and distilled water. Lithium and iron nitrates were dissolved in 35 ml of distilled water with continuous mechanical stirring at 25 °C. After complete dissolution of the salts, 2–3 ml of 5M nitric acid and glycine were added, with glycine in a ratio of f = 0.05 relative to the stoichiometric amount. Nitric acid was included to prevent the formation of lithium and iron complex compounds. The synthesis procedure is described in more detail in [27]. The resulting solution was heated on a ceramic plate until nearly all the water evaporated, reaching the autoignition point. This process produced significant gas evolution and resulted in a solid brown product. The synthesized powder was ground mechanically in a mortar and then thermally treated in an air atmosphere for 6 hours at temperatures ranging from 500 to 750 °C, with 50 °C increments. After heat treatment, the powder was again ground mechanically and subsequently analyzed.

The chemical composition of the synthesized samples was determined using energy-dispersive spectroscopy (EDS) for iron (Fe) and oxygen (O), and atomic absorption spectroscopy (AAS) for lithium (Li), employing an Oxford INCA attachment and a Shimadzu AA-7000 atomic absorption spectrometer, respectively. The powder morphology was characterized by scanning electron microscopy (SEM) on a Tescan Vega 3 SBH microscope, and the average particle size was calculated from the micrographs using ImageJ software. X-ray diffraction (XRD) analysis was conducted using a Rigaku SmartLab 3 diffractometer with $CuK_{\alpha 1}$ radiation (λ = 0.154056 nm) at 40 kV and 30 mA. Diffraction patterns were collected over a 2θ range of 20° to 80°, with a step size of 0.01° and a 3-second exposure time per step. Crystallite size distribution was evaluated using the fundamental parameter method, and the average crystallite size was estimated using the Scherrer equation. Unit cell parameters, crystallinity degree, and lattice microstrains were analyzed using Rigaku SmartLab Studio II software. Magnetic hysteresis loops (M-H) were obtained at room temperature (278 K) using a Lake Shore 7410 vibrating sample magnetometer (VSM) with an applied field up to 10 kOe. Measurements were conducted using a standard cell.

3. Results and Discussion

The morphology of the synthesized powders was investigated using scanning electron microscopy (SEM), as shown in Fig. 1.

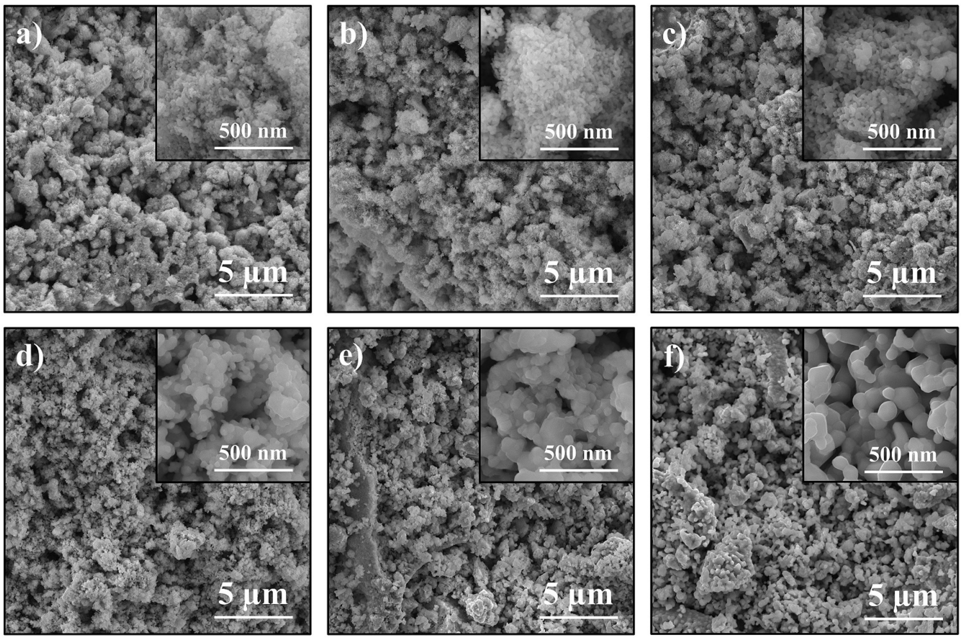

FIG. 1. SEM micrographs of α-$Li_{0.5}Fe_{2.5}O_4$ synthesized via thermal treatment of X-ray amorphous combustion products at 500 °C (a), 550 °C (b), 600 °C (c), 650 °C (d), 700 °C (e), 750 °C (f)

The SEM results demonstrate that the morphology of the lithium ferrite nanopowders depends significantly on the heat treatment temperature. All samples exhibit micron-sized clusters formed by nanoparticles, with the particle size increasing as the temperature rises. At 500 °C, the clusters appear loosely packed with weakly isolated small particles, and the surface shows noticeable porosity. Samples treated at 550 °C and 600 °C display similar features, with comparable porosity and particle size. However, at 650 °C and 700 °C, the clusters become more distinct, with clearer particle boundaries, though the surface remains loose. The 750 °C sample exhibits the most organized structure, with well-defined particle boundaries and reduced porosity. Thus, SEM analysis indicates that increasing the heat treatment temperature leads to larger particle sizes and a reduction in porosity.

To further quantify the particle size, distribution graphs were generated from the SEM images using ImageJ software (Fig. 2), with all histograms shown on the same scale for comparison. The data reveal that the average particle size increases steadily with temperature, ranging from 14.24 nm at 500 °C to 59.48 nm at 750 °C. The most significant growth occurs between 700 °C and 750 °C, where the average particle size nearly doubles, from 25.69 nm to 59.48 nm. The distributions remain monomodal across all samples, indicating a high degree of homogeneity and suggesting that particle growth occurred uniformly. This consistent growth points to the presence of an amorphous lithium ferrite phase in the initial X-ray amorphous powder, allowing direct particle growth without the formation of intermediate oxide phases. Additionally, the consistent particle growth across all samples suggests that diffusion limitations were similar at each temperature, preventing significant variations in growth rates and leading to uniform particle size increases.

The elemental composition of the synthesized samples, as determined by energy-dispersive spectroscopy (EDS) and atomic absorption spectroscopy (AAS), is summarized in Table 1. AAS confirmed the lithium content, while EDS verified the iron composition. The results indicate that the synthesized powders closely match the theoretical composition, with deviations of no more than 0.4%. Notably, these deviations increase with temperature, ranging from 0.1% at 500 °C to 0.4% at 750 °C. This increase is likely due to the volatility of lithium at higher temperatures, which can lead to lithium evaporation during heat treatment [28].

The X-ray diffraction (XRD) patterns of the initial lithium ferrite powder and the heat-treated samples are presented in Fig. 3a. The initial sample is nearly X-ray amorphous, displaying a single low-intensity amorphous halo around the 35° region. In contrast, the other samples exhibit clear diffraction peaks corresponding to the crystal planes (220), (311), (222), (400), (422), (511), and (440) of the crystalline α-$Li_{0.5}Fe_{2.5}O_4$ phase (JCPDS # 38-0259). As the processing temperature increases, a notable rise in peak intensity is observed, indicating a higher degree of crystallinity in the samples. At lower temperatures, particularly in the initial state, the diffraction peaks are less intense and more diffuse, which signifies a less ordered structure. Additionally, peak width decreases with increasing temperature, suggesting an increase in crystallite size. This observation is further supported by the shape of the crystallite size distribution, which shows a steady increase

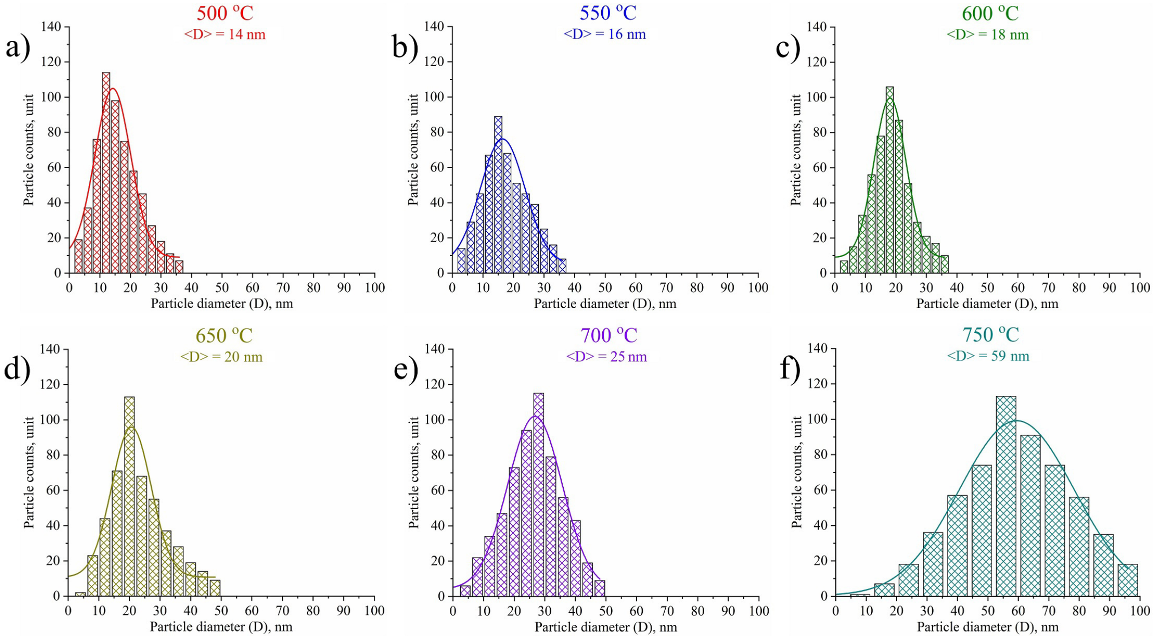

FIG. 2. Particle size distributions of lithium ferrite obtained via thermal treatment of X-ray amorphous combustion products at 500 °C (a), 550 °C (b), 600 °C (c), 650 °C (d), 700 °C (e), 750 °C (f)

TABLE 1. Elemental composition of synthesized lithium ferrite at different temperature modes

Sample	Li, at. %	Fe, at. %
500 °C	16.8	83.2
550 °C	16.8	83.2
600 °C	16.6	83.4
650 °C	16.5	83.5
700 °C	16.5	83.5
750 °C	16.4	83.6

in size with temperature (Fig. 3b). The crystallite size distribution data obtained using the fundamental parameters method align well with the visual estimates of average particle size (Fig. 2). The distributions reveal that the crystallite sizes across all samples are centered between 13±2 nm and 50±5 nm. The average crystallite size increases linearly as the processing temperature rises.

The values of the average crystallite size, degree of crystallinity, lattice parameters, and microstresses, determined using the Rigaku SmartLab Studio II software package, are shown in Fig. 4a,b. The average crystallite size was calculated using the Scherrer formula for the main crystallographic directions (220), (311), (400), (422), (511), and (440). It is evident that as the processing temperature increases from 500 °C to 750 °C, a significant rise in the average crystallite size is observed, from 10.2 nm to 49.6 nm. These results are consistent with the visual assessment of the average particle size, obtained from the micrographs (Fig. 2), and the data from the fundamental parameters method (Fig. 3b). The most pronounced increase in crystallite size occurs between 650 °C and 750 °C, suggesting an intensive crystallite growth process within this temperature range.

The degree of crystallinity was estimated using an internal standard (α-Si) with the Rietveld method, and it also increases with temperature. In the range from 500 °C to 650 °C, a moderate increase in the crystalline phase percentage is observed, but after 650 °C, the growth rate accelerates, reaching nearly 90% crystallinity at 750 °C. This high degree of crystallinity at elevated temperatures may indirectly reflect improved structural ordering of the lithium ferrite, which is further confirmed by the temperature dependence of the lattice parameters. These parameters decrease significantly, reaching values close to those reported in the literature (a = b = c = 8.324(7) Å) for the sample annealed at 750 °C [25,27]. Hence, the reduction in lattice parameters within the 500 °C to 750 °C range may be attributed to lattice compression during crystallite growth and the corresponding increase in crystallinity.

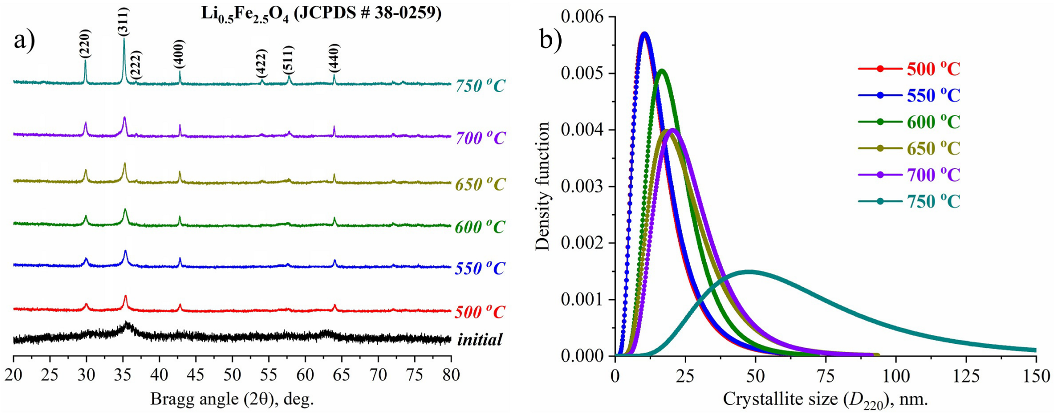

FIG. 3. Diffraction patterns (a) and crystallite size distribution (b) of α-$Li_{0.5}Fe_{2.5}O_4$ synthesized via thermal treatment of X-ray amorphous combustion products at the range of temperature from 500 to 750 °C

Microstress values also decrease notably as the temperature rises, with the most significant reduction occurring between 600 °C and 750 °C. This decline in microstresses may be linked to the relaxation of defects within the lattice at higher temperatures, coinciding with the increase in crystallinity. Therefore, the observed reduction in lattice parameters indicates a compaction of the structure, while the decreasing microstresses suggest the relaxation of internal stresses and defects.

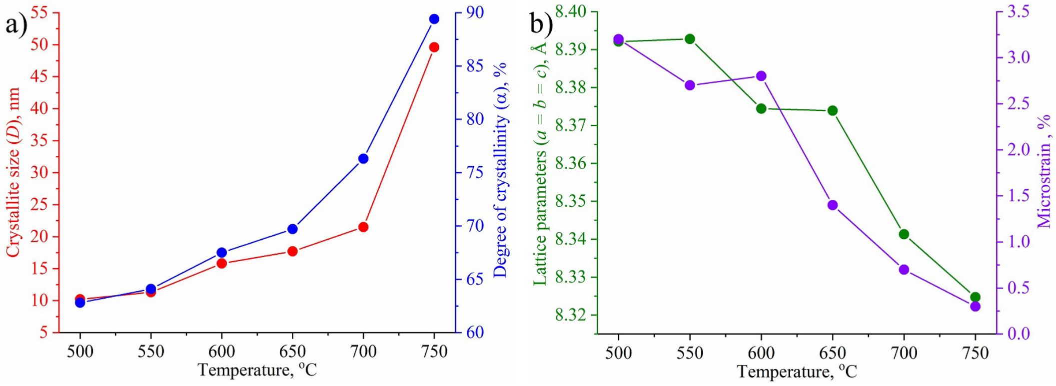

FIG. 4. Structural parameters of lithium ferrite nanopowders synthesized via thermal treatment of X-ray amorphous combustion products at the range of temperature from 500 to 750 °C

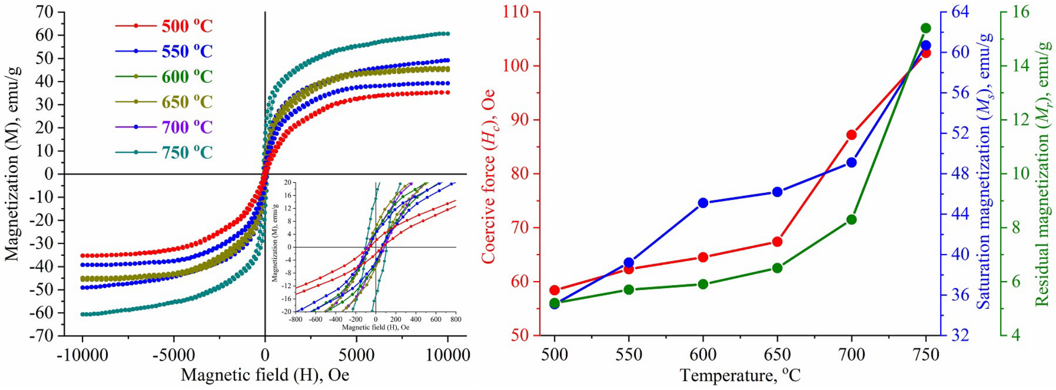

FIG. 5. M-H hysteresis loops (a) and magnetic parameters (b) of lithium ferrite nanopowders synthesized via thermal treatment of X-ray amorphous combustion products at different temperature modes

Figure 5 shows the magnetic hysteresis loops (M-H) and magnetic parameters of the lithium ferrite nanopowders (Fig. 5a,b). The hysteresis loops exhibit the characteristic shape of ferrimagnetic materials. Notably, as the temperature increases from 500 °C to 750 °C, a significant change in the loop shape is observed. At 750 °C, the hysteresis loop is the widest, indicating higher magnetic performance, with a residual magnetization of 15.4 emu/g, saturation magnetization of 60.7 emu/g, and coercive force of 102.4 Oe. As the heat treatment temperature decreases, the loop width narrows, and both saturation magnetization and residual magnetization decline considerably. The lowest values are observed in the sample treated at 500 °C, where the coercive force, residual magnetization, and saturation magnetization are 58.4 Oe, 5.2 emu/g, and 35.1 emu/g, respectively. This behavior suggests a reduction in magnetic order at lower temperatures, likely due to thermal fluctuations that disturb magnetic domains [29, 30]. Therefore, the data clearly demonstrate that the main magnetic parameters of lithium ferrite improve with increasing heat treatment temperature, which corresponds with the observed increases in both average particle size and degree of crystallinity.

4. Conclusion

This study demonstrates the successful synthesis of the crystalline phase of α-$Li_{0.5}Fe_{2.5}O_4$ without impurity oxide phases through the heat treatment of X-ray amorphous products derived from solution combustion. The formation of lithium ferrite begins at 500 °C, and as the processing temperature increases, the average particle size grows from 14.2 nm to 59.5 nm, while the degree of crystallinity improves from 62.8% to 89.4%. The unit cell parameters change linearly with temperature, reflecting structural evolution in the samples, with the sample treated at 750 °C showing the closest match to reference values. Given that this sample also exhibits the lowest percentage of amorphous phase, the 750 °C temperature regime is deemed optimal for obtaining well-crystallized lithium ferrite. Furthermore, the key magnetic parameters – coercive force, residual magnetization, and saturation magnetization – also increase linearly with temperature, corresponding to the rise in both particle size and crystallinity.

References

[1] Salih S.J., Mahmood W.M. Review on magnetic spinel ferrite (MFe_2O_4) nanoparticles: From synthesis to application. *Heliyon*, 2023, **9**(6), P. e16601.

[2] Martinson K.D., Cherepkova I.A., Sokolov V.V. Formation of cobalt ferrite nanoparticles via glycine-nitrate combustion and their magnetic properties. *Glass Physics and Chemistry*, 2018, **44**, P. 21–25.

[3] Askarzadeh N., Shokrollahi H. A review on synthesis, characterization and properties of lithium ferrites. *Results in Chemistry*, 2024, **10**, P. 101679.

[4] Liandi A.R., Cahyana A.H., Kusumah A.J.F., Lupitasari A, Alfariza D.N., Nuraini R., Sari R.W., Kusumasari F.C. Recent trends of spinel ferrites (MFe_2O_4: Mn, Co, Ni, Cu, Zn) applications as an environmentally friendly catalyst in multicomponent reactions: A review. *Case Studies in Chemical and Environmental Engineering*, 2023, **7**, P. 100303.

[5] Martinson K.D., Panteleev I.B., Steshenko K.A., Popkov V.I., Effect of Bi_2O_3 contents on magnetic and electromagnetic properties of LiZnMn ferrite ceramics. *Journal of the European Ceramic Society*, 2022, **42**(8), P. 3463–3472.

[6] Dastjerdi O.D., Shokrollahi H., Mirshekari S. A review of synthesis, characterization, and magnetic properties of soft spinel ferrites. *Inorganic Chemistry Communications*, 2023, **153**, P. 110797.

[7] Sagayaraj R. A review on structural and magnetic properties of magnesium ferrite nanoparticles. *International Nano Letters*, 2022, **12**, P. 345–350.

[8] Harris V.G., Geiler A., Chen Y., Yoon S.D., Wu M., Yang A., Chen Z., He P., Parimi P.V., Zuo X., Patton C.E., Abe M., Acher O., Vittoria C. Recent advances in processing and applications of microwave ferrites. *Journal of Magnetism and Magnetic Materials*, 2009, **321**, P. 2035–2047.

[9] Dyachenko S.V., Martinson K.D., Cherepkova I.A., Zhernovoi A.I. Particle size, morphology, and properties of transition metal ferrospinels of the MFe_2O_4 (M = Co, Ni, Zn) type, produced by glycine-nitrate combustion. *Russian Journal of Applied Chemistry*, 2016, **89**, P. 535–539.

[10] Verma R., Thakur P., Sun A.-C. A., Thakur A. Investigation of structural, microstructural and electrical characteristics of hydrothermally synthesized $Li_{0.5-0.5x}Co_xFe_{2.5-0.5x}O_4$, ($0.0\leq x \leq 0.4$) ferrite nanoparticles. *Physica B: Condensed Matter*, 2023, **661**, P. 414926.

[11] Malathi S., Wayessa S.G. A Study of Lithium Ferrite and Vanadium-Doped Lithium Ferrite Nanoparticles Based on the Structural, Optical, and Magnetic Properties. *Journal of Nanomaterials*, 2023, **2023**, P. 6752950.

[12] Verma V., Gairola S.P., Pandey V., Kotanala R.K., Su H. Permeability of Nb and Ta doped lithium ferrite in high frequency range. *Solid State Communications*, 2008, **148**(3-4), P. 117–121.

[13] Mazen S.A., Abu-Elsaad N.I., Structural, magnetic and electrical properties of the lithium ferrite obtained by ball milling and heat treatment. *Applied Nanoscience*, 2015, **5**, P. 105–114.

[14] Lysenko E.N., Nikolaev E.V., Vlasov V.A., Svirkov A.S., Surzhikov A.P., Sheveleva E.A., Plotnikova I.V., Artishchev S.A. Structural and Electromagnetic Properties of Lithium Ferrite Manufactured by Extrusion Printing. *Russian Physics Journal*, 2024, **67**, P. 960–965.

[15] Martinson K.D., Ivanov A.A., Panteleev I.B., Popkov V.I., Effect of sintering temperature on the synthesis of LiZnMnFe microwave ceramics with controllable electro/magnetic properties. *Ceramics International*, 2021, **47**(21), P. 0071–30081.

[16] Dasari M., Gajula G.R., Rao D.H., Chintabathini A.K., Kurimella S., Somayajula B. Lithium ferrite: the study on magnetic and complex permittivity characteristics. *Processing and Application of Ceramics*, 2017, **11**(1), P. 7–12.

[17] Rezlescu N., Doroftei C., Rezlescu E., Papa P.D. Lithium ferrite for gas sensing applications. *Sensors and Actuators B: Chemical*, 2008, **133**(2), P. 420–425.

[18] Ateia E.E., Ateia M.A., Fayed M.G., El-Hout S.I., Mohamed S.G., Arman M.M., Synthesis of nanocubic lithium cobalt ferrite toward high-performance lithium-ion battery. *Applied Physics A*, 2022, **128**, P. 483.

[19] Teixeira S.S., Graca M.P.F., Lucas J., Valente M.A., Soares P.I.P., Lanca M.C., Vieira T., Silva J.C., Borges J.P., Jinga L.I., Socol G., Salgueiro C.M., Nunes J., Costa L.C., Nanostructured $LiFe_5O_8$ by a Biogenic Method for Applications from Electronics to Medicine. *Nanomaterials*, 2021, **11**(1), P. 193.

[20] Berbenni V., Marini A., Matteazzi P., Ricceri R., Walham N.J., Solid-state formation of lithium ferrites from mechanicallyactivated Li_2CO_3-Fe_2O_3 mixtures. *Journal of European Ceramic Society*, 2003, **23**(3), P. 527–536.

[21] Ahmad M., Shahid M., Alanazi Y.M., Rehman A.U., Asif M., Dunnill C.W., Lithium ferrite ($Li_{0.5}Fe_{2.5}O_4$): synthesis, structural, morphological and magnetic evaluation for storage devices. *Journal of Materials Research and Technology*, 2022, **18**, P. 3386–3395.

[22] Venkatachalapathy R., Manoharan C., Venkateshwarlu M., Elfadeel G.A., Saddeek Y., Solution combustion route for Ni and Al co-doped lithium ferrite nanoparticles: Synthesis, the effect of doping on the structural, morphological, optical, and magnetic properties. *Ceramics International*, 2023, **49**(4), P. 6594–6607.

[23] Mohanty V., Govindaraj G., $\mathrm{Li}_{0.5}\mathrm{Ce}_x\mathrm{Fe}_{2.5-x}\mathrm{O}_4$ (x = 0, 0.05): hydrothermal synthesis, electrical and magnetic properties. *Materials Research Express*, 2018, **5**, P. 055014.

[24] Fu, Y.-P., Lin C.-H., Liu C.-W., Yao Y.-D. Microwave-induced combustion synthesis of $\mathrm{Li}_{0.5}\mathrm{Fe}_{2.5}\mathrm{O}_4$ powder and their characterization. *Journal of Alloys and Compounds*, 2005, **395**(1-2), P. 247–251.

[25] Naderi P., Masoudpanah S.M., Alamolhoda S. Magnetic properties of $\mathrm{Li}_{0.5}\mathrm{Fe}_{2.5}\mathrm{O}_4$ nanoparticles synthesized by solution combustion method. *Applied Physics A*, 2017, **123**, P. 702.

[26] Randhawa B.S., Dosanjh H.S, Kumar N. Synthesis of lithium ferrite by precursor and combustion methods: A comparative study. *Journal of Radioanalytical and Nuclear Chemistry*, 2007, **274**, P. 581–591.

[27] Martinson K.D., Panteleev I.B., Shevchik A.P., Popkov V.I. Effect of the Red/Ox ration on the structure and magnetic behavior of $\mathrm{Li}_{0.5}\mathrm{Fe}_{2.5}\mathrm{O}_4$ nanocrystals synthesized by solution combustion approach. *Letters on Materials*, 2019, **9**(4), P. 475–479.

[28] Iida Y. Evaporation of Lithium Oxide from Solid Solution of Lithium Oxide in Nickel Oxide. *Journal of American Ceramic Society*, 1960, **43**(3), P. 171–172.

[29] Jing X., Guo M., Li Z., Qin C., Chen Z., Li Z., Gong H. Study on structure and magnetic properties of rare earth doped cobalt ferrite: The influence mechanism of different substitution positions. *Ceramics International*, 2023, **49**(9), P. 14046–14056.

[30] Sun B., Ma D., Bai G., Lu X., Yang J., Wang K., Xu X., Zhai Y., Quan W., Han B. Correlating the microstructure of Mn-Zn ferrite with magnetic noise for magnetic shield applications. *Ceramics International*, 2023, **49**(8), P. 11960–11967.

Submitted 5 November 2024; revised 9 November 2024; accepted 10 November 2024

Information about the authors:

Kirill D. Martinson – Ioffe Institute, Politekhnicheskaya st., 26, Saint Petersburg, 194064, Russia; ORCID 0000-0001-9313-4267; martinsonkirill@mail.ru

Vadim I. Popkov – Ioffe Institute, Politekhnicheskaya st., 26, Saint Petersburg, 194064, Russia; ORCID 0000-0002-8450-4278; vip-07@yandex.ru

Conflict of interest: the authors declare no conflict of interest.

NANOSYSTEMS:
PHYSICS, CHEMISTRY, MATHEMATICS

Original article

Khrapova E.K., et al. *Nanosystems: Phys. Chem. Math.*, 2024, **15** (6), 821–836.
http://nanojournal.ifmo.ru
DOI 10.17586/2220-8054-2024-15-6-821-836

Intermetallic compounds obtained from $Me_3Ge_2O_5(OH)_4$ (*Me* = Mg, Ni, Fe, Co) phyllogermanates: synthesis of single-phase precursors

Ekaterina K. Khrapova, Anastasia A. Ivanova, Demid A. Kirilenko, Andrei A. Krasilin

Ioffe Institute, St. Petersburg, Russia

Corresponding author: Ekaterina K. Khrapova, e.k.khrapova@mail.ioffe.ru

ABSTRACT Typically, intermetallic compounds are prepared by solid-state method at high temperatures. We propose a simple method to obtain intermetallic compounds by reduction in Ar–H_2 atmosphere from precursors. In particular, Co^{2+} and Fe^{2+} oxidation in hydrothermal conditions grants additional experimental challenge. Here, we report successful Fe phyllogermanate synthesis for the first time. We identify general patterns of formation and determine the effect of hydrothermal treatment on phase composition and morphology for the whole series of phyllogermanates. Formation of phyllogermanates under hydrothermal conditions is studied in the 100 – 200 °C temperature range in three hydrothermal media: H_2O, NaOH, Na_2SO_3. The latter inhibits the oxidation of Co^{2+} and Fe^{2+} during the synthesis. An increase in temperature favors to the formation of phase described by three-layers unit cell. Heat treatment in an Ar–H_2 atmosphere allows us to obtain intermetallic compounds and Me_xGe_y alloys, and to establish the temperature regimes of the reduction processes.

KEYWORDS intermetallic compounds, phyllogermanate, hydrothermal synthesis, reduction

ACKNOWLEDGEMENTS The work was financially supported by the Russian Science Foundation (Project No. 23-22-00245, https://rscf.ru/project/23-22-00245/). Powder X-ray diffraction was performed using the equipment of the Engineering Centre of St. Petersburg State Technical University (Technical Institute). TEM studies were performed using equipment of the Federal Joint Research Center “Material science and characterization in advanced technology” supported by the Ministry of Science and Higher Education of the Russian Federation.

FOR CITATION Khrapova E.K., Ivanova A.A., Kirilenko D.A., Krasilin A.A. Intermetallic compounds obtained from $Me_3Ge_2O_5(OH)_4$ (*Me* = Mg, Ni, Fe, Co) phyllogermanates: synthesis of single-phase precursors. *Nanosystems: Phys. Chem. Math.*, 2024, **15** (6), 821–836.

1. Introduction

Class of 1:1 phyllogermanates is a poorly studied, although they are structural analogues of 1:1 phyllosilicates. These phyllosilicates have a unique structure consisting of two sublayers, tetrahedral SiO_4 and octahedral MeO_6. The octahedral sublayer has a larger size compared to the tetrahedral one, which leads to folding into nanoscrolls. [1,2]. This morphology is typical for chrysotile. Lizardite is a platy analog of chrysotile. It has a similar structure but does not fold [3]. The chrysotile structure allows isomorphic substitution in the cation sublattice of Mg^{2+} and Si^{4+} by Ni^{2+} [4–7], Co^{2+} [7–9], Fe^{2+} [7, 10], Fe^{3+} [11, 12], Ti^{4+} [13], Ge^{4+} [14, 15] with preservation of the scrolled morphology or formation of plates. Attempts to obtain phyllosilicates with partial or complete replacement of Si^{4+} by Ge^{4+} have been made for several compounds. $Mg_3Ge_2O_5(OH)_4$ and $Ni_3Ge_2O_5(OH)_4$ phyllogermanates and are the first phyllogermanates obtained on the basis of chrysotile. The substitution of Si^{4+} by Ge^{4+} led to the formation of hexagonal plates [14]. In another related group of layered phyllosilicates $Al_2Si_2O_5(OH)_4$, the substitution of Si^{4+} by Ge^{4+} led to the folding of kaolinite sheet into scrolls with halloysite-like structure. It was possible to obtain multi-walled or single-walled nanotubes, as well as curved nanosheets, by varying the Ge/(Ge+Si) ratio [16]. In another nanotubular phyllosilicate, imogolite $Al_2SiO_3(OH)_4$, the Ge/Si ratio affected the diameter of the nanotubes as well as their length [17].

In this work, phyllogermanates with the stoichiometric formula $Me_3Ge_2O_5(OH)_4$ (*Me* = Mg, Ni, Fe, Co) were selected for study. The structure of such compounds has not been studied in details. The only one that has been determined was $Mg_3Ge_2O_5(OH)_4$. Only for this compound, it was possible to construct a unit cell. It had six layers with some layers shifted by $\pm b/3$, which was also typical for other serpentine compounds, including their polytypes [18]. $Co_3Ge_2O_5(OH)_4$ also had a layered structure, but the number of layers in the unit cell was limited to three [19]. Such a structure and morphology create a number of advantages that make such compounds perspective in catalysis and adsorption application. Advantages include the presence of a large number of surface hydroxyl groups, the provision of a redox cycle through rapid electron transfer, and the control of surface-active centers by changing the number of layers in the particles [20–23]. The most actively studied are cobalt and nickel phyllogermanates, which, in addition to the properties listed, can also be used as anode materials due to the presence of transition elements in their composition [24, 25]. Their electronic [23] and magnetic [19] properties can potentially ensure their applicability in spintronics [26].

It is possible to obtain the corresponding orthogermanates or intermetallic compounds based on phyllogermanates. Although Ge-intermetallic compounds are promising materials for use in semiconductor devices [27, 28] and energy storage devices [29], as well as in various catalytic processes [29–31]. Intermetallic compounds are obtained by solid-state methods requiring high temperatures in most cases [31]. The reduction of Ge and transition elements from a single precursor, in particular phyllogermanates, would allow to obtain intermetallic compounds of a given composition. This article presents a new simple method for the preparation of Ge-intermetallic compounds, consisting of the reduction of phyllogermanates in an Ar–H_2 atmosphere. The synthesis parameters for the preparation studies of Mg, Ni, Co and, in particular, Fe phyllogermanates, which were obtained for the first time, are also presented.

2. Experimental

2.1. Samples preparation

$Me_3^{2+}Ge_2O_5(OH)_4$ (*Me* = Mg, Ni, Co, Fe) phyllogermanates were obtained by reverse coprecipitation followed by hydrothermal treatment. The synthesis was carried out in a glove box under an inert argon atmosphere for Co- and Fe-phyllogermanates. Oxygen-free water was used in the synthesis, obtained by distillation in an inert Ar atmosphere followed by 2 – 3 cycles of vacuum evacuation. All phyllogermanates were obtained according to the general scheme: crystalline GeO_2 (1 g) was dissolved in a 0.3 M NaOH aqueous solution (0.1 L). Then 0.15 M aqueous solution (0.1 L) of the salt ($FeSO_4 \cdot 7H_2O$, $NiCl_2 \cdot 6H_2O$, $CoCl_2 \cdot 6H_2O$ or $MgCl_2 \cdot 6H_2O$) was added dropwise at constant stirring to obtain a molar ratio Me/Ge = 1.5. The precipitate was then washed by decantation until there was negative reaction for chloride ions with $AgNO_3$ solution in the case of Mg and Ni phyllogermanates. Then the precipitate was ground in an agate mortar. Washing to remove impurity ions was not performed to minimize sample contact with oxygen for Co- and Fe phyllogermanates. All samples (0.2 g) placed in 25 mL Teflon crucibles in high-pressure vessels and 20 mL of distilled water or aqueous solutions of 0.1 M NaOH, 0.1 M Na_2SO_3 were added as hydrothermal medium (HTM). Na_2SO_3 was used only for Co- and Fe-phyllogermanates to prevent oxidation during the hydrothermal treatment [9]. The hydrothermal treatment temperatures for all samples were 100, 150, and 200 °C. The holding time was 72 h, and the estimated pressure was 2 MPa. The samples were dried in air at a temperature of 80 °C after the hydrothermal treatment.

The samples were reduced in a tube furnace in an Ar–H_2 flow (5 % vol. H_2) at $T = 900$ °C for 5 h at a heating rate of 10 °/min. The samples were cooled together with the furnace in an inert atmosphere.

2.2. Samples characterization

Powder X-ray diffraction (PXRD) was performed on a Rigaku SmartLab 3 (Japan) with a cobalt anode ($\lambda = 1.789$ Å) and a K_β-filter in the Bragg–Brentano geometry in the range of 5 – 80°, a step of 0.01°, and a shooting rate of 1 °/min. The cathode heating current was 35 mA and the accelerating voltage was 40 kV. X-ray phase analysis was performed using the PDF-2 crystallographic database. The lattice parameters were determined in the Rigaku SmartLab Studio II software package by the direct derivation method [32]. Crystallite size was determined by the WPPF method [33]. Temperature programmed reduction (TPR) was performed on a Chemosorb (Russia). Samples in the form of tablets (0.03 g) were placed in quartz crucibles and heated to $T = 110$ °C at a rate of 10 °/min in an inert argon atmosphere until there was no change in sample mass. The sample was heated to $T = 950$ °C in an Ar–H_2 atmosphere (10 % vol. H_2) at a rate of 10 °/min.

The elemental analysis of the samples was determined by energy-dispersive spectroscopy (EDS) on a FEI Quanta 200 scanning electron microscope (USA) with an X-ray Si(Li) microanalyzer. The morphology of the samples was also determined with this microscope. A transmission electron microscope (TEM) JEM 2100-F Jeol (USA) was additionally used for samples with nano-sized particles. The overage particle size of the basis of 100 particles for each sample was calculated using the ImageJ program [34].

3. Results and discussion

3.1. Products of hydrothermal treatment

Phyllogermanates, as 1:1 analogues of phyllosilicates, had a similar layered structure. They were characterized by partial displacement of the layers with an increase in their number in the lattice. To determine the phase composition and the lattice parameters, one-, two- and three-layer unit cells were constructed based on the three-layer unit cell from [19], with the second layer shifted by $-b/3$. The proposed model was a kind of averaging and reflected the general tendency for the adjacent layers to shift. Based on the processing results, the number of layers in the unit cell could be determined for each sample, as well as the lattice parameters and crystallite size. The phase composition of phyllogermanate samples after hydrothermal treatment in the temperature range of 100 – 200 °C in different hydrothermal media is shown in Fig. 1. Both temperature and hydrothermal media affected the formation of phyllogermanates.

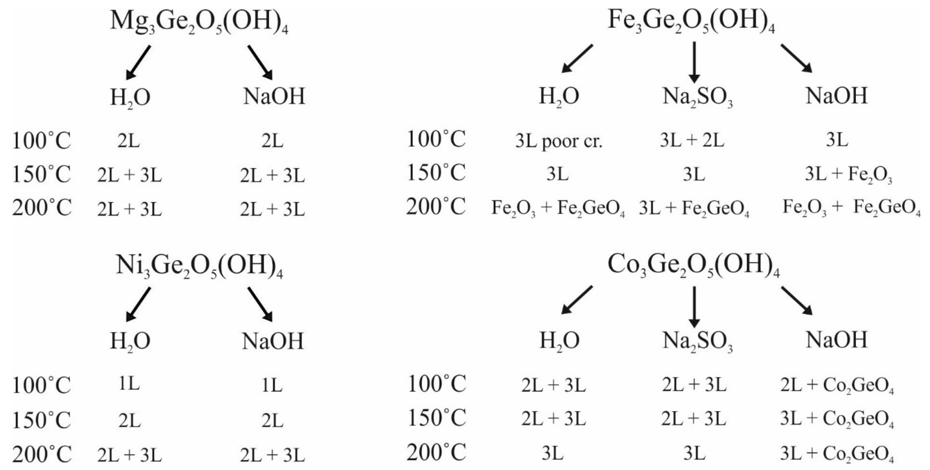

FIG. 1. Phase composition of samples obtained in different hydrothermal media in the 100 – 200 °C temperature range (L – layer, poor cr. – poor crystalline)

3.1.1. Mg-phyllogermanate. Crystal structure of Mg-phyllogermanate formed at $T = 100$ °C was described by a two-layer unit cell. The NaOH-HTM sample (Fig. A1, Appendix) possessed higher crystallinity in comparison to the H_2O-HTM sample (Fig. A2, Appendix). Temperature increased up to 150 °C yielded formation of phase described by three-layer unit cell. More active formation of that phase occurred in the H_2O-HTM sample, and it dominated at $T = 200$ °C. Phase described by two-layer unit cell predominated in the NaOH-HTM sample in the whole temperature range. Lattice parameters did not change significantly (Fig. A3, Appendix), and the reduced unit cell volume (the cell volume divided by the number of layers) did not change either with temperature or with hydrothermal medium change (Fig. 2e). Phyllogermanate phase formation occurred already at 100 °C, and then only the number of layers increased with increasing temperature, while the layer structure itself remained mostly unchanged. TEM and SEM micrographs are shown in Fig. 3. All the particles had platy morphology. The particle shape approached hexagonal, and the plates average size increased with increase in temperature. The particle size was 9 ± 4 nm in the H_2O-HTM sample and 25 ± 6 nm in the NaOH-HTM sample at $T = 100$ °C. Temperature increase up to 150 °C yielded increase in particle sizes to 23 ± 7 and 73 ± 30 nm, respectively, and they grew up to 1.7 ± 0.3 μm (H_2O-HTM) and 1 ± 0.2 μm (NaOH-HTM) at $T = 200$ °.

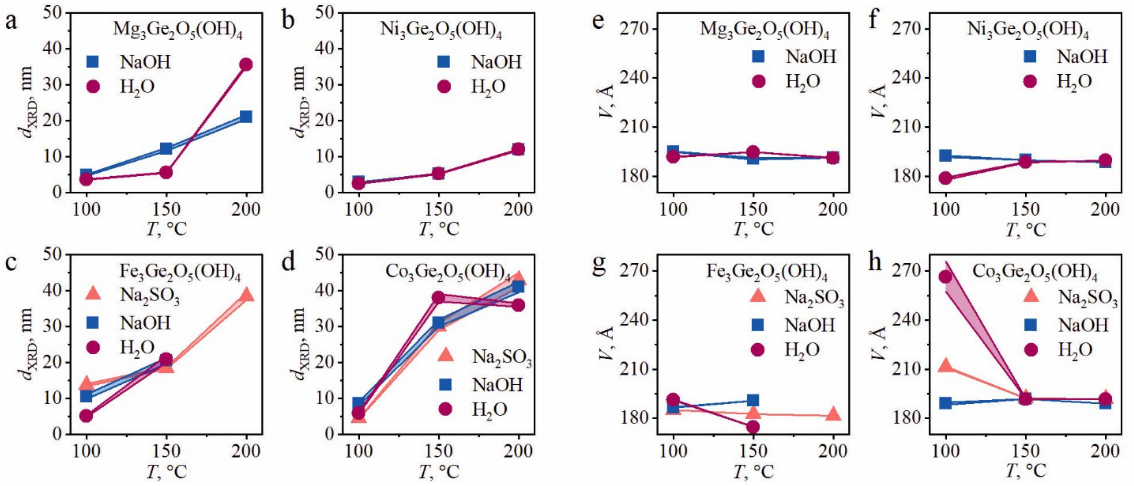

FIG. 2. Crystallite size of samples for all hydrothermal media in the temperature range 100 – 200 °C for: a) $Mg_3Ge_2O_5(OH)_4$; b) $Ni_3Ge_2O_5(OH)_4$; c) $Fe_3Ge_2O_5(OH)_4$; c) $Co_3Ge_2O_5(OH)_4$ and unit cell volume reduced to one layer for all hydrothermal media in the temperature range 100 – 200 °C for: e) $Mg_3Ge_2O_5(OH)_4$; f) $Ni_3Ge_2O_5(OH)_4$; g) $Fe_3Ge_2O_5(OH)_4$; h) $Co_3Ge_2O_5(OH)_4$

Unusual size dependence could be related with concurrent effect of pH and temperature on the particles aggregation and components solubility. It is believed that particles growth occurs via two main mechanisms: dissolution/precipitation (Ostwald ripening) and oriented attachment [35]. The first mechanism involves the gradual growth of large particles due to the dissolution of small ones. In this point of view, increase in components solubility by rising the pH value would promote particles growth, that was observed in practice. Breakage of this trend at high temperature occurred, apparently, because of dramatic increase in both GeO_2 [36] and $Mg(OH)_2$ solubility, so even the large phyllogermanate particles

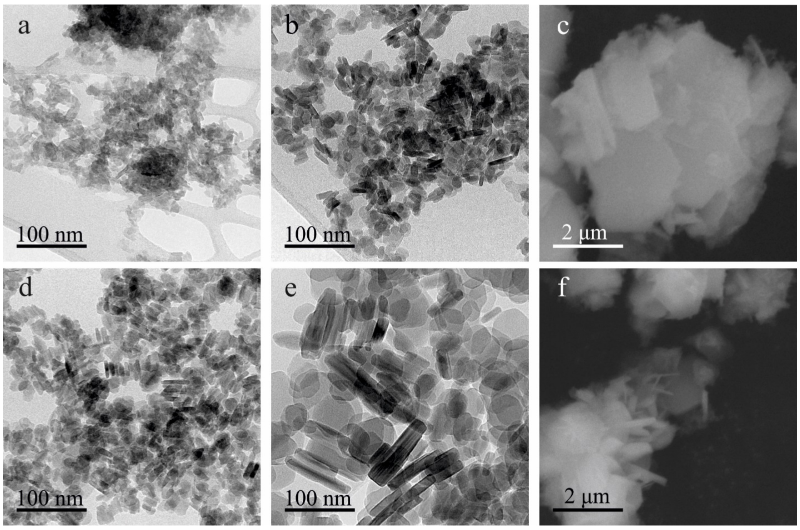

FIG. 3. TEM and SEM micrographs of $Mg_3Ge_2O_5(OH)_4$ in H_2O hydrothermal medium at a) 100 °C (TEM); b) 150 °C (TEM); c) 200 °C (SEM) and in NaOH hydrothermal medium at d) 100 °C (TEM); e) 150 °C (TEM); f) 200 °C (SEM).

began to dissolve. Therefore, a lot of nuclei appeared in bulk of HTM during the cooling step of the high-pressure vessel, resulting in decrease of average particle size. This was indirectly confirmed by the EDS data shown in Table 1. A given Mg/Ge = 1.5 ratio was maintained in the H_2O-HTM sample, while the ratio increased to 1.65 due to partial dissolution of GeO_2 in the NaOH-HTM sample.

On the other hand, the particle size and crystallinity may sharply increase because of oriented attachment. Availability of related surfaces of adjacent particles is key condition for the attachment. Platy particle morphology facilitates this process along *00l* direction thus yielding thick plates and multi-layer polytypes. However, high pH value could inhibit the oriented attachment via increase in ζ-potential (by absolute value) and suspension stability. For example, high concentration of alkali (pH = 13) caused decrease in $Mg(OH)_2$ ζ-potential down to –25 mV [37], that might be the case of the NaOH-HTM sample. As a result, the particles repelled each other and their possibility for the attachment decreased. The crystallite size shown in Fig. 2a gradually increased from 5 to 20 nm for the NaOH-HTM sample. In the H_2O-HTM sample, a sharp jump in the crystallite size was observed at $T = 200$ °C (40 nm). This was apparently due to the active formation of phase described by three-layer unit cells and the emergence of preferential directions of oriented attachment. For phases described by two-layer unit cells, the most intense diffraction maxima corresponded to the *00l* and *h00* directions, which were associated with crystallite growth both along and perpendicular to the layers. Texturing also contributed to the increase in diffraction maxima with 00*l* indices. The appearance of the third layer was characterized by an increase in intensity along the *113* direction, which was also almost perpendicular to the layers in the unit cell.

3.1.2. Ni-phyllogermanate. Ni-phyllogermanate showed similar trends to Mg-phyllogermanate (Fig. 1). However, Ni-phyllogermanate was characterized by the formation of phase described by one-layer unit cell at $T = 100$ °C. Phase described by two-layer unit cell was formed at $T = 150$ °C, and a slight presence of phase described by tree-layer unit cell was observed (Fig. A4 and Fig. A5, Appendix). It was possible that Ni-phyllogermanate required higher temperatures to form phases with multi-layer unit cells, as indicated by the tendency for the number of layers to increase with increase in temperature, but no dependence on the HTM type was observed. Unit cell volume (Fig. 2f) was significantly different for the two hydrothermal media only at $T = 100$ °C. The rest of the lattice parameters were also HTM-independent in the 150 – 200 °C range (Fig. A6, Appendix). The crystallite size in both media gradually increased from 4 to 12 nm with increase in hydrothermal treatment temperature (Fig. 2b). The particles themselves also had the shape of plates. The particles of the NaOH-HTM sample were smaller than 7 nm at $T = 100$ °C (Fig. A7a, Appendix). A significant difference in particle size was observed depending on the HTM type at high temperature. While the average particle size of the H_2O-HTM reached 2 μm and more at $T = 200$ °C (Fig. A7b, Appendix), for individual particles of the NaOH-HTM sample were almost indistinguishable in the SEM. In addition to the reasons discussed for the Mg-phyllogermanate case (including high ζ-potential value of NiO and $Ni(OH)_2$ [38, 39]), greater sensitivity of Ni-containing systems to pH value should be noted for the case of Mg- and Ni-phyllosilicate nanoscrolls formation [40, 41]. Comparing these observations with our previously published paper [15], in which Ni-phyllogermanate particle sizes reached 0.5 μm independently on pH, we are once again convinced of the importance of the role of chemical prehistory in the formation and growth of crystals. Thus, the usage of crystalline compounds mechanical mixtures ($Ni(OH)_2$ and GeO_2 [15]) demanded for comparatively high temperatures (240 °C) to start recrystallization, and particle sizes were predetermined by the less soluble compound.

TABLE 1. Elemental composition of phyllogermanates for all hydrothermal media in the 100 – 200 °C temperature range

$\mathbf{Mg_3Ge_2O_5(OH)_4}$					
HTM	T, °C	Element content, at.%			Mg/Ge
		Mg	Ge	O	
H_2O	100	22.79±0.21	15.36±0.15	61.86±0.16	1.48±0.03
	150	24.31±0.21	15.50±0.14	60.19±0.33	1.57±0.03
	200	24.41±0.19	16.52±0.31	59.07±0.47	1.48±0.04
NaOH	100	24.54±0.18	14.84±0.15	60.62±0.29	1.65±0.03
	150	25.06±0.16	15.23±0.23	59.71±0.34	1.65±0.04
	200	25.36±0.23	15.42±0.11	59.26±0.30	1.64±0.03

$\mathbf{Ni_3Ge_2O_5(OH)_4}$					
HTM	T, °C	Element content, at.%			Ni/Ge
		Ni	Ge	O	
H_2O	100	22.20±0.45	15.45±0.04	62.36±0.43	1.44±0.03
	150	26.76±0.61	18.40±0.31	54.84±0.33	1.45±0.06
	200	29.16±0.35	19.46±0.45	51.38±0.67	1.50±0.05
NaOH	100	27.48±0.70	17.30±0.07	55.21±0.73	1.59±0.05
	150	24.87±0.96	19.13±0.05	56.00±0.95	1.30±0.05
	200	27.08±0.83	19.46±0.11	53.46±0.77	1.39±0.05

$\mathbf{Co_3Si_2O_5(OH)_4}$					
HTM	T, °C	Element content, at.%			Co/Ge
		Co	Ge	O	
H_2O	100	26.26±0.76	18.31±0.18	55.43±0.79	1.43±0.06
	150	23.73±0.87	18.38±0.12	57.89±0.76	1.29±0.06
	200	26.29±0.70	18.14±0.21	55.57±0.59	1.45±0.06
NaOH	100	23.51±6.36	15.90±1.46	60.59±7.18	1.48±0.54
	150	24.41±0.90	16.68±0.10	58.91±0.84	1.46±0.06
	200	34.39±8.38	14.65±1.11	50.96±7.34	2.35±0.75
Na_2SO_3	100	22.75±0.69	15.09±0.08	62.16±0.75	1.51±0.05
	150	26.32±0.99	17.95±0.18	55.73±0.95	1.47±0.07
	200	27.05±0.94	17.37±0.39	55.58±1.12	1.56±0.09

$\mathbf{Fe_3Si_2O_5(OH)_4}$					
HTM	T, °C	Element content, at.%			Fe/Ge
		Fe	Ge	O	
H_2O	100	22.22±0.47	14.82±0.09	62.97±0.41	1.50±0.04
	150	22.41±0.44	15.47±0.14	62.12±0.35	1.45±0.04
	200	45.65±5.66	11.99±1.43	42.36±4.25	3.81±0.93
NaOH	100	26.10±1.28	16.55±0.72	57.35±1.02	1.58±0.15
	150	27.45±1.37	16.33±0.34	56.22±1.22	1.68±0.12
	200	50.16±4.24	10.26±1.27	39.57±3.18	4.89±1.02
Na_2SO_3	100	22.86±0.73	15.41±0.09	61.73±0.77	1.48±0.06
	150	20.22±0.77	15.28±0.16	64.50±0.84	1.32±0.06
	200	27.45±0.81	17.06±0.07	55.49±0.76	1.61±0.05

3.1.3. Fe-phyllogermanate. Unlike the previous phyllogermanates, the main obstacle for Fe-phyllogermanate synthesis is an intensive oxidation of Fe^{2+} to Fe^{3+} during precipitation and hydrothermal treatment. Except paper [42], Fe^{2+}-phyllosilicates with chrysotile or lizardite structure were not obtained, but Fe-phyllosilicate $Fe_{3-2}Si_2O_5(OH)_4$ was obtained with the greenalite structure. The iron in this compound had oxidation states of 2+ and 3+ [43, 44]. Previously obtained $Me_3Ge_2O_5(OH)_4$ phyllogermanates contained divalent metal ions in the octahedral position, so an important task was to stabilize iron in the 2+ oxidation state.

In analogy with other phyllogermanates, Fe-phyllogermanates tended to form phase described by three-layer unit cell in water (Fig. A9, Appendix) because of oriented attachment. Addition of NaOH increased crystallinity (Fig. A8, Appendix) and inhibited the growth along *113* direction. Increase in temperature resulted in the formation of Fe_2O_3 impurity phase. Moreover, Fe-phyllogermanate dehydroxylated with formation of Fe_2GeO_4 and Fe_2O_3 in H_2O and NaOH at 200 °C (using of mother liquor as HTM allowed to obtain single-phase Fe_2GeO_4, see Fig. A11, Appendix). The formation of Fe_2O_3 and Fe_2GeO_4 led to a sharp increase in the Fe/Ge ratio (Table 1) due to the presence in the sample of well-crystallized particles of volumetric shape, from which the signal was most intense and overlapped the signal from particles of smaller size. Addition of Na_2SO_3 prevented Fe_2O_3 and inhibited Fe_2GeO_4 formation at 200 °C (Fig. 1 and Fig. A10, Appendix).

The lattice parameters of Fe-phyllogermanate varied unsystematically (Fig. A12, Appendix), but the unit cell volume did not change significantly with temperature or HTM (Fig. 2g). The crystallite size was about 5 nm for H_2O-HTM samples at $T = 100$ °C, while for Na_2SO_3-HTM and NaOH-HTM samples it was 13 and 11 nm, respectively. The crystallite size increased, reaching about 20 nm at $T = 150$ °C for all HTMs (Fig. 2c). Only Na_2SO_3-HTM retained Fe-phyllogermanate at $T = 200$ °C, the crystallite size was almost 40 nm. Fe-phyllogermanate also had a plate-like morphology, the largest particle size was also characteristic of the H_2O-HTM sample and was about 1 μm at $T = 150$ °C. The same sizes were observed for particles obtained at $T = 200$ °C in the Na_2SO_3-HTM sample. The particles had a size of about 0.5 μm and their size did not change with increasing temperature in NaOH-HTM (Fig. A13(a,b), Appendix).

It is worth noting that the morphology of Fe_2GeO_4 differed significantly depending on HTM. They were plate-like particles similar to Fe-phyllogermanate in the H_2O-HTM sample (Fig. A14a, Appendix). The particles joined into flower-like agglomerates with sizes of 5 μm and larger in the NaOH-HTM sample (Fig. A13c, Appendix), that was probably due to more active particle growth in NaOH-HTM. And in the mother liquor, isomeric particles were formed (Fig. A14b, Appendix). The homogeneity of the composition and distribution of the primary particles, the absence of additional oxidation sources could contribute to this effect.

3.1.4. Co-phyllogermanate. Phases described by two-layer unit cell were formed in all HTMs at $T = 100$ °C, phases described by three-layer unit cells began to form in H_2O-HTM (Fig. A15, Appendix) and Na_2SO_3-HTM (Fig. A16, Appendix) in analogy with previous phyllogermanates. Cobalt orthogermanate Co_2GeO_4 was formed in NaOH-HTM (Fig. A17, Appendix) at 100 °C, which was present in this HTM at all subsequent processing temperatures (Fig. 1). Increasing the temperature to 150 °C resulted in more intense formation of phases described by three-layer unit cells, whereas phases described by two-layer unit cells were practically absent. At $T = 200$ °C only phases described by three-layer unit cells were observed. Growth was observed in the preferred directions *00l*, *h00*, and *113* in all samples with three-layer unit cells, similar to Fe-phyllogermanate, but the texturing effect in these directions was stronger. The lattice parameters remained virtually unchanged at $T = 150$ °C and above, while they changed unsystematically at $T = 100$ °C (Fig. A18, Appendix) comparing different HTMs. The unit cell volume decreased in Na_2SO_3-HTM, while a strong volume decrease occurred in H_2O-HTM (Fig. 2h). While NaOH-HTM promoted the formation of Co-phyllogermanate, the particles in the other two HTMs could be weakly crystallized, resulting in a larger unit cell volume.

Crystallite size increased from an average of 5 nm at $T = 100$ °C to 30 – 40 nm at $T = 150$ °C. Subsequent increased in temperature caused the crystallite size of NaOH-HTM and Na_2SO_3-HTM samples to increase to 45 nm, while the crystallite size in the H_2O-HTM sample remained virtually unchanged (Fig. 2d). The particles were hexagonal plates [19] and had sizes much smaller than the phyllogermanates considered above. The sample contained thin plates of 36 ± 8 nm in size at $T = 100$ °C in the H_2O-HTM sample (Fig. A7c, Appendix). The Co/Ge ratio was kept within the error limits in all samples, except for the Co-phyllogermanate obtained in NaOH-HTM at 200 °C due to the presence of Co2GeO4 in significant amounts, as well as in the sample obtained in H_2O-HTM at 150 °C due to probably strong texturing.

Thus, hydrothermal treatment promoted the formation of phyllogermanates and each series contained single-phase samples, which allowed us to establish the optimal phyllogermanates synthesis parameters. Increase in temperature yielded increase in the number of layers in the unit cell. Neutral pH (H_2O-HTM) enhanced particles attachment with formation of bigger plates. Na_2SO_3-HTM minimized undesirable oxidation of Co^{2+} and Fe^{2+} in hydrothermal conditions.

3.2. Products of heat treatment in Ar–H_2 atmosphere

The reduction of phyllogermanates was carried out in an Ar–H_2 atmosphere to obtain intermetallic compounds or metallic germanium in the case of Mg-phyllogermanate. Single phase samples were selected for the reduction (Fig. 4). The TPR curves are shown in Fig. 5. The reduction took place in one or two stages, depending on the sample. It is worth noting that the shape of the TPR profiles also depended on the H_2O released during the process [45].

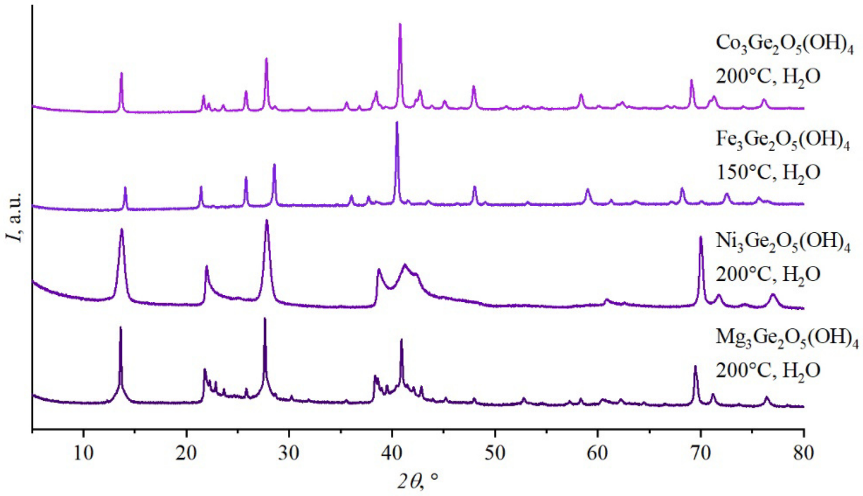

FIG. 4. PXRD patterns of single-phase samples of phyllogermanates obtained in H_2O hydrothermal medium at 150 – 200 °C

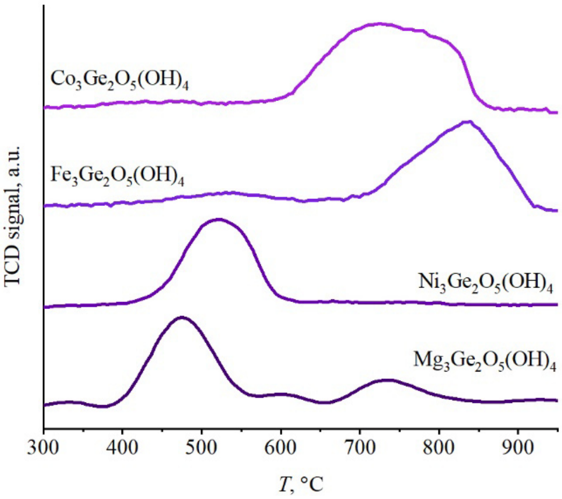

FIG. 5. TPR curves of single-phase samples of phyllogermanates obtained in H_2O hydrothermal medium at 150 – 200 °C

The reduction began at about 400 °C with $T_{\max} = 480$ °C for Mg-phyllogermanate. The second reduction stage started at 665 °C with $T_{\max} = 730$ °C. This was in agreement with literature data on the reduction of GeO_2: hydroxylated GeO_2 had higher reduction temperatures compared to other germanium oxides [46]. Structurally bound water could also affect the reduction process of germanium in the case of Mg-phyllogermanate. Presence of three phases was observed in the sample after the reduction: metallic germanium, orthorhombic Mg_2GeO_4 and cubic Mg_2GeO_4 (Fig. 6). It is possible that the reduction of germanium from phyllogermanate occurred in parallel with the formation of cubic Mg_2GeO_4 and continued until the stoichiometric ratio Mg/Ge = 2 was reached. The increase in temperature contributed to its stabilization and prevented further reduction of germanium from the system. Traditionally, Mg_2GeO_4 is obtained by the solid phase synthesis method [47], therefore the temperatures of its preparation from the corresponding phyllogermanate could be significantly lower. The presence of cubic Mg_2GeO_4 could be associated with an incomplete transition from the cubic to the orthorhombic phase. The second stage of Mg phyllogermanate reduction was weakly intense and could be associated with the phase transition from cubic to orthorhombic Mg_2GeO_4 [48].

The reduction occurred in a single step for Ni-phyllogermanate (Fig. 5), and it was accompanied by the formation of $Ni_{19}Ge_{12}$ intermetallic compound (Fig. 6). It existed in a rather narrow region of the phase diagram. The Ni/Ge ratio in the initial phyllogermanate was 1.5, which was close to the Ni/Ge ratio in the resulting intermetallic compound, and the reduction temperature corresponded exactly to the formation temperature of $Ni_{19}Ge_{12}$ in the phase diagram [49]. The reduction start temperature of Ni-phyllogermanate was 435 °C with a maximum at 520 °C. It was higher than that of Mg-phyllogermanate due to the presence of nickel in the system and the simultaneous reduction of germanium and nickel.

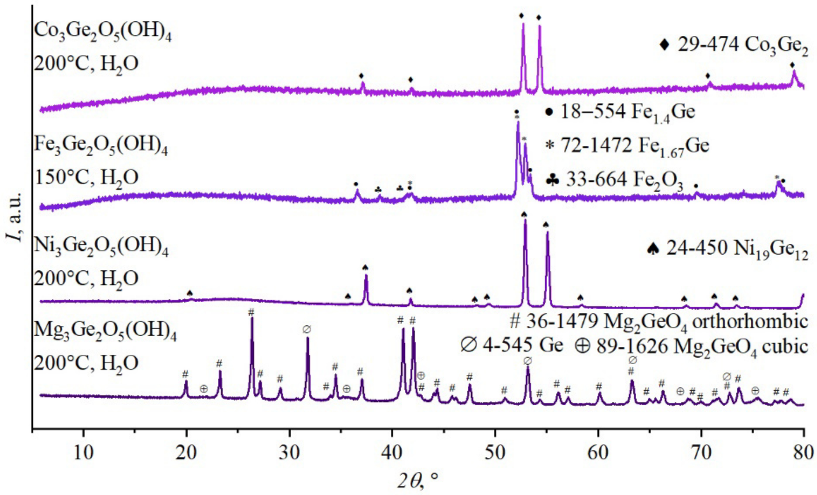

FIG. 6. PXRD patterns of phyllogermanate reduction products in Ar–H$_2$ (5 % vol. H$_2$)

The reduction start temperature of Fe-phyllogermanate was 705 °C with $T_{\max} = 845$ °C. This sample had the highest reduction temperature. Structurally bound water greatly slowed down the process of iron reduction [45]. The initial ratio Fe/Ge = 1.5 corresponded to the region of two solid solutions [50], possibly due to this, the formation of two alloys with approximate ratios of $Fe_{1.4}Ge$ and $Fe_{1.67}Ge$ was observed by PXRD (Fig. 6). In addition, a small amount of Fe_2O_3 was present in the sample. This oxide could have formed in air after the reduction process due to the oxidation of metallic iron, which was a reduction product.

The reduction from Co-phyllogermanate occurred in one step (or several steps, indistinguishable due to peaks overlap) with the formation of the intermetallic compound Co_3Ge_2 (Fig. 6), which was a high-temperature phase [51]. The reduction start temperature was 600 °C with a $T_{\max} = 750$ °C, which was higher than the reduction start temperature of a similar phyllosilicate [8]. Apparently, the reduction start temperature increased due to the simultaneous reduction of the transition element and Ge, which led to the destruction of the structure and the formation of the intermetallic compound.

The formation of intermetallic compounds was observed in all samples containing transition elements. Mg-phyllogermanate contained germanium and magnesium orthogermanate. It was possible to obtain intermetallic compounds with a given germanium/transition element ratio by varying the initial *Me*/Ge ratio.

4. Conclusion

Here, we have demonstrated unified approach to Mg-, Ni-, Fe- and Co-phyllogermanates synthesis by soft chemistry methods. Additional precautions to prevent oxidation were required to obtain Co- and Fe-phyllogermanates, so the synthesis was performed in an inert Ar atmosphere using oxygen-free water.

Phyllogermanates tended to form unit cells, the number of layers in which depended on the temperature conditions of the hydrothermal treatment. Ni-phyllogermanate required the highest temperatures to initiate the formation of phases described by three-layer unit cell, while Fe-phyllogermanate required the lowest. The samples were particles with three-layer cells already at 100 °C. Orthogermanates were also formed in Fe- and Co-phyllogermanates under elevated temperature conditions, besides temperature of their formation was much lower than that in the solid phase synthesis method. Therefore, hydrothermal synthesis could be successfully used to obtain not only phyllogermanates, but also orthogermanates.

Temperature-programmed reduction made it possible to estimate the reduction start temperature of germanium in Mg-phyllogermanate and germanium intermetallic compounds in other samples. This method of obtaining intermetallic compounds is quite simple, and the possibility of varying the composition of the initial phyllogermanates to obtain a series of intermetallic compounds with a given ratio makes them promising objects for further research.

Appendix

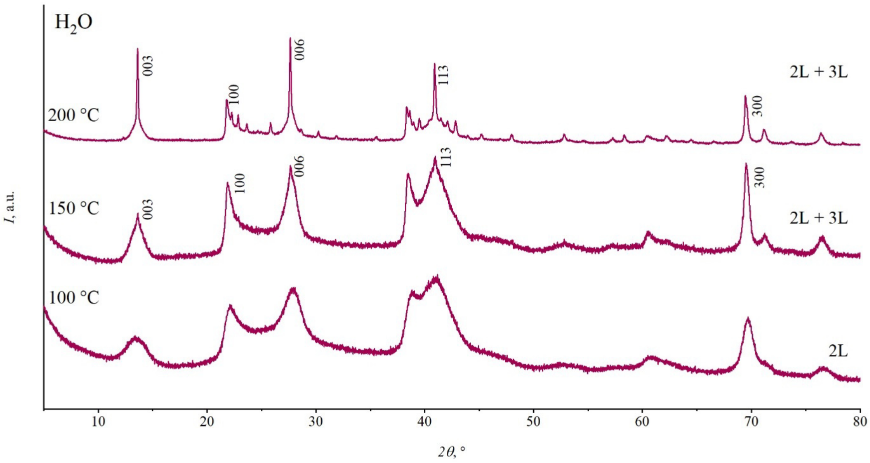

FIG. A1. PXRD patterns of $Mg_3Ge_2O_5(OH)_4$ in H_2O hydrothermal medium at three different temperatures

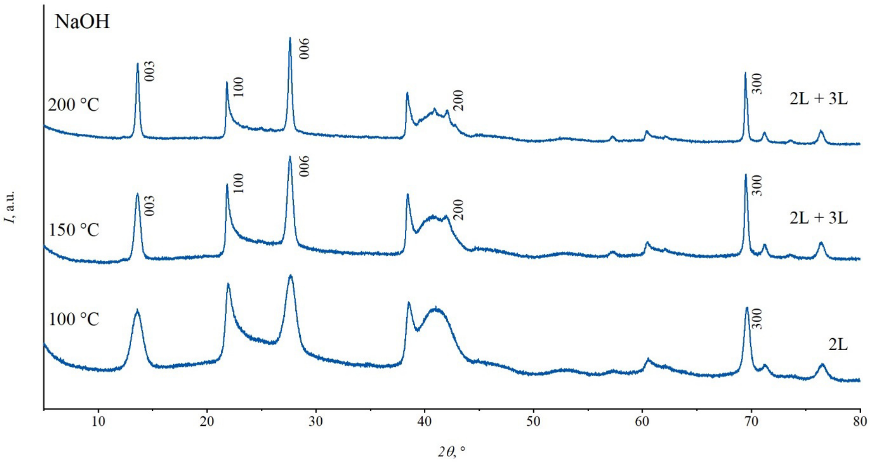

FIG. A2. PXRD patterns of $Mg_3Ge_2O_5(OH)_4$ in NaOH hydrothermal medium at three different temperatures

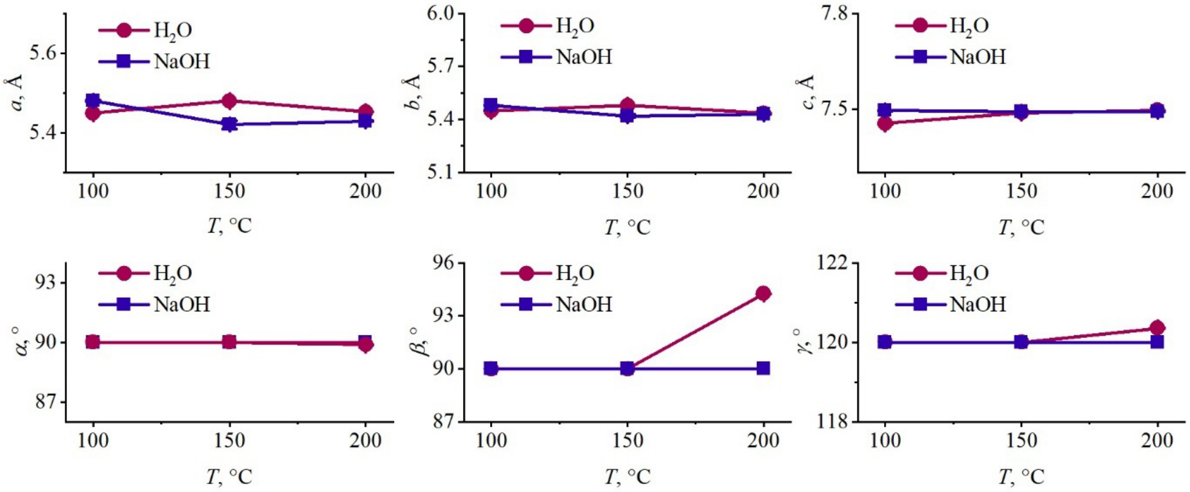

FIG. A3. Lattice parameters of $Mg_3Ge_2O_5(OH)_4$ in H_2O and NaOH hydrothermal media at three different temperatures

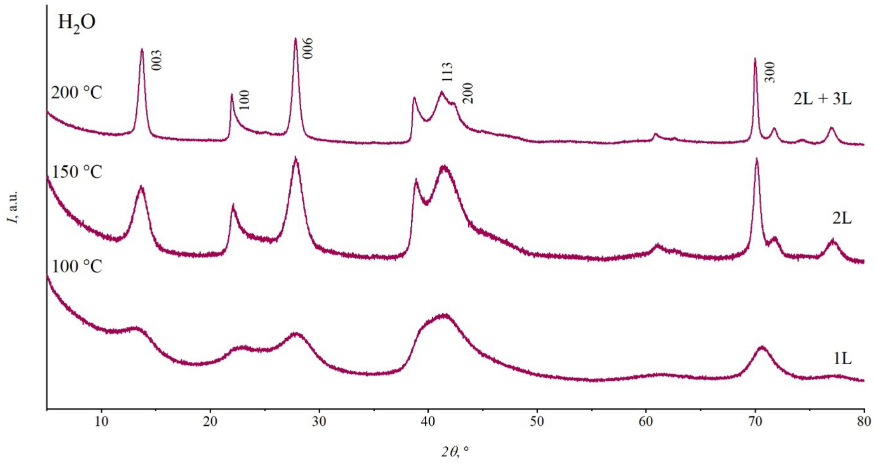

FIG. A4. PXRD patterns of $Ni_3Ge_2O_5(OH)_4$ in H_2O hydrothermal medium at three different temperatures

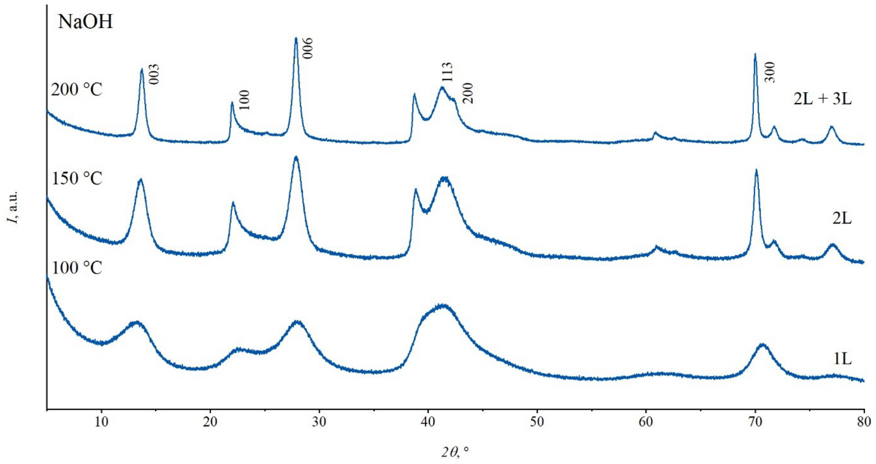

FIG. A5. PXRD patterns of $Ni_3Ge_2O_5(OH)_4$ in NaOH hydrothermal medium at three different temperatures

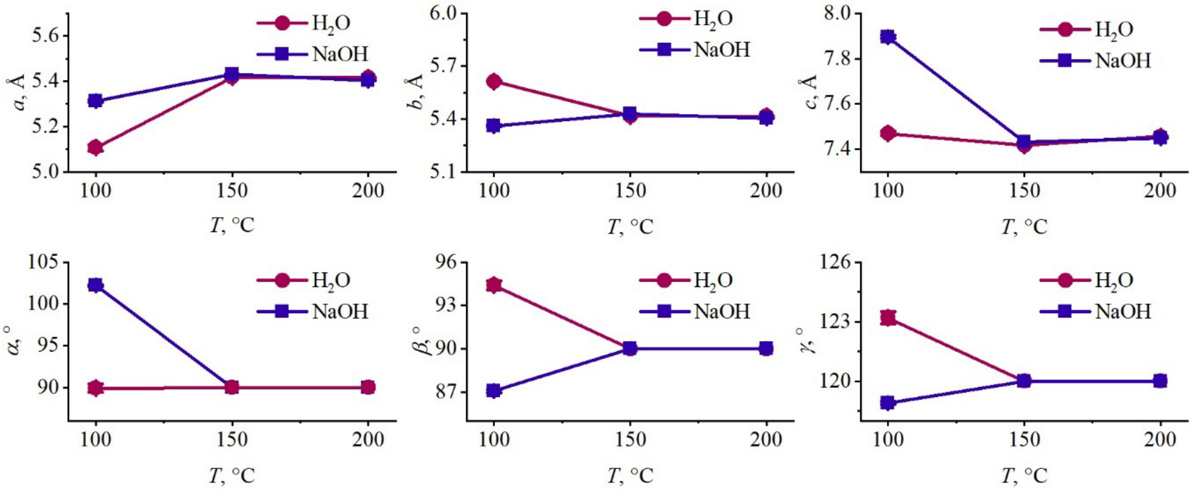

FIG. A6. Lattice parameters of $Ni_3Ge_2O_5(OH)_4$ in H_2O and NaOH hydrothermal media at three different temperatures

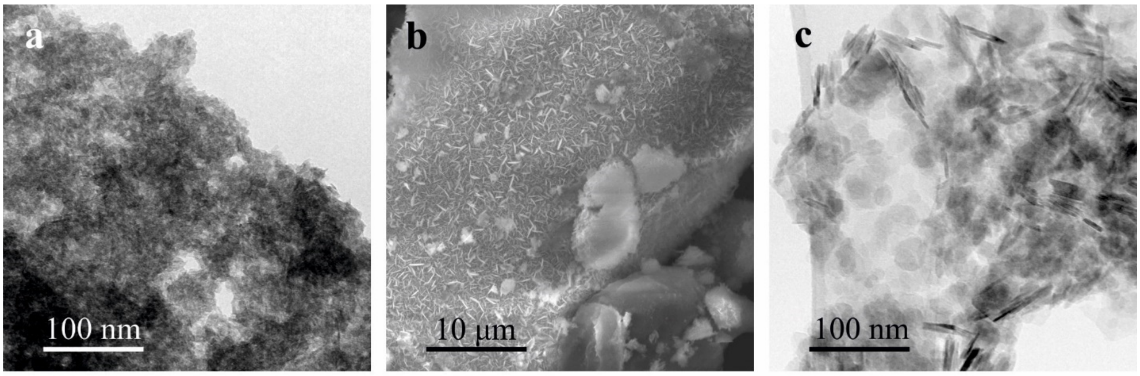

FIG. A7. a) TEM micrograph of $Ni_3Ge_2O_5(OH)_4$ at 100 °C in NaOH hydrothermal medium; b) SEM micrograph of $Ni_3Ge_2O_5(OH)_4$ at 200 °C in H_2O hydrothermal medium; and c) TEM micrographs of $Co_3Ge_2O_5(OH)_4$ at 100 °C in H_2O hydrothermal medium

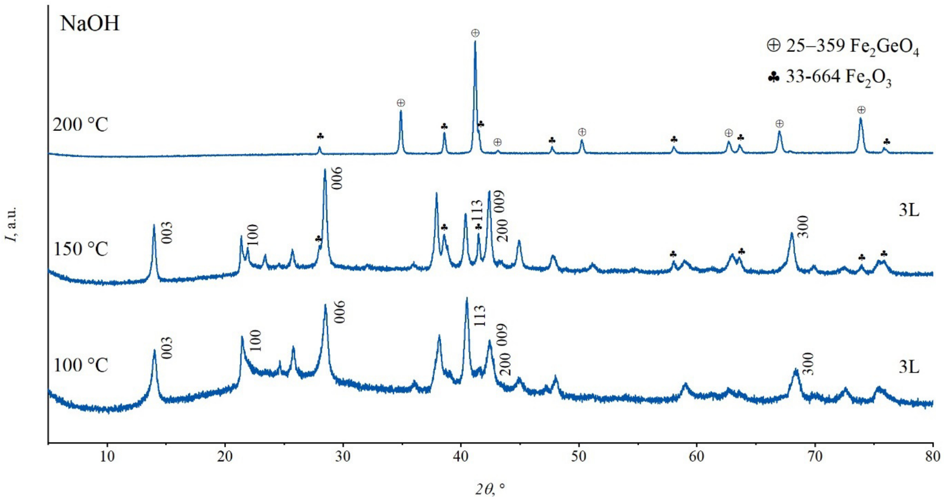

FIG. A8. PXRD patterns of $Fe_3Ge_2O_5(OH)_4$ in NaOH hydrothermal medium at three different temperatures

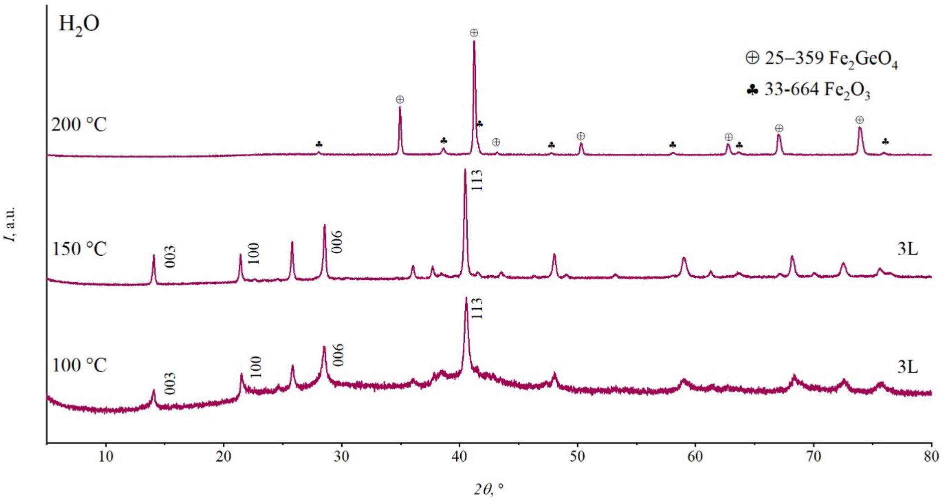

FIG. A9. PXRD patterns of $Fe_3Ge_2O_5(OH)_4$ in H_2O hydrothermal medium at three different temperatures

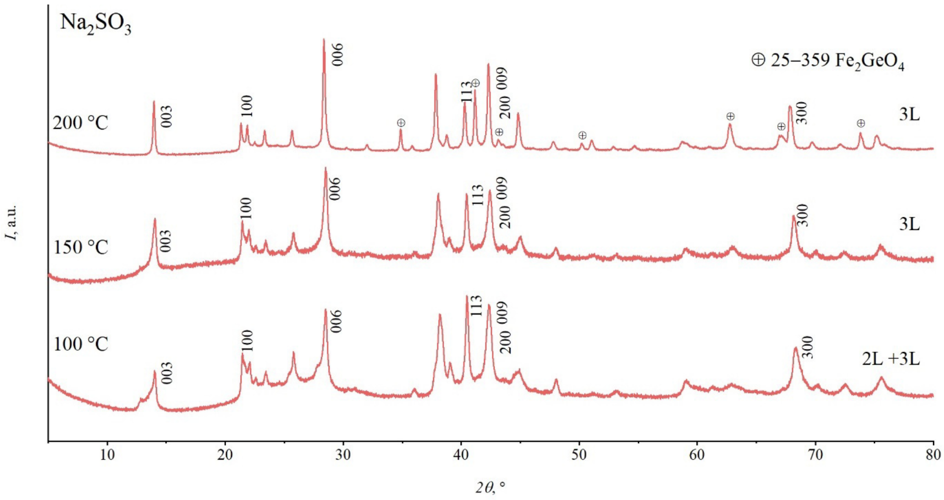

FIG. A10. PXRD patterns of $Fe_3Ge_2O_5(OH)_4$ in Na_2SO_3 hydrothermal medium at three different temperatures

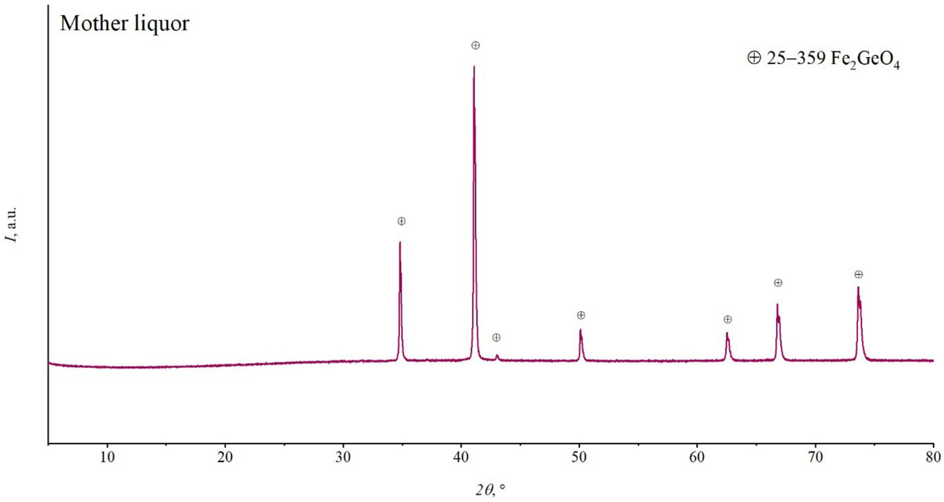

FIG. A11. PXRD pattern of $Fe_3Ge_2O_5(OH)_4$ treated in mother liquor at 200 °C

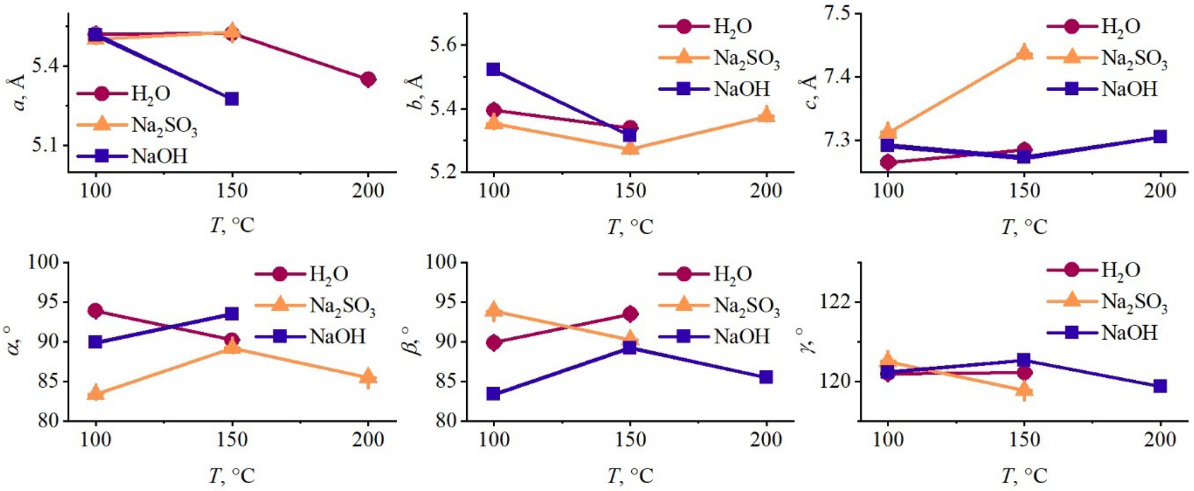

FIG. A12. Lattice parameters of $Fe_3Ge_2O_5(OH)_4$ in H_2O, NaOH and Na_2SO_3 hydrothermal media at three different temperatures

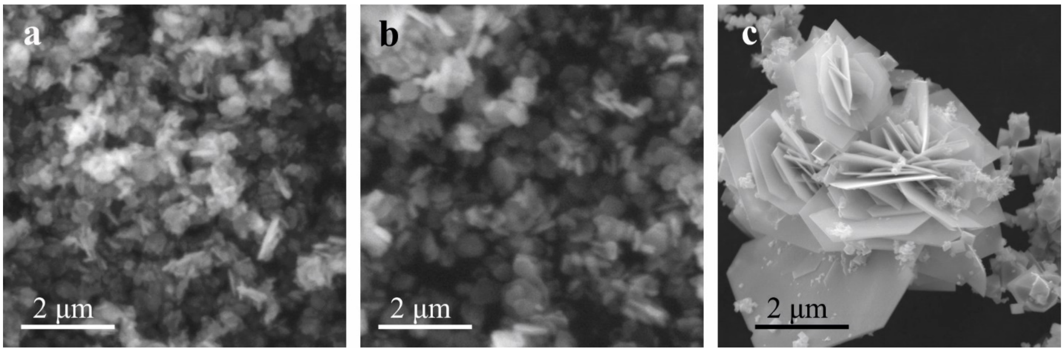

FIG. A13. SEM micrographs of $Fe_3Ge_2O_5(OH)_4$ in NaOH hydrothermal medium: a) at 100 °C; b) at 150 °C; c) at 200 °C

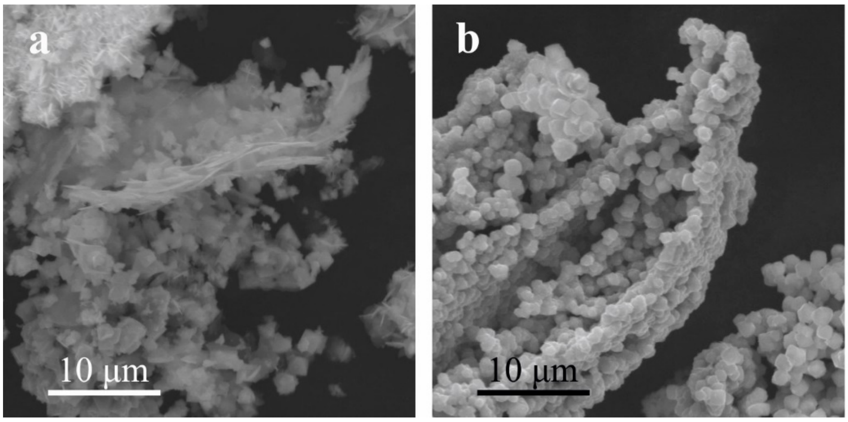

FIG. A14. SEM micrographs of $Fe_3Ge_2O_5(OH)_4$ at 200 °C a) in H_2O hydrothermal medium; b) in mother liquor

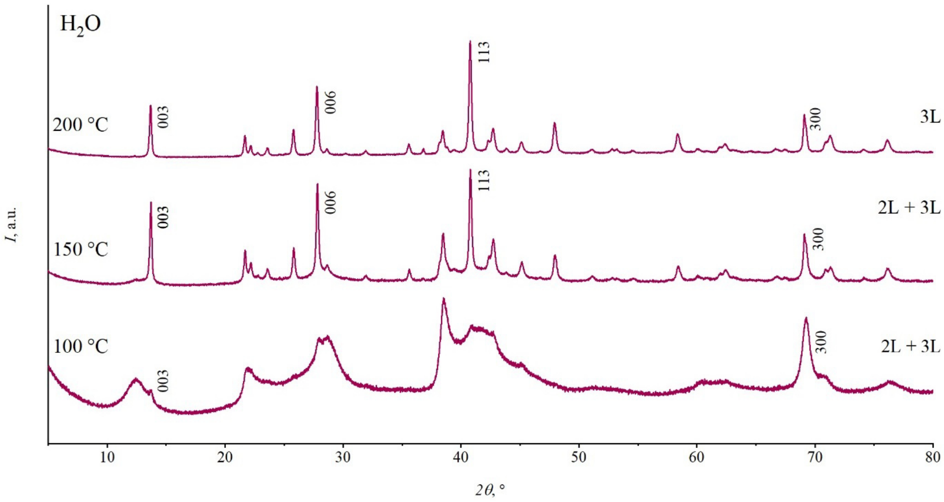

FIG. A15. PXRD patterns of $Co_3Ge_2O_5(OH)_4$ in H_2O hydrothermal medium at three different temperatures

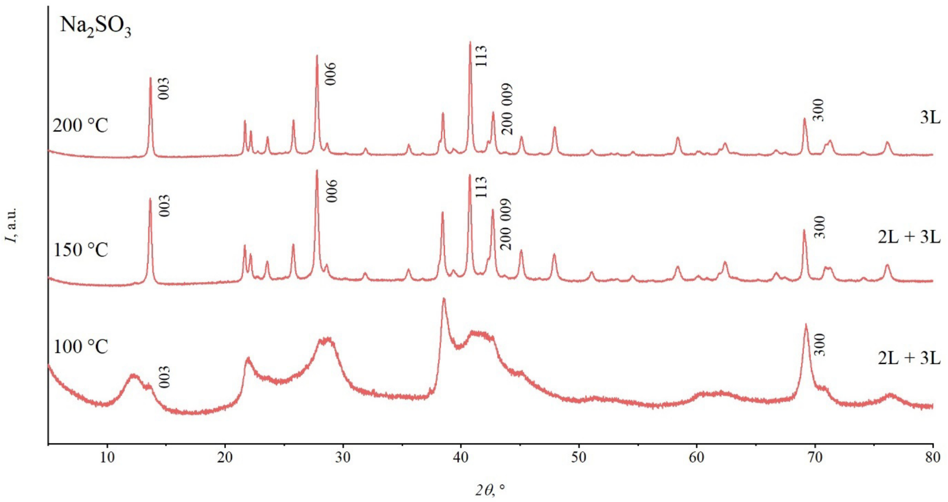

FIG. A16. PXRD patterns of $Co_3Ge_2O_5(OH)_4$ in Na_2SO_3 hydrothermal medium at three different temperatures

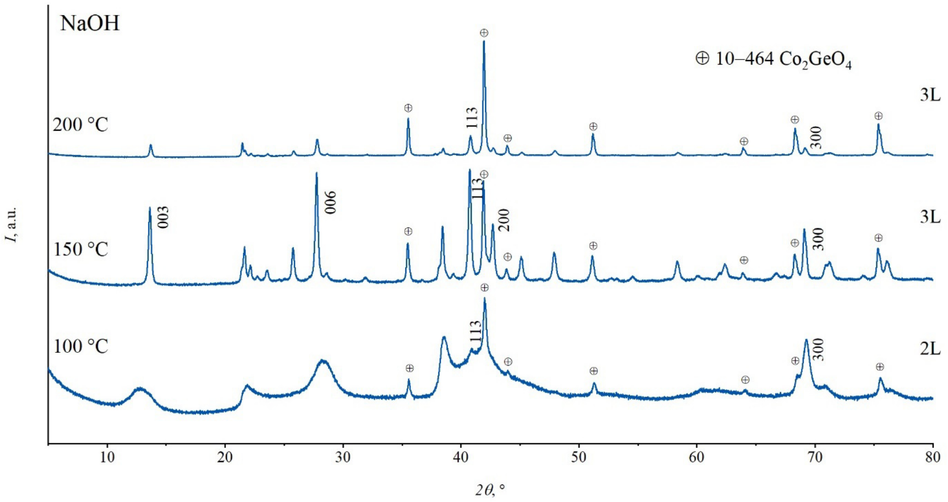

FIG. A17. PXRD patterns of $Co_3Ge_2O_5(OH)_4$ in NaOH hydrothermal medium at three different temperatures

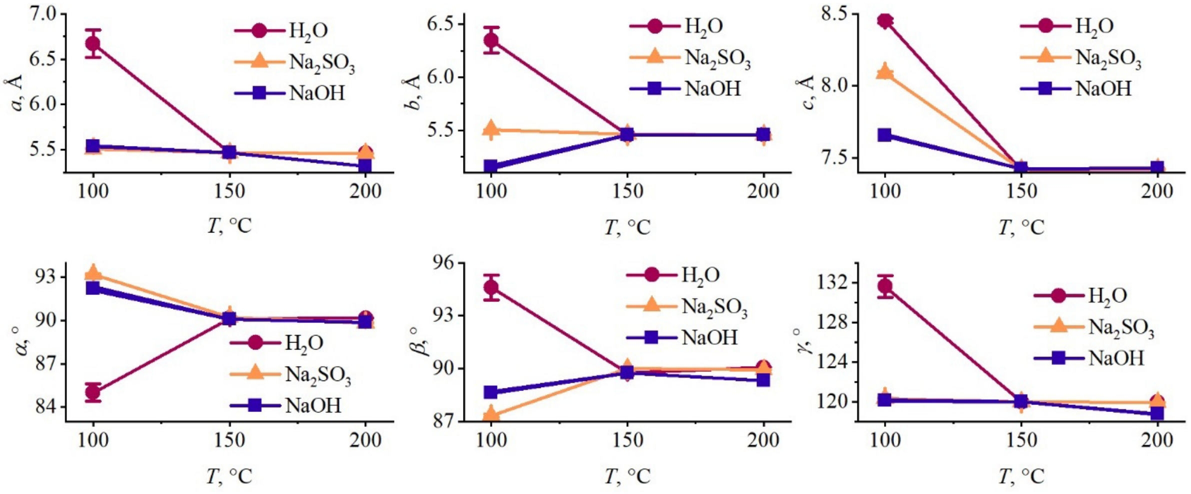

FIG. A18. Lattice parameters of $Co_3Ge_2O_5(OH)_4$ in H_2O, NaOH and Na_2SO_3 hydrothermal media at three different temperatures

References

[1] Roveri N., Falini G., Foresti E., Fracasso G., Lesci I.G., Sabatino P. Geoinspired synthetic chrysotile nanotubes. *J. of materials research*, 2006, **21** (11), P. 2711–2725.

[2] Korytkova E.N., Maslov A.V., Pivovarova L.N., Drozdova I.A., Gusarov V.V. Formation of $Mg_3Si_2O_5(OH)_4$ nanotubes under hydrothermal conditions. *Glass Physics and Chemistry*, 2004, **30**, P. 51–55.

[3] Mellini M. The crystal structure of lizardite 1 T: hydrogen bonds and polytypism. *American Mineralogist*, 1982, **67** (5–6), P. 587–598.

[4] Alvarez-Ramírez F., Toledo-Antonio J.A., Angeles-Chavez C., Guerrero-Abreo J.H., López-Salinas E. Complete structural characterization of Ni3$Si_2O_5(OH)_4$ nanotubes: theoretical and experimental comparison. *The J. of Physical Chemistry C*, 2011, **115** (23), P. 11442–11446.

[5] Krasilin A.A., Semenova A.S., Kellerman D.G., Nevedomsky V.N., Gusarov V.V. Magnetic properties of synthetic $Ni_3Si_2O_5(OH)_4$ nanotubes. *Europhysics Letters*, 2016, **113** (4), 47006.

[6] Korytkova E.N., Maslov A.V., Pivovarova L.N., Polegotchenkova Y.V., Povinich V.F., Gusarov V.V. Synthesis of nanotubular $Mg_3Si_2O_5(OH)_4$–$Ni_3Si_2O_5(OH)_4$ silicates at elevated temperatures and pressures. *Inorganic materials*, 2005, **41**, P. 743–749.

[7] Korytkova E.N., Pivovarova L.N. Hydrothermal synthesis of nanotubes based on (Mg, Fe, Co, Ni)$_3Si_2O_5(OH)_4$ hydrosilicates. *Glass Physics and Chemistry*, 2010, **36**, P. 53–60.

[8] Khrapova E.K., Ivanova A.A., Kirilenko D.A., Levin A.A., Bert N.A., Ugolkov V.L., Krasilin A.A. Phase transformations of $(Co_xMg_{1-x})_3Si_2O_5(OH)_4$ phyllosilicate nanoscrolls upon heating in Ar, O_2 and H_2 containing atmospheres. *Applied Clay Science*, 2024, **250**, 107282.

[9] Khrapova E.K., Kozlov D.A., Krasilin A.A. Hydrothermal Synthesis of Hydrosilicate Nanoscrolls $(Mg_{1-x}Co_x)_3Si_2O_5(OH)_4$ in a Na_2SO_3 Solution. *Russian J. of Inorganic Chemistry*, 2022, **67** (6), P. 839–849.

[10] Korytkova E.N., Pivovarova L.N., Gusarov V.V. Influence of iron on the kinetics of formation of chrysotile nanotubes of composition (Mg, Fe)$_3Si_2O_5(OH)_4$ under hydrothermal conditions. *Geochemistry International*, 2007, **45**, P. 825–831.

[11] Krasilin A.A., Panchuk V.V., Semenov V.G., Gusarov V.V. Formation of variable-composition iron (III) hydrosilicates with the chrysotile structure. *Russian J. of General Chemistry*, 2016, **86**, P. 2581–2588.

[12] Foresti E., Hochella Jr M.F., Kornishi H., Lesci I.G., Madden A.S., Roveri N., Xu H. Morphological and Chemical/Physical Characterization of Fe-Doped Synthetic Chrysotile Nanotubes. *Advanced Functional Materials*, 2005, **15** (6), P. 1009–1016.

[13] Bloise A., Barrese E., Apollaro C. Hydrothermal alteration of Ti-doped forsterite to chrysotile and characterization of the resulting chrysotile fibers. *Neues Jahrbuch für Mineralogie*, 2009, **185** (3), P. 297–304.

[14] Roy D.M., Roy R. An experimental study of the formation and properties of synthetic serpentines and related layer silicate minerals. *American Mineralogist: J. of Earth and Planetary Materials*, 1954, **39** (11–12), P. 957–975.

[15] Krasilin A.A., Khrapova E. K. Effect of hydrothermal treatment conditions on formation of nickel hydrogermanate with platy morphology. *Russian J. of Applied Chemistry*, 2017, **90**, P. 22–27.

[16] White R.D., Bavykin D.V., Walsh F.C. Spontaneous scrolling of kaolinite nanosheets into halloysite nanotubes in an aqueous suspension in the presence of GeO_2. *The J. of Physical Chemistry C*, 2012, **116** (15), P. 8824–8833.

[17] Paineau E. Imogolite nanotubes: a flexible nanoplatform with multipurpose applications. *Applied Sciences*, 2018, **8** (10), 1921.

[18] Hall S.H., Guggenheim S., Moore P., Bailey S.W. The structure of Unst-type 6-layer serpentines. *The Canadian Mineralogist*, 1976, **14** (3), P. 314–321.

[19] Belskaya N.A., Khrapova E.K., Ivanova A.A., Eremin E.V., Pavlov S.I., Krasilin A.A. Structure refinement and magnetic properties of synthetic $Co_3Ge_2O_5(OH)_4$ phyllogermanate. *J. of Magnetism and Magnetic Materials*, 2023, **587**, 171262.

[20] Abdelkrim Y., Wu J., Jiao F.Z., Wang Z.H., Hou S.X., Zhang T.T., Qu J. Cobalt germanium hydroxides with asymmetric electron distribution and surface hydroxyl groups for superb catalytic degradation performances. *J. of Colloid and Interface Science*, 2025, **677**, P. 282–293.

[21] Xu Z., Li W., Wang X., Wang B., Shi Z., Dong C., Zou Z. Novel cobalt germanium hydroxide for electrochemical water oxidation. *ACS applied materials & interfaces*, 2018, **10** (36), P. 30357–30366.

[22] Zhang N., Yang B., He Y., He Y., Liu X., Liu M., Roy V.A. Serpentine $Ni_3Ge_2O_5(OH)_4$ nanosheets with tailored layers and size for efficient oxygen evolution reactions. *Small*, 2018, **14** (48), 1803015.

[23] Yang B., Zhang N., Chen G., Liu K., Yang J., Pan A., Qiu T. Serpentine $Co_xNi_{3-x}Ge_2O_5(OH)_4$ nanosheets with tuned electronic energy bands for highly efficient oxygen evolution reaction in alkaline and neutral electrolytes. *Applied Catalysis B: Environmental*, 2020, **260**, 118184.

[24] Wen N., Chen S., Feng J., Zhang K., Zhou Z., Li X., Zhao Y. In situ hydrothermal synthesis of double-carbon enhanced novel cobalt germanium hydroxide composites as promising anode material for sodium ion batteries. *Dalton transactions*, 2021, **50** (12), P. 4288–4299.

[25] Li H.S., Qu J., Hao S.M., Wang Z.Z., Zhang Y.J., Yu Z.Z. Enhanced lithium storage performances of novel layered nickel germanate anodes inspired by the spatial arrangement of lotus leaves. *Nanoscale*, 2018, **10** (23), P. 10963–10970.

[26] Liu F., Ye S., Guo H., Zhai M., Qian J. Assembled β-Co(OH)$_2$ Nanoparticles on Reduced Graphene Oxide for Enhanced Magnetism. *J. of Superconductivity and Novel Magnetism*, 2014, **27**, P. 787–791.

[27] Gaudet S., Detavernier C., Kellock A.J., Desjardins P., Lavoie C. Thin film reaction of transition metals with germanium. *J. of Vacuum Science & Technology A*, 2006, **24** (3), P. 474–485.

[28] Sadoh T., Kamizuru H., Kenjo A., Miyao M. Low-temperature formation ($< 500\ ^\circ$ C) of poly-Ge thin-film transistor with NiGe Schottky source/drain. *Applied physics letters*, 2006, **89** (19).

[29] Kauzlarich S.M., Ju Z., Tseng E., Lundervold J. Recent developments in germanium containing clusters in intermetallics and nanocrystals. *Chemical Society Reviews*, 2021, **50** (23), P. 13236–13252.

[30] Menezes P.W., Yao S., Beltrán?Suito R., Hausmann J.N., Menezes P.V., Driess M. Facile access to an active γ-NiOOH electrocatalyst for durable water oxidation derived from an intermetallic nickel germanide precursor. *Angewandte Chemie*, 2021, **133** (9), P. 4690–4697.

[31] Walter C., Menezes P. W., Driess M. Perspective on intermetallics towards efficient electrocatalytic water-splitting. *Chemical Science*, 2021, **12** (25), P. 8603–8631.

[32] Toraya H. Quantitative phase analysis using observed integrated intensities and chemical composition data of individual crystalline phases: quantification of materials with indefinite chemical compositions. *J. of Applied Crystallography*, 2017, **50** (3), P. 820–829.

[33] Toraya H. Whole-powder-pattern fitting without reference to a structural model: application to X-ray powder diffraction data. *J. of Applied Crystallography*, 1986, **19** (6), P. 440–447.

[34] Schneider C.A., Rasband W.S., Eliceiri K.W. NIH Image to ImageJ: 25 years of image analysis. *Nature methods*, 2012, **9** (7), P. 671–675.

[35] Ivanov V.K., Fedorov P.P., Baranchikov A.Y., Osiko V.V.E. Oriented attachment of particles: 100 years of investigations of non-classical crystal growth. *Russian Chemical Reviews*, 2014, **83** (12), 1204.

[36] Pokrovski G.S., Schott J. Thermodynamic properties of aqueous Ge (IV) hydroxide complexes from 25 to 350 C: implications for the behavior of germanium and the Ge/Si ratio in hydrothermal fluids. *Geochimica et Cosmochimica Acta*, 1998, **62** (9), P. 1631–1642.

[37] Lin J.X., Wang L. Adsorption of dyes using magnesium hydroxide-modified diatomite. *Desalination and Water Treatment*, 2009, **8** (1–3), P. 263–271.

[38] Hernández N., Moreno R., Sánchez-Herencia A.J., Fierro J.L. Surface behavior of nickel powders in aqueous suspensions. *The J. of Physical Chemistry B*, 2005, **109** (10), P. 4470–4474.

[39] Lorenzen A.L., Rossi T.S., Riegel-Vidotti I.C., Vidotti M. Influence of cationic and anionic micelles in the (sono) chemical synthesis of stable $Ni(OH)_2$ nanoparticles: "In situ" zeta-potential measurements and electrochemical properties. *Applied Surface Science*, 2018, **455**, P. 357–366.

[40] White R.D., Bavykin D.V., Walsh F.C. Morphological control of synthetic $Ni_3Si_2O_5(OH)_4$ nanotubes in an alkaline hydrothermal environment. *J. of Materials Chemistry A*, 2013, **1** (3), P. 548–556.

[41] Krasilin A.A., Nevedomsky V.N., Gusarov V.V. Comparative energy modeling of multiwalled $Mg_3Si_2O_5(OH)_4$ and $Ni_3Si_2O_5(OH)_4$ nanoscroll growth. *The J. of Physical Chemistry C*, **121** (22), P. 12495–12502.

[42] Bloise A., Belluso E., Barrese E., Miriello D., Apollaro C. Synthesis of Fe-doped chrysotile and characterization of the resulting chrysotile fibers. *Crystal Research and Technology: J. of Experimental and Industrial Crystallography*. **44** (6), P. 590–596.

[43] Dzene L., Brendle J., Limousy L., Dutournie P., Martin C., Michau N. Synthesis of iron-rich tri-octahedral clay minerals: A review. *Applied Clay Science*, 2018, **166**, P. 276–287.

[44] Pignatelli I., Mosser-Ruck R., Mugnaioli E., Sterpenich J., Gemmi M. The effect of the starting mineralogical mixture on the nature of Fe-serpentines obtained during hydrothermal synthesis at 90 C. *Clays and Clay Minerals*, 2020, **68** (4), P. 394–412.

[45] Zieliñski J., Zglinicka I., Znak L., Kaszkur Z. Reduction of Fe_2O_3 with hydrogen. *Applied Catalysis A: General*, 2010, **381** (1–2), P. 191–196.

[46] Bielz T., Soisuwan S., Girgsdies F., Klo?tzer B., Penner S. Reduction of different GeO_2 polymorphs. *The J. of Physical Chemistry C*, 2012, **116** (18), P. 9961–9968.

[47] Chen C.X., Wu S.P., Fan Y.X. Synthesis and microwave dielectric properties of B_2O_3-doped Mg_2GeO_4 ceramics. *J. of alloys and compounds*, 2013, **578**, P. 153–156.

[48] Yamaguchi O., Matumoto H., Morikawa S., Shimizu K. Preparation and Thermal Behavior of Magnesium?Germanium Hydroxide. *J. of the American Ceramic Society*, 1983, **66** (9), P. c169–c170.

[49] Liu Y.Q., Ma D.J., Du Y. Thermodynamic modeling of the germanium–nickel system. *J. of Alloys and Compounds*, 2010, **491** (1–2), P. 63–71.

[50] Okamoto H. Fe–Ge (iron-germanium). *J. of Phase Equilibria and Diffusion*, 2008, **29** (3), 292.

[51] Audebrand N., Ellner M., Mittemeijer E J. High-temperature ordering of structural vacancies in the cobalt-rich portion of the binary system Co–Ge. *J. of alloys and compounds*, 2005, **388** (2), P. 230–234.

Submitted 15 November 2024; accepted 25 November 2024

Information about the authors:

Ekaterina K. Khrapova – Ioffe Institute, 194021 St. Petersburg, Russia; ORCID 0000-0003-2674-9653; e.k.khrapova@mail.ioffe.ru

Anastasia A. Ivanova – Ioffe Institute, 194021 St. Petersburg, Russia; ORCID 0000-0002-8134-1506; a.a.ivanova@mail.ioffe.ru

Demid A. Kirilenko – Ioffe Institute, 194021 St. Petersburg, Russia; ORCID 0000-0002-1571-209X; demid.kirilenko@mail.ioffe.ru

Andrei A. Krasilin – Ioffe Institute, 194021 St. Petersburg, Russia; ORCID 0000-0002-3938-3024; ikrasilin@mail.ioffe.ru

Conflict of interest: the authors declare no conflict of interest.

NANOSYSTEMS:
PHYSICS, CHEMISTRY, MATHEMATICS

Nadeina K.A., et al. *Nanosystems: Phys. Chem. Math.*, 2024, **15** (6), 837–854.
http://nanojournal.ifmo.ru
DOI 10.17586/2220-8054-2024-15-6-837-854

Original article

Granular Ni–Mo–W bulk hydrotreating catalyst: the effects from precursor calcination

Ksenia A. Nadeina, Yuliya V. Vatutina, Polina P. Mukhacheva, Sergey V. Budukva, Irina G. Danilova, Vera P. Pakharukova, Evgeniy Yu. Gerasimov, Maxim A. Panafidin, Oleg V. Klimov

Boreskov Institute of Catalysis SB RAS, Pr. Lavrentieva 5, 630090 Novosibirsk, Russia

Corresponding author: Ksenia A. Nadeina, lakmallow@catalysis.ru

PACS 81.05.-t, 81.05.Rm, 81.20.-n, 81.40.-z

Abstract This paper presents a study on the effect of the Ni–Mo–W precursor calcination (300, 450 and 500 °C) on properties of granulated bulk Ni–Mo–W catalysts. The Ni–Mo–W precursor and bulk catalysts were studied by XRD, nitrogen adsorption-desorption method, CHNS analysis, thermal analysis, Raman spectroscopy, UV-Vis DR spectroscopy, HRTEM and XPS. It is shown that the increase in calcination temperature of the precursor to 500 °C leads to stepwise decomposition of citric acid, transformation of active metals and re-structurization of the samples. Active metals in sulfide catalysts are present in the bulk mixed or individual sulfides and interact with alumina binder to form "NiMoS-like" sulfide phase. Increased crystallinity of the precursor results in the enlargement of bulk nickel particles, capsulation of Mo and W and their rounding by Ni atoms. Catalysts testing in hydrotreatment of SRVGO demonstrates that the best choice of temperature regimes is 300 °C for the precursor.

Keywords bulk catalyst, NiMoW, calcination, HDS, HDN

Acknowledgements The study was funded by the Russian Science Foundation according to the research project No. 22-73-10144 (https://rscf.ru/en/project/22-73-10144/).

For citation Nadeina K.A., Vatutina Yu.V., Mukhacheva P.P., Budukva S.V., Danilova I.G., Pakharukova V.P., Gerasimov E.Yu., Panafidin M.A., Klimov O.V. Granular Ni–Mo–W bulk hydrotreating catalyst: the effects from precursor calcination. *Nanosystems: Phys. Chem. Math.*, 2024, **15** (6), 837–854.

1. Introduction

Hydroprocessing catalysts are attracting constant interest from scientists working in catalysts development. It is caused by the constantly emerging requirements for the resulting fuels and heavy feedstocks of secondary processing and, consequently, the requirements for the catalytic action of the corresponding catalysts.

Hydrotreating (HDT) catalysts used in industrial units can be supported or bulk systems. The main similarity between them is the nature of active metals. Typically, Co or Ni are used in the pair with Mo or W [1, 2]. Combination of these metals in a catalyst followed by their transition in active sulfide phase provides high activity in target hydrotreating reactions.

The structure of active component of hydrotreating catalysts is sufficiently well determined, if bimetallic NiMo or CoMo catalysts are considered. According to Topsøe et al. [3], the active component of such CoMo systems consists of molybdenum sulfide particles being decorated with the promotor atom. However, the formation of Co–Mo–S phase is observed at Co/Mo ratios < 0.4, while greater Co contents result in the formation of Co–Mo–S phase and individual CoxSy sulfides. In general, NiMo catalysts have similar structure of Ni–Mo–S phase [4].

When adding the third element, Co/Ni or Mo/W, a synergetic effect can be observed. It is known that Ni–Mo and Co–Mo catalysts have better hydrogenolysis activity, while Ni–W catalyst is stronger in hydrogenation. Combining these advantages of bimetallic catalysts, Albemarle, ExxonMobil, and the Nippon Ketjen Corporation jointly developed the bulk catalyst (NEBULA) [5, 6], which presents of Ni–Mo–W component and demonstrates a breakthrough catalytic activity. The preparation procedure of NEBULA is know-how of the producer company. That is why, numerous investigations in this field are carried out by the catalysts developers to understand the nature of Ni–Mo–W catalysts and to create new high-active bulk catalysts.

Obviously, the presence of three different metals in the Ni–Mo–W system significantly increases the complexity of the system. Density functional theory (DFT) calculations confirmed the formation of synergetic effect of the addition of Ni to Mo–W–S system [7]. Moreover, it is shown that the best HDT catalysts must exhibit sulfur metal bond energies close to $NiMo_{0.5}W_{0.5}S_2$ system, meaning between NiMoS and NiWS ones. The data in [8] shows that the surface of NiMoW catalysts is easily formed comparing to bimetallic systems and the edge of NiMoW particle exhibits the highest occupation density of d-type states near the Fermi level. The equilibrium morphologies of the sulfide particles of the active component CoMoS or NiMoS phase are hexagonal or trigonal particles, according to DFT calculations [9]. According to the calculations, the shape of the main particle is close to the bimetallic one. In the case of the supported system, the active component particles were highly dispersed, highly reducible, and highly sulfidable W/Mo species, that provided the formation of $W_xMo_{1-x}S_2$ phases with increased capability for accommodating NiS_x at the edges of sulfide slabs [10].

For the bulk NiMoW catalysts, the establishment of the composition of active particles is complicated by the absence of the support, which can unify the active phase, as well as the use of numerous preparation techniques and conditions of activation procedures. Moreover, some preparation procedures can lead to the formation of the bulk hydrodesulfurization (HDS) catalysts with low atom efficiency and intrinsic activity due to the large amount of unused active sites embedded in the bulk catalyst, leading to the limitation of the practical application in HDS process [11, 12]. Therefore, optimization of bulk catalyst preparation is a complicated task.

In our previous research, it is shown that among all widely used preparation techniques for the bulk NiMoW catalysts, the best method includes the synthesis of the active metals precursor in the solution followed by spray drying [13]. It allows a synthesis of a set of compounds with high activity in HDS and hydrodenitrogenation (HDN) reactions. We found that the more preferred calcination temperature of the granulated catalyst prepared by the above-mentioned method is 300 °C [14]. However, the question on calcination of the precursor, which would define final structure of the oxide system before calcination, still arises.

For example, Wang et al. [15] used a surfactant-assisted co-precipitation method from the starting materials including basic nickel carbonate followed by a sulfidation process to obtain the final Ni–Mo–W sulfide catalyst without previous calcination of the precursor. The given data showed the formation of hydrotalcite-like structures, where Mo–W–S particles are located between Ni_7S_6 layers that significantly improves promotion effect from Ni.

On the contrary, in a number of works and patents, calcination temperature of bulk catalysts is usually in the range of 300 – 400 °C, however, there are no arguments for the chosen temperatures [12, 16, 17]. The report [18] demonstrates the data on the influence of thermal treatment at 250, 350, 450, 550 and 650 °C of a bulk NiMo catalyst being prepared by coprecipitation method on HDS activity of DBT. It is shown that the catalyst calcined at 350 °C is the most active in HDS than other samples. Similar results are shown in the report [19] for bimetallic NiMo catalysts, where calcination procedure is carried out under hydrogen or nitrogen atmosphere in the temperature range from 350 to 600 °C. It is shown that the best activity is achieved at calcination temperature of 400 °C. However, hydrothermal synthesis procedure of the precursor used in the above-mentioned papers, as well as calcination conditions, are not optimal for industrial application. Moreover, these works do not consider the necessity to use binding agent, such as pseudoboehmite, for granulation. It should also significantly influence the formation of the oxide active component precursor and then catalysts activity.

In the present work, we tried to clarify in detail the effect of calcination temperature on the NiMoW precursor for the bulk hydrotreating catalysts. The work focuses on the preparation of granulated system and, therefore, on the use of pseudoboehmite as a binding agent and its interaction with active component in the bulk system. Catalysts activity was assessed in a real feedstock hydrotreating.

2. Experimental

2.1. Preparation of catalysts

NiMoW precursor was synthesized by dissolution of nickel hydroxide, ammonium heptamolybdate and ammonium metatungstate with citric acid using the procedure described in [20]. Citric acid was dissolved in a distilled water under stirring at 70 °C. Then nickel hydroxide was added to the solution followed by complete dissolution and preparation of green transparent solution. Ammonium heptamolybdate and ammonium metatungstate were added to the green solution and it was stirred until complete dissolution. Molar ratio of Ni/Mo/W was 1/0.5/0.5. The obtained solution with the precursor was spray dried to prepare NiMoW powder. Then, the NiMoW powder was calcined at 300, 400, 450 or 500 °C in air flow. It should be emphasized that after studies by XRD and TGA the NiMoW sample calcined at 400 °C was not chosen for other investigations.

Granulated NiMoW catalysts were prepared by the following procedure. First, a dry mixing of the powder of the NiMoW precursor and a binder (pseudoboehmite) was carried out to obtain a kneading paste. A pseudoboehmite powder (SSA – 241 m^2/g, V_p – 0.6 cm^3/g, CSR: [100] – 14.5 nm, [010] – 4.0 nm, [001] – 11.5 nm) was synthesized by the procedure described in [21]. The weight ratio of pseudoboehmite and NiMoW precursor was 0.6. Then, an aqueous solution of plasticizing agent (nitric acid) was prepared. The amount of nitric acid was calculated from molar ratio of $HNO_3/Al_2O_3 = 0.07$. The obtained solution was added to the mix of powders and stirred to obtain plastic paste. The paste was extruded via fluoroplastic spinneret with trilobe holes of 1.3 ± 0.1 mm. The extrudate was then dried at 110 ± 10 °C and then calcined at 300 ± 10 °C.

2.2. Sulfiding and testing of catalysts

To assess catalysts activity in HDS and HDN reactions, catalysts were tested in hydrotreatment (HDT) of the real feedstock. Hydrotreatment of the real feedstock was carried out in a fixed-bed pilot unit using straight-run vacuum gas oil (SRVGO) (7080 ppm S and 958 ppm N). The 30 cm^3 of a catalyst sample was diluted with silicon carbide (0.1 – 0.2 mm) in a volume ratio of 1:2 and loaded in the isothermal zone of the reactor. Before testing, catalysts were sulfided in a liquid phase using the mixture of straight-run gasoil and dimethyl disulfide (20 g of DMDS per 1 l of straight-run gasoil).

Sulfidation of catalysts was carried out at 8.0 MPa, sulfidation mixture flow – 2 h^{-1} and volume ratio H_2/sulfidation mixture – 300 Nm^3/m^3 at 240 °C for 16 h and at 340 °C for 16 h. After sulfidation catalysts were tested in the following conditions: liquid hourly space velocity = 1.5 h^{-1}, H_2/feedstock = 600 Nm^3/m^3, $P = 8.0$ MPa, $T = 340$, 350 and 360 °C. Catalysts were tested for 48 h at each temperature. There were no liquid samples during first 24 h at each temperature. That period was marked as no steady state. Then, 4 liquid product samples were selected for analysis each 4 h. Content of nitrogen and sulfur in the feedstock and hydrotreating products was determined on Xplorer-NS Analyzer (TE Instruments).

2.3. Characterization methods

CHNS analysis was carried out on the analyzer VARIO EL CUBE according to ASTM D3176-15.

X-ray diffraction experiments in the transmitted light mode were carried out with MoKα radiation ($\lambda = 0.7093$ Å) at STOE STADI MP (STOE, Germany) installation using the detector MYTHEN2 1K. Measurements were carried out by scanning in the angles range 2 – 69° at 0.015° step at 2θ. The obtained data were analyzed to define average crystallite size. The size of coherent scattering region (CSR – D_{XRD}) was calculated from the width of diffraction peaks. Phase analysis was made using diffraction database ICDD PDF-2.

The textural properties of the catalysts were determined by nitrogen physisorption using an ASAP 2400 instrument (Micrometrics, USA). Prior to analysis, samples were subjected to a N_2 flow at 150 °C for 2 h. The Brunauer–Emmett–Teller method (BET) was used to calculate BET surface areas from the nitrogen uptakes at relative pressures ranging (P/P_0) from 0.05 to 0.30. The total pore volume was derived from the amount of nitrogen adsorbed at a relative pressure close to 1 (in practice, $P/P_0 = 0.995$). The pore size distribution was calculated by the Barrett–Joyner–Halenda (BJH) method using the desorption branch of the isotherm [22]. The uncertainty of the results was 10 %.

Sulfide catalysts were studied by X-ray photoelectron spectroscopy (XPS) on a SPECS photoelectron spectrometer using non-monochromatic MgKα radiation ($h\nu = 1253.6$ eV). The binding energy scale (E_b) was previously calibrated by the position of photoelectronic lines of core levels of gold, silver and copper: Au4$f_{7/2}$ – 84.0 eV, Ag3$d_{5/2}$ – 368.3 eV and Cu2$p_{3/2}$ – 932.7 eV, measured for corresponding metallic foils. Samples were applied to a double-sided conductive copper tape. The charging effect that occurs during electron photoemission was taken into account using the internal standard method, which used the Al2p line from aluminum in the support ($E_b = 74.5$ eV) [23]. In addition to the survey spectrum, high resolved spectral regions of elements being included to the samples were recorded. All obtained spectra were recorded at pass energy of 20 eV. The definition of a relative elements content on catalysts surface and a ratios of their atomic concentration were made from integral intensity of photoelectron lines being corrected by atomic sensitive factors [24].

Sulfide catalysts before reaction were studied by high-resolution transmission electron microscopy (HRTEM) to investigate their morphology and structure. For imaging in TEM and STEM modes, a ThemisZ two-corrector transmission electron microscope (USA, Thermo Fisher Scientific) with an accelerating voltage of 200 kV and a limiting resolution of 0.07 nm (TEM) and 0.06 nm (SEM) was used. The micrographs were recorded using a Ceta 16 CCD matrix (Thermo Fisher Scientific, USA). High-angle annular dark field (HAADF) technique was performed to evaluate distribution of active metals.

Thermal analysis of the catalysts was carried out using NETZSCH STA 449 Jupiter. A sample was loaded into corundum crucibles and placed in a chamber. An air flow rate was 30 ml/min. A sample was heated up to 600 °C at a rate of 10 °C/min. Experimental data was analyzed by the NETZSCH Proteus Thermal Analysis software.

UV-Vis diffuse reflectance spectra (UV-Vis DRS) of the catalysts in the oxide states were recorded on an UV-2501 PC Shimadzu spectrometer with an IRS-250A diffusion reflection attachment. The measurements were performed in a quartz cell (optical path length 2 mm) in air at room temperature using $BaSO_4$ as a reference.

Raman spectra of the catalysts in the oxide states were recorded with the use of a LabRAM HR spectrometer, Evolution, Horiba, equipped by a multichannel CCD detector, which was cooled by liquid nitrogen. The spectra were excited by a 633 nm He–Ne laser with a power of about 0.5 mW on the sample surface. The diameter of the laser light spot on the sample surface was about 2 μm. The scattering geometry was 180°. The spectrometer resolution was 2.4 cm^{-1}.

The structural properties of the samples were analyzed by Infrared (IR) spectroscopy using a KBr wafer technique (a typical wafer containing 1 wt. % of a sample). IR spectra were recorded on a Shimadzu IRTracer-100 spectrometer within the spectral range of 350 – 4000 cm^{-1} with a resolution of 2 cm^{-1}.

3. Results and discussion

3.1. Structure of NiMoW precursor after calcination at high temperatures

Before explanation of the data, which are given below for the precursor and catalysts, it would be better to justify the choice of the calcination temperature for the NiMoW precursor. The first point is based on the granulation of the catalysts. It is experimentally established that the NiMoW precursor has very poor plasticizing properties, when the calcination temperature is less than 300 °C. The second point is related to phase transitions seen in TG/DTG/DSC curves and XRD patterns.

The DTG curve (Fig. 1) of the NiMoW precursor contains specific features being characteristic for the decomposition of citrate ligands [25–27]. A weight loss at 50 – 150 °C can be assigned to the removal of adsorbed water and ammonia. A great weight loss (25 % of the total weight) is observed at 180 – 350 °C due to the citrate ligands decomposition to acetondicarboxylate compounds or oxycarbonate compounds [25, 28]. The decomposition of citrate complexes to carbon deposits occurs at $\sim$ 300 °C. It possibly explains poor plasticizing properties of the NiMoW powder. The weight loss over 400 – 600 °C is accompanied by a strong exo-effect, which is related to the oxidation of residual fragments of organic molecules and amorphous carbon, and to the formation of nickel, molybdenum and tungsten oxide compounds, and their phase transformation [29–31]. When the calcination temperature is higher than 300 °C, two areas can be pointed out: 400 – 450 °C and 500 – 550 °C. To choose calcination temperature in these two areas for further studies, the NiMoW precursors calcined at 300, 400, 450 and 500 °C were studied by XRD analysis (Fig. 2).

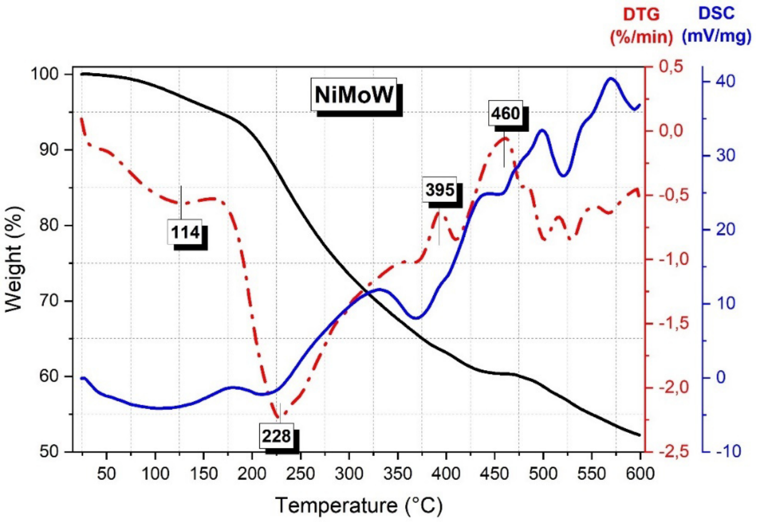

FIG. 1. TG and DTG curves of NiMoW precursor

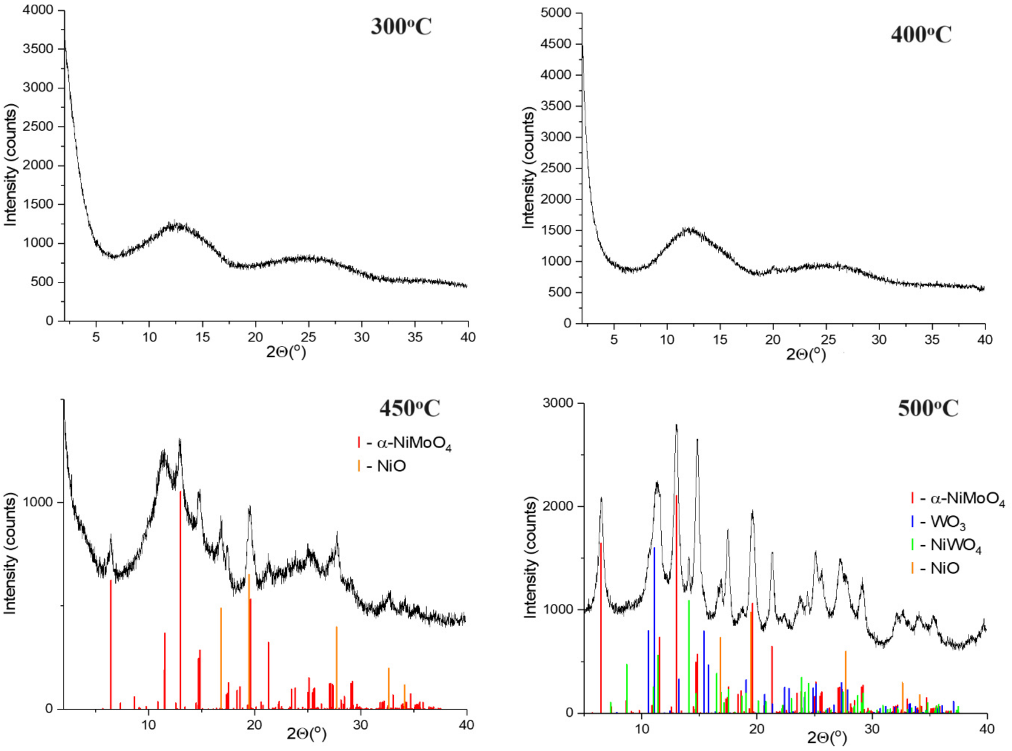

FIG. 2. XRD patterns of Ni–Mo–W precursor calcined at 300, 400, 450 and 500 °C

It is seen that only calcination at temperatures higher than 400 °C leads to the formation of crystal phases. Moreover, crystallinity of the samples calcined at 450 and 500 °C strongly changes. Then, we choose one of the X-ray amorphous samples, which were calcined at 300 °C, and two samples calcined at 450 and 500 °C for further studies.

3.1.1. NiMoW precursor calcined at 300 °C. As it is noted above, the XRD data of the precursor calcined at 300 °C does not show any crystal phases. On the contrary, the Raman spectrum (Fig. 3A) of the NiMoW sample calcined at 300 °C contains a set of bands in the range of 1100 – 1700 cm^{-1} with two intense poor resolved signals at 1360 and 1590 – 1600 cm^{-1} typical for most kinds of carbonaceous materials such as graphite, carbon black and soot. Considering calcination temperature, the peak at 1590 – 1600 cm^{-1} (G-band) can be assigned to graphitized coke, while the peaks at around 1360 cm^{-1} (D-band) can be due to disordered pseudographite deposits [32, 33]. The band at 1445 – 1465 cm^{-1} (D3-band) corresponds to the loss of aromatic bonding in a purely sp2 network [34]. The signal at 1250 – 1265 cm^{-1} corresponds to the Raman shift of C–H bond vibrations, while the shoulder at 1150 – 1200 cm^{-1} could be attributed to sp^2-sp^3 bonds or C–C and C=C stretching vibrations of polyene-like coke. In addition, a strong fluorescence background is detected in the sample calcined at 300 °C, probably caused by residual fragments of the organic matrix [35]. The observed features can indicate the effects from deposits of citric acid in the catalysts. A small signal at $\sim$ 220, 650 – 690 and $\sim$ 960 cm^{-1} can be assigned to bridged Mo–O–Mo and terminal M=O in polymolybdate-like structures [36].

The UV-Vis DR spectrum of NiMoW precursor (Fig. 4A) calcined at 300 °C represents a very intense broad signal in the region of 400 – 700 nm with the maximum at around 500 nm and shoulders at about 420 – 430, 350 – 360 and 280 – 300 nm. This set of bands may belong to π-π^* and n-π^* transitions of charged alkylated aromatics and polyaromatics with oxygen-containing substituents (the products of citric acid decomposition after calcinations) [37]. The absence of clearly defined bands of d-d transitions of Ni^{2+} ions may indicate shielding by a carbon matrix.

3.1.2. NiMoW precursors calcined at > 450 °C. When calcination temperature is higher than 450 °C, XRD patterns contain peaks from α-$NiMoO_4$ (PDF#00-033-0948, $a = 9.509$, $b = 8.759$, $c = 7.667$ Å) with the average CSR size $D = 10$ nm (content prevails). Moreover, the precursor calcined at 450 °C contains NiO phase (PDF#00-047-1049,

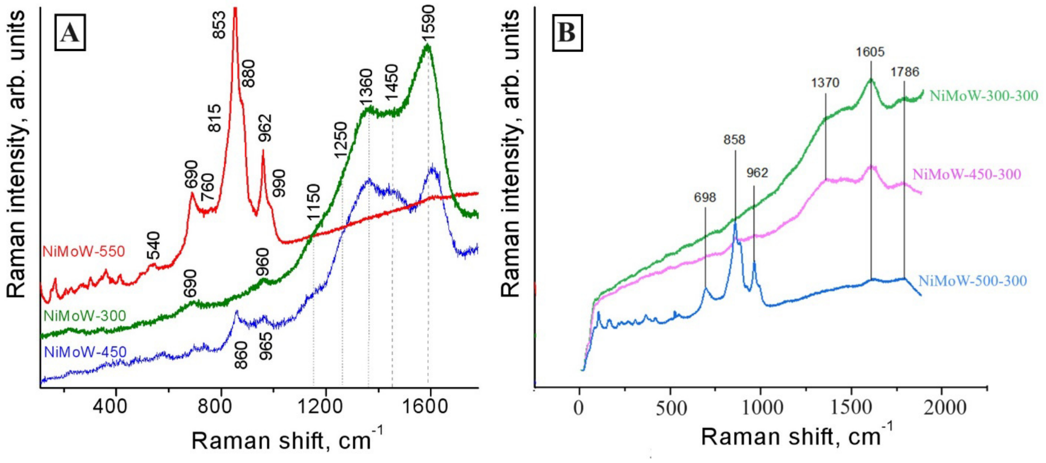

FIG. 3. Raman spectra of Ni–Mo–W precursor (A) and corresponding catalysts (B) calcined at 300, 450 and 500 °C

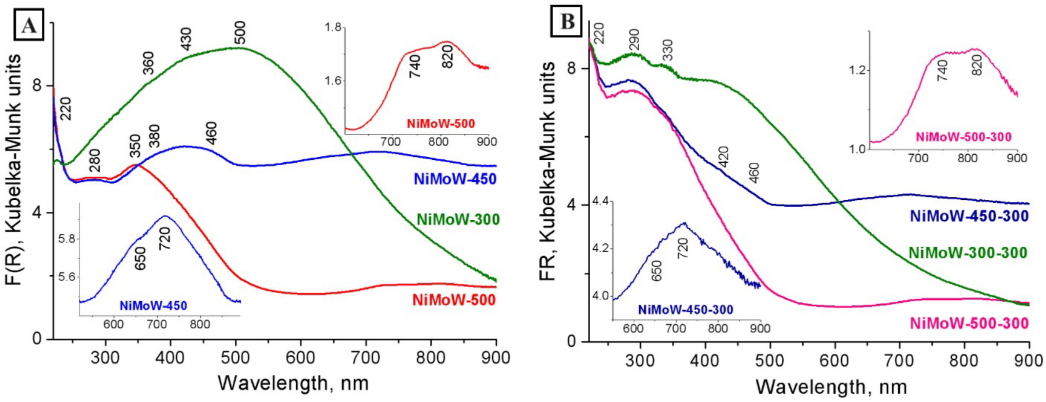

FIG. 4. UV-Vis DR spectra: A) Ni–Mo–W precursor calcined at 300, 450 and 500 °C; B) NiMoW–X-300 (where X = 300, 450 and 500 °C) catalysts. The insets show enlarged fragment of spectra

$a = b = c = 4.177$ Å) with $D = 10$ nm and with high probability highly dispersed WO_3 phase (PDF#00-033-1387), since there is an increase in the intensity near 11° at 2θ.

The set of bands in the Raman spectra (Fig. 3A) in the region of 1100 – 1700 cm^{-1} decreases in intensity and new peaks appear at about 540, 705, 740, 860 and 920 cm^{-1}. The band at 860 cm^{-1} can be attributed to W=O bonds in isolated WO_4 structures, while the signal at *ca.* 740 cm^{-1} is assigned to W=O bonds in isolated WO_6 structures [38]. The set of bands at 965, 920 and 705 cm^{-1} belongs to the MoO_6 symmetric stretch and corresponding MoO_6 asymmetric vibrations of bulk β-$NiMoO_4$ [36], while the band at 760 cm^{-1} is attributed to bridging Mo–O–Mo bond that confirms the presence of polymolybdate structures. The peak at about 540 cm^{-1} is typical for NiO.

Treatment at 450 °C is accompanied by the appearance of the intense peak at 720 nm with the shoulder at 650 nm in the UV-Vis DR spectra (Fig. 4A). This signal as well as the bands located at about 380 – 460 nm result from d-d transitions of Ni^{2+} ions hosted by octahedral sites in the dispersed NiO [39]. The n-π^* transitions in carboxylate substituents of the carbon matrix likely have an additional contribution to the adsorption in the 350 – 460 nm region and the increased background in the long wavelength region. The UV region of this spectrum contains three strong broad bands centered at 220, 280 and 350 nm, which could be assigned to $O^{2-} \rightarrow Mo^{6+}$ (W^{6+}) charge transfer (CT) transitions. First peak is usually observed in compounds, which contain isolated tetrahedral coordinated MoO_4 or WO_4 species [38, 40]. The second peak most likely refers to polymolybdate-like structure containing octahedral coordinated Mo ions (MoO_6 species) [36], while the third signal probably related to polytungstates or WO_3 cluster contained octahedral coordinated W ions (WO_6 species) [38]. The intensity of the band from isolated tetrahedral coordinated molybdate (tungstate) ions is much higher than from polymolydates (polytungstates).

Besides α-$NiMoO_4$ phase, the precursor calcined at 500 °C contains WO_3 (PDF#00-033-1387, $a = b = 7.298$, $c = 3.899$ Å) with the CSR size $D \sim 8$ nm, $NiWO_4$ (PDF#00-015-0755, $a = 4.912$, $b = 4.60$, $c = 5.665$ Å) with CSR size $D = 19$ nm, and NiO (PDF#00-047-1049, $a = b = c = 4.177$ Å), $D \sim 10$ nm.

The Raman spectra of the NiMoW-500 sample is characterized by the set of bands at 540, 690, 760, 853 cm^{-1} with the shoulders at 815, 880 and 920 cm^{-1}, as well as 962 and 990 cm^{-1}. Signals at 990 cm^{-1} with the 815 cm^{-1} belong to the modes from MoO_3. The peaks at 962, 920 and $\sim$ 700 cm^{-1} characterize nickel molybdate, and the bands at 880 and 690 cm^{-1} correspond to nickel tungstate. On the other hand, the band in the range of 715 cm^{-1} accompanied by the band at around 805 cm^{-1} can be attributed to the W–O–W deformation mode, W–O bending modes and a W–O stretching vibration characteristic of octahedral WO_3-like species (or crystalline WO_3) and may overlap with the signals of the above compounds [38]. The modes from carbon compounds completely disappear.

The UV-Vis DR spectrum of the NiMoW-500 precursor contains the new bands at 740 and 820 nm which are likely associated with Ni^{2+} ions octahedral coordinated to molybdate ions in nickel molybdate [41, 42]. The last band is coming from the distortion of octahedral Ni^{2+} by incorporation to MoO_4^{2-}. Nickel ions in the $NiWO_4$ structure can also absorb in this area too [43].

3.1.3. Intermediate conclusions. Summarizing effects seen in the precursor samples, the following scheme can be provided (Fig. 5). First, the precursor obtained after spray drying contains molybdenum, tungsten and nickel citrate complexes. When heat treatment temperature increases to 300 °C, citrates decompose and form variations of acotonic and itaconic compounds followed by the formation of carbon-containing compounds, like coke. Then, the heating to more than 450 °C results in the removal of carbon and other products of citrate's decomposition and formation of crystal phases – both individual Ni, Mo or W oxides and mixed oxides.

FIG. 5. Scheme on the possible reactions being occurred in the NiMoW precursor

3.2. Structure of NiMoW catalysts

Before describing and discussing the structural data on the bulk NiMoW catalyst, it should be emphasized that all structural changes of the NiMoW precursor are not significantly affected by calcination of catalysts granules, because final calcination temperature is equal or less than calcination of the NiMoW precursor.

According to CHNS analysis (Table 1), residuals of citric acid decomposition products present in the catalysts even at high temperatures. Carbon content decreases from 7 to 0.8 wt.%, when calcination temperature increases from 300 to 500 °C. It is noted that carbon content is high in the NiMoW-300-300 and NiMoW-450-300 catalysts. Then, we can suggest that decomposition of citric acid is complicated in bulk catalysts comparing to supported samples [35, 44, 45] possibly due to its hiding in the catalyst volume. Moreover, X-ray amorphous properties seen for the NiMoW precursor calcined at 300 °C could be caused by even distribution of atoms of active metals in the presence of high amount of carbon in the samples [46].

TABLE 1. CHNS analysis data of catalysts

Sample	C% wt.	H% wt.	N% wt.	S% wt.
NiMoW-300-300	7.4	1.4	1.4	0
NiMoW-450-300	3.2	0.7	0.7	0
NiMoW-500-300	0.8	0.6	0	0

Another point is the presence of nitrogen in granulated catalysts. Obviously, nitrogen is caused by the use of nitric acid during plasticization and can be also present as a residual nitrogen in pseudoboehmite (specified by the synthesis procedure). Then, the increase in calcination temperature of granules results in the decrease of nitrogen content. Some of nitrogen could be present from ammonium heptamolybdate used in the synthesis. It explains the difference between the NiMoW-300-300 and NiMoW-450-300 samples. It is not obvious, how nitrogen will influence catalysts activity. Possibly, similar effects of HDS activity worsening can be pointed out [47].

The features of the precursor transformation during its calcination are confirmed by data of thermal analysis (Fig. 6). DTG curves demonstrate three-stages weight loss. The first stage at 80 – 100 °C is caused by desorption of physically adsorbed water. The second one at 430 – 445 °C is due to phase transformation of pseudoboehmite to γ-Al_2O_3 [21,48] or to decomposition of various citrates to oxides. The main difference between the samples is observed in DTG/DSC curves. The NiMoW-300-300 and NiMoW-450-300 catalysts demonstrate strong endo-effect at 554 and 578 °C, respectively, due to the formation of stable nickel molybdates and tungstates ($NiMoO_4$ and $NiWO_4$) [29,31]. The TG/DTG/DSC curves of the NiMoW-500-300 catalyst in this temperature region are plateau.

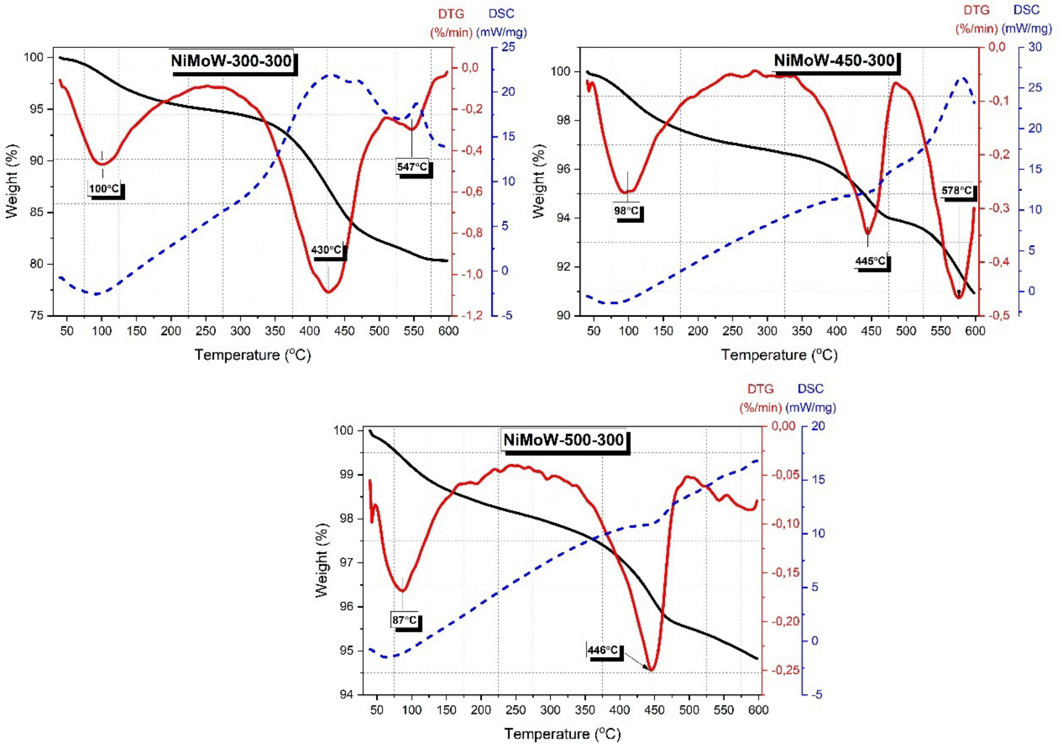

FIG. 6. TG and DTG curves of NiMoW-300-300, NiMoW-450-300, NiMoW-500-300, catalysts

Using IR, UV-Vis DR and Raman spectroscopy, the structural properties of the NiMoW granulated catalyst samples in the oxide form were compared. The UV-Vis DR spectrum of the NiMoW-300-300 catalysts (Fig. 4B) shows a decrease in signals associated with the carbon material compared to the spectrum of the NiMoW-300 precursor (Fig. 4A). The appearance of three strong broad bands centered at 220, 290 and 330 nm could be assigned to $O^{2-} \rightarrow Mo^{6+}$ (W^{6+}) CT transitions. Apparently, some of the polyoxometalate anions react with Al–OH groups of pseudoboehmite to form probably $(Al_s)_2Mo(W)O_4$ surface species. This promotes the release of polymolybdate (polytungstate anions) from the organic matrix. Most of the Ni^{2+} ions remain uniformly distributed and shielded by the organic amorphous matrix. Calcination of the NiMoW precursor at higher temperatures leads to the disappearance of the signal from the carbon material in the spectra of the NiMoW-450-300 and NiMoW-500-300 catalysts. The spectra of the NiMoW-450-300 and NiMoW-500-300 catalysts demonstrate more intense signals in the region of $O^{2-} \rightarrow Mo^{6+}$ (W^{6+}) CT transitions compared with the corresponding precursors. This may be the result of the anchoring of polymolybdate and polytungstate structures on the Al–OH groups of pseudoboehmite. The state of Ni^{2+} ions in NiMoW-450-300 and NiMoW-500-300 catalysts differs slightly from corresponded precursors. In all compounds, Ni^{2+} ions are stabilized in octahedral coordination. Additionally, there is an increase in intensity in the long-wavelength region of the spectrum of the NiMoW-450-300 sample, which may indicate Ni^{2+} ions in the structure of molybdate or tungstate.

The IR spectra of the NiMoW catalysts are shown in Fig. 7. Three intense bands at 480, 630 and 740 cm^{-1} in the framework vibration range as well as four peaks at 1070, 1160 and 3090, 3303 cm^{-1} characterize a well crystallized boehmite [49]. Moreover, the spectra of all samples demonstrate a weak signal at 1384 cm^{-1} related to residual NO_3- ions. The bands at 1715 (νC=O in –COOH) and 2855, 2925, 2960 cm^{-1} (ν ($-CH_2-$, $-CH_3$)) in the spectrum of the NiMoW-300-300 sample are assigned to residual citric acid fragments, while the bands at 1590 (ν_{as} COO–) and 1410 cm^{-1} (ν_s COO–) are attributed to carboxylate groups that were binding with the aluminum atoms of the boehmite surface [50]. The bands at about 1590 – 1300 cm^{-1} in the spectrum of the NiMoW-450-300 sample relate to carbonate-carboxylate compounds, but the only peak at 1630 cm^{-1} in this region for the NiMoW-500-300 sample is due to adsorbed water. The intensity of the boehmite signals for the NiMoW-500-300 catalyst is the highest, while it is slightly higher for the NiMoW-450-300 then for the NiMoW-300-300 catalyst. Thus, higher calcination temperature of the NiMoW precursor decreases the residual content of carbon-containing fragments (it is also shown in Table 1). It complicates the transformation of pseudoboehmite structure to alumina. To confirm that, we made additional studies of the samples by XRD method (Fig. A1, Appendix).There was no alumina phase in the samples, which granules were calcined at 300 °C. But when calcination temperature of the granules becomes 400 °C, alumina phase is observed from high-intensive peaks in XRD curves. Possibly, the samples calcined at 300 °C also contain some γ-Al_2O_3, but its amount is very small, and reflections are overlapped by other phases. Another point is that boehmite starts to transform at higher temperatures as it seen from IR spectroscopy.

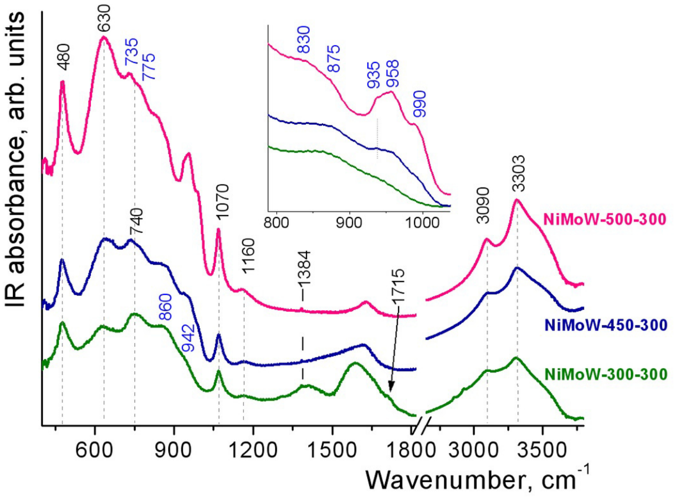

FIG. 7. IR spectra of NiMoW-X-300 (where $X = 300$, 450 and 500 °C) catalysts. The inset shows enlarged fragment of spectra

Two bands at 942 and 860 cm^{-1} in the spectrum of the NiMoW-300-300 sample could be attributed to the vibrations of the distorted MoO_6 units in polymolybdate anions. The band at 958 with the shoulder at 935 cm^{-1} in the spectra of the NiMoW-450-300 and NiMoW-500-300 samples characterize a bulk α-$NiMoO_4$ [51, 52]. A group of signals at about 990 and 875 cm^{-1} is assigned to bulk MoO_3 [53]. The intensity of the signals associated with nickel molybdate and molybdenum oxide is higher for the NiMoW-500-300 catalyst than for the NiMoW-300-300 catalyst. Therefore, the higher calcination temperature of the NiMoW precursor leads to higher crystallization degree of nickel molybdate and molybdenum oxide that is confirmed by UV-Vis DRS. In addition, the well resolved peaks at 830, 775 and 735 cm^{-1} are observed in the spectrum of the NiMoW-500-300 sample. The first band is attributed to a bulk $NiWO_4$ [43, 54], while the second and the third peaks may be associated with the formation of WO_3 [38, 55]. The signal of Ni–O bonds in NiO overlaps with the intense absorbance of pseudoboehmite and cannot be detected by the used method.

The Raman spectra of the catalysts confirm the observed results (Fig. 3B). The background significantly grows for all catalysts that is probably caused by the presence of OH groups in the alumina binder. The addition of the binding agent leads to the decrease in the intensity of the signals from carbon in both catalysts calcined at 300 and 450 °C. Moreover, the signals in the spectrum of the NiMoW-450-300 from Mo and W oxides also decrease and almost disappear. The spectrum of the NiMoW-500-300 is similar to the precursor one. The spectra also contain the band at 1786 cm^{-1}, which is related to vibrations of the keto group >C=O in aliphatic or aromatic esters, products of the decomposition of citric acid.

The granulated bulk catalysts were studied by nitrogen adsorption-desorption method. Specific surface area (SSA) and pore volume (V_p) significantly decrease from 122 to 61 m^2/g with the increase of calcination temperature of the precursor from 300 to 450 °C (Table 2). It can be caused by decomposition and removal of citrate in complexes, transformation of Ni, Mo and W compounds and possible sintering of formed oxides. The SSA and especially V_p values increase from 61 to 83 m^2/g and from 0.12 to 0.17 cm^3/g when calcination temperature of the precursor was increased to 500 °C (Table 2). The average pore diameter (D_p) shifts slightly toward higher values from 5.2 to 8.4 nm with increasing precursor calcination temperature from 300 to 450 – 500 °C.

TABLE 2. Textural properties of the calcined catalysts

Sample	SSA, m^2/g	V_p, cm^3/g	D_p, nm
NiMoW-300-300	122	0.16	5.2
NiMoW-450-300	61	0.12	7.7
NiMoW-500-300	83	0.17	8.4

Formation of bulk systems requires consideration of porous structure for the transportation of feedstock molecules. Shape of pores in bulk catalysts can be defined from adsorption-desorption isotherms (Fig. A2, Appendix). According to classification [22], the form of isotherms is similar to IV(a) type specific for mesoporous materials. Hysteresis loops of isotherms indicate capillary condensation of nitrogen in mesopores. All studied catalysts have similar hysteresis loops classified to H3 type, which is characteristic for materials consisting of non-rigid particle aggregates of irregular size and/or shape. On other point of view, this type of hysteresis loop can be observed for macroporous structures, which are not filled by condensate. Since nitrogen adsorption-desorption method cannot measure macropores, we can assume that the lack of the developed mesoporous structure (especially small mesoporous volume) is compensated by transportation pores. This assumption was confirmed by the results of mercury porosimetry (Fig. 8). The increase in the volume of macropores occurred when the calcination temperature of the precursor was increased.

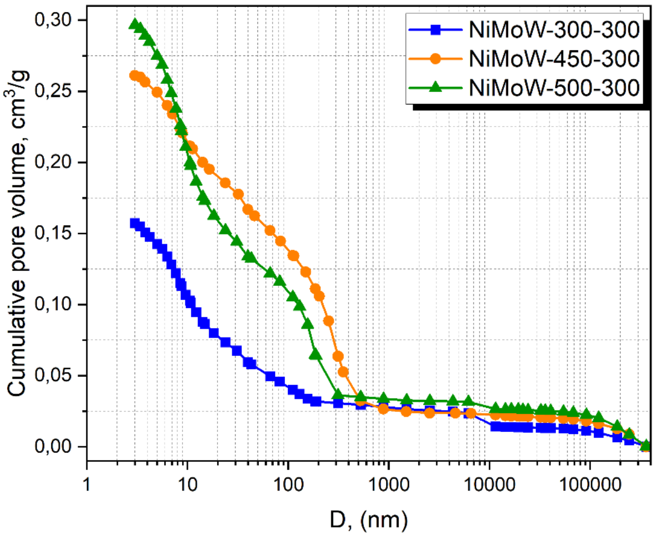

FIG. 8. Dependences of the volume of cumulative on the pore diameter (log D) obtained from the results of mercury intrusion for calcined catalysts

The changes in mesoporosity are better seen from the pore size distribution from nitrogen adsorption-desorption (Fig. A2, Appendix). The NiMo-300-300 catalyst has wide pore size distribution with a strong maximum at 4 nm and smooth curve in the range of 5 – 15 nm. Calcination at 450 – 500 °C resulted in the formation of bimodal pore size distribution curves with the first maxima at 4 nm and the second maxima at 5 – 15 nm. Comparing three catalysts we can conclude that calcination led to the formation of mesopores of 5 – 15 nm.

3.3. Effect of calcination temperature on catalysts activity in HDT of real feedstocks and structure of sulfide catalysts

The data of hydrotreating of SRVGO at 340 – 360 °C are given in Table 3. The catalysts show worsening in HDS activity with the increase in the calcination temperature from 300 to 500 °C. HDN activity also becomes worse. This tendency is actual for all process temperature range. Therefore, the best choice of temperature regimes is 300 °C. It should be noted that the comparison of the bulk catalyst prepared in a similar way as NiMoW-300-300 catalyst with the supported catalyst was carried out earlier [56]. It was shown that the bulk catalyst was superior in activity to the supported one. Then, we can suppose that the activity of the NiMoW-300-300 catalyst in SRVGO hydrotreatment will be also higher.

TABLE 3. Results of catalytic tests in hydrotreating of SRVGO

Temperature, °C / Sample	340		350		360	
	S, ppm	N, ppm	S, ppm	N, ppm	S, ppm	N, ppm
NiMoW-300-300	1461	800	1061	711	775	597
NiMoW-450-300	2112	913	1596	835	1157	738
NiMoW-500-300	2345	937	1812	854	1406	796

The catalysts in the sulfide state were washed in toluene after testing and investigated by low-temperature nitrogen adsorption-desorption method (Table 4). Values of SSA and V_p decreased compared to the calcined catalysts. The observed result is related to the transition of active metals into sulfide form and to the acceleration of carbon during testing. The formation of active metal sulfides in the catalysts is described below in the description of the XPS results. However, the difference between the samples in SSA and V_p values became insignificant considering the method error of 5 %. The exception is the NiMoW-500-300 sample. The pore volume (0.10 cm^3/g) for the mentioned sample is higher than that of the other samples (Table 4). The trends in the change of pore size distribution with increasing precursor calcination temperature after the reaction are maintained (Fig. A3, Appendix). The NiMoW-500-300 sample contains large number of pores with the diameters of 5 – 15 nm compared to the others. Thus, in terms of textural characteristics, it is the most preferable catalyst. However, this catalyst has the lowest activity in HDS and HDN reactions (Table 3). Then, the changes in the catalytic activity are related to the properties of the active metals.

TABLE 4. Textural properties of the sulfided catalysts

Sample	SSA, m^2/g	V_p, cm^3/g	D_p, nm
NiMoW-300-300	35	0.07	8.4
NiMoW-450-300	22	0.06	11.0
NiMoW-500-300	43	0.10	9.6

Sulfide catalysts before testing were studied by HRTEM and SEM methods. Fig. 9 shows HRTEM images of the studied catalysts. It is seen that there are slabs of active component particles which are localized over alumina as well as bulk particles. The transition of active metals to alumina binder can occur at the granulation stage. On the one hand, this phenomenon can be an advantage for catalysts activity due to the formation of more dispersed active phase, which is similar in structure to the high active “Ni–Mo–S” phase. On the other hand, there can be the decrease of “bulk active sites” concentration that could decrease catalysts activity. However, it is a question for the future discussion.

The increase in the calcination temperature of the precursor powder used for granulation results in the increase of the length of active component particles and their stacking. In addition, there is a visual enlargement of bulk particles in catalysts.

Metals distribution in catalysts given in Figs. 10 and A4–5 (Appendix) demonstrates separately allocated nickel particles that is likely caused by the extraction of nickel from the volume to the surface during sulfidation procedure. The images of the NiMoW-300-300 (Fig. 10) catalyst also show that sulfur and nickel have similar distribution areas that can indicate the formation of nickel sulfides. Similar areas of sulfur and tungsten accumulations are pointed out, while molybdenum distribution is uniform.

The images of the NiMoW-450-300 (Fig. A4, Appendix) and NiMoW-500-300 (Fig. A5, Appendix) catalysts additionally contain areas, where Mo and W are concentrated in the inner part, while Ni is in the outside part forming rim (Fig. 11). The increase in calcination temperature leads to the pronunciation of the effect. It is seen that the higher calcination temperature, the greater encapsulation of Mo and W by Ni. At the same time, sulfur is distributed evenly over all areas of localization of three metals.

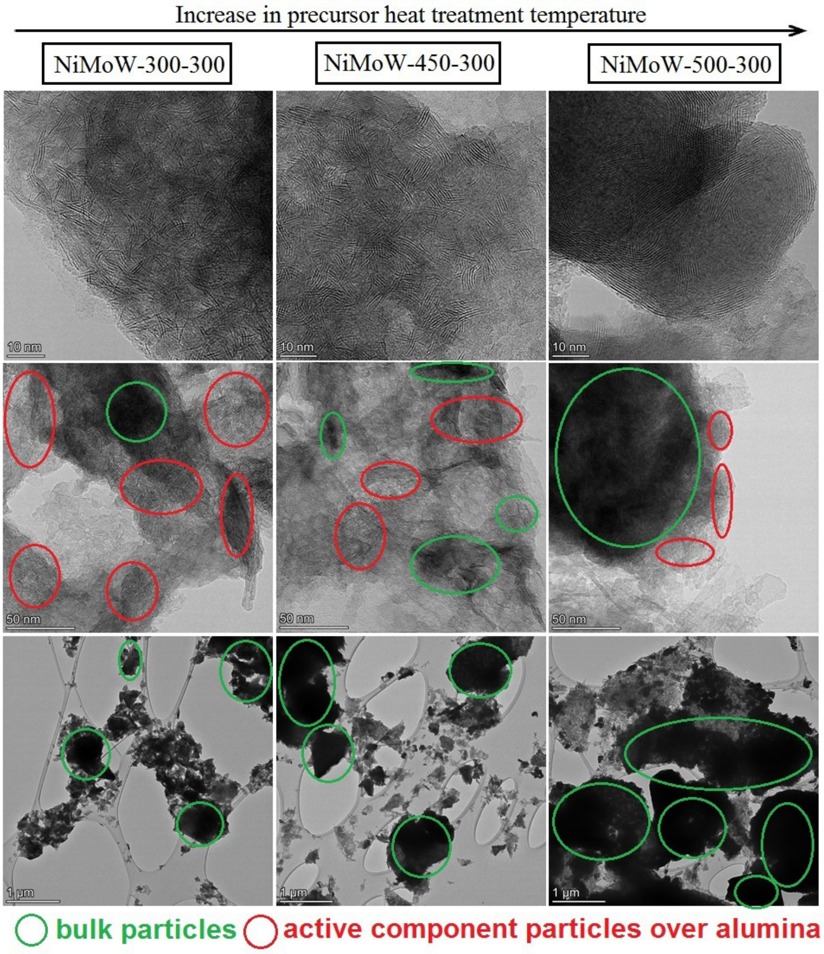

FIG. 9. HRTEM images of the NiMoW-300-300, NiMoW-450-300 and NiMoW-500-300 catalysts before testing

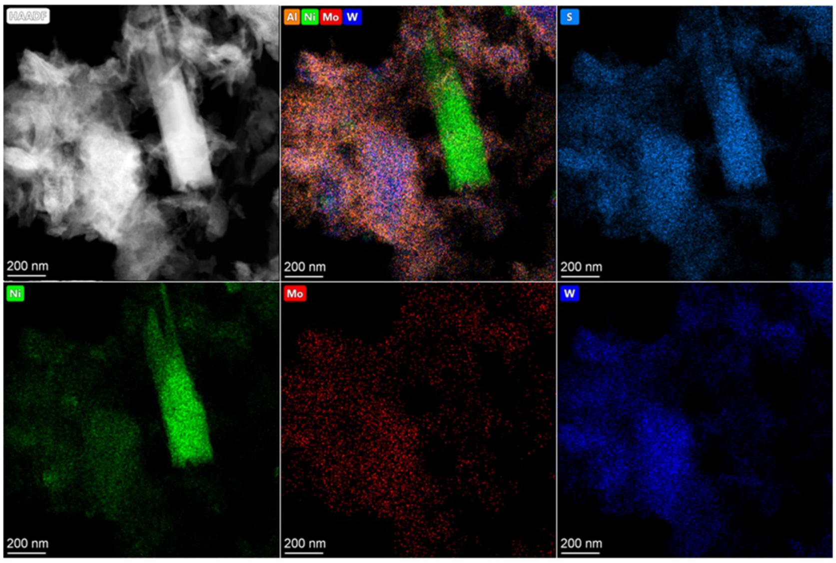

FIG. 10. HAADF data on the NiMoW-300-300 catalyst before testing

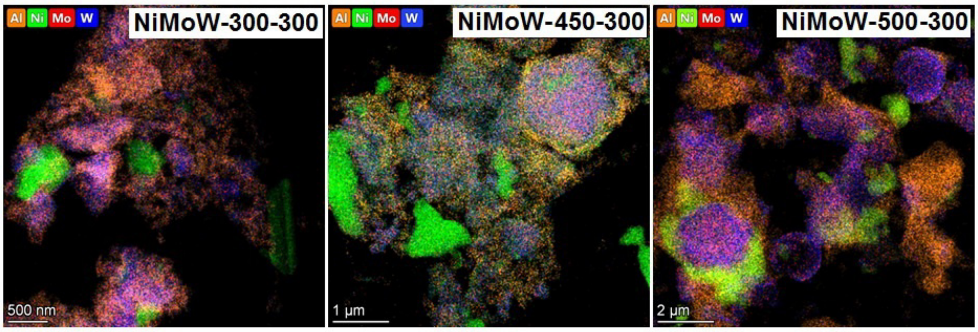

FIG. 11. HAADF data on the catalysts after testing to demonstrate encapsulation of metals

The NiMoW-300-300 and NiMoW-500-300 catalysts were studied by XPS to obtain additional information on the state of active metals. Fig. 12A demonstrates Mo3d spectra for the studied samples. The catalysts have different surface concentration of molybdenum. The surface concentration of Mo in the NiMoW-300-300 catalyst is 2.6 %, and in the NiMoW-500-300 catalyst – 0.9 % (Table 5). All detected Mo on the catalysts surface is in the Mo^{4+} state in both catalysts, because Mo3d spectrum contains only one doublet with the binding energy of $Mo3d_{5/2} \sim 228.9$ eV [57, 58]. There are no peaks with E_b close to 230.7 and $\sim$ 232.6 eV corresponding to Mo^{5+} and Mo^{6+}, respectively. The peaks at $\sim$ 226.3 and $\sim$ 233.4 eV in all samples relate to sulfur (region S2s) and are characterized for sulfur in sulfides (S^{2-} and S_2^{2-}) and sulfates (S^{6+}), respectively.

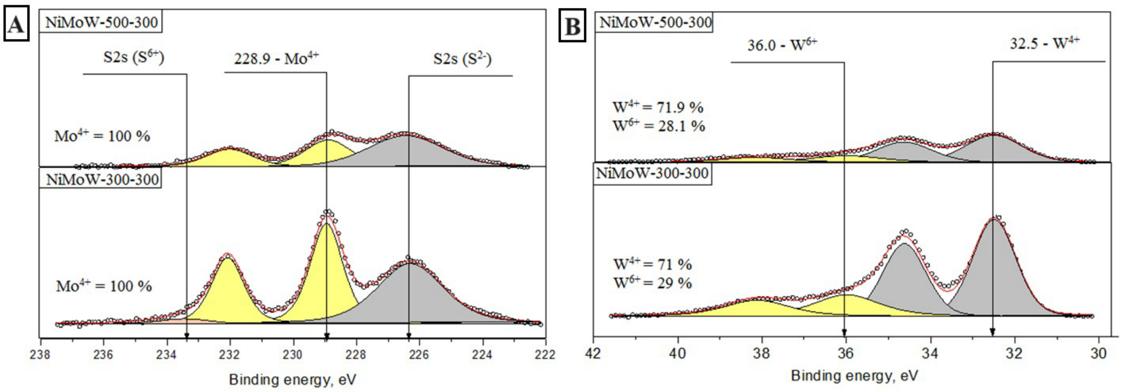

FIG. 12. Mo3d (A) and W4f (B) XPS spectra of the NiMoW-300-300 and NiMoW-500-300 catalysts after testing

TABLE 5. XPS data of studied catalysts

Parameter	NiMoW-300-300	NiMoW-500-300
Al – %	19.4	17.7
S – %	21.7	11.1
Mo – %	2.6	0.9
W – %	2.9	1.0
Ni – %	3.6	1.7
Mo/S	0.12	0.08
Ni/S	0.16	0.16
W/Mo	1.13	1.14

The surface concentration of tungsten is also lower in NiMoW-500-300 catalyst (1 %) than in NiMoW-300-300 (2.9 %) (Table 5, Fig. 12B). It can be caused by capsulation of tungsten during calcination of the precursor. W4f spectra of studied catalysts are decomposed by two doublets with binding energies $W4f_{7/2} \sim 32.5$ and 36.0 eV, respectively

(Fig. 12B). The peak with the binding energy ~ 32.5 eV can be assigned to tungsten in the W^{4+} state that is caused by the transition of WO_3 to WS_2 during sulfidation [59]. The fraction of W^{4+} from detected surface tungsten is 71.9 % in the NiMoW-300-300 catalyst and 71.0 % in the NiMoW-500-300 catalyst. The rest of tungsten is in the W^{6+} state (i.e. tunsten oxide) and is confirmed by the peak at ~ 36.0 eV [13,60].

The intensity of the Ni2p spectra was 2.1 times higher in the NiMoW-300-300 sample compared to NiMoW-500-300 (Fig. 13A). The $Ni2p_{3/2}$ spectra of both catalysts contain two peaks with the binding energies ~ 854.0 and ~ 856.2 eV. The peak at ~ 854.0 eV relates to the Ni^{2+} in NiMoS phase [61] and/or to trimetallic NiMoWS phase [13]. The fraction of nickel in these phases is more than 80 % in both catalysts. However, the amount of NiMoS phase in NiMoW-300-300 catalyst is much higher considering the surface concentration of nickel. The peak at 856.2 eV is specific for the Ni^{2+} in NiO that is confirmed by the presence of intensive satellite at $\sim 861 – 862$ eV [61].

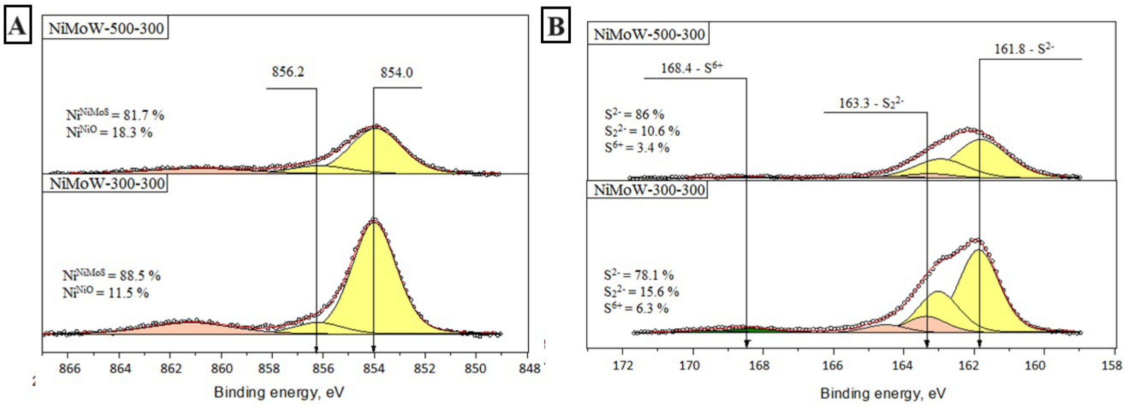

FIG. 13. Ni2p (A) and S2p (B) XPS spectra of the NiMoW-300-300 and NiMoW-500-300 catalysts after testing

The S2p XPS spectra of studied samples contain the $S2p_{3/2}$ peak with the binding energy at 168.4 eV (Fig. 13B). The surface sulfur concentration is also significantly higher in the NiMoW-300-300 catalyst than in the NiMoW-500-300 sample (Table 5). It is the feature of the S^{6+} in sulfates SO_4^{2-} [62]. In the range of lower binding energy values there are two doublets with the binding energy at 161.8 and ~ 163.3 eV. They are characteristic for sulfides like S^{2-} and S_2^{2-}, respectively [62–64]. The ratio of S^{2-} to S_2^{2-} increases with calcination temperature of the precursor as well as there is the decrease in sulfate sulfur.

Summarizing the XPS data it was noted that an increase in the precursor calcination temperature from 300 to 500 leads to a decrease in the number of surface atoms of active metals. The NiMoW-300-300 catalyst is the best in the content of the most active form of Ni, Mo and W. The higher calcination temperature results in the formation of more oxide forms of active metals possibly due to the removal of citric acid residuals. Moreover, there is the decrease in the ratio of active metals to the binding component – alumina, which could indirectly indicate the aggregation of active metals.

4. Conclusion

The present work studies the effect of calcination temperature of the precursor on physico-chemical properties of bulk NiMoW catalysts. According to thermal analysis and plasticizing properties of the NiMoW precursor, three calcination temperatures were chosen – 300, 450 and 500 °C.

It is found that calcination of the precursor at 300 °C results in the formation of X-ray amorphous NiMoW precursor that is likely caused by incomplete decomposition of citric acid and its transformation into amorphous carbon. XRD patterns of the catalysts with calcination temperature 450 and 500 °C demonstrate reflexes from nickel molybdate, individual nickel and tungsten oxides and nickel tungstate. These data are also confirmed by UV-Vis spectra, which show the increase of crystallization degree of nickel molybdate and molybdenum oxide as well as the decrease of the amount of carbon containing compounds. It makes it difficult to convert pseudoboehmite into alumina.

The influence of calcination temperature of the precursor on textural properties of the related bulk catalysts is not obvious. When temperature is 300 or 450 °C, there is the decrease in the specific surface area and pore volume of the catalysts that is likely caused by decomposition of citric acid and other transformations of the precursor compounds formed during plasticizing with nitric acid and by possible sintering of the obtained oxides. On the contrary, the increase in precursor's calcination temperature to 500 °C results in the increase in textural characteristics of granulated catalyst due to its re-structurization. Despite the improved textural properties, the bulk catalyst prepared from the Ni–Mo–W precursor calcined at 500 °C did not demonstrate high activity in hydrotreating of SRVGO. The most active catalyst in hydrotreatment of SRVGO was the one prepared from the precursor calcined at 300 °C.

Investigation of the sulfide catalysts showed that after granulation of the catalysts some part of active metals reacted with the alumina binding agent and formed “Ni–Mo–S”-like particles. The other part was presented in the form of various bulk species, individual or mixed. The increase in calcination temperature from 300 to 500 °C resulted in the increase in the formation of more amount of bulk nickel sulfides and capsulation of Mo and W which were rounded by nickel atoms. According to the XPS analysis data, it led to the decrease in the number of active metals in their most active sulfide forms. The catalysts with higher calcination temperature of the precursor or granules contain more active metals in the oxide form.

Appendix

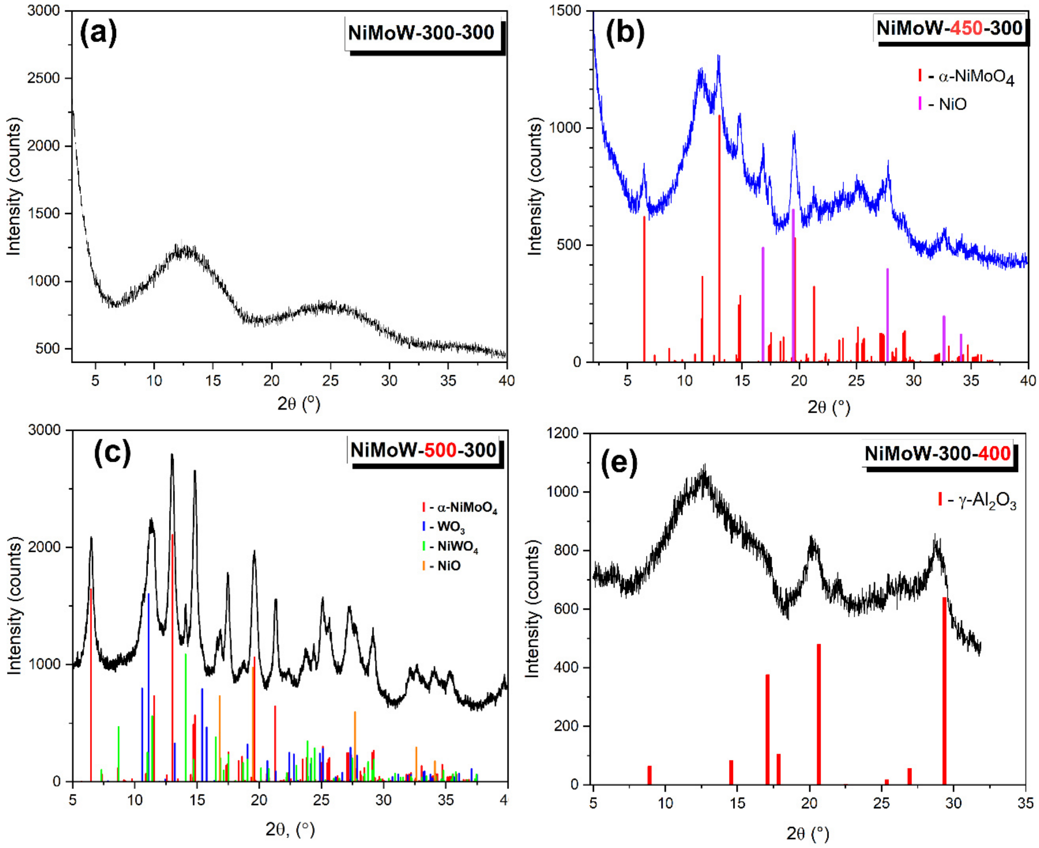

FIG. A1. XRD data of granulated catalyst with different precursor calcination temperature and catalysts calcination temperature

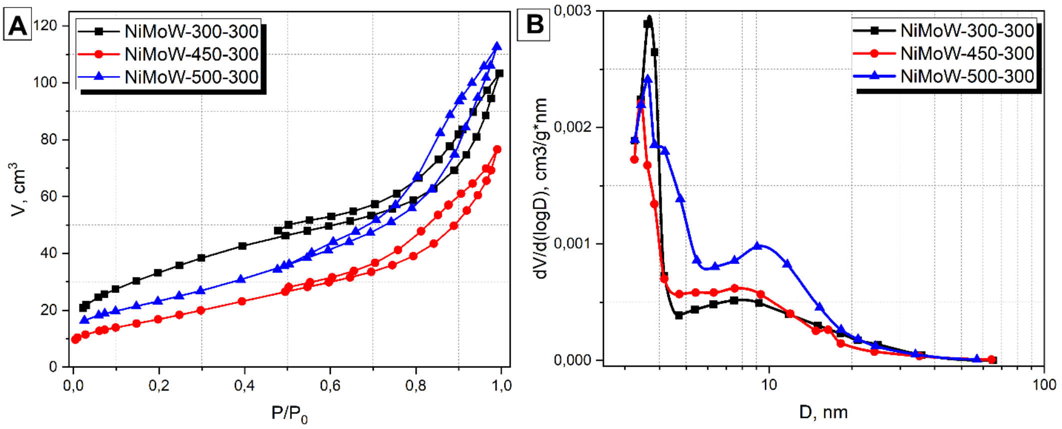

FIG. A2. Nitrogen adsorption-desorption isotherms and pore size distribution curves for granulated calcined catalysts

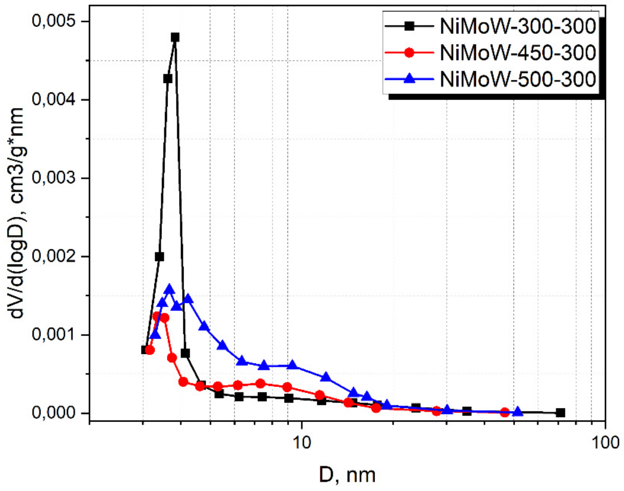

FIG. A3. Pore size distribution curves for sulfided catalysts after reaction

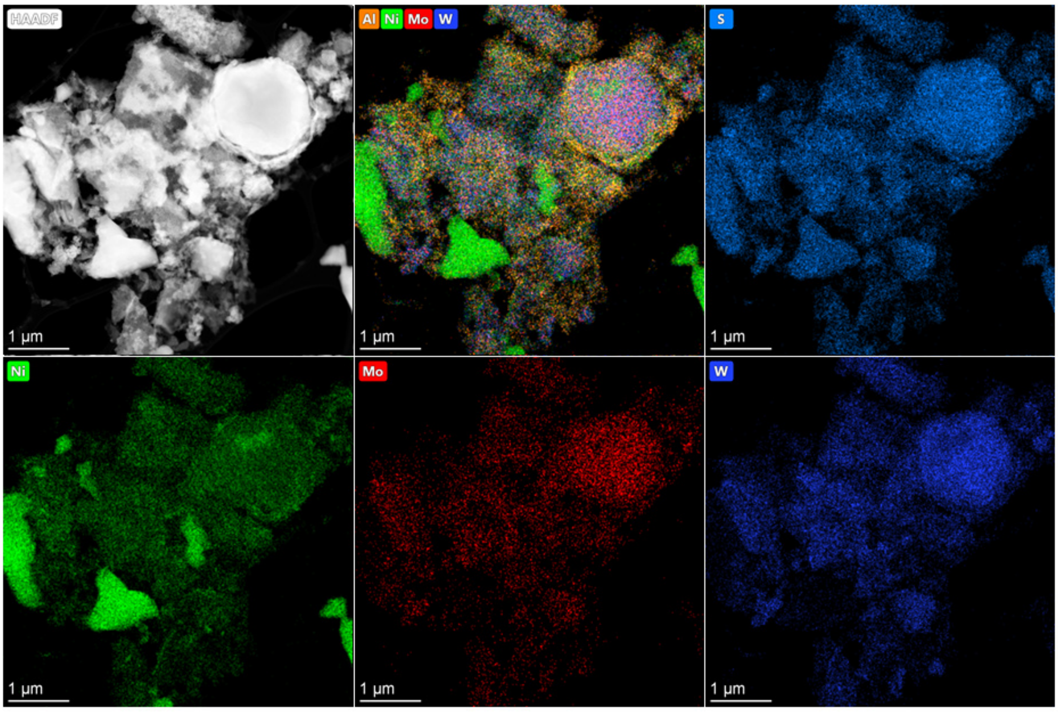

FIG. A4. HAADF data on the NiMoW-450-300 catalyst before testing

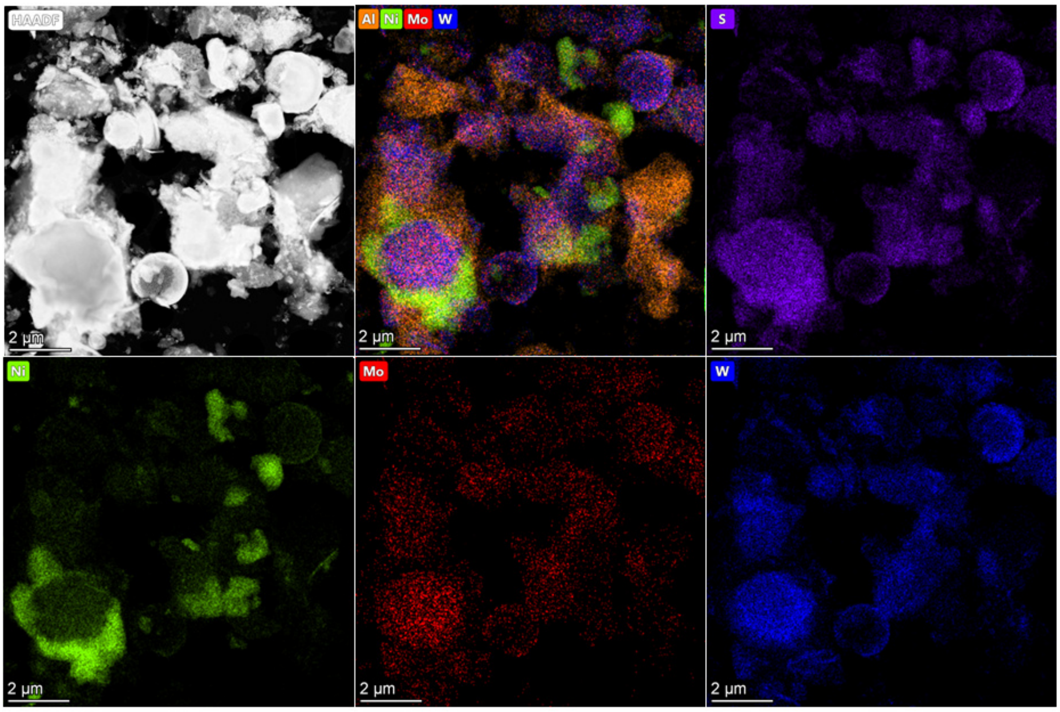

FIG. A5. HAADF data on the NiMoW-500-300 catalyst before testing

References

[1] Tanimu A., Alhooshani K. Advanced Hydrodesulfurization Catalysts: A Review of Design and Synthesis. *Energy and Fuels*, 2019, **33**, P. 2810–2838.

[2] Díaz de León J.N., Ramesh Kumar C., Antúnez-García J., Fuentes-Moyado S. Recent Insights in Transition Metal Sulfide Hydrodesulfurization Catalysts for the Production of Ultra Low Sulfur Diesel: A Short Review. *Catalysts*, 2019, **9**, 87.

[3] Topsøe H., Clausen B.S., Candia R., Wivel C., Mørup S. In situ Mössbauer emission spectroscopy studies of unsupported and supported sulfided Co-Mo hydrodesulfurization catalysts: Evidence for and nature of a Co–Mo–S phase. *J. Catal.*, 1981, **68**, P. 433–452.

[4] Lauritsen J.V., Kibsgaard J., Olesen G.H., Moses P.G., Hinnemann B., Helveg S., Nørskov J.K., Clausen B.S., Topsøe H., Lægsgaard E., Besenbacher F. Location and coordination of promoter atoms in Co- and Ni-promoted MoS_2-based hydrotreating catalysts. *J. Catal.*, 2007, **249**, P. 220–233.

[5] Plantenga F.L., Cerfontain R., Eijsbouts S., Houtert F., Anderson G.H., Miseo S., Soled S., Riley K., Fujita K., Inoue Y. "NEBULA": A hydroprocessing catalyst with breakthrough activity. *Stud. Surf. Sci. Catal.*, 2003, **145**, P. 407–410.

[6] Eijsbouts S., Plantenga F., Leliveld B., Inoue Y., Fujita K. STARS and NEBULA – New Generations of Hydroprocessing Catalysts for the Production of Ultra Low Sulfur Diesel. *Prepr. Symp. – Am. Chem. Soc., Div. Fuel Chem.*, 2003, **48**, P. 494–495.

[7] Thomazeau C., Geantet C., Lacroix M., Danot M., Harlé V., Raybaud P. Predictive approach for the design of improved HDT catalysts: γ-Alumina supported (Ni, Co) promoted $Mo_{1-x}W_xS_2$ active phases. *Appl. Catal. A Gen.*, 2007, **322**, P. 92–97.

[8] Cervantes-Gaxiola M.E., Arroyo-Albiter M., Pérez-Larios A., Balbuena P.B., Espino-Valencia J. Experimental and theoretical study of NiMoW, NiMo, and NiW sulfide catalysts supported on an AlTiMg mixed oxide during the hydrodesulfurization of dibenzothiophene. *Fuel*, 2013, 113, P. 733–743.

[9] Krebs E., Silvi B., Daudin A., Raybaud P. A DFT study of the origin of the HDS/HydO selectivity on Co(Ni)MoS active phases. *J. Catal.*, 2008, **260**, P. 276–287.

[10] Shan S., Liu H., Yue Y., Shi G., Bao X. Trimetallic WMoNi diesel ultra-deep hydrodesulfurization catalysts with enhanced synergism prepared from inorganic–organic hybrid nanocrystals. *J. Catal.*, 2016, **344**, P. 325–333.

[11] Varakin A.N., Mozhaev A.V., Pimerzin A.A., Nikulshin P.A. Comparable investigation of unsupported MoS_2 hydrodesulfurization catalysts prepared by different techniques: Advantages of support leaching method. *Appl. Catal. B Environ.*, 2018, **238**, P. 498–508.

[12] Yin C., Dong C., Kong Y., Li K., Zhang H., Liu D., Liu C. Effects of Aging Treatment on the Hydrotreating Performance of the Unsupported Catalyst. *Ind. & Eng. Chem. Res.*, 2019, **58**, P. 2683–2688.

[13] Nadeina K.A., Budukva S.V., Vatutina Y.V., Mukhacheva P.P., Gerasimov E.Y., Pakharukova V.P., Prosvirin I.P., Larina T.V., Klimov O.V., Noskov A.S., Atuchin V.V. Optimal Choice of the Preparation Procedure and Precursor Composition for a Bulk Ni–Mo–W Catalyst. *Inorganics*, 2023, **11**, 89.

[14] Mukhacheva P.P., Vatutina Y.V., Nadeina K.A., Budukva S.V., Pakharukova V.P., Danilova I.G., Panafidin M.A., Klimov O.V., Noskov A.S. Effects of Heat Treatment Temperature on the Physicochemical Properties and Catalytic Performance of Bulk Ni–Mo–W Catalysts. *Pet. Chem.*, 2023, **63**, P. 1302–1310.

[15] Wang L., Zhang Y., Zhang Y., Jiang Z., Li C. Ultra-Deep Hydrodesulfurization of Diesel Fuels on Trimetallic NiMoW Sulfide Catalysts. *Chem. – A Eur. J.*, 2009, **15**, P. 12571–12575.

[16] Chowdari R.K., Díaz de León J.N., Fuentes-Moyado S. Effect of sulfidation conditions on the unsupported flower-like bimetallic oxide microspheres for the hydrodesulfurization of dibenzothiophene. *Catal. Today*, 2022, **394–396**, P. 13–24.

[17] Ouyang X., Kuperman A. Multi-metallic bulk hydroprocessing catalysts, Patent 2022269376, 2021.

[18] Liu H., Yin C., Liu B., Li X., Li Y., Chai Y., Liu C. Effect of Calcination Temperature of Unsupported NiMo Catalysts on the Hydrodesulfurization of Dibenzothiophene. *Energy & Fuels*, 2014, **28**, P. 2429–2436.

[19] Yang C., Hu A., Dai Q., Yang Q., Hou R., Liu Z. Study on the Performance of Ni–MoS_2 Catalysts with Different MoS_2 Structures for Dibenzothiophene Hydrodesulfurization. *ACS Omega*, 2023, **8**, P. 41182–41193.

[20] Nadeina K.A., Budukva S.V., Vatutina Y.V., Mukhacheva P.P., Gerasimov E.Y., Pakharukova V.P., Klimov O.V., NoskovA.S. Unsupported Ni–Mo–W Hydrotreating Catalyst: Influence of the Atomic Ratio of Active Metals on the HDS and HDN Activity. *Catalysts*, 2022, **12**, 1671.

[21] Danilevich V.V., Nadeina K.A., Gerasimov E.Y., Shefer K.I., Klimov O.V., Noskov A.S. Synthesis and characterization of lanthanum-modified pseudoboehmite – The precursor of alumina supports and catalysts. *Microporous Mesoporous Mater.*, 2022, **335**, 111800.

[22] Thommes M., Kaneko K., Neimark A.V., Olivier J.P., Rodriguez-Reinoso F., Rouquerol J., Sing K.S.W. Physisorption of gases, with special reference to the evaluation of surface area and pore size distribution (IUPAC Technical Report). *Pure Appl. Chem.*, 2015, **87**, P. 1051–1069.

[23] Moulder J.F. *Handbook of X-ray Photoelectron Spectroscopy*, Physical Electronics Division, Perkin-Elmer Corporation, 1992.

[24] Scofield J.H. Hartree-Slater subshell photoionization cross-sections at 1254 and 1487 eV. *J. Electron Spectros. Relat. Phenomena*, 1976, **8**, P. 129–137.

[25] Gajbhiye N.S., Balaji G. Synthesis, reactivity, and cations inversion studies of nanocrystalline $MnFe_2O_4$ particles. *Thermochim. Acta*, 2002, **385**, P. 143–151.

[26] Bocher L., Aguirre M.H., Robert R., Trottmann M., Logvinovich D., Hug P., Weidenkaff A. Chimie douce synthesis and thermochemical characterization of mesoporous perovskite-type titanate phases. *Thermochim. Acta*, 2007, **457**, P. 11–19.

[27] Rajendran M., Rao M.S. Formation of $BaTiO_3$ from Citrate Precursor. *J. Solid State Chem.*,1994, **113**, P. 239–247.

[28] Rajendran M., Rao S.M. Synthesis and characterization of barium bis(citrato) oxozirconate(IV) tetrahydrate: A new molecular precursor for fine particle $BaZrO_3$. *J. Mater. Res.*, 1994, **9**, P. 2277–2284.

[29] Kovács T.N., Hunyadi D., de Lucena A.L.A., Szilágyi I.M. Thermal decomposition of ammonium molybdates. *J. Therm. Anal. Calorim.*, 2016, **124**, P. 1013–1021.

[30] Fait M.J.G., Lunk H.-J., Feist M., Schneider M., Dann J.N., Frisk T. Thermal decomposition of ammonium paratungstate tetrahydrate under non-reducing conditions: Characterization by thermal analysis, X-ray diffraction and spectroscopic methods. *Thermochim. Acta*, 2008, **469**, P. 12–22.

[31] Hunyadi D., Sajó I., Szilágyi I.M. Structure and thermal decomposition of ammonium metatungstate. *J. Therm. Anal. Calorim.*, 2014, **116**, P. 329–337.

[32] Marafi M., Stanislaus A. Influence of catalyst acidity and feedstock quality on hydrotreating catalyst deactivation by coke deposition. *Pet. Sci. Technol.*, 2001, **19**, P. 697–710.

[33] Dychalska A., Popielarski P., Franków W., Fabisiak K., Paprocki K., Szybowicz M. Study of CVD diamond layers with amorphous carbon admixture by Raman scattering spectroscopy. *Mater. Sci.*, 2015, **33**.

[34] Guichard B., Roy-Auberger M., Devers E., Rebours B., Quoineaud A.A., Digne M. Characterization of aged hydrotreating catalysts. Part I: Coke depositions, study on the chemical nature and environment. *Appl. Catal. A Gen.*, 2009, **367**, P. 1–8.

[35] González-Cortés S.L., Qian Y., Almegren H.A., Xiao T., Kuznetsov V.L., Edwards P.P. Citric acid-assisted synthesis of γ-alumina-supported high loading CoMo sulfide catalysts for the hydrodesulfurization (HDS) and hydrodenitrogenation (HDN) reactions. *Appl. Petrochemical Res.*, 2015, **5**, P. 181–197.

[36] Tian H., Roberts C.A., Wachs I.E. Molecular Structural Determination of Molybdena in Different Environments: Aqueous Solutions, Bulk Mixed Oxides, and Supported MoO_3 Catalysts. *J. Phys. Chem. C*, 2010, **114**, P. 14110–14120.

[37] Goetze J., Meirer F., Yarulina I., Gascon J., Kapteijn F., Ruiz-Martínez J., Weckhuysen B.M. Insights into the Activity and Deactivation of the Methanol-to-Olefins Process over Different Small-Pore Zeolites As Studied with Operando UV-vis Spectroscopy. *ACS Catal.*, 2017, **7**, P. 4033–4046.

[38] Ross-Medgaarden E.I., Wachs I.E. Structural Determination of Bulk and Surface Tungsten Oxides with UV-vis Diffuse Reflectance Spectroscopy and Raman Spectroscopy. *J. Phys. Chem. C*, 2007, **111**, P. 15089–15099.

[39] Garbarino G., Riani P., Infantes-Molina A., Rodríguez-Castellón E., Busca G. On the detectability limits of nickel species on NiO/γ-Al_2O_3 catalytic materials. *Appl. Catal. A Gen.*, 2016, **525**, P. 180–189.

[40] Jeziorowski H., Knoezinger H. Raman and ultraviolet spectroscopic characterization of molybdena on alumina catalysts. *J. Phys. Chem.*, 1979, **83**, P. 1166–1173.

[41] da Silva V.L.S., Frety R., Schmal M. Activation and Regeneration of a NiMo/Al_2O_3 Hydrotreatment Catalyst. *Ind. Eng. Chem. Res.*, 1994, **33**, P. 1692–1699.

[42] Romanova T.S., Nadeina K.A., Danilova I.G., Danilevich V.V., Pakharukova V.P., Gabrienko A.A., Glazneva T.S., Gerasimov E.Y., Prosvirin I.P., Vatutina Y.V., Kazakov M.O., Klimov O.V., Noskov A.S. Modification of HDT catalysts of FCC feedstock by adding silica to the kneading paste of alumina support: Advantages and disadvantages. *Fuel*, 2022, **324**, 124555.

[43] Mohamed M.M., Ahmed S.A., Khairou K.S. Unprecedented high photocatalytic activity of nanocrystalline WO_3/$NiWO_4$ hetero-junction towards dye degradation: Effect of template and synthesis conditions. *Appl. Catal. B Environ.*, 2014, **150–151**, P. 63–73.

[44] Leonova K.A., Klimov O.V., Kochubey D.I., Chesalov Y.A., Gerasimov E.Y., Prosvirin I.P., Noskov A.S. Optimal pretreatment conditions for Co–Mo hydrotreatment catalysts prepared using ethylenediamine as a chelating agent. *Catal. Today*, 2014, **220–222**, P. 327–336.

[45] Bukhtiyarova G.A., Klimov O.V., Kochubey D.I., Noskov A.S., Pashigreva A.V. EXAFS study of oxide precursors of the high active Co–Mo hydrotreating catalysts: Effect of drying conditions. *Nucl. Instruments Methods Phys. Res. Sect. A Accel. Spectrometers, Detect. Assoc. Equip.*, 2009, **603**, P. 119–121.

[46] Courty P., Ajot H., Marcilly C., Delmon B. Oxydes mixtes ou en solution solide sous forme très divisée obtenus par décomposition thermique de précurseurs amorphes. *Powder Technol.*, 1973, **7**, P. 21–38.

[47] Leonova K.A., Klimov O.V., Kochubey D.I., Chesalov Y.A., Gerasimov E.Y., Prosvirin I.P., Noskov A.S. Optimal pretreatment conditions for Co–Mo hydrotreatment catalysts prepared using ethylenediamine as a chelating agent. *Catal. Today*, 2014, **220–222**, P. 327–336.

[48] Guzmán-Castillo M.L., Bokhimi X., Toledo-Antonio A., Salmones-Blásquez J., Hernández-Beltrán F. Effect of Boehmite Crystallite Size and Steaming on Alumina Properties. *J. Phys. Chem. B*, 2001, **105**, P. 2099–2106.

[49] Boumaza A., Favaro L., Lédion J., Sattonnay G., Brubach J.B., Berthet P., Huntz A.M., Roy P., Tétot R. Transition alumina phases induced by heat treatment of boehmite: An X-ray diffraction and infrared spectroscopy study. *J. Solid State Chem.*, 2009, **182**, P. 1171–1176.

[50] Liu Q., Wang A., Wang X., Zhang T. Mesoporous γ-alumina synthesized by hydro-carboxylic acid as structure-directing agent. *Microporous Mesoporous Mater.*, 2006, **92**, P. 10–21.

[51] Tichit D., El Alami D., Figueras F. Influence of the Preparation and of the Activation Treatments on the Catalytic Activity of Mechanical Mixtures of Sulfated Zirconia and Pt/Al_2O_3. *J. Catal.*,1996, **163**, P. 18–27.

[52] Ozkan U., Schrader G.L. $NiMoO_4$ selective oxidation catalysts containing excess MoO_3 for the conversion of C_4 hydrocarbons to maleic anhydride: I. Preparation and characterization. *J. Catal.*,1985, **95**, P. 120–136.

[53] Pampararo G., Garbarino G., Ardoino N., Riani P., Busca G. A study of molybdena catalysts in ethanol oxidation. Part 1. Unsupported and silica-supported MoO_3. *J. Chem. Technol. Biotechnol.*, 2021, **96**.

[54] Horsley J.A., Wachs I.E., Brown J.M., Via G.H., Hardcastle F.D. Structure of surface tungsten oxide species in the tungsten trioxide/alumina supported oxide system from x-ray absorption near-edge spectroscopy and Raman spectroscopy. *J. Phys. Chem.*, 1987, **91**, P. 4014–4020.

[55] Busca G. Differentiation of mono-oxo and polyoxo and of monomeric and polymeric vanadate, molybdate and tungstate species in metal oxide catalysts by IR and Raman spectroscopy. *J. Raman Spectrosc.*, 2002, **33**, P. 348–358.

[56] Mukhacheva P.P., Vatutina Y.V., Nadeina K.A., Budukva S.V., Panafidin M.A., Pakharukova V.P., Parfenov M.V., Gerasimov E.Y., Klimov O.V., Noskov A.S. Comparison of the HDS DBT Reaction Using Bulk and Supported Catalysts. *Chim. Techno Acta*, 2024, **11**, 202411206.

[57] Saih Y., Segawa K. Catalytic activity of CoMo catalysts supported on boron-modified alumina for the hydrodesulphurization of dibenzothiophene and 4.6-dimethyldibenzothiophene. *Appl. Catal. A Gen.*, 2009, **353**, P. 258–265.

[58] Okamoto Y., Nakano H., Shimokawa T., Imanaka T., Teranishi S. Stabilization effect of Co for Mo phase in Co-$MoAl_2O_3$ hydrodesulfurization catalysts studied with X-Ray photoelectron spectroscopy. *J. Catal.*, 1977, **50**, P. 447–454.

[59] Ben Tayeb K., Lamonier C., Lancelot C., Fournier M., Payen E., Bonduelle A., Bertoncini F. Study of the active phase of NiW hydrocracking sulfided catalysts obtained from an innovative heteropolyanion based preparation. *Catal. Today*, 2010, **150**, P. 207–212.

[60] Orsini G., Tricoli V. Facile nonhydrolytic sol–gel route to mesoporous mixed-conducting tungsten oxide. *J. Mater. Chem.*, 2011, **21**, P. 14530–14542.

[61] Lorenz M., Schulze M. XPS analysis of electrochemically oxidized nickel surfaces. *J. Anal. Chem.*, 1999, **365**, P. 154–157.

[62] Kazakova M.A., Kuznetsov V.L., Bokova-Sirosh S.N., Krasnikov D.V., Golubtsov G.V., Romanenko A.I., Prosvirin I.P., Ishchenko A.V., Orekhov A.S., Chuvilin A.L., Obraztsova E.D. Fe–Mo and Co–Mo Catalysts with Varying Composition for Multi-Walled Carbon Nanotube Growth. *Phys. Status Solidi*, 2018, **255**, 1700260.

[63] Klimov O.V., Nadeina K.A., Vatutina Y.V., Stolyarova E.A., Danilova I.G., Gerasimov E.Y., Prosvirin I.P., NoskovA.S. CoMo/Al_2O_3 hydrotreating catalysts of diesel fuel with improved hydrodenitrogenation activity. *Catal. Today*, 2018, **307**, P. 73–83.

[64] Bremmer G.M., van Haandel L., Hensen E.J.M., Frenken J.W.M., Kooyman P.J. The effect of oxidation and resulfidation on (Ni/Co)MoS_2 hydrodesulfurisation catalysts. *Appl. Catal. B Environ.*, 2019, **243**, P. 145–150.

Submitted 29 July 2024; revised 2 October 2024; accepted 7 November 2024

Information about the authors:

Ksenia A. Nadeina – Boreskov Institute of Catalysis SB RAS, Pr. Lavrentieva 5, 630090 Novosibirsk, Russia;
ORCID 0000-0003-2671-5146; lakmallow@catalysis.ru

Yuliya V. Vatutina – Boreskov Institute of Catalysis SB RAS, Pr. Lavrentieva 5, 630090 Novosibirsk, Russia;
ORCID 0000-0001-8898-9762; y.vatutina@catalysis.ru

Polina P. Mukhacheva – Boreskov Institute of Catalysis SB RAS, Pr. Lavrentieva 5, 630090 Novosibirsk, Russia;
ORCID 0000-0002-5005-0781; mpp@catalysis.ru

Sergey V. Budukva – Boreskov Institute of Catalysis SB RAS, Pr. Lavrentieva 5, 630090 Novosibirsk, Russia;
ORCID 0000-0001-7450-3960; zsm@catalysis.ru

Irina G. Danilova – Boreskov Institute of Catalysis SB RAS, Pr. Lavrentieva 5, 630090 Novosibirsk, Russia;
ORCID 0000-0003-1476-9825; danig@catalysis.ru

Vera P. Pakharukova – Boreskov Institute of Catalysis SB RAS, Pr. Lavrentieva 5, 630090 Novosibirsk, Russia;
ORCID 0000-0001-8808-0161; verapakharukova@yandex.ru

Evgeniy Yu. Gerasimov – Boreskov Institute of Catalysis SB RAS, Pr. Lavrentieva 5, 630090 Novosibirsk, Russia;
ORCID 0000-0002-3230-3335; gerasimov@catalysis.ru

Maxim A. Panafidin – Boreskov Institute of Catalysis SB RAS, Pr. Lavrentieva 5, 630090 Novosibirsk, Russia;
ORCID 0000-0001-6897-7692; mpanafidin@catalysis.ru

Oleg V. Klimov – Boreskov Institute of Catalysis SB RAS, Pr. Lavrentieva 5, 630090 Novosibirsk, Russia;
ORCID 0000-0002-8089-2357; klm@catalysis.ru

Conflict of interest: the authors declare no conflict of interest.

NANOSYSTEMS:
PHYSICS, CHEMISTRY, MATHEMATICS

Original article

Korotkova N.A., et al. *Nanosystems: Phys. Chem. Math.*, 2024, **15** (6), 855–866.
http://nanojournal.ifmo.ru
DOI 10.17586/2220-8054-2024-15-6-855-866

Development of spectral methods for the analysis of nanocized ferrogarnets of the $Y_{3-x}Ce_xFe_{5-y}Ga_yO_{12}$ composition

Natalia A. Korotkova[1,a], Alexandra A. Arkhipenko[1,b] , Maria N. Smirnova[1,c], Vasilisa B. Baranovskaya[1,d], Marina S. Doronina[1,e], Valerii A. Ketsko[1,f], Galina E. Marina[1,g]

[1]Kurnakov Institute of General and Inorganic Chemistry of the Russian Academy of Sciences, Moscow, Russia

[a]natalya.korotkova.95@mail.ru, [b]alexandra622@mail.ru, [c]smirnovamn@igic.ras.ru, [d]baranovskaya@list.ru, [e]ms.semenova@gmail.com, [f]ketsko@igic.ras.ru, [g]gelim@mail.ru

Corresponding author: N. A. Korotkova, natalya.korotkova.95@mail.ru

---

PACS 81.07.Wx, 62.20.Qp, 78.20.-e

ABSTRACT The study and development of yttrium-iron garnets are in demand and promising when creating materials for integrated optics and magnetic microelectronics. The authors synthesized nanosized cerium-substituted yttrium-iron-gallium garnet of the composition $Y_{3-x}Ce_xFe_{5-y}Ga_yO_{12}$ (where x = 0.4 – 0.5, and y = 2.4 – 2.6), which is characterized by improved magnetic and optical properties. However, the efficiency of applying this material directly depends on the chemical purity of the source materials, as well as the elemental composition of the intermediate and final products. In this regard, the development of multi-element, selective and accurate methods of analysis is an urgent task. As a result of the studies, methods for spectral analysis of cerium-substituted yttrium-iron-gallium garnet were developed. The conditions for determining target analytes (Mg, Al, Si, Ca, Sc, Cr, Mn, Fe, Co, Ni, Cu, Zn, Ga, Se, Y, Cd, Sn, Te, La, Ce, Pr, Nd, Sm, Eu, Gd, Tb, Dy, Ho, Er, Tm, Yb, Lu, Pb) in the materials in question were studied and established using X-ray fluorescence spectrometry (XRF), arc atomic emission spectrometry (AAES) and inductively coupled plasma mass spectrometry (ICP-MS). Approaches to reducing and eliminating the main spectral and non-spectral interferences in the methods studied were proposed. A comprehensive complementary approach to the analytical control of garnets of the $Y_{3-x}Ce_xFe_{5-y}Ga_yO_{12}$ composition was developed, which ensures high accuracy and reliability of the results, and allows one to expand the nomenclature of target analytes and the boundaries of the determined contents.

KEYWORDS yttrium-iron-gallium garnet, X-ray fluorescence spectrometry, arc atomic emission spectrometry, inductively coupled plasma mass spectrometry, analysis.

ACKNOWLEDGEMENTS This research was performed using the equipment of the JRC PMR IGIC RAS and JRC of GIREDMET. This work was supported by the Ministry of Science and Higher Education of the Russian Federation as part of the State Assignment of the Kurnakov Institute of General and Inorganic Chemistry of the Russian Academy of Sciences.

FOR CITATION Korotkova N.A., Arkhipenko A.A., Smirnova M.N., Baranovskaya V.B., Doronina M.S., Ketsko V.A., Marina G.E. Development of spectral methods for the analysis of nanocized ferrogarnets of the $Y_{3-x}Ce_xFe_{5-y}Ga_yO_{12}$ composition. *Nanosystems: Phys. Chem. Math.*, 2024, **15** (6), 855–866.

---

1. Introduction

One of the promising and rapidly developing directions in modern materials science is the development of functional materials for integrated optics and magnetic microelectronics. Ferrogarnets have been progressed among the materials with the necessary magnetic and optical properties [1]. Cerium containing yttrium ferrogranates have the best characteristics in terms of the combination of optical, magneto-optical activity and magneto-optical quality factor [1–6].

However, due to the large ionic radius of Ce^{3+} (1.14 Å) ferrogarnet of the hypothetical elemental composition – $Ce_3Fe_5O_{12}$ does not exist in the form of ceramics and single crystals [7, 8]. Because of this fact, the possibility of obtaining single-phase cerium-substituted ferrogarnets with the maximum possible Ce^{3+} content is of particular relevance, for example, by replacing part of the Y^{3+} ions in $Y_3Fe_5O_{12}$ with Ce^{3+} [7–11]. Such materials were obtained in a number of studies [12–14]. At the same time, the Ce^{3+} content in garnet in these studies, according to X-ray diffraction (XRD), did not reach 8 wt. %, for example, $Ce_{0.122}Y_{2.878}Fe_5O_{12}$ [12–14].

The authors previously obtained a single-phase ferrogarnet with an increased Ce content – $Y_{2.5}Ce_{0.5}Fe_{2.5}Ga_{2.5}O_{12}$ [7]. The Ce^{3+} content in the material was increased by annealing $Y_{2.5}Ce_{0.5}Fe_{2.5}Ga_{2.5}O_{12}$ in a vacuum and replacing some of the Fe^{3+} ions with Ga^{3+}. The introduction of Ga^{3+} ions into the composition together with Ce^{3+} enabled to compensate for structural limitations and contributed to the stabilization of $Y_{2.5}Ce_{0.5}Fe_{2.5}Ga_{2.5}O_{12}$ [7].

It is noteworthy that while developing materials for integrated optics, the presence of impurity elements (Mg, Al, Si, Ca, Sc, Cr, Mn, Co, Ni, Cu, Zn, Se, Cd, Sn, Te, La, Pr, Nd, Sm, Eu, Gd, Tb, Dy, Ho, Er, Tm, Yb, Lu, Pb) and a disturbance of the matrix and alloying component ratio (Fe, Ga, Y, Ce) can lead to a decrease in the magnetic and optical properties of the final product [15–19]. In this regard, analytical control of ferrogarnets is necessary at all stages of its production. Spectral methods, namely X-ray fluorescence (XRF), arc atomic emission (AAES) and inductively coupled plasma mass spectrometry (ICP-MS), are promising for solving this task. The analytical methods listed have high accuracy, sensitivity and versatility [20–34]. XRF has a wide range of detectable concentrations and is prospective to express control of the matrix and alloying component ratio in the process of developing and producing complex materials [23–26]. The advantages of AAES method are the possibility of simultaneous determination of a large number of elements, high sensitivity and the absence of the need to dissolve the sample [20–22]. ICP-MS is one of the most widely used methods to determine low levels of trace elements in sample solutions. The advantages of ICP-MS include high sensitivity, a wide range of contents being determined, the possibility of using universal standard solutions to construct a calibration curve and verify the result accuracy [27–34]. Accordingly, the use of XRF, AAES and ICP-MS methods is promising for allowing for the control of the target composition of complex materials, including cerium-substituted yttrium-iron-gallium garnet.

However, the presented methods (XRF, AAES, ICP-MS) have a number of limitations. Namely, spectral and non-spectral interference of various types [20–34]. The overlapping of analyte signals is primarily highlighted. This problem is especially acute when analyzing materials containing rare earth elements (REE) as the main ones. This problem is solved by conducting a set of studies aimed at a detailed study of the obtained spectra and the influence of the analysis conditions on the intensity and stability of the signal of the analytes determined, and searching for an approach to considering the background signal and constructing a calibration dependence [20–34].

This article is devoted to the development of approaches to reducing and eliminating various types of interference in XRF, AAES and ICP-MS analysis of nanosized ferrogarnets of the composition $\mathrm{Y}_{3-x}\mathrm{Ce}_x\mathrm{Fe}_{5-y}\mathrm{Ga}_y\mathrm{O}_{12}$ (x = 0.4–0.5, y = 2.4–2.6).

2. Experimental part

2.1. Materials

Synthesis of $\mathrm{Y}_{3-x}\mathrm{Ce}_x\mathrm{Fe}_{5-y}\mathrm{Ga}_y\mathrm{O}_{12}$($x$ = 0.4–0.5, y = 2.4–2.6) was carried out by gel combustion [7]. For this purpose, stoichiometric amounts of high-purity yttrium carbonate ($Y_2(CO_3)_3{\cdot}3H_2O$), cerium nitrate ($Ce(NO_3)_3$), carbonyl iron (Fe) and metallic gallium (Ga) were dissolved in dilute nitric acid (HNO_3 – 70 %). Then polyvinyl alcohol $[–CH_2CH(OH)–]_n$ (PVA) was added to the resulting solution, based on the calculation of 0.12 mol PVA per 0.01 mol ferrite, as well as ammonium nitrate (NH_4NO_3) in the amount of 0.12 mol per 0.01 mol ferrite. The reaction mixtures were evaporated in a reactor at 90°C with constant stirring until they became gels.

As the temperature increased above 100°C, the gels burnt into finely dispersed yellow-beige powders. After cooling, the powders were dispersed using a ball mill and annealed at 750°C in a furnace for 5 hours at a pressure of $\approx 1{\cdot}10^{-2}$ Pa. This mode of heat treatment was due to the need to exclude the possibility of Ce^{3+} cation oxidation.

2.2. Methods

X-ray diffraction was performed using a Bruker D8 Advance diffractometer (BrukerOptik Gmb H, Germany). The following operating parameters were used to obtain the results: a radiation – CuKα, an angle range 2θ = 10°–70°, a scanning step – 0.0133° and a counting time of 0.3 sec per step.

The morphology of the powders was performed using scanning electron microscopy (SEM) on a TESCAN AMBER GMH device (Tescan, Czech Republic).

To primarily determine the ratio of the matrix and alloying components in the material, XRF analysis method was used. A wavelength-dispersive X-ray fluorescence spectrometer SPECTROSCAN MAX GVM (Spectron Ltd., St. Petersburg, Russian Federation) was performed (Table 1). Quantitative determination was carried out using the fundamental parameters method (FPM).

TABLE 1. Instrumental operating conditions of the X-ray fluorescence spectrometer

Element	Analytical Line	Wavelength, nm	Crystal analyzer	Reflection Order	Exposure Time, sec	Tube Current, mÅ
Fe	Kβ	0.1757	LiF200	1	10	0.5
Ga	Kβ	0.1208	LiF200	1	10	0.5
Y	Kα	0.0830	LiF200	1	10	0.1
Ce	Lα	0.2561	LiF200	1	10	1.5

Arc atomic emission spectrometry and inductively coupled plasma mass spectrometry were performed to determine target impurity elements.

The studies into the analysis conditions of arc atomic emission method were carried out on a high-resolution spectrometer Grand-Globula (VMK-Optoelectronics, Russian Federation) (Table 2).

TABLE 2. Instrumental operating conditions of the arc atomic emission spectrometer

Current type	Direct
Current strength,Å	15
Configuration of the lower graphite electrode	Electrode with a neck below the bottom of the crater (“glass”)
The thickness of the walls of the lower electrode is not more than, mm	1
Configuration of the upper graphite electrode	Cone 60°
Mass ratio of the sample to the graphite powder	5:1
Carrier	NaCl
Distance between the upper and lower electrodes, mm	3
Exposure time, sec	60
Analytical lines of elements being determined, nm	Mg 277.98, 285.21; Al 266.04, 309.27; Si 288.16, 243.52; Ca 317.93; Cr 284.98, 301.49; Mn 279.48; Co 242.49, 340.92; Ni 225.38; 305.08; Cu 240.67; Zn 213.86; Se 206.28; Cd 226.50; Sn 224.61, 242.17; Te 214.28, 238.58; La 338.09; Pr 316.37; Nd 430.36; Sm 442.43; Eu 281.39; Cd 301.01; Tb 332.44; Dy 317.00, 340.78; Ho 311.85, 345.60; Er 339.20; Tm 313.13; Yb 328.94; Lu 261.54, 291.14; Pb 244.62, 261.42

ICP-MS analysis conditions were studied using a NexION® 1000 spectrometer (PerkinElmer, USA) (Table 3).

Inductively coupled plasma optical-emission spectrometry (ICP-OES) was used as a control method. Earlier we studied and selected the conditions for analyzing the material under examination using ICP-OES method [35].

2.3. Sample preparation

Before conducting XRF analysis, the sample was pressed on a boric acid substrate using a PLG-12 laboratory hydraulic press (LabTools, Russian Federation). The pressure did not exceed 100 bar. The mass of the nanocrystalline ferrogarnet powder sample was (0.50 ± 0.01 g). The resulting pellet was placed in an aluminum holder, pressed with a polyurethane foam sealant and secured with a lid.

Graphite electrodes used in AAES method were made of graphite rods with a diameter of 6 mm (AO Karbotek, Russian Federation), and ready-made electrodes of the “glass” shape (AO Karbotek, Russian Federation) were also applied. Graphite electrodes were prepared by means of a Krater-2M device (VMK-Optoelectronics, Russian Federation). The sample was diluted with graphite powder, pure in terms of target impurities (AO Karbotek, Russian Federation). High-purity sodium chloride (NaCl); sodium fluoride (NaF); elemental sulfur (S); potassium chloride (KCl); germanium oxide (GeO) were used as carriers. Reference samples to plot the calibration curve were made of high purity iron (Fe_3O_4), yttrium (Y_2O_3), gallium (Ga_2O_3), and cerium (CeO_2) oxides in a ratio of 2.5:2.5:2.5:1, which were then mixed with graphite powder with a known content of the impurities being determined.

High-purity nitric (HNO_3 – 70%) and hydrochloric (HCl – 35–38%) acids were used for sample preparation for ICP-MS and ICP-OES analysis. All dissolutions and dilutions were conducted by means of deionized water with a resistivity of 18.2 MΩ cm at 25°C. Aqueous calibration solutions for ICP-MS and ICP-OES were prepared from multi-element and single-element standard solutions (High-Purity Standards, USA) by serial dilution to different volumes with a 2 % HNO_3 mixture. The calibration dependence in ICP-MS method was constructed by means of multielement solutions with concentrations of the analytes being determined of 1–100 μg/L, and in the ICP-OES method of 0.1–100 mg/L for Mg,

TABLE 3. Instrumental operating conditions of the mass spectrometer

Forward power, W	1300
Coolant gas flow, L·min^{-1}	15
Auxiliary gas flow, L·min^{-1}	12
Nebulizer gas flow, L·min^{-1}	0.95
Sample flow rate, rpm	30
Sampling depth, relative units	0
Helium flow rate, mL·min^{-1}	6.5
Level of oxide ions, %	< 2
Level of doubly charged ions, %	< 1.5
Measurement mode	Peak hopping
Pneumatic nebulizer	Meinhard, PerkinElmer
Spray chamber	Quartzconical, Peltiercooled
Isotopes of elements being determined, m/z	$^{24/25}$Mg, ^{27}Al, ^{29}Si, ^{42}Ca, ^{45}Sc, $^{52/53}$Cr, ^{55}Mn, ^{59}Co, ^{62}Ni, ^{63}Cu, ^{68}Zn, ^{82}Se, $^{111/112}$Cd, ^{117}Sn, ^{125}Te, ^{139}La, ^{141}Pr, $^{145/146}$Nd,$^{147/149}$Sm, ^{151}Eu, ^{160}Gd, ^{159}Tb, $^{161/162}$Dy, ^{165}Ho, $^{167/168}$Er, ^{169}Tm, $^{172-174}$Yb, ^{175}Lu, $^{207/208}$Pb
Internal standard	^{103}Rh, ^{115}In

Al, Si, Ca, Sc, Cr, Mn, Co, Ni, Cu, Zn, Se, Cd, Sn, Te, La, Pr, Nd, Sm, Eu, Gd, Tb, Dy, Ho, Er, Tm, Yb, Lu, Pb; and 10–500 mg/L for Fe, Ga, Y, Ce.

The decomposition of the samples was carried out using a MARS6 microwave autoclave system with microwave heating (CEM Corp., USA) and Easy-PrepiWave vessels (CEM Corp., USA). The dissolution was performed using previously established conditions, namely, using an acid mixture (5 ml H_2O, 2 ml HNO_3, 5 HCl) and a temperature-time program (hold time – 30 min, hold temperature – 220°C). The decomposition method was estimated for a sample weight of 0.1 g [35].

3. Results and discussion

3.1. Materials

According to the results of XRD, after synthesis and annealing in vacuum, the particle size of $Y_{3-x}Ce_xFe_{5-y}Ga_yO_{12}$ was $\sim$100 nm, the phase composition was homogeneous.

Fig. 1 shows a SEM-image of $Y_{2.5}Ce_{0.5}Fe_{2.4}Ga_{2.6}O_{12}$ powder. The powder is seen not to have any heterogeneous formations. The particles themselves are characterized by unimodality, and the crystallite growth faces are clearly expressed. The particle size is $\sim$100 nm.

3.2. X-ray fluorescence analysis

The studies into the XRF conditions of multicomponent materials, such as cerium-doped yttrium ferrogarnet, are aimed at increasing the selectivity of the signal of the elements being determined to achieve the required accuracy of the analysis results (RSD $\leq$ 10%). It is necessary to control the ratio and uniformity of the matrix and alloying element distribution in the sample, which are fundamental indicators in the development and production of garnets. It is particularly difficult to achieve the required accuracy indicators when using the FPM. Despite its advantage – the absence of standardization, it can be difficult to achieve the required metrological indicators, which needs a competent choice of analysis conditions.

The algorithm for studying and selecting the XRF conditions includes a number of operating parameters of the spectrometer (Fig. 2).

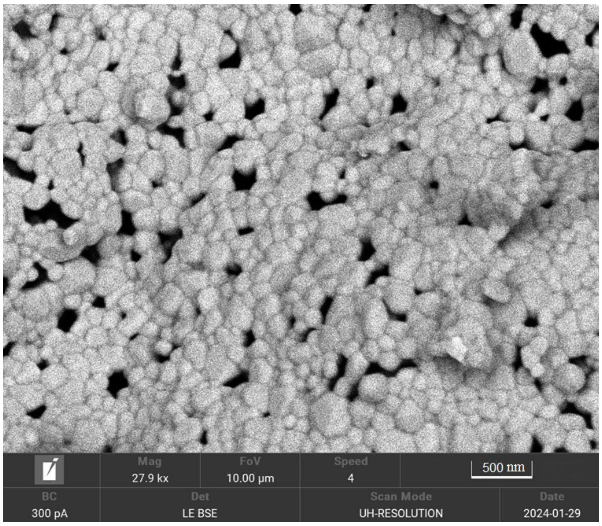

FIG. 1. SEM-image of the obtained particles of yttrium-iron garnet ($Y_{2.5}Ce_{0.5}Fe_{2.4}Ga_{2.6}O_{12}$)

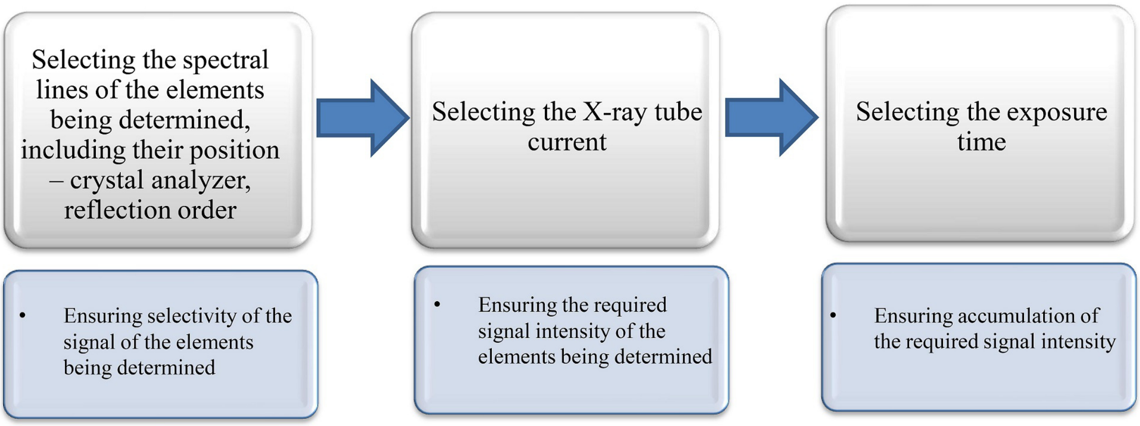

FIG. 2. Methodological approach to the selection of the XRF conditions

First, it is necessary to select the spectral lines of the elements being determined. While selecting analytical lines, one must focus on the absence of spectral interference from matrix and impurity elements on the signal of target analytes, as well as the ability to assess the noise level near the lines being studied. The SPECTROSCAN MAX-GVM spectrometer is equipped with four analyzer crystals (LiF200, PET, RbAP, C002) with different values of inter-planar distances, which allows optimizing the conditions to determine elements in different wavelength ranges and to establish the most optimal and overlap-free lines. Each analyzer crystal has 2 reflection orders.

To select the spectral lines of Fe, Ga, Y and Ce, the spectral line atlas embedded in the instrument software was used, with it taking into account the overlaps of all the elements being determined. Fig. 3 shows the spectrum of the $Y_{2.5}Ce_{0.5}Fe_{2.5}Ga_{2.5}O_{12}$ sample, recorded using the LiF200 crystal analyzer in the first reflection order. To determine the target elements, the lines recorded using this crystal analyzer were selected, since they are the least susceptible to mutual overlaps. The selected lines of elements being determined are presented in Table 1.

The criterion for selecting the X-ray tube current and exposure time is the fulfillment of the condition: [Signal intensity] $\times$ [Exposure time] $\leq$ 300.000 pulses. This rule is due to the detector capabilities, since too high current leads to its failure. The exposure time should be sufficient for signal accumulation, but not too long, in order to avoid unnecessary interference and reduce the analysis time. We were faced with the task of determining the main and alloying components; in order to prevent the detector overload and the spectrometer failure. While determining Fe, Ga, Y and Ce, the effect of the current near the lower limit of the range – from 0.1 to 3.5 mÅ and the exposure time – from 10 to 50 sec was studied. For Fe and Ga, the currents selected were 0.5 mÅ, for Y – 0.1 mÅ (such low currents are due to the high intensities of the selected spectral lines), and for Ce – 1.5 mÅ. The exposure time for all elements was 10 sec (Table 1).

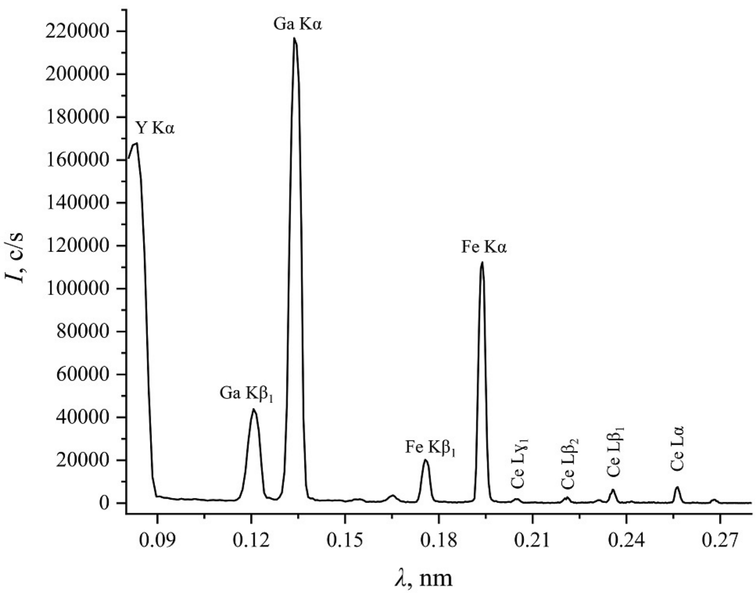

FIG. 3. XRF spectrum of $Y_{2.5}Ce_{0.5}Fe_{2.5}Ga_{2.5}O_{12}$ sample

3.3. Arc atomic emission analysis

The study of arc atomic emission analysis (AAEA) conditions is aimed at ensuring selectivity, intensity (I) and stability of the signal of the elements to be determined. In the light of this, a number of analysis conditions were studied to develop AAES to determine target impurities in cerium-doped yttrium ferrogarnets (Fig. 4).

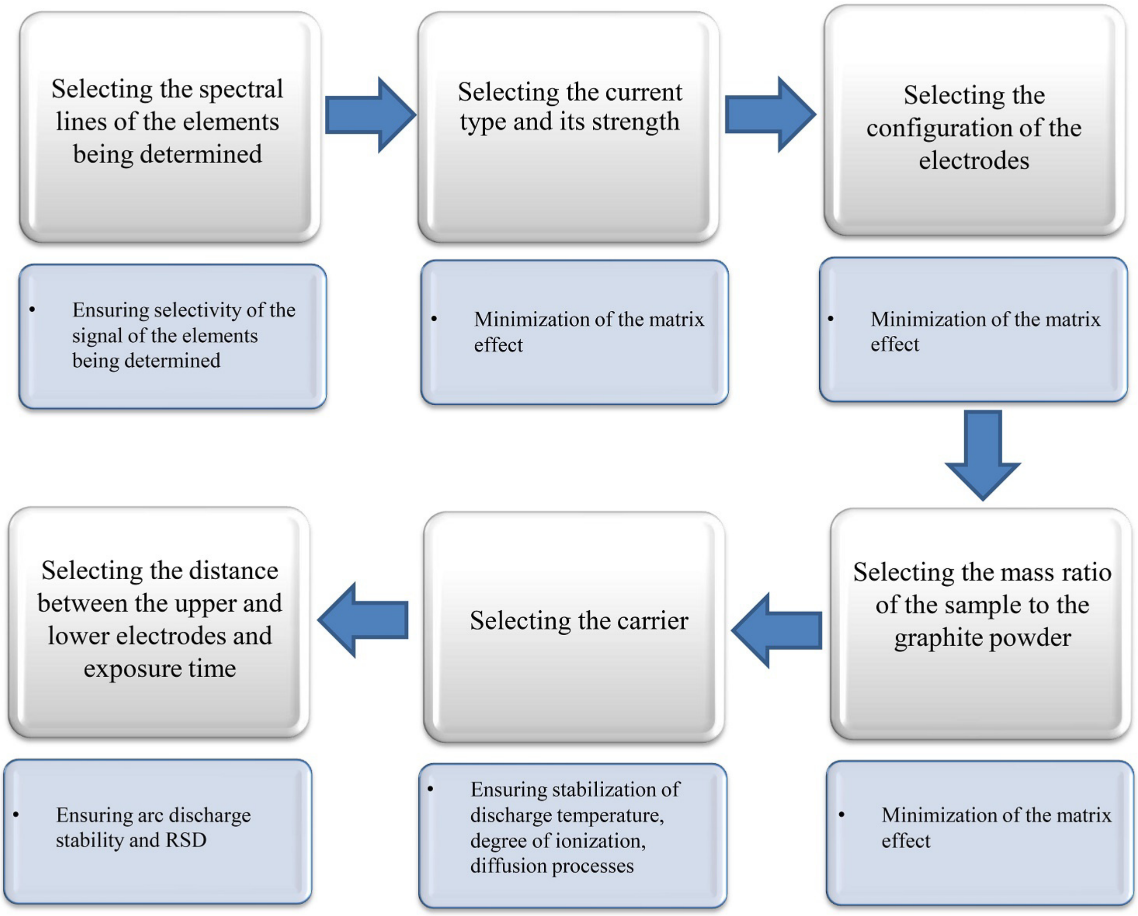

FIG. 4. Methodological approach to the selection of conditions for AAEA

Selecting the analytical lines of the elements being determined is based on the sample composition. Analytical lines are usually selected from the most sensitive lines of the spectrum; these include lines with the lowest excitation potential values. A large number of sensitive lines of rare earth elements are located in the range of 250–350 nm. The most sensitive lines of rare earth elements are in the range of 300–450 nm. The atlas of spectral lines and the signal/noise ratio were used to select the lines. In cases where it was not possible to select a line free of spectral overlaps, the contribution of spectral interference to the signal intensity of the analyte being determined was taken into account using software. The selected analytical lines are presented in Table 2.

One of the most important factors influencing the processes of evaporation, atomization and excitation of elements is the current type and its strength. The current shape, its polarity and intensity have a direct effect on the evaporation of the analytes being determined and the resulting spectrum. Given this, the behavior of the impurities being determined was studied under conditions of direct, alternating and intermittent current. In addition, the current strength was varied from 5 to 20Å. The best result was obtained with a direct positive current of 15Å.

The shape and size of graphite electrodes affect the flow of the sample into the arc plasma. The configuration of the electrode used allows one to set the temperature in the arc cloud and, accordingly, the evaporation rate of impurities. REE are slowly evaporating substances. In the volatility series, they are located at the end of the series together with low-volatile metals. Therefore it is reasonable to use electrodes with a narrow constriction below the bottom of the recess (configuration of the lower graphite electrode is “glass”) with thin walls (up to 1 mm) (Fig. 5).

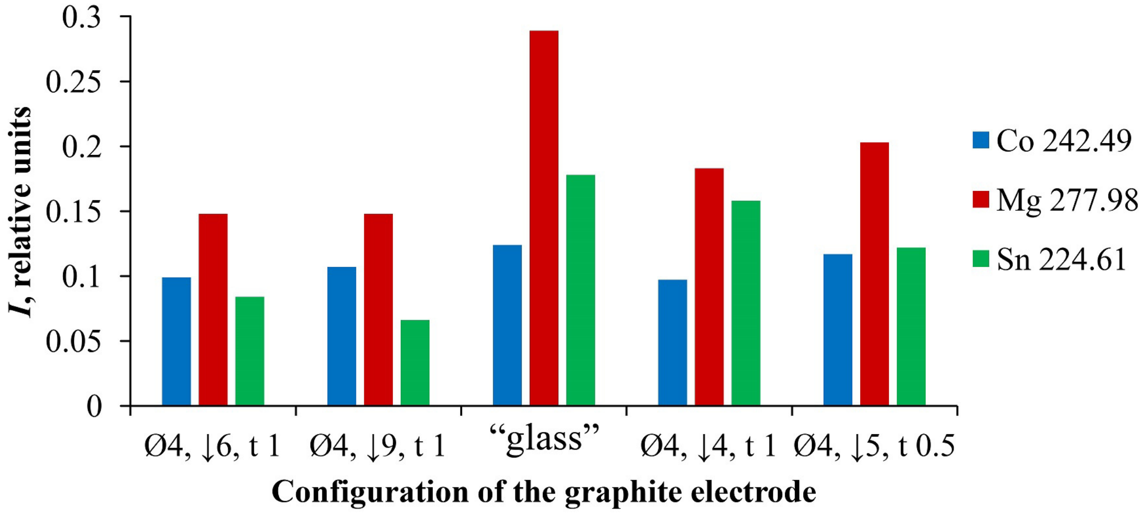

FIG. 5. Selection of an electrode for the determination of target impurities in nanosized yttrium-iron-gallium garnets (↓ — crater depth, mm; Ø — diameter, mm; t — crater wall thickness, mm)

The configuration of the upper graphite electrode of a cone 60° was chosen, since the discharge is more stable and is evenly distributed over the entire working surface of the electrode during the arc burning process.

To ensure robust conditions to determine target impurities, the analyzed sample was mixed with graphite powder (g.p.) in a certain ratio. This minimized the matrix effect. However, if the dilution is too great, the signal intensity of the analytes decreases. Therefore, it is necessary to select the optimal mass ratio of the sample to the g.p. Studies on selecting the mass ratio of the sample to the g.p. showed that the most optimal ratio is 5:1.

To stabilize the discharge temperature, the degree of elements ionization and diffusion processes in a direct or alternating current arc, special chemically active additives (carriers) – were introduced into the sample. Their introduction into the arc cloud led to an increase in the conductivity of the arc plasma column, caused a decrease in the voltage between the electrodes and a decrease in the voltage gradient in the arc plasma column, which in turn led to a decrease in the temperature in the plasma and an increase in the electron concentration [36, 37]. All these processes resulted in an increase in the intensities of the lines being determined and an increase in the sensitivity of the method. In this work, NaCl showed the best result as a carrier for target impurities.

The distance between the upper and lower electrodes (inter-electrode distance) can be varied to achieve the most stable sample burnout. The greater the inter-electrode distance, the higher the voltage on it, which helps to reduce the signal intensity of the analytes. This leads to the fact that the limits of detection and determination (LOD) of target elements increase. Reducing the length of the inter-electrode distance helps to spatially stabilize the discharge. It is important that the distance remains constant, otherwise the repeatability standard deviation (RSD) of the analysis results increases. An inter-electrode distance of 3 mm was chosen for all materials, since it was the most appropriate from the viewpoint of the stability of the plasma discharge during the arcing.

To control the exposure time, it is necessary to study the evaporation curves in detail. Since different elements evaporate at different rates, it is necessary to set the exposure time during which all impurities will completely evaporate. If the time is too long, a noise signal will accumulate; if it is too short, the sample or impurities in it will not have time to completely ionize. Given the chance, it is better to set an individual determination time for each element due to its different volatility. It was established that 60 sec is sufficient to determine all target impurities (Fig. 6).

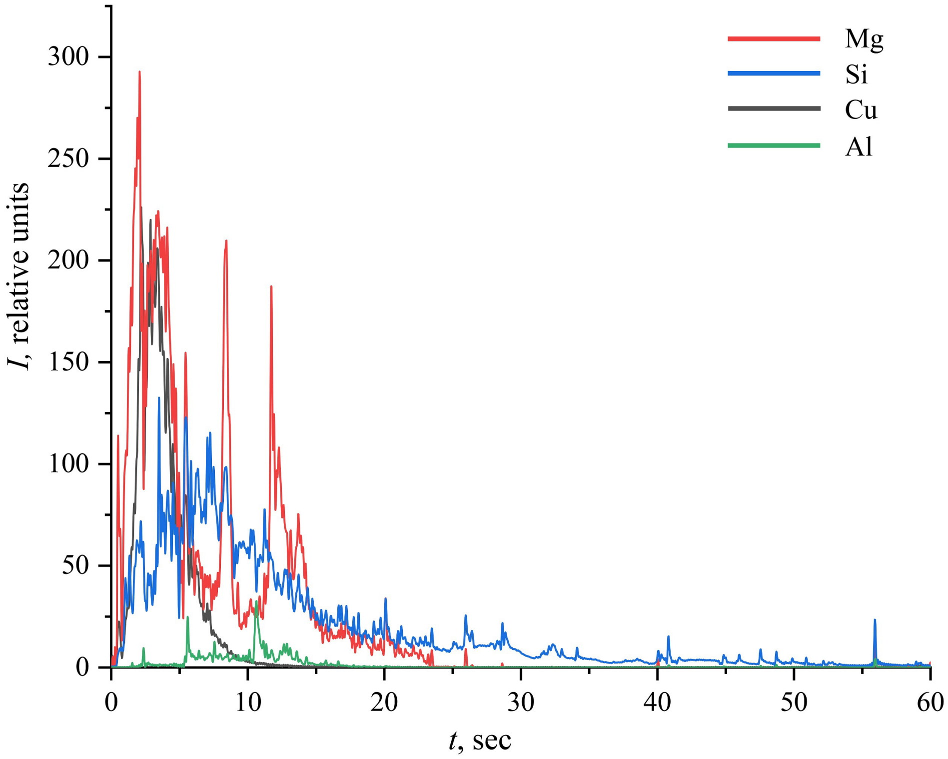

FIG. 6. Evaporation curves of Mg, Si, Cu, Al

The conditions of AAEA selected during the study are presented in Table 2. The use of these conditions (Table 2) provides the LOD of target impurity elements at the level of $3.0{\cdot}10^{-6}$–$6.0{\cdot}10^{-4}$ wt. %.

3.4. Inductively coupled plasma mass spectrometry analysis

The study of the ICP-MS conditions is aimed at minimizing the matrix effect, ensuring selectivity and signal intensity of target analytes. A number of analysis conditions were accordingly studied to develop ICP-MS to determine target impurities in cerium-doped yttrium ferrogarnets (Fig. 7).

Selecting the isotopes of the elements being determined in ICP-MS is justified by the complex composition of cerium-substituted yttrium iron garnets. The presence of several matrix elements (Fe, Ga, Y, Ce) leads to the formation of a large number of polyatomic ($^{n}M^{1}H^{+}$, $^{n}M^{12/13}C^{+}$, $^{n}M^{14/15}N^{+}$, $^{n}M^{16}O^{+}$, $^{n}M^{16}O^{1}H^{+}$) and doubly charged ($^{n}M^{++}$) ions. The formation of these ions in plasma causes an increase in the signal intensity of a number of target analytes and, accordingly, to an increase in their LOD (Table 4).

The greatest influence on the LOD was exerted by oxide and hydroxide ions ($^{n}Ce^{16}O^{+}$, $^{n}Ce^{16}O^{1}H^{+}$) formed from Ce (Table 4). This resulted in a significant increase in the apparent concentration for elements such as Gd and Tb, which was a prerequisite for studying the effect of the He consumption rate in the collision cell in their determination. The isotopes of the target analytes selected for analysis are given in Table 3.

The matrix effect was expressed as the suppression of the signal intensity of the elements being determined with increasing concentration of the matrix element [33]. Several complementary approaches were used to minimize the matrix effect: dilution of the analyzed solutions, introduction of an internal standard, selection of the operating parameters of the spectrometer (nebulizer gas flow, voltage on the extractor lens, provided that it is present in the optical system of the spectrometer) [29]. The nebulizer gas flow in the study varied in the range of 0.6–1.2 L·min^{-1}. The minimum matrix effect and maximum analytical signals for most elements were obtained at nebulizer gas flow of 0.95 L·min^{-1}. The level of doubly charged ions did not exceed 2.0 %. Fig. 8 shows the dependence of the signal intensity of the elements characterizing the mass scale (^{25}Mg, ^{65}Cu, ^{137}Ba, ^{232}Th) on the concentration of the main elements simulating the composition of the material ($Y_{2.5}Ce_{0.5}Fe_{2.5}Ga_{2.5}O_{12}$). The magnitude of the matrix effect was estimated as I_i/I_0, where I_i is the signal intensity of the analyte isotope in a solution with the main elements (0–500 μg/ml matrix), I_0 is the signal

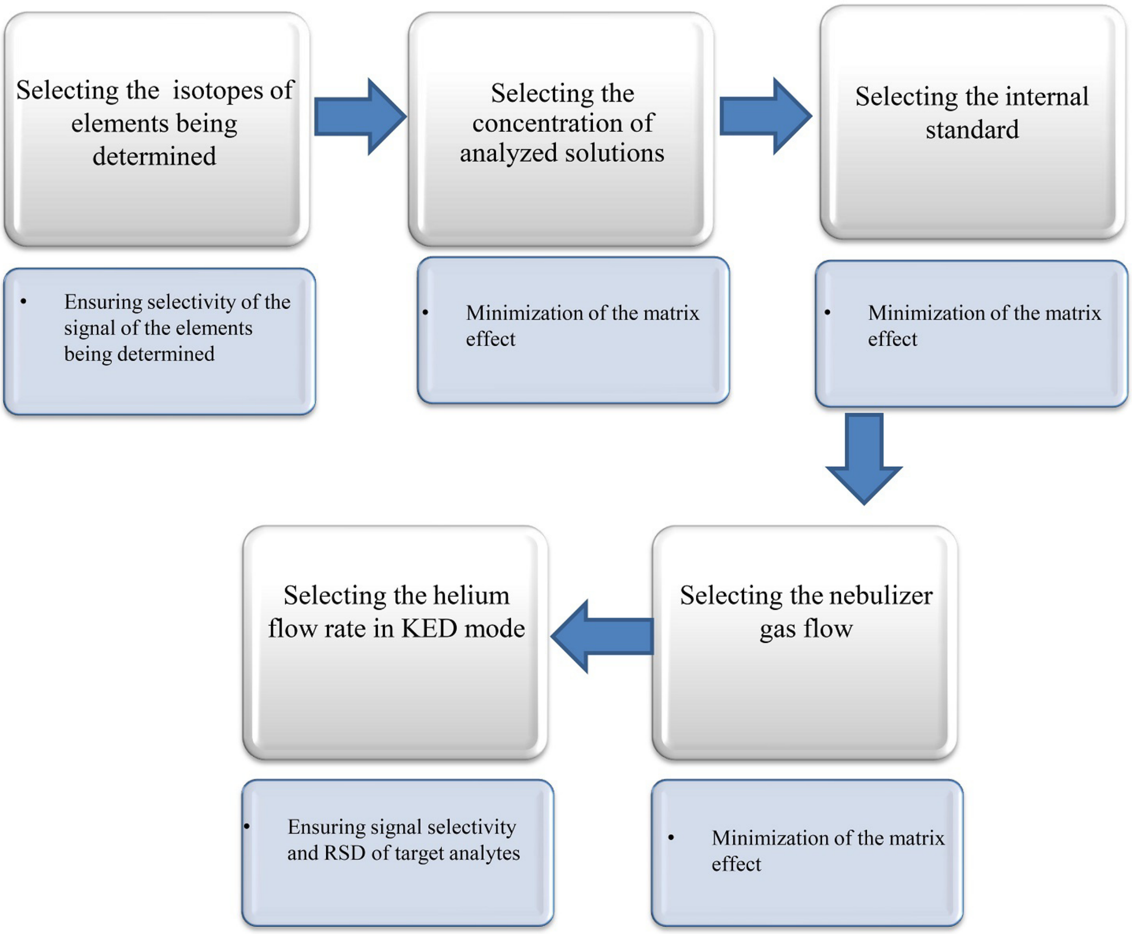

FIG. 7. Methodological approach to the selection of conditions for ICP-MS analysis

intensity of the element being determined in a pure nitric acid solution. ^{103}Rh and ^{115}In were used as internal standards to reduce the matrix effect (Fig. 8).

As can be seen in Fig. 8, both the introduction of two elements as an internal standard and a nebulizer gas flow of 0.95 L·min^{-1} lead to a noticeable reduction in the matrix effect, which allows for the analysis of more concentrated solutions (up to 500 mg/l).

One of the most common techniques to reduce the influence of polyatomic ions on the LOD of analytes is the use of a collision cell with an inert gas – He (KED mode). With that in mind, the effect of helium flow rate on the apparent concentration of ^{n}Ce^{16}O^{+}, ^{n}Ce^{16}O^{1}H^{+} ions was studied in determining of Gd and Tb in the KED mode. The studied solutions contained 500 mg/L of the main elements simulating the composition of $Y_{2.5}Ce_{0.5}Fe_{2.5}Ga_{2.5}O_{12}$. With an increase in a helium flow rate, the apparent concentration of ^{n}Ce^{16}O^{+}, ^{n}Ce^{16}O^{1}H^{+} ions was expected to decrease (Table 5).

The results showed that the optimal helium flow rate is 6.5 mL·min^{-1}. While using this helium flow rate, an order-of-magnitude decrease in the apparent concentration of ^{n}Ce^{16}O^{+}, ^{n}Ce^{16}O^{1}H^{+} ions was achieved.

The conditions of ICP-MS analysis selected during the study (Table 3) provide the LOD of target impurity elements at the level of $1\cdot10^{-6}$–$2.5\cdot10^{-3}$ wt. %.

3.5. The accuracy of the obtained results

The accuracy of the obtained results was confirmed using the added-found method and analysis of a sample by ICP-OES method using a previously developed technique [35]. For the added-found method, solutions containing 1.0, 10.0, and 50.0 μg/L of target impurity elements (Mg, Al, Si, Ca, Sc, Cr, Mn, Co, Ni, Cu, Zn, Se, Cd, Sn, Te, La, Pr, Nd, Sm, Eu, Gd, Tb, Dy, Ho, Er, Tm, Yb, Lu, Pb). The repeatability standard deviation for the target analytes in ICP-MS was 1–5 relative %, in DAES was 3–10 relative %, in XRF was 7–10 relative %.

The use of AAES and ICP-MS ensures control of the impurity composition of yttrium iron garnets in the ranges from $1\cdot10^{-6}$ to 1 wt. %. ICP-MS method has lower LOD for the determination of Sc ($2\cdot10^{-6}$ wt. %), Cr ($6\cdot10^{-6}$ wt. %), Ni ($8\cdot10^{-6}$ wt. %), Cu ($6\cdot10^{-6}$ wt. %), Zn ($6\cdot10^{-6}$ wt. %), Cd ($2\cdot10^{-6}$ wt. %), Te ($2\cdot10^{-6}$ wt. %), La ($2\cdot10^{-6}$ wt. %), Nd ($2\cdot10^{-6}$ wt. %), Sm ($2\cdot10^{-6}$ wt. %), Eu ($3\cdot10^{-6}$ wt. %), Ho ($2\cdot10^{-6}$ wt. %), Tm ($2\cdot10^{-6}$ wt. %), Yb ($1\cdot10^{-6}$ wt. %), Lu

TABLE 4. Polyatomic ions that interfere with the determination of target analytes in a solution containing 500 mg/L of main elements simulating the composition $Y_{2.5}Ce_{0.5}Fe_{2.5}Ga_{2.5}O_{12}$

Element	Isotop	Polyatomic Ion	Apparent Concentration of the Element,μg/L
Mn	^{55}Mn	$^{54}Fe^{1}H^{+}$	0.30
Co	^{59}Co	$^{58}Fe^{1}H^{+}$	0.48
Zn	^{66}Zn	$^{54}Fe^{12}C^{+}$	0.10
Pr	^{141}Pr	$^{140}Ce^{1}H^{+}$	1.20
Nd	^{143}Nd	$^{142}Ce^{1}H^{+}$	0.85
Sm	^{149}Sm	$^{136}Ce^{13}C^{+}$	0.04
	^{152}Sm	$^{136}Ce^{16}O^{+}$, $^{138}Ce^{14}N^{+}$, $^{140}Ce^{12}C^{+}$	36.5
	^{154}Sm	$^{138}Ce^{16}O^{+}$, $^{140}Ce^{14}N^{+}$, $^{142}Ce^{12}C^{+}$	57.0
Eu	^{151}Eu	$^{136}Ce^{15}N^{+}$	0.001
	^{153}Eu	$^{136}Ce^{16}O^{1}H^{+}$, $^{138}Ce^{13}C^{+}$, $^{138}Ce^{15}N^{+}$, $^{140}Ce^{13}C^{+}$	1.5
Gd	^{155}Gd	$^{138}Ce^{16}O^{1}H^{+}$, $^{140}Ce^{15}N^{+}$	0.60
	^{156}Gd	$^{140}Ce^{16}O^{+}$, $^{142}Ce^{14}N^{+}$	3583
	^{157}Gd	$^{140}Ce^{16}O^{1}H^{+}$, $^{142}Ce^{15}N^{+}$	1982
	^{158}Gd	$^{142}Ce^{16}O^{+}$	468
Tb	^{159}Tb	$^{142}Ce^{16}O^{1}H^{+}$	44.0

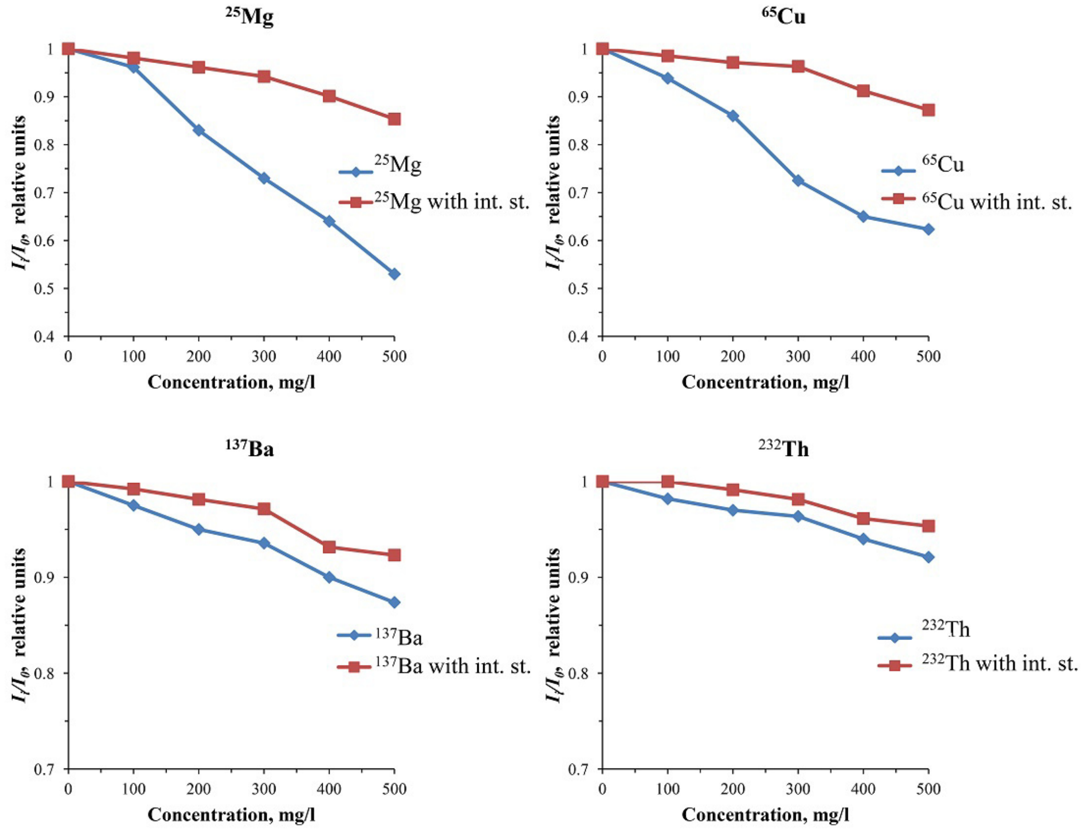

FIG. 8. Dependence of the signal intensity of the determined elements on the concentration of matrix elements in the solutio

TABLE 5. Apparent concentration of the elements being determined depending on a helium flow rate

Isotop	Apparent Concentration of the Element, μg/L			
	He – 0 mL·min^{-1}	He –5.0 mL·min^{-1}	He –6.5 mL·min^{-1}	He –7.25 mL· min^{-1}
^{155}Gd	0.60	0.08	0.01	0.003
^{159}Tb	44.0	0.62	0.02	0.01

(4·10^{-6} wt. %). The use of AAES allowed one to reduce the LOD in determining of Si (5·10^{-4} wt. %), Mn (3·10^{-6} wt. %), Co (2·10^{-5} wt. %), Pr (8·10^{-5} wt. %), Tb (9·10^{-6} wt. %). AAES and ICP-MS have similar LOD for Mg (2·10^{-5} wt. %), Al (2·10^{-5} wt. %), Ca (1·10^{-4} wt. %), Se (4·10^{-4} wt. %), Sn (1·10^{-5} wt. %), Gd (1·10^{-5} wt. %), Dy (1·10^{-6} wt. %), Er (2·10^{-6} wt. %), Pb (2·10^{-6} wt. %). The joint use of the studied spectral methods ensures high accuracy and reliability of the results and allows for the expansion of the range of target analytes and the boundaries of the contents being determined.

4. Conclusions

The conditions of XRF, AAES and ICP-MS analysis of synthesized nanocrystalline cerium-substituted yttrium-iron-gallium garnets of the composition $Y_{3-x}Ce_xFe_{5-y}Ga_yO_{12}$ (where x = 0.4–0.5, and y = 2.4–2.6) were studied. Due to the optimization of the conditions of XRF, AAES and ICP-MS analysis, it was possible to improve the analytical characteristics in determining the target elements of the materials. In particular, the selected operating parameters of XRF (exposure time – 10 sec, tube current – 0.5–1.5 mÅ) enabled to achieve RSD less than 10 relative %. By the AAES determination of target impurity elements, the use of a “glass” shaped electrode, NaCl as a carrier, current strength of 15 Å, inter-electrode distance of 3 mm and a mass ratio of the sample to the graphite powder of 5:1 provided the best intensity and stability of the analyte signal, which allowed one to reduce the LOD to 3.0·10^{-6}–6.0·10^{-4} wt. % and RSD no more than 10 relative %. When determining Gd and Tb by ICP-MS, the use of helium flow rate of 6.5 mL·min^{-1} in the KED mode enabled to reduce the LOD for these elements by an order of magnitude. The use of two internal standards (^{103}Rh, ^{115}In) and nebulizer gas flow of 0.95 L·min^{-1} allowed for a minimal matrix effect when analyzing solutions with a concentration of up to 500 mg/l of the base, which ensured the LOD of 1·10^{-6}–2.5·10^{-3} wt. % and RSD 1–5 relative %. The combined use of AAES and ICP-MS methods ensured the LOD for target impurity elements at the level of n·10^{-6}–n·10^{-4} wt. %.

References

[1] Dehghani D.O., Shokrollahi H., Yang H. The enhancement of the Ce-solubility limit and saturation magnetization in the $Ce_{0.25}Bi_xPr_yY_{2.75-x-y}Fe_5O_{12}$ garnet synthesized by the conventional ceramic method. *Ceramics International*, 2020, **46**(3), P. 2709–2723.

[2] Shen T., Dai H., Song M., Liu H., Wei X. Structure and Magnetic Properties of Ce-Substituted Yttrium Iron Garnet Prepared by Conventional Sintering Techniques. *Journal of Superconductivity and Novel Magnetism*, 2017, **30**, P. 937–941.

[3] Jung H.K., Kim C.H., Hong A.-R., Lee S.H., Kim T.C., Jang H.S., Kim D.H. Luminescent and magnetic properties of cerium-doped yttrium aluminum garnet and yttrium iron garnet composites. *Ceramics International* 2019, **45**, P. 9846–9851.

[4] Hapishah A.N., Hamidon M.N., Syazwan M.M., Shafiee F.N. Effect of grain size on microstructural and magnetic properties of holmium substituted yttrium iron garnets ($Y_{1.5}Ho_{1.5}Fe_5O_{12}$), *Results in Physics*, 2019, **14**, P. 102391.

[5] Gota T., Onbasli M.C., Kim D.H., Singh V., Inoue M., Kimerling L.C., Ross C.A. A nonreciprocal racetrack resonator based on vacuum-annealed magnetooptical cerium-substituted yttrium iron garnet. *Optics Express*, 2014, **22**, P. 19047–19054.

[6] Randoshkin V.V., Chervonenkis A.Ya. *Applied magneto-optics*, Moscow, Energoatomizdat, 1990, 320 p.

[7] Smirnova M.N., Glazkova I.S., Nikiforova G.E., Kop’eva M.A., Eliseev A.A., Gorbachev E.A., Ketsko V.A. Synthesis of Ce:YIG nanopowder by gel combustion. *Nanosystems: Physics, Chemistry, Mathematics*, 2021, **12**(2), P. 210–217.

[8] Sharm V., Kuanr B.K. Magnetic and crystallographic properties of rare-earth substituted yttrium-iron garnet. *Journal of Alloys and Compounds*, 2018, **748**, P. 591–600.

[9] Bokshyts Y.V., Kichanov S.E., Shevchenko G.P., Tratsiak E.V., Parshikova E.A., Kozlenko D.P. Structure and luminescence properties of $(Y_{1-x}La_x)_3(La_{1-y}Ga_y)O_{12}$:Ce^{+3}. *Inorganic Materials*, 2019, **55**(8), P. 820–826.

[10] Smirnova M.N., Nikiforova G.E., Goeva L.V. One-stage synthesis of $(Y_{0,5}Bi_{0,5})_3(Fe_{0,5}Ga_{0,5})_5O_{12}$ garnet using the organometallic gel auto-combustion approach. *Ceramics international*, 2018, **45**(4), P. 4509–4513.

[11] Smirnova M.N., Nipan G.D., Nikiforova G.E. $(Y_{1-x}Bi_x)_3(Fe_{1-y}Ga_y)_5O_{12}$ Solid Solution Region in the Ieneke Diagram, *Inorganic materials*, 2018, **54**(7), P. 683–688.

[12] Shen T., Dai H., Song M. Structure and Magnetic Properties of Ce-Substituted Yttrium Iron Garnet Prepared by Conventional Sintering Techniques. *Journal of Superconductivity and Novel Magnetism*, 2017, **30**, P. 937–941.

[13] Lisnevskaya I.V., Bobrova I.A., Lupeiko T.G. $Y_3Fe_5O_{12}$/Na,Bi,Sr-doped PZT particulate magnetoelectric composites. *Journal of Magnetism and Magnetic Materials*, 2016, **397**, P. 86–95.

[14] Huang M., Zhang S. Growth and characterization of cerium-substituted yttrium iron garnet single crystals for magneto-optical applications *Applied Physics A*, 2002, **74**, P. 177–180.

[15] Teterina Yu.A., Smirnova M.N., Maslakov K.I., Teterin A.Yu., Kop’eva M.A., Nikiforova G.E., Ketsko V.A. Ionic and Phase Compositions of $Y_{2.5}Ce_{0.5}Fe_{2.5}Ga_{2.5}O_{12}$. Ferrogarnet Powder Produced by Gel Combustion. *Doklady Physical Chemistry*, 2022, **5032**, P. 45–49.

[16] Yushchuk S.I., Yuryev S.O., Moklyak V.V. Monocrystalline ferrogarnet films with low magnetizations and small magnetic losses. *Materials Today: Proceedings*, 2022, **62**, P. 5771–5774.

[17] Khivintsev Y.V., Sakharov V.K., Kozhevnikov A.V., Dudko G.M., Filimonov Y.A., Khitun A. Spin waves in YIG based magnonic networks: Design and technological aspects. *Journal of Magnetism and Magnetic Materials*, 2022, **545**, P. 168754.

[18] Jin L., Jia K., He Y., Wang G., Zhong Z., Zhang H. Pulsed laser deposition grown yttrium-iron-garnet thin films: Effect of composition and iron ion valences on microstructure and magnetic properties. *Applied Surface Science*, 2019, **483**, P. 947–952.

[19] Rao Y., Zhang D., Zhang H., Jin L., Yang Q., Zhong Z., Li M., Hong C., Ma B.O. Thickness dependence of magnetic properties in submicron yttrium iron garnet films. *Journal Physics D: Applied Physics*, 2018, **51**(43), P. 435001.

[20] Arkhipenko A.A., Koshel E.S., Baranovskaya V.B. Analysis of cerium oxide by arc atomic emission spectrometry. *Zavodskaya laboratoriya. Diagnostika materialov*, 2021, **87**(11), P. 19–25.

[21] Koshel E.S., Arkhipenko A.A., Baranovskaya V.B.. Lutetium oxide analysis by direct arc atomic emission spectrometry. *Analytics and control*, 2021, **25**(2), P. 70–83.

[22] Vasilyeva I.E. Shabanova E.V. Stages of arc atomic emission spectrometry development as applied to the solid geological samples' analysis. *Analytics and Control*, 2021, **25**(4), P. 280–295.

[23] Schramm R. Use of X-ray Fluorescence Analysis for the Determination of Rare Earth Elements. *Physical Sciences Reviews*, 2016, **1**(1), P. 20160061.

[24] Sitko R., Zawisza B., Czaja M. Fundamental parameters method for determination of rare earth elements in apatites by wavelength-dispersive X-ray fluorescence spectrometry. *Journal of Analytical Atomic Spectrometry*, 2005, **20**, P. 741–745.

[25] Bondarenko A.V., Belonovsky A.V., Katsman Ya.M. Application of the method of fundamental parameters in X-ray fluorescence analysis of pulp products of ore enrichment. *Mining Industry*, 2021, **5-2**, P. 84–88

[26] Beckhoff B., Kanngießer B., Langhoff N., Wedell R., Wolff H. H*andbook of Practical X-ray Fluorescence Analysis*; Part 5 Quantitative Analysis, Berlin/Heidelberg, Springer, 2006, 863 p.

[27] Karandashev V.K., Orlova T.V., Zybinsky A.M., Kordyukov S.V., Simakov V.A., Kolotov V.P. Analysis of niobium-rare-earth ores by inductively coupled plasma mass spectrometry. *Journal of Analytical Chemistry*, 2018, **7**, P. 364–373.

[28] Salem D.B., Barrat J.A. Determination of rare earth elements in gadolinium-based contrast agents by ICP-MS. *Talanta*, 2021, **221**, P. 121589.

[29] Korotkova N.A., Baranovskaya V.B., Petrova K.V. Microwave Digestion and ICP-MS Determination of Major and Trace Elements in Waste Sm-Co Magnets. *Metals*, 2022, **12**(8), P. 1308.

[30] eiga M., Mattiazzi P., S. de Gois J., Nascimentod P.C., Borgese D.L.G., Bohrer D. Presence of other rare earth metals in gadolinium-based contrast agents. *Talanta*, 2020, **216**, P. 120940.

[31] Tanner S.D., Baranov V.I., Bandura D.R. Reaction cells and collision cells for ICP-MS: a tutorial review. *Spectrochimica Acta Part B*, 2002, **57**, P. 1361–1452.

[32] Balaram V. Strategies to overcome interferences in elemental and isotopic geochemical analysis by quadrupole inductively coupled plasma mass spectrometry: A critical evaluation of the recent developments. *Rapid Commun Mass Spectrom*, 2021, **35**, P. e9065.

[33] Agatemor C., Beauchemin D. Matrix effects in inductively coupled plasma mass spectrometry: A review. *Analytica Chimica Acta*, 2011, **706**(1), P. 66–83.

[34] Makonnen Y., Beauchemin D. Investigation of a measure of robustness in inductively coupled plasma mass spectrometry. *Spectrochimica Acta Part B*, 2015, **103–104**, P. 57–62.

[35] Korotkova N.A, Petrova K.V., Baranovskaya V.B. Analysis of cerium-substituted yttrium iron garnet by inductively coupled plasma atomic emission spectrometry with preliminary microwave decomposition. *Zavodskaya laboratoriya. Diagnostika materialov*, 2023, **89**(11), P. 24–33.

[36] Rusanov A.K. *Fundamentals of quantitative spectral analysis of ores and minerals*, M., Nedra, 1971, 360 p.

[37] Baranovskaya V.B., Koshel E. *Arc atomic emission analysis of rare earth metals and their oxides*, M., Technosfera, 132 p.

Submitted 20 November 2024; accepted 25 November 2024

Information about the authors:

Natalia A. Korotkova – Kurnakov Institute of General and Inorganic Chemistry of the Russian Academy of Sciences, Leninskii prosp., 31, Moscow, 119991, Russia; ORCID 0000-0003-1269-6570; natalya.korotkova.95@mail.ru

Alexandra A. Arkhipenko – Kurnakov Institute of General and Inorganic Chemistry of the Russian Academy of Sciences, Leninskii prosp., 31, Moscow, 119991, Russia; ORCID 0000-0002-2242-8572; alexandra622@mail.ru

Maria N. Smirnova – Kurnakov Institute of General and Inorganic Chemistry of the Russian Academy of Sciences, Leninskii prosp., 31, Moscow, 119991, Russia; ORCID 0000-0003-2707-7975; smirnovamn@igic.ras.ru

Vasilisa B. Baranovskaya – Kurnakov Institute of General and Inorganic Chemistry of the Russian Academy of Sciences, Leninskii prosp., 31, Moscow, 119991, Russia; ORCID 0000-0002-0076-9990; baranovskaya@list.ru

Marina S. Doronina – Kurnakov Institute of General and Inorganic Chemistry of the Russian Academy of Sciences, Leninskii prosp., 31, Moscow, 119991, Russia; ORCID 0000-0003-4553-1019; ms.semenova@gmail.com

Valerii A. Ketsko – Kurnakov Institute of General and Inorganic Chemistry of the Russian Academy of Sciences, Leninskii prosp., 31, Moscow, 119991, Russia; ORCID 0000-0002-2075-1755; ketsko@igic.ras.ru

Galina E. Marina – Kurnakov Institute of General and Inorganic Chemistry of the Russian Academy of Sciences, Leninskii prosp., 31, Moscow, 119991, Russia; ORCID 0009-0000-2872-2150; gelim@mail.ru

Conflict of interest: the authors declare no conflict of interest.

NANOSYSTEMS:
PHYSICS, CHEMISTRY, MATHEMATICS

Original article

Ikim M.I., et al. *Nanosystems: Phys. Chem. Math.*, 2024, **15** (6), 867–878.
http://nanojournal.ifmo.ru
DOI 10.17586/2220-8054-2024-15-6-867-878

Effect of synthesis method on the structural, conductive and sensor properties of NiO–In_2O_3 nanocomposites

Mariya I. Ikim[1,a], Vladimir F. Gromov[1,b], Genrikh N. Gerasimov[1,c], Valentin G. Bekeshev[1,d],
Leonid I. Trakhtenberg[1,2,3,c]

[1]N. N. Semenov Federal Research Center for Chemical Physics RAS, Moscow, Russia

[2]Chemical Faculty, Lomonosov Moscow State University, Moscow, Russia

[3]Moscow Institute of Physics and Technology(State University), Moscow, Russia

[a]ikimmary1104@gmail.com, [b]vfgromov@mail.ru, [c]gerasimovgen@mail.ru, [d]bvg495@yandex.ru,
[e]litrakh@gmail.com

Corresponding author: Mariya I. Ikim, ikimmary1104@gmail.com

PACS 73.63.-b

ABSTRACT The structural, conductive and sensor properties of NiO–In_2O_3 composites synthesized by hydrothermal and impregnation methods are investigated and compared. The mixed oxide considered consists of nanoparticles with electronic (In_2O_3) and hole (NiO) conduction bands. The lattice parameters of indium oxide decrease with the introduction of NiO into composites synthesized by the hydrothermal method. The addition of 3 % NiO to the hydrothermal composite also increases its specific surface area. The specific surface area and In_2O_3 lattice parameters in the impregnated samples are essentially independent of the NiO content. The conductivity of impregnated composites is an order of magnitude lower than that of hydrothermal composites. An increase in NiO content leads to a significant enhancement of the sensor response to H_2 and CO. In addition, there is a decrease in the optimal operating temperature of hydrothermal and impregnated samples by 60 and 20 °C, respectively.

KEYWORDS composite, hydrothermal method, impregnation, indium oxide, conductivity, sensor response, hydrogen, carbon monoxide

ACKNOWLEDGEMENTS The work was supported by the Russian Science Foundation (grant No. 22-19-00037).

FOR CITATION Ikim M.I., Gromov V.F., Gerasimov G.N., Bekeshev V.G., Trakhtenberg L.I. Effect of synthesis method on the structural, conductive and sensor properties of NiO–In_2O_3 nanocomposites. *Nanosystems: Phys. Chem. Math.*, 2024, **15** (6), 867–878.

1. Introduction

The presence in the atmosphere of various gases that can have harmful effects on human health has led to the development of research aimed at effective detection of these compounds. A considerable attention has been paid to the detection of reducing compounds such as H_2, CO, CH_4, NH_3 and others. One of the most effective detection methods is the use of metal oxide compounds whose conductivity changes in the presence of the above-mentioned reducing gases.

Previous studies have shown that mixtures of n-type metal oxides with different conductivity and catalytic activity can be used as sensors for detection of reducing and oxidizing gases (see, for example, [1–4]). However, despite the enough high sensitivity of the oxides considered in these studies, such as SnO_2, In_2O_3, CeO_2, ZnO, their sensor effect is fully observed only at sufficiently high temperatures, usually above 400 °C. In addition, metal oxide-based composites with an electronic type of conductivity are characterized by relatively low selectivity.

The gas sensitivity of p-type metal oxides is generally much lower than that of n-type metal oxides [5], however, their efficiency and selectivity are manifested at significantly lower temperatures (from room temperature to 150 – 200 °C). The use of mixtures consisting of n- and p-type metal oxides for detection can lead to more efficient composites. In this regard, the creation of p-n or n-p heterojunctions is one of the most important methods for obtaining metal oxide sensor materials. The formation of p-n heterostructures, as well as the introduction of p-type metal oxide into an n-type semiconductor produces an increase in the specific surface area of the composites, an increase in the number of active centers and more intensive generation of adsorbed oxygen due to the formation of an extended electron-depleted layer in the p-n junction [6–10].

The Fermi level for n-type metal oxides is higher than for p-type compounds. Therefore, in a mixture of such oxides, electrons with higher energy will transfer from the n-type metal oxide across the interface to unoccupied states with lower energy, which will lead to an equalization of the Fermi energy of both components. The potential barrier that must be overcome in the process of such electron transfers increases or decreases significantly in the presence of oxidizing and reducing gases, respectively, while ensuring the occurrence of a sensory effect (see, for example, paper [11]).

Indeed, the addition of even small amounts of p-type semiconductor Co_3O_4 to In_2O_3 having electronic conductivity leads to a significant increase in the sensor response to hydrogen [12]. In addition, when detecting H_2S, the ZnO–CuO nanofiber has a higher sensor activity compared to the ZnO nanofiber [13]. The sensitivity to H_2S of CuO-doped SnO_2 nanofibers increases relative to the undoped SnO_2-based layer [14].

One of the components of sensor materials is nickel oxide, which has strong oxidizing properties, excellent catalytic activity and good electrical conductivity [15, 16]. The addition of metal oxides such as Fe_2O_3, MoO_3, ZnO, WO_3, TiO_2 to NiO, which is a p-type semiconductor, leads to a significant increase in sensitivity to acetone [6–10]. The response to 100 ppm acetone of α-Fe_2O_3/NiO heterostructures increases by almost 7 folds over pure NiO [10]. The response of the α-MoO_3–NiO composite with a core/shell structure is 6.6 times higher than that of pure NiO [6]. Hollow NiO–SnO_2 particles have a much higher response to triethylamine than the original hollow spheres of SnO_2 [17]. The n-p heterojunction occurring in the SnO_2/NiO system provides ultra-high sensitivity and selectivity of this material to H_2S [18].

The gas-sensitive properties of NiO nanofibers and one-dimensional heterogeneous NiO–In_2O_3 nanofibers obtained by electrospinning were investigated for acetone detection [19]. It was shown that the heterogeneous nanofibers formed from In_2O_3 and NiO demonstrate increased sensitivity to acetone. At the optimal operating temperature, the response of ZnO–In_2O_3 nanofibers to 50 ppm of acetone was more than 10 times higher than the response of pure NiO nanofibers. The acetone detection limit for heterogeneous nanofibers reached 10 ppm, while it was 100 ppm for NiO nanofibers. The response of heterogeneous NiO–In_2O_3 nanofibers to acetone exceeds the response to methanol, ethanol, triethylamine, ethyl acetate and benzene [19]. In addition, heterogeneous nanofibers have demonstrated a higher recovery rate after removal of the analyzed gas and good long-term stability. These results demonstrate that one- dimensional heterogeneous NiO-In_2O_3 nanofibers have great potential for detection of low concentrations of acetone.

A significant sensor activity to ethanol of NiO–In_2O_3 nanofibers obtained by electrospinning and calcination has been demonstrated [20]. The most active composite among the samples containing up to 7.5 mol. % NiO is the 5 % NiO – 95 % In_2O_3 composite which has a response of 78 to 100 ppm ethanol at 300 °C. It is assumed that the improved sensor characteristics are due to the formation of p-n-transitions between NiO and In_2O_3, the ability to adsorb various forms of oxygen and an increase in the specific surface area of nanofibers when NiO is added to In_2O_3.

Here, composites consisting of In_2O_3 and p-type hole conductive NiO are synthesized by the hydrothermal and impregnated methods. The effect is then investigated of the composition on the electronic state, the spatial structure of such composites, as well as their conductivity and sensor activity in the detection of H_2 and CO.

2. The experimental part

Nickel nitrate $Ni(NO_3)_2 \cdot 6H_2O$ (99 %) and indium nitrate $In(NO_3)_3 \cdot 4H_2O$ (99.5 %) were used as precursors in the hydrothermal synthesis of mixed NiO–In_2O_3 oxides. The required amount of nickel nitrate was added to the indium nitrate solution in distilled water or ethanol and kept in an ultrasonic bath for 1 hour at 30 °C. The solution was then placed in a Teflon-coated autoclave (volume 100 ml) and kept for 3 hours at 160 °C. The resulting suspension was separated in a centrifuge, and the powder washed with distilled water and annealed in air at 500 °C.

Commercial In_2O_3 powder (AnalaR brand, 99.5 %, BDH/Merck Ltd., Lutterworth, Leicestershire, UK), as well as chemically pure $Ni(NO_3)_2 \cdot 6H_2O$ were used to obtain NiO–In_2O_3 composites by impregnation. Indium oxide nanopowder was placed in an aqueous solution of nickel nitrate with concentration of 0.015 mol/l and the resulting suspension was maintained for a long time. This treatment causes complete wetting the surface of the solid oxide by the salt solution. Moreover, salt molecules are not only adsorbed on the surface of In_2O_3, but also diffuse into its near-surface layers. To obtain impregnated samples water was removed at a temperature of about 70 – 80 °C, and the samples were subsequently heated for several hours at 500 °C. The phase composition and crystal lattice parameters of the composites synthesized by the two methods considered were determined by X-ray diffraction (XRD) using the Rigaku Smartlab GP X-ray diffractometer (CuKa radiation with a wavelength of 1.5406 Å). The morphology of the particles in the composites and the distribution of metal ions between the components of the composite were determined by TEM and EDX methods on a JEOL OSM-6000PLUS device equipped with an energy dispersion analysis system. The electronic structure of the composites was determined by X-ray photoelectron spectroscopy (XPS) on a Prevac EA15 spectrometer using Mg(Ka) (1253.6 eV) as the radiation source. The specific surface area and pore size distribution in the synthesized composites were determined by low-temperature nitrogen adsorption on the NOVA 1200e Quantachrome device (USA).

The conductivity and sensor properties were investigated in the temperature range 300 – 550 °C. The chip with the applied sensor layer was placed in a special chamber of about 1 cm^3 volume into which purified air or a gas mixture was supplied. The mixture consisted of purified air and H_2 or CO. We used two concentrations of the analyzed gas: 0.9 or 0.1 %. The rate of gas pumping through the chamber was 200 ml/min, and the accuracy of temperature maintenance was within 1 °C. The sensor response was determined by the relation $S = R_0/R_g$, where R_0 is the initial resistance of the sensor in air, and R_g is the minimal value of the sensor resistance after the introduction of the mixture being investigated.

The response time of the sensor t_{resp} (the time required to achieve a 90 % change in the resistance of the sensor after introducing the analyzed gas) and the recovery time of the sensor t_{rec} (the time required to reach 90 % of the initial resistance of the sensor after removal of the mixture considered) were determined by the change in the resistance of the sensor layer. The change in the sensor resistance was recorded using a Keysight digital multimeter, the signal from which was transmitted to a computer.

3. Results and discussion

3.1. Structural characteristics of NiO–In_2O_3 composites

X-ray analysis data show that, regardless of the synthesis method, when up to 3 wt. % NiO is added to In_2O_3, there are no peaks characterizing nickel or its compounds in the XRD spectra of the composite (Fig. 1). This result may be caused by the dissolution of nickel ions in the In_2O_3 lattice, the formation of an X-ray amorphous phase, or simply the small amount of NiO in the composites. Only peaks corresponding to the cubic phase of indium oxide (c-In_2O_3) with a predominant orientation (222) are recorded in the spectra of impregnated and hydrothermal composites synthesized from aqueous solutions of indium and nickel nitrates (Fig. 1(1,2)). In turn, all the observed diffraction peaks in the spectra of composites synthesized from an alcohol solution of the salts belong to the rhombohedral phase of indium oxide of the corundum type (rh-In_2O_3) with a predominant orientation (104) and (110) (Fig. 1(3)).

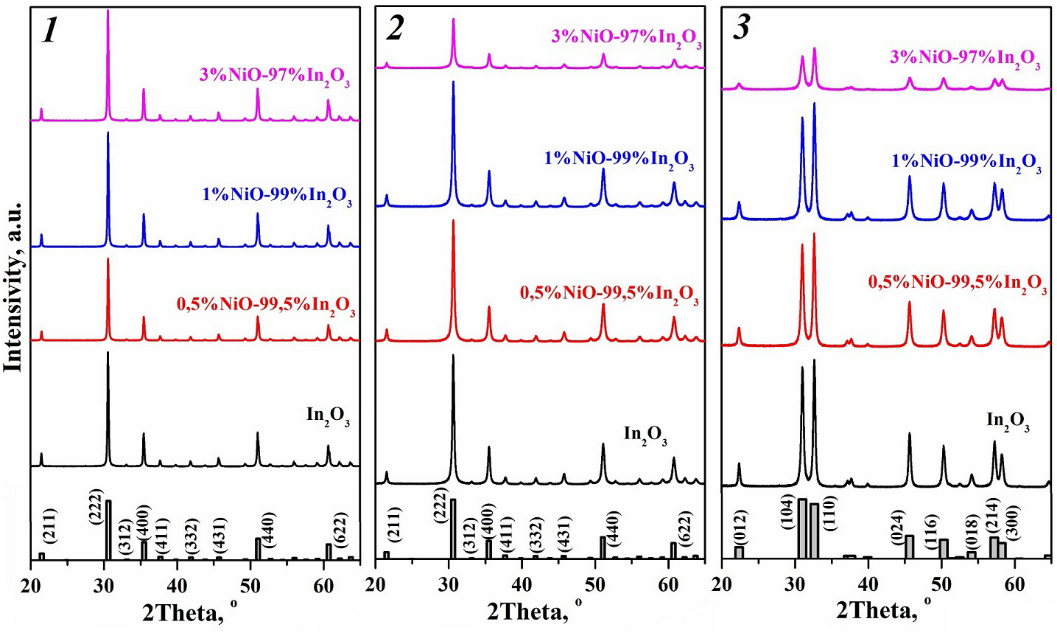

FIG. 1. XRD pattern of NiO–In_2O_3 composites synthesized by impregnation (1) and hydrothermal method in water (2) and ethanol (3)

Increase in the nickel content in the synthesized composites results in a shift in the diffraction angles of the reflex (222) for the cubic phase and reflex (104) for the rhombohedral phase of In_2O_3. It can be assumed that nickel ions are embedded in the indium oxide lattice, which leads to the angular shift due to the difference in the sizes of In^{3+} (0.81 Å) and Ni^{2+} (0.69 Å) ions.

As NiO is introduced into the composites obtained by the hydrothermal method, the lattice parameters of both cubic and rhombohedral indium oxide decrease, which is also due to the difference in the ionic radii of In and Ni. In impregnated samples, the lattice parameters are – nickel is embedded in the structure of indium oxide in hydrothermal samples. In the case of impregnated samples, X-ray data indicate that amorphous NiO is formed on the surface of In_2O_3, but some Ni ions can be embedded in the near-surface layers.

The particle size calculated by the Debye–Scherrer formula is about 60 nm for impregnated composites and does not depend on the nickel oxide content. At the same time, in hydrothermal samples, the introduction of nickel into the indium oxide structure leads to a decrease in particle size from 34.5 to 30.5 nm for samples with a cubic structure and 24.6 to 15.5 nm for the rhombohedral phase. The introduction of nickel ions into different crystalline phases of In_2O_3 hydrothermal composites prevents crystal growth. This finding is attributed to the occurrence of deformations due to indium substitution in the lattice.

TEM data for impregnated NiO–In_2O_3 nanocomposites show that spherical particles of up to 20 nm in size are formed on the surface of indium oxide particles of about 100 nm size as a result of their impregnation with nickel nitrate and further heat treatment (Fig. 2(1)). Hydrothermal samples synthesized from an aqueous solution are agglomerates of heterogeneous in size rectangular nanoparticles (Fig. 2(2)). The nanoparticles in the rhombohedral samples have a shape close to spherical and are uniform in size (Fig. 2(3)).

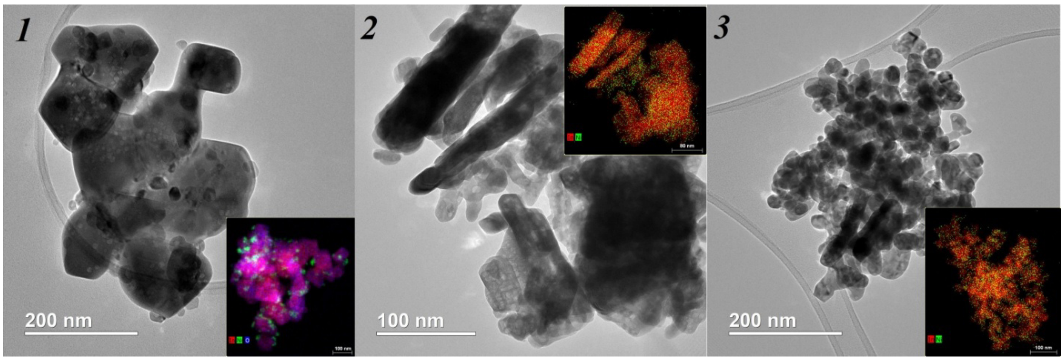

FIG. 2. TEM and EDA analysis (in the insert) of 3 % NiO – 97 % In_2O_3 composites synthesized by impregnation (1) and hydrothermal method from solutions of indium and nickel nitrates in water (2) and ethanol (3)

The data on energy dispersion mapping of In, O and Ni in hydrothermal composites show that nickel ions are evenly distributed in indium oxide particles. The particles containing only nickel ions are also observed on the surface of indium oxide in impregnated composites. In the latter case, a small quantity of nickel is distributed in the surface layer of indium oxide particles.

The adsorption-desorption of nitrogen by the samples at 77 K was studied in order to determine the specific surface area and porosity of the synthesized samples. The isotherms of the impregnated samples have a shape characteristic of nonporous or macroporous samples (Fig. 3(1)). Regardless of the Ni content in such composites, the isotherms are almost identical, with only minor differences in the filling area of the macropores.

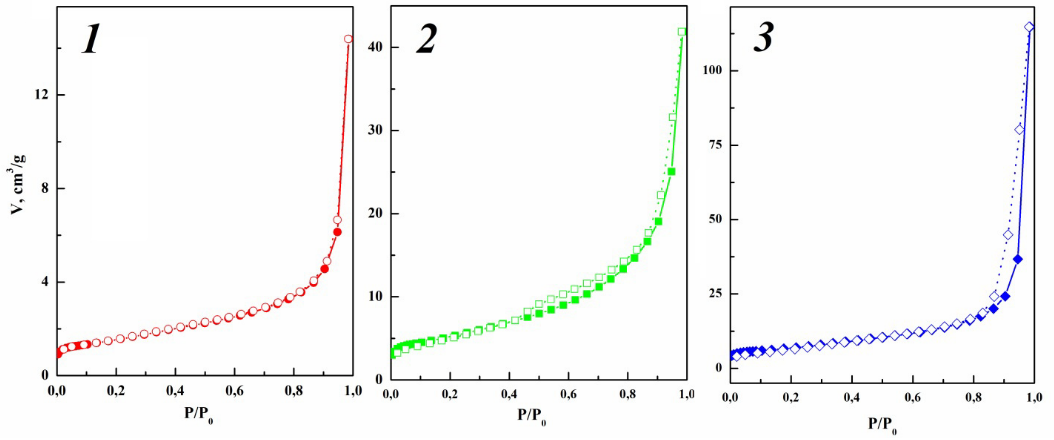

FIG. 3. Isotherms of adsorption (filled symbols) and desorption (empty symbols) of nitrogen at 77 K of 1 % NiO – 99 % In_2O_3 composites synthesized by impregnation (1) and hydrothermal method using solutions of indium and nickel nitrates in water (2) and ethanol (3)

Based on the IUPAC classification, the isotherms of hydrothermal samples have a type IV shape with a hysteresis loop H3, which indicates a mesoporous nature of these samples (Fig. 3(2 and 3)). The shape of the hysteresis loop of hydrothermal composites depends on the mesoporous structure of the crystalline phase of indium oxide present in the samples. For composites with a rhombohedral structure (Fig. 3(3)) the hysteresis closes in the region of relative pressures P/P_0 (P is the partial pressure of the adsorbed substance, and P_0 is the pressure of saturated vapors of the adsorbed gas), close to 0.8. In addition, the hysteresis closes in the region of P/P_0 values close to 0.4 in samples with a cubic structure of In_2O_3 (Fig. 3(2)).

The specific surface area of impregnated composites (S_{BET}), calculated by the BET method, is 5.1 – 5.6 m^2/g and essentially independent of the concentration of NiO in the samples. For hydrothermal samples synthesized from an alcoholic solution, the S_{BET} value varies from 21.9 m^2/g for pure In_2O_3 to 26.1 m^2/g for a sample containing 3 % NiO. Samples synthesized from an aqueous solution have a slightly lower specific surface area S_{BET}, which is 16.1 m^2/g for pure In_2O_3 and reaches 18.2 m^2/g for a sample containing 3 % NiO. The specific surface area becomes greater with increase in the concentration of NiO in such composites.

The mesoporous structure of the samples, on which their sensor properties largely depend, was studied by the BJH method (Fig. 4). The pore size distribution for these samples also differs significantly. As can be seen from the data shown in Fig. 4, the diameter of the mesopores of the rhombohedral hydrothermal sample synthesized from an alcoholic solution is mainly 20 nm. In the diagram of this sample there is also a very small peak in the 3 nm region, but the total pore volume of this size is negligible compared to the pore volume of a larger diameter. With an increase in the concentration of NiO in such composites, the volume of mesopores increases, which leads to an increase in the specific surface area S_{BET}.

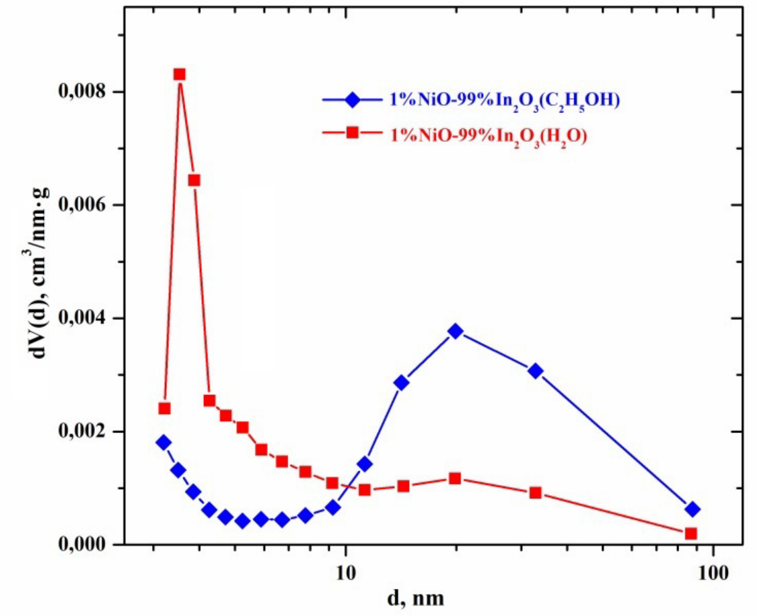

FIG. 4. Pore size distribution for hydrothermal samples containing 1 % NiO

The pore size distribution for hydrothermal samples of cubic structure has an acute peak in the region of pores with a diameter of 3.5 nm, followed by a wide decreasing plume of pores with a larger diameter (see Fig. 4). With an increase in the concentration of NiO in composites of this type, the volume of mesopores increases slightly. This, apparently, explains the smaller increase in the specific surface area S_{BET} of such samples compared to nanocomposites of rhombohedral structure. In addition, the total volume of 3.5 nm pores in samples synthesized from aqueous solution is approximately 3 times smaller than the total volume of 20 nm pores for samples synthesized from ethanol. It can be assumed that in hydrothermal composites of cubic structure, narrow pores with a diameter of 3.5 nm correspond to pores inside the nanoparticles, while in samples with a rhombohedral structure, 20 nm pores correspond to pores between the nanoparticles.

The composition and valence state of the surface elements and active oxygen centers were determined by the XPS method. Only peaks In, O, C and Ni are present in the survey spectra, which indicates the high purity of the synthesized samples. Two intense peaks with binding energies of 452.3 and 444.7 eV, observed for all samples, belong to the spin-orbital energy states In $3d_{3/2}$ and In $3d_{5/2}$, respectively (Fig. 5). The XPS study indicates that the valence state of indium ions in the samples is 3+.

It should be noted that regardless of the method of obtaining NiO–In_2O_3, the introduction of NiO in the composite leads to a decrease in the binding energy In $3d_{3/2}$ and In $3d_{5/2}$. This result is due to the substitution of nickel ions in the crystal lattice, leading to the formation of In–O–Ni with a relatively low binding energy, and once again indicates the introduction of Ni into the In_2O_3 lattice. In the high-resolution Ni 2p XPS spectra for all the composites obtained, peaks characterized by binding energies of 854 and 873 eV are observed, which corresponds to the valence state 2+ of nickel ions. The spectra of XPS O 1s are also analyzed in this study. The asymmetric peak of O 1s can be divided into several peaks that are characteristic of three forms of oxygen, namely: lattice oxygen (O_L) with a binding energy of 530.1 eV, oxygen vacancies (O_V) with a binding energy of 531.5 eV and chemisorbed oxygen (O_C) with a binding energy of 532.4 eV (see Fig. 6).

The O_L signal is caused by the presence of O^{2-} ions in the crystal structure. The O_V characterizes the region of oxygen vacancies in the matrix and plays an important role in gas-sensitive characteristics. The O_C is associated with oxygen ions adsorbed on the surface of the sample. The content of various oxygen forms in the samples depends on the synthesis method. Thus, the impregnation of In_2O_3 with nickel nitrate leads to a decrease in the number of oxygen vacancies by 8 % and an increase in the concentration of chemisorbed oxygen by 17 %. In hydrothermal samples, the introduction of NiO increases the number of oxygen vacancies by 18 % for the cubic In_2O_3 phase and 2 % for

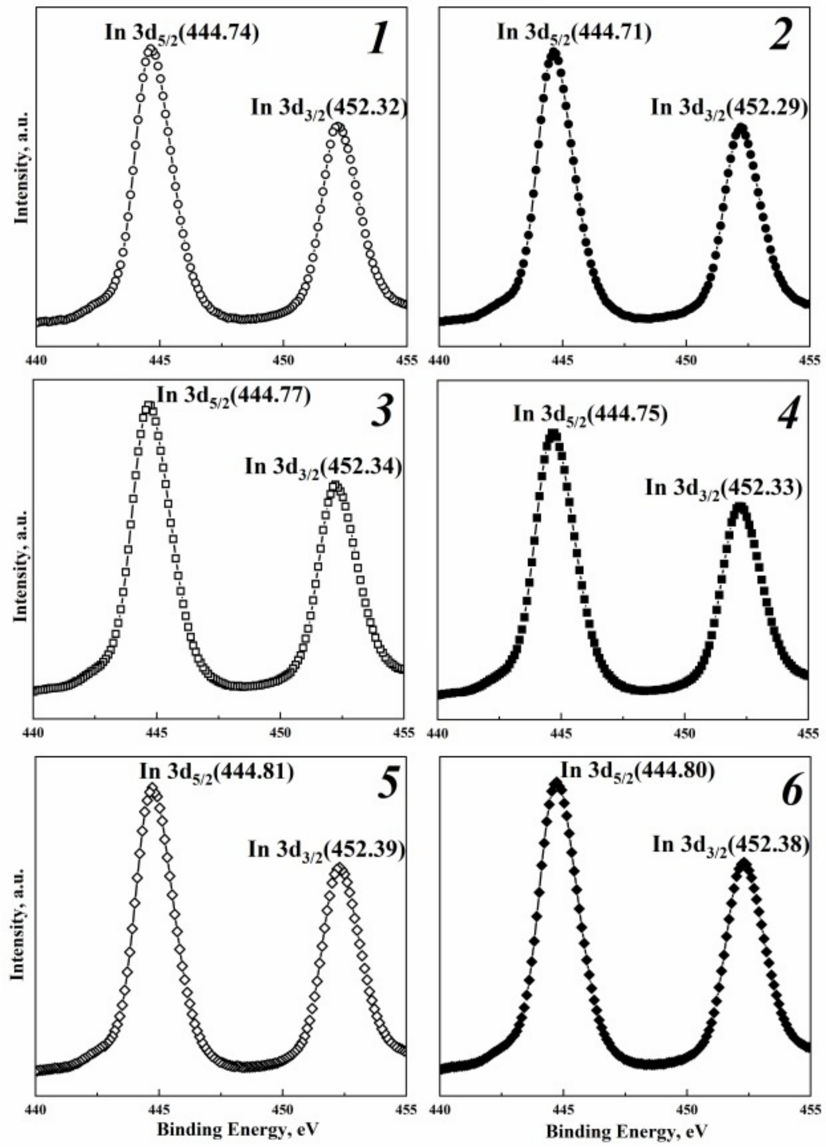

FIG. 5. High-resolution XPS spectra In 3d: In_2O_3 (1), impregnated composite of 1 % NiO – 99 % In_2O_3 (2), hydrothermal samples In_2O_3 (3) and 3 % NiO – 97 % In_2O_3 (4) synthesized from aqueous solutions of In and Ni salts, as well as In_2O_3 (5) and 3 % NiO – 97 % In_2O_3 (6) synthesized from salt solutions in ethanol

the rhombohedral phase and thereby affects the sensory activity of the composites. In addition, the concentration of chemisorbed oxygen decreases in the composites with a cubic structure but increases in rhombohedral samples.

3.2. Conductivity of NiO–In_2O_3 composites

The conductivity of NiO–In_2O_3 composites synthesized by different methods are enhanced with the increase of sensor layer temperature from 300 to 520 °C (Fig. 7), which is typical for n-type semiconductors. Moreover, violations of this pattern decrease with increase in the fraction of nickel oxide. This trend is not surprising considering the peculiarities of the temperature dependence of In_2O_3 conductivity [21]. The composites synthesized by In_2O_3 impregnation with nickel nitrate have the highest conductivity at all the temperatures investigated.

It was also found that the conductivity of the composites decreases with an increase in the nickel oxide content (see Fig. 7(4)). In the process of impregnation, X-ray amorphous NiO is formed on the surface of indium oxide nanoparticles, while some nickel ions can be embedded in its near-surface layers. The electron work function from NiO (5.5 eV) is higher than from indium oxide (4.3 eV). Thus, upon contact of these oxides, electrons are transferred from In_2O_3 nanoparticles with a high concentration of conduction electrons to the NiO nanoparticles. This transfer is accompanied by a decrease in the conductivity of the composites.

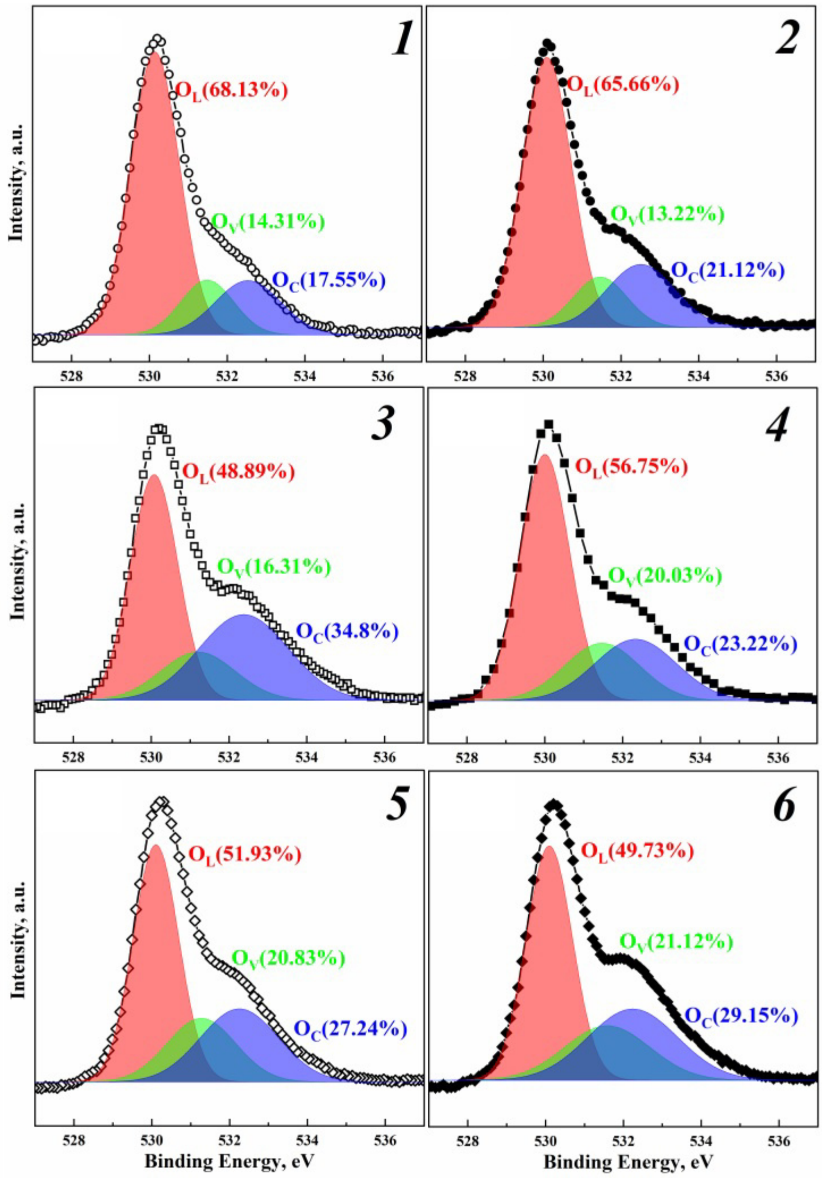

FIG. 6. High-resolution XPS spectra of O 1s: (1) In_2O_3; (2) composite 1 % NiO – 99 % In_2O_3 obtained by impregnation; hydrothermal samples synthesized from aqueous solutions of indium and nickel nitrates: In_2O_3 (3) and 3 % NiO – 97 % In_2O_3 (4); hydrothermal samples synthesized from solutions of salts in ethanol: In_2O_3 (5) and 3 % NiO – 97 % In_2O_3 (6)

In the process of hydrothermal synthesis, nickel ions (Ni^{2+}) are introduced into the lattice of both cubic and rhombohedral In_2O_3, replacing In^{3+} ions. In addition, positively charged oxygen vacancies V_O^+ are formed in the composite, which ensures a balance of positive and negative charges.

The conductivity of hydrothermal composites, regardless of the nature of the In_2O_3 crystalline phase, is an order of magnitude lower than that of impregnated ones. This result is due to the fact that during the hydrothermal synthesis of composites, the quantity of In^{3+} ions replaced by Ni^{2+} ions is greater than during impregnation. This in turn leads to a decrease in the conductivity of hydrothermal samples relative to impregnated ones. It should also be noted that the interaction of nanoparticles during impregnation is concentrated mainly in the surface layers of the nanocrystals. In addition, the conductivity of hydrothermal composites depends on the phase state of the In_2O_3 crystals.

Composites with a rhombohedral structure have higher conductivity than similar composites of a cubic structure (see Fig. 7(4)). In the rhombohedral lattice of In_2O_3 crystals, unlike the cubic type, there are elongated and, consequently, weakened In–O bonds. This may be responsible for the increase in the concentration of vacancies and the corresponding increase in the concentration of conduction electrons generated by these vacancies in the composites with a rhombohedral structure compared to a cubic structure.

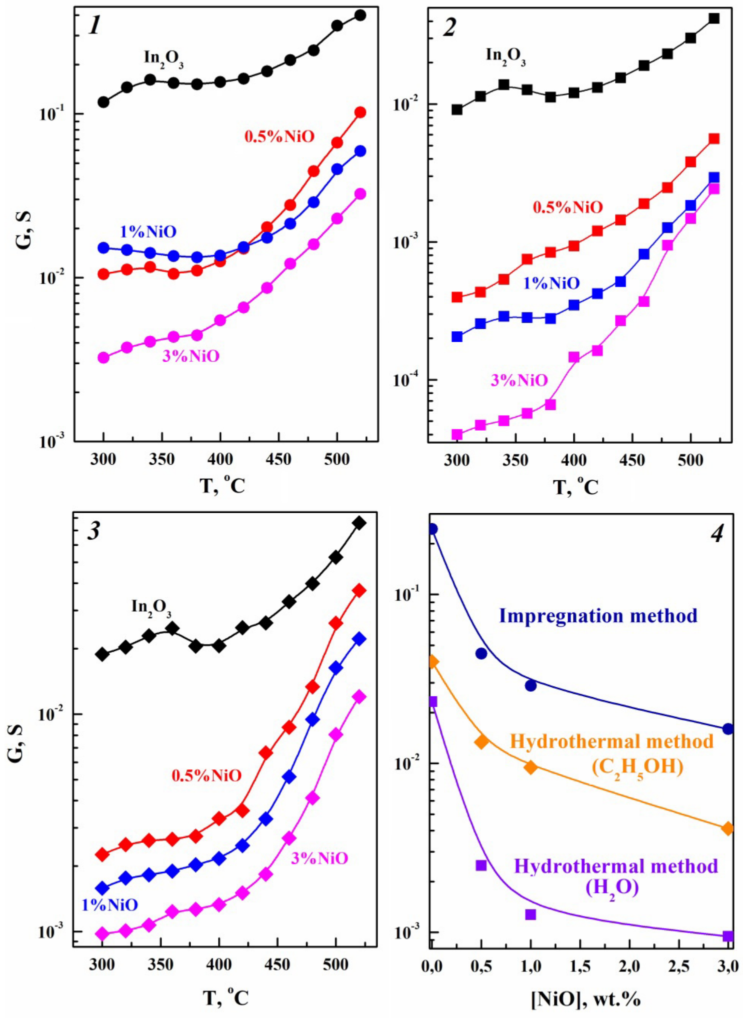

FIG. 7. Temperature dependence of the conductivity of NiO–In_2O_3 composites synthesized by impregnation (1) and hydrothermal method using solutions of indium and nickel nitrates in water (2) and ethanol (3). Dependence of the conductivity of NiO–In_2O_3 composites synthesized by different methods on the concentration of NiO at $T = 460$ °C (4)

3.3. Sensor properties of NiO–In_2O_3 composites

In NiO–In_2O_3 composites, regardless of the synthesis method, the temperature dependence of sensor response to H_2 and CO has a curve that is typical for semiconductor sensors with a maximum $S_{\max}$ at a certain temperature $T_{\max}$ (see Fig. 8). In all cases, the sensor activity of composites exceeds the activity of pure In_2O_3 (Fig. 9).

Oxygen vacancies are centers of chemisorption of oxygen and the analyzed gas, therefore, an increase in their concentration contributes to a higher sensor response of rhombohedral indium oxide. Since the introduction of nickel oxide in the sample enhances the number of vacancies, the sensor response increases accordingly. In addition, the magnitude of the response to different concentrations of hydrogen and carbon monoxide depends on the method used for synthesizing the composite (see Fig. 9).

A hydrothermal composite of 3 % NiO – 97 % In_2O_3 synthesized from an alcoholic solution of the corresponding nitrates and containing rhombohedral indium oxide has the highest sensor response to 0.9 % H_2. However, at 0.1 % H_2 detection, the highest response has the hydrothermal composite 3 % NiO – 97 % In_2O_3, synthesized from an aqueous solution in which cubic indium oxide is present. When detecting carbon monoxide, the hydrothermal composite based on cubic indium oxide containing 3 % nickel oxide shows the highest efficiency. It should be noted that impregnated composites have the lowest response to hydrogen and carbon monoxide, which is due to the lower specific surface area of such samples compared to hydrothermal samples.

The method of synthesis of NiO–In_2O_3 composites significantly affects the dependence of the sensor response on the concentration of nickel oxide (Fig. 9). The highest efficiency of impregnated samples is observed when they contain 0.5 – 1 % NiO.

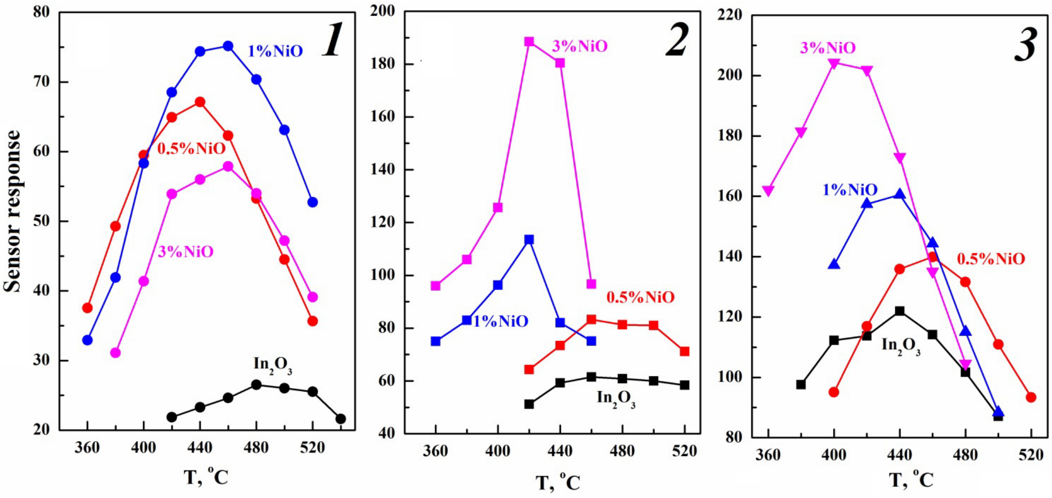

FIG. 8. Temperature dependences of the sensor response to 0.9 % H_2 of NiO–In_2O_3 composites synthesized by impregnation (1) and hydrothermal method using solutions of indium and nickel nitrates in water (2) and ethanol (3)

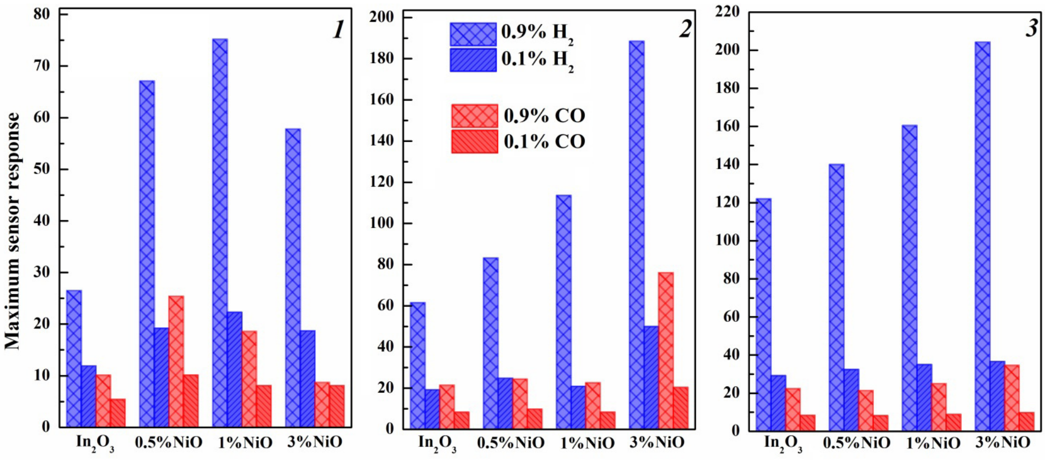

FIG. 9. Concentration dependence of the maximum sensor response to different concentrations of H_2 and CO of NiO–In_2O_3 composites synthesized by impregnation (1) and hydrothermal method using solutions of indium and nickel nitrates in water (2) and ethanol (3)

A further increase of the NiO content in impregnated composites results in a slight decrease in sensor response, while the addition of 3 % NiO to a hydrothermal composite causes a sharp increase in the sensitivity to H_2 and CO. Such a behavior takes place due to the various types of interactions between the components in the composites synthesized by different methods.

Nickel ions are embedded in the indium oxide lattice in hydrothermal samples, which leads to an increase in the defectiveness of the nanoparticles, the concentration of atomic oxygen on the surface and the sensor effect. In composites synthesized by impregnation, NiO nanoclusters are formed on the surface of In_2O_3 nanoparticles and do not affect their structure, size and defects. Consequently, nickel oxide additives in this case have a lesser effect on the sensor response compared to hydrothermal samples. It should be noted that the mechanisms considered here affecting the response of sensors prepared by impregnation and hydrothermal method differ from the mechanism proposed in [20], where samples were obtained by electrospinning and calcination methods. The increased sensitivity with the addition of nickel oxide was attributed to the formation of p-n-transitions between NiO and In_2O_3 and a decrease in particle size.

An increase in the nickel oxide content leads to a decrease in the optimal operating temperature for hydrothermal samples by 40 – 60 °C, and for impregnated samples by 20 °C. This decrease is caused by the high catalytic activity of NiO nanoparticles.

A comparison of the sensor properties of indium oxide and NiO–In_2O_3 composites obtained by different methods and under various conditions is presented in Table 1.

TABLE 1. Sensor properties of NiO and In_2O_3-based materials at detecting different concentrations of H_2 and CO

Sample	**Synthesis method**	**Gas concentration**	**Sensor response**	T, **°C**	**Reference**
In_2O_3	one-step hydrothermal and thermal treatment process using MOF	100 ppm H_2	7.9	100	[22]
3 % Ni–In_2O_3			12.5		
In_2O_3	solvothermal method	10 ppm CO	2.5	200	[23]
1 %Ni-In_2O_3			4.8		
In_2O_3	nanocasting method	1 ppm CO	—	58	[24]
Ni-doped In_2O_3			2.7		
In_2O_3	solvothermal method	100 ppm CO	2	140	[25]
5 % Ni–In_2O_3			11.03		
In_2O_3	hydrothermal method	100 ppm H_2	4.8	150	[26]
		100 ppm CO	1.2		
NiO/In_2O_3 – 0.2		100 ppm H_2	4.9		
		100 ppm CO	1.3		
In_2O_3	hydrothermal method	100 ppm CO	1.2	280	[27]
NiIn – 2			6.4		
In_2O_3	impregnation method	0.9 % / 0.1 % H_2	26.5/11.9	480	**This work**
		0.9 % / 0.1 % CO	10.1/5.4		
1 % NiO–In_2O_3		0.9 % / 0.1 % H_2	75.2/22.3	460	
		0.9 % / 0.1 % CO	18.6/8.1		
In_2O_3	hydrothermal method (water)	0.9 % / 0.1 % H_2	61.5/19.2	460	
		0.9 % / 0.1 % CO	21.4/8.3		
3 %NiO–In_2O_3		0.9 % / 0.1 % H_2	188.5/49.9	400	
		0.9 % / 0.1 % CO	76.1/20.4		
In_2O_3	hydrothermal method (ethanol)	0.9 % / 0.1 % H_2	122/29.2	440	
		0.9 % / 0.1 % CO	22.36/8.4		
3 %NiO–In_2O_3		0.9 % / 0.1 % H_2	204.3/36.6	400	
		0.9 % / 0.1 % CO	34.6/8.9		

It turned out that the introduction of nickel into indium oxide at various concentrations of the additive, regardless of the production method, increases the sensor response. Compared with the literature data, the NiO–In_2O_3 composites synthesized by us have higher sensory response values to H_2 and CO, but at a higher operating temperature. The introduction of nickel results in a decrease of operating temperature compared to pure indium oxide, which was not observed in other studies. Note also that in works [22–27], the composites based on NiO–In_2O_3 containing only the cubic phase of indium oxide are considered. We have shown that the magnitude of the sensor response and selectivity in detecting H_2 and CO are higher for composites based on rhombohedral In_2O_3 than for cubic ones.

The response/recovery time of samples when detecting 0.9 % hydrogen depends on the method of sample preparation. However, in all cases, the introduction of nickel oxide into the composite leads to a decrease in the response and recovery time of the sensor. Thus, with the introduction of 1 % NiO in impregnated samples, the response time decreases from 1.3 to 0.8 s, and the recovery time – from 6.5 to 5.4 s. In the case of samples obtained by the hydrothermal method and having cubic structure, t_{resp} decreases from 0.4 to 0.2 s, and t_{rec} from 14 to 10 s, and in the samples with a rhombohedral structure, t_{resp} decreases from 0.3 to 0.1 s, t_{rec} from 5 to 4.7 s. A longer recovery time compared to other samples is also observed in hydrothermal sensitive layers with a cubic structure of indium oxide.

The sensor properties of the synthesized samples were measured regularly for 5 months at the optimal operating temperature. Over this period, the resistance of the sensor layer in the air and the magnitude of the response to H_2 were found to vary by less than 5 – 10 % depending on the synthesis method, indicating the long-term stability of the samples obtained.

4. Conclusions

Composites consisting of metal oxides with different types of conductivity (In_2O_3 and NiO) have been synthesized by impregnation and hydrothermal methods. The structural characteristics, as well as conductive and sensor properties of the samples obtained have been studied. It is shown that the introduction of NiO into composites obtained by the hydrothermal method leads to a decrease in the value of In_2O_3 lattice parameters. The lattice parameters in impregnated samples are practically independent of the NiO content.

The specific surface area of impregnated composites is 5.1 – 5.6 m^2/g and does not depend much on the concentration of NiO in the samples. However, the addition of 3 % NiO to indium oxide increases the specific surface area of a hydrothermal sample with rhombohedral structure from 21.9 to 26.1 m^2/g and from 16.1 to 18.2 m^2/g for samples with cubic structure. The conductivity of hydrothermal composites is an order of magnitude lower than that of impregnated composites. It is shown that an increase in the NiO content in the composite leads to an increase in their sensor response to H_2 and CO, as well as a decrease in the optimal operating temperature for hydrothermal samples by 60 °C, and for impregnated samples by 20 °C.

The conducted studies allowed us to compare the properties of NiO–In_2O_3 sensor systems depending on the synthesis method used. Thus, the maximum response to 0.9 % H_2 sensors, with a sensitive layer prepared by the impregnation method, was achieved when the NiO additive was 1 %, but the optimal additive value at the hydrothermal method was 3 %. At the same time, the maximum response value was slightly larger for sensors prepared using solutions of indium and nickel nitrates in ethanol. Note that in this case, rhombohedral indium oxide is formed. However, the maximum response to 0.1 % H_2 is achieved for the sensitive layer obtained using solutions nitrates in water with cubic indium oxide. In other words, the properties of the studied systems are strongly dependent not only on the method of preparation and concentration of the additive, but also on the concentration of the gas being studied. It is also important that the introduction of nickel oxide into the composite leads to a decrease in the optimal operating temperature and response/recovery time of the sensor, as well as to an increase in selectivity.

It follows from the above that sensors prepared by hydrothermal method are more effective compared to impregnated systems. The choice between using alcohol or water as a solvent for hydrothermal synthesis of the sensitive layer depends on which sensor characteristic is most important in a particular case.

References

[1] Zappa D., Galstyan V., Kaur N., Arachchige H.M.M., Sisman O., Comini E. Metal oxide-based heterostructures for gas sensors – A review. *Anal. Chim. Acta*, 2018, **1039**, P. 1–23.

[2] Gerasimov G.N., Gromov V.F., Ilegbusi O.J., Trakhtenberg L.I. The mechanisms of sensory phenomena in binary metal-oxide nanocomposites. *Sens. Actuators B Chem.*, 2017, **240**, P. 613–624.

[3] Hu J., Sun Y., Xue Y., Zhang M., Li P., Lian K., Chen Y. Highly sensitive and ultra-fast gas sensor based on CeO_2-loaded In_2O_3 hollow spheres for ppb-level hydrogen detection. *Sens. Actuators B Chem.*, 2018, **257**, P. 124–135.

[4] Vasiliev A., Shaposhnik A., Moskalev P., Kul O. Kinetics of chemisorption on the surface of nanodispersed SnO_2-PdO_x and selective determination of CO and H_2 in air. *Sensor*, 2023, **23**, 3730.

[5] Kim H.J., Lee J.H. Highly sensitive and selective gas sensors using p-type oxide semiconductors: overview. *Sens. Actuators B Chem.*, 2014, **192**, P. 607–627.

[6] Xu K., Duan S.L., Tang Q., Zhu Q., Zhao W., Yu X., Yang Y., Yu T., Yuan C.L., P-N heterointerface-determined acetone sensing characteristics in α-MoO_3-NiO core-shell nanobelts. *Cryst. Eng. Comm.*, 2019, **21**, P. 5834–5844.

[7] Kavitha G., Arul K.T., Babu P. Enhanced acetone gas sensing behavior of n-ZnO/p-NiO nanostructures. *J. Mater. Sci.: Mater. Electron.*, 2018, **29**, P. 6666–6671.

[8] Choi S., Lee J.K., Lee W.S., Lee C., Lee W.I. Acetone sensing of multi-networked WO_3-NiO core-shell nanorod sensors. *J. Korean Phys. Soc.*, 2017, **71**, P. 487–493.

[9] Sun G.J., Kheel H., Choi S., Hyun S.K., Lee C. Prominent gas sensing performance of TiO_2-core/NiO-shell nanorod sensors. *J. Nanosci. Nanotechnol.*, 2017, **17**, P. 4099–4102.

[10] Haq M.U., Wen Z., Zhang Z.Y., Khan S., Lou Z.R., Ye Z.Z., Zhu L.P. A two-step synthesis of nanosheet-covered fibers based on α-Fe_2O_3/NiO composites towards enhanced acetone sensing. *Sci. Rep.*, 2018, **8**, 1705.

[11] Lee H., Mirzaei A., Kim H.W., Kim S.S. SnO_2(n)–NiO(p) composite nanowebs: Gas sensing properties and sensing mechanisms. *Sens. Actuators B Chem.*, 2018, **258**, P. 204–214.

[12] Ikim M.I., Gerasimov G.N., Gromov V.F., Ilegbusi O.J., Trakhtenberg L.I. Synthesis, structural and sensor properties of nanosized mixed oxides based on In_2O_3 particles. *Int. J. Mol. Sci.*, 2023, **24**, 1570.

[13] Katoch A., Choi S.-W., Kim J.-H., Lee J.-H., Lee J.-S., Kim S.S. Importance of the nanograin size on the H_2S-sensing properties of ZnO-CuO composite nanofibers. *Sens. Actuators B Chem.*, 2015, **214**, P. 111–116.

[14] Choi S.-W., Zhang J., Katoch A., Kim S.S. H_2S sensing performance of electrospun CuO-loaded SnO_2 nanofibers. *Sens. Actuators B Chem.*, 2012, **160**, P. 54–60.

[15] Liu Y., Bai J., Li Y., Yang L., Wang Y., Li Y., Liu F., Zhang Y., Lu G. Preparation of PdO-decorated NiO porous film on ceramic substrate for highly selective and sensitive H_2S detection. *Ceramics Int.*, 2022, **48**, P. 4787–4794.

[16] Liu H., Wang Z., Cao G., Pan G., Yang X., Qiu M., Sun C., Shao J., Li Z., Zhang H. Construction of hollow NiO/ZnO p-n heterostructure for ultrahigh performance toluene gas sensor. *Mater. Scie. in Semicond. Proc.*, 2022, **141**, 106435.

[17] Ju D., Xu H., Xu Q., Gong H., Qiu Z., Guo J., Zhang J., Cao B. High triethylamine-sensing properties of NiO/SnO_2 hollow sphere P-N heterojunction sensors. *Sens. Actuators B Chem.*, 2015, **215**, P. 39–44.

[18] Kaur M., Dadhich B.K., Singh R., Ganapathi K., Bagwaiya T., Bhattacharya S., Gadkari S.C., RF sputtered SnO_2: NiO thin films as sub-ppm H_2S sensor operable at room temperature. *Sens. Actuators B Chem.*, 2017, **242**, P. 389–403.

[19] Fan X., Xu Y., He W. High acetone sensing properties of In_2O_3-NiO one-dimensional heterogeneous nanofibers based on electrospinning. *RSC Advances.*, 2021, **19**, P. 11215–11223.

[20] Yan C., Lu H.B., Gao J.Z., Zhu G.Q., Yin F., Yang Z.B., Liu Q.R., Li G. Synthesis of porous NiO-In_2O_3 composite nanofibers by electrospinning and their highly enhanced gas sensing properties. *J. Alloys Compd.*, 2017, **699**, P. 567–574.

[21] Belysheva T.V., Gerasimov G.N., Gromov V.F., Spiridonova E.Yu., Trakhtenberg L.I. Conductivity of SnO_2–In_2O_3 nanocrystalline composite films. *Russ. J. Phys. Chem. A*, 2010, **84**, P. 1554–1559.

[22] Qin W., Lu B., Xu X., Shen Y., Meng F. Metal organic framework-derived porous Ni-doped In_2O_3 for highly sensitive and selective detection to hydrogen at low temperature. *Sens. Actuators B Chem.*, 2024, **417**, 136123.

[23] Jin Z., Wang C., Wu L., Song H., Yao X., Liu J., Wang, F. Fast responding and recovering of NO_2 sensors based on Ni-doped In_2O_3 nanoparticles. *Sens. Actuators B Chem.*, 2023, **377**, 133058.

[24] Yang Q., Cui X., Liu J., Zhao J., Wang Y., Gao, Y., Lu G. A low temperature operating gas sensor with high response to NO_2 based on ordered mesoporous Ni-doped In_2O_3. *New J. Chem.*, 2016, **40** (3), P. 2376–2382.

[25] Zhang Y., Cao J., Wang Y. Ultrahigh methane sensing properties based on Ni-doped hierarchical porous In_2O_3 microspheres at low temperature. *Vacuum*, 2022, **202**, 111149.

[26] Liang Z., Zhang Y., Wang M., Liu S., Zhang X., Lei S., Liu G. Facile preparation of flower-like NiO/In_2O_3 composite for sensitively and selectively detecting NO_2 at room and lower temperatures. *Appl. Surf. Sci.*, 2024, **657**, 159805.

[27] Zhang S., Li J., Han L., Zhang B., Wang Y., Zhang Z. Preparation of porous NiO/In_2O_3 nanoflower-like composites and their dual selectivity for CO/CH_4. *Mater. Res. Bull.*, 2023, **165**, 112332.

Submitted 1 July 2024; revised 29 August 2024; accepted 13 October 2024

Information about the authors:

Mariya I. Ikim – N. N. Semenov Federal Research Center for Chemical Physics RAS, 4 Kosygin Street, Moscow, 119991, Russia; ORCID 0000-0003-4411-1119; ikimmary1104@gmail.com

Vladimir F. Gromov – N. N. Semenov Federal Research Center for Chemical Physics RAS, 4 Kosygin Street, Moscow, 119991, Russia; ORCID 0000-0002-9401-1717; vfgromov@mail.ru

Genrikh N. Gerasimov – N. N. Semenov Federal Research Center for Chemical Physics RAS, 4 Kosygin Street, Moscow, 119991, Russia; ORCID 0000-0001-8692-0382; gerasimovgen@mail.ru

Valentin G. Bekeshev – N. N. Semenov Federal Research Center for Chemical Physics RAS, 4 Kosygin Street, Moscow, 119991, Russia; ORCID 0000-0001-8989-3965; bvg495@yandex.ru

Leonid I. Trakhtenberg – N. N. Semenov Federal Research Center for Chemical Physics RAS, 4 Kosygin Street, Moscow, 119991, Russia; Chemical Faculty, Lomonosov Moscow State University, Moscow, 119991, Russia; Moscow Institute of Physics and Technology(State University), Moscow, Russia; ORCID 0000-0001-9139-5754; litrakh@gmail.com

Conflict of interest: the authors declare no conflict of interest.

NANOSYSTEMS:
PHYSICS, CHEMISTRY, MATHEMATICS

Smal E., et al. *Nanosystems: Phys. Chem. Math.*, 2024, **15** (6), 879–892.
http://nanojournal.ifmo.ru
DOI 10.17586/2220-8054-2024-15-6-879-892

Original article

Chemical looping methane dry reforming over Ni-containing modified ceria-zirconia

Ekaterina Smal[1,a], Valeria Fedorova[1,b], Konstantin Valeev[1,c], Amir Hassan[2,d], Evgeny Gerasimov[1,e], Mikhail Simonov[1,f]

[1]Boreskov Institute of Catalysis SB RAS, Novosibirsk, Russia
[2]Novosibirsk State University, Novosibirsk, Russia

[a]smal@catalysis.ru, [b]valeria@catalysis.ru, [c]valeev@catalysis.ru, [d]a.khassan1@g.nsu.ru, [e]gerasimov@catalysis.ru, [f]smike@catalysis.ru

Corresponding author: Ekaterina Smal, smal@catalysis.ru

PACS 61.46.+w, 82.40.-g, 82.65.+r

ABSTRACT Modified ceria-zirconia oxides were prepared in supercritical fluids in flow-type installation. Ni was added by wetness impregnation. All materials were studied by a complex of physicochemical techniques (XRD, TEM, H_2-TPR). Catalysts have been investigated in a modern process – chemical looping methane dry reforming (CLMDR). Conversions of CH_4 and CO_2, H_2/CO ratio, H_2 and CO productivities were calculated. The features of CLMDR process were compared with results obtained in MDR steady-state conditions.

KEYWORDS chemical looping, methane dry reforming, hydrogen, ceria-zirconia, supercritical synthesis

ACKNOWLEDGEMENTS This work was supported by the Ministry of Science and Higher Education of the Russian Federation within the governmental assignment for Boreskov Institute of Catalysis (project FWUR-2024-0033).
The studies were carried out using the facilities of the shared research center “National Center of Investigation of Catalysts” at Boreskov Institute of Catalysis.
Authors thank to T. Krieger and O. Bulavchenko for XRD, V. Rogov for H_2-TPR and A. Ishchenko for TEM studies.

FOR CITATION Smal E., Fedorova V., Valeev K., Hassan A., Gerasimov E., Simonov M. Chemical looping methane dry reforming over Ni-containing modified ceria-zirconia. *Nanosystems: Phys. Chem. Math.*, 2024, **15** (6), 879–892.

1. Introduction

Methane dry reforming process (MDR) (1) is a route to utilize and convert two major greenhouse gases – CH_4 and CO_2 – to syngas and hydrogen [1–3]. Syngas can be obtained with a low H_2/CO molar ratio equal to 1, which is suitable for obtaining valuable liquid hydrocarbons through Fischer–Tropsch synthesis [4].

$$\mathrm{CH_4 + CO_2 \rightarrow 2H_2 + 2CO}, \quad \Delta H^0_{298\,\mathrm{K}} = 247\ \mathrm{kJ/mol}. \tag{1}$$

However, the side reaction of reverse water gas shift (RWGS) (2) caused by the simultaneous presence of CO_2 and hydrogen results to decrease of H_2/CO ratio during MDR [5]. So, it is important to find a way to carry out the MDR reaction in order to exclude the occurrence of RWGS reaction.

$$\mathrm{CO_2 + H_2 \rightleftarrows CO + H_2O}, \quad \Delta H^0_{298\,\mathrm{K}} = -41\ \mathrm{kJ/mol}. \tag{2}$$

Another problem of conventional MDR is rapid coke formation which occurs due to methane decomposition (3) at low temperatures and CO disproportionation (Boudouard reaction) at high temperatures (4) [6].

Both side reactions lead to active centers blocking and catalyst deactivation.

$$\mathrm{CH_4 \rightarrow C + 2H_2}, \quad \Delta H^0_{298\,\mathrm{K}} = 75\ \mathrm{kJ/mol}, \tag{3}$$

$$\mathrm{2CO \rightarrow C + CO_2}, \quad \Delta H^0_{298\,\mathrm{K}} = -171\ \mathrm{kJ/mol}. \tag{4}$$

Chemical looping methane dry reforming process (CLMDR) is the attractive way to resolve both these issues. In this mode, consistent feed of CH_4 and CO_2 is implemented, which eliminates the contribution of RWGS side reaction [7–9].

The first step of CLMDR includes reaction of methane with support reactive oxygen with its partial oxidation and selective production of syngas (5). Further, the reduced support would be re-oxidized by CO_2 to regenerate the reactive oxygen (6). Successive red-ox cycles drive the continuous conversion of CO_2 and methane to syngas with a higher H_2/CO molar ratio. The total process stoichiometrically corresponds to the conventional catalytic MDR although it is divided in time into two independent heterogeneous reactions [7–9].

$$\mathrm{CH_4 + cat_{Ox} \rightarrow 2H_2 + CO + cat_{Red}}, \tag{5}$$

$$\mathrm{CO_2} + \mathrm{cat_{Red}} \rightarrow \mathrm{cat_{Ox}} + \mathrm{CO}, \tag{6}$$

$$\mathrm{cat_{Ox}} = \text{oxidized catalyst} \quad \text{and} \quad \mathrm{cat_{Red}} = \text{reduced catalyst [8].}$$

Moreover, compared with MDR process, during CLMDR, the carbon generated by CH_4 pyrolysis can be oxidized by CO_2 at the oxidation step, which can reduce the carbon deposition to a certain extent and also produce syngas with adaptable hydrogen/carbon molar ratio [7].

In the literature, catalysts for the chemical looping processes are called oxygen carriers. They consist of reducible metal oxides, which must have the following characteristics: ability to generate oxygen ions or vacancies and electrons or holes, facilitate their diffusion in the bulk phase and provide active sites for surface reactions [10–12].

Another important factor is strength of the surface M–O bonds. If they are too weak, the full oxidation will occur at the reduction stage instead of partial one. However, they should also not be too strong, otherwise the material will be a weak oxidant. An ideal oxygen carrier has intermediate bond strength and mobility of lattice O atoms to drive the process both selectively and kinetically fast. Such materials include oxides with fluorite, perovskite and rocksalt structures, and most of investigated catalysts are based on them [12].

Furthermore, for practical applications these materials should exhibit long-term redox stability, fast reaction kinetics, reasonable oxygen and heat capacity and conductivity, be mechanically and thermally robust under the operation conditions [12].

It is well known that CeO_2 has a good thermal stability and a high oxygen mobility/storage capacity due to its redox couple (Ce^{4+}/Ce^{3+}) being perspective support for high temperature processes such as MDR and CLMDR [7–9, 13, 14]. However, different ways to increase oxygen mobility of CeO_2 oxide are under investigation. For example, ceria modification by zirconium with solid solution formation leads to increased oxygen mobility [15]. Besides, partial replacement of cerium with zirconium in CeO_2 can improve the oxygen storage capacity and catalytic performance in MDR process because of the easy formation of oxygen vacancies [16].

It was shown that Ni-containing catalysts based on ceria-zirconia are attractive for MDR process due to their low price and high activity [13,17–19]. In recent years, the influence of dopant metals (Ti, Nb, Pr) in ceria or ceria-zirconia on catalytic activity in MDR was investigated by our research group [20–25] and other groups as well [26–29]. Ni-containing catalysts based on Ce–Pr mixed oxide show higher activity in MDR process at 700 °C compared with Ce–Zr-based catalyst [23,25,30].

It is well known that the preparation method has a great influence on the properties of the resulting oxides, which consequently affects their interaction with the supported metal component and catalytic activity in the target reaction. There are a lot of various methods for the preparation of mixed Ce–Zr oxides described in the literature: solid-phase synthesis [31], the Pechini method [32], coprecipitation [33], sol-gel technology [34, 35], hydrothermal synthesis [36], solvothermal method [37], microemulsions [38], the microwave method [39], the sonochemical method [40], solution combustion [41] and spray pyrolysis reactions [42].

In recent years, synthesis in supercritical alcohols is of growing interest, since it is characterized by low energy consumption, simple implementation, allows obtaining mixed oxides with high structural homogeneity and affecting their morphology by varying synthesis conditions such as pressure, temperature and nature of supercritical solvent [25, 43]. In our previous study [20], it was shown that synthesis in supercritical isopropanol allows obtaining single-phase mixed Ce–Zr-(Ti/Nb) oxides, in contrast to the Pechini method.

The CLMDR was studied earlier using Ni-containing catalysts based on pure ceria [7–9] only. It was shown in [8] that conversions of CH_4 and CO_2 were equal to 85 % after 12 cycles at 700 °C for initial reaction mixture containing 5 % of CH_4 or CO_2. However, this concentration is too low for practical use. It should be emphasized that CLMDR is a process potentially capable of producing synthesis gas suitable for the synthesis of hydrocarbons, so the design of highly active catalysts is an urgent task.

The objective of the present work is to study the Ni-containing catalysts based on modified ceria-zirconia prepared in supercritical fluids in chemical looping methane dry reforming reaction. The novelty of this work is using namely modified ceria-zirconia as supports in the process of CLMDR. Moreover, in our work, we use more concentrated reaction mixtures containing 15 % of reagents.

$Ni/Ce_{0.75}Zr_{0.25}O_2$, $Ni/Ce_{0.75}Ti_{0.1}Zr_{0.15}O_2$, $Ni/Ce_{0.75}Ti_{0.05}Nb_{0.05}Zr_{0.15}O_2$ and $Ni/Ce_{0.75}Pr_{0.1}Zr_{0.15}O_2$ compositions were earlier investigated as catalysts for conventional MDR process [20, 25] and demonstrated high activity in this reaction. So they were chosen in the present work for further studies as catalysts for CLMDR process. The influence of dopant metals in supports and comparison with results obtained in MDR steady-state conditions are presented.

2. Experimental section

2.1. Preparation of Ni-containing modified ceria-zirconia materials

The modified ceria-zirconia supports were synthesized by the solvothermal method using supercritical conditions in the flow-type reactor [20]. $Ce(NO_3)_3 \cdot 6H_2O$ (pure for analysis, Vecton, Russia), $Zr(OBu)_4$ (80 wt% in n-butanol, Alfa Aesar, Germany), $Ti(OC_4H_9)_4$ (Acros Organics, Belgium), $NbCl_5$ (Acros Organics, Belgium) and $Pr(NO_3)_3 \cdot 6H_2O$

(chemically pure, Krane, Russia) were used as supports precursors. Starting salts were dissolved in isopropanol (particularly pure, Soyuzkhimprom, Russia); only $Zr(OBu)_4$ was dissolved in n-butanol (chemically pure, Komponent-Reaktiv, Russia) with acetylacetonate (pure, Interhim, Russia) as complexing agent. Isopropanol was used as a supercritical alcohol in the synthesis process. The molar concentrations of Ce and Zr were 0.25 and 0.8 – 1 mol/L, respectively. The temperature of oxide synthesis was 400 °C, the pressure in the reaction system was 120 atm, the feed rate of the salts solution was 5 mL/min, and the solvent feed rate was 9 mL/min. After leaving the reactor, the exit stream was depressurized and cooled, and suspension of solid particles in the mother liquid was collected in a storage container. Obtained powders were decanted, dried at 200 °C and calcined at 700 °C during 2 h.

All catalysts were obtained by the incipient wetness impregnation of the supports with water solution of $Ni(NO_3)_2 \cdot 6H_2O$ (pure for analysis, Vecton, Russia) and subsequent drying and calcination at 700 °C during 2 h. Ni amount was 5 wt.% in all samples.

2.2. Catalysts characterization

X-Ray diffraction analysis (XRD) was carried out using a D8 Advance (Bruker, Germany) diffractometer with Cu Kα radiation and LynxEye detector. The XRD pattern was collected in the 2θ range 20 – 85 °C with a 0.05 step size and 3 s accumulation times.

The *in situ* XRD experiment was carried out using XRK-900 high-temperature flow chamber (Anton Paar, Graz, Austria). The sample was placed in a chamber and purged with He flow. Next, the heating of the chamber was turned on (heating rate 12 °C/min). The mixture of H_2 in He (H_2:He = 1:2) was fed at a temperature about 300 °C. The sample was reduced by hydrogen to 700 °C. Then the chamber was purged with He for 0.5 h and flow of pure CO_2 was supplied. The first diffractogram under CO_2 was recorded after 0.5 h, the second one – after 2 h. Then the sample was cooled to a room temperature under He flow. The final diffractogram was recorded after night under air. The lattice parameters were calculated using the least squares method by Polycrystal software [44].

Specific surface area (SSA) was defined by the BET method using a Quadrasorb evo (Quantachrome Instruments, USA) installation.

Reducibility of samples pretreated in O_2 at 500 °C were studied by the temperature programmed reduction by H_2 (H_2-TPR) with the temperature ramp 10 °/min from 60 to 900 °C using 10 % H_2 in Ar mixture and GC Tsvet 500 (Russia).

TEM (transmission electron microscopy) micrographs were obtained with a Themis-Z3.1 instrument (TFS, USA) equipped with X-FEG monochromator and CS/S double corrector, accelerating voltage 200 kV and with a JEM-2200FS transmission electron microscope (JEOL Ltd., Japan, acceleration voltage 200 kV, lattice resolution $\sim$ 1 Å) equipped with a Cs corrector. Elemental analysis was performed with a Super-X EDS detector (energy resolution about 120 eV) in HAADF-STEM mode. Samples for the TEM study were prepared by ultrasonic dispersing in ethanol and subsequent deposition of the suspension upon a "holey" carbon film supported on a copper grid.

2.3. Catalytic Tests

2.3.1. Chemical looping methane dry reforming technique (CLMDR). Before reaction the catalysts were pretreated in 10 vol. % O_2/N_2 at 600 °C for 30 min and then in 5 vol. % H_2/He at 600 °C for 1 h. Chemical looping methane dry reforming process (CLMDR) was carried out at 700 °C under atmospheric pressure in flow-type installation. Contact time was 10 ms. The gas stream was switched periodically between inert gas (He) to one containing 15 vol.% CH_4/He at reduction step and 15 vol.% CO_2/He at oxidation step. Each cycle consists of a reduction step of 1 min, He purge of 2 min, an oxidation step of 1 min, and again He purge of 2 min. Cycles were repeated 12 times.

During the cyclic supply of reagents, the concentrations of products in the reaction mixture were continuously measured using a gas analyzer Test-1 (Boner, Russia). The measured concentrations were recalculated to reagents and products flow (mol·min^{-1}) and integrated over time into the amount of substance in each cycle.

The reagents conversions were calculated as follows:

$$X_{\mathrm{CH_4}}\,(\%) = \frac{\upsilon_0 - \upsilon}{\upsilon_0} \cdot 100\,\%$$

at reduction step,

$$X_{\mathrm{CO_2}}\,(\%) = \frac{\upsilon_0 - \upsilon}{\upsilon_0} \cdot 100\,\%$$

at oxidation step, where υ_0, υ – initial and final reagent amount of substance, respectively (mol).

H_2/CO ratio was calculated both at reduction step and taking into account the total amount of CO produced during each cycle:

$$\frac{\mathrm{H_2}}{\mathrm{CO}}\text{ratio} = \frac{\upsilon(\mathrm{H_2})}{\upsilon(\mathrm{CO})}.$$

H_2 productivity was calculated at reduction step (mol·g^{-1}):

$$Y_{\mathrm{H_2}} = \frac{\upsilon(\mathrm{H_2})}{m_{\mathrm{cat}}}.$$

CO productivity was calculated at reduction and oxidation step (mol·g^{-1}):

$$Y_{\mathrm{CO}} = \frac{\upsilon(\mathrm{CO}^{R}) + \upsilon(\mathrm{CO}^{O})}{m_{\mathrm{cat}}}.$$

Carbon balances were calculated both separately at each stage and in total at each cycle using the following formulas:

$$\mathrm{CarbonBalance(R)} = \frac{\upsilon(\mathrm{CH_4}^{\mathrm{R}})+\upsilon(\mathrm{CO_2}^{\mathrm{R}})+\upsilon(\mathrm{CO}^{\mathrm{R}})}{\upsilon_0(\mathrm{CH_4})} \cdot 100\,\%,$$

$$\mathrm{CarbonBalance(O)} = \frac{\upsilon(\mathrm{CO_2}^{\mathrm{O}})+\upsilon(\mathrm{CO}^{\mathrm{O}})}{\upsilon_0(\mathrm{CO_2})} \cdot 100\,\%,$$

$$\mathrm{CarbonBalance(All)} = \frac{\upsilon(\mathrm{CH_4}^{\mathrm{R}})+\upsilon(\mathrm{CO_2}^{\mathrm{R}})+\upsilon(\mathrm{CO}^{\mathrm{R}})+\upsilon(\mathrm{CO_2}^{\mathrm{O}})+\upsilon(\mathrm{CO}^{\mathrm{O}})}{\upsilon_0(\mathrm{CH_4})+\upsilon_0(\mathrm{CO_2})} \cdot 100\,\%.$$

Hydrogen balances was also calculated:

$$\mathrm{HydrogenBalance} = \frac{2 \cdot \upsilon(\mathrm{H_2}^{R}) + 4 \cdot \upsilon(\mathrm{CH_4}^{R})}{4\upsilon_0(\mathrm{CH_4})} \cdot 100\,\%.$$

2.3.2. Methane dry reforming performance in steady-state conditions. Pretreatment before reaction was the same as in the case of CLMDR. The experiments were carried out in the temperature range of 600 – 750 °C, contact time was 10 ms. The initial mixture was 15 vol. % CH_4 + 15 vol. % CO_2 + balance N_2 following the earlier described procedure [20, 22].

3. Results and discussion

3.1. Textural and structural properties

Figure 1 shows XRD patterns for catalysts. Reflections corresponding to the cubic fluorite lattice CeO_2–ZrO_2 (PDF 81–0792) and NiO phase (PDF 47–1049) are observed.

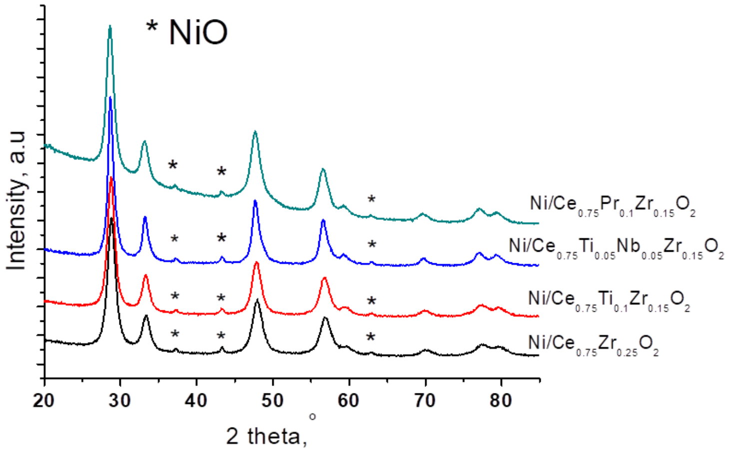

FIG. 1. XRD patterns of fresh catalysts

Table 1 shows specific surface area of studied catalysts and cell parameter and crystallite size of fluorite phase. The S_{BET} is close for three of studied catalysts, but is significantly lower for Pr-containing sample. The values of crystallite size of fluorite phase estimated from diffraction patterns are 9 – 14 nm. The crystallite size of NiO is between 20 – 30 nm for all samples. The change of cell parameter of ceria-zirconia fluorite phase after addition of Ti, Nb and Pr confirms incorporation of dopant cations into fluorite lattice.

A more detailed characterization of the samples is presented in our previous works, where the presence of oxygen vacancies in ceria-based catalysts prepared in supercritical isopropanol was shown based on XRD and Raman data [20, 21, 25].

The morphology of catalysts was studied by transmission electronic microscopy (TEM). The TEM images of fresh catalysts are presented in the Figure 2. Particles of fluorite phase have near-spherical shape with sizes about 15 – 20 nm and are packed into large ($\sim$ 100 nm) agglomerates [20, 25].

Nickel is presented on the support surface in the form of NiO particles, the corresponding interplanar distances are shown in the Fig. 2(b,d). NiO particles are also marked by blue circles in the Fig. 2(a,c). The particle size of NiO is about 10 – 20 nm for TiNb-doped sample and 20 – 30 nm for Pr-doped sample. It also should be noted, that NiO particles for Pr-containing sample have close to cubic shape, which, together with their larger size, also suggests their weak bound with the support.

TABLE 1. Surface area (BET) and fluorite crystallites size (from XRD) of the studied catalysts

Catalyst	S_{BET} (m^2/g)	$d_{fluorite}$ (nm)	d_{NiO} (nm)	Cell parameter of fluorite phase (Å)
$Ni/Ce_{0.75}Zr_{0.25}O_2$	21	9.4	30	5.368
$Ni/Ce_{0.75}Ti_{0.1}Zr_{0.15}O_2$	23	10.4	20	5.379
$Ni/Ce_{0.75}Ti_{0.05}Nb_{0.05}Zr_{0.15}O_2$	26	14.5	24	5.392
$Ni/Ce_{0.75}Pr_{0.1}Zr_{0.15}O_2$	9	11	23	5.394

The homogeneous distribution of support cations in all catalysts was shown by dark-field images with EDX analysis (Fig. 3).

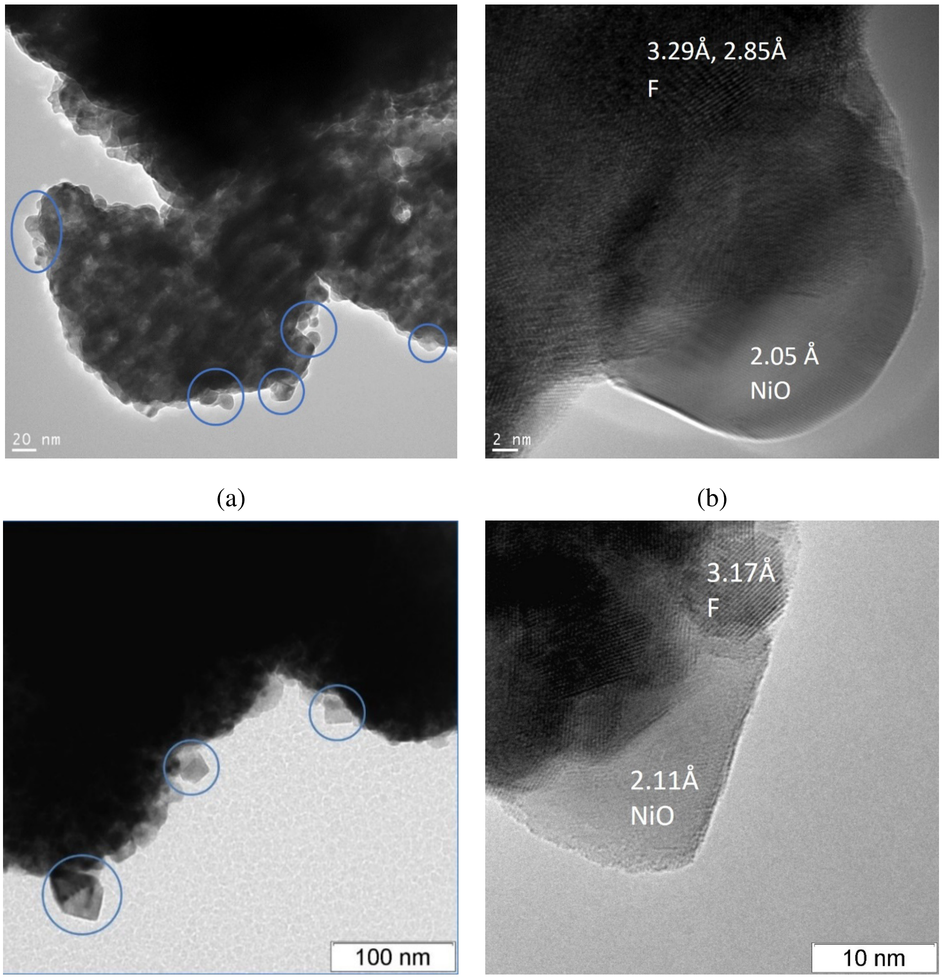

(a) (b)

(c) (d)

FIG. 2. TEM images of fresh catalysts $Ni/Ce_{0.75}Ti_{0.05}Nb_{0.05}Zr_{0.15}O_2$ (a,b [22]), $Ni/Ce_{0.75}Pr_{0.1}Zr_{0.15}O_2$ (c [25], d). F denotes the fluorite phase. NiO particles are marked by circles

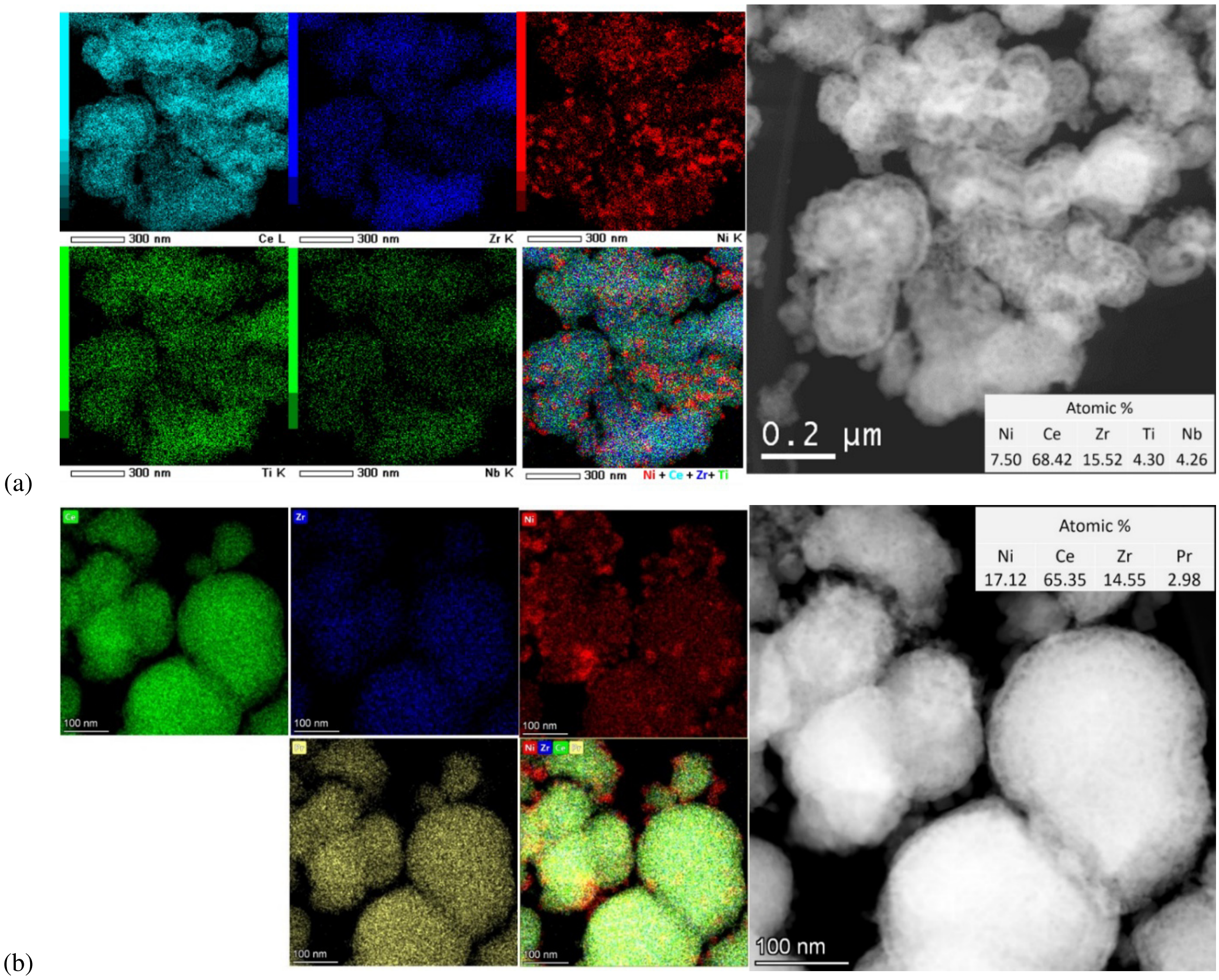

FIG. 3. HAADF-STEM images with EDX analysis of fresh catalysts a) $Ni/Ce_{0.75}Ti_{0.05}Nb_{0.05}Zr_{0.15}O_2$, b) $Ni/Ce_{0.75}Pr_{0.1}Zr_{0.15}O_2$

3.2. Catalysts reduction by H_2

Figure 4 shows H_2-TPR curves for supports and corresponding catalysts calcined at 700 °C [20, 25, 45]. For ceria, reduction peaks corresponding to removal of the surface/near-surface and bulk lattice oxygen are usually observed at 500 – 600 and 800 – 850 °C, respectively [46, 47].

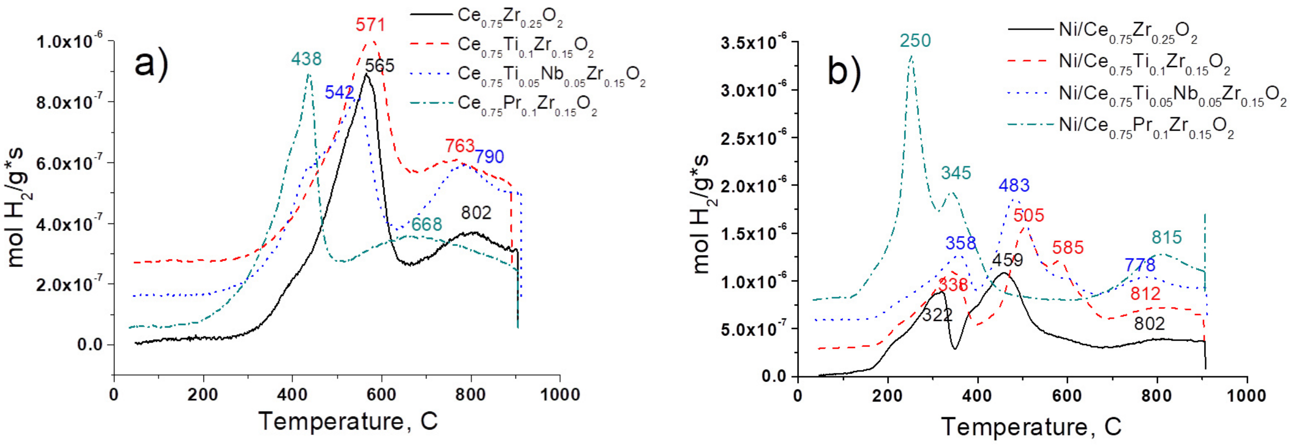

FIG. 4. H_2-TPR curves for supports (a) and corresponding catalysts (b) [20, 25]

It is worth noting, that the introduction of doping cations can promote the oxygen mobility and reactivity in modified CeO_2. For example, zirconium cations incorporated into ceria lead to reduction of the lattice oxygen at temperature below 800 °C [48]. In this work, the $Ce_{0.75}Zr_{0.25}O_2$ has peaks at 565 and 802 °C corresponding to reduction of the surface and bulk oxygen, respectively. The incorporation of Ti and Nb cations leads to a slight decrease of reduction temperatures compared with ceria-zirconia [20, 45]. At the same time, for Pr-doped sample, reduction peaks are shifted to lower temperatures by more than 100 °C which suggests its higher oxygen reactivity [25].

Amounts of hydrogen spent for the reduction of all samples are presented in the Table 2 and are quite close for all supports.

TABLE 2. H_2 consumption for studied supports and catalysts

	H_2 consumption, mmol/g_{cat}	
	Support	Ni/Support
$Ce_{0.75}Zr_{0.25}O_2$	1.36	2.21 [20]
$Ce_{0.75}Ti_{0.1}Zr_{0.15}O_2$	1.20	2.32 [20]
$Ce_{0.75}Ti_{0.05}Nb_{0.05}Zr_{0.15}O_2$	1.30	2.06 [20]
$Ce_{0.75}Pr_{0.1}Zr_{0.15}O_2$	1.21	2.14 [25]

The H_2-TPR reduction curves of the Ni-containing catalysts are presented in the Fig. 4(b). It is well known that metal-support interaction has very important role to red-ox properties of corresponding catalysts. This interaction can be very complex and results in presence of various forms of Ni species in the catalysts.

A weak shoulder at 200 °C corresponds to reduction of highly reactive oxygen surface species [49, 50]. For Ni/$Ce_{0.75}Zr_{0.25}O_2$ sample, there are two peaks in the region of middle temperatures, in contrast to one peak for the $Ce_{0.75}Zr_{0.25}O_2$ support. The first peak at 322 °C is due to the reduction of nickel oxide weakly interacting with support [51], while the second peak at 459 °C can be associated with the reduction of NiO particles strongly interacting with the oxide support [52].

Simultaneously with the reduction of nickel, the reduction of support cations also occurs [24, 45]. For Ti-containing catalysts, shift of these peaks to higher temperature is observed suggesting stronger interaction of supported Ni with oxide support [24].

For Pr-doped sample, on the contrary, reduction begins at lower temperature. In our earlier work [25], it was shown by XRD with *in situ* H_2 reduction, that peak at 250 °C can be attributed to reduction of active surface oxygen. Such shift for Ni-containing samples is associated with the facilitation of support reduction due to hydrogen spillover in the presence of nickel atoms [25]. The reduction of nickel also begins together with the support cations and finish at a lower temperature due to its weaker interaction with the support.

A more detailed characterization of TPR data can be found in our previous works [20, 25, 45].

3.3. Kinetic features of CLMDR

Figure 5(a) demonstrates the typical dependence of reagents and products concentration on reaction time at 700 °C using the Ni/$Ce_{0.75}Zr_{0.25}O_2$ catalyst as an example.

The catalyst reacts separately with methane and carbon dioxide at the reduction and oxidation stages, respectively.

It is assumed that several parallel processes occur at the reduction stage. First, the lattice oxygen interacts with CH_4 forming CO and H_2 by reaction of partial oxidation (7). The concentration of methane gradually increases, while the concentrations of H_2 and CO first increase to a maximum and then decrease due to limited amount of reactive oxygen of the catalyst.

$$CH_4 + [O] \rightarrow 2H_2 + CO^R. \tag{7}$$

Figure 6(a) presents data of H_2/CO^R ratio at reduction step. It is higher than 7 at the beginning of reaction and drops to 3 – 4 for last cycles which is still higher than 2 for partial oxidation (7). The formation of superstoichiometric H_2 can be explained by the occurrence of the second process, namely, the decomposition of methane according to reaction at (2). It can be seen that H_2/CO^R ratio decreases with the cycle number, so decrease in the contribution of methane decomposition reaction can be assumed.

Moreover, presence of a few amount of CO_2 at reduction stage indicates occurring reaction of complete oxidation of methane by highly reactive oxygen on the catalyst surface (8). Unfortunately, we have no information about formation of water because products concentration was measured by gas analyzer. However, both these products were observed at reduction step by Löfberg et al. [9].

$$CH_4 + 2[O] \rightarrow H_2O + CO_2^R. \tag{8}$$

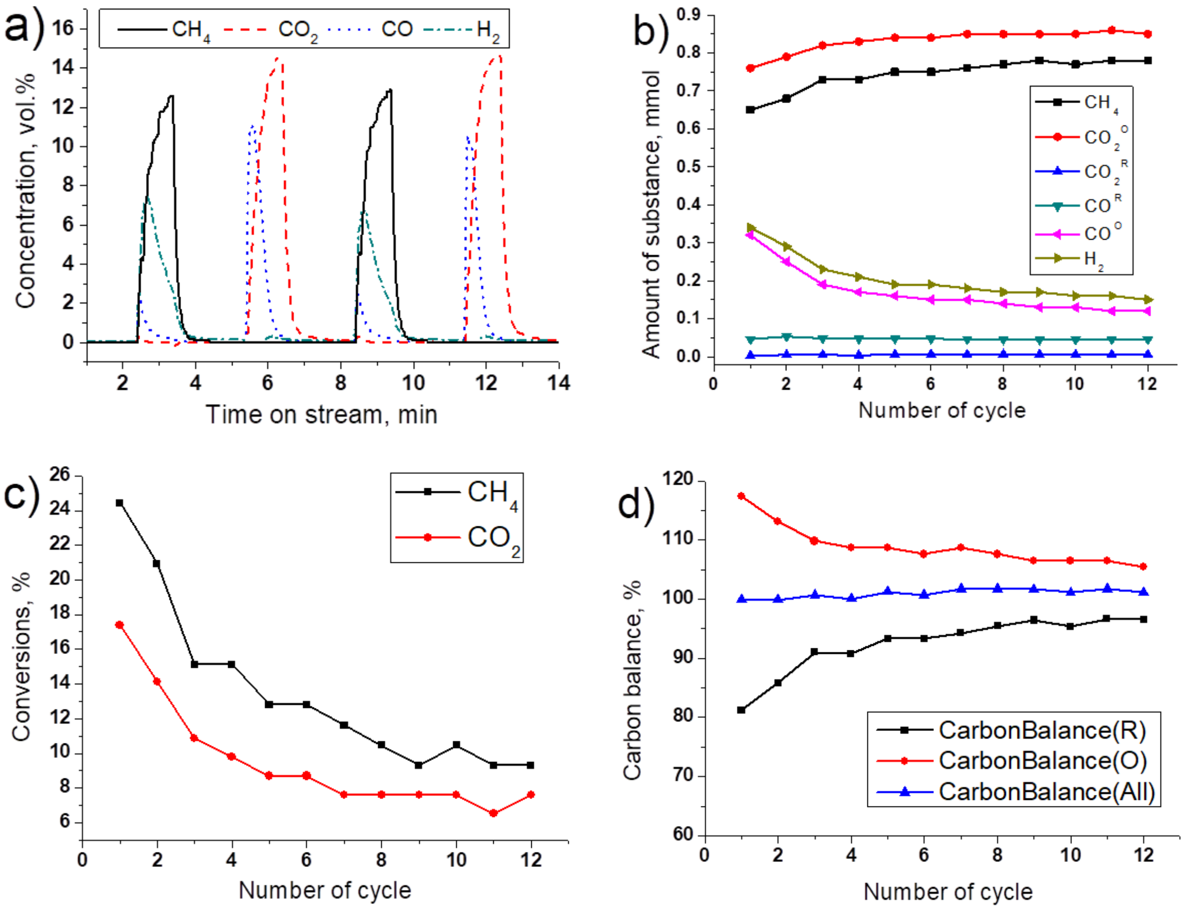

FIG. 5. Results of CLMDR experiment for Ni/$Ce_{0.75}Zr_{0.25}O_2$: a) the dependence of reagents and products concentrations on reaction time during 1st and 2nd cycles; b) the dependencies of CH_4, CO_2, CO, H_2 amounts on cycle number. CO^R/CO_2^R is CO/CO_2 produced at reduction step, CO^O/CO_2^O is CO/CO_2 produced at oxidation step; c) CH_4 and CO_2 conversions; d) carbon balances. Conditions: 15 vol.% CH_4 +15 vol.% CO_2 + 70 vol.% He, $T = 700$ °C, $\tau = 10$ ms

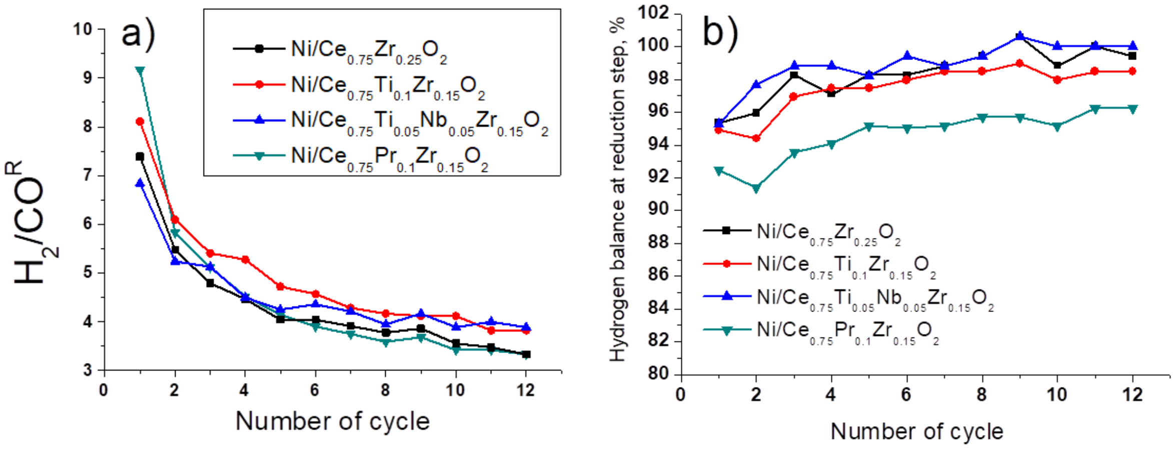

FIG. 6. a) The H_2/CO ratio at reduction step; b) hydrogen balance at reduction step

The hydrogen balances estimated at reduction step are presented in the Fig. 6(b). It can be seen that hydrogen balance is rather close to 100 % for the most of catalysts and is slightly lower for the Pr-doped sample. Based on the TPR data, it can be assumed that this sample contains more highly reactive oxygen, which leads to an increased oxidizing ability and lower hydrogen balance due to water formation.

Based on the data of CO_2 and CO formation at the reduction stage, the number of oxygen monolayers removed from the catalyst was calculated. It reaches $\sim$ 7 – 9 monolayers for the Pr-containing sample and $\sim$ 3 – 4 monolayers for other catalysts. So, this amount exceeds a monolayer even without taking into account the produced water, which indicates participation both of surface and lattice oxygen in the reaction process.

At the oxidation step there are also two routes of CO_2 consumption. The carbon generated by CH_4 decomposition can be oxidized by CO_2 forming CO (9). In addition, a negligible formation of hydrogen is observed, probably due to oxidation of CH_x species on the catalyst surface. The second parallel route of CO_2 consumption is oxidation of Ce_xO_y reduced species, during which the lattice oxygen consumed at the reduction stage is replenished (10). Another parallel route of CO_2 consumption, Ni oxidation by CO_2, is thermodynamically forbidden at the reaction temperature [8]. So, during oxidation stage, CO_2 conversion is gradually decreased due to replenishing of support oxygen and oxidation of carbon deposits.

$$\mathrm{CO_2} + \mathrm{C_{ads}} \rightarrow 2\mathrm{CO^O}, \tag{9}$$

$$\mathrm{CO_2} + [\,] \rightarrow \mathrm{CO^O} + [\mathrm{O}]. \tag{10}$$

Both of these processes lead to return of the catalyst to its initial oxidized state, which was before the reduction cycle, and the catalytic cycle is closed.

To some extent, this behavior is similar to that proposed for the red-ox Mars and Van Krevelen mechanism of such type reactions. It has been suggested that the mechanism of action of catalysts based on fluorites and perovskites with a high reactivity of lattice oxygen is of the red-ox type, and methane dry reforming proceeds with the participation of lattice oxygen [53]. In the present study, this assumption is also confirmed, since without the participation of lattice oxygen, the conversion of methane and CO_2 during the periodic supply of these reagents would be impossible.

3.4. Influence of the support composition on catalytic activity

One of the key tasks was to compare influence of doping cation on catalytic activity in CLMDR. In earlier investigations of our group, all these compositions were investigated in the conventional MDR [20,22,23,45]. Catalysts doped by Pr and both Ti and Nb showed the highest activity due to their high defectiveness and presence of oxygen vacancies. So it was interesting how these features will affect the activity in CLMDR mode.

The dependencies of the substance amount of reagents and products on cycle number are presented in Fig. 5(b) using the example of $Ni/Ce_{0.75}Zr_{0.25}O_2$. Each point on the graphs is obtained by integrating the corresponding concentration curve at the stages of reduction or oxidation. The H_2 amount at oxidation step is not presented since it is close to zero. Based on these data, reagents conversions, products productivities and carbon balances were calculated.

Figures 5(c,d) presents reagents conversions and carbon balances for $Ni/Ce_{0.75}Zr_{0.25}O_2$ which are typical for all studied catalysts. It is known that CO_2 conversion is higher than CH_4 conversion in conventional MDR reaction because of influence of reverse water gas shift reaction (RWGS) [20]. However, in all cases in the present experiments in CLMDR, the values of CH_4 conversion are higher than CO_2 conversion that corresponds to decreasing influence of RWGS due to the separation of CO_2 and H_2 in time.

The features of carbon balances correspond to coke deposition at the reduction stage ($<$ 100 %) with subsequent oxygenation of deposited carbon at oxidation stage ($>$ 100 %). The carbon balance at the reduction stage in the first cycles is much lower, which, as was mentioned above, is due to higher contribution of the methane decomposition reaction. It should be taken into account that before the first cycle the catalyst is already in a reduced state with most of the support reactive oxygen being removed. Therefore, the contribution of the methane decomposition reaction is larger than that of the methane oxidation reaction.

The larger amount of carbon formed at the reduction step also leads to higher carbon balance at the oxidation step due to formation of additional CO from carbon deposits. It reaches 117 % and decreases with increasing cycle number. As a result, the total carbon balance at each cycle is close to 100 %.

For all studied catalysts, the similar behavior is shown (Fig. 7). The CH_4 and CO_2 conversions decrease from first cycles and reaches stationary values with an increase of the cycle number. The H_2 and CO productivities similarly decrease from 8 – 10 to 3 – 4 mmol/g.

Some differences are observed for the Pr-doped sample, for which, despite the highest methane conversion, lower H_2 and CO productivities are obtained. Since this sample also exhibits the lowest hydrogen and carbon (not shown) balances at the reduction stage, this may be due to loss of hydrogen in the form of water or CH_x species.

Another notable difference is the lowest CO_2 conversion for the TiNb-doped sample. This may be due to low methane conversion and high carbon balance at the reduction stage. So, for this sample, there is less deposited carbon, which can subsequently be oxidized at the oxidation stage, and less CO_2 is converted.

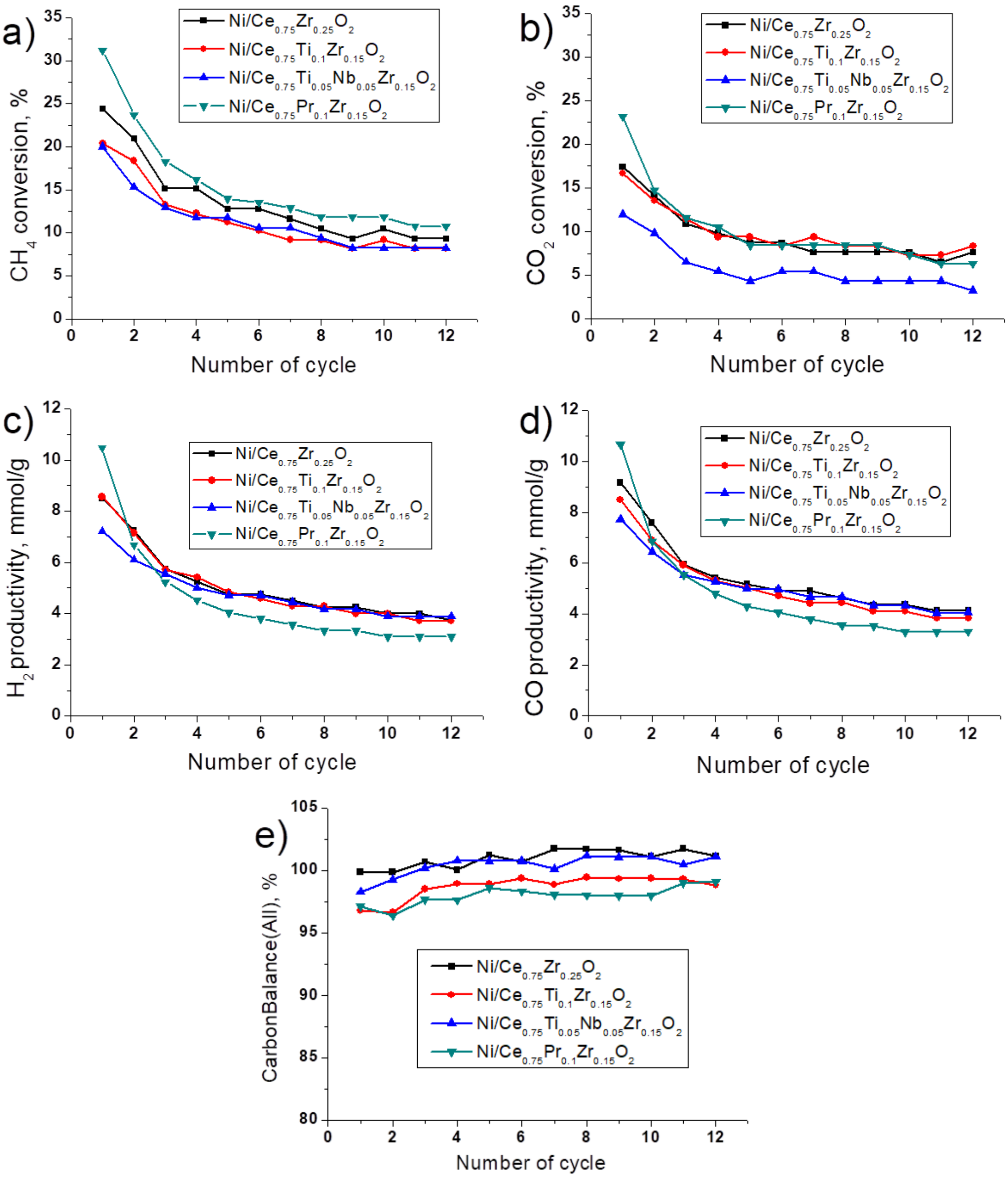

FIG. 7. The dependencies of CH_4 and CO_2 conversions (a,b), H_2 and CO productivities (c,d) and total carbon balances (e) on cycle number in CLMDR over studied catalysts

Catalysts after reaction were also investigated by HRTEM. Fig. 8 shows the micrographs for samples doped by TiNb (a) and Pr (b). There are metal nickel particles with sizes from 10 to 110 nm and small amounts of carbon fibers (not shown). However, there is no obvious difference in particle sizes depending on the composition of the oxide support.

To study the changes in catalyst structure at the oxidation stage, an additional *in situ* XRD experiment was carried out for $Ni/Ce_{0.75}Pr_{0.1}Zr_{0.15}O_2$ sample. A detailed description of the experiment is given in the experimental part. Fig. 9 shows the diffraction patterns and the lattice parameters of fluorite phase.

As was mentioned above, peaks of the fluorite and NiO phases are observed for the initial sample. After treatment in hydrogen, NiO is reduced to metallic nickel. The peaks of the fluorite phase shift towards smaller angles due to change in the lattice parameter, which increases from 5.4166 to 5.4892 Å. As was shown in [54], such increase is associated not only with the thermal expansion of the oxide crystal lattice, but also with the reduction of Ce^{4+} cations to Ce^{3+}.

After CO_2 supply, the lattice parameter decreases to 5.4599 Å as a result of the Ce^{3+} cations being oxidized back to Ce^{4+}. It is important to note that the formation of NiO does not occur. This is consistent with the results of thermodynamic calculations in [8], where it was shown that nickel is not oxidized by CO_2 at these temperatures. The second diffraction pattern under CO_2 stream was recorded after 2 hours later. During this time, the fluorite lattice parameter is further

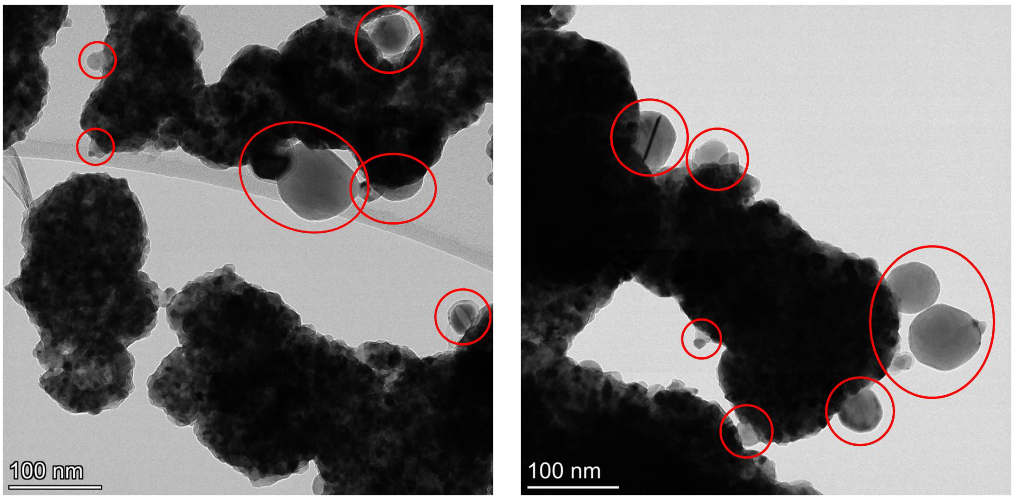

FIG. 8. TEM images of catalysts a) Ni/$Ce_{0.75}Ti_{0.05}Nb_{0.05}Zr_{0.15}O_2$; b) Ni/$Ce_{0.75}Pr_{0.1}Zr_{0.15}O_2$ after testing in CLDRM. Ni particles are marked by circles

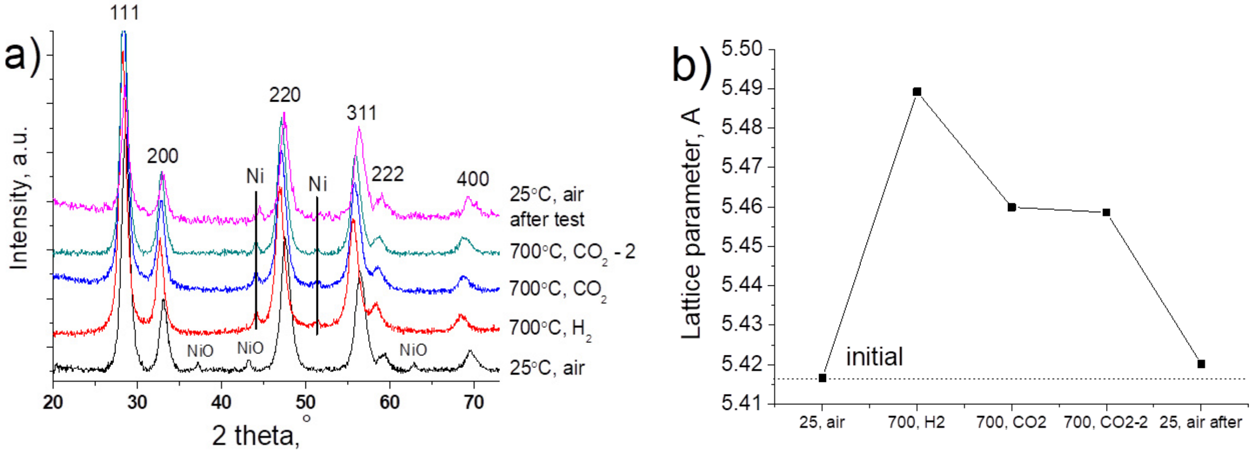

FIG. 9. Results of *in situ* XRD experiments on Ni/$Ce_{0.75}Pr_{0.1}Zr_{0.15}O_2$: a) diffraction patterns; b) dependence of lattice parameters of fluorite phase vs temperature

decreased to 5.4586 Å. Thus it can be concluded that the kinetics of support oxidation by CO_2 is quite slow [8]. However, this should not affect the catalytic activity, since the surface oxidation process is faster than the O diffusion in the bulk [55].

The last diffractogram was recorded after the sample was cooled in an inert environment and kept overnight in air. The lattice parameter is 5.4202 Å, which is slightly higher than the initial value and indicates a higher content of Ce^{3+} cations, so it can be concluded that complete oxidation of the oxide support to the initial state does not occur.

Thus, it was confirmed by *in situ* XRD that reduced oxide support is oxidized, while nickel remains in the metallic state under the CO_2 stream. Thus, even under conditions of CLMDR process, nickel particles remain in metallic form and only the support undergoes reduction and oxidation.

3.5. Comparison of MDR in steady-state condition and CLMDR

Detailed description of catalysts investigation in conventional steady-state MDR reaction is presented in our earlier works [20, 25] and will not be completely repeated here for the brevity. In general, the methane conversion at 700 °C decreases in the series Ni/$Ce_{0.75}Pr_{0.1}Zr_{0.15}O_2$ (50 %) $>$ Ni/$Ce_{0.75}Ti_{0.05}Nb_{0.05}Zr_{0.15}O_2$ (44 %) $>$ Ni/$Ce_{0.75}Zr_{0.25}O_2$ (35 %) $>$ Ni/$Ce_{0.75}Ti_{0.1}Zr_{0.15}O_2$ (27 %). It is clear that the catalytic performance in the processes of CLMDR and MDR is not entirely correct to compare directly. However, it can be concluded, that carrying out reaction in the CLMDR mode for the studied samples eliminates the difference between various support compositions compared with conventional MDR process. Probably, it can be due to methane decomposition reaction, which occurs on metal nickel particles without participation of oxide support.

The ability of studied catalysts to conduct a cyclic process confirms our assumption that these catalysts with a high reactivity of oxygen implement a staged mechanism with independent stages of methane and CO_2 activation. The presence of reactive oxygen species makes it possible to separately feed the reagents, which leads to minimization of the influence of RWGS side reaction. Indeed, if we compare the ratios of H_2 to total CO, it becomes clearly seen that these ratios on all catalysts are close to unity, being much higher than those in the course of the conventional MDR process (Fig. 10). If we take into account that in this study, the reduction step takes 1/6 of the cycle time and assume that the productivity by H_2 at the reduction stage tends to the value of 3 – 4 $\text{mmol}\cdot\text{g}^{-1}\text{h}^{-1}$, then we can estimate some average performance, which will be about 0.5 – 0.7 $\text{mmol}\cdot\text{g}^{-1}\text{h}^{-1}$. The productivity can be multiplied by using a two-reactor unit, in one reactor it is possible to carry out the reduction stage, in the other – the oxidation stage, alternately switching the oxidizer and reductant flows.

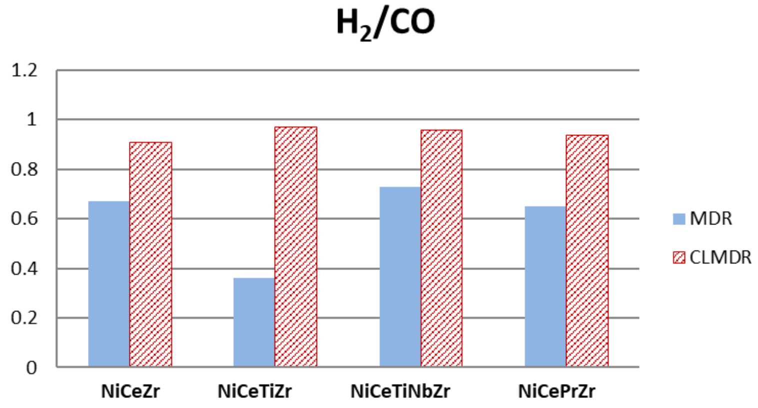

FIG. 10. The values of H_2/CO ratios for MDR and CLMDR (at the last cycle) processes. $T = 700$ °C, $\tau = 10$ ms

4. Conclusions

The principle of chemical looping methane dry reforming reaction for Ni-containing catalysts based on modified ceria-zirconia was demonstrated. During the process, nickel remains in the form of metallic particles, and the support consistently participates in the processes of CH_4 oxidation and CO_2 reduction. Support modification has a weak effect on catalytic activity in CLMDR process compared with conventional MDR reaction. Using the CLMDR process, synthesis gas with a high H_2/CO ratio was obtained, which is acceptable for using as a feedstock for the production of hydrocarbons, which cannot be achieved on these catalysts with a conventional MDR process. The possibility of separating gas flows after the stage of oxidation and reduction can be used to obtain hydrogen-enriched gas for the needs of hydrogen energy.

References

[1] Wang Y., Yao L., Wang S., Mao D., Hu C. Low-temperature catalytic CO_2 dry reforming of methane on Ni-based catalysts: A review. *Fuel Process. Technol.*, 2018, **169**, P. 199–206.

[2] Manfro R.L., Souza M.M.V.M. Overview of Ni-Based Catalysts for Hydrogen Production from Biogas Reforming. *Catalysts*, 2023, **13**, 1296.

[3] Cai Y., Zhang Y., Zhang X., Wang Y., Zhao Y., Li G., Zhang G. Recent Advances in Ni-Based Catalysts for CH_4-CO_2 Reforming (2013–2023). *Atmosphere*, 2023, **14**, 1323.

[4] Zhang G., Liu J., Xu Y., Sun Y. A review of CH_4-CO_2 reforming to synthesis gas over Ni-based catalysts in recent years (2010–2017). *Int. J. Hydrogen Energy*, 2018, **43**, P. 15030–15054.

[5] Bradford M.C.J., Vannice M.A. CO_2 reforming of CH_4. *Catal. Rev.*, 1999, **41**, P. 1–42.

[6] Marinho A.L.A., Toniolo F.S., Noronha F.B., Epron F., Duprez D., Bion N. Highly active and stable Ni dispersed on mesoporous CeO_2–Al_2O_3 catalysts for production of syngas by dry reforming of methane. *Appl. Catal. B*, 2021, **281**, 119459.

[7] Li R., Zhang J., Shi J., Li K., Liu H., Zhu X. Regulation of metal-support interface of Ni/CeO_2 catalyst and the performance of low temperature chemical looping dry reforming of methane. *J. Fuel Chem. Technol.*, 2022, **50** (11), P. 1458–1470.

[8] Löfberg A., Guerrero-Caballero J., Kane T., Rubbens A., Jalowiecki-Duhame L. Ni/CeO_2 based catalysts as oxygen vectors for the chemical looping dry reforming of methane for syngas production. *Appl. Catal. B*, 2017, **212**, P. 159–174.

[9] Löfberg A., Kane T., Guerrero-Caballero J., Jalowiecki-Duhamel L. Chemical looping dry reforming of methane: towards shale-gas and biogas valorization. *Chem. Eng. Process.: Process Intensif.*, 2017, **122**, P. 523–529.

[10] Tang M., Xu L., Fan M. Progress in oxygen carrier development of methane-based chemical-looping reforming: A review. *Appl. Energy*, 2015, **151**, P. 143–156.

[11] Dawa T., Sajjadi B. Exploring the potential of perovskite structures for chemical looping technology: A state-of-the-art review. *Fuel Process. Technol.*, 2024, **253**, 108022.

[12] Zeng L., Cheng Z., Fan J.A., Fan L.-S., Gong J. Metal oxide redox chemistry for chemical looping processes. *Nat. Rev. Chem.*, 2018, **2**, P. 349–364.

[13] Kambolis A., Matralis H., Trovarelli A., Papadopoulou Ch. Ni/CeO_2–ZrO_2 catalysts for the dry reforming of methane. *Appl. Catal. A*, 2010, **377**, P. 16–26.

[14] Chen W., Zhao G., Xue Q., Chen L., Lu Y. High carbon-resistance Ni/$CeAlO_3$–Al_2O_3 catalyst for CH_4/CO_2 reforming. *Appl. Catal. B*, 2013, **136–137**, P. 260–268.

[15] Chen J., Wu Q., Zhang J., Zhang J. Effect of preparation methods on structure and performance of Ni/$Ce_{0.75}Zr_{0.25}O_2$ catalysts for CH_4–CO_2 reforming. *Fuel*, 2008, **87**, P. 2901–2907.

[16] Wu L., Xie X., Ren H., Gao X. A short review on nickel-based catalysts in dry reforming of methane: Influences of oxygen defects on anti-coking property. *Mater. Today Proc.*, 2021, **42** (1), P. 153–160.

[17] Safavinia B., Wang Y.M., Jiang C.Y., Roman C., Darapaneni P., Larriviere J., Cullen D.A., Dooley K.M., Dorman J.A. Enhancing $Ce_xZr_{1-x}O_2$ Activity for Methane Dry Reforming Using Subsurface Ni Dopants. *ACS Catal.*, 2020, **10** (7), P. 4070–4079.

[18] Pavlova S., Smirnova M., Bobin A., Cherepanova S., Kaichev V., Ishchenko A., Selivanova A., Rogov V., Roger A.-C., Sadykov V. Structural, Textural, and Catalytic Properties of Ni-$Ce_xZr_{1-x}O_2$ Catalysts for Methane Dry Reforming Prepared by Continuous Synthesis in Supercritical Isopropanol. *Energies*, 2020, **13**, 3728.

[19] Radlik M., Adamowska-Teyssier M., Krzton' A., Kozieł K., Krajewski W., Turek W., Costa P.D. Dry Reforming of methane over Ni/$Ce_{0.62}Zr_{0.38}O_2$ catalysts: Effect of Ni loading on the catalytic activity and on H_2/CO production. *C. R. Chim.*, 2015, **18**, P. 1242–1249.

[20] Simonov M., Bespalko Y., Smal E., Valeev K., Fedorova V., Krieger T., Sadykov V. Nickel-Containing Ceria-Zirconia Doped with Ti and Nb. Effect of Support Composition and Preparation Method on Catalytic Activity in Methane Dry Reforming. *Nanomaterials*, 2020, **10**, 1281.

[21] Bespalko Y., Smal E., Simonov M., Valeev K., Fedorova V., Krieger T., Cherepanova S., Ishchenko A., Rogov V., Sadykov V. Novel Ni/Ce(Ti)ZrO_2 Catalysts for Methane Dry Reforming Prepared in Supercritical Alcohol Media. *Energies*, 2020, **13**, 3365.

[22] Fedorova V., Simonov M., Valeev K., Bespalko Y., Smal E., Eremeev N., Sadovskaya E., Krieger T., Ishchenko A., Sadykov V. Kinetic Regularities of Methane Dry Reforming Reaction on Nickel-Containing Modified Ceria-Zirconia. *Energies*, 2021, **14**, 2973.

[23] Smal E., Bespalko Y., Arapova M., Fedorova V., Valeev K., Eremeev N., Sadovskaya E., Krieger T., Glazneva T., Sadykov V., et al. Carbon Formation during Methane Dry Reforming over Ni-Containing Ceria-Zirconia Catalysts. *Nanomaterials*, 2022, **12**, 3676.

[24] Smal E., Bespalko Y., Arapova M., Fedorova V., Valeev K., Eremeev N., Sadovskaya E., Krieger T., Glazneva T., Sadykov V., Simonov M. Dry Reforming of Methane over 5 % Ni/$Ce_{1-x}Ti_xO_2$ Catalysts Obtained via Synthesis in Supercritical Isopropanol. *Int. J. Mol. Sci.*, 2023, **24**, 9680.

[25] Arapova M., Smal E., Bespalko Y., Valeev K., Fedorova V., Hassan A., Bulavchenko O., Sadykov V., Simonov M. Methane Dry Reforming Catalysts Based on Pr-Doped Ceria-Zirconia Synthesized in Supercritical Propanol. *Energies*, 2023, **16**, 4729.

[26] Zagaynov I., Loktev A., Arashanova A., Ivanov V., Dedov A., Moiseev I. Ni(Co)-$Gd_{0.1}Ti_{0.1}Zr_{0.1}Ce_{0.7}O_2$ mesoporous materials in partial oxidation and dry reforming of methane into synthesis gas. *Chem. Eng. J.*, 2016, **290**, P. 193–200.

[27] Kim S.S., Lee S.M., Won J.M., Yang H.J., Hong S.C. Effect of Ce/Ti ratio on the catalytic activity and stability of Ni/CeO_2–TiO_2 catalyst for dry reforming of methane. *Chem. Eng. J.*, 2015, **280**, P. 433–440.

[28] Azevedo I.R., da Silva A.A.A., Xing Yu.T., Rabelo-Neto R.C., Luchters N.T.J., Fletcher J.C.Q., Noronha F.B., Mattos L.V. Long-term stability of Pt/$Ce_{0.8}Me_{0.2}O_{2-\gamma}$/$Al_2O_3$ (Me = Gd, Nb, Pr, and Zr) catalysts for steam reforming of methane. *Int. J. Hydrogen Energy*, 2022, **47**, P. 15624–15640.

[29] Wang Y., Zhang R., Yan B. Ni/$Ce_{0.9}Eu_{0.1}O_{1.95}$ with enhanced coke resistance for dry reforming of methane. *J. Catal.*, 2022, **407**, P. 77–89.

[30] Makri M.M., Vasiliades M.A., Petallidou K.C., Efstathiou A.M. Effect of support composition on the origin and reactivity of carbon formed during dry reforming of methane over 5 wt.% Ni/$Ce_{1-x}M_xO_2$-I (M = Zr^{4+}, Pr^{3+}) catalysts. *Catal. Today*, 2016, **259**, P. 150–164.

[31] Mastelaro V.R., Briois V., de Souza D.P.F., Silva C.L. Structural studies of a ZrO_2–CeO_2 doped system. *J. Eur. Ceram. Soc.*, 2003, **23**, P. 273–282.

[32] Kuznetsova T.G., Sadykov V.A., Moroz E.M., Trukhan S.N., Paukshtis E.A., Kolomiichuk V.N., Burgina E.B., Zaikovskii V.I., Fedotov M.A., Lunin V.V., Kemnitz E. Preparation of Ce–Zr–O composites by a polymerized complex method. *Stud. Surf. Sci. Catal.*, 2002, **143**, P. 659–667.

[33] Kambolis A., Matralis H., Trovarelli A., Papadopoulou Ch. Ni/CeO_2–ZrO_2 catalysts for the dry reforming of methane. *Appl. Catal. A*, 2010, **377**, P. 16–26.

[34] Montoya J.A., Romero-Pascual E., Gimon C., Del Angel P., Monzón A. Methane reforming with CO_2 over Ni/ZrO_2–CeO_2 catalysts prepared by sol-gel. *Catal. Today*, 2000, **63**, P. 71–85.

[35] Luisetto I., Tuti S., Romano C., Boaro M., Di Bartolomeo E., Kesavan J.K., Kumar S.S., Selvakumar K. Dry reforming of methane over Ni supported on doped CeO_2: New insight on the role of dopants for CO_2 activation. *J. CO_2 Util.*, 2019, **30**, P. 63–78.

[36] Hirano M., Hirai K. Effect of hydrolysis conditions on the direct formation of nanoparticles of ceria-zirconia solid solutions from acidic aqueous solutions. *J. Nanopart. Res.*, 2003, **5**, P. 147–156.

[37] Pradeep E., Habu T., Tooriyama H., Ohtani M., Kobiro K. Ultra-simple synthetic approach to the fabrication of CeO_2–ZrO_2 mixed nanoparticles into homogeneous, domain, and core-shell structures in mesoporous spherical morphologies using supercritical alcohols. *J. Supercrit. Fluids*, 2015, **97**, P. 217–223.

[38] Basile F., Mafessanti R., Fasolini A., Fornasari G., Lombardi E., Vaccari, A. Effect of synthetic method on CeZr support and catalytic activity of related Rh catalyst in the oxidative reforming reaction. *J. Eur. Ceram.*, 2019, **39**, P. 41–52.

[39] Manjunatha S., Dharmaprakash M.S. Thermal stability, optical and Photoluminescence properties of spherical $Ce_xZr_{1-x}O_2$ ($x = 0.05$) crystalline blue-emitting nanophosphors synthesized by microwave method. *Mater. Res. Express*, 2018, **5**, 035043.

[40] Guo J., Xin X., Zhang X., Zhang S. Ultrasonic-induced synthesis of high surface area colloids CeO_2–ZrO_2. *J. Nanopart. Res.*, 2009, **11**, P. 737–741.

[41] Khani Y., Bahadoran F., Shariatinia Z., Varmazyari M., Safari N. Synthesis of highly efficient and stable Ni/$Ce_xZr_{1-x}Gd_xO_4$ and Ni/X–Al_2O_3 (X = Ce, Zr, Gd, Ce–Zr–Gd) nanocatalysts applied in methane reforming reactions. *Ceram. Int.*, 2020, **46**, P. 25122–25135.

[42] Lovell E., Horlyck J., Scott J., Amal R. Flame spray pyrolysis-designed silica/ceria-zirconia supports for the carbon dioxide reforming of methane. *Appl. Catal.*, 2017, **546**, P. 47–57.

[43] Aymonier C., Loppinet-Serani A., Reveron H., Garrabos Y., Cansell F. Review of supercritical fluids in inorganic materials science. *J. Supercrit. Fluids*, 2006, **38**, P. 242–251.

[44] Tsybulya S.V., Cherepanova S.V., Soloviyova L.P. Polycrystal software package for IBM/PC. *J. Struct. Chem.*, 1996, **37** (2), P. 332–334.

[45] Arapova M., Smal E., Bespalko Yu., Fedorova V., Valeev K., Cherepanova S., Ischenko A., Sadykov V., Simonov M. Ethanol dry reforming over Ni supported on modified ceria-zirconia catalysts: the effect of Ti and Nb dopants. *Int. J. Hydrogen Energy*, 2021, **46**, P. 39236–39250.

[46] Luo M., Chen J., Chen L., Lu J., Feng Z., Li C. Structure and Redox Properties of CexTi1-xO2 Solid Solution. *Chem. Mater.*, 2001, **13**, P. 197–202.

[47] Zhu H., Qin Z., Shan W., Shen W., Wang J. Pd/CeO_2–TiO_2 catalyst for CO oxidation at low temperature: a TPR study with H_2 and CO as reducing agents. *J. Catal.*, 2004, **225**, P. 267–277.

[48] Kim J.R., Myeong W.J., Ihm S.K. Characteristics in oxygen storage capacity of ceria-zirconia mixed oxides prepared by continuous hydrothermal synthesis in supercritical water. *Appl. Catal. B*, 2007, **71**, P. 57–63.

[49] Ye J.L., Wang Y.Q., Liu Y., Wang H. Steam reforming of ethanol over Ni/$Ce_xTi_{1-x}O_2$ catalysts. *Int. J. Hydrogen Energy*, 2008, **33**, P. 6602–6611.

[50] Shan W., Luo M., Ying P., Shen W., Li C. Reduction property and catalytic activity of $Ce_{1-x}Ni_xO_2$ mixed oxide catalysts for CH_4 oxidation. *Appl. Catal. A*, 2003, **246**, P. 1–9.

[51] Montoya J.A., Romero-Pascual E., Gimon C., Del Angel P., Monzón A. Methane reforming with CO_2 over Ni/ZrO_2–CeO_2 catalysts prepared by sol-gel. *Catal. Today*, 2000, **63**, P. 71–85.

[52] Romero-Núñez A., Díaz G. High oxygen storage capacity and enhanced catalytic performance of NiO/$Ni_xCe_{1-x}O_{2-\delta}$ nanorods: Synergy between Ni-doping and 1D morphology. *RSC Adv.*, 2015, **5**, P. 54571–54579.

[53] Sadykov V., Rogov V., Ermakova E., Arendarsky D., Mezentseva N., Alikina G., Sazonova N., Bobin A., Pavlova S., Schuurman Y., Mirodatos C. Mechanism of CH_4 dry reforming by pulse microcalorimetry: metal nanoparticles on perovskite/fluorite supports with high oxygen mobility. *Thermochim. Acta*, 2013, **567**, P. 27–34.

[54] Pakharukova V.P., Potemkin D.I., Stonkus O.A., Kharchenko N.A., Saraev A.A., Gorlova A.M. Investigation of the Structure and Interface Features of Ni/$Ce_{1-x}Zr_xO_2$ Catalysts for CO and CO_2 Methanation. *J. Phys. Chem. C*, 2021, **125**, P. 20538–20550.

[55] Demoulin O., Navez M., Mugabo J.-L., Ruiz P. The oxidizing role of CO_2 at mild temperature on ceria-based catalysts. *Appl. Catal. B*, 2007, **70**, P. 284–293.

Submitted 3 June 2024; revised 10 October 2024; accepted 7 November 2024

Information about the authors:

Ekaterina Smal – Boreskov Institute of Catalysis SB RAS, 630090, Lavrentieva prospect, 5, Novosibirsk, Russia;
ORCID 0000-0001-5068-8964; smal@catalysis.ru

Valeria Fedorova – Boreskov Institute of Catalysis SB RAS, 630090, Lavrentieva prospect, 5, Novosibirsk, Russia;
ORCID 0000-0002-0551-1892; valeria@catalysis.ru

Konstantin Valeev – Boreskov Institute of Catalysis SB RAS, 630090, Lavrentieva prospect, 5, Novosibirsk, Russia;
ORCID 0000-0001-5981-5018; valeev@catalysis.ru

Amir Hassan – Novosibirsk State University, 630090, Pirogova st., 1, Novosibirsk, Russia;
ORCID 0000-0002-8725-186X; a.khassan1@g.nsu.ru

Evgeny Gerasimov – Boreskov Institute of Catalysis SB RAS, 630090, Lavrentieva prospect, 5, Novosibirsk, Russia;
ORCID 0000-0002-3230-3335; gerasimov@catalysis.ru

Mikhail Simonov – Boreskov Institute of Catalysis SB RAS, 630090, Lavrentieva prospect, 5, Novosibirsk, Russia;
ORCID 0000-0002-5161-5684; smike@catalysis.ru

Conflict of interest: the authors declare no conflict of interest.

NANOSYSTEMS:
PHYSICS, CHEMISTRY, MATHEMATICS

Smyslova V.G., et al. *Nanosystems: Phys. Chem. Math.*, 2024, **15** (6), 893–901.
http://nanojournal.ifmo.ru
DOI 10.17586/2220-8054-2024-15-6-893-901

Original article

Effect of nanostructuring of coprecipitated precursors on the morphology and scintillation properties of multication ceramics with a garnet structure

Valentina G. Smyslova[1,a], Vasiliy M. Retivov[1,b], Valery V. Dubov[1,c], Lidia V. Ermakova[1,d], Vladimir K. Ivanov[2,e], Petr V. Karpyuk[1,f], Ilya Yu. Komendo[1,g], Daria E. Lelekova[1,h], Vitaly A. Mechinsky[1,3,j], Andrey N. Vasil'ev[4,k], Artemii S. Ilyushin[4,l], Petr S. Sokolov[1,m], Mikhail V. Korzhik[1,3,n]

[1]National Research Center "Kurchatov Institute", Moscow, 123182, Russian Federation

[2]Kurnakov Institute of General and Inorganic Chemistry, Moscow, 119071, Russian Federation

[3]"Institute for Nuclear Problems" of the Belarusian State University, Minsk, 220030, Republic of Belarus

[4]Skobeltsyn Institute of Nuclear Physics, Moscow State University, Moscow, 119234, Russian Federation

[a]smyslovavg@gmail.com, [b]vasilii_retivov@mail.ru, [c]valery_dubov@mail.ru, [d]ermakova_lv@nrcki.ru, [e]van10@mail.ru, [f]karpyuk_pv@nrcki.ru, [g]komendo_iyu@nrcki.ru, [h]daria_kyznecova@inbox.ru, [j]vitaly.mechinsky@gmail.com, [k]anv@sinp.msu.ru, [l]artyom2833@mail.ru, [m]sokolov_ps@nrcki.ru, [n]korjikmikhail@gmail.com

Corresponding author: V. G. Smyslova, smyslovavg@gmail.com, smyslova_vg@nrcki.ru

PACS 81.20.Ev; 82.40.Qt

ABSTRACT Single-phase polycrystalline samples of the $(Gd,Y)_3Al_2Ga_3O_{12}$:Ce,Tb composition with a garnet structural type were obtained. Using various approaches to the preparation of the initial powders of hydroxycarbonate precursors and compaction methods, the grain size of the ceramics was varied. The scanning electron microscopy method was used to establish the features of the microstructure of the initial powders with different processing temperatures and the microstructure of the resulting ceramics. It is shown that an increase in the grain size of the ceramics and a decrease in the residual porosity gives a noticeable increase in optical transparency in the visible region of the spectrum, in which Ce^{3+} and Tb^{3+} ions emit during scintillation. The effect of intergrain boundaries of the ceramics on the diffusion features of nonequilibrium carriers, electrons and holes, as well as excitons formed during the absorption of ionizing radiation on the scintillation yield and energy resolution is considered.

KEYWORDS precursor, ceramics, garnet, microstructure, scintillation, light yield.

ACKNOWLEDGEMENTS Calculations of the dependence of the fluctuation contribution to the energy resolution of a crystalline scintillator on the grain size, the development of a scheme for the recombination of electrons and holes with the formation of charge-transfer excitons in a homogeneous crystal and in ceramics were obtained with the financial support of the Russian Federation represented by the Ministry of Education and Science of Russia, agreement No. 075-15-2021-1353 dated October 12, 2021. Research was done using equipment of "Research Chemical and Analytical Center NRC "Kurchatov Institute" Shared Research Facilities.

FOR CITATION Smyslova V.G., Retivov V.M., Dubov V.V., Ermakova L.V., Ivanov V.K., Karpyuk P.V., Komendo I.Yu., Lelekova D.E., Mechinsky V.A., Vasil'ev A.N., Ilyushin A.S., Sokolov P.S., Korzhik M.V. Effect of nanostructuring of coprecipitated precursors on the morphology and scintillation properties of multication ceramics with a garnet structure. *Nanosystems: Phys. Chem. Math.*, 2024, **15** (6), 893–901.

1. Introduction

Crystalline materials of the garnet structural type are widely used in various fields of photonics, especially in solid-state lasers [1] and in ionizing radiation detectors as scintillators [2]. Compounds of the garnet structural type based on triply charged cations have the space group $Ia-3d$ (#230, O_{10}^h), and their general formula can be represented as $C_3[B]_2(A)_3O_{12}$, where the C position and the positions in brackets, [] and (), correspond to cations in three different oxygen coordinations: distorted dodecahedral, octahedral and tetrahedral, respectively. Rare earth ions are localized in dodecahedral positions. Further progress in improving their consumer properties is associated with the complication of the cationic composition [3]. The use of garnet isomorphism is an exceptional opportunity to obtain multicomponent compounds of this structural type. The high tolerance of the garnet crystal lattice allows a wide variation of the elemental composition. Isovalent substitution is provided by changing the corresponding length of the metal-oxygen bond, which affects the luminescent properties of rare earth ions and is an additional tool for restructuring their spectral-luminescent properties. The most significant results in the field of scintillators were obtained for gadolinium-aluminum-gallium garnets $Gd_3Al_2Ga_3O_{12}$ (GAGG), in which the [] and () positions are mixed with Al^{3+} and Ga^{3+} ions, and the Gd^{3+} ions either completely occupy dodecahedral positions in the lattice or are partially diluted with lanthanide or yttrium ions. Such materials are obtained by drawing from a melt [4–8] or by micro-pulling down method [9], and also in the form of ceramics by hot pressing [10, 11].

The listed methods require either expensive tooling made of platinum group metals or expensive equipment for high pressure sintering. To obtain transparent GAGG or more complex materials based on it, ceramic technology is of particular importance. Its advantages include obtaining the product without the stage of melting the precursor, which significantly minimizes the problem of defect formation in it due to evaporation at high temperatures and the difference in the pressure of saturated vapors of different components of the batch in the synthesis chamber. Ceramics of complex compounds can be obtained from a premix of simpler compounds of the same structural type [12], which allows controlling the spatial distribution of activator ions in the grains of the ceramics. Finally, hot pressing is not an exclusive approach to obtaining transparent ceramics of garnet compounds; it can also be obtained as a result of annealing in an oxygen atmosphere using nanoscabe precursors to obtain raw materials [13–17].

Nanostructuring of precursors in the technology of ceramics of the GAGG family of compounds allows solving two important problems: minimizing the evaporation of gallium from the compound and thereby maintaining a composition close to the specified one [18] and increasing the rate of compaction of the raw material during sintering due to the high reactivity of the precursor particles, which have a well-developed surface.

In this paper, it is shown that the use of co-precipitated nanoscale precursors of complex garnet compounds containing more than three cations allows us to solve a number of chemical engineering problems in the production of transparent scintillation ceramics. In particular, it is shown that ensuring a given composition of the compound with high accuracy at the stage of preparing the precursor for further pressing and sintering provides the ability to effectively adjust the scintillation properties by controlling the compositional disordering of the crystalline matrix.

2. Obtaining precursors of multicationic compounds by the coprecipitation method

The hydroxycarbonate precursor of following compositions $Gd_3Al_2Ga_3O_{12}$ (GAGG:Ce) and $(Gd,Y)_3Al_2Ga_3O_{12}$:Ce, Tb (GYAGG:Ce,Tb) were synthesized by co-precipitation from a mixed nitric acid solution containing Gd, Y, Ce, Tb, Al, and Ga. The following were used as feedstock materials: Gd_2O_3 (99.995%), Y_2O_3 (99.995%), AlOOH (99.998%), Ga (99.999%), $Ce(NO_3)_3$ $6H_2O$, and $Tb(NO_3)_3$ $6H_2O$ (99.95%). The feedstock of the main components was dissolved in the nitric acid of special purity grade 18-4, and the feedstock of the activators $Ce(NO_3)_3$ $6H_2O$ and $Tb(NO_3)_3$ $6H_2O$ was dissolved in deionized water (specific resistance 18 MOhm×cm). Solutions of individual metals with known concentrations determined gravimetrically were mixed in the required ratio and diluted with water to a total metal concentration of 1 mol Me/l. The mixed solution was then gradually added to a solution of the ammonium hydrocarbonate NH_4HCO_3 with a concentration of 1.5 mol/l under constant stirring with an overhead stirrer. The resulting precipitate was filtered through a Buchner funnel, washed with a mixture of water and isopropanol, and dried for 6 h at 100 °C in a drying cabinet with forced convection. The precursor thus obtained was then subjected to heat treatment in a muffle furnace at temperatures above 600 °C for 2 h to convert it to the oxide form and form a garnet phase ($\geq$900 °C).

The completeness of precipitation was assessed using the inductively coupled plasma mass spectrometry (ICP-MS) method using a Perkin Elmer Elan DRC-e spectrometer. For this purpose, the content of the metals in the mother liquor and washing liquid determined, and the proportion of elements that did not precipitate relative to their initial amount in the mixed solution was calculated based on the data obtained. The analysis results for 10 syntheses are presented in Table 1.

TABLE 1. Completeness of precipitation during the synthesis of the GYAGG:Ce,Tb precursor

Element	The proportion of the element that did not pass into the sediment, % of the initial amount
Al	$< 0,02$
Ga	0,31±0,04
Y	0,10±0,02
Ce	$< 0,02$
Gd	$< 0,02$
Tb	$< 0,02$

The amounts of the elements which were not precipitated are within narrow limits that allows take them into account when planning syntheses and preparing mixed solutions. This ensures the preservation of the specified composition of the precipitate and the oxide with the garnet structure obtained from it, as well as the reproducibility of the syntheses.

The temperature of the garnet phase formation was estimated using differential scanning calorimetry (DSC) data. Fig. 1 shows the DSC results obtained on a TA Instruments SDT Q 600 at a heating rate of 10 °C/min, and the weight loss according to thermogravimetry (TG) data.

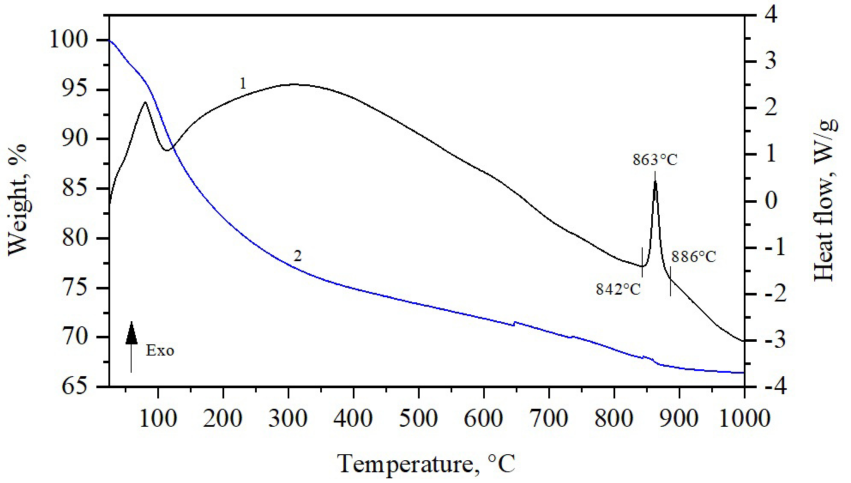

FIG. 1. TG (left axis) and DSC (right axis) curves of the GYAGG:Ce,Tb precursor: 1 – differential curve, 2 – mass loss curve

Solid samples treated at different temperatures for 2 h were analyzed by X-ray diffraction (XRD) on a BRUKER D2 PHASER diffractometer (CuK$_\alpha$ radiation, 2θ angle range from 15 to 95°, 0.02° step, Bragg-Brentano geometry) at room temperature. The results are shown in Fig. 2.

XRD data show that the samples are X-ray amorphous when annealed at temperatures up to 700°C. The cubic garnet phase ($Ia - 3d$) is already formed and becomes predominant when the samples are annealed at 850 °C, which is close to the exothermic peak on the DSC curve. Its content is about 92 vol.%, and the remaining 8 vol.% is the impurity phase with the hexagonal perovskite structure *P63/mmc*. The reflections of these impurity phases are not observed in the diffraction pattern of the samples obtained at 900 °C. The low temperature of the garnet phase formation achieved in this production method allows reducing the evaporation of gallium oxide [19] during annealing, which ensures the production of single-phase samples with a given elemental composition.

Figure 3 shows the results of the study of the powder microstructure obtained on a Jeol JSM 7100 F scanning electron microscope (secondary electron mode, accelerating voltage 10 kV).

It is noticeable that the microstructure of the precursor and oxide powder does not undergo significant changes in the considered temperature range. This serves as additional confirmation of the uniform distribution of components at the level of nanosized primary particles.

The grain size of the final ceramics may depend on various factors. In particular, the structural features of the original powder or the presence of special additives - fluxes - may have an impact. Fig. 4 shows photo images and scanning electron microscopy images for ceramic samples of the GYAGG:Ce,Tb composition.

It can be seen that a significant increase in the grain size of ceramics and an increase in its optical transparency can be achieved by using a mixture of powders with different heat treatment temperatures during the production of ceramics: 850 and 1500 °C, respectively (Fig. 4, b, d). The grain size of the ceramics increases from an average value of 1 μm to 5 μm. A similar effect can be achieved by adding a sintering additive SiO_2 to the powder in an amount of 0.01 wt.% (Fig. 4, c, e), however, a certain heterogeneity in the grain size and a noticeable number of closed pores are observed, which may be associated with a sharp increase in the grain size during the sintering process. Thus, using a nanostructured precursor, it becomes possible to apply various approaches to control the morphology of ceramics.

Using the 3D printing method – stereolithography – it is possible to obtain ceramic elements of complex shape [20]. This method significantly expands traditional ceramic approaches, such as semi-dry pressing (compacting) and slip casting. Objects of complex geometry, such as openwork and mesh structures, are created due to controlled and local layer-by-layer polymerization of a photocurable suspension with ceramic particles when exposed to ultraviolet radiation. The composition of photocurable suspensions suitable for 3D printing consists of a mixture of the ceramic powder, low-viscosity acrylate monomer, UV photoinitiator and dispersing additive. We used 1,6-hexanediol diacrylate as an acrylate monomer. Another important advantage of this method is the relative availability of source materials for the preparation of suspensions and the low cost of modern desktop printers. After manufacturing by stereolithography, the green body – a

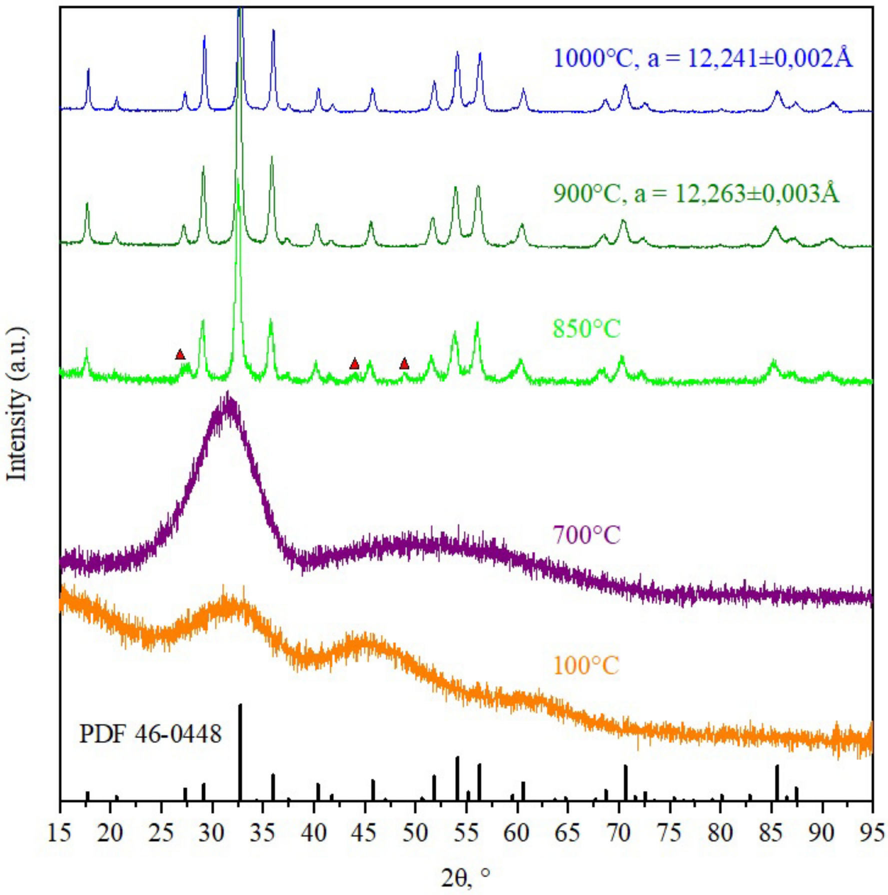

FIG. 2. Results of XRD analysis of the precursor and oxide powders GYAGG:Ce,Tb. Red triangles mark reflections related to the impurity phase

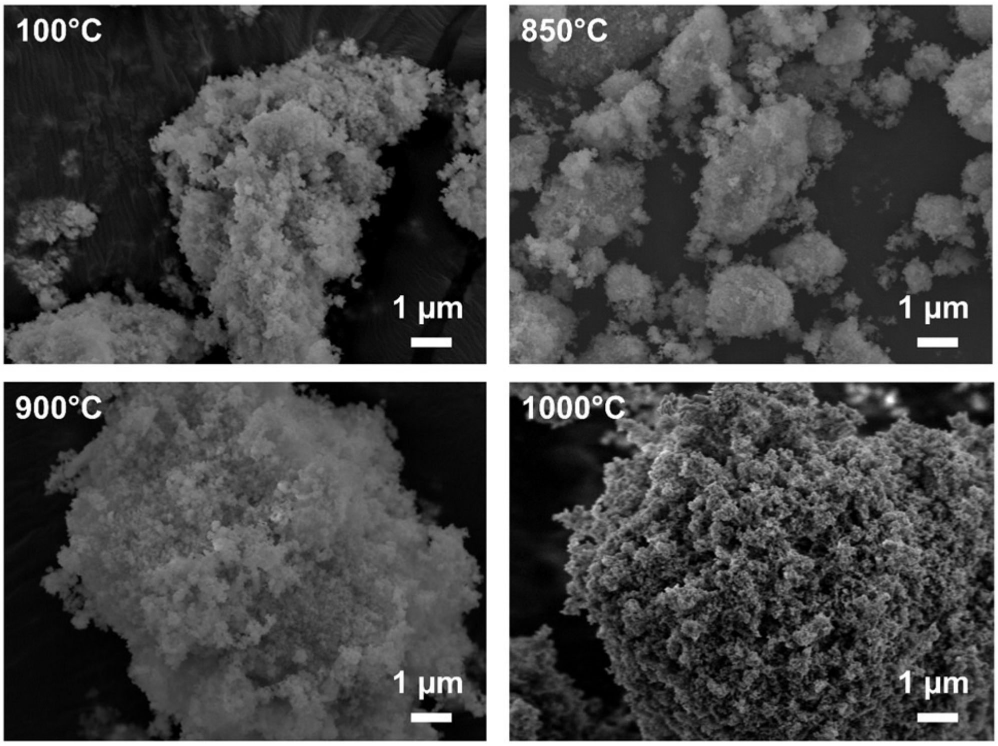

FIG. 3. SEM images of precursor and oxide powders of GYAGG:Ce,Tb after heat treatment at 100–1000 °C

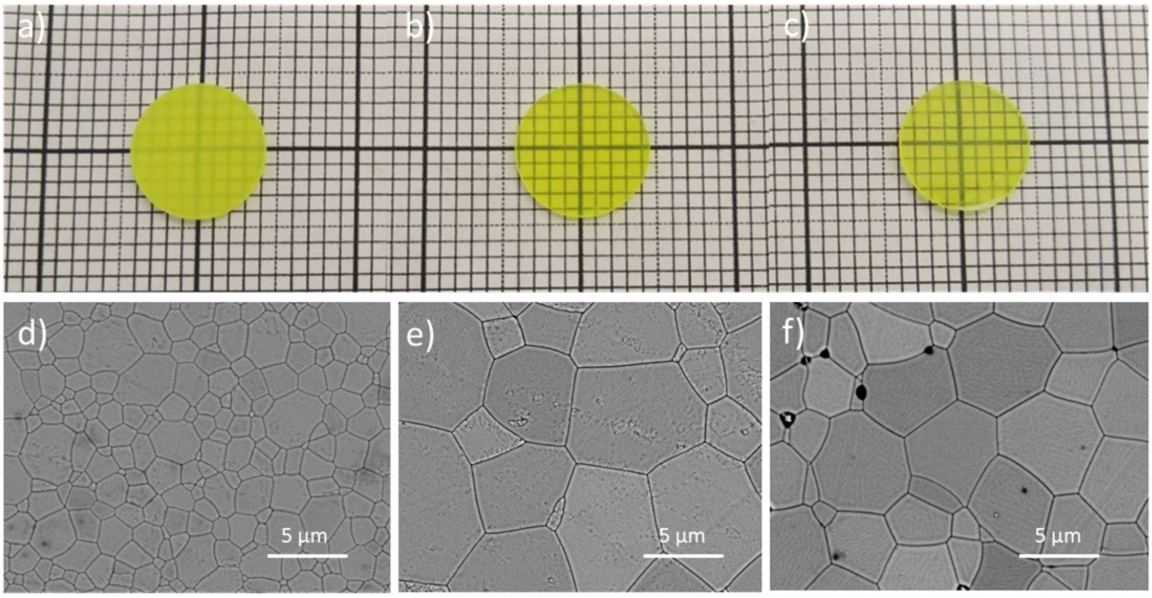

FIG. 4. Photographs and SEM images of GYAGG:Ce,Tb ceramic samples based on powder with a heat treatment temperature of 850 °C (a, d), based on a mixed powder of 850 °C + 1500 °C (b, e) and powder with heat treatment at 850 °C and the addition of 0.01 wt.% SiO_2 (c, f)

composite consisting of an acrylate polymer with encapsulated ceramic particles – requires burning out the organic binder and high-temperature sintering. These two operations are standard for the ceramic approach in general, but in the case of stereolithography, burning out in an inert atmosphere is usually required to remove the organic components from the green body without defects. A typical appearance of green bodies and ceramics of multicomponent garnets activated by cerium is shown in Fig. 5.

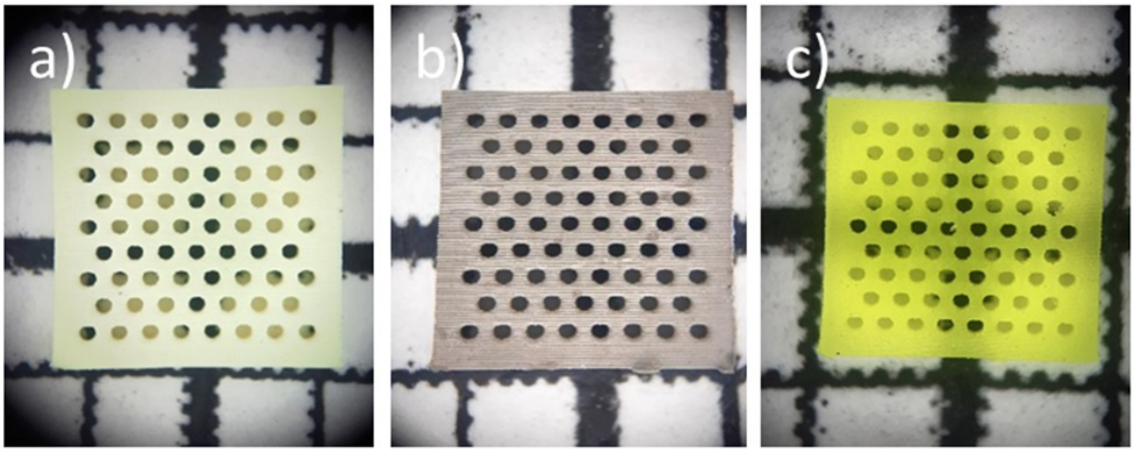

FIG. 5. Typical appearance of GYAGG:Ce,Tb raw materials after 3D printing (a), after burning out the organic binder (b) and high-temperature sintering (c) into dense oxide ceramics. The ceramic surfaces are not polished

Using the stereolithography method, it is possible to produce planar periodic structures from ceramics with a garnet structure.

3. Discussion of the results

The obtained data show that the morphology of transparent ceramics can vary significantly: the average grain size can vary from a few microns to more than 10 microns. Therefore, the question of the dependence of the scintillation parameters on the morphology of the ceramics, in particular, the grain size, is natural. From the point of view of the development of the scintillation process, ceramics differs from a single-crystal material by a number of factors. Firstly, a violation of the spatial periodicity of the crystal occurs at the boundaries between the grains and, as a consequence, nonequilibrium electrons and holes formed by ionizing radiation are additionally scattered at this boundary. In addition, potential barriers to the movement of carriers may appear. Grain boundaries, clearly visible using scanning microscopy, can act as such energy barriers. The height of such barriers to the movement of electrons should not exceed the work function of the electron exit from the crystal into vacuum and depends on the orientation of the axes of the basis vectors of neighboring crystallites, and their spatial width depends on how tightly the ceramic grains fit together, that is, on the presence of pores in the ceramics. It can be assumed that electrons, holes and excitons can diffuse inside the grain with the same diffusion coefficients as in the crystal, but can move from one grain to another only due to slow tunneling processes. The boundary between the grains is a defect layer on which carriers can be captured and undergo nonradiative recombination. Finally, the grain boundary is enriched with the activator due to the large radius of the cerium ions Ce^{3+}. In this case, cerium at the boundary is predominantly in the state Ce^{4+} [21].

Let us consider some of the consequences of this difference. The elementary acts of fast electron scattering and the Auger processes for a hole in crystalline and ceramic samples do not differ from each other. In this regard, the structure of the track before thermalization will be the same in the crystalline and ceramic samples. The cascade of electron excitation multiplication ends when all secondary electrons and holes have an energy below the multiplication threshold (of the order of the band gap). Thus, in the garnets under consideration, by the end of multiplication, the electrons and holes will be distributed over kinetic energy within the range from zero to approximately 6 eV. Further relaxation is associated with the emission of optical phonons, as a result of which the electrons and holes fly away from their birthplace due to the hot diffusion process [22]. The average distance over which hot charge carriers fly away in the parabolic zone model increases with increasing initial energy E_{kin} of secondary electrons as $E_{kin}^{3/2}$. In oxide crystals with a typical optical phonon energy of about 100 meV, electrons with an energy of about 5 eV fly away from their birthplace on average by l_{term} ~30 nm, with the main flight occurring while their energy is sufficiently high (about 1 eV) [23]. Due to this, such electrons can fly over the intergranular barrier and enter the neighboring grain if they are born in a layer of thickness l_{term} near the intergranular boundary (the fraction of such electrons is about l_{term}/d, where d is the typical grain size). After thermalization, their return to the grain in which they were born and in which the hole remains is hindered by the presence of barriers. Thus, the number of electrons and holes born by the primary ionizing particle in different grains is not the same. If we assume that N_e electrons and N_h holes remain inside the grain, then the maximum number of excitons created by them should not exceed $\mathrm{Min}(N_e, N_h)$. This creates additional fluctuations in the number of generated electrons and holes due to the unequal number of carriers of different signs in the grains. As the grain size decreases, these fluctuations increase. Fig. 6 shows the dependence of this fluctuation contribution to the energy resolution of a crystalline element obtained by dividing the track of a primary electron with energy of 50 to 400 keV after thermalization into cells (grains) depending on the grain size. The simulation was carried out based on 100 (for 400 keV) to 800 (for 50 keV) generated tracks in a GAGG crystal. The simulation algorithm is described in [24]. It is evident that with an average grain size of ~5 μm, the contribution does not exceed 0.2%, i.e. it becomes insignificant. For small energies the contribution increases when the track length is about the grain size.

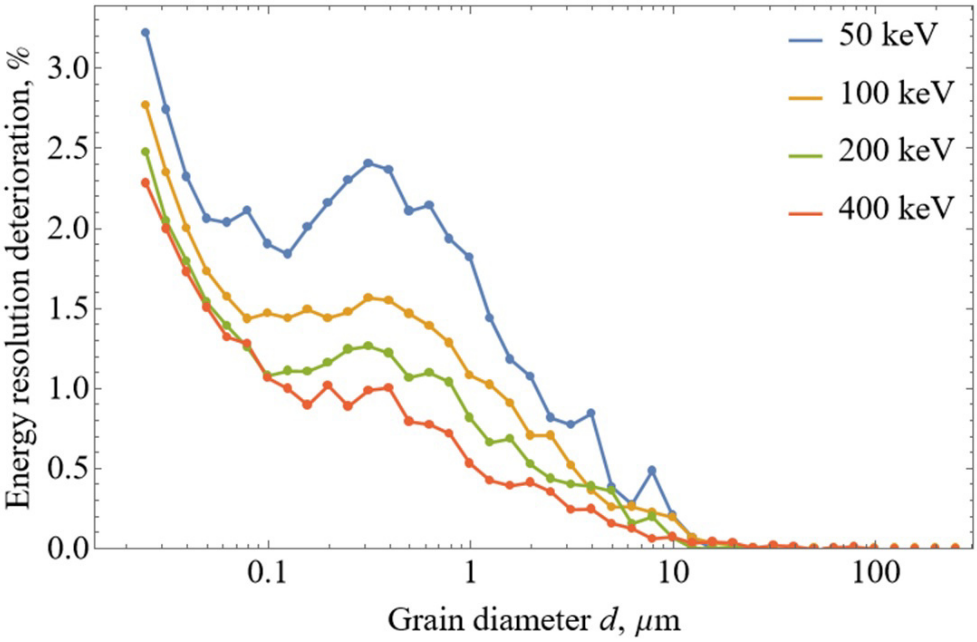

FIG. 6. Additional contribution to the energy resolution of a ceramic scintillator due to the difference in the numbers of electrons and holes in ceramic grains depending on the grain size. For a primary electron with an energy labeled in legend in GAGG

Assuming that all electrons and holes in the grains are bound into excitons, the yield of the ceramic scintillator should decrease compared to the crystalline one, since unpaired electrons and holes remain in the grains (over time, due to the long process of tunneling through barriers and due to capture by defects, including intergranular ones, these uncompensated charge carriers also recombine).

In a homogeneous crystal, during the process of diffusion-controlled recombination of an electron-hole pair, not all electrons and holes generated in one scattering event and located at a distance of the order of l_{term} from each other recombine, but only their share of the order of Min(1,R_c/l_{term}) [25, 26]. Here, the capture radius R_c is approximately equal to the Onsager radius – the distance at which the potential energy of attraction of an electron and a hole is of the order of thermal energy (at room temperature, the typical value of R_c is approximately 6–10 nm). The remaining electrons fly far from the hole and do not return to it, being captured by defects or recombining with “foreign holes” (in the region where the concentration of charge carriers is sufficiently high). On the other hand, if the electron thermalization occurs in the same grain in which it was born, it has a lower probability of moving away from the hole at a large distance, and thus the probability of its recombination with the hole increases. These processes are shown schematically in Fig. 7.

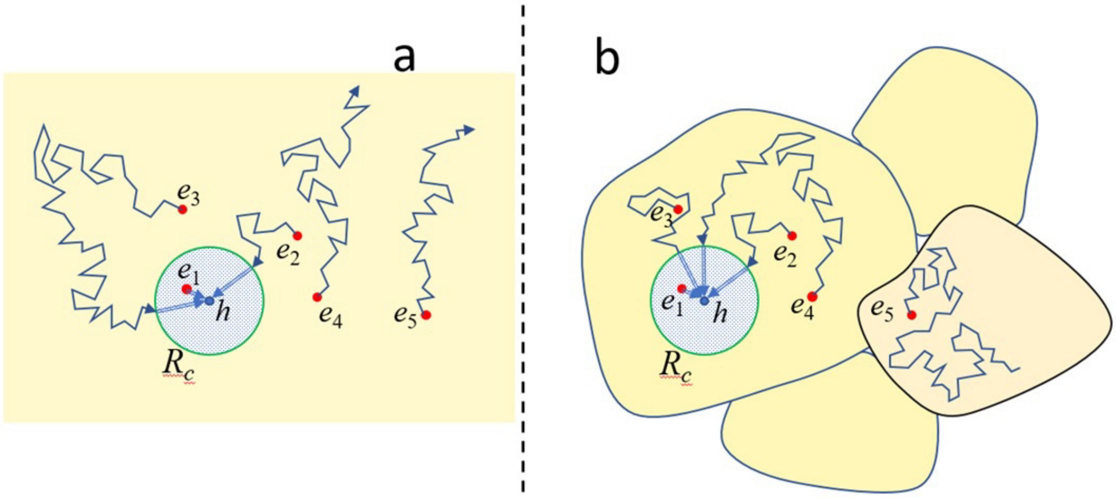

FIG. 7. Scheme of diffusion-controlled recombination of electrons and holes with the formation of charge-transfer excitons in a homogeneous crystal (a) and in ceramics (b)

The sphere of electron capture by a hole has a radius R_c (about 10 nm). Various cases of the location of a thermalized electron relative to a hole are shown (Fig. 7). Electron e_1 quickly recombines with the hole to form a charge-transfer exciton, electron e_2 recombines after a short diffusion, electron e_3 in a crystal recombines after a long diffusion in the crystal, and in ceramics its diffusion is limited by the grain size, and it enters the capture sphere faster. In a crystal, electrons e_4 and e_5 escape genetic recombination and can then recombine with other holes or be captured by defects. In ceramics, electron e_4 will recombine with a hole due to the diffusion region being limited by grain boundaries, and electron e_5 will be captured by another grain.

Due to the limitation of the scattering of electrons and holes, the yield of a ceramic scintillator can exceed the yield of a crystalline scintillator, despite the appearance of uncompensated electrons and holes in the grains. However, this also changes the kinetics of scintillations, in particular, the proportion of slow components decreases if they arise in the crystal due to the long migration of electron excitations over distances exceeding the grain sizes in the ceramics.

4. Conclusion

The influence of precursor morphology and sintering conditions on the characteristics of four-cation scintillation ceramics $(Gd,Y)_3Al_2Ga_3O_{12}$:Ce,Tb was analyzed. It was found that the grain size in transparent ceramics can vary within fairly wide limits. At the same time, it was found that the effects associated with the influence of grain boundaries on scintillation parameters become insignificant at grain sizes of $\sim$3–5 μm and above.

References

[1] Kaminskii A.A. *Laser crystals: their physics and properties*. Springer Ser. Opt. Sci., 1990, P. 214.

[2] Gektin A., Korzhik M. *Inorganic scintillators for detector systems*. Berlin: Springer, 2017, P. 20-77.

[3] Retivov V., Dubov V., Komendo I., Karpyuk P., Kuznetsova D., Sokolov P., Talochka Y., Korzhik M. Compositionally disordered crystalline compounds for next generation of radiation detectors. *Nanomaterials*, 2022, **12**(23), P. 4295.

[4] Kamada K., Endo T., Tsutumi K., Yanagida T., Fujimoto Y., Fukabori A., Yoshikawa A., Pejchal J., Nikl M. Composition engineering in cerium-doped $(Lu,Gd)_3(Ga,Al)_5O_{12}$ single-crystal scintillators. *Cryst. Growth Des.*, 2011, **11**(10), P. 4484–4490.

[5] Kamada K., Yanagida T., Pejchal J., Nikl M., Endo T., Tsutumi K., Fujimoto Y., Fukabori A., Yoshikawa A. Scintillator-oriented combinatorial search in Ce-doped $(Y,Gd)_3(Ga,Al)_5O_{12}$ multicomponent garnet compounds *J. Phys. D: Appl. Phys.*, 2011 **44**(50), P. 505104.

[6] Kamada K., Yanagida T., Endo T., Tsutumi K., Usuki Y., Nikl M., Fujimoto Y., Fukabori A., Yoshikawa A. 2 inch diameter single crystal growth and scintillation properties of Ce:$Gd_3Al_2Ga_3O_{12}$. *J. Cryst Growth*, 2012, **352**(1), P. 88–90.

[7] Kurosawa S., Shoji Y., Yokota Y., Kamada K., Chani V., Yoshikawa A. Czochralski growth of $Gd_3(Al_{5-x}Ga_x)O_{12}$ (GAGG) single crystals and their scintillation properties. *J. Cryst. Growth*, 2014, **393**, P. 134–137.

[8] Korzhik M., Alenkov V., Buzanov O., Dosovitsky G., Fedorov A., Kozlov D., Mechinsky V., Nargelas S., Tamulaitis G., Vaitkevicius A. Engineering of a new single-crystal multi-ionic fast and high-light-yield scintillation material $(Gd_{0.5}–Y_{0.5})_3Al_2Ga_3O_{12}$:Ce,Mg. *CrystEngComm*, 2020, **22**(14), P. 2502–2506.

[9] Sakthong O., Chewpraditkul W., Pattanaboonmee N., Chewpraditkul W., Yamaji A., Kamada K., Nikl M. Light yield and timing characteristics of $Lu_{0.8}Gd_{2.2}(Al_{5-x}Ga_x)O_{12}$: Ce,Mg single crystals. *IEEE Transactions on Nuclear Science*, 2020, **67**(10), P. 2295–2299.

[10] Seeley Z., Cherepy N., Payne S. Expanded phase stability of Gd-based garnet transparent ceramic scintillators. *J. Mater. Res.*, 2014, **29**(19), P. 2332–2337.

[11] Cherepy N., Kuntz J., Roberts J., Hurst T., Drury O., Sanner R., Tillotson T., Payne S. Transparent ceramic scintillator fabrication, properties, and applications. *Proc. SPIE*, 2008, **7079**, P. 263–268.

[12] Smyslova V., Kuznetsova D., Bondaray A., Karpyuk P., Korzhik M., Komendo I., Pustovarov V., Retivov V. and Tavrunov D. Advances of the cubic symmetry crystalline systems to create complex, bright luminescent ceramics. *Photonics*, 2023, **10**(5), P. 603.

[13] Luo Z., Jiang H., Jiang J. Synthesis of cerium-doped $Gd_3(Al,Ga)_5O_{12}$ powder for ceramic scintillators with ultrasonic-assisted chemical coprecipitation method. *J. Am. Ceram. Soc.*, 2013, **96**(10), P. 3038–3041.

[14] Drozdowski W., Witkowski M., Solarz P., Głuchowski P., Głowacki M., Brylew K. Scintillation properties of $Gd_3Al_2Ga_3O_{12}$:Ce (GAGG:Ce): a comparison between monocrystalline and nanoceramic samples. *Opt. Mater.*, 2018, **79**, P. 227–231.

[15] Yang S., Sun Y., Chen X., Zhang Y., Luo Z., Jiang J., Jiang H. The effects of cation concentration in the salt solution on the cerium doped gadolinium gallium aluminum oxide nanopowders prepared by co-precipitation method. *IEEE Trans. Nucl. Sci.*, 2014, **61**(1), P. 301–305.

[16] Sun Y., Yang S., Zhang Y., Jiang J., Jiang H. Coprecipitation synthesis of gadolinium aluminum gallium oxide (GAGG) via different precipitants. *IEEE Trans. Nucl. Sci.*, 2014, **61**(1), P. 306–311.

[17] Zhang J., Luo Z., Jiang H., Jiang J., Gui Z., Chen C., Ci M. Sintering of GGAG:Ce^{3+}, xY^{3+} transparent ceramics in oxygen atmosphere. *Ceram. Int.*, 2017, **43**(17), P. 16036–16041.

[18] Korzhik M., Alenkov V., Buzanov O., Fedorov A., Dosovitskiy G., Grigorjeva L., Mechinsky V., Sokolov P., Tratsiak Y., Zolotarjovs A., Dormenev V., Dosovitskiy A., Agrawal D., Anniyev T., Vasilyev M., Khabashesku V. Nanoengineered $Gd_3Al_2Ga_3O_{12}$ scintillation materials with disordered garnet structure for novel detectors of ionizing radiation. *Cryst. Res. Technol*, 2019, **54**(4), P. 1800172.

[19] Lamoreaux H., Hildenbrand D., Brewer L. High-temperature vaporization behavior of oxides II. Oxides of Be, Mg, Ca, Sr, Ba, B, Al, Ga, In, Tl, Si, Ge, Sn, Pb, Zn, Cd, and Hg. *J. Phys. Chem. Ref. Data*, 1987, **16**(3), P. 419–443.

[20] Dosovitskiy G., Karpyuk P., Evdokimov P., Kuznetsova D., Mechinsky V., Borisevich A., Fedorov A., Putlayev V., Dosovitskiy A., Korjik M. First 3D-printed complex inorganic polycrystalline scintillator. *CrystEngComm*, 2017, **19**(30), P. 4260–4264.

[21] Dosovitskiy G., Dubov V., Karpyuk P., Volkov P., Tamulaitis G., Borisevich A., Vaitkevičius A., Prikhodko K., Kutuzov L., Svetogorov R., Veligzhanin A., Korzhik M. Activator segregation and micro-luminescence properties in GAGG:Ce ceramics. *J. Lumin.*, 2021, **236**, P. 118140.

[22] Dosovitskiy G., Dubov V., Karpyuk P., Volkov P., Tamulaitis G., Borisevich A., Vaitkevičius A., Prikhodko K., Kutuzov L., Svetogorov R., Veligzhanin A., Korzhik M. Activator segregation and micro-luminescence properties in GAGG:Ce ceramics. *J. Lumin.*, 2021, **236**, P. 118140.

[23] Kirkin R., Mikhailin V., Vasil'ev A. Recombination of correlated electron-hole pairs with account of hot capture with emission of optical phonons. *IEEE Trans. Nucl. Sci.*, 2012, **59**, P. 2057–2064.

[24] Vasil'ev A., Korzhik M., Gektin A. Microtheory of scintillation in crystalline materials. *Eng. Scint. Mat. Rad. Technol.: Proc. ISMART – Springer Int. Publ.*, 2017, P. 3-34.

[25] Korzhik M., Tamulaitis G., Vasil'ev A. *Physics of Fast Processes in Scintillators*. Cham : Springer, 2020, **262**, P. 250.

[26] Vasil'ev A., Gektin A. Multiscale Approach to Estimation of Scintillation Characteristics. *IEEE Trans. Nucl. Sci.*, 2014, **61**, P. 235–245.

Submitted 13 November 2024; revised 25 November 2024; accepted 30 November 2024

Information about the authors:

Valentina G. Smyslova – National Research Center "Kurchatov Institute", Moscow, 123182, Russian Federation; ORCID 0000-0001-8475-2602; smyslovavg@gmail.com; smyslova_vg@nrcki.ru

Vasiliy M. Retivov – National Research Center "Kurchatov Institute", Moscow, 123182, Russian Federation; ORCID 0000-0002-3649-2778; vasilii_retivov@mail.ru

Valery V. Dubov – National Research Center "Kurchatov Institute", Moscow, 123182, Russian Federation; ORCID 0000-0002-5816-1582; valery_dubov@mail.ru

Lidia V. Ermakova – National Research Center "Kurchatov Institute", Moscow, 123182, Russian Federation; ORCID 0000-0001-7263-5724; ermakova_lv@nrcki.ru

Vladimir K. Ivanov – Kurnakov Institute of General and Inorganic Chemistry, Moscow, 119071, Russian Federation; ORCID 0000-0003-2343-2140; van10@mail.ru

Petr V. Karpyuk – National Research Center "Kurchatov Institute", Moscow, 123182, Russian Federation; ORCID 0000-0003-0002-3483; karpyuk_pv@nrcki.ru

Ilya Yu. Komendo – National Research Center "Kurchatov Institute", Moscow, 123182, Russian Federation; ORCID 0000-0003-3622-173X; komendo_iyu@nrcki.ru

Daria E. Lelekova – National Research Center "Kurchatov Institute", Moscow, 123182, Russian Federation; ORCID 0000-0001-5538-1726; daria_kyznecova@inbox.ru

Vitaly A. Mechinsky – National Research Center “Kurchatov Institute”, Moscow, 123182, Russian Federation; “Institute for Nuclear Problems” of the Belarusian State University, Minsk, 220030, Republic of Belarus; vitaly.mechinsky@gmail.com

Andrey N. Vasil’ev – Skobeltsyn Institute of Nuclear Physics, Moscow State University, Moscow, 119234, Russian Federation; anv@sinp.msu.ru

Artemii S. Ilyushin – Skobeltsyn Institute of Nuclear Physics, Moscow State University, Moscow, 119234, Russian Federation; ORCID 0009-0007-0850-988X; artyom2833@mail.r

Petr S. Sokolov – National Research Center “Kurchatov Institute”, Moscow, 123182, Russian Federation; ORCID 0000-0003-3516-3953; sokolov_ps@nrcki.ru

Mikhail V. Korzhik – National Research Center “Kurchatov Institute”, Moscow, 123182, Russian Federation; “Institute for Nuclear Problems” of the Belarusian State University, Minsk, 220030, Republic of Belarus; korjikmikhail@gmail.com

Conflict of interest: the authors declare no conflict of interest.

NANOSYSTEMS:
PHYSICS, CHEMISTRY, MATHEMATICS

Klimonsky S.O., et al. *Nanosystems: Phys. Chem. Math.*, 2024, **15** (6), 902–909.
http://nanojournal.ifmo.ru
DOI 10.17586/2220-8054-2024-15-6-902-909

Original article

SERS substrates based on opal films with gold coating

Mikhail O. Astafurov[1], Elena V. Perevedentseva[2], Nikolay N. Melnik[2], Alexander E. Baranchikov[3], Sergey G. Dorofeev[1], Alexander A. Ezhov[1], Anastasia V. Grigorieva[1], Sergey O. Klimonsky[1]

[1]Lomonosov Moscow State University, Moscow, Russia

[2]P. N. Lebedev Physical Institute of the Russian Academy of Sciences, Moscow, Russia

[3]Kurnakov Institute of General and Inorganic Chemistry of the Russian Academy of Sciences, Moscow, Russia

Corresponding author: Sergey O. Klimonsky, klimonskyso@my.msu.ru

---

ABSTRACT Substrates for Surface-Enhanced Raman Spectroscopy (SERS) were fabricated by gold sputtering onto surface of synthetic opal films and their characteristics were studied at wavelengths $\lambda = 532$ and 785 nm. Synthetic opal films were fabricated by self-assembly of spherical SiO_2 particles on vertical substrates. It was found that at the concentration of the analyte methylene blue equal to 10^{-5} M the intensity of SERS at the wavelength of 785 nm increased with increasing amount of sputtered gold up to a certain optimal thickness exceeding 35 nm, while at the concentration of 10^{-6} M this dependence was not observed. It is assumed that this is due to the complex amount-dependent morphology of the sputtered gold coating and the presence of "hot spots" of different strengths. For the best samples at a wavelength of $\lambda = 785$ nm, the SERS enhancement factor was of $7\cdot10^4$ and a detection limit for methylene blue reached $3\cdot10^{-7}$ M that exceeds the results published for similar substrates previously. The SERS parameters obtained for $\lambda = 532$ nm were less attractive, despite the additional enhancement due to this wavelength was at the edge of the photonic stop-band.

KEYWORDS silica opal, gold coating, Surface-Enhanced Raman spectroscopy

ACKNOWLEDGEMENTS The authors are grateful to the Russian Science Foundation for financial support of the present research (Grant No. 23-23-00252). This work was partially performed using the scanning probe microscope NT-MDT NTEGRA Prima upgraded up to NT-MDT NTEGRA II by Nova SPb from Program for the Development of Moscow State University. Scanning electron microscopy was performed using the equipment of the JRC PMR IGIC RAS. The authors also thank Daniil Kozlov for assistance with electron microscopy.

FOR CITATION Astafurov M.O., Perevedentseva E.V., Melnik N.N., Baranchikov A.E., Dorofeev S.G., Ezhov A.A., Grigorieva A.V., Klimonsky S.O. SERS substrates based on opal films with gold coating. *Nanosystems: Phys. Chem. Math.*, 2024, **15** (6), 902–909.

---

1. Introduction

Surface-Enhanced Raman Spectroscopy (SERS) is one of the most promising branches of optical spectroscopy. Research in this field is mainly aims to create new materials (SERS substrates) that would have high Raman enhancement factor (*EF*) and low detection limit in combination with reproducibility of their properties, uniformity, stability and manufacturability. The key point here is the creation of so-called "hot spots" between metal nanoparticles or on nanoscale features of topography of the metal surface. The electromagnetic field in hot spots at the frequency of the light wave is to be as strong as possible, and the number of molecules of the detected compound (analyte) should be as large as possible.

In recent years, several different approaches have been proposed to create SERS substrates with record high characteristics based on the uniform distribution of silver nanoparticles on the substrate surface [1, 2], creation of a monolayer of silver nanoparticles on the surface of multilayer metal-dielectric structures [3], using films of silver inverse opals [4], as well as inverse opals decorated with various gold or silver nanoparticles [5, 6], construction of honeycomb gold nanostructures [7], silver wrinkles with gold nanoparticles lined at the tips [8], sputtering of silver on polydimethylsiloxane substrates with nanopits [9], etc. Despite the impressive results achieved in some of these works (a detection limit of the order of 10^{-20} M was achieved in [8], for example), in most cases the described technologies are rather complicated and have not been confirmed by other authors. At the same time, there is still a steady interest in simpler methods which although do not give record-breaking performance are characterized by good manufacturability and high reproducibility of the properties of the obtained SERS substrates. In particular, such methods include the use of noninverted opal-type films on which silver or gold is sputtered on top [10–14]. It is assumed that hot spots in this case can arise in places where the spheres forming the opal film are in contact with each other [10, 13, 14].

Responsible for the large electric field strength in such hot spots are plasmons localized in the metal layers around the contact points of neighboring spheres [13]. In most cases [11–14], silver has been used for sputtering. In the best works of this type [13,14], the surface morphology was further complicated by the addition of polystyrene spheres of small diameter [13] or the thermal conversion of the silver layer into nanoparticles [14]; a SERS enhancement factor of about $1 \cdot 10^8$ and a rhodamine 6G detection limit of about 10^{-14} [13] or 10^{-13} M [14] were obtained. Gold may be more attractive due to its high chemical stability, but we are aware of only one work on the SERS [10] in which it was used for sputtering onto a silica opal film. In this work a 5 nm thick gold coating was deposited by electron beam evaporation. No explanation as to why this particular thickness was chosen was given by the authors. The detection limit of rhodamine 6G was obtained in the order of $1 \cdot 10^{-6}$ M in the case when the photonic stop band normal to the opal film coincided with the wavelength of the SERS laser, and it was of $1 \cdot 10^{-5}$ M when there was no such coincidence. No estimates of the *EF* were given in Ref. [10].

Note that the influence of the photonic stop band is due to the slow photon effect inside photonic crystal (see reviews [15, 16]). In the case of SERS, the additional enhancement factor due to this effect can be more than one order of magnitude [17]. The synergistic effect between SERS and photonic stop band was reported not only in [10] but also in [11, 12]. In these studies, very thin (5 nm in [10, 12]) or island-like [11] metal coatings were used. However, this effect was not mentioned in [13], where a silver thickness of 80 nm was established as optimal. Obviously, in the latter case, light passes poorly through the metal layer and cannot effectively interact with the photonic crystal. Thus, a dilemma arises whether it is necessary to optimize the metal thickness to achieve maximum plasmon-assisted SERS or to reduce it as much as possible to obtain additional enhancement due to the photonic stop band.

In the present work, we performed a more detailed study of the SERS activity of gold-coated opal films. We collected data on the influence of the amount of sputtered gold on the properties of Au/SiO_2 opal composite, estimated the *EF* and obtained a better detection limit compared to [10]. The influence of the photonic stop band is also discussed.

2. Experimental methods

Films with opal structure were obtained using a vertical deposition self-assembly process using a colloid of SiO_2 spheres [18]. Fine-distribution SiO_2 particles with diameter of about $D \approx 250$ nm were prepared by seeded growth from nanosized nuclei [19], which were obtained by Stöber method [20]. Growing up of nuclei was provided by dropping of additional tetraethyl orthosilicate (TEOS, 99 %, Sigma-Aldrich) to the reactionary vessel performed every 10 mins according to the scheme described in Ref. [19]. Properties of the films prepared are presented in Refs. [19,21]. Sputtering of gold was carried out by thermal evaporation of metal gold (99.9 %, Sberbank) using a PVD coating machine VUP-5 equipped with a direct expansion molybdenum evaporator at a pressure of 10^{-5} torr. Amount of gold deposited was controlled with a precision of ±7 % using the samples of even gold coatings on bare glass substrates by atomic-force microscopy (AFM). To determine a thickness of the gold coating d it was partly removed in specially formed grooves, the depth of groves was examined by atomic-force microscope NT-MDT NTEGRA Prima modernized by Nova SPb company up to the level of NT-MDT NTEGRA II. A thickness of gold coating d was varied in different experiments from 12 to 100 nm (Table 1).

TABLE 1. Parameters and properties of the studied samples

The sample number	d, nm	S, mm^2		SERS Enhancement Factor*	
		10^{-5} M	10^{-6} M	$\lambda = 785$ nm	$\lambda = 532$ nm
1	12	12 ± 1	8.3 ± 0.3	$9 \cdot 10^3$	$1.4 \cdot 10^3$
2	16	12 ± 1	8.3 ± 0.3	$2 \cdot 10^4$	$0.8 \cdot 10^3$
3	34	19 ± 1	8.3 ± 0.3	$7 \cdot 10^4$	$1 \cdot 10^4$
4	100	23 ± 1	—	$5 \cdot 10^3$	—

S – area of deposited droplets of the analyte (MB),

d – the thickness of gold coating at the test substrates.

*SERS *EF* was estimated for the concentration of analyte of $C = 10^{-5}$ M.

Before the SERS experiment 5 μl droplets of aqueous solutions of methylene blue (MB, 99 %, LLC "Nasklade") with concentrations from $C = 10^{-5}$ to $C = 10^{-7}$ M were deposited to the top of samples with gold coatings. The surface area of droplets varied from 8 to 19 mm^2 (see Table 1). Variation of the surface area of the droplets originated from using of different pipettes for analyte deposition. We did not find any evident effect of thickness of a gold coating on droplet spreading and its final surface area. The surface area of droplets was taken into account when compared intensities of SERS peaks and *EF*s. Measurements of Raman scattering of a model analyte methylene blue (MB) were performed after the droplets were dried completely. SERS spectra were averaged using 4 – 6 randomly selected points. Typical standard deviations of the intensities of the obtained MB peaks over a sample were $\pm 15 - 17\ \%$. As a reference sample for further calculating the *EF*, a quartz glass plate with a drop of MB with a concentration of $C_0 = 0.08$ M was used.

All the samples were characterized with a high resolution scanning electron microscope with a field emission cathode (SEM) Carl Zeiss NVision 40, and a scanning spectrophotometer Perkin-Elmer Lambda 950. SERS spectra were collected using Renishaw InVia Raman Microscope with laser emission wavelengths $\lambda = 785$ and 532 nm (average power 45 and 25 mW, laser spot diameter 1 and 3 μm, respectively), equipped with long focal length lens Leica N Plan 50/0.50. Attenuation filters of 0.1 and 1 % were used for 785 and 532 nm lasers, respectively, with an accumulation time of 100 s in all cases.

3. Results and discussion

We examined four samples that differed in the amount of sputtered gold (Table 1). SEM images of the first three of these samples are shown in Fig. 1. As can be seen, the morphology of the gold coating changes at a thickness of $d \approx 15$ nm. At lower thickness, gold forms a non-continuous film with branched narrow grooves on the surface of SiO_2 spheres (Fig. 1a). The characteristic lateral size of continuous parts was approximately of 100 – 150 nm. On the contrary, at greater thickness it covers them with a continuous layer, but between SiO_2 particles there still remain gaps and channels not filled with gold even in this case (Fig. 1, panels b and c). It is interesting to note that the formation of non-continuous silver coating of "island-like metal particles" of approximately the same size (125 – 150 nm) was also reported in Ref. [11]. The composites were synthesized by sputtering small amounts of silver on silica opal films ($D = 242$ nm), and such coatings showed the highest SERS spectra intensity for methylene blue (MB).

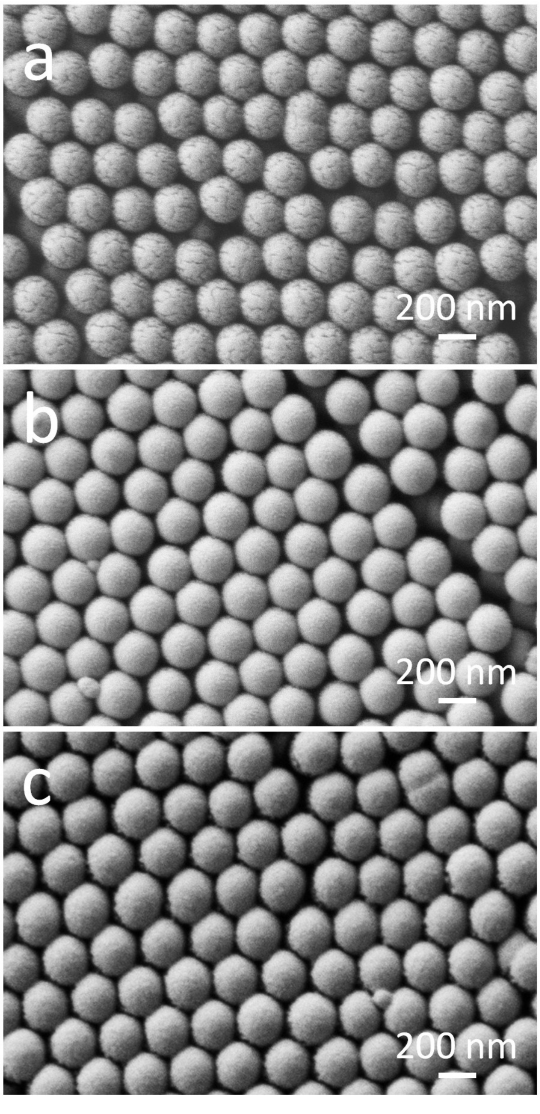

FIG. 1. SEM images of the surface of samples with different amounts of sputtered gold. Thickness of the gold film d on the corresponding bare glass plates were as following: a – 12 nm, b – 16 nm, c – 34 nm (samples 1, 2 and 3 from Table 1, respectively)

The specular reflectance spectra for all three samples are shown in Fig. 2. At both longer and shorter wavelengths, the reflectance increases with increasing amount of sputtered gold. A different sequence of curves is observed around 540 nm, where the photonic stop band is located. With increasing amount of gold, the associated reflectance maximum decreases as less light passes through the gold coating and enters deep into the film. As a result, the reflection from the film with $d = 34$ nm (see curve 3) appears to be less in this region than the others.

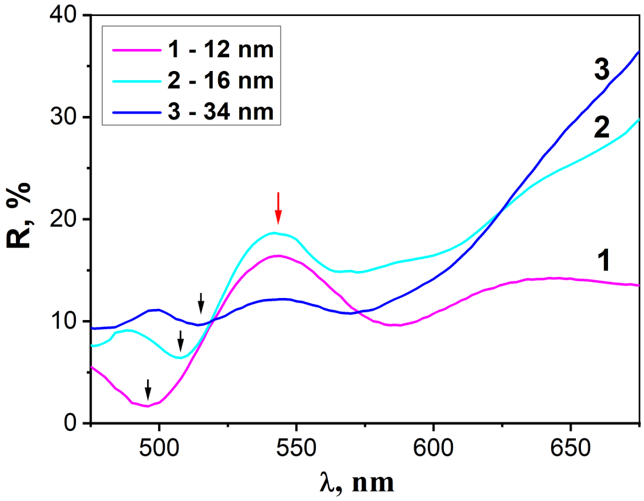

FIG. 2. Specular reflectance spectra at the angle 8° for samples with different amounts of sputtered gold. The numbers of curves correspond to the numbers of samples in Table 1

To the left of the maximum in all three curves (Fig. 2), there is a minimum, marked by black arrows, which is natural to associate with plasmon resonance. These may be plasmons localized on the protrusions and pits on the gold coating. As the thickness of the coating increases, its topography becomes smoother, and, accordingly, the plasmon resonance shifts toward longer wavelengths. It is remarkable that this plasmon resonance effect is not relevant to the SERS spectra at wavelength $\lambda = 785$ nm. Probably, the SERS effect could be associated in this case with far-away plasmons whose spectrum can be much broader than the minima marked by black arrows in Fig. 2.

Figure 3 shows the SERS spectra collected at a wavelength $\lambda = 785$ nm at different concentrations of MB in droplets. It is noticeable that at $C = 10^{-5}$ M the height of the strongest peak at about 1622 cm^{-1} (the C – C stretching mode of toluene ring) increases significantly with increasing amount of sputtered gold, while at MB concentration of $C = 10^{-6}$ M the changes are less significant and the maximum height is obtained for the sample with gold coating thickness of 16 nm. The changes in the height of this peak as a function of the sputtered gold thickness d are shown in Fig. 4. We took into account that the intensity of the SERS modes depends on the number of analyte molecules per a unit area of the substrate. This amount is inversely proportional to the area of the droplets, so for a more correct comparison in Fig. 4 the height of the SERS peak is multiplied by the droplet area S, namely, in Fig. 4 the "height $\times S$" is plotted vertically. The plotted values are also normalized to one for $d = 12$ nm. By the way, the droplet area (see Table 1) has a significant effect on the position of the points in Fig. 4 for $d = 34$ nm at $C = 10^{-5}$ M.

Most likely, the peak at 957 – 970 cm^{-1} in Fig. 3 is not related to the spectrum of the analyte. It increased with a growth of gold coating thickness and was significant in spectra of MB at concentration of 10^{-6} M only, while the strongest maximum at 1622 cm^{-1} became less intensive. Most likely, this peak originated as vibration modes of substrates.

The different character of the dependences in Fig. 4 is related, in our opinion, to the complex structure of the gold coatings which cover silica opal films. At low concentrations of the MB dye, it apparently enters the nanopores and grooves of gold where weak SERS hot spots could be formed. At small thicknesses of the gold coatings, the dye, most likely, is also there even at a concentration of $C = 10^{-5}$ M. In this case, the ratio between the height of the SERS peaks at different MB concentrations corresponds roughly to the concentration ratio. However, as the thickness of gold increases the grooves disappear, the volume of nanopores, apparently, decreases, and at high concentrations of dye it can no longer be placed in pores and grooves falling under the action of capillary forces into the contact area between the spherical SiO_2 particles covered with gold. It seems so the strongest SERS hot spots are located there [10, 13], caused by plasmons localized not on the islands, but on the metal coatings of the neighboring spheres as a whole fragment, that could explain the growth of the SERS intensity with increasing gold thickness at $C = 10^{-5}$ M. It is noticeably that for the sample with gold coating thickness of $d = 34$ nm (sample 3, Table 1) the ratio of peak heights at different MB concentrations (Fig. 3) is much larger than the concentration ratio, probably, indicating different localization of molecules, namely: at $C = 10^{-6}$ M – mainly in the nanopores of the gold coating, and at $C = 10^{-5}$ M – also in the contact regions between the spheres.

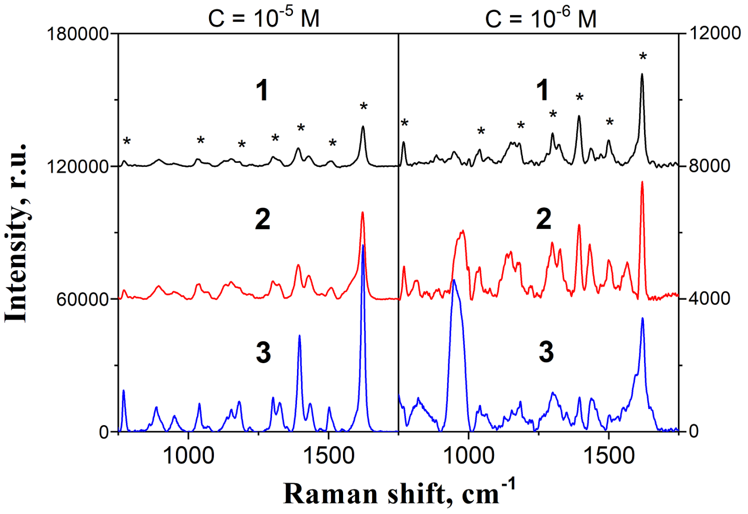

FIG. 3. SERS spectra for samples with different amounts of sputtered gold ($\lambda = 785$ nm). Concentration of MB solutions: $C = 1 \cdot 10^{-5}$ and $1 \cdot 10^{-6}$ M for the left and right panels, respectively. The curve numbers correspond to the sample numbers in Table 1. For better view, curves 1 and 2 are shifted vertically. The asterisks indicate the characteristic modes of MB

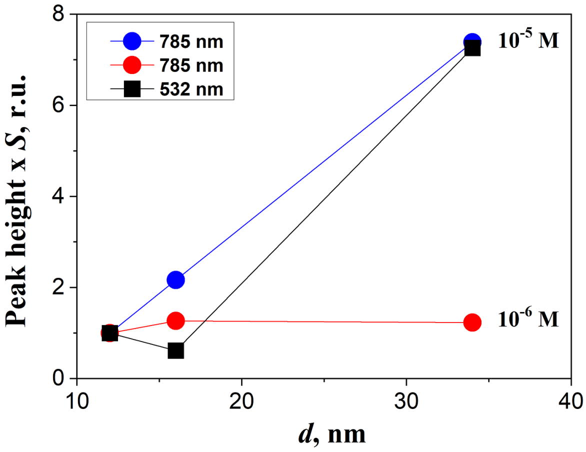

FIG. 4. Height of the main peak in SERS spectrum of MB multiplied by the surface area of the droplet S as a function of the sputtered gold thickness d. Points indicated by blue and red circles are obtained for $\lambda = 785$ nm, and black squares are obtained for $\lambda = 532$ nm. For a gold thickness of 12 nm, the peak heights are normalized to 1

When the MB concentration decreases below $C = 10^{-6}$ M the intensity of SERS maximum continues to drop rapidly. For sample 1 (Table 1) at the wavelength of incident light $\lambda = 785$ nm, we obtained a detection limit of $3 \cdot 10^{-7}$ M. At this concentration, it is still possible to sustainably detect MB in solution. In this respect, we have improved the results of Ref. [10] whose authors could not obtain for similar samples a detection limit below $1 \cdot 10^{-6}$ M even for the case when the photonic stop band coincided with the laser wavelength. Remarkable that according to Ref. [10], as the stop band approached the laser wavelength the intensity of the SERS increased several times, while the detection limit decreased by an order of magnitude. For silver-coated samples, a similar effect was reported in Ref. [12] and a weaker one in Ref. [11].

In our case, the stop-band was near 544 nm (see red arrow in Fig. 2) and the wavelength $\lambda = 532$ nm of the other laser fell on its edge. The SERS spectra collected with this laser for sample 1 (Table 1) are shown in Fig. 5. As it was shown in Ref. [17], matching the wavelength of the incident light with the stop band can give an additional enhancement of the SERS intensity by a factor of about 20. However, for our samples the electromagnetic field enhanced by Bragg reflections in the photonic crystal was weakened by the gold on the surface when leaving it. This is also evident from the height of the reflection peaks associated with the stop band, namely, for 12 nm gold it was about 11 %, for 16 nm – about 8 % (curves 1 and 2 in Fig. 2, respectively), and for 34 nm – already only about 2 % (curve 3). Accordingly, the additional enhancement due to the photonic stop-band should also decrease rapidly with a growth of gold coating thickness. For this reason, increase of the gold coating thickness from 12 to 16 nm resulted not in an increase but in a decrease of the height of the main SERS maximum for $\lambda = 532$ nm and $C = 10^{-5}$ M (see the corresponding points in Fig. 4). Further, for $d = 34$ nm (sample 3, see Table 1), the influence of the photonic stop band effectively nullified, and a significant increase in peak height was obtained for the same reasons as for $\lambda = 785$ nm. In addition, at large d value, the intensity of the SERS modes could be further enhanced due to the approach to the laser wavelength ($\lambda = 532$ nm) of the plasmon resonance, marked in Fig. 2 by arrows. At this wavelength, we obtained for sample 1 (Table 1) the detection limit of MB $1 \cdot 10^{-6}$ M (see the lower curve in Fig. 5), which corresponds to the data of Ref. [10].

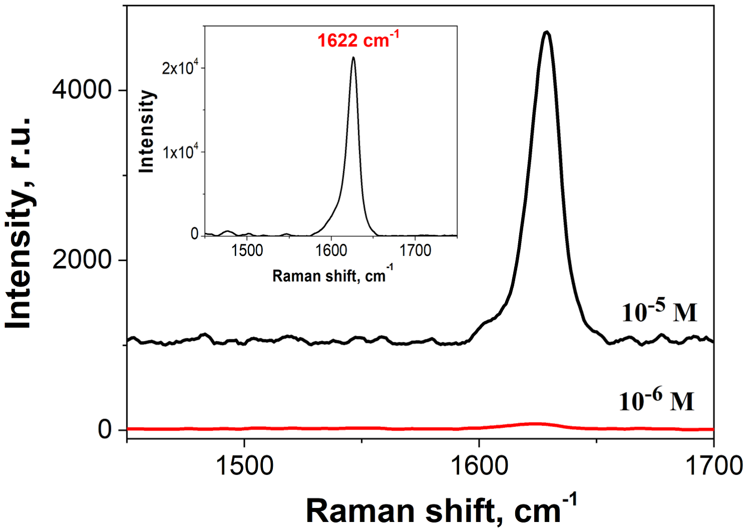

FIG. 5. Raman spectra for sample 1 (Table 1) taken at wavelength $\lambda = 532$ nm at different MB concentrations. Inset: Raman spectrum for 0.08 M of MB on a quartz glass reference sample

The *EF* of Raman scattering was determined by comparing the heights of the SERS peaks of MB deposited onto a gold-coated opal films and a reference sample of quartz glass plate, and it was calculated by the following Eq. 1 [22]:

$$EF = \frac{I_{\mathrm{SERS}}/N_{\mathrm{SERS}}}{I_0/N_0}, \tag{1}$$

where N_{SERS} and N_0 are the average number of analyte molecules in the region of SERS and reference Raman spectra collecting, respectively, and I_{SERS} and I_0 are the heights of the main peak at 1622 cm^{-1} in those and other spectra, respectively. We considered that the ratio N_{SERS}/N_0 is proportional to the ratio C/C_0 of MB concentrations in the corresponding solutions (at the reference sample $C_0 = 0.08$ M) and it is inversely proportional to the ratio of surface areas S/S_0 of the corresponding droplets (for the reference sample $S_0 = 12 \pm 1$ mm^2 – surface area of the droplet on quartz glass). The resulting formula looks as follows (Eq. 2):

$$EF = \frac{I_{\mathrm{SERS}} C_0 S}{I_0 C S_0}. \tag{2}$$

As a result, we obtained for $C = 10^{-5}$ M the *EF* values summarized in Table 1.

The dependences of the *EF* on the gold thickness d repeat the dependences shown in Fig. 4 for the height of the main SERS peak. The maximum *EF* value reached $\sim 7 \cdot 10^4$ at laser wavelength $\lambda = 785$ nm for the sample 3 ($d = 34$ nm). This value is about 1 – 2 orders of magnitude below the results reported previously for silver-coated silica opal films [11, 12]. A reasonable question arises whether the SERS intensity will increase with a further increase in d. From Table 1, we see that this is not the case: increasing d to 100 nm (sample 4) leads to a sharp drop in *EF*. Probably, the optimal thickness of gold lies in the vicinity of 40 nm. Note, that the highest SERS intensity was detected for an Ag coating with a thickness of 80 nm in [13] and only 5 nm in [12]; in both cases, a laser with a different wavelength $\lambda = 532$ nm was used.

4. Conclusions

In the present study, the issues related to gold-coated opal-type SERS substrates were addressed. It was demonstrated that at high analyte concentration $C = 10^{-5}$ M, the intensity of SERS at a wavelength of 785 nm increased with increasing amount of sputtered gold, while at $C = 10^{-6}$ M similar dependence was not observed. We believe that this is due to the complex morphology of the gold coating causing the existence of SERS hot spots of different strength. Electron microscopy has shown that at small amounts of sputtered gold, a coating with branched narrow grooves on the surface of SiO$_2$ spheres is obtained. At the same time, at large amounts of gold (the thickness of the gold coating on the bare glass plates above 15 nm), the upper surface of silica spheres is covered with metal completely but there are still gaps and channels between SiO$_2$ spheres which are not filled with gold. As a result, at concentration of the analyte MB of 10^{-6} M and at lower concentrations, as well as in case of thin island-like gold coatings, the analyte molecules fall mainly into weak hot spots, presumably, associated with grooves and nanopores in the gold coating. Otherwise, at higher concentrations of the analyte (of $C = 10^{-5}$ M and above) and sufficient thickness of the gold coating the molecules appear in the strongest SERS hot spots in the contact areas between the SiO_2 spheres. In this case, the highest values of the SERS *EF* (see Table 1) and the best detection limits of the analyte (of about $1 \cdot 10^{-6}$ and $3 \cdot 10^{-7}$ M for $\lambda = 532$ and 785 nm, respectively) were obtained.

Despite the fact that the photonic stop band contributed to the additional enhancement of SERS signal at $\lambda = 532$ nm, this factor turned out not to be the leading one. The SERS characteristics detected with $\lambda = 785$ nm exceeded significantly both the data discussed above for $\lambda = 532$ nm and those published previously in Ref. [10]. At the same time, the fabricated samples with gold coating were inferior in enhancement factor and detection limit to similar opal materials with silver coatings [11, 12]. Despite this, they may be quite promising for practical applications due to a great thermodynamic stability of gold. The data presented in this work were collected within a year after the samples were fabricated and no particular methods of surface protection were taken, that confirms the high stability of gold-coated silica opals as promising SERS materials. To scale up the production of the proposed SERS substrates, it is desirable to replace the slow laboratory-oriented vertical deposition with a more productive process, such as the drop casting and drying method [14] or the inward-growing self-assembly [23], for example. Otherwise, our method of sputtering gold onto an opal-type layer can be easily adapted for large-scale production of efficient, reproducible and stable SERS substrates.

References

[1] Liang L., Zhao X., Wen J., Liu J., Zhang F., Guo X., Zhang K., Wang A., Gao R., Wang Y., Zhang Y. Flexible SERS Substrate with a Ag–SiO_2 Cosputtered Film for the Rapid and Convenient Detection of Thiram. *Langmuir*, 2022, **38**, P. 13753–13762.

[2] Varasteanu P., Bujor A.M., Pachiu C., Craciun G., Mihalache I., Tucureanu V., Romanitan C., Pascu R., Boldeiu A. Close-packed small nanocubes assemblies as efficient SERS substrates. *J. of Molecular Structure*, 2023, **1294**, 136441.

[3] Zha Z., Liu R., Yang W., Li C., Gao J., Shafi M., Fan X., Li Z., Du X., Jiang S. Surface-enhanced Raman scattering by the composite structure of Ag NP-multilayer Au films separated by Al2O3. *Optics Express*, 2021, **29** (6), P. 8890–8901.

[4] Cai Z., Yan Y., Liu L., Lin S., Hu X. Controllable fabrication of metallic photonic crystals for ultra-sensitive SERS and photodetectors. *RSC Adv.*, 2017, **7**, P. 55851–55858.

[5] He L., Huang J., Xu T., Chen L., Zhang K., Han S., He Y., Lee S.T. Silver nanosheet-coated inverse opal film as a highly active and uniform SERS substrate. *J. Mater. Chem.*, 2012, **22**, P. 1370–1374.

[6] Martynova N.A., Goldt A.E., Grigorieva A.V. Au-Au composites with inverse opal structure for surface-enhanced Raman spectroscopy. *Gold Bulletin*, 2018, **51**, P. 57–64.

[7] Zhu A., Zhao X., Cheng M., Chen L., Wang Y., Zhang X., Zhang Y., Zhang X. Nanohoneycomb Surface-Enhanced Raman Spectroscopy-Active Chip for the Determination of Biomarkers of Hepatocellular Carcinoma. *ACS Appl. Mater. Interfaces*, 2019, **11**, P. 44617–44623.

[8] Guo H., Qian K., Cai A., Tang J., Liu J. Ordered gold nanoparticle arrays on the tip of silver wrinkled structures for single molecule detection. *Sensors & Actuators: B. Chemical*, 2019, **300**, 126846.

[9] Ke X., Chen J., Chang L., Zhou Z., Zhang W. Casting liquid PDMS on self-assembled bilayer polystyrene nanospheres to prepare a SERS substrate with two layers of nanopits for detection of p-nitrophenol. *Anal. Methods*, 2023, **15**, P. 4582–4590.

[10] Wei M.-X., Liu C.-H., Lee H., Lee B.-W., Hsu C.-H., Lin H.-P., Wu Yu-C. Synthesis of High-Performance Photonic Crystal Film for SERS Applications via Drop-Coating Method. *Coatings*, 2020, **10**, 679.

[11] Chen G., Zhang K., Luo B., Hong W., Chen J., Chen X. Plasmonic-3D photonic crystals microchip for surface enhanced Raman spectroscopy. *Biosensors and Bioelectronics*, 2019, **143**, 111596.

[12] Chen H., Song C., Peng Z., Mao J., Zhang Y., Chen S., Zhang W., Zhang S., Zhao W., Ouyang G. The Fabrication of Photonic Crystal Microchip with Controllable Wettability and SERS Activity based on Surface Roughness for Trace Organic Compounds Determination. *Adv. Mater. Interfaces*, 2022, 2102178.

[13] Li W., Lu X., Yang R., Liang F., Chen W., Xie Z., Zheng J., Zhu J., Huang Y., Yue W., Li L., Su Y. Highly sensitive and reproducible SERS substrates with binary colloidal crystals (bCCs) based on MIM structures. *Applied Surface Science*, 2022, **597**, 153654.

[14] Dzhagan V., Mazur N., Kapush O., Skoryk M., Pirko Y., Yemets A., Dzhahan Vl., Shepeliavyi P., Valakh M., and Yukhymchuk V. Self-Organized SERS Substrates with Efficient Analyte Enrichment in the Hot Spots. *ACS Omega*, 2024, **9**, P. 4819–4830.

[15] Galisteo-Lopez J.F., Ibisate M., Sapienza R., Froufe Perez L.S., Blanco A., Lopez C. Self-Assembled Photonic Structures. *Adv. Mater.*, 2011, **23**, P. 30–69.

[16] Liu J., Zhao H., Wu M., Van der Schueren B., Yu Li, Deparis O., Ye J., Ozin G.A., Hasan T., Su B.-L. Slow Photons for Photocatalysis and Photovoltaics. *Adv. Mater.*, 2017, **29**, 1605349.

[17] Ashurov M., Abdusatorov B., Baranchikov A., Klimonsky S. Surface-enhanced Raman scattering in ETPTA inverse photonic crystals with gold nanoparticles. *Phys. Chem. Chem. Phys.*, 2021, **23**, P. 20275–20281.

[18] Jiang P., Bertone J.F., Hwang K.S., Colvin V.L. Single-Crystal Colloidal Multilayers of Controlled Thickness. *Chem. Mater.*, 1999, **11**, P. 2132–2140.

[19] Klimonsky S.O., Bakhia T., Knotko A.V., Lukashin A.V. Synthesis of Narrow_Dispersed SiO_2 Colloidal Particles and Colloidal Crystal Films Based on Them. *Doklady Chemistry,* 2014, **457** (1), P. 115–117.

[20] Stöber W., Fink A., Bohn E. Controlled Growth of Monodisperse Silica Spheres in the Micron Size Range. *J. Colloid Interface Sci.*, 1968, **26**, P. 62–69.

[21] Bakhia T., Baranchikov A.E., Gorelik V.S., Klimonsky S.O. Local Optical Spectroscopy of Opaline Photonic Crystal Films. *Crystallography Reports*, 2017, **62** (5), P. 783–786.

[22] Le Ru E., Blackie E., Meyer M., Etchegoin P.G. Surface Enhanced Raman Scattering Enhancement Factors: A Comprehensive Study. *J. Phys. Chem. C*, 2007, **111** (37), P. 13794–13803.

[23] Yan Q., Zhou Z., Zhao X.S. Inward-Growing Self-Assembly of Colloidal Crystal Films on Horizontal Substrates. *Langmuir*, 2005, **21** (7), P. 3158–3164.

Submitted 5 June 2024; revised 29 October 2024; accepted 31 October 2024

Information about the authors:

Mikhail O. Astafurov – Lomonosov Moscow State University, 119991 Leninskie gory 1, bld. 3, Moscow, Russia; mihast0707@mail.ru

Elena V. Perevedentseva – P. N. Lebedev Physical Institute of the Russian Academy of Sciences, Leninskii prospekt 53, 119991, Moscow, Russia; ORCID 0000-0002-1489-6747; perevedencevaev@lebedev.ru

Nikolay N. Melnik – P. N. Lebedev Physical Institute of the Russian Academy of Sciences, Leninskii prospekt 53, 119991, Moscow, Russia; ORCID 0000-0002-0212-9903; melniknn@lebedev.ru

Alexander E. Baranchikov – Kurnakov Institute of General and Inorganic Chemistry of the Russian Academy of Sciences, Leninskii prospekt 31, 119071, Moscow, Russia; ORCID 0000-0002-2378-7446; a.barantchikov@yandex.ru

Sergey G. Dorofeev – Lomonosov Moscow State University, 119991 Leninskie gory 1, bld. 3, Moscow, Russia; ORCID 0000-0003-3820-4853; dorofeev@inorg.chem.msu.ru

Alexander A. Ezhov – Lomonosov Moscow State University, 119991 Leninskie gory 1, bld. 3, Moscow, Russia; ORCID 0000-0001-6221-3093; alexander-ezhov@yandex.ru

Anastasia V. Grigorieva – Lomonosov Moscow State University, 119991 Leninskie gory 1, bld. 3, Moscow, Russia; ORCID 0000-0001-6102-9024; anastasia@inorg.chem.msu.ru

Sergey O. Klimonsky – Lomonosov Moscow State University, 119991 Leninskie gory 1, bld. 3, Moscow, Russia; ORCID 0000-0001-6102-1305; klimonskyso@my.msu.ru

Conflict of interest: the authors declare no conflict of interest.

NANOSYSTEMS:
PHYSICS, CHEMISTRY, MATHEMATICS

Original article

Veselova V.O., et al. *Nanosystems: Phys. Chem. Math.*, 2024, **15** (6), 910–920.
http://nanojournal.ifmo.ru
DOI 10.17586/2220-8054-2024-15-6-910-920

Prolonged antibacterial action of CuO-coated cotton fabric in tropical climate

Varvara O. Veselova[1,a], Andrey N. Kostrov[2,b], Vladimir A. Plyuta[3,c], Anna V. Kamler[1,d], Roman V. Nikonov[1,e], Olga E. Melkina[3,f], Vo Thi Hoai Thu[4,g], Le Thi Hue[4,h], Dinh Thi Thu Trang[4,i], Inessa A. Khmel[3,j], Viktor A. Nadtochenko[2,k], Mikhail G. Kiselev[5,l], Vladimir K. Ivanov[1,m]

[1]N. S. Kurnakov Institute of General and Inorganic Chemistry RAS, Moscow, Russia
[2]N. N. Semenov Federal Research Center for Chemical Physics, Moscow, Russia
[3]Complex of NBICS Technologies, National Research Center "Kurchatov Institute", Russia, Moscow, Russia
[4]Joint Vietnam-Russia Tropical Science and Technology Research Center, Hanoi, Vietnam
[5]G. A. Krestov Institute of Solution Chemistry of the Russian Academy of Sciences, Ivanovo, Russia

[a]ibvarvara@yandex.ru, [b]andreikostrov@rambler.ru, [c]plyuta_va@nrcki.ru, [d]abramova@physics.msu.ru, [e]novita@mail.ru, [f]compleanno@mail.ru, [g]hoaithu@mail.ru, [h]huelebiotech85@gmail.com, [i]trangdt1806@gmail.com, [j]iakhmel@yandex.ru, [k]nadtochenko@gmail.com, [l]mgk@isc-ras.ru, [m]van@igic.ras.ru

Corresponding author: V. O. Veselova, ibvarvara@yandex.ru

ABSTRACT The paper reports the results of a large-scale testing of antibacterial textiles with extremely stable and long-lasting copper oxide coating. Using disk diffusion method, ICP-OES and specific *lux* biosensors it was shown that the coating does not leach copper ions into the environment. Laboratory experiments performed according to the ISO 20743 protocol showed high antibacterial activity of the produced coating, up to complete growth suppression for some strains. The long-term field tests were carried out in a tropical climate, at the Climate test station "Hoa Lac" (Hanoi city, Vietnam). The number of microorganisms on the textile materials remained within the range of 1–3% in comparison with the control sample for the entire duration of the field exposure (12 months).

KEYWORDS climate test, composite materials, metal oxide nanoparticles, ultrasonic cavitation, antimicrobial activity, field testing.

FUNDING The work on textile coating and physico-chemical characterisation of the obtained materials was carried out within the State Assignment of the Kurnakov Institute of General and Inorganic Chemistry of the Russian Academy of Sciences. The work on *in vitro* characterisation of the antibacterial activity of the textile materials was carried out within the framework of the Thematic Plan of the State Assignment of the National Research Center "Kurchatov Institute".

ACKNOWLEDGEMENTS This research was performed using the equipment of the JRC PMR IGIC RAS. SEM measurements were performed using core research facilities of FRCCP RAS (no. 506694). The field tests were conducted using the facilities of the Program of research and technological works of the joint Russian-Vietnamese Tropical Research and Technology Centre for 2020-2024 (ECOLAN T-1.13).

FOR CITATION Veselova V.O., Kostrov A.N., Plyuta V.A., Kamler A.V., Nikonov R.V., Melkina O.E., Vo Thi Hoai Thu, Le Thi Hue, Dinh Thi Thu Trang, Khmel I.A., Nadtochenko V.A., Kiselev M.G., Ivanov V.K. Prolonged antibacterial action of CuO-coated cotton fabric in tropical climate. *Nanosystems: Phys. Chem. Math.*, 2024, **15** (6), 910–920.

1. Introduction

Woven fabrics effectively absorb sweat and other body exudate, retain moisture and warmth. Textiles which are worn close to the skin offer an ideal environment for microbial growth. With the problem of antibiotic-resistant bacteria being an ever-increasing concern and the rising awareness in public and personal hygiene, textiles with antimicrobial properties are becoming attractive for both the manufacturers and researchers. An emerging trend in textile finishing is the use of metal oxide nanoparticles (NP) [1].

Copper compounds have found numerous applications as bactericide, algaecide, fungicide, nematocide, molluscicide, and anti-fouling agent [2]. They are especially attractive for pretreatment of fabrics intended for the use in warm tropical climate with high biodiversity, because they exhibit both bactericidal and fungicidal properties simultaneously. In previous work related to textile testing in tropical climate, it was shown that fungi are the more prominent type of microorganism in these conditions and make a significant contribution to the fabric deterioration [3].

To be used in textile production, the chemical compounds should be safe for the final consumer. Copper ions are known for their toxicity and associated health risks [4], which requires use of copper compounds that do not leach copper ions, do not dissolve, do not penetrate the skin barrier, etc. In this regard, copper oxide is one of the suitable copper compounds. Compared to the other commonly used antibacterial agents, CuO has low cytotoxicity to human hepatocellular carcinoma (HepG2) cells [5]. Recent studies have shown that CuO nanoparticles (NPs) do not translocate though the skin barrier [6]. In a recent paper [7], a detailed study of the cytotoxic effects of fabrics treated with CuO nanoparticles was conducted. Human dermal fibroblast (HDF) cell viability above 95 % was observed for all the tested fabrics. Hence, the risk of NP-mediated damage to human cells is minimal and the NP-coated fabrics could be used safely. Moreover, CuO-loaded wound dressings were found to improve and accelerate wound healing, and no histological differences were found between open wounds treated with conventional dressings and CuO-treated dressings [8].

While the human skin does not experience any negative effects upon contact with copper oxide nanoparticles, microorganisms are extremely susceptible to it. A significant bactericidal effect was reported even for fabric coated with 1wt.% of CuO nanoparticles [9, 10]. Several studies (primarily short-term laboratory experiments with individual strains of microorganisms) have shown that impregnation or coating of fabrics with CuO nanoparticles endows them with broad-spectrum antimicrobial properties [11, 12]. It is suggested that in case of CuO NPs the cellular damage to the microorganisms is caused by the hydroxyl radicals produced on its surface [12, 13].

As previously mentioned, the textile coating must not release any ions into the surrounding media. The long-term stability of bactericidal materials is crucial for their application [14–16]. In order to produce long-lasting stable coating, various ways of immobilizing the metal oxide nanoparticles in organic or inorganic matrices have been actively studied in recent years [17].

One of the possible approaches to production of stable fabric coatings is the use of ultrasonic cavitation for the incorporation of nanoparticles into the textile fibres. This method ensures even distribution of the coating components, allows for large-scale production and provides stability of the coating for at least 20 washing cycles [18–20].

Though some studies of CuO-coated cotton fabrics have already been reported [9, 21], the vast majority of these studies were limited to testing with the model objects only, such as *E. coli* and *S. aureus* [22–29]. Data characterizing the performance of these composites in field conditions are very limited. The effect of the climate might be extremely significant, and it could also severely affect the speed of fabric deterioration [30]. Antibacterial activity strongly depends on the temperature [31], humidity [32], and insolation conditions as well. Tropical climate is characterized by high temperature and high humidity. Biological diversity of microorganisms occurring in a tropical climate is significantly higher compared to other climatic zones [33]. Thus, the materials intended for use in the tropical climate will be subjected to very harsh environmental conditions, and therefore these materials require special testing.

In this paper, we report the whole production cycle of the textiles coated with copper oxide nanoparticles and the results of their testing both according to the standard laboratory-scale procedures and in the long-term field tests in the tropical climate at the Climate test station “Hoa Lac” (Hanoi city, Vietnam).

2. Materials and methods

2.1. Preparation of the fabric samples

CuO nanoparticles were purchased from ROTH and used without any preliminary processing. Chemical purity of the nanopowder is $\geq$99 %. CuO particle size according to the manufacturer is 15–50 nm. Surface area (BET) is $\geq$15 m^2/g. White calico (100% cotton) with density of 140 g/m^2 (manufactured by IvanovoTextile ltd., Russia) was placed in a 1.25 g/L suspension of CuO nanoparticles in water at 20°C at 20 mm from the ultrasonic emitter and treated with ultrasound. The frequency of the ultrasound was 22 kHz, the power was 750 W. The fabric was moved along the ultrasonic emitter with the speed of 1.5 m/min. The sample was dried at 120°C for 3 h. The procedure for the immobilization of metal oxide nanoparticles on a substrate of fibrous material using high power ultrasound was reported earlier by Abramova et al. [19, 20, 34].

2.2. Study of the physical and mechanical characteristics of composite materials

For the quantitative characterization of the prepared coated textile samples, approximately 1 g of the coated cotton was ashed in a platinum crucible for 6 hours at 900°C in a resistance furnace under air.

Analysis of the elemental composition was performed by energy dispersive X–ray (EDX) spectroscopy using a high resolution scanning electron microscope (Carl Zeiss NVision40) equipped with an Oxford Instruments X-Max detector. The analysis was carried out at an accelerating voltage of 20 kV and the working distance of 11 mm. For calibration, standard cobalt reference sample was used.

The surface morphology of the obtained composite materials was studied by scanning electron microscopy (SEM). SEM images were obtained using a Prisma E microscope (Thermo Scientific, Czech Republic) with an accelerating voltage of 3.5 kV. The samples were preliminarily coated with 10 nm thick gold layer by a Q150R ES plus sputter coater (Quorum Technologies, UK).

The tensile strength of the samples was measured according to the TCVN 1754–1986 standard on a Zwick/Roell Z010TH Proline device (Germany).

Assessment of copper ions leaching into the aqueous media was performed by inductively coupled plasma optical emission spectroscopy (ICP-OES) using a Thermo Scientific iCAP XP (USA). To prepare the solutions for analysis, 10×10 mm fabric fragments were submerged in 1.5 mL of water for five days at 30°C. Then the fabric fragments were removed and the resulting solution was analysed.

2.3. *In vitro* evaluation of antibacterial activity of composite materials

The antibacterial activity of the obtained composite materials was tested *in vitro* using the following model objects: 1) opportunistic Gram-negative bacteria *Escherichia coli* strain BW25113 (the parent strain for the Keio Collection of single-gene knockouts) [35], the strain was kindly provided by Dr. Alexander Mironov (Engelhardt Institute of Molecular Biology, Russian Academy of Science, Moscow, Russia); 2) Gram-positive bacteria *Staphylococcus aureus*; 3) opportunistic human pathogen *Chromobacterium violaceum* strain CV12472 (a characteristic representative of the soil and water microbiome in tropical and subtropical climatic zones [36]), the strain was kindly provided by Dr. Leonid Chernin (The Hebrew University of Jerusalem, Rehovot, Israel); 4) rhizosphere *Pseudomonas chlororaphis* strain 449 [37], which was obtained from rhizosphere of maize (Ukraine) [38]; and strains isolated from fabric samples studied in 2020 in the field tests at the Climate test station “Hoa Lac” (Hanoi city, Vietnam) [3] which were the strains most commonly found on the surface of cotton fabric after exposure at the test station, namely 5) *Stenotrophomonas rhizophila*; 6) *Exiguobacterium indicum*; 7) *Brachybacterium paraconglomeratum*; 8) *Bacillus amyloliquefaciens*.

Two variations of the laboratory-scale experimental procedure were used to conduct preliminary tests of the antibacterial activity.

a. Evaluation of antibacterial activity of the composite materials on a solid nutrient medium

Antibacterial activity of the composite materials was tested using the disk diffusion test as described elsewhere [3]. Briefly, the fabric composite materials were sterilized, cut into 10×10 mm pieces and placed on the surface of the Petri dishes. After 24 hours of incubation at 30°C, the Petri dishes were examined for the presence of growth inhibition zones around the studied samples. The diameters of inhibition zones were measured. All the assays were carried out in triplicate.

b. Evaluation of antibacterial activity of composite materials based on ISO 20743.

An experimental protocol was developed on the basis of ISO 20743 [39]. The studied fabric (in three replicates) was cut to size of 6×15 cm and sprayed with microbial suspension (using the strains listed above). After adding the strain, the fabric was suspended in an airtight vessel with sterile water at the bottom to provide moisture and then incubated under humid conditions at 30°C for 28 days. At the “zero point” and after the contact period (28 days of incubation at 30°C) the microorganisms were counted. The antimicrobial effect of the fabric samples on microorganisms was assessed by analysing the growth of microorganisms on the surface of the samples and by comparing of number of surviving organisms, counted as the number of colonies forming unit (CFU), of CuO-coated cotton fabric samples with that of reference sample (without CuO coating, control).

2.4. Evaluation of the leaching of copper ions from cotton fabric with CuO coating into an aqueous solution using specific *lux* biosensor

Specific *lux* biosensor based on Gram-negative bacteria *E. coli* JM83 with hybrid plasmid pCopA’::lux was used to evaluate the rate of copper ions release from CuO-coated cotton fabric and to assess the degree of bacterial cell damage caused by these ions. The tests were carried out as described elsewhere [40,41], with some modifications. Briefly, sterile fabric pieces (10×10 mm) (1, 2 or 3 pieces) were placed in 2 mL centrifuge tubes containing 1.5 mL of sterile mQ water. The tubes were placed on a vortex and then moved into a thermostat and incubated for 5 days at 30°C. After 5 days, the content of copper ions in the aqueous solution (with or without fabric pieces) was measured using the *lux* biosensor *E. coli* JM83 (pCopA’::lux). Copper sulfate (aqueous solutions of $CuSO_4$, 5, 10 and 50 μg/mL) was used as reference compound for the induction of bioluminescence in *lux* biosensors.

2.5. Field Tests

All field experiments were carried out at the Climate test station “Hoa Lac” (Hanoi city, Vietnam). The experiments were carried out in three repetitions. The coated textile was sterilized at 120°C for 30 minutes and cut into 5×10 cm pieces. The fabric samples were placed on the following test sites:

a. “Concrete site”: the site is located in a field with no shading. The fabric samples were placed at a height of 1 m from the ground, with 3 cm distance between the samples.

b. “Mycological site”: the site is located in a shaded wooded area. The fabric samples were placed in a closed cabinet with a roof at 0.5 m from the ground, with 3 cm distance between the samples.

2.6. Evaluation of microorganisms’ growth on studied materials after various duration of field tests

The fabric samples were collected after 1, 3, 4, 6, 9 and 12 months of exposure at the test sites. Microorganisms from the collected samples were isolated and counted according to procedure described elsewhere [3].

2.7. Statistical Analysis

The statistical analysis was carried out using the IBM SPSS software v.26 (New York, NY, USA). Significant differences were determined using a one-way analysis of variance (ANOVA), followed by Tukey's HSD (Honestly Significant Difference) post hoc test. Differences were considered to be significant at $p \leq 0.05$.

3. Results and discussion

3.1. Production and characterization of coated textiles

Cotton fabric coated with CuO nanoparticles was prepared using ultrasonic treatment. Details of this procedure along with the study of the coating stability during washing can be found elsewhere [19,20,34]. The content of CuO NPs in the obtained fabric was determined gravimetrically and was found to be 5.25 g/m^2. The experiment was carried out in four repetitions and the standard deviation of this value was 10%. Chemical composition of the samples was also analysed by EDX (Fig. 1a). EDX mapping proved the loading of copper atoms to be 5 at.% showing a sufficiently uniform distribution of the CuO nanoparticles on the cotton fibres.

The surface morphology of the obtained samples is shown in Fig.1b. The role of surface texture for the antibacterial efficiency was demonstrated previously in numerous reports [42,43]. Coating cotton textiles with TiO_2 was shown to create a hydrophobic surface, which additionally prevented bacterial adhesion [3,44]. However, in the case of the CuO coating, the fabric demonstrated full wetting, which means that any observed antibacterial effect is associated with the action of CuO and not with hydrophobicity.

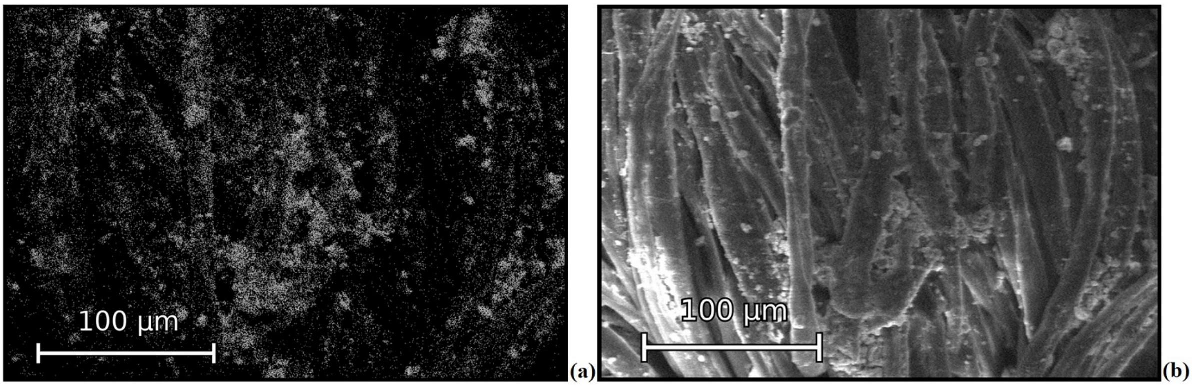

FIG. 1. EDX mapping (a) and SEM image (b) of fabric coated with CuO nanoparticles

3.2. Study of the antibacterial effect of CuO coating on solid nutrient medium

Preliminary laboratory-scale tests were carried out using the disk diffusion method. The results of *in vitro* tests of the CuO-coated fabrics on solid nutrient medium with bacteria of different taxonomic groups are presented in Table 1.

The experiments were carried out using both gram-positive (*S. aureus, E. indicum, B. paraconglomeratum*, and *B. amyloliquefaciens*) and gram-negative (*E. coli, C. violaceum, P. chlororaphis, and S. rhizophila*) bacteria. For the majority of the tested strains the growth inhibition zone is almost negligible after short incubation time. This means that CuO nanoparticles have very low diffusion rate in solid nutrient medium, which prevents their diffusion into the agar. The absence of an inhibition zone cannot be interpreted as the absence of an antibacterial effect, since it is only an indicator of low release rate and poor diffusion of the active component of the coating during short-term exposure of the test samples to bacteria.

The data presented in Table 1 confirm minor antimicrobial activity of CuO coating on gram-positive *B. amyloliquefaciens* and gram-negative *S. rhizophila* species after 24 h. This might evidence higher susceptibility of these bacteria to copper ions. It should be noted, however, that the presence of the growth inhibition zone does not necessarily imply that microorganisms have been killed – they might have only been prevented from growing.

3.3. Evaluation of the leaching of copper ions from cotton fabric with CuO coating into an aqueous solution

The disk diffusion method showed that CuO nanoparticles are strongly bound to the textile and do not leach copper ions into the solid nutrient medium after 24 h. To evaluate Cu^{2+} ions leaching over a longer period of time and in "harsher" conditions, the ICP-OES method was used. To prepare the solutions for analysis, 10*10 mm fabric piece was submerged in 1.5 mL of water for five days at 30°C. After five days the fabric was removed and the resulting solution was analysed. The concentration of copper ions in the solution was found to be 0.2 mg/L with relative standard deviation of 2%.

TABLE 1. Antibacterial activity of the textiles coated with CuO on solid medium

Bacterial strain	Diameters of inhibition zone (DIZ)[a], mm	
	the reference sample	fabric coated with CuO nanoparticles
E. coli	0 ± 0.1	0 ± 0.1
C. violaceum	0 ± 0.1	0 ± 0.1
P. chlororaphis	0 ± 0.1	0 ± 0.1
S. aureus	0 ± 0.1	0 ± 0.1
E. indicum	0 ± 0.1	0 ± 0.1
B. paraconglomeratum	0 ± 0.1	0 ± 0.1
B. amyloliquefaciens	0 ± 0.1	0.8 ± 0.1
S. rhizophila	0 ± 0.1	0.5 ± 0.1

[a] Diameter of the growth inhibition zone (DIZ) is calculated as the size of entire growth inhibition zone around the fabric sample minus the size of the fabric sample (which is 10 mm); all the assays were carried out in triplicate and the data were recorded as mean ± standard error.

In vitro studies using a specific *lux* biosensor were employed to elucidate whether defence systems responsible for protection against excess of copper ions of living bacterial cells were triggered in the presence of the coated fabric at such concentration of leached ions. In the case of *E.coli* JM83 strain used in this study, it is the induction of the *copA* gene (encoding the CopA protein, a member of the P-type ATPase cation transporter family) that indicate the activation of defense system of bacterial cells, since CopA is known to confer resistance to copper ions in *E. coli* as an ATP-dependent exporter of monovalent copper [45].

The solutions for analysis were prepared in the same way as for ICP-OES, by incubation of a fabric piece in 1.5 mL of water for five days at 30°C. Solutions with varied number of fabric pieces were prepared. The obtained data are presented in Fig. 2. It can be seen that aqueous solutions containing fabric coated with CuO nanoparticles do activate luminescence of *E. coli* pCopA *lux*-biosensor (induce expression from the P*copA* promoter). Specifically, fabric samples coated with CuO nanoparticles increase luminescence intensity of *lux*-biosensor by 5–10 times after 30 minutes of measurement compared to the control (aqueous solution without fabric samples) or aqueous solutions containing fabric samples without nanoparticles.

Thus, the obtained data indicate that copper ions are capable of leaching from CuO-coated cotton fabric into the aqueous medium to induce expression from the promoter of the *cop*A gene responsible for copper homeostasis in *E. coli.*

However, even the samples prepared with 3 pieces of the fabric coated with CuO nanoparticles (to achieve higher concentration of Cu^{2+} ions) had luminescence intensity of *E. coli* pCopA *lux*-biosensor 4.5–6 times lower (after 30 minutes of measurement) compared to that of the reference compound (5 μg/mL aqueous solution of $CuSO_4$). It means that the rate of the Cu^{2+} ions release from the CuO coating after 5 days of incubation is relatively low. This makes the ultrasonically treated coated fabrics suitable for prolonged use.

3.4. Determination of antimicrobial activity of CuO-coated fabric samples using ISO 20743 standard

The experiments described above provide evidence towards the slow leaching of Cu^{2+} ions in aqueous medium and in agar. However, the prepared fabric is not intended for use in aqueous medium (underwater use). Thus, the antibacterial activity of the CuO-coated textile was additionally evaluated in accordance with ISO 20743 standard, as presented in Table 2. The ISO 20743 (Textiles - Determination of antibacterial activity of textile products) is a commonly used test for evaluation of the antimicrobial efficiency. It is applicable to all textile products and allows for comparison between various antimicrobial treatments, as well as various treatment-levels on the same textile [39]. This approach includes applying aerosol of bacterial suspension onto the samples and then incubating these samples in a dry enclosed space.

The data obtained demonstrate that the CuO-coated fabric has high bactericidal activity compared to reference samples. Antibacterial effect of CuO coating was the highest against bacteria *B. amyloliquefaciens* (complete growth suppression), then against *B. paraconglomeratum* and *E. indicum* (4-log(10) CFU' reduction), and *S. rhizophila* (with a 3-log(10)

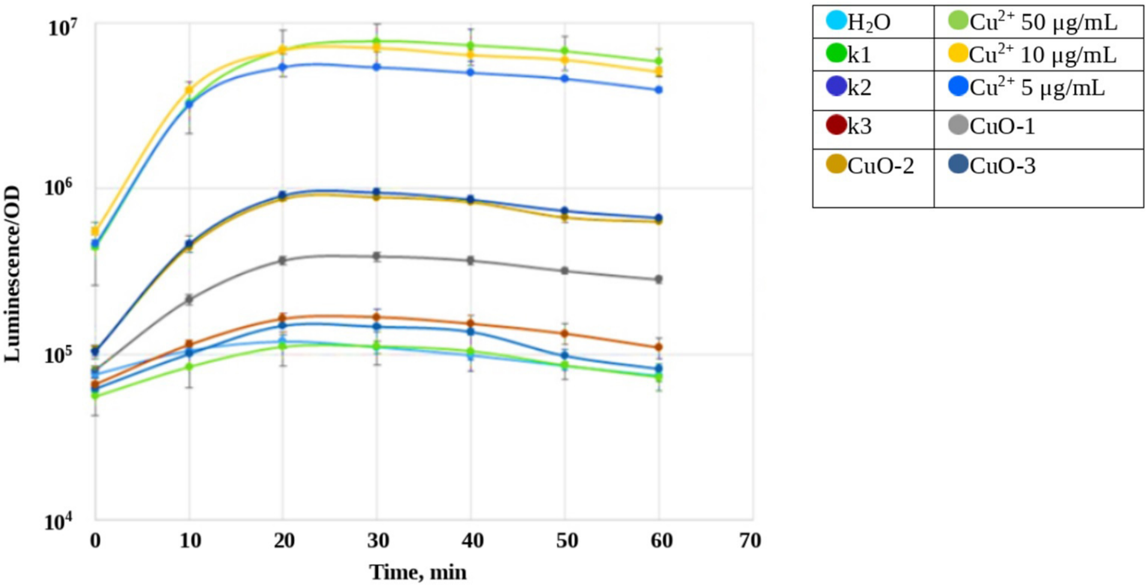

FIG. 2. Response of the biosensor strain *E. coli* JM83 (pCopA'::lux) to the presence of copper ions in aqueous environment. The curves show the change in the luminescence response of the sensor over time, which is expressed as the ratio of the average values of light emission (in RLU) measured at time t (every 10 min in the time interval 0–60 min) to its optical density (OD600) measured at 600 nm in the presence of various concentrations of $CuSO_4$ (5, 10, and 50 μg/mL) and aqueous solutions of the samples (k1, k2, and k3 - aqueous solutions with 1, 2 or 3 pieces of cotton fabric without CuO coating, and CuO-1, CuO-2, CuO-3 - aqueous solutions with 1, 2 or 3 pieces of CuO-coated cotton fabric, respectively). All values were means ± standard deviations (SD) for n = 3. $CuSO_4$ is a reference compound for the *E. coli* JM83 (pCopA'::lux) sensor and is used as a positive control to check activity (induction of bioluminescence) of the *lux* sensor strain.

CFU' reduction) after 28 days of incubation (Table 2). It must be noted that in the previously described experiments on solid nutrient medium, no growth inhibition zone was observed for *E. indicum* and *B. paraconglomeratum* compared to the uncoated sample of textile.

This highlights that the antibacterial efficiency rate depends strongly on the testing method and the conditions of bacterial cultivation. The long-term (28 days) experiments studying the antibacterial activity of the CuO-coated textile according to ISO 20743 standard confirm a high antibacterial potential of CuO nanoparticle coating compared to short-term laboratory experiments.

3.5. Field Tests

3.5.1. Determination of the antimicrobial activity of CuO-coated textiles after field tests in the tropical climate. Two types of conditions were used for field testing of the fabrics coated with CuO nanoparticles. Open concrete site had high degree of insolation and good air circulation; the samples were placed on a stand without any roof, shielding or coverage. The mycological test site was located in a forested area, and the samples were closer to the ground in shelves with doors and a roof. Presumably, the conditions at the mycological test site would promote faster leaching of the active coating component due to higher humidity at this site. The results of the field tests on these two test sites are presented in Table 3.

The data obtained show that the growth of microorganisms on the control samples of textile (original cotton fabric without a nanoparticle coating) was not suppressed and the number of colonies per sample increased over time during exposure to the tropical environment. On the other hand, the samples of textile coated with CuO nanoparticles have fewer colonies per sample compared to the reference samples, proving the inhibitory ability of the composite material. In general, composite materials had 30–100 times less CFU per sample than the control (Table 3). It should be noted that textile samples coated with CuO nanoparticles retain their antimicrobial activity during the entire period of field testing which indicates the microbiostatic effect of such coatings. No considerable differences in the long-term antibacterial activity of the samples on the two test sites were found. The number of CFU on the samples is comparable, though after 6 months of exposure the ratio of the average CFU value of microorganisms on the CuO-coated sample to the average CFU value on the reference sample became slightly higher for the samples placed on the concrete open site. The difference is small and should be interpreted with caution, but it might be suggested that the presence of the copper ions due the minor leaching occurring at the mycological test site invokes additional mechanisms of antibacterial action. Toxicity of copper ions to microorganisms, including toxicity to viruses, may occur through the displacement of essential metals from their native binding sites, from interference with oxidative phosphorylation and osmotic balance as well as from

TABLE 2. Results of laboratory-scale testing of CuO-coated textiles for antibacterial activity based on ISO 20743. The average value of CFU derived from three repetitions is given

Bacterial strain	Type of coating	Sample incubation time	
		“zero point”	After 28 days of incubation
		Colonies/Sample, CFU	
S. rhizophila	Reference sample	2.1×10^6	6.2×10^6([a]295%)
	CuO coating		3.4×10^3 ([a]0.2%; [b]0.05%)
B. paraconglomeratum	Reference sample	4.3×10^6	1.6×10^7 ([a]372%)
	CuO coating		9.4×10^2 ([a]0.02%;[b]0.005%)
B. amyloliquefaciens	Reference sample	5.8×10^5	2.4×10^6 ([a]413%)
	CuO coating		0
E. indicum	Reference sample	3.2×10^6	7.5×10^6 ([a]234%)
	CuO coating		2.0×102 ([a]0.006%; [b]0.003%)

[a] The ratio of the average CFU value for the CuO-coated sample after 28 days of incubation to the average CFU value of the sample at the “zero point” of the experiment

[b] The ratio of the average CFU value for the CuO-coated sample to the average CFU value of the reference sample after 28 days of incubation

TABLE 3. Results of the field tests of CuO-coated textiles at the Climate test station “Hoa Lac” (Hanoi city, Vietnam). The averaged value of CFU from three repetitions is given

Type of test site	Type of coating	Duration of exposure to a tropical environment				
		1 month	3 months	6 months	9 months	12 months
		Colonies/Sample, (CFU)				
Concrete open test site	Reference sample	1.6×10^6	3.3×10^7	4.3×10^7	8.2×10^7	4.2×10^8
	CuO	9.4×10^4 ([a]5.9%)	1.3×10^5 ([a]0.1%)	1.6×10^5 ([a]0.4%)	2.4×10^5 ([a]0.3%)	3.8×10^5 ([a]0.1%)
Mycological shelf test site	Reference sample	1.1×10^6	3.7×10^7	9.0×10^7	1.2×10^8	7.2×10^8
	CuO	3.4×10^4 ([a]3.1%)	9.4×10^4 ([a]0.3%)	1.0×10^5 ([a]0.1%)	1.2×10^5 ([a]0.1%)	2.5×10^5 ([a]0.04%)

[a] The ratio of the average CFU value of microorganisms on the the CuO-coated sample to the average CFU value on the reference sample;

alterations in the conformational structure of nucleic acids, membranes and proteins [2]. The experiment with specific *lux* biosensor described above shows that the amount of copper ions leached from the fibres is sufficient to have an input in the antibacterial activity of the textile.

As discussed previously, the antimicrobial properties of metal oxide nanoparticles are commonly attributed to the formation of reactive oxygen species (ROS) under UV-irradiation [2, 44–47]. The high efficiency of the coating on the shaded test site indicates that intense UV-irradiation is not necessary and it does not contribute significantly to the antibacterial performance.

Our research group previously reported similar case of tropical field tests for fabrics with TiO_2 and ZnO coatings, and these types of coatings were only able to decrease the number of CFU by 35–50 times in similar conditions [3]. This comparison shows higher efficiency of the CuO coating in tropical environment.

3.5.2. Determination of the types of microorganisms on the fabric surface after the field tests. The number of different types of microorganisms found on the samples after field testing is presented in Table 4. As can be seen from Table 4, the ratio of the microorganism types on the fabric coated with CuO nanoparticles did not change significantly over time on both of the test sites.

TABLE 4. Number of different types of microorganisms on the CuO-coated textile after different periods of exposure at the Climate test station "Hoa Lac" (Hanoi city, Vietnam). An average value from three repetitions is given

Time of exposure		Number of Species After														
		1 months			3 months			6 months			9 months			12 months		
Type of Microorganism		B	F	Y	B	F	Y	B	F	Y	B	F	Y	B	F	Y
Mycological shelf test site	Reference sample	3	5	2	4	6	2	4	7	2	5	7	2	5	7	2
		10			12			13			14			14		
	CuO	2	3	2	2	5	2	1	5	2	2	5	2	3	5	2
		7			9			8			9			10		
Concrete open test site	Reference sample	4	4	1	5	5	2	5	5	2	6	6	2	6	7	2
		9			12			12			14			15		
	CuO	2	4	2	2	4	2	2	3	1	2	4	1	3	4	1
		8			8			6			7			8		

B – Bacteria, Y – Yeast, F – Fungi

Yeasts were the least common, and the biggest variety of species was determined for fungi. The samples at both test sites were found to have very similar proportions and amounts of various microorganisms at 'zero point'. However, over time, slightly bigger variety of microorganisms was found in the samples collected from the mycological site. The difference is not very significant and can be explained by the difference in the environment conditions during the period of field testing. It is logical that greater variety of species was observed at the site with favourable conditions for microbial diversity such as high moisture and the absence of intense insolation. Fungi prevailed among identified types of microorganisms both on coated and uncoated textiles during the entire period of field testing. The mycelium species can significantly contribute to material deterioration in tropical conditions. Copper oxide nanoparticles were originally chosen because of their fungicidal properties, but it can be seen that while the number of organism decreases, the diversity is not affected as much.

3.6. Tensile strength evaluation

To estimate the deterioration of the textile samples, the tensile strength was evaluated according to the TCVN 1754-1986 protocol. The results of the measurements are summarized in Table 5 and visualized in Fig. 3.

TABLE 5. Tensile strength of the CuO-coated textiles after different periods of exposure at the Climate test station "Hoa Lac" (Hanoi city, Vietnam). Average values from three repetitions are given

Type of exposure	Type of coating	Duration of exposure to the tropical environment			
		0 (before the field test)	1 month	3 months	4 months
		Tensile strength, MPa			
Concrete open test site	Reference sample	23.1	17.4	14.1	13.2
	Fabric coated with CuO nanoparticles	27.1	15.5	12.2	10.5
Mycological shelf test site	Reference sample	23.1	21.3	17.3	16.0
	Fabric coated with CuO nanoparticles	27.1	16.0	15.4	14.9

The application of metal oxide nanoparticles was previously shown to improve the mechanical properties of a textile [48]. However this effect is not always observed even with similar fabric, coatings and coating techniques [3]. In the present work, it was found that application of CuO NPs coating initially increases the tensile strength by ∼17%.

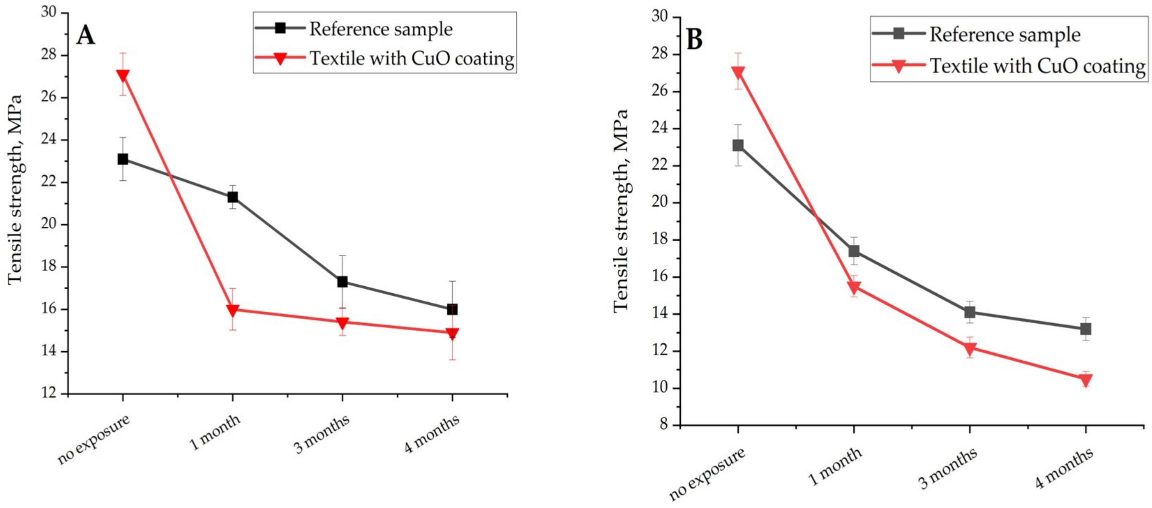

FIG. 3. Tensile strength of the fabric samples after different periods of exposure at the mycological shelf test site (A) and at the open concrete site (B). Standard deviation represents the average from three separate experiments

After exposure at the open concrete test site for one month, both the control sample and the coated sample showed a significant decrease in tensile strength. The decrease rate over the next three months was similar, but the sample coated with CuO nanoparticles had a slightly higher rate of degradation. This might be explained with high insolation at the test site, with CuO nanoparticles acting as photocatalysts. A more interesting and unexpected trend is observed in the case of the samples placed at the mycological test site: the CuO-coated fabric shows a major decrease in the tensile strength after the first month of exposure, while the control sample deteriorates more steadily over the course of 4 months. The reasons for this effect will be analysed in the further studies of the textiles coated with metal oxide nanoparticles.

4. Conclusions

Cotton fabric with CuO coating was produced using ultrasonic cavitation technique. It was shown that this method is quite effective for the immobilization of the nanoparticles. The release rate of copper ions was estimated by disk diffusion method, ICP-OES and using specific *lux* biosensors. Field tests of the coated fabrics carried out at the "Hoa Lac" test site (Hanoi city, Vietnam) showed that the coated fabrics reduced the number of microorganisms to 1–3% compared with the reference at both test sites. No significant difference cased by insolation degree or air humidity was observed. The types of microorganisms found on the textile samples after exposure in tropical climate were identified, with fungi being the most prevalent species despite the previously reported fungicidal activity of copper oxide.

The textile materials coated with CuO nanoparticles not only exhibit antimicrobial activity in short-term and long-term laboratory experiments, but also retain it for a long time (up to 12 months) during field tests in tropical climate. The data obtained on antimicrobial activity, analysis of the species found on the samples, and the mechanical characteristics of the fabrics coated with copper oxide nanoparticles in a tropical climate, after field testing both at open concrete and mycological sites, clearly demonstrate the potential for the use of this textile composite materials in a tropical environment.

References

[1] Bhandari V., Jose S., Badanayak P., Sankaran A., Anandan V. Antimicrobial Finishing of Metals, Metal Oxides, and Metal Composites on Textiles: A Systematic Review. *Industrial & Engineering Chemistry Research*, 2022, **61**, P. 86–101.

[2] Borkow G., Gabbay J. Copper as a biocidal tool. *Current Medicinal Chemistry*, 2005, **12**(18), P. 2163–2175.

[3] Veselova V.O., Plyuta V.A., Kostrov A.N., Vtyurina D.N., Abramov V.O., Abramova A. V, Voitov Y.I., Padiy D.A., Thu V.T.H., Hue L.T. J., Trang D.T.T., Baranchikov A.E., Khmel I.A., Nadtochenko V.A., Ivanov V.K. Long-Term Antimicrobial Performance of Textiles Coated with ZnO and TiO_2 Nanoparticles in a Tropical Climate. *Journal of Functional Biomaterials*, 2022, **13**(4), P. 233.

[4] Ashish B., Neeti K., Himanshu K. Copper toxicity: a comprehensive study. *Research Journal of Recent Sciences*, 2013, **2**, P. 58–67.

[5] Bondarenko O., Juganson K., Ivask A., Kasemets K., Mortimer M., Kahru A. Toxicity of Ag, CuO and ZnO nanoparticles to selected environmentally relevant test organisms and mammalian cells in vitro: a critical review. *Archives of Toxicology*, 2013, **87**, P. 1181–1200.

[6] Vandebriel R.J., De Jong W.H. A review of mammalian toxicity of ZnO nanoparticles. *Nanotechnology Science and Applications*, 2012, **5**, P. 61–71.

[7] Singh G., Beddow J., Mee C., Maryniak L., Joyce E.M., Mason T.J. Cytotoxicity Study of Textile Fabrics Impregnated With CuO Nanoparticles in Mammalian Cells. *International Journal of Toxicology*, 2017, **36**, P. 478–484.

[8] Borkow G., Okon-Levy N., Gabbay J. Copper Oxide Impregnated Wound Dressing: Biocidal and Safety Studies. *Wounds*, 2010, **22**(12), P. 301.

[9] Perelshtein I., Applerot G., Perkas N., Wehrschuetz-Sigl E., Hasmann A., Guebitz G., Gedanken A. CuO–cotton nanocomposite: Formation, morphology, and antibacterial activity. *Surface and Coatings Technology*, 2009, **204**, P. 54–57.

[10] Alagarasan D., Harikrishnan A., Surendiran M., Indira K., Khalifa A.S., Elesawy B.H. Synthesis and characterization of CuO nanoparticles and evaluation of their bactericidal and fungicidal activities in cotton fabrics. *Applied Nanoscience*, 2023, **13**(3), P. 1797.

[11] Román L.E., Gomez E.D., Solís J.L., Gómez M.M. Antibacterial Cotton Fabric Functionalized with Copper Oxide Nanoparticles. *Molecules*, 2020, **25**(24), P. 5802.

[12] Madkhali O.A. A comprehensive review on potential applications of metallic nanoparticles as antifungal therapies to combat human fungal diseases. *Saudi Pharmaceutical Journal*, 2023, **31**(9), P. 101733.

[13] Gabbay J., Borkow G., Mishal J., Magen E., Zatcoff R., Shemer-Avni Y. Copper Oxide Impregnated Textiles with Potent Biocidal Activities. *Journal of Industrial Textiles*, 2006, **35**(4), P. 323–335.

[14] Liao C., Li Y., Tjong S.C. Bactericidal and Cytotoxic Properties of Silver Nanoparticles. *International Journal of Molecular Sciences*, 2019, **20**, P. 449.

[15] Li J., Zheng J., Yu Y., Su Z., Zhang L., Chen X. Facile synthesis of rGO–MoS_2–Ag nanocomposites with long-term antimicrobial activities. *Nanotechnology*, 2020, **31**, P. 125101.

[16] Ferdous Z., Nemmar A. Health Impact of Silver Nanoparticles: A Review of the Biodistribution and Toxicity Following Various Routes of Exposure. *International Journal of Molecular Sciences*, 2020, **21**, P. 2375.

[17] Moritz M., Geszke-Moritz M. The newest achievements in synthesis, immobilization and practical applications of antibacterial nanoparticles. *Chemical Engineering Journal*, 2013, **228**, P. 596–613.

[18] Abramov O.V., Gedanken A., Koltypin Y., Perkas N., Perelshtein I., Joyce E., Mason T.J. Pilot scale sonochemical coating of nanoparticles onto textiles to produce biocidal fabrics. *Surface and Coatings Technology*, 2009, **204**, P. 718–722.

[19] Abramova A.V., Abramov V.O. Bayazitov V.M., Voitov Y., Straumal E.A., Lermontov S.A., Cherdyntseva T.A., Braeutigam P., Weiße M., Günther K. A sol-gel method for applying nanosized antibacterial particles to the surface of textile materials in an ultrasonic field. *Ultrasonics Sonochemistry*, 2020, **60**, P. 104788.

[20] Abramova A.V., Abramov V.O., Gedanken A., Perelshtein I., Bayazitov V.M., Beilstein J. An Ultrasonic Technology for Production of Antibacterial Nanomaterials and Their Coating on Textiles. *Nanotechnology*, 2014, **5**, P. 532–536.

[21] Giannossa L.C., Longano D., Ditaranto N., Nitti M.A., Paladini F., Pollini M., Rai M., Sannino A., Valentini A., Cioffi N. Metal nanoantimicrobials for textile applications. *Nanotechnology Reviews*, 2013, **2**, P. 307–331.

[22] Ehiasarian A., Pulgarin C., Kiwi J. Inactivation of bacteria under visible light and in the dark by Cu films. Advantages of Cu-HIPIMS-sputtered films. *Environmental science and pollution research international*, 2012, **19**, P. 3791–3797.

[23] Berendjchi A., Khajavi R., Yazdanshenas M.E. Fabrication of superhydrophobic and antibacterial surface on cotton fabric by doped silica- based sols with nanoparticles of copper. *Nanoscale Research Letters*, 2011, **6**, P. 1–8.

[24] Mary G., Bajpai S.K., Chand N. Copper (II) ions and copper nanoparticles-loaded chemically modified cotton cellulose fibers with fair antibacterial properties. *Journal of Applied Polymer Science*, 2009, **113**, P. 757–766.

[25] Grace M., Chand N., Bajpai S.K. Copper Alginate-Cotton Cellulose (CACC) Fibers with Excellent Antibacterial Properties. *Journal of Engineered Fibers and Fabric*, 2009, **4**(3), P. 24–35.

[26] Castro C., Sanjines R., Pulgarin C., Osorio P., Giraldo S.A., Kiwi J. Structure–reactivity relations for DC-magnetron sputtered Cu-layers during E. coli inactivation in the dark and under light. *Journal of Photochemistry and Photobiology A: Chemistry*, 2010, **216**, P. 295–302.

[27] Torres A., Ruales C., Pulgarin C., Aimable A., Bowen P., Sarria V., Kiwi J. Innovative high-surface-area CuO pretreated cotton effective in bacterial inactivation under visible light. *ACS Applied Materials & Interfaces Journal*, 2010, **2**, P. 2547–2552.

[28] Crookes W.S. On Radiant Matter; a Lecture Delivered to the British Association for the Advancement of Science, at Sheffield, Friday, August 22, 1879.

[29] Anita S., Ramachandran T., Rajendran R., Koushik C. V, Mahalakshmi M. A study of the antimicrobial property of encapsulated copper oxide nanoparticles on cotton fabric. *Textile Research Journal*, 2011, **81**, P. 1081–1088.

[30] Thaysen A.C., Bunker H.J., Butlin K.R., Williams L.H. The effect of climatic exposure on textile fibres and fabrics. *Annals of Applied Biology*, 1939, **26**, P. 750–781.

[31] Saliani M., Jalal R., Goharshadi E.K. Effects of pH and Temperature on Antibacterial Activity of Zinc Oxide Nanofluid Against Escherichia coli O157: H7 and Staphylococcus aureus. *Jundishapur Journal of Microbiology*, 2015, **8**(2), P. 17115.

[32] Lipovsky A., Nitzan Y., Gedanken A., Lubart R. Antifungal activity of ZnO nanoparticles -the role of ROS mediated cell injury. *Nanotechnology*, 2011, **22**, P. 105101.

[33] De Azevedo J.L. Quecine M.C. *Diversity and Benefits of Microorganisms from the Tropics*, Springer, 2017.

[34] Abramova A., Gedanken A., Popov V., Ooi E.-H., Mason T.J., Joyce E.M., Beddow J., Perelshtein I., Bayazitov V. A. A sonochemical technology for coating of textiles with antibacterial nanoparticles and equipment for its implementation. *Materials Letters*, 2013, **96**, P. 121–124.

[35] Datsenko K.A., Wanner B.L. One-step inactivation of chromosomal genes in Escherichia coli K-12 using PCR products. *The Proceedings of the National Academy of Sciences*, 2000, **97**, P. 6640–6645.

[36] De Vasconcelos A.T.R., De Almeida D.F., Hungria M., Guimaraes C.T., Antônio R.V., Almeida F.C., De Almeida L.G.P., De Almeida R., Alves-Gomes J.A., Andrade E.M. The complete genome sequence of Chromobacterium violaceum reveals remarkable and exploitable bacterial adaptability. The Proceedings of the National Academy of Sciences U.S.A., 2003, P. 11660–11665.

[37] Veselova M., Lipasova V., Protsenko M.A., Buza N., Khmel I.A. GacS-dependent regulation of enzymic and antifungal activities and synthesis of N-acylhomoserine lactones in rhizospheric strain Pseudomonas chlororaphis 449. *Folia Microbiologica* (Praha), 2009, **54**, P. 401–408.

[38] Veselova M.A., Klein S.H., Bass I.A., Lipasova V.A., Metlitskaya A.Z., Ovadis M.I., Chernin L.S., Khmel I.A. Quorum sensing systems of regulation, synthesis of phenazine antibiotics, and antifungal activity in rhizospheric bacterium pseudomonas chlororaphis 449. *Russian Journal of Genetics*, 2008, **44**, P. 1400–1408.

[39] Ristić T., Zemljič L.F., Novak M., Kunčič M.K., Sonjak S., Cimerman N.G. Strnad S. Antimicrobial efficiency of functionalized cellulose fibres as potential medical textiles. *Science against microbial pathogens: communicating current research and technological advances*, 2011, **6**, P. 36–51.

[40] Melkina O.E., Plyuta V.A., Khmel I.A., Zavilgelsky G.B. The mode of action of cyclic monoterpenes $(-)$-limonene and $(+)$-α-pinene on bacterial cells. *Biomolecules*, 2021, **11**(6), P. 806.

[41] Plyuta V.A., Sidorova D.E., Zavigelsky G.B., Kotova V.Y., Khmel I.A. Effects of Volatile Organic Compounds Synthesized by Bacteria on the Expression from Promoters of the zntA, copA, and arsR Genes Induced in Response to Copper, Zinc, and Arsenic. *Molecular Genetics, Microbiology and Virology*, 2020, **35**, P. 152–158.

[42] Banner D.J., Firlar E., Jakubonis J., Baggia Y., Osborn J.K., Shahbazian-Yassar R., Megaridis C.M., Shokuhfar T. Correlative ex situ and Liquid-Cell TEM Observation of Bacterial Cell Membrane Damage Induced by Rough Surface Topology. *International Journal of Nanomedicine*, 2020, **15**, P. 1929–1938.

[43] Jana T.K., Jana S.K., Kumar A., De K., Maiti R., Mandal A.K., Chatterjee T., Chatterjee B.K., Chakrabarti P., Chatterjee K. The antibacterial and anticancer properties of zinc oxide coated iron oxide nanotextured composites. *Colloids Surfaces B Biointerfaces*, 2019, **177**, P. 512–519.

[44] Jang Y., Choi W.T., Johnson C.T., García A.J., Singh P.M., Breedveld V., Hess D.W., Champion J.A. Inhibition of Bacterial Adhesion on Nanotextured Stainless Steel 316L by Electrochemical Etching. *ACS Biomaterials Science & Engineering Journal*, 2018, **4**, P. 90–97.

[45] Rensing C., Fan B., Sharma R., Mitra B., Rosen B.P. CopA: An Escherichia coli Cu(I)-translocating P-type ATPase. The Proceedings of the National Academy of Sciences U.S.A., 2000, **97**, P. 652–656.

[46] Kairyte K., Kadys A., Luksiene Z. Antibacterial and antifungal activity of photoactivated ZnO nanoparticles in suspension. *Journal of Photochemistry and Photobiology B: Biology*, 2013, **128**, P. 78–84.

[47] Ilkhechi N.N., Mozammel M., Khosroushahi A.Y. Antifungal effects of ZnO, TiO_2 and ZnO–TiO_2 nanostructures on Aspergillus flavus. *Pesticide Biochemistry and Physiology*, 2021, **176**, P. 104869.

[48] Eskani I.N., Astuti W., Farida, Haerudin A., Setiawan J., Lestari D.W., Isnaini, Widayatno T. Antibacterial Activities of Synthesised ZnO Nanoparticles Applied on Reactive Dyed Batik Fabrics. *The Journal of the Textile Institute*, 2022, **113**, P. 430–439.

Submitted 14 August 2024; revised 24 November 2024; accepted 25 November 2024

Information about the authors:

Varvara O. Veselova – N. S. Kurnakov Institute of General and Inorganic Chemistry RAS, Leninskii prosp., 31, Moscow, 119991, Russia; ORCID 0000-0002-8548-7959; ibvarvara@yandex.ru

Andrey N. Kostrov – N. N. Semenov Federal Research Center for Chemical Physics, Kosygina str. 4, Building 1, Moscow, 119991, Russia; ORCID 0000-0003-2198-7134; andreikostrov@rambler.ru

Vladimir A. Plyuta – Complex of NBICS Technologies, National Research Center "Kurchatov Institute", Russia, Akademika Kurchatova sq. 2, Moscow, 123182, Russia; ORCID 0000-0002-3127-4114; plyuta_va@nrcki.ru

Anna V. Kamler – N. S. Kurnakov Institute of General and Inorganic Chemistry RAS, Leninskii prosp., 31, Moscow, 119991, Russia; ORCID 0009-0004-3940-6638; abramova@physics.msu.ru

Roman V. Nikonov – N. S. Kurnakov Institute of General and Inorganic Chemistry RAS, Leninskii prosp., 31, Moscow, 119991, Russia; ORCID 0009-0005-0563-3813; novita@mail.ru

Olga E. Melkina – Complex of NBICS Technologies, National Research Center "Kurchatov Institute", Russia, Akademika Kurchatova sq. 2, Moscow, 123182, Russia; compleanno@mail.ru

Vo Thi Hoai Thu – Joint Vietnam-Russia Tropical Science and Technology Research Center, Nguyen Van Huyen street, Nghia Do, Cau Giay district, Hanoi, Vietnam; ORCID 0009-0009-2245-7179; hoaithu@mail.ru

Le Thi Hue – Joint Vietnam-Russia Tropical Science and Technology Research Center, Nguyen Van Huyen street, Nghia Do, Cau Giay district, Hanoi, Vietnam; ORCID 0009-0002-2722-5798; huelebiotech85@gmail.com

Dinh Thi Thu Trang – Joint Vietnam-Russia Tropical Science and Technology Research Center, Nguyen Van Huyen street, Nghia Do, Cau Giay district, Hanoi, Vietnam; ORCID 0009-0008-9404-6654; trangdt1806@gmail.com

Inessa A. Khmel – Complex of NBICS Technologies, National Research Center "Kurchatov Institute", Russia, Akademika Kurchatova sq. 2, Moscow, 123182, Russia; ORCID 0000-0002-3079-7845; iakhmel@yandex.ru

Viktor A. Nadtochenko – N. N. Semenov Federal Research Center for Chemical Physics, Kosygina str. 4, Building 1, Moscow, 119991, Russia; ORCID 0000-0002-6645-692X; nadtochenko@gmail.com

Mikhail G. Kiselev – G. A. Krestov Institute of Solution Chemistry of the Russian Academy of Sciences, Akademicheskaya str. 1, Ivanovo 153045, Russia; ORCID 0000-0003-1189-3679; mgk@isc-ras.ru

Vladimir K. Ivanov – N. S. Kurnakov Institute of General and Inorganic Chemistry RAS, Leninskii prosp., 31, Moscow, 119991, Russia; ORCID 0000-0003-2343-2140; van@igic.ras.ru

Conflict of interest: the authors declare no conflict of interest.

NANOSYSTEMS:
PHYSICS, CHEMISTRY, MATHEMATICS

Semenov K.N., et al. *Nanosystems: Phys. Chem. Math.*, 2024, **15** (6), 921–935.
http://nanojournal.ifmo.ru
DOI 10.17586/2220-8054-2024-15-6-921-935

Original article

Biomedical applications of graphene-based nanomaterials in gene delivery, tissue engineering, biosensing and for the development antibacterial agents

Konstantin N. Semenov[1,2,3], Sergei V. Ageev[1,2], Olga S. Shemchuk[1,3], Gleb O. Iurev[1,3], Abdelsattar O. E. Abdelhalim[4], Igor V. Murin[2], Pavel K. Kozhukhov[1], Anastasia V. Penkova[2], Dmitriy N. Maystrenko[3], Oleg E. Molchanov[3], Vladimir V. Sharoyko[1,2,3]

[1]Pavlov First St. Petersburg State Medical University, St. Petersburg, Russia

[2]St. Petersburg State University, St. Petersburg, Russia

[3]A. M. Granov Russian Research Centre for Radiology and Surgical Technologies, St. Petersburg, Russia

[4]Environmental Research Department, National Centre for Social and Criminological Research (NCSCR), Giza, Egypt

Corresponding author: Konstantin N. Semenov, knsemenov@gmail.com; Vladimir V. Sharoyko, sharoyko@gmail.com

PACS 87.85.Qr, 87.85.Rs

ABSTRACT Graphene and graphene oxide have emerged as promising materials in various biomedical applications due to their unique physicochemical properties. This review provides a comprehensive overview of their utilization in gene delivery, tissue engineering, biosensors and antibacterial and antimicrobial agents. In gene delivery, graphene-based materials offer efficient delivery platforms with enhanced cellular uptake and minimal cytotoxicity, promising advancements in gene therapy. Additionally, in tissue engineering, graphene and graphene oxide scaffolds exhibit excellent biocompatibility, electrical conductivity, and mechanical properties, facilitating cell adhesion, proliferation, and differentiation for tissue regeneration. Moreover, graphene-based biosensors demonstrate high sensitivity, selectivity, and stability, enabling rapid and accurate detection of biomolecules for diagnostic and therapeutic purposes. This review highlights the recent advancements, challenges, and future prospects of graphene and graphene oxide in revolutionizing biomedical technologies, paving the way for innovative solutions in healthcare.

KEYWORDS graphene, graphene oxide, composites, nanostructures, biocompatibility, biomedical applications

ACKNOWLEDGEMENTS The authors acknowledge St. Petersburg State University for a research project 11602266.

FOR CITATION Semenov K.N., Ageev S.V., Shemchuk O.S., Iurev G.O., Abdelhalim A.O.E., Murin I.V., Kozhukhov P.K., Penkova A.V., Maystrenko D.N., Molchanov O.E., Sharoyko V.V. Biomedical applications of graphene-based nanomaterials in gene delivery, tissue engineering, biosensing and for the development antibacterial agents. *Nanosystems: Phys. Chem. Math.*, 2024, **15** (6), 921–935.

Abbreviations

A549 – hypotriploid human alveolar basal epithelial cell line; AA – alginic acid; ADR – Adriamycin; AgNP – silver nanoparticle; anti-miR-21 – miRNA against miR-21; APTES – (3-aminopropyl)triethoxysilane; ATP – adenosine triphosphate; AuNP – gold nanoparticles; BPEI – branched polyethyleneimine; C2C12 – immortalized mouse myoblast cell line; CS – chitosan; DOX – doxorubicin; EGFP – enhanced green fluorescent protein; FA – folic acid; FAM – fluorescein amidite; GAP43 – growth associated protein 43; GBN – graphene-based nanomaterials; GFP – green fluorescent protein; GO – graphene oxide; GO–AgNP – conjugate of GO and silver nanoparticles; GONS – chemically synthesized graphene oxide nanosheet; GO–TCP/AA – nanocomposite based on GO, TCP and AA; ITO – indium tin oxide; HA – hydroxyapatite; HDAC1 – histone deacetylase 1; HEK293 – human embryonic kidney epithelial-like cell line; HepG2 – hepatocellular carcinoma cell line; HL-60 – human leukemia cell line; HRP – horseradish peroxidase; K-Ras – protein from Kirsten rat sarcoma encoded by KRAS proto-oncogene; MC3T3-E1 – osteoblastic cell line; MCF-7 – human breast adenocarcinoma cell line; MSC – mesenchymal stem cells; NIR – near-infrared light; NSC – neuronal stem cells; OPF – oligo(poly(ethylene glycol) fumarate; PAA – polyacrylic acid; PAMAM – polyamidoamine; PLC – polycaprolactone; PLC–GO–Ag–Arg – nanocomposite based on GO, PLC, argentum nanoparticles and L-arginine; pDNA – DNA plasmid; PEDOT – poly(3,4-ethylenedioxythiophene); PEG – polyethylene glycol; PEI – polyethylenimine; PLC – phospholipase C; PPI – polypropylenimine; PTT – photothermal therapy; rBMSCs – rat bone marrow stem cells; rGO – reduced graphene oxide; rGO–AgNP – composite based on rGO and argentum nanoparticles; ROS – reactive oxygen species; SF – silk fibroin; shRNA – small hairpin RNA; SiNPs – silica nanoparticles ; siRNA – small interfering RNA; Stat 3-siRNA – targeted small interfering RNA against signal transducer and activator of transcription 3; TCP – calcium orthophosphate; TMC – trimethyl chitosan; TuJ1 – neuron-specific class III beta-tubulin.

1. Introduction

The analysis of recent publications shows that interest in studying graphene-based materials (GBN) remains strong. This is due to their unique structure and physicochemical properties, as well as the wide range of possibilities for their practical applications in various fields, including medicine [1] (for the creation of targeted drug delivery systems [2], bioimaging [3], tissue engineering [4], biosensors [5], and new materials with antibacterial [6] and antiviral properties [7]). Traditionally, GBN includes graphene, graphene oxide (GO), reduced graphene oxide (rGO), and graphene quantum dots (GQD) (Fig. 1). Let us briefly describe GBN.

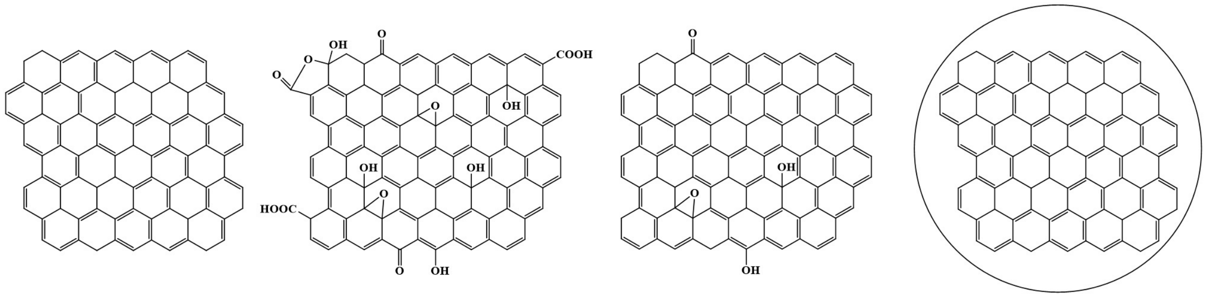

Graphene **Graphene oxide (GO)** **Reduced graphene oxide (rGO)** **Graphene quantum dots (GQDs)**

FIG. 1. Graphene-based materials

Graphene is two-dimensional material made of a single layer of carbon atoms arranged in a honeycomb lattice. Graphene was synthetized and characterized in 2004 by Andre Geim and Konstantin Novoselov. Due to the fact that carbon atoms in graphene are linked by both σ- and π- bonds, a very strong monoatomic structure with unique properties is formed. Graphene can be synthesized by chemical vapour deposition [8–14], electrochemical exfoliation [15–18] and mechanochemical exfoliation [19].

Graphene consisting oxygen-containing functional groups (epoxy, lactol, carboxyl, carbonyl, hydroxyl) [20,21] in its structure called graphene oxide (GO) [21,23,24]. GO can be obtained by two main chemical methods: from nanosheets graphene and graphite [25]. The first method has not become widespread due to the complexity of the hardware and high costs: graphene sheets are oxidized in a vacuum chamber using atomic oxygen. In the second version of the synthesis, graphite is oxidized with strong oxidizing agents. This approach was a key to Hammers' [25], Brody [26] and Staudenmaier methods [27].

Reduced graphene oxide (rGO) is GBN, which is produced by reducing of GO using thermal and chemical reduction, for example by hydrazine hydrate, L-cysteine and other reducing agents [28–36]. rGO can been used as energy storage [37], as material for biomedical applications [38,39] as well as in catalysis [40].

Graphene quantum dots (GQDs) are small, quasi-spherical graphene-based nanoparticles typically less than 10 nm in size. They can be used in bioimaging, drug delivery, sensors, and optoelectronics [41]. The following methods of obtaining of GQDs can be used: chemical synthesis [42–44], electron beam lithography [45], GO reduction [46,47] and carbon nanotubes (CNTs) disintegration transformation [48]. In comparison with bulk graphene, GQDs offer the advantage of size-dependent properties due to quantum confinement and edge effects, which are absent in larger graphene sheets. This makes GQDs especially valuable in research areas focused on nanoscale phenomena, where precise control over material properties is crucial. Thus, while they share a common origin with graphene, GQDs stand out due to their unique properties that emerge specifically at the nanoscale, broadening the scope of applications for GBN.

In this review, we explore the recent advancements and challenges in utilizing graphene for gene delivery, tissue engineering, creation of biosensors and antibacterial and antimicrobial agents. By elucidating the underlying mechanisms and highlighting the promising outcomes, we aim to provide insights into the future directions of graphene-based technologies in biomedical research and clinical applications.

2. Gene delivery

Great interest of researchers in the field of nanobiomedicine is concentrated on the method of targeted correction of cell dysfunctions at the molecular genetic level. A key factor for the success of gene therapy is the development of delivery systems that can efficiently transport genetic material to the site of their therapeutic action without causing any associated side effects. Over the past ten years, much effort has been devoted to the creation of more efficient and biocompatible vectors that can transfer nucleic acids into cells without inducing an immune response. There is an urgent need to develop a 'smart' nanocarrier, which can be loaded by various genetic materials, the carrier will transfer this material through various cellular structures without causing any immune response of the body and toxicity [49]. Currently, the Unified Register of Registered Medicines of the Eurasian Economic Union has not yet contained any nanoparticle drug for use in gene therapy. Thus, the development of optimal multifunctional nanoparticles for the delivery of genetic material is an urgent task [50, 51].

GO nanomaterials are suitable candidates for gene delivery due to their high loading rate and efficient gene transfection [52–56]. This has led to a number of research articles aimed at studying of covalent and non-covalent conjugates GO for gene delivery as shown in Table 1.

A number of studies have developed biomaterials for targeted delivery of axons and stimulation of the growth of transplanted neurons in the damaged spinal cord [64]. For this purpose, neuronal stem cells (NSCs) are used, which can differentiate into neurons and glial cells. Solanki *et al.* reported the creation of hybrid structures based on GO modified with silica nanoparticles (SiNPs) with immobilised NSCs. These hybrid structures (GO–SiNP) resulted in the formation of highly aligned axons from differentiating NSCs [65]. Immunocytochemical staining confirmed the presence of the neuronal marker TuJ1 and the axonal marker GAP43. In summary, the authors demonstrate the potential of using GO–SiNP as a novel hybrid material to enhance neuronal differentiation and axonal alignment, leading to accelerated functional recovery of injured spinal cord (Fig. 2).

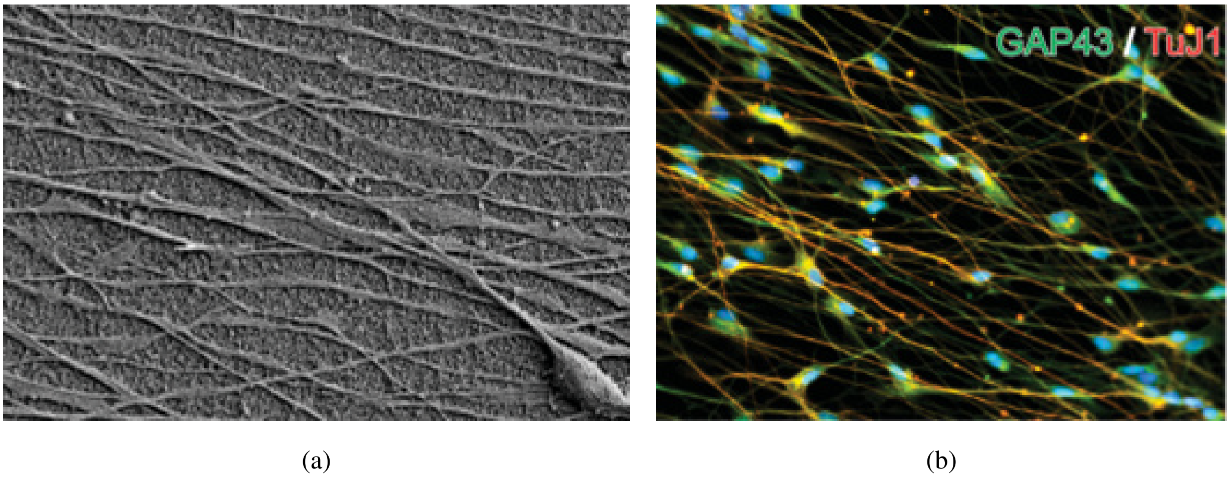

(a) (b)

FIG. 2. SEM image of GO–SiNP on a polydimethylsiloxane substrate showing highly aligned NSC axons at day 14 (*a*); immunocytochemistry results demonstrating the expression of the neuronal marker TuJ1 and the axonal marker GAP43 in NSCs (*b*) [65]

The success of gene therapy depends on the development of effective delivery systems for genetic material. Thus, the creation of biocompatible systems capable of transporting nucleic acids without side effects is a pressing issue. Nanomaterials such as GO are promising in this area due to their high loading capacity, gene transfection efficiency, and low toxicity.

3. Tissue engineering

Tissue engineering has become an important new field in medicine. A critical requirement in tissue engineering is the development of biomaterials that can mimic the biological environment and create a matrix for interaction with living cells, allowing cell attachment, proliferation and differentiation. GO-based materials have attracted attention due to their ease of functionalization coupled with high mechanical strength, stiffness, and electrical conductivity. One application of GO-based materials in tissue engineering is their use as reinforcements in hydrogels, films, fibres and fabrics to improve their physical and mechanical properties [66–73] (Table 2).

It has been shown that the creation of composite materials containing GBN leads to a significant improvement in physicochemical and mechanical properties, as well as biocompatibility, which collectively determines the promising potential of these materials in tissue engineering.

3.1. Tissue regeneration

Liu *et al.* [81] reported modification of GO with gelatine to biomimic charged proteins present in the ECM during bone formation. A GO–gelatine composite was used for biomimetic surface mineralisation with hydroxyapatite (HA). A detailed structural and morphological characterisation of the mineralised composite was carried out. In addition, the

TABLE 1. Modifications of graphene-based nanoplatforms for gene delivery systems

Characteristics of the conjugate	Effect	Ref.
GO conjugates with PEI, PPI), PAMAM and glycine, *N1*-(3-aminopropyl)butane-1.4-diamine	All conjugates showed significantly lower cellular toxicity compared to the individual polymer. The most successful effect was observed in the case of PEI conjugates, among which the most effective vector was the conjugate GO–PEI containing a glycine linker. This conjugate was nine times more effective in terms of the number of cells transfected with EGFP.	[55]
Conjugate based on GO modified with TMC and FA, for delivery of Survivin shRNA-expressing pDNA	Cytotoxicity of the conjugate was studied on HeLa cell line (cell survival after incubation for 24 h was 80 %) and A549 cell line (cell survival after incubation for 24 h is 98 %).	[56]
Non-covalent conjugate GO with PEI and PEG and Stat 3-siRNA	Results *in vivo* indicate significant regression of tumour growth and tumour weight after delivery of miRNA to block Stat3 using a plasmid supported by GO–PEI–PEG.	[57]
Non-covalent conjugate based on GO, modified with PEI and adriamycin (ADR), with miRNA against miR-21 (anti-miR-21)	Conjugate significantly enhanced the accumulation of ADR in MCF-7/ADR cells (an ADR-resistant mammary adenocarcinoma cell line) and exhibited much higher cytotoxicity than free ADR.	[58]
Non-covalent conjugate based on rGO modified with AuNP and PEI, with labelled FAM siRNA	The resulting composites allow efficient loading of siRNA, forming complexes for transport into HL-60 cells and suppressing the anti-apoptotic protein Bcl-2, which indicates that GBN conjugates are a suitable platform for gene delivery.	[59]
Non-covalent conjugates GO with grafted PEI and DNA plasmid against DNaseI; siRNA against GFP	Conjugate was used to sequentially deliver GFP-specific siRNA, resulting in $\sim$70 % suppression of target gene expression.	[60]
Non-covalent conjugate GO modified with PEI, PEG, chitosan-aconitic anhydride and chitosan-carballylic acid with shRNA (isolated from HepG2 cells) and DOX	The resulting systems effectively disrupted the endosome, significantly facilitating the release of DOX and shRNA into the cytoplasm. The systems demonstrated high efficiency of co-delivery of shRNA and DOX into HepG2 cell line.	[61]
Non-covalent conjugate based on GO, decorated with PEG and FA, and HDAC1 and K-Ras siRNAs targeting the HDAC1 gene and the mutant K-Ras gene, respectively	The synergistic combination of gene suppression and near-infrared PTT showed significant antitumour efficacy by inhibiting bulk tumour growth *in vivo* by more than 80 %.	[62]
GO conjugate with PEI, decorated with DNA plasmid and EGFP	The results demonstrate that GO is an effective platform for gene delivery, has low cytotoxicity, and may be promising in the field of virus-free gene therapy.	[63]

TABLE 2. GO containing nanocomposites used in tissue engineering

Application area	Characteristics of the conjugate	Effect	Ref.
Engineering and regeneration of cardiovascular tissue	Chitosan framework doped with GO nanoparticles decorated with AuNPs	The possibility of using a GO–AuNP nanocomposite as a reinforcing agent was demonstrated, which increased conduction velocity, contractility, and electrical circulation in the myocardium after infarction compared to individual chitosan	[74]
Engineering and regeneration of cardiovascular tissue	Adsorbed MSC on GO nanoparticles	MSC–GO implantation improved cardiac function, increased the number of engrafted MSCs and the amount of secreted paracrine factors that enhance angiogenesis and prevent further progression of myocardial infarction	[75]
Regeneration of skeletal muscles	Hybrid matrices based on a copolymer of lactic and glycolic acid and collagen, doped with GO	The introduction of composites increased the proliferation, differentiation and attachment of skeletal myoblasts of the C2C12 cell line	[76]
Regeneration of skeletal muscles	Composites based on PCL and GO	In cell viability experiments, the ratio levels and expression of genes encoding the myogenic markers CD56, myogenin and desmin were significantly increased with GO nanoparticles compared to control surfaces	[77]
Skin regeneration	PCL nanocomposite containing GO and AgNP nanoparticles decorated with l-arginine (Arg)	The PCL–GO–Ag–Arg conjugate showed biocompatibility with L929 mouse fibroblast cells. The composite exhibited proangiogenic effects on human endothelial cells	[78]
Bone tissue regeneration	Nanocomposite based on calcium orthophosphate (TCP) and alginic acid (AA) with the addition of GO	The cylindrical hybrid scaffolds were composed of GO–TCP/AA nanocomposite. The results showed that GO–TCP/AA scaffolds exhibited increased porosity, improved swelling profile, and better mechanical properties compared to TCP/AA	[79]
Creation of prostheses	GO nanosheet (GONS) and PAA/gelatine hydrogels	Tensile strength increased by 71 % and elongation at break increased by 26 % after adding 0.3 *wt.* % GONS	[80]

preosteoblast cell line MC3T3-E1 was cultured on the surface of GO–gelatine to visualise cellular activity and HA mineralisation. Higher cellular activities, namely cell adhesion, cell proliferation, and alkaline phosphatase activity, were observed on the GO–gelatine surface compared to the individual GO or glass surface. GO–gelatine composite promotes osteogenic differentiation of MC3T3-E1 cells. Moreover, the degree of surface mineralisation was studied using scanning electron microscopy (SEM) and alizarin red staining, and the formation of a native osteoid matrix was proven (Fig. 3). Taken together, the obtained data suggest that the GO–gelatine composite can be used as a scaffold material for osteogenesis and applied in orthopedic surgery.

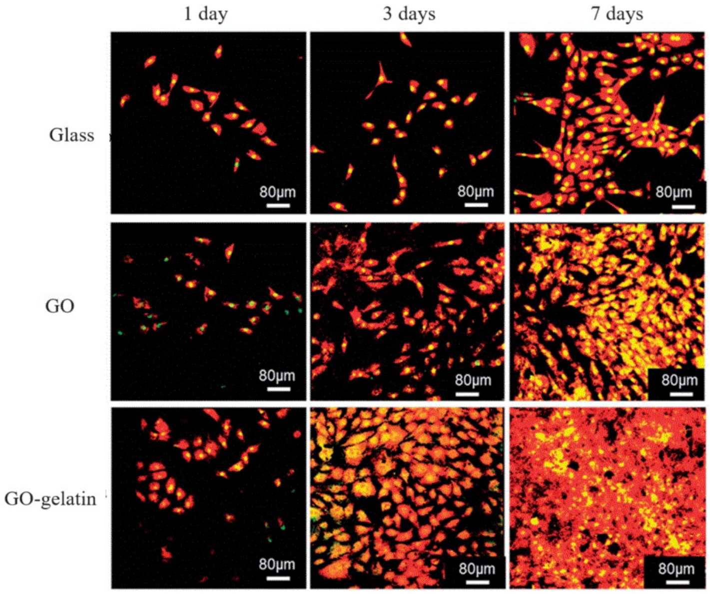

FIG. 3. Confocal fluorescence images of MC3T3-E1 cells cultured on glass, GO, and GO–gelatine composite for 1, 3, and 7 days [81]

Peng *et al.* [82] described a method for synthesizing a high-strength composite graphene hydrogel for bone tissue engineering. By combining GO, HA nanoparticles, and chitosan (CS) with crosslinking and reducing agents, researchers created a dense and oriented microstructure with improved mechanical strength, HA fixation capacity, and porosity. The study also highlights the importance of porosity and pore size for osteoblast proliferation and differentiation (porosity of nanomaterial was determined to be 84.37 %, the average pore size was 122 μm). Preliminary cell culture experiment using rat bone marrow stem cells (rBMSCs) demonstrated high viability and proliferation of osteoblasts on the composite hydrogel, suggesting its potential for use in bone tissue engineering applications.

The study [83] focuses on constructing a stem cell composite hydrogel scaffold for bone tissue engineering. Silk fibroin (SF) hydrogels were prepared with enzyme-catalyzed crosslinking, incorporating GO. The addition of GO resulted in more regular pore size and stable silk structure with excellent mechanical properties. Bone marrow stromal cells (BMSCs) encapsulated in the hydrogel showed enhanced growth, proliferation, and osteogenic differentiation, particularly at low GO concentrations. SEM revealed a porous structure conducive to cell proliferation and nutrient transport, with pore size influenced by GO content (addition of 0.05 % GO increases porosity by 2 %). Mechanical testing demonstrated improved anti-deformation ability and failure strain with the addition of GO. Osteogenic differentiation markers, such as alkaline phosphatase (ALP) and calcium nodules, increased significantly with SF/GO hydrogels, indicating promotion of osteogenesis. The SF/GO hydrogel exhibited excellent biocompatibility and potential for bone defect repair, highlighting its suitability for biomedical applications in bone tissue engineering.

The authors of [84] prepared a GO-based nanocomplex functionalized with polyethyleneglycol (PEG) and PEI for loading and delivering miR-29b, a key player in bone formation. The nanocomplex exhibited good biocompatibility, miR-29b loading capacity, and transfection efficiency. Encapsulating the miR-29b/GO-PEG-PEI nanocomplex into CS hydrogel for osteogenesis showed promising results *in vitro* and *in vivo*, promoting BMSC osteogenic differentiation and bone regeneration. The study suggests that PEG/PEI functionalized GO could serve as a promising candidate for miRNA cellular delivery, and the miR-29b/GO-PEG-PEI@CS hydrogel holds potential for repairing bone defects *in vivo*. Cytotoxicity testing revealed good biocompatibility of the GO-PEG-PEI complex, with efficient miRNA loading demonstrated through agarose gel electrophoresis and cellular uptake observed via laser scanning confocal microscopy. The transfection efficiency of miR-29b/GO-PEG-PEI varied with different mass ratio of nanoparticles to plasmid content (N/P), with the complex showing the highest transfection efficiency at an N/P ratio of 40. *In vivo* evaluation indicated increased bone formation in defects treated with miR-29b/GO-PEG-PEI@CS hydrogel compared to control groups, demonstrating its potential for bone regeneration. Overall, the study suggests that the miR-29b/GO-PEG-PEI@CS hydrogel is a promising candidate for bone defect repair.

The studies presented show that GO-based composites with gelatin, hydrogels and other high-molecular compounds enhance cellular activity, making them promising for use in osteogenesis and orthopedic surgery. The presence of GO in composite materials improves mechanical properties, structural stability and porosity, which increases their suitability for bone tissue engineering.

3.2. Soft tissue regeneration

Graphene and its derivatives, have shown promise in promoting the growth of fibroblasts and keratinocytes, making them valuable in skin tissue engineering and wound healing. For instance, Khan *et al.* [85] developed a cost-effective composite hydrogel by crosslinking GO-functionalized arabinoxylan with polyvinyl alcohol (PVA), exhibiting improved antibacterial properties and biocompatibility, as well as efficacy in anticancer evaluations. Xue *et al.* [86] crafted a single-layer hydrogel artificial skin by incorporating dispersed peptide-coated graphene (PCG), resulting in a hydrogel with remarkable stretchability, mechanical sensing capabilities, and rapid self-healing abilities. Zhao *et al.* [87] designed a flexible hydrogel dressing for wound care, offering effective antibacterial properties through a photothermal mechanism. Additionally, conductive hydrogel design must consider both mechanical strength and electrical activity to mimic ECM properties. Zhou *et al.* [88] investigated the integration of GO into oligo(poly(ethylene glycol) fumarate) (OPF) hydrogels to enhance mechanical support and improve cellular electrical signaling, showing promise in myocardial infarction treatment. Yuan *et al.* [89] engineered a self-healing hydrogel within a silk protein (SP) framework, incorporating GO and growth factors for regenerative treatment in myocardial infarction therapy. Moreover, a novel injectable gel composed of rGO and alginate was created to transport mesenchymal stem cells, fostering the regeneration of injured cardiac tissue following a heart attack and supporting the viability and maturation of cardiac myocytes. These advancements hold significant potential in addressing complex tissue interactions and managing emergencies related to hemostasis outside the body.

As can be seen from the presented studies, functionalized graphene improves antibacterial properties and biocompatibility, as it promotes skin cell growth and wound healing; graphene-based hydrogels exhibit stretchability, self-healing ability, and are applicable for wound care. These materials can maintain mechanical strength, which can be used in the treatment of cardiovascular diseases such as myocardial infarction. These developments open up new possibilities in regenerative medicine and bleeding management.

4. Antimicrobial agents

Resistance of pathogenic bacteria to antibiotics has become a serious health care problem throughout the world, so replacing existing antibacterial agents is an urgent problem in material science [90, 91]. GBN have been intensively studied due to their antibacterial activity towards a wide range of bacteria [38, 92–95].

Metal composites containing graphene or GO have improved bactericidal properties than pure metal surfaces. In the composite, GO serves as an electron acceptor and captures electrons from the bacterial cell wall, and then transfers them to the metal substrate and thereby generates ROS production. This interrupts mitochondrial electron transport and ATP production in the bacterial cell, inhibiting its growth and viability [96].

Abdollahzadeh *et al.* carried out the synthesis of a metal-organic framework nanocomposite based on CS and GO. The resulting material has a high level of antibacterial activity with a maximum concentration of 2000 μg/mL. The studies were carried out using the disk diffusion method on Mueller–Hinton agar medium on bacteria of the species *Staphylococcus aureus* and *Escherichia coli* [97].

Bentedlaouti *et al.* prepared nanomaterials based on GO and rGO decorated with silver nanoparticles (AgNPs) [98]. Analysis of nanomaterials using SEM confirmed the intercalation of AgNPs into intermediate layers as nanosheets GO and rGO. Fig. 4 shows the results of a study of antibacterial activity using the paper disk method. The introduction of silver nanoparticles into tGO and trGO increased the antibacterial effect in relation to the individual GBN towards *Staphylococcus aureus* (by 2 – 3 times), *Bacillus cereus* (by 2 – 3 times), *Bacillus subtilis* (by 1.5 – 3 times), *Escherichia coli* (by 1.5 – 2 times), *Pseudomonas aeruginosa* (by 1.5 – 2 times) and *Candida albucans* (by 2.5 – 3 times).

A non-covalent nanocomposite based on GO and bimetallic Ag–Zr nanoparticles showed superior antibacterial and anti-biofilm activity of GO-decorated nanoparticles compared to bimetallic nanoparticles [99]. This effect may be due to the synergistic effect of the interaction between GO and Ag–Zr. This work showed a dose-dependent anti-biofilm activity of nanocomposites *in vitro* against biofilm-forming bacteria methicillin-resistant strain *Staphylococcus aureus* (MRSA). Ag–Zr nanoparticles inhibited 68.11 % and Ag–Zr/GO inhibited 71.12 % of MRSA biofilm formation (Fig. 5). MRSA biofilms were visualised using confocal scanning laser microscopy.

Nitrogen doped quantum carbon dots have been produced by hydrothermal synthesis [100]. The study of their antibacterial activity was determined using the minimum inhibitory concentration (MIC) test on *Bacillus subtilis* strain. The results showed no inhibition in carbon quantum dot samples without nitrogen, while samples containing 4.2 and 5 g of nitrogen had inhibitory activity at concentrations of 100 – 200 ppm. Moreover, the sample with the maximum nitrogen content demonstrated maximum activity [100].

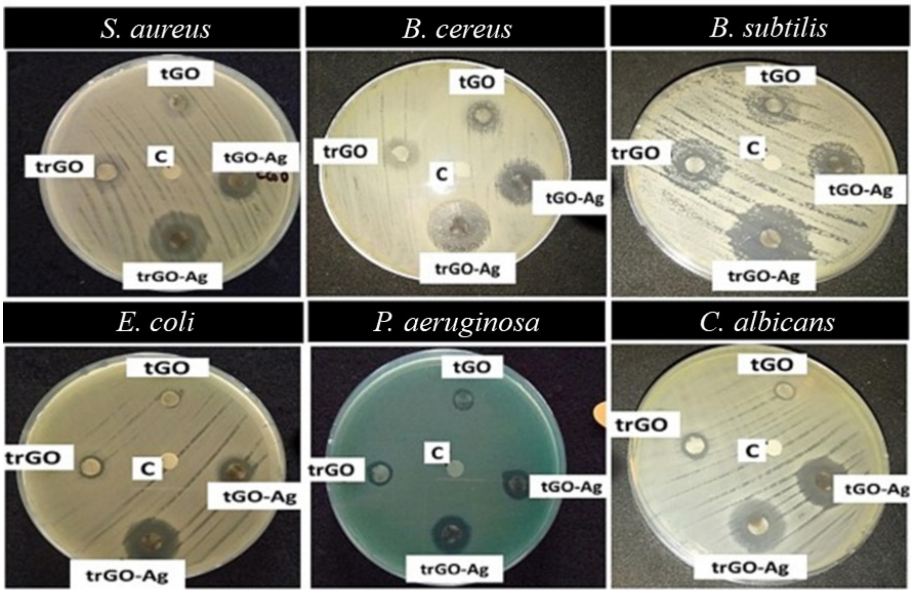

FIG. 4. Antibacterial test results using the paper disc diffusion method against microorganisms, (*c*) – control [98]. tGO and trGO are GO and rGO obtained by thermal synthesis, tGO-Ag and, trGO-Ag are GO and rGO obtained by thermal synthesis with silver nanoparticles

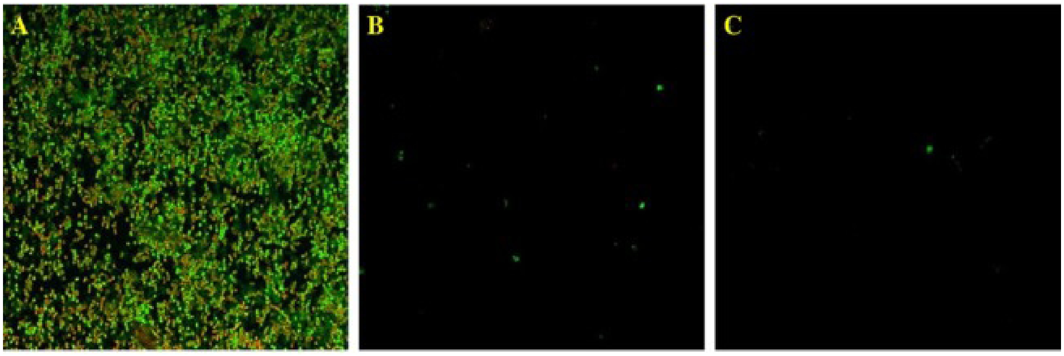

FIG. 5. Confocal images of anti-biofilm activity of nanoparticles. Control (*a*), bimetallic Ag–Zr NPs (*b*), Ag–Zr/GO nanocomposite (*c*) [99]

Hemmat *et al.* revealed that GO non-covalently functionalised with CuI using a hydrothermal method, the nanocomposite managed to inhibit the growth of gram-negative (*Escherichia coli*) and gram-positive (*Staphylococcus aureus*) bacteria. The mechanism of antibacterial activity was attributed to the oxidative stress due to generation of ROS, physical disruption, and wrapping of bacterial membranes owing to the GO sharp edges [101]. Metal oxide nanoparticles such as copper oxide were decorated on GO surface using ginger essential oil (GEO) as eco-friendly approach, the nanocomposite showed enhanced at about two times antibacterial activity against *Staphylococcus aureus* and *Escherichia coli* [102].

Metal nanoparticles such as copper nanopowders were incorporated with graphene surface, the nanocomposite exhibited strong antibacterial activity and achieved 99 % reduction of *Escherichia coli* bacteria within 1 h [103]. Yang *et al.* demonstrated that the antibacterial activity of medical titanium was strengthened through coating its surface by GO and copper, the GO–Cu–Ti has proved *in vitro* and *in vivo* antibacterial activity (over 99 %) against Staphylococcus aureus, and *Escherichia coli* bacteria due to synergistic effect of both GO and Cu, generation of ROS, and sharp-edged GO sheets that physically damage bacterial membranes [104]. Moreover, the functionalised graphene surface with aliphatic molecules such as diaminohexane was also activated using AgNPs for the antibacterial activity against total and faecal coliform bacteria [105]. Derakhshi *et al.* revealed that AgNPs were stabilised on rGO using dimethyl formamide (DMF), and the distributed AgNPs have different shapes depending on the synthesis method. The authors displayed that the shape of AgNPs formed on the amine functionalised rGO, have significant effect on the inhibition of bacterial growth, where triangular AgNPs exhibited highest antibacterial activity against both *Escherichia coli* and *Staphylococcus aureus* in comparison with the spherical AgNPs and silver nanowires [106].

The antibacterial activity was increased through the synergistic effect produced as a result of combining organic polymer of tetraethynyl porphyrin with GO surface for enhancing the antibacterial activity against gram-positive (*Staphylococcus aureus*) and gram-negative (*Escherichia coli*) pathogens in comparison with the free counterparts (the bare GO, and porphyrin), the synergistic effect could significantly accelerate the healing of open wound infected by bacteria [107].

Graphene–bismuth oxychloride 2D heterojunction killed *Staphylococcus aureus* bacteria with 99.36 % under simulated sunlight irradiation for 20 min, the antibacterial properties of heterojunction was attributed to graphene by 57.31 %. In the latter case graphene has the ability to transfer the excited electrons of BiOCl semiconductor exposed to visible light irradiation conjugated with the electrons on graphene surface for enhancing the photocatalytic antibacterial performance through surface plasmon resonance effect [108].

Sun *et al.* displayed that rGO was covalently attached to silanised titanium surface ((3-aminopropyl)triethoxysilane–titanium sheets) and showed high antibacterial activity against *Escherichia coli* and *Staphylococcus aureus* bacteria in comparison with titanium sheets, the SEM results of bacterial morphology illustrated that the dead bacteria were recorded on the graphene coated titanium more than the titanium sheets, the size and shape of both types of bacteria changed, the bacterial membranes were deformed and damaged. Levofloxacin antibiotic was noncovalently anchored on the graphene coated titanium through π–π stacking interaction, hydrogen bonds, and electrostatic interactions and proved inhibition for the abovementioned types of bacteria *in vivo* for the potential applications in oral implant surfaces for treatment of bacterial infection [109].

Thus, the growing resistance of bacteria to antibiotics requires the development of new antibacterial materials. GBN (GO, rGO) have shown effectiveness against various pathogens. Composites with graphene enhance bactericidal properties by suppressing bacterial activity due to the generation of ROS. The incorporation of metal nanoparticles, such as copper and silver, into graphene structures increases antibacterial activity, which can accelerate wound healing. These developments offer new approaches to combating infections, including application in medical implants.

5. Nanobiosensors

Nanobiosensors are nanomaterials that are applied in the field of biosensors for different applications such as diagnosis of diseases, viruses and bacteria, environmental monitoring, food industry, healthcare and clinical uses [110–115]. Different components contribute to the composition of a biosensor:

- blood, urine, saliva, bacteria, virus, fungi, water, food, soil, gases or air samples can serve as analytes;
- antibodies, enzymes, DNA, RNA, peptides, aptamers, organic molecules or metals and nanoparticles can act as a recognition element or bioreceptor;
- the transducer part is responsible for the transferring of the signal to the detector when exposed to any change happening on its surface such as chemical redox reactions, or physical changes. Carbon nanomaterials are widely used as transducers due to their high surface area, special electronic, optical, thermal and mechanical properties;
- the detector can translate the electrical signal received from the transducer to quantitative and qualitative data [116].

The nanobiosensors are divided into electrochemical, optical calorimetric and piezoelectric:

- electrochemical nanobiosensors are based on transducing the biochemical signals to electrical ones [117];
- optical nanobiosensors are based on the interaction between analyte and sensor which leads to a change in the morphology and fluorescence of the transducer under irradiation. The optical sensing can be achieved through Raman scattering, fluorescence, and plasmon resonance [118];
- calorimetric nanobiosensors are based on the detection of the heat liberated or consumed by a reaction between the analyte and the bioreceptor on the transducer surface [119];
- in case of piezoelectric nanobiosensors, the mechanical force produced due to the conjugation of the analyte with the sensor is transferred into electrical signal by the transducer and recognised by the detector [120].

Hernández *et al.* demonstrated that DNA aptamers were covalently and non-covalently attached to GBN (GO and rGO) as the transducer surfaces for the detection of living organisms such as *Staphylococcus aureus* with high selectivity detecting even single CFU/mL of the bacteria [121]. Electrochemical biosensor was developed from graphene functionalised with black phosphorus and gold nanoparticles for the detection of sortase enzyme which can catalyse the covalent attachment of surface proteins to the cell walls of gram-positive bacteria. A linear dynamic range was obtained between 1 pM – 100 nM with LOD of 0.65 pM, compared to the fluorimetric method, where linear range was 300 pmol/L – 100 nmol/L and LOD was 0.16 nM [122].

Yang *et al.* demonstrated that the biosensors fabricated from rGO modified with poly(methylene blue) and poly(ionic liquids) were applied in detecting SARS-CoV2-spike protein in clinical serum samples for the diagnosis and treatment of COVID-19, with a detection range of $0.1\sim1000$ ng/mL and LOD 38 pg/mL, compared to AuNPs/carbon cloth nanomaterial with linear range $0 \sim 1000$ ng/mL and LOD 110 pg/mL [123]. Field effect transistor biosensor based on GO was applied to detect SARS-CoV2 spike protein. Sheets of GO were π–π stacked to the graphene surface and formed Van der Waals heterostructure, the antibody was immobilised on the GO surface providing high affinity to interact with the protein with LOD around 8 fg/mLwith detection range between 10 fg/mL to 100 pg/mL, which showed enhancement of sensitivity in three times compared to biosensor based on graphene field effect transistor [124]. A genosensor was developed by Malla *et al.* where rGO was modified by gold nanoparticles and covalently functionalised with DNA probes for targeting the SARS-CoV2 gene efficiently in human saliva, urine, and serum with LOD 0.37, 0.33, and 0.19 fM, respectively, compared to gold electrode with LOD 26 fM [125].

Laser scribed graphene modified with gold nanoparticles and molecularly imprinted polymer was developed to detect the human epidermal growth factor receptor 2 (HER2) protein, a biomarker for breast cancer. Detection of HER2 was performed in the concentration range from 1 to 200 ng/mL with a LOD of 0.43 ng/mL, leading to early diagnosis of breast cancer [126]. Chemiresistive biosensors were fabricated from crumpled graphene modified by polystyrene as a heat shrinkable material. The DNA was covalently immobilised on GO surface through amide bond formation for the purpose of targeting miRNA-21; the rate of changing electrical resistance was measured when the target miRNA-21 interacts with GO surface. A linear change occurs with increasing the concentration of miRNA-21 from 10 nM to 1 pM with LOD of 1.47 pM, revealing the high sensitivity and selectivity of the biosensor for cancer biomarkers [127]. Yan *et al.* developed the electrochemical aptasensor from graphene nanosheets modified with AgNPs and thiolated aptamer for the detection of the carcinoembryonic antigen with high selectivity, reproducibility, and sensitivity proved in a wide linear range from 0.001 to 10 pg/mL with LOD of 0.5 fg/mL, compared to $Ag/MoS_2@Fe_3O_4$ with linear range 0.1 – 20000 pg/mL and LOD 0.03 pg/mL, applied in human serum samples [128].

Rajaji *et al.* showed that an electrochemical nanosensor was efficiently prepared from rGO decorated with iron nitride nanoparticles immobilised on carbon electrode for the rapid detection of the cancer biomarker of 4-nitroquinoline *N*-oxide; the fabricated nanosensor showed a wide range of detection from 0.05 – 574.2 μM and LOD of 9.24 nM, the nanosensor was applied for analysis in human blood and urine samples [129].

Rauf *et al.* developed an electrochemical immunosensor based on GO enriched with carboxylic groups covalently modified with antibody against the cancer biomarker mucin-1. The immunosensor was fabricated on screen-printed carbon electrodes and showed high sensitivity with linear range of detection from 0.1 to 2 U/mL with LOD of 0.04 U/mL in human serum samples, compared to coated PMMA beads with linear range 0.3 – 20 U/mL and LOD 0.21 U/mL. At the electrode surface, methylene blue probe was redox catalysed by the active nanosensor and reduced to a leucomethylene blue as an indicator for detection of antibody-protein interactions [130].

Kumar *et al.* constructed a nanosensor from yttria-doped zirconia-reduced GO nanocomposite that was functionalised with 3-(triethoxysilyl)propan-1-amine. The nanocomposite was then electrophoretically deposited onto an electrode of indium tin oxide coated glass substrate. CYFRA-21-1 antibody cancer biomarker were then covalently immobilised on the nanocomposite surface. The obtained nanobiosensor proved highly sensitive detection for the salivary cancer biomarker CYFRA-21-1 with linear detection range from 0.01 – 50 ng/mL with LOD of 7.2 pg/mL, compared to $APTES/nHfO_2/ITO$ nanoparticles with linear range 2 – 18 ng/mL and LOD 0.21 ng/mL [131].

Singh *et al.* deposited layers of graphene sheets on copper substrate through chemical vapour deposition technique with subsequent non-covalent functionalisation with 1-pyrenebutanoic acid succinimidyl ester through π–π stacking interaction followed by covalent functionalisation with the antibody for the detection of the cancer biomarker carcinoembryonic antigen (CEA). The constructed biosensor approved high sensitivity and selectivity with linear detection range from 1.0 to 25.0 ng/mL and LOD of 0.23 ng/mL, compared to complex material of HRP, AuNPs, Carboxylic magnetic beads, graphene, hexacyanoferrates and SiO_2 with linear range 5 – 60 ng/mL and LOD 5 ng/mL [132].

Sadeghi *et al.* fabricated aptasensor based on electrochemically synthesised GO layers on graphite electrode and covalently conjugated through amide bonds with aptamers that are specific to the HER2. The nanobiosensor confirmed the ability for early diagnosis of breast cancer, high sensitivity and selectivity with a linear detection range from 0.5 to 25 ng/mL with LOD of 0.59 ng/mL [133].

The GBN can also be used in the diagnosis of neurodegenerative diseases such as Alzheimer's and Parkinson's. Chen *et al.* developed an electrochemical sensor from the nanocomposite based on rGO and manganese sulphide nanoparticles. The authors revealed high selectivity and sensitivity towards Parkinson's disease biomarker (dopamine). The nanosensor demonstrated a wide linear range of detection of dopamine between 0.02 and 438.6 μM and LOD of 3.5 nM in human and rat serum, compared to PEDOT/Pd with linear range 0.5 – 1.0 μM and LOD 0.5 μM [134].

Nanobiosensors play an important role in disease diagnostics. They demonstrate high selectivity, for example, for detecting bacteria, viruses and cancer biomarkers. The use of graphene modified with various nanoparticles (gold, silver and others) allows creating effective electrochemical biosensors. These sensors are also promising in the diagnosis of neurodegenerative diseases with high accuracy and sensitivity.

6. Conclusion

GBN materials are of great benefit to modern science in particular due to their potential applications in medicine and bioengineering (Fig. 6). In this review it was shown that GBN can be effectively used for development of nanobiosensors, to deliver genetic material with minimal toxicity, as well as to improve the mechanical properties of biomaterials in tissue engineering. GBN composites promote bone tissue regeneration and can be applied in orthopedic surgery; GBN improves the antibacterial properties of materials, accelerating wound healing and suppressing pathogen activity, which is useful for medical implants.

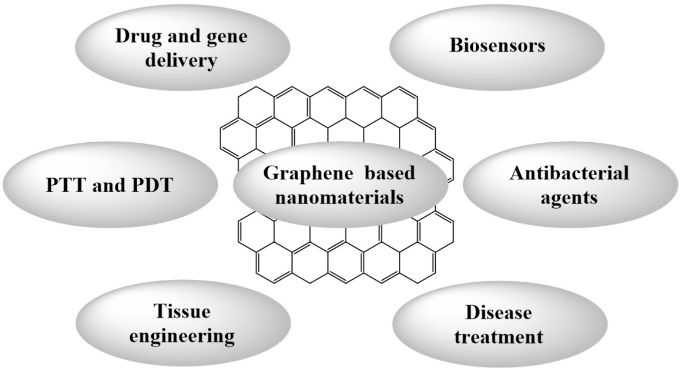

FIG. 6. Directions of GBN application in biomedicine

It is well known that one of the main problems of using nanomaterials in medicine is that their properties are determined not only by the chemical composition, but also by the variety of their surface characteristics and morphology, that implies the complexity their standardization. At present, detailed analysis of the literature data reveals the following problems in the field of GBN investigation: (*i*) lack of data on identification of the synthesized nanomaterial; (*ii*) non-sufficient reproducibility of GBN syntheses; (*iii*) lack of studies devoted to the stability of GBN dispersions; (*iv*) absence of data on the metabolic stability, mechanisms of action, signaling pathways and pharmaco- and toxicokinetics of GBN.

References

[1] Abdelhalim A.O.E., Semenov K.N., Nerukh D.A., Murin I V., Maistrenko D.N., Molchanov O.E., Sharoyko V.V. Functionalisation of graphene as a tool for developing nanomaterials with predefined properties. *J. Mol. Liq.*, 2022, **348**, 118368.

[2] Saharan R., Paliwal S.K., Tiwari A., Tiwari V., Singh R., Beniwal S.K., Dahiya P., Sagadevan S. Exploring graphene and its potential in delivery of drugs and biomolecules. *J. Drug. Deliv. Sci. Technol.*, 2023, **84**, 104446.

[3] Lin J., Huang Y., Huang P. Graphene-Based Nanomaterials in Bioimaging, In *Biomedical Applications of Functionalized Nanomaterials: Concepts, Development and Clinical Translation*, 2018, Elsevier, P. 247–287.

[4] Cao Z., Bian Y., Hu T., Yang Y., Cui Z., Wang T., Yang S., Weng X., Liang R., Tan C. Recent advances in two-dimensional nanomaterials for bone tissue engineering. *J. of Materiomics*, 2023, **9** (5), P. 930–958.

[5] Prasad S.V.S., Kumar M., Arulananth T.S., Ravi B., Kumar B., Kiran Kumar B. Graphene/ZnO nanocomposite based optical biosensors. *Mater Today Proc*, 2023.

[6] Kumar P., Huo P., Zhang R., Liu B. Antibacterial Properties of Graphene-Based Nanomaterials. *Nanomaterials*, 2019, **9** (5), 737.

[7] Palmieri V., Papi M. Can graphene take part in the fight against COVID-19? *Nano Today*, 2020, **33**, 100883.

[8] Zhang Y., Zhang L., Zhou C. Review of chemical vapor deposition of graphene and related applications. *Acc. Chem. Res.*, 2013, **46** (10), P. 2329–2339.

[9] Muñoz R., Gómez-Aleixandre C. Review of CVD synthesis of graphene. *Chemical Vapor Deposition*, 2013, **19** (10–12), P. 297–322.

[10] Li X., Colombo L., Ruoff R.S. Synthesis of Graphene Films on Copper Foils by Chemical Vapor Deposition. *Advanced Materials*, 2016, **28** (29), P. 6247–6252.

[11] Chen K., Shi L., Zhang Y., Liu Z. Scalable chemical-vapour-deposition growth of three-dimensional graphene materials towards energy-related applications. *Chem. Soc. Rev.*, 2018, **47** (9), P. 3018–3036.

[12] Yang X., Zhang G., Prakash J., Chen Z., Gauthier M., Sun S. Chemical vapour deposition of graphene: layer control, the transfer process, characterisation, and related applications. *Int. Rev. Phys. Chem.*, 2019, **38** (2), P. 149–199.

[13] Mattevi C., Kim H., Chhowalla M. A review of chemical vapour deposition of graphene on copper. *J. Mater. Chem.*, 2011, **21** (10), P. 3324–3334.

[14] Zhou H., Yu W.J., Liu L., Cheng R., Chen Y., Huang X., Liu Y., Wang Y., Huang Y., Duan X. Chemical vapour deposition growth of large single crystals of monolayer and bilayer graphene. *Nat. Commun.*, 2013, **4** (1), P. 1–8.

[15] Yu P., Lowe S.E., Simon G.P., Zhong Y.L. Electrochemical exfoliation of graphite and production of functional graphene. *Curr. Opin. Colloid Interface Sci.*, 2015, **20** (5–6), P. 329–338.

[16] Rao K.S., Senthilnathan J., Liu Y.F., Yoshimura M. Role of peroxide ions in formation of graphene nanosheets by electrochemical exfoliation of graphite. *Sci. Rep.*, 2014, **4** (1),P. 1–6.

[17] Wan H., Wei C., Zhu K., Zhang Y., Gong C., Guo J., Zhang J., Yu L. Zhang J. Preparation of graphene sheets by electrochemical exfoliation of graphite in confined space and their application in transparent conductive films. *ACS Appl. Mater. Interfaces*, 2017, **9** (39), P. 34456–34466.

[18] Mir A., Shukla A. Bilayer-rich graphene suspension from electrochemical exfoliation of graphite. *Mater. Des.*, 2018, **156**, P. 62–70.

[19] Melezhik A.V., Pershin V.F., Memetov N.R. Tkachev A.G. Mechanochemical synthesis of graphene nanoplatelets from expanded graphite compound. *Nanotechnol. Russ.*, 2016, **11** (7–8), P. 421–429.

[20] Abdelhalim A.O.E., Semenov K.N., Nerukh D.A., Murin I. V., Maistrenko D.N., Molchanov O.E., Sharoyko V.V. Functionalisation of graphene as a tool for developing nanomaterials with predefined properties. *J. Mol. Liq.*, 2022, **348**, 118368.

[21] Abdelhalim A.O.E., Sharoyko V.V., Ageev S.V., Farafonov V.S., Nerukh D.A., Postnov V.N., Petrov A.V., Semenov K.N. Graphene Oxide of Extra High Oxidation: A Wafer for Loading Guest Molecules. *J. Phys. Chem. Lett.*, 2021, **12** (41), P. 10015–10024.

[22] Abdelhalim A.O.E., Meshcheriakov A.A., Maistrenko D.N., Molchanov O.E., Ageev S.V., Ivanova D.A., Iamalova N.R., Luttsev M.D., Vasina L.V., Sharoyko V.V., Semenov K.N. Graphene oxide enriched with oxygen-containing groups: on the way to an increase of antioxidant activity and biocompatibility. *Colloids Surf B Biointerfaces*, 2021, 112232.

[23] Taneva S.G., Krumova S., Bogár F., Kincses A., Stoichev S., Todinova S., Danailova A., Horváth J., Násztor Z., Kelemen L., Dér A. Insights into graphene oxide interaction with human serum albumin in isolated state and in blood plasma. *Int. J. Biol. Macromol.*, 2021, **175**, P. 19–29.

[24] Anirudhan T.S., Chithra Sekhar V., Athira V.S. Graphene oxide based functionalized chitosan polyelectrolyte nanocomposite for targeted and pH responsive drug delivery. *Int. J. Biol. Macromol.*, 2020, **150**, P. 468–479.

[25] Hummers W.S., Offeman R.E) Preparation of Graphitic Oxide. *J. Am. Chem. Soc.*, 1958, **80** (6), P. 1339–1339.

[26] Brodie B.C. On the atomic weight of graphite. *Philos. Trans. R. Soc. Lond.*, 1859, **149** (1859), P. 249–259.

[27] Staudenmaier L. Verfahren zur Darstellung der Graphitsäure. *Berichte der deutschen chemischen Gesellschaft*, 1898, **31** (2), P. 1481–1487.

[28] Abdelhalim A.O.E., Sharoyko V.V., Meshcheriakov A.A., Martynova S.D., Ageev S.V., Iurev G.O., Al Mulla H., Petrov A.V., Solovtsova I.L., Vasina L.V., Murin I.V., Semenov K.N. Reduction and functionalization of graphene oxide with L-cysteine: Synthesis, characterization and biocompatibility. *Nanomedicine*, 2020, **29**, 102284.

[29] Lavin-Lopez M.P., Paton-Carrero A., Sanchez-Silva L., Valverde J.L., Romero A. Influence of the reduction strategy in the synthesis of reduced graphene oxide. *Advanced Powder Technology*, 2017, **28** (12), P. 3195–3203.

[30] Guex L.G., Sacchi B., Peuvot K.F., Andersson R.L., Pourrahimi A.M., Ström V., Farris S., Olsson R.T. Experimental review: Chemical reduction of graphene oxide (GO) to reduced graphene oxide (rGO) by aqueous chemistry. *Nanoscale*, 2017, **9** (27), P. 9562–9571.

[31] De Silva K.K.H., Huang H.H., Joshi R.K., Yoshimura M. Chemical reduction of graphene oxide using green reductants. *Carbon N.Y.*, 2017, **119**, P. 190–199.

[32] Wang J., Salihi E.C., siller L. Green reduction of graphene oxide using alanine. *Materials Science and Engineering C*, 2017, **72**, P. 1–6.

[33] Alam S.N., Sharma N., Kumar L. Synthesis of Graphene Oxide (GO) by Modified Hummers Method and Its Thermal Reduction to Obtain Reduced Graphene Oxide (rGO)*. *Graphene*, 2017, **06** (01), P. 1–18.

[34] Saleem H., Haneef M., Abbasi H.Y. Synthesis route of reduced graphene oxide via thermal reduction of chemically exfoliated graphene oxide. *Mater. Chem. Phys.*, 2018, **204**, P. 1–7.

[35] Oliveira A.E.F., Braga G.B., Tarley C.R.T., Pereira A.C. Thermally reduced graphene oxide: synthesis, studies and characterization. *J. Mater. Sci.*, 2018, **53** (17), P. 12005–12015.

[36] Schedy A., Oetken M. The thermal reduction of graphene oxide – A simple and exciting manufacturing process of graphene. *CHEMKON*, 2020, **27** (5), P. 244–249.

[37] Liu Z., Navik R., Tan H., Xiang Q., Wahyudiono Goto M., Ibarra R.M., Zhao Y. Graphene-based materials prepared by supercritical fluid technology and its application in energy storage. *J. Supercrit. Fluids*, 2022, **188**, 105672.

[38] Mann R., Mitsidis D., Xie Z., McNeilly O., Ng Y.H., Amal R., Gunawan C. Antibacterial Activity of Reduced Graphene Oxide. *J. Nanomater.*, 2021, **2021**, P. 1–10.

[39] Robinson J.T., Perkins F.K., Snow E.S., Wei Z., Sheehan P.E. Reduced Graphene Oxide Molecular Sensors. *Nano Lett.*, 2008, **8** (10), P. 3137–3140.

[40] Dong N., Ye Q., Zhang D., Xiao Y., Dai H. Reduced graphene oxide as an effective promoter to the layered manganese oxide-supported Ag catalysts for the oxidation of ethyl acetate and carbon monoxide. *J. Hazard Mater.*, 2022, **431**, 128518.

[41] Zhao J., Tang L., Xiang J., Ji R., Yuan J., Zhao J., Yu R., Tai Y., Song L. Chlorine doped graphene quantum dots: Preparation, properties, and photovoltaic detectors. *Appl. Phys. Lett.*, 2014, **105** (11).

[42] Mueller M.L., Yan X., McGuire J.A., Li L. Triplet States and Electronic Relaxation in Photoexcited Graphene Quantum Dots. *Nano Lett.*, 2010, **10** (7), P. 2679–2682.

[43] Tang L., Ji R., Li X., Teng K.S., Lau S.P. Energy-level structure of nitrogen-doped graphene quantum dots. *J. Mater. Chem. C Mater.*, 2013, **1** (32), 4908.

[44] Peng J., Gao W., Gupta B.K., Liu Z., Romero-Aburto R., Ge L., Song L., Alemany L.B., Zhan X., Gao G., Vithayathil S.A., Kaipparettu B.A., Marti A.A., Hayashi T., Zhu J.-J., Ajayan P.M. Graphene Quantum Dots Derived from Carbon Fibers. *Nano Lett.*, 2012, **12** (2), P. 844–849.

[45] Ponomarenko L.A., Schedin F., Katsnelson M.I., Yang R., Hill E.W., Novoselov K.S., Geim A.K. Chaotic Dirac Billiard in Graphene Quantum Dots. *Science*, 2008, **320** (5874), P. 356–358.

[46] Shen J., Zhu Y., Yang X., Zong J., Zhang J., Li C. One-pot hydrothermal synthesis of graphenequantum dots surface-passivated by polyethylene glycol and their photoelectric conversion under near-infrared light. *New J. Chem.*, 2012, **36** (1), P. 97–101.

[47] Gupta V., Chaudhary N., Srivastava R., Sharma G.D., Bhardwaj R., Chand S. Luminscent Graphene Quantum Dots for Organic Photovoltaic Devices. *J. Am. Chem. Soc.*, 2011, **133** (26), P. 9960–9963.

[48] Lin L., Zhang S. Creating high yield water soluble luminescent graphene quantum dots via exfoliating and disintegrating carbon nanotubes and graphite flakes. *Chemical Communications*, 2012, **48** (82), 10177.

[49] Danaeifar M. Recent advances in gene therapy: genetic bullets to the root of the problem. *Clin. Exp. Med.*, 2022, **23** (4), P. 1107–1121.

[50] Wong J.K.L., Mohseni R., Hamidieh A.A., MacLaren R.E., Habib N., Seifalian A.M. Will Nanotechnology Bring New Hope for Gene Delivery? *Trends Biotechnol.*, 2017, **35** (5), P. 434–451.

[51] Yin H., Kanasty R.L., Eltoukhy A.A., Vegas A.J., Dorkin J.R., Anderson D.G. Non-viral vectors for gene-based therapy. *Nat. Rev. Genet.*, 2014, **15** (8), P. 541–555.

[52] Cao X., Zheng S., Zhang S., Wang Y., Yang X., Duan H., Huang Y., Chen Y. Functionalized Graphene Oxide with Hepatocyte Targeting as Anti-Tumor Drug and Gene Intracellular Transporters. *J. Nanosci. Nanotechnol.*, 2015, **15** (3), P. 2052–2059.

[53] Choi H.Y., Lee T.-J., Yang G.-M., Oh J., Won J., Han J., Jeong G.-J., Kim J., Kim J.-H., Kim B.-S., Cho S.-G. Efficient mRNA delivery with graphene oxide-polyethylenimine for generation of footprint-free human induced pluripotent stem cells. *J. of Controlled Release*, 2016, **235**, P. 222–235.

[54] Goenka S., Sant V., Sant S. Graphene-based nanomaterials for drug delivery and tissue engineering. *J. of Controlled Release*, 2014, **173**, P. 75–88.

[55] Teimouri M., Nia A.H., Abnous K., Eshghi H., Ramezani M. Graphene oxide–cationic polymer conjugates: Synthesis and application as gene delivery vectors. *Plasmid.*, 2016, **84–85**, P. 51–60.

[56] Hu H., Tang C., Yin C. Folate conjugated trimethyl chitosan/graphene oxide nanocomplexes as potential carriers for drug and gene delivery. *Mater. Lett.*, 2014, **125**, P. 82–85.

[57] Yin D., Li Y., Lin H., Guo B., Du Y., Li X., Jia H., Zhao X., Tang J., Zhang L. Functional graphene oxide as a plasmid-based Stat3 siRNA carrier inhibits mouse malignant melanoma growth *in vivo*. *Nanotechnology*, 2013, **24** (10), 105102.

[58] Zhi F., Dong H., Jia X., Guo W., Lu H., Yang Y., Ju H., Zhang X., Hu Y. Functionalized Graphene Oxide Mediated Adriamycin Delivery and miR-21 Gene Silencing to Overcome Tumor Multidrug Resistance In Vitro. *PLoS One*, 2013, **8** (3), e60034.

[59] Cheng F.-F., Chen W., Hu L.-H., Chen G., Miao H.-T., Li C., Zhu J.-J. Highly dispersible PEGylated graphene/Au composites as gene delivery vector and potential cancer therapeutic agent. *J. Mater. Chem. B*, 2013, **1** (38), 4956.

[60] Tripathi S.K., Goyal R., Gupta K.C., Kumar P. Functionalized graphene oxide mediated nucleic acid delivery. *Carbon N.Y.*, 2013, **51**, P. 224–235.

[61] He Y., Zhang L., Chen Z., Liang Y., Zhang Y., Bai Y., Zhang J., Li Y. Enhanced chemotherapy efficacy by co-delivery of shABCG2 and doxorubicin with a pH-responsive charge-reversible layered graphene oxide nanocomplex. *J. Mater. Chem. B*, 2015, **3** (31), P. 6462–6472.

[62] Yin F., Hu K., Chen Y., Yu M., Wang D., Wang Q., Yong K.-T., Lu F., Liang Y., Li Z. SiRNA Delivery with PEGylated Graphene Oxide Nanosheets for Combined Photothermal and Genetherapy for Pancreatic Cancer. *Theranostics*, 2017, **7** (5), P. 1133–1148.

[63] Feng L., Zhang S., Liu Z. Graphene based gene transfection. *Nanoscale*, 2011, **3** (3), 1252.

[64] Teng Y.D., Lavik E.B., Qu X., Park K.I., Ourednik J., Zurakowski D., Langer R., Snyder E.Y. Functional recovery following traumatic spinal cord injury mediated by a unique polymer scaffold seeded with neural stem cells. *Proceedings of the National Academy of Sciences*, 2002, **99** (5), P. 3024–3029.

[65] Solanki A., Chueng S.D., Yin P.T., Kappera R., Chhowalla M., Lee K. Axonal Alignment and Enhanced Neuronal Differentiation of Neural Stem Cells on Graphene? Nanoparticle Hybrid Structures. *Advanced Materials*, 2013, **25** (38), P. 5477–5482.

[66] Setia Budi H., Javed Ansari M., Abdalkareem Jasim S., Abdelbasset W.K., Bokov D., Fakri Mustafa Y., Najm M.A.A., Kazemnejadi M. Preparation of antibacterial Gel/PCL nanofibers reinforced by dicalcium phosphate-modified graphene oxide with control release of clindamycin for possible application in bone tissue engineering. *Inorg. Chem. Commun.*, 2022, **139**, 109336.

[67] Amiryaghoubi N., Fathi M., Barar J., Omidian H., Omidi Y. Recent advances in graphene-based polymer composite scaffolds for bone/cartilage tissue engineering. *J. Drug Deliv. Sci. Technol.*, 2022, **72**, 103360.

[68] Sharifi S., Ebrahimian-Hosseinabadi M., Dini G., Toghyani S. Magnesium-zinc-graphene oxide nanocomposite scaffolds for bone tissue engineering. *Arabian J. of Chemistry*, 2023, **16** (6), 104715.

[69] Ghosal K., Mondal P., Bera S., Ghosh S. Graphene family nanomaterials- opportunities and challenges in tissue engineering applications. *FlatChem*, 2021, **30**, 100315.

[70] Challa A.A., Saha N., Szewczyk P.K., Karbowniczek J.E., Stachewicz U., Ngwabebhoh F.A., Saha P. Graphene oxide produced from spent coffee grounds in electrospun cellulose acetate scaffolds for tissue engineering applications. *Mater Today Commun.*, 2023, **35**, 105974.

[71] Motiee E.-S., Karbasi S., Bidram E., Sheikholeslam M. Investigation of physical, mechanical and biological properties of polyhydroxybutyrate-chitosan/graphene oxide nanocomposite scaffolds for bone tissue engineering applications. *Int. J. Biol. Macromol.*, 2023, **247**, 125593.

[72] Babakhani A., Peighambardoust S.J., Olad A. Fabrication of magnetic nanocomposite scaffolds based on polyvinyl alcohol-chitosan containing hydroxyapatite and clay modified with graphene oxide: Evaluation of their properties for bone tissue engineering applications. *J. Mech. Behav. Biomed. Mater*, 2024, **150**, 106263.

[73] Amiryaghoubi N., Fathi M., Barar J., Omidian H., Omidi Y. Hybrid polymer-grafted graphene scaffolds for microvascular tissue engineering and regeneration. *Eur. Polym. J.*, 2023, **193**, 112095.

[74] Saravanan S., Sareen N., Abu-El-Rub E., Ashour H., Sequiera G.L., Ammar H.I., Gopinath V., Shamaa A.A., Sayed S.S.E., Moudgil M., Vadivelu J., Dhingra S. Graphene Oxide-Gold Nanosheets Containing Chitosan Scaffold Improves Ventricular Contractility and Function After Implantation into Infarcted Heart. *Sci. Rep.*, 2018, **8** (1), 15069.

[75] Park J., Kim B., Han J., Oh J., Park S., Ryu S., Jung S., Shin J.-Y., Lee B.S., Hong B.H., Choi D., Kim B.-S. Graphene Oxide Flakes as a Cellular Adhesive: Prevention of Reactive Oxygen Species Mediated Death of Implanted Cells for Cardiac Repair. *ACS Nano*, 2015, **9** (5), P. 4987–4999.

[76] Shin Y.C., Lee J.H., Jin L., Kim M.J., Kim Y.-J., Hyun J.K., Jung T.-G., Hong S.W., Han D.-W. Stimulated myoblast differentiation on graphene oxide-impregnated PLGA-collagen hybrid fibre matrices. *J. Nanobiotechnology*, 2015, **13** (1), 21.

[77] Chaudhuri B., Bhadra D., Moroni L., Pramanik K. Myoblast differentiation of human mesenchymal stem cells on graphene oxide and electrospun graphene oxide–polymer composite fibrous meshes: importance of graphene oxide conductivity and dielectric constant on their biocompatibility. *Biofabrication*, 2015, **7** (1), 015009.

[78] Shahmoradi S., Golzar H., Hashemi M., Mansouri V., Omidi M., Yazdian F., Yadegari A., Tayebi L. Optimizing the nanostructure of graphene oxide/silver/arginine for effective wound healing. *Nanotechnology*, 2018, **29** (47), 475101.

[79] Boga J.C., Miguel S.P., de Melo-Diogo D., Mendonça A.G., Louro R.O., Correia I.J. In vitro characterization of 3D printed scaffolds aimed at bone tissue regeneration. *Colloids Surf B Biointerfaces*, 2018, **165**, P. 207–218.

[80] Faghihi S., Karimi A., Jamadi M., Imani R., Salarian R. Graphene oxide/poly(acrylic acid)/gelatin nanocomposite hydrogel: Experimental and numerical validation of hyperelastic model. *Materials Science and Engineering: C*, 2014, **38**, P. 299–305.

[81] Liu H., Cheng J., Chen F., Bai D., Shao C., Wang J., Xi P., Zeng Z. Gelatin functionalized graphene oxide for mineralization of hydroxyapatite: biomimetic and in vitro evaluation. *Nanoscale*, 2014, **6** (10), 5315.

[82] Yu P., Bao R.-Y., Shi X.-J., Yang W., Yang M.-B. Self-assembled high-strength hydroxyapatite/graphene oxide/chitosan composite hydrogel for bone tissue engineering. *Carbohydr. Polym.*, 2017, **155**, P. 507–515.

[83] Wang L., Lu R., Hou J., Nan X., Xia Y., Guo Y., Meng K., Xu C., Wang X., Zhao B. Application of injectable silk fibroin/graphene oxide hydrogel combined with bone marrow mesenchymal stem cells in bone tissue engineering. *Colloids Surf A Physicochem. Eng. Asp.*, 2020, **604**, 125318.

[84] Qin H., Ji Y., Li G., Xu X., Zhang C., Zhong W., Xu S., Yin Y., Song J. MicroRNA-29b/graphene oxide–polyethyleneglycol–polyethylenimine complex incorporated within chitosan hydrogel promotes osteogenesis. *Front Chem.*, 2022, **10**.

[85] Khan M.R., Huang C., Ullah R., Ullah H., Qazi I.M., Nawaz T., Adnan M., Khan A., Su H., Ren L. Effects of Various Polymeric Films on the Pericarp Microstructure and Storability of Longan (cv. Shixia) Fruit Treated with Propyl Disulfide Essential Oil from the Neem (Azadirachta indica) Plant. *Polymers (Basel)*, 2022, **14** (3), 536.

[86] Xue B., Sheng H., Li Y., Li L., Di W., Xu Z., Ma L., Wang X., Jiang H., Qin M., Yan Z., Jiang Q., Liu J.-M., Wang W., Cao Y. Stretchable and self-healable hydrogel artificial skin. *Natl. Sci. Rev.*, 2022, **9** (7).

[87] Zhao, P., Zhang Y., Chen X., Xu C., Guo J., Deng M., Qu X., Huang P., Feng Z., Zhang J. Versatile Hydrogel Dressing with Skin Adaptiveness and Mild Photothermal Antibacterial Activity for Methicillin?Resistant Staphylococcus Aureus?Infected Dynamic Wound Healing. *Advanced Science*, 2023, **10** (11).

[88] Zhou J., Yang X., Liu W., Wang C., Shen Y., Zhang F., Zhu H., Sun H., Chen J., Lam J., Mikos A.G., Wang C. Injectable OPF/graphene oxide hydrogels provide mechanical support and enhance cell electrical signaling after implantation into myocardial infarct. *Theranostics*, 2018, **8** (12), P. 3317–3330.

[89] Yuan Z., Qin Q., Yuan M., Wang H., Li R. Development and novel design of clustery graphene oxide formed Conductive Silk hydrogel cell vesicle to repair and routine care of myocardial infarction: Investigation of its biological activity for cell delivery applications. *J. Drug Deliv. Sci. Technol.*, 2020, **60**, 102001.

[90] Chinemerem Nwobodo D., Ugwu M.C., Oliseloke Anie C., Al-Ouqaili M.T.S., Chinedu Ikem J., Victor Chigozie U., Saki M. Antibiotic resistance: The challenges and some emerging strategies for tackling a global menace. *J. Clin. Lab. Anal.*, 2022, **36** (9).

[91] Mitsunaga M., Ito K., Nishimura T., Miyata H., Miyakawa K., Morita T., Ryo A., Kobayashi H., Mizunoe Y., Iwase T. Antimicrobial strategy for targeted elimination of different microbes, including bacterial, fungal and viral pathogens. *Commun. Biol.*, 2022, **5** (1), 647.

[92] Kulakova I.I., Lisichkin G.V. Potential Directions in the Use of Graphene Nanomaterials in Pharmacology and Biomedicine (Review). *Pharm. Chem. J.*, 2022, **56** (1), P. 1–11.

[93] Bousiakou L.G., Qindeel R., Al-Dossary O.M., Kalkani H. Synthesis and characterization of graphene oxide (GO) sheets for pathogen inhibition: Escherichia coli, Staphylococcus aureus and Pseudomonas aeruginosa. *J. King Saud. Univ. Sci.*, 2022, **34** (4), 102002.

[94] Dan S., Bagheri H., Shahidizadeh A., Hashemipour H. Performance of graphene Oxide/SiO_2 Nanocomposite-based: Antibacterial Activity, dye and heavy metal removal. *Arabian J. of Chemistry*, 2023, **16** (2), 104450.

[95] Tariq M., Khan A.U., Rehman A.U., Ullah S., Jan A.U., Zakareya Khan Z.U.H., Muhammad N., Islam Z.U., Yuan Q. Green synthesis of Zno@GO nanocomposite and its' efficient antibacterial activity. *Photodiagnosis Photodyn. Ther.*, 2021, **35**, 102471.

[96] Bhatt S., Punetha V.D., Pathak R., Punetha M. Graphene in nanomedicine: A review on nano-bio factors and antibacterial activity. *Colloids Surf B Biointerfaces*, 2023, **226**, 113323.

[97] Abdollahzadeh S., Sayadi M.H., Shekari H. Synthesis of biodegradable antibacterial nanocomposite (metal–organic frameworks supported by chitosan and graphene oxide) with high stability and photocatalytic activities. *Inorg. Chem. Commun.*, 2023, **156**, 111302.

[98] Bentedlaouti K., Belouatek A., Kebaili N. Antibacterial and antioxidant activities of graphene and graphene oxide synthesis coated silver nanoparticules. *J. Cryst. Growth*, 2024, **627**, 127527.

[99] Khan A., Zaid M., Ameen F., Khan Mo.A., Kumar S., Al-Masri A.A., Islam M.A. Colossal antibacterial, antibiofilm and solar light-driven photocatalytic activity of nanoenhanced conjugate of bimetallic Ag-Zr nanoparticles with graphene oxide. *J. Mol. Struct.*, 2024, **1300**, 137223.

[100] Dwitya S.S., Hsueh Y.-H., Wang S.S.-S., Lin K.-S. Ultrafine nitrogen-doped graphene quantum dot structure and antibacterial activities against Bacillus subtilis 3610. *Mater. Chem. Phys.*, 2023, **295**, 127135.

[101] Avatefi Hemmat M., Asghari S., Bakhshesh M., Mahmoudifard M. Copper iodide decorated graphene oxide as a highly efficient antibacterial and antiviral nanocomposite. *Inorg. Chem. Commun.*, 2023, **156**, 111214.

[102] Fardinpour P., Ghafouri Taleghani H., Reza Zakerimehr M. Facile green synthesis of graphene oxide/copper oxide nanocomposites using ginger essential oil and its enhanced antibacterial properties. *Materials Science and Engineering: B*, 2024, **300**, 117100.

[103] Aissou T., Jann J., Faucheux N., Fortier L.-C., Braidy N., Veilleux J. Suspension plasma sprayed copper-graphene coatings for improved antibacterial properties. *Appl. Surf. Sci.*, 2023, **639**, 158204.

[104] Yang F., Huo D., Zhang J., Lin T., Zhang J., Tan S., Yang L. Fabrication of graphene oxide/copper synergistic antibacterial coating for medical titanium substrate. *J. Colloid Interface Sci.*, 2023, **638**, P. 1–13.

[105] Abdelhalim A.O.E., Galal A., Hussein M.Z., El Sayed I.E.-T. Graphene Functionalization by 1,6-Diaminohexane and Silver Nanoparticles for Water Disinfection. *J. Nanomater.*, 2016, **2016**, P. 1–7.

[106] Derakhshi M., Ashkarran A.A., Bahari A., Bonakdar S. Shape selective silver nanostructures decorated amine-functionalized graphene: A promising antibacterial platform. *Colloids Surf. A Physicochem. Eng. Asp.*, 2018, **545**, P. 101–109.

[107] Chen P., Ze R., Xia X., Zhang Z., Lu K., Wei L., Zhou B. Composite porphyrin-based conjugated microporous polymer/graphene oxide capable of photo-triggered combinational antibacterial therapy and wound healing. *Biomaterials Advances*, 2023, **154**, 213662.

[108] Wang Z., Liu G., Chen W., Zhang L., Qi Z., Bai G., Fan Y., Liu C., Xiao C., Li W., Chang Y., Liang G., Zhou Z., Yu P., Song Z., Ning C. Contribution of surface plasmonic resonance to enhanced photocatalytic antibacterial performance of graphene-based two-dimensional heterojunction. *Chemical Engineering J.*, 2023, **460**, 141720.

[109] Sun J., Liu X., Lyu C., Hu Y., Zou D., He Y.S., Lu J. Synergistic antibacterial effect of graphene-coated titanium loaded with levofloxacin. *Colloids Surf. B Biointerfaces*, 2021, **208**, 112090.

[110] Kumar S., Singh H., Feder-kubis J., Nguyen D.D. Recent advances in nanobiosensors for sustainable healthcare applications: A systematic literature review. *Environ. Res.*, 2023, **238** (P2), 117177.

[111] Arshad F., Nabi F., Iqbal S., Khan R.H. Applications of graphene-based electrochemical and optical biosensors in early detection of cancer biomarkers. *Colloids Surf. B Biointerfaces*, 2022, **212**, 112356.

[112] Oliveira M.E., Lopes B.V., Rossato J.H.H., Maron G.K., Gallo B.B., La Rosa A.B., Balboni R.D.C., Alves M.L.F., Ferreira M.R.A., da Silva Pinto L., Conceição F.R., Piva E., de Pereira C.M.P., Escote M.T., Carreño N.L.V. Electrochemical Biosensor Based on Laser-Induced Graphene for COVID-19 Diagnosing: Rapid and Low-Cost Detection of SARS-CoV-2 Biomarker Antibodies. *Surfaces*, 2022, **5** (1), P. 187–201.

[113] Bai Y., Xu T., Zhang X. Graphene-Based Biosensors for Detection of Biomarkers. *Micromachines*, 2020, **11** (1), 60.

[114] Peña-Bahamonde J., Nguyen H.N., Fanourakis S.K., Rodrigues D.F. Recent advances in graphene-based biosensor technology with applications in life sciences. *J. Nanobiotechnology*, 2018, **16** (1), P. 1–17.

[115] Sharifi M., Hasan A., Attar F., Taghizadeh A., Falahati M. Development of point-of-care nanobiosensors for breast cancers diagnosis. *Talanta*, 2020, **217**.

[116] Irkham I., Ibrahim A.U., Pwavodi P.C., Al-Turjman F., Hartati Y.W. Smart Graphene-Based Electrochemical Nanobiosensor for Clinical Diagnosis: Review. *Sensors (Basel)*, 2023, **23** (4).

[117] Achi F., Attar A.M., Ait Lahcen A. Electrochemical nanobiosensors for the detection of cancer biomarkers in real samples: Trends and challenges. *TrAC Trends in Analytical Chemistry*, 2023, 117423.

[118] Wu T., Shen J., Li Z., Xing F., Xin W., Wang Z., Liu G., Han X., Man Z., Fu S. Microfluidic-integrated graphene optical sensors for real-time and ultra-low flow velocity detection. *Appl. Surf. Sci.*, 2021, **539**, 148232.

[119] Mondal R., Dam P., Chakraborty J., Paret M.L., Kati A., Altuntas S., Sarkar R., Ghorai S., Gangopadhyay D., Mandal A.K., Husen A. Potential of nanobiosensor in sustainable agriculture: the state-of-art. *Heliyon*, , **8** (12), e12207.

[120] Bakhshpour M., Göktürk I., Gür S.D., Yilmaz F., Denizli A. Sensor Applications for Detection in Agricultural Products, Foods, and Water, in *Pesticides Bioremediation*, 2022, Springer International Publishing, Cham, P. 311–352.

[121] Hernández R., Vallés C., Benito A.M., Maser W.K., Xavier Rius F., Riu J. Graphene-based potentiometric biosensor for the immediate detection of living bacteria. *Biosens. Bioelectron.*, 2014, **54**, P. 553–557.

[122] Cai Y., Chen D., Chen Y., Li T., Wang L., Jiang J., Guo Z., Jaffrezic-Renault N., Zhang Z., Huang S. An electrochemical biosensor based on graphene intercalated functionalized black phosphorus/gold nanoparticles nanocomposites for the detection of bacterial enzyme. *Microchemical J.*, 2023, **193**, 109255.

[123] Yang X., Yin Z.Z., Zheng G., Zhou M., Zhang H., Li J., Cai W., Kong Y. Molecularly imprinted miniature electrochemical biosensor for SARS-CoV-2 spike protein based on Au nanoparticles and reduced graphene oxide modified acupuncture needle. *Bioelectrochemistry*, 2023, **151**, 108375.

[124] Gao J., Wang C., Chu Y., Han Y., Gao Y., Wang Y., Wang C., Liu H., Han L., Zhang Y. Graphene oxide-graphene Van der Waals heterostructure transistor biosensor for SARS-CoV-2 protein detection. *Talanta*, 2022, **240**, 123197.

[125] Malla P., Liu C.H., Wu W.C., Kabinsing P., Sreearunothai P. Synthesis and characterization of Au-decorated graphene oxide nanocomposite for magneto-electrochemical detection of SARS-CoV-2 nucleocapsid gene. *Talanta*, 2023, **262**, 124701.

[126] Lahcen A.A., Rauf S., Aljedaibi A., de Oliveira Filho J.I., Beduk T., Mani V., Alshareef H.N., Salama K.N. Laser-scribed graphene sensor based on gold nanostructures and molecularly imprinted polymers: Application for Her-2 cancer biomarker detection. *Sens Actuators B Chem.*, 2021, **347**, 130556.

[127] Wu T.Z., Jian C.R., Govindasamy M., Li Y.C., Lin Y.T., Su C.Y., Samukawa S., Huang C.H. Crumpled graphene induced by commercial Heat-Shrinkable material for chemiresistive biosensors toward cancer biomarker detection. *Microchemical J.*, 2023, **195**, 109469.

[128] Yan M., Fu L. ling Feng H. chao Namadchian M. Application of Ag nanoparticles decorated on graphene nanosheets for electrochemical sensing of CEA as an important cancer biomarker. *Environ. Res.*, 2023, **239**, 117363.

[129] Rajaji U., Muthumariyappan A., Chen S.M., Chen T.W., Ramalingam R.J. A novel electrochemical sensor for the detection of oxidative stress and cancer biomarker (4-nitroquinoline N-oxide) based on iron nitride nanoparticles with multilayer reduced graphene nanosheets modified electrode. *Sens Actuators B Chem.*, 2019, **291**, P. 120–129.

[130] Rauf S., Mishra G.K., Azhar J., Mishra R.K., Goud K.Y., Nawaz M.A.H., Marty J.L., Hayat A. Carboxylic group riched graphene oxide based disposable electrochemical immunosensor for cancer biomarker detection. *Anal. Biochem.*, 2018, **545**, P. 13–19.

[131] Kumar S., Gupta N., Malhotra B.D. Ultrasensitive biosensing platform based on yttria doped zirconia-reduced graphene oxide nanocomposite for detection of salivary oral cancer biomarker. *Bioelectrochemistry*, 2021, **140**, 107799.

[132] Singh V.K., Kumar S., Pandey S.K., Srivastava S., Mishra M., Gupta G., Malhotra B.D., Tiwari R.S., Srivastava A. Fabrication of sensitive bioelectrode based on atomically thin CVD grown graphene for cancer biomarker detection. *Biosens. Bioelectron.*, 2018, **105**, P. 173–181.

[133] Sadeghi M., Kashanian S., Naghib S.M., Haghiralsadat F., Tofighi D. An Efficient Electrochemical Biosensor Based on Pencil Graphite Electrode Mediated by 2D Functionalized Graphene Oxide to Detect HER2 Breast Cancer Biomarker. *Int. J. Electrochem. Sci.*, 2022, **17** (4), 220459.

[134] Chen T.W., Rajaji U., Chen S.M., Li Y.L., Ramalingam R.J. Ultrasound-assisted synthesis of α-MnS (alabandite) nanoparticles decorated reduced graphene oxide hybrids: Enhanced electrocatalyst for electrochemical detection of Parkinson's disease biomarker. *Ultrason. Sonochem.*, 2019, **56**, P. 378–385.

Submitted 21 June 2024; revised 8 October 2024; accepted 7 November 2024

Information about the authors:

Konstantin N. Semenov – Pavlov First St. Petersburg State Medical University, 6–8 L'va Tolstogo Street, St. Petersburg, 197022, Russia; St. Petersburg State University, 7–9 Universitetskaia Embankment, St. Petersburg, 199034, Russia; A. M. Granov Russian Research Centre for Radiology and Surgical Technologies, 70 Leningradskaia Street, St. Petersburg, 197758, Russia; ORCID ; knsemenov@gmail.com

Sergei V. Ageev – Pavlov First St. Petersburg State Medical University, 6–8 L'va Tolstogo Street, St. Petersburg, 197022, Russia; St. Petersburg State University, 7–9 Universitetskaia Embankment, St. Petersburg, 199034, Russia; ORCID ; ageev.sergey06@gmail.com

Olga S. Shemchuk – Pavlov First St. Petersburg State Medical University, 6–8 L'va Tolstogo Street, St. Petersburg, 197022, Russia; A. M. Granov Russian Research Centre for Radiology and Surgical Technologies, 70 Leningradskaia Street, St. Petersburg, 197758, Russia; ORCID ; olja.shemchuk17@gmail.com

Gleb O. Iurev – Pavlov First St. Petersburg State Medical University, 6–8 L'va Tolstogo Street, St. Petersburg, 197022, Russia; A. M. Granov Russian Research Centre for Radiology and Surgical Technologies, 70 Leningradskaia Street, St. Petersburg, 197758, Russia; ORCID ;

Abdelsattar O. E. Abdelhalim – Environmental Research Department, National Centre for Social and Criminological Research (NCSCR), Giza 11561, Egypt; ORCID ; abdelsattarosama@yahoo.com

Igor V. Murin – St. Petersburg State University, 7–9 Universitetskaia Embankment, St. Petersburg, 199034, Russia; ORCID ; igormurin@mail.ru

Pavel K. Kozhukhov – Pavlov First St. Petersburg State Medical University, 6–8 L'va Tolstogo Street, St. Petersburg, 197022, Russia; ORCID ; kozhukhovpk@yandex.ru

Anastasia V. Penkova – St. Petersburg State University, 7–9 Universitetskaia Embankment, St. Petersburg, 199034, Russia; ORCID ;

Dmitriy N. Maystrenko – A. M. Granov Russian Research Centre for Radiology and Surgical Technologies, 70 Leningradskaia Street, St. Petersburg, 197758, Russia; ORCID ; may68@mail.ru

Oleg E. Molchanov – A. M. Granov Russian Research Centre for Radiology and Surgical Technologies, 70 Leningradskaia Street, St. Petersburg, 197758, Russia; ORCID ; molchanovo@mail.ru

Vladimir V. Sharoyko – Pavlov First St. Petersburg State Medical University, 6–8 L'va Tolstogo Street, St. Petersburg, 197022, Russia; St. Petersburg State University, 7–9 Universitetskaia Embankment, St. Petersburg, 199034, Russia; A. M. Granov Russian Research Centre for Radiology and Surgical Technologies, 70 Leningradskaia Street, St. Petersburg, 197758, Russia; ORCID ; sharoyko@gmail.com

Conflict of interest: the authors declare no conflict of interest.

NANOSYSTEMS:
PHYSICS, CHEMISTRY, MATHEMATICS

Original article

Klimshina V.I., et al. *Nanosystems: Phys. Chem. Math.*, 2024, **15** (6), 936–949.
http://nanojournal.ifmo.ru
DOI 10.17586/2220-8054-2024-15-6-936-949

Natural polyphenols as potential antibacterial agents and their delivery systems of nanosized level

Vladislava I. Klimshina[1], Roman O. Shaikenov[1], Svetlana N. Morozkina[1,2],
Aleksey E. Romanov[1], Petr P. Snetkov[1,a]

[1]ITMO University, St. Petersburg, Russia
[2]Kabardino-Balkarian State University, Nalchik, Russia

[a]ppsnetkov@itmo.ru

Corresponding author: P. P. Snetkov, ppsnetkov@itmo.ru

ABSTRACT Bacterial infections associated with multidrug-resistant pathogens are a serious danger to both humans and farm animals. For this reason, natural biologically active agents (BAA), in particular, polyphenols, with a wide range of biological activity could become promising molecules for effective antibacterial therapy. Despite the potentially high antibacterial activity and other beneficial biological effects, the use of such BAA is hindered due to their low water solubility. To overcome this problem, various approaches are used, for example, loading BAA into nanosized delivery systems (nanoparticles, nanocapsules, micelles, etc.). Such approaches allow not only to increase the effectiveness of natural BAA, but also to ensure their targeted (local) effect, which is important in the treatment of bacterial diseases, and in some cases result in synergic action. This review describes the antibacterial properties of the most promising polyphenols and key approaches for their delivery at the nanoscale level, as well as the methods for their development.

KEYWORDS polyphenolic agents, antibacterial activity, natural biologically active agents, carnosic acid, curcumin, mangiferin, rosmarinic acid, drug resistance, nanoparticles, analysis methods.

ACKNOWLEDGEMENTS This research was funded by the Russian Science Foundation, project number 24-23-00269. Link to information about the project: https://rscf.ru/en/project/24-23-00269/

FOR CITATION Klimshina V.I., Shaikenov R.O., Morozkina S.N., Romanov A.E., Snetkov P.P. Natural polyphenols as potential antibacterial agents and their delivery systems of nanosized level. *Nanosystems: Phys. Chem. Math.*, 2024, **15** (6), 936–949.

1. Introduction

In recent years, there has been a significant spread of resistant bacterial infections; therefore, antibiotic resistance has become a major public health problem [1]. To address this problem, numerous studies are being conducted worldwide to find alternative treatment options. One such option is the use of natural biologically active agents (BAA) derived from plants with unique antibacterial properties and low side effects.

Plants have long been used by humans as therapeutic agents and their secondary metabolites show promising antimicrobial activity. The effectiveness of these natural compounds is determined by their chemical structure, which allows them to affect bacterial cells and disrupt their essential biological processes. In addition, due to their diverse mechanisms of action, plant secondary metabolites are less likely to lead to the development of resistance in pathogens. Importantly, natural agents have fewer side effects and less environmental impact than traditional antibiotics.

However, most natural BAA have a hydrophobic nature, which limits their use as highly effective antibacterial agents. To increase the activity of such agents and ensure their targeted action, various approaches are used, in particular, "loading" (encapsulation) of BAA into polymer matrices with subsequent production of various dosage forms: films, fibers, nanoparticles, etc.

In this work, natural polyphenols, namely mangiferin, curcumin, rosmarinic and carnosic acids, were selected as natural biologically active agents with pronounced antibacterial activity. The aim of this review is to conduct a comparative analysis of the antibacterial properties of these natural agents in order to determine the potential for their use in the composition of new effective drugs to combat resistant bacterial infections, including those based on nanoscale polymeric carriers.

2. Antibacterial activity of natural biologically active agents

A unique feature of plants is the ability to produce not only primary metabolites necessary for the vital activity of all cells, but also secondary metabolites that do not participate in the main metabolism. These agents allow plants to adapt to various abiotic and biotic environmental conditions [2]. Secondary metabolites determine the unique properties of plants such as colour, odour and taste and also possess biological activity, thereby affecting other plants, microorganisms, animals and humans [3].

As a result of the microbial evolution, namely the continuous expansion of the spectrum of antibiotic resistance genes, the development of new antibacterial drugs has become necessary in the last decade [4]. Currently, natural BAA are of particular interest as antimicrobial agents due to their easy availability and therapeutic potential [5].

The antibacterial activity is mainly mediated to two mechanisms. The first is by affecting the synthesis or function of vital components of bacteria. For example, bacterial protein biosynthesis or bacterial DNA replication and repair can serve as targets for antibacterial drugs. The second way is alternative mechanisms for the development of antibiotic resistance, for example, through antibiotic modification [6].

Based on the structure of the cell wall, there are two main groups of bacteria: Gram-negative and Gram-positive. Their main difference is the structure of cell walls (Fig. 1). Gram-negative bacteria have a thinner layer of peptidoglycan in their walls than Gram-positive bacteria, and also acquire a red color when stained by Gram staining, in contrast to Gram-positive bacteria, which stain purple [7].

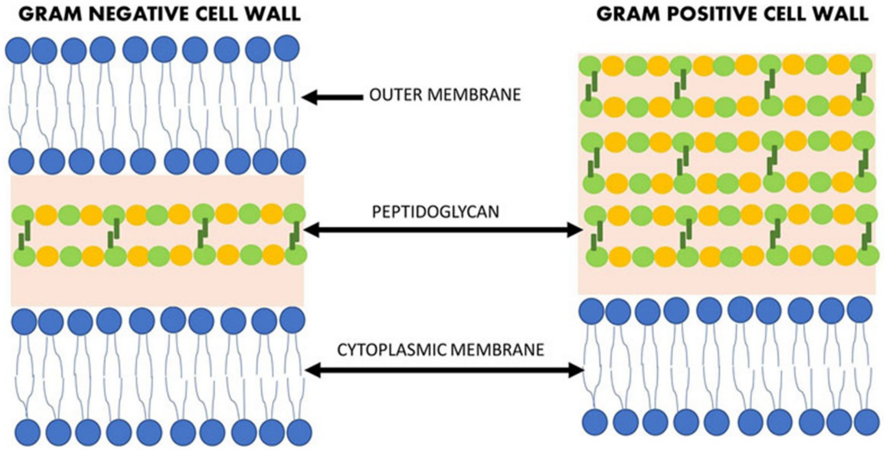

FIG. 1. Structural differences between the cell wall of gram-negative and gram-positive bacteria. Reproduced under the terms of the CC-BY 4.0 license. [8] Copyright 2021, Collective authors. Published by Frontiers Media S.A. (Frontiers in Pharmacology)

Antibacterial activity of secondary metabolites of plants has been confirmed in numerous studies. These compounds can be classified into three main groups: phenolic compounds, terpenoids and alkaloids [9]. Depending on the structural characteristics of bacteria, the efficacy of antibacterial agents may greatly vary [8]. In this paper, the antibacterial properties of a subgroup of phenolic BAA, namely polyphenols, have been considered.

3. Polyphenols

Polyphenols are natural compounds synthesized exclusively by plants and have at least two phenolic groups and one or more hydroxyl substituents in the molecule. These agents are mainly present in fruits, vegetables, green tea and whole grains, and are widely recognized for their antioxidant properties [10].

Polyphenols can be classified into two large groups: flavonoids and non-flavonoids. All flavonoids have a basic structure of diphenylpropanes, where the phenolic rings are usually linked by a heterocyclic ring [11]. Nonflavonoid compounds include phenolic acids, stilbenes (Fig. 2) and lignans (Fig. 3) [10–13].

Polyphenolic BAA have a huge range of biological properties such as antioxidant, anti-oncological, anti-inflammatory and antidiabetic. In addition, numerous studies have shown that polyphenols also possess antiviral, antifungal and antibacterial properties [14]. Thus, polyphenols can be considered as an alternative or complementary treatment for infectious diseases.

3.1. Mangiferin

The fruits and leaves of the mango tree contain a unique xanthone derivative, mangiferin. This compound is present in different plant families in varying concentrations and is usually found as a glycoside [15]. However, one of the major sources of mangiferin is *Mangifera indica*. Mangiferin is a secondary metabolite of this plant and its presence has been

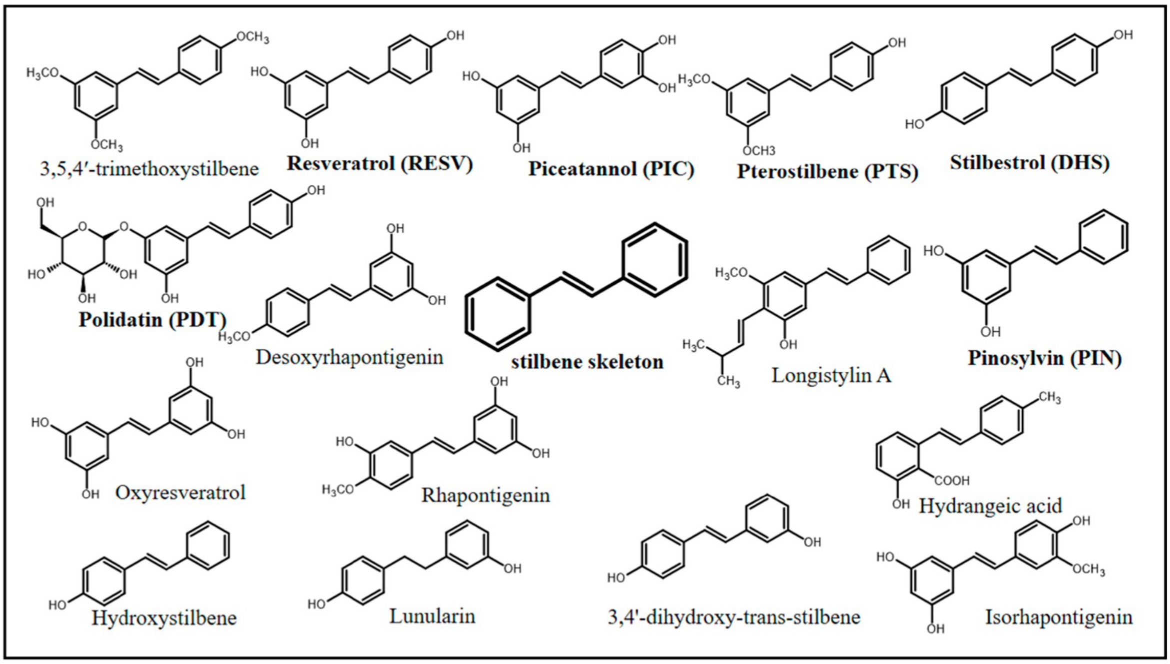

FIG. 2. Chemical structures of stilbenes with documented biological activity. Reproduced under the terms of the CC-BY 4.0 license.[12] Copyright 2024, Collective authors. Published by MDPI

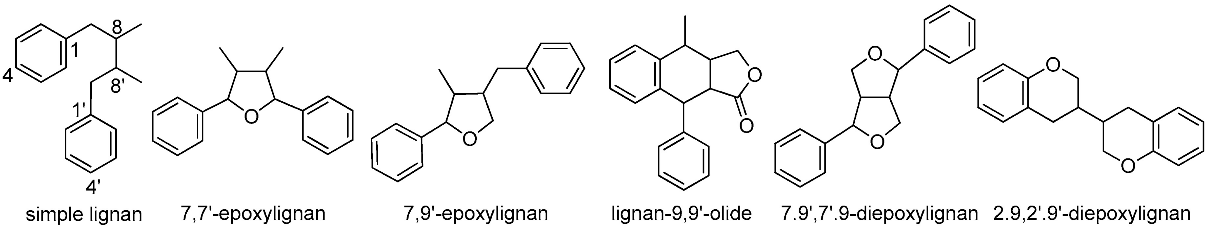

FIG. 3. Subtypes of classical lignans. Reproduced under the terms of the CC-BY 4.0 license.[13] Copyright 2018, Collective authors. Published by MDPI

detected in extracts of bark, peel and pips but the highest amount is found in the leaves [16]. Mangiferin isolated from mango leaves, for example, is a light-yellow crystalline powder [17].

Since the 1960s studies of the structure of mangiferin [18] confirmed that this molecule is 2-C-β-D-glucopyranosyl-1,3,6,7-tetrahydroxyxanthone (Fig. 4).

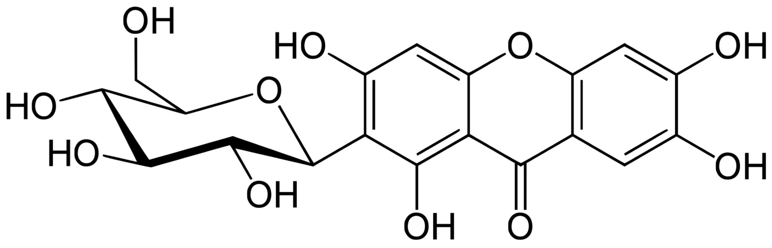

FIG. 4. Mangiferin structure

Besides antibacterial properties, mangiferin has numerous biological properties, including antioxidant, antiviral, antidiabetic, anticancer, immunomodulatory, hepatoprotective, analgesic and anti-aging [19].

Contact dermatitis is the most common inflammatory skin disease characterized by pruritus, immune dysregulation and epidermal barrier dysfunction [20]. Mangiferin also demonstrated anti-inflammatory activity in animal models (mice with oxazolone-induced contact dermatitis). The active ingredient reduced the levels of inflammatory mediators, namely interleukin-1-beta, interleukin-6 and inducible nitric oxide synthase, through the inhibition of the NF-kB signalling pathway, thereby reducing epithelial thickness [21]. In addition, mangiferin is able to inhibit collagenase and elastase activity and penetrate through the stratum corneum into the epidermis and dermis [22]. It is the stratum corneum of the skin that is the main barrier to transdermal penetration of drugs.

3.2. Curcumin

The plant *Curcuma longa*, belonging to the ginger family, is widely cultivated in southern and south-eastern tropical Asia. The rhizome of this plant is the most useful part of the plant for culinary and medicinal purposes. The most active component of turmeric is curcumin, which makes up 2-5 % of the spice. The characteristic yellow color of turmeric is due to curcuminoids, first isolated by Vogel in 1842. Curcumin is an orange-yellow crystalline powder that is insoluble in water. The structure of curcumin was first described in 1910 and is diferuloylmethane (Fig. 5) [23].

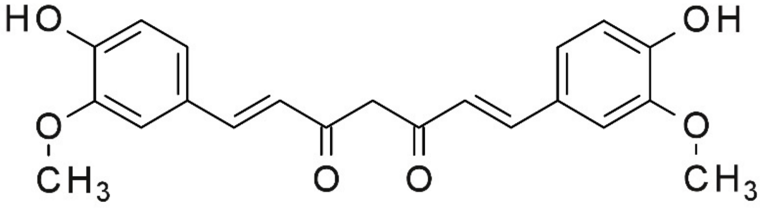

FIG. 5. Curcumin structure

Curcumin has a number of unique properties, which makes it possible to use this substance in various fields of medicine. For example, it has antioxidant, antibacterial, anti-inflammatory, anticancer, antidiabetic, antiviral, cardioprotective properties and is also active against dementia [24].

In addition, curcumin has been shown to be effective against various skin diseases including skin cancer, psoriasis, scleroderma, and dermatitis [25]. Numerous evidences suggest that curcumin accelerates wound healing, also prevents scarring and plays an important role in muscle regeneration after the injury.

3.3. Natural phenolic acids

Although the position of hydroxyl groups in aromatic rings play an important role in biological properties possessing, phenolic acids can be divided according to the skeleton structure into two main groups: hydroxycinnamic acids and hydroxybenzoic acids. Hydroxybenzoic acids occur as free acids or in conjugated forms, namely as glycosides or esters. The most common compounds belonging to this group are gallic, syringic and vanillic acids [26]. Hydroxycinnamic acids have a three-carbon side chain at the aromatic ring, and the most commonly found representatives are caffeic acid, ferulic acid and sinapic acid [27].

Rosmarinic acid is classified as hydroxycinnamic acid. This compound is an ester of caffeic acid (Fig. 6) [28]. It was first isolated from *Rosmarinus officinalis* and named after this plant. Rosmarinic acid has also been found in other plant families such as *Boraginaceae*, *Apiaceae* and *Cucurbitaceae* [29].

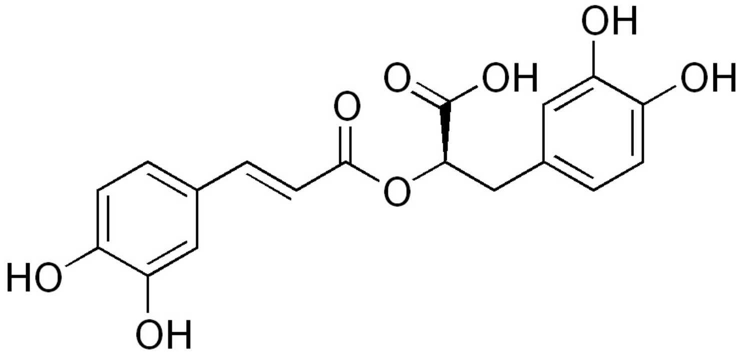

FIG. 6. Rosmarinic acid structure

Rosmarinic acid has a wide range of pharmacological properties such as antibacterial, anti-inflammatory, anti-oncological, anti-aging, anti-diabetic, hepatoprotective, antiviral and nephroprotective [30].

Carnosic acid belongs to hydroxybenzoic acids. This compound has been found in the family Lamiaceae, which includes plants such as *Salvia*, *Rosmarinus*, *Rosmarinus*, *Lepechinia*, *Oreganum* and *Thymus* [31]. The structural formula of carnosic acid is shown in Fig. 7.

Carnosic acid has antibacterial, anti-inflammatory, antioxidant and anti-oncological properties [32].

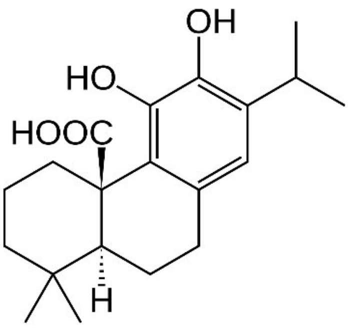

FIG. 7. Carnosic acid structure

4. Analysis of antibacterial activity of polyphenols

In 2017, the World Health Organization (WHO) published the list of 12 families of bacteria that pose the greatest threat to human health. The focus was on Gram-negative bacteria, which have a greater ability to develop resistance to antibiotics through the transfer of genetic material, allowing other bacteria to also develop resistance to the drugs. This list has been divided into three categories according to the urgency of the need for new antibiotics: critical, high priority and medium priority. The top priority is the fight against bacteria with the highest developed resistance, such as *Acinetobacter baumannii*, *Pseudomonas aeruginosa* and *Enterobacteriaceae*. These pathogens are capable of causing pneumonia and infection in the bloodstream. Bacteria capable of causing gonorrhea and food poisoning were categorized as high and medium priority. Examples of these groups are *Entorococcus faecium*, *Staphylococcus aureus*, *Salmonella*, *Streptococcus pneumoniae* and *Haemophilus influenza* [33].

There is also another classification of bacteria with the increasing multidrug resistance and virulence consisting of 6 pathogens. This group is called ESKAPE, and this abbreviation is made from the first letters of bacterial names: *Enterococcus faecium* (Gram-positive), *Staphylococcus aureus* (Gram-positive), *Klebsiella pneumoniae* (Gram-negative), *Acinetobacter baumannii* (Gram-negative), *Pseudomonas aeruginosa* (Gram-negative) and *Enterobacter spp* (Gram-negative). It is these pathogens that cause the majority of hospital-acquired infections [34]. In this analytical review, the antibacterial activity of polyphenols against ESKAPE group was considered.

The specificity of the diseases caused by *Enterococcus faecium* is the formation of a bacterial film. In one study, *Enterococcus faecium* was cultured on dentin biofilm to evaluate the bacterial activity of mangiferin. It was shown that after three weeks, methanolic mango seed extract with the concentration of 5 mg/ml killed 99.8 % of the bacterial colonies on the biofilm [35]. A similar study on dentin biofilm was carried out with 10.2 % aqueous curcumin extract. After three weeks, the significant reduction in *Enterococcus faecium* colonies (approximately 53 %) was found [36].

Staphylococcus aureus is capable to cause a large number of diseases ranging from skin infections to pneumonia and meningitis. Mangiferin has antibacterial activity against this pathogen. For example, disc diffusion method showed that 4 mg/disc of xanthone derivative was able to inhibit about 12.3 mm of *Staphylococcus aureus*, while the antibiotic ampicillin inhibited about 19.7 mm [37]. The same method of study showed that an organic solution (isopropyl alcohol/hexane) of curcumin (1 g / 10 ml) was able to inhibit about 22.3 mm *Staphylococcus aureus* [38].

Klebsiella pneumoniae was first isolated from the person who died of pneumonia, but this pathogen is also capable to cause diseases such as pyelonephritis, septicemia and meningitis. In one study, a methanolic extract of mango fruit containing mangiferin showed inhibitory activity against the growth of *Klebsiella pneumoniae*. The inhibitory zone was 12 mm (100 mg/disc) while the antibiotic kanamycin inhibited 18 mm (30 mg/disc) [39]. Another study showed that curcumin was able to inhibit the growth of *Klebsiella pneumoniae*. Curcumin dissolved in 2 % dimethyl sulfoxide had the minimum inhibitory concentration of 128 μg/ml, the antibiotic meropenem had an identical value [40].

Acinetobacter baumannii is responsible for the development of infections in the bloodstream, respiratory tract, skin and soft tissues. Mangiferin and curcumin have no pronounced antibacterial activity against this microorganism; however, when used in combination with antibiotics, these polyphenols show a synergistic effect [41,42].

Pyocyanic infection caused by *Pseudomonas aeruginosa* is a leading nosocomial infection. Ethanol solution of mangiferin exhibits an inhibitory effect against this pathogen at the minimum concentration of 62.5 μg/ml [43]. Curcumin dissolved in ethanol showed the minimum inhibitory concentration of 175 μg/ml in an antibacterial study against *Pseudomonas aeruginosa* [44].

Enterobacter spp is also one of the most frequent causes of nosocomial infections, this pathogen causes urinary and respiratory tract, skin and soft tissue infections. Acetone extract of mango peel containing mangiferin was able to inhibit the growth of *Enterobacter spp* (the zone of inhibition was 16 mm) [45]. Acetone solution of curcumin (10 mmol/L) also has antibacterial activity against this microorganism, but its zone of inhibition was only 9 mm [46].

The study of antibacterial activity against *Enterococcus faecium* and *Staphylococcus aureus* of methanol solutions of rosmarinic and carnosic acids showed that the minimum inhibitory concentration against strains of these pathogens for carnosic acid was 60 μg/ml, and rosmarinic acid was inactive even at high concentrations (480 μg/ml) [47]. In addition, the methanolic solution of carnosic acid has the minimum inhibitory concentration of 30 μg/ml against *Klebsiella pneumoniae*, while rosmarinic acid was unable to inhibit the growth of this bacterium [48]. Also, the methanolic extract of *Rosmarinus officinalis* leaves, with high content of rosmarinic and carnosic acids, is able to inhibit the growth of *Acinetobacter baumannii*. The best result was obtained using the solution with the concentration of 100 μg/ml, which had the inhibitory zone of 33 mm [49]. Another study on the antibacterial properties against *Pseudomonas aeruginosa* showed that ethanolic extract of *Rosmarinus officinalis* leaves, achieved the minimum inhibitory concentration at 128 μg/ml [50]. Despite this, neither aqueous nor ethanolic extracts of the same plant (2000 μg/ml) had antibacterial activity against *Enterobacter spp* [51].

The antibacterial activity of the considered polyphenols depends on many factors such as extraction method, degree of purification, solution composition and concentration of bioactive agent. Table 1 summarizes the ability of mangiferin, curcumin, rosmarinic acid and carnosic acid to inhibit the growth of ESKAPE bacteria.

TABLE 1. Comparative analysis of polyphenols antibacterial activity

Pathogen	Polyphenol			
	Mangiferin	Curcumin	Rosmarinic acid	Carnosic acid
Enterococcus faecium	+	+	-	+
Staphylococcus aureus	+	+	-	+
Klebsiella pneumoniae	+	+	-	+
Acinetobacter baumannii	-	-	+	+
Pseudomonas aeruginosa	+	+	+	+
Enterobacter spp	+	+	-	-

Table 1 shows that polyphenols such as curcumin and mangiferin have antibacterial activity against ESKAPE group of pathogens except *Acinetobacter baumannii* strain.

Phenolic acids are also capable of inhibiting the growth of multidrug resistant microorganisms. However, rosmarinic acid is not active against this group of pathogens, while *Rosmarinus officinalis* leaf extracts are likely to have antibacterial properties due to the carnosic acid included in the extract, which has good inhibitory ability against the ESKAPE group of bacteria except *Enterobacter spp*.

Thus, polyphenols are potential candidates for the control of infectious diseases caused by pathogens with high antimicrobial resistance. Their relevance for the use against highly resistant bacteria is due to their synergistic effect when used with existing antibiotics, as well as their different mechanisms of action on microorganisms than conventional drugs [52]. In addition, there is an opportunity to improve the antibacterial properties of polyphenols using various methods, including their introduction into delivery systems based on polymer matrices [53].

5. Nanoscale delivery systems for natural compounds with antibacterial action

Currently there are a lot of carriers which could be used for the incorporation of biologically active agent into nanoscale delivery systems. Schematic representation of the most promising nanocarriers is demonstrated in Fig. 8. More detailed information was published earlier [54, 55]. Summarized information of various nanocarriers is shown in Table 2.

5.1. Mangiferin

Mangiferin-loaded delivery systems are described in the recently published review [56].

It was many times documented that mangiferin have antioxidant, anti-infection, anti-cancer, anti-diabetic, cardiovascular, neuroprotective properties and this molecule also enhance immunity, without demonstrating any toxicity even at high doses. To improve the solubility, increase the biological effects and bioavailability, mangiferin was integrated into polymer systems. This review summarizes molecular mechanisms of anti-cancer action and also a number of designed polymer-mangiferin systems.

TABLE 2. Summarized information of various nanocarriers Reproduced under the terms of the CC-BY 4.0 license.[54] Copyright 2020, Collective authors. Published by MDPI

Nanosystems	Advantages	Limitations
Liposomes	Biodegradability Biocompatibility Reduced systemic toxicity Improved stability and circulation time of the drugs	Low drug loading Lack of colloidal stability Difficulties in sterilization Some leakage of the encapsulated agent
SLNs	Suitable for a variety of routes of administration Good physiological compatibility A wide range of drug adaptability Improve the stability of drugs	Requires organic solvent during preparation Low loading capacity compared with other nanocarriers Possibly containing other colloidal structures and complex physical state
NLCs	Stability Good biocompatibility High drug-loading capacity Targeting and controlled release Improved bioavailability of drugs	No data
Micelles	Suitable for water-insoluble drugs due to hydrophobic core	Poor chemical versatility and structural instability
PMs	Good stability Allow drugs to avoid mononuclear macrophages phagocytosis Water-insoluble drugs can be easily incorporated into PMs by the simple act of mixing	Premature drug leakage Toxicity of materials, fixed functionality after synthesis Response mechanism in the human body unknown
Polymeric NPs	Targeted, controlled drug release Easy surface functionalization	The polymer cytotoxicity Difficulty in large-scale industrial production The residual organic solvent in the preparation process
Dendrimers	Structural symmetry and stable nature Has a strong EPR Enhancement in the blood circulation time Multiple functional groups in its surface Customize the drug release profiles	Time-consuming synthesis and increased production costs Difficulties in mass production Cytotoxic and hemolytic properties
Niosomes	Overcome phospholipid oxidation	No data
Nanoemulsions	Improve drug stability To avoid drug inactivation in the gastrointestinal tract Increase drug solubility and improve bioavailability With lymphatic targeting and sustained release to reduce the side effects of drugs	No data

Nanocrystals	Free of organic solvents or other solubilizing chemicals Carrier-free delivery system High-drug loading efficiency Steady dissolution rates Great structural stability	Difficulty in large-scale industrial production
Bio-NPs	Overcome various biological barriers Lower immunogenicity and toxicity Biocompatibility and biodegradability	Limited drug loading capacity
Exosomes	High capacity to pass through various biological barriers High stability Less immunogenity Natural targeting capacity	Specific approaches to load the desired additional drugs without disturbing the exosomes
Metal NPs	Simple synthesis procedures Modifiable (control of pore size) Multifunctional surface functionalization	Poor biocompatibility Low stability Poor water solubility
Inorganic non-metallic NPs	Simple synthesis procedures	Low loading capacities
Hybrid nanomedicines	Targeted delivery of drugs Has high structural integrity Stable storage of drugs and the controlled release of drugs Increased drug encapsulation efficiency and biocompatibility	Potential material toxicity

5.2. Curcumin

Curcumin-loaded delivery systems are extremely numerous and are presented in main reviews [57–59]. However, its clinical use is extremely difficult due to the pH-dependent structure transformations of curcumin [60].

Commercially available curcumin, commonly used *in vitro* and *in vivo* studies, is the mixture of curcuminoids derived from the rhizome of *Curcuma longa Linn*, it is a mixture of three main diarylheptanoids: 75-77% is curcumin (C) (diferuloyl methane; MW $C_{21}H_{20}O_6$; log P = 3.29; MM = 368.38), 15-18% – demethoxycurcumin (DMC) (p-Hydroxycinnamoyl feruloyl methane; $C_{20}H_{18}O_5$; log P = 2.792; MM= 338.35), 5-7% –bis-demethoxycurcumin (BDMC) (di-p-hydroxycinnamoylmethane; $C_{19}H_{16}O_4$; log P = 2,649; MM = 308,33) [61–63].

According to the chemical structure, the main component of the curcuminoid mixture, curcumin is bis-α, β, an unsaturated β-diketone formed as the result of the conjugation of two ferulic acid molecules connected by a methylene bridge [64]. In the solution curcuminoid molecules are in keto-enol form stabilized by hydrogen bonds. The direction of the equilibrium shift in keto-enol tautomerism depends from the polarity of the solvent and the pH value of the solution. In nonpolar solvents, curcumin is mainly represented in the enol form, which is maintained by the formation of an intramolecular hydrogen bond, and in polar solvents curcumin passes into the diketo form [62–64]. Fig. 9 shows the structural formulas of the main diarylheptanoids and structural transitions in keto-enol tautomerism of the curcumin molecules [65].

There are three proton-donating groups in the curcumin molecule that dissociate at different pH values of the medium: a proton of the enol group (pKa=8.5) and two phenolic OH groups (pKa=10–10.5). Fig. 10 shows the ionization scheme of the hydroxyl groups of curcumin.

5.3. Rosmarinic acid

Rosmarinic acid (RA) is an important antitumour phytochemical due to its multi-targeted anti-oncological mechanisms. However, its bioavailability when ingested is limited due to poor solubility and permeability. In recent years, tremendous efforts have been made to develop nanoforms of rosmarinic acid for the treatment of cancer. However, these

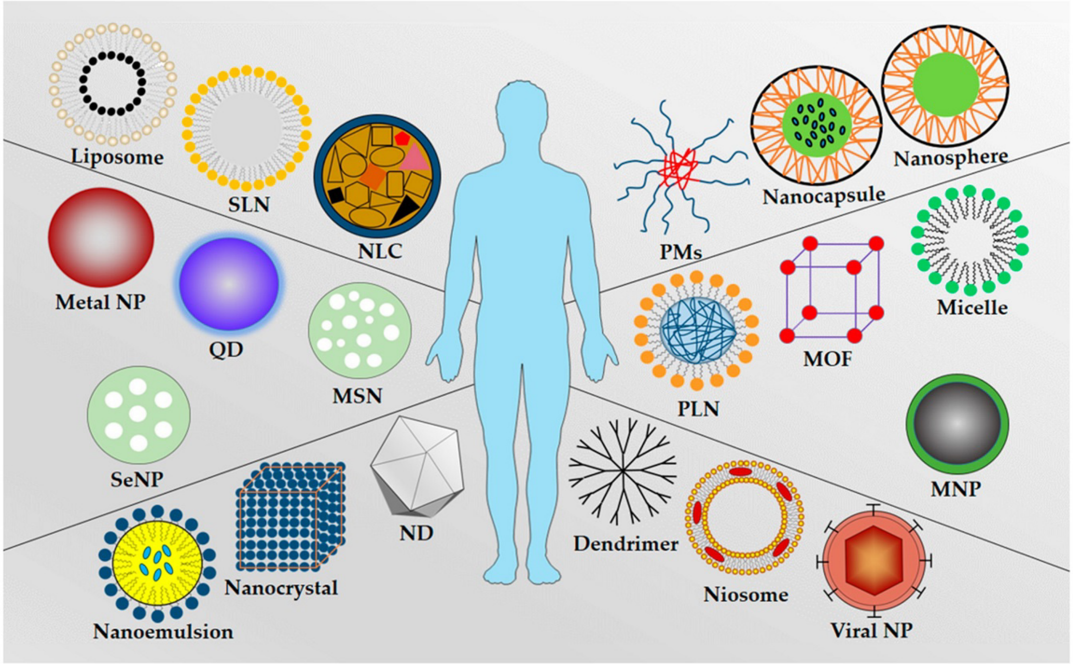

FIG. 8. Typical nanocarriers used for the loading (incorporation) of biologically active agents: dendrimer, liposome, magnetic nanoparticle (MNP), mesoporous silica nanoparticle (MSN), metal nanoparticle, metal–organic framework (MOF), micelle, nanocapsule, nanodiamond (ND), nanoemulsion, nanocrystal, nanosphere, nanostructured lipid carrier (NLC), niosome, polymer–lipid hybrid nanoparticle (PLN), polymeric micelles (PMs), selenium nanoparticle (SeNP), quantum dot (QD), solid lipid nanoparticle (SLN), viral nanoparticle. Reproduced under the terms of the CC-BY 4.0 license.[54] Copyright 2020, Collective authors. Published by MDPI

studies are at an early stage as bringing nanoparticles to the market is itself associated with numerous challenges such as stability, toxicity and scalability of the synthesis process [66].

Xue et al. developed liposomes with RA and doxorubicin, named rososomes (RS). RS were synthesized by the classical thin film hydration method. Phospholipid choline and 1-polmitoyl-2-hydroxy-sn-glycero-3-phosphocholine were taken as lipid matrix (RA-L). RA-L was obtained through the conjugation of an amphiphilic lipid to RA by the esterification method. RA-L was combined with polyethylene glycol and phosphotidylcholine to obtain RS. RS was found to have the diameter of 198.9 nm and the polydispersity index (PDI) of 0.194, indicating a rather narrow size distribution of the rhososomes. Cross-linking was carried out with trivalent iron to stabilize the structure of liposomes. *In vivo* experiments on mice with breast cancer showed that RS cross-linked with iron exhibited significant activity in cancer treatment [67].

Subongkot et al. developed ultra-deformable liposomes (ULS) of RA with fatty acids such as oleic, linoleic and linolenic acids to improve the skin penetration of RA in skin cancer. The size, zeta potential, size distribution, shape, encapsulation efficiency (% EE) and polymer matrix capacity (% DL) of the prepared ULSs were evaluated. The obtained ULSs with fatty acids had negative zeta potential and average particle size ranging from 50.37 ± 0.3 to 59.82 ± 17.3 nm. The average EE and DL were 9 % and 24 %, respectively. RA has been shown to penetrate the skin much more easily with ULS containing oleic acid than ULS without added fatty acids [68].

Fuster et al. developed silk fibroin nanoparticles containing RA (RA-SFN) and investigated their activity against breast cancer cells (MCF-7) and human cervical cancer cells (HeLa). The characteristics of the synthesized nanoparticles were determined: the average particle diameter was 255 nm, zeta potential was −17 mV, and PDI was 0.187. About 50 % of the total drug content was released in 0.5 h, indicating rapid release under physiological conditions. Studies on cell lines showed that concentration-dependent cancer cell death was observed after the treatment by RA-SNs. MCF-7 and HeLa cell death was observed at IC_{50} values of 1.568 and 1.377 mg/ml, respectively. In addition, the inhibition of cell proliferation was observed in cancer cell lines following cell cycle and apoptosis studies [69].

Tabatabaeian et al. developed a unique conjugate of NH_2-UiO-66 with nitrogen-doped carbon nanodots (N-CND) with embedded rosmarinic acid to target adenocarcinoma. The size range of the obtained particles was 35±10 nm and the zeta potential was −03.6 mV. To study the apoptotic effect, MTT assay was performed on cell line A549: apoptosis increased with the increasing nanoparticle concentration from 25 to 150 μg/ml. Thus, a new carrier of rosmarinic acid was found to be promising and cost-effective for drug delivery systems for cancer treatment [70].

Chung et al. developed PEGylated rosmarinic acid nanoparticles, (RA-NPs), for the treatment of inflammatory bowel disease and colorectal cancer. Particles with the diameter of 63.5 ± 4.0 nm were prepared from PEG-containing

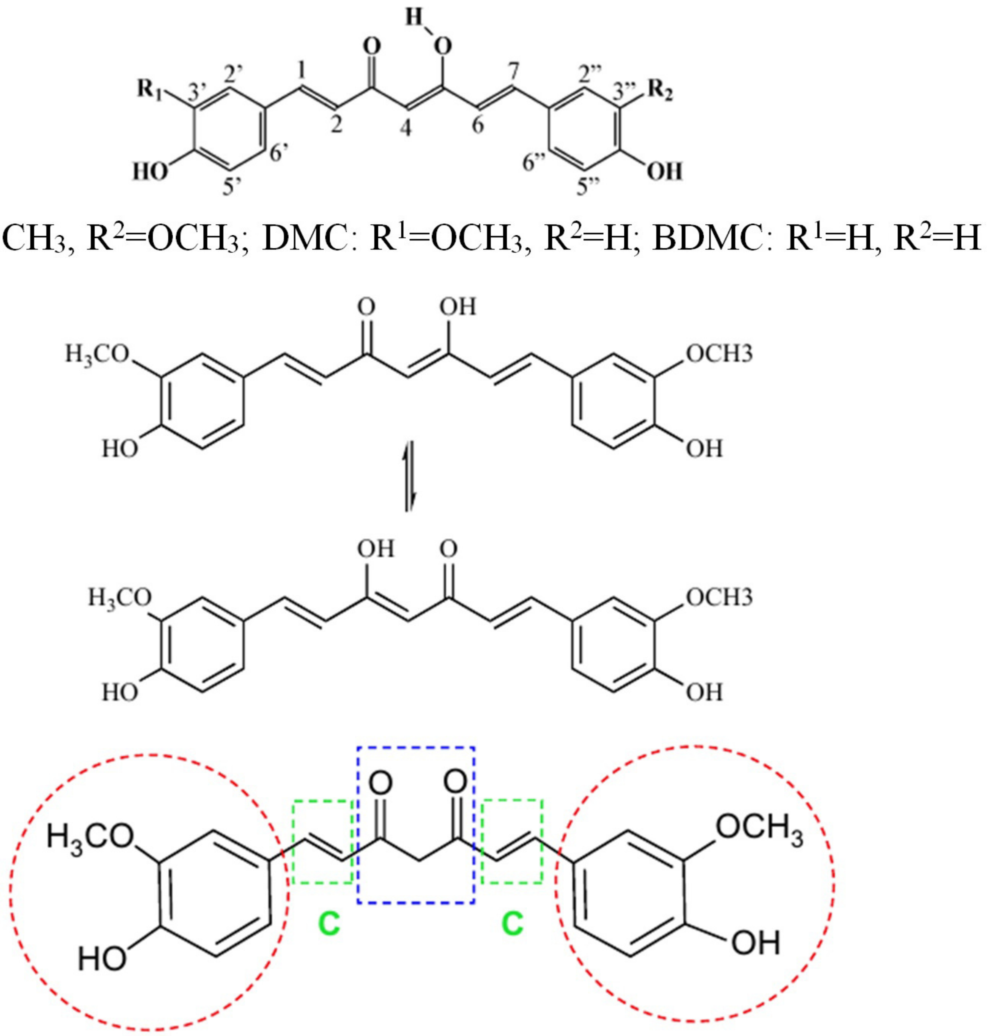

FIG. 9. Structural formulas of the main diarylheptanoids [60]

amine and rosmarinic acid in a single step followed by self-assembly in the buffer solution. In physiological media, the obtained RA-NPs exhibited good colloidal stability for a fortnight. RA-NPs could efficiently absorb hydrogen peroxide, preventing cell damage due to the oxidative stress. In inflamed colon, RA-NPs reduced the expression and production of pro-inflammatory cytokines [71].

Campos et al. developed lipid nanoparticles with rosmarinic acid. Witepsol H15 was used as a lipid shell and Tween 80 was used as the surfactant. The hot melt ultrasonication method was used. The authors used different formulations: 1 %, 2 % and 3 % vol/vol of lipid and 0.5 %, 1 % and 1.5 % wt/vol of surfactant. The results showed that nanoparticles with an average diameter ranging from 270 to 1000 nm could be obtained using Witepsol H15. The obtained particles were found to be extremely stable: during 28 days in aqueous solution at 5°C, they maintained their morphological characteristics and had no tendency to aggregate. The encapsulation efficiency of rosmarinic acid was 99 %, and rosmarinic acid was not washed out from the matrix during the storage [72].

Interestingly, rosmarinic acid in the composition of nanoparticles can be used not only as an antibacterial agent, but also as a modifier. Thus, Bhatt et al. proposed silver nanoparticles whose surface was modified with rosmarinic acid (Ro-AgNPs). Such particles can be used to create sensitive colorimetric probe sensors for the rapid determination of cyanide (CN-) and chromium (VI) [Camr(VI)] in aqueous solutions, including waste water [73].

In addition to nanoparticles, other types of nanomaterials, such as nanofibers, can be fabricated with rosmarinic acid. One of the possible methods to produce such fibers is the electroforming method of polymer solutions [74]. Thus, nanofibers based on cellulose acetate with rosmarinic acid were prepared and investigated. To evaluate the biological activity of nanofibers containing BAS, their ability to inhibit protein denaturation was analyzed as an indicator of anti-inflammatory properties, and their antioxidant activity was determined by free radical capture method. Homogeneous distribution of the drug throughout the volume of nanofibers provided high loading efficiency, absence of explosive release at the initial stages, and prolonged release for 64 h by the mechanism of diffusion according to Fick's law. The nanofibers

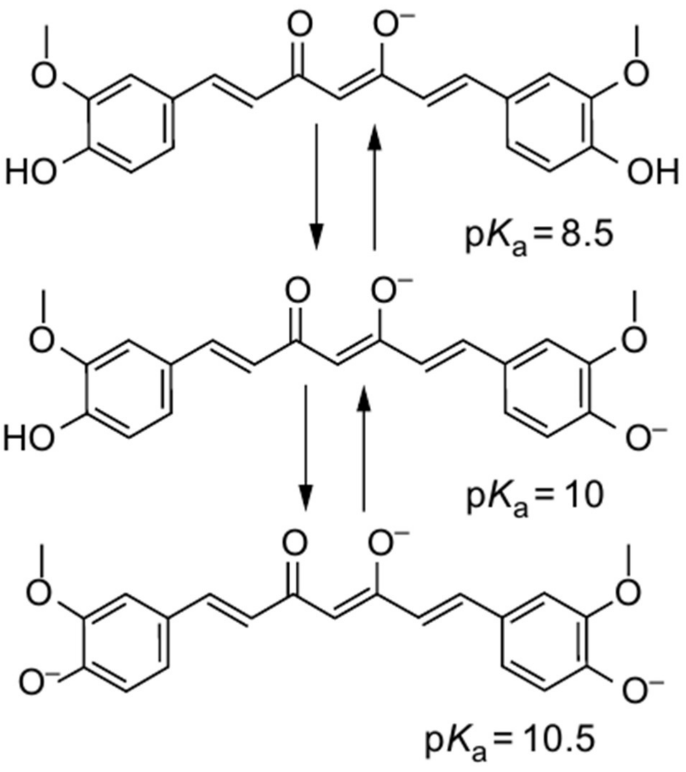

FIG. 10. Scheme of ionization of hydroxyl groups of curcumin at pH values of medium >8 [60]

with higher RA content exhibited anti-inflammatory activity comparable to ibuprofen and higher antioxidant activity compared to nanofibers with low bioactive agent content. In addition, the nanofibers did not have any significant cytotoxic effects on cells. The delayed release of RA and the biological activity of RA-containing nanofibers confirmed the potential of the obtained matrix as a drug delivery system [75].

5.4. Carnosic acid

Chitosan nanoparticles containing carnosic acid were prepared by ionotropic gelation method. The effect of factors such as chitosan concentration (0.1–1.0 % by weight), tripolyphosphate concentration (0.1–1.0 % by weight) and ultrasonic treatment time (2–10 min) on key particle parameters such as size and morphology, zeta potential, drug encapsulation efficiency and drug release kinetics were evaluated. The protein level of neurotrophins in rat brain during intranasal administration of optimized dose of carnosic acid nanoparticles was determined. The experimental values of the drug doses correlated well with those predicted by mathematical models. A single intranasal administration of carnosic acid nanoparticles was sufficient to achieve the required level of endogenous neurotrophins in the brain, which was almost the same as when chitosan solution with carnosic acid was intranasally administered to rats once a day for four days. The results clearly demonstrated the fact that the nanoparticle drug delivery system for intranasal administration of carnosic acid requires fewer injections to achieve the required pharmacological activity due to its ability to localize on the nasal mucosa and provide controlled delivery of carnosic acid over a long period of time [76].

A lecithin-based nanoemulsion (CA-NE) was developed to enhance the bioavailability and biological activity of carnosic acid (CA). The investigated material was found to have high capacity (2.80 ± 0.15 %), small particle size (172.0 ± 3.5 nm) with homogeneous particle distribution (PDI index is 0.231 ± 0.025) and zeta potential value of -57.2 ± 0.24 mV. More importantly, the bioavailability of CA-NE was improved 2.8-fold compared to the CA content of MCT oil. In addition, cellular antioxidant assay (CAA) and cellular uptake study of CA-NE in HepG2 cell model demonstrate a longer endocytosis process, indicating a controlled release of CA from CA-NE. In addition, improved anti-inflammatory activity was assessed by inhibition of the production of pro-inflammatory cytokines, nitric oxide (NO) and TNF-α in lipopolysaccharide-stimulated RAW 264.7 macrophage cells [77].

Carnosic acid was encapsulated in bovine serum albumin (BSA), chitosan (CH) and cellulose (CL) nanoparticles to enhance its activity against breast cancer (MCF-7) and colon cancer (Caco-2) cells. CA-enriched BSA nanoparticles (CA-BSA-NPs) showed good drug encapsulation efficiency and best release profile as the drug concentration reached 80 % after 10 hours. The antitumour activity of CA-BSA-NPs was evaluated by the measuring of cell viability, apoptosis rate and gene expression of GCLC, COX-2 and BCL-2 in MCF-7 and Caco-2. Cytotoxicity (MTT) assay showed enhanced antitumour activity of CA-BSA-NPs against MCF-7 and Caco-2 compared to free CA and BSA-NPs. Moreover, apoptosis test data showed growth arrest of Caco-2 cells at G2/M (10.84 %) and MCF-7 cells at G2/M (4.73 %) when treated with CA-BSA-NPs. Gene expression analysis based on OT-PCR showed the increased activity of GCLC gene and the decreased activity of BCL-2 and COX-2 genes in cells treated with CA-BSA-NPs compared to the untreated cells. In conclusion, CA-BSA-NPs have been presented as a promising formula for the treatment of breast cancer and colorectal cancer [78].

6. Conclusion

In this paper, an analytical review of natural biologically active agents exhibiting antibacterial activity, namely such polyphenols as mangiferin, curcumin, rosmarinic acid and carnosic acid has been carried out. A comparative analysis of the antibacterial properties of these natural substances against a group of microorganisms possessing multidrug resistance and virulence was also carried out.

Comparative analysis of antimicrobial activity showed that mangiferin, curcumin and carnosic acid are potential candidates to address the problem of multidrug resistance to antibacterial drugs. These natural agents can be recommended for the incorporation into advanced drug delivery systems such as nanoparticles, nanomicelles, nanocapsules, etc.

Analysis of data on delivery systems for these natural molecules has shown that for rosmarinic and carnosic acids, the number of delivery systems is extremely limited and require development based on biocompatible and biodegradable matrices with targeted action. Equally important is the review of methods used to characterize nanoscale delivery systems.

Thus, this review not only highlights the known data on natural agents with antibacterial action, but also points to new directions in the development of nanosystems and nanoscale materials for the delivery of potential drugs to combat multidrug resistance.

References

[1] Miller W.R., Arias C.A. ESKAPE pathogens: antimicrobial resistance, epidemiology, clinical impact and therapeutics. *Nat. Rev. Microbiol.*, 2024, **22**(10), P. 598–616.

[2] Zagoskina N.V. Nazarenko L.V. Secondary Plant Metabolites: Distribution, History of Study, Practical Application. *MCU J. Nat. Sci.*, 2019, **2**(34), P. 8–19.

[3] Hartmann T. The lost origin of chemical ecology in the late 19th century. *Proc. Natl. Acad. Sci. USA*, 2008, **105** (12), P. 4541–4546.

[4] Kırmusaoğlu S. *Antimicrobials, Antibiotic Resistance, Antibiofilm Strategies and Activity Methods*. Intechopen eBooks, 2019, 152 p.

[5] Boccolini P.M.M., de Lima Sírio Boclin K., de Sousa I.M. C., Boccolini C.S. Prevalence of complementary and alternative medicine (CAM) use in Brazil: results of the National Health Survey, 2019. *BMC Complement. Med. Ther.*, 2022, **20**, 205.

[6] Khameneh B., Iranshahy M., Soheili V. Fazly Bazzaz B.S. Review on plant antimicrobials: a mechanistic viewpoint. *Antimicrob. Resist. Infect. Control*, 2019, **8**, P. 118.

[7] Zvereva V.V., Boychenko M.N. *Fundamentals of microbiology and immunology*. GEOTAR-Media, Moscow, 2021, 368 p.

[8] Stan D., Enciu A.-M., Mateescu A.L., Ion A.C., Brezeanu A.C., Stan D., Tanase C. Natural Compounds With Antimicrobial and Antiviral Effect and Nanocarriers Used for Their Transportation. *Front. Pharmacol.*, 2021, **12**, P. 723233.

[9] Varaprasad B. *Antimicrobial Agents*. Intechopen, Rijeka, 2012, 434 p.

[10] Singla R.K., Dubey A.K., Garg A., Sharma R.K., Fiorino M., Ameen S.M., Haddad M.A., Al-Hiary M. Natural Polyphenols: Chemical Classification, Definition of Classes, Subcategories, and Structures. *J. AOAC Int.*, 2019, **102**(5), P. 1397–1400.

[11] Khoddami A., Wilkes M.A., Roberts T.H. Techniques for Analysis of Plant Phenolic Compounds. *Molecules*, 2013, **18**(2), P. 2328–2375.

[12] Mendonça E.L.S.S., Xavier J.A., Fragoso M.B.T., Silva M.O., Escodro P.B., Oliveira A.C.M., Tucci P., Saso L., Goulart M.O.F. *E*-Stilbenes: General Chemical and Biological Aspects, Potential Pharmacological Activity Based on the Nrf2 Pathway. *Pharmaceuticals*, 2024, **17**, P. 232.

[13] Li Y., Xie S., Ying J., Wei W., Gao K. Chemical Structures of Lignans and Neolignans Isolated from Lauraceae. *Molecules*, 2018, **23**, P. 3164.

[14] Manso T., Lores M., de Miguel T. Antimicrobial Activity of Polyphenols and Natural Polyphenolic Extracts on Clinical Isolates. *Antibiotics*, 2022, **11**(1), P. 46.

[15] Vyas A., Syeda K., Ahmad A., Padhye S., Sarkar F.H. Perspectives on medicinal properties of mangiferin. *Mini-Rev. Med. Chem.*, 2012, **12**(5), P. 412–425.

[16] Barreto J.C., Trevisan M.T., Hull W.E., Erben G., Brito E.S., Pfundstein B., Würtele G., Spiegelhalder B., Owen R.W. Characterization and quantitation of polyphenolic compounds in bark, kernel, leaves, and peel of mango (*Mangifera indica L.*). *J. Agric. Food Chem.*, 2008, **56**(14), P. 5599–5610.

[17] Pang C., Tian H., Guo X., Wang P., Han B., Yang X. Facile extraction of high-purity mangiferin from mango industrial wastes. *J. Chin. Pharm. Sci.*, 2021, **30**(10), P. 831–837.

[18] Bhatia V.K., Ramanathan J.D., Seshadri T.R. Constitution of mangiferin. *Tetrahedron*, 1967, **23**(3), P. 1363–1368.

[19] Jangra A., Arora M.K., Kisku A., Sharma S. The multifaceted role of mangiferin in health and diseases: a review. *Advances in Traditional Medicine*, 2020, **21**(3), P. 619–643.

[20] Patel K., Nixon R. Irritant Contact Dermatitis - a Review. *Curr. Dermatol. Rep.*, 2022, **11**(2), P. 41–51.

[21] Zhao Y., Wang W., Wu X., Ma X., Qu R., Chen X., Liu C., Liu Y., Wang X., Yan P., Zhang H., Pan J., Li W. Mangiferin antagonizes TNF-α mediated inflammatory reaction and protects against dermatitis in a mice model. *Int. Immunopharmacol.*, 2017, **45**, P. 174–179.

[22] Ochocka R., Hering A., Stefanowicz-Hajduk J., Cal K., Baranska H. The effect of mangiferin on skin: penetration, permeation and inhibition of ECM enzymes. *PLOS ONE*, 2017, **12**(7), P. e0181542.

[23] Karomatov I.D., Atamuradova Sh.T. Anti-inflammatory, antioxidant, immunomodulatory properties of turmeric. *Biol. Integr. Med.*, 2018, **2**(19), P. 117–131.

[24] Fu Y.-S., Chen T.-H., Weng L., Huang L., Lai D., Weng C.-F. Pharmacological properties and underlying mechanisms of curcumin and prospects in medicinal potential. *Biomed. & Pharmacother.*, 2021, **141**, P. 111888.

[25] Utz S.R., Talnikova E.E. Use of curcumin in dermatology. *Saratov Sci. Med. J.*, 2016, **12**(3), P. 484–487.

[26] Singala R.K., Dubey A.K. Phytochemical Profiling, GC-MS Analysis and α-Amylase Inhibitory Potential of Ethanolic Extract of *Cocos nucifera* Linn. Endocarp. *Endocr. Metab. & Immune Disord.: Drug Targets*, 2019, **19**(4), P. 419–442.

[27] Bankar G.R., Nayak P.G., Bansal P., Paul P., Pai K.S., Singla R.K., Bhat V.G. Vasorelaxant and antihypertensive effect of *Cocos nucifera* Linn. endocarp on isolated rat thoracic aorta and DOCA salt-induced hypertensive rats. *J. Ethnopharmacol.*, 2011, **134**(1), P. 50–54.

[28] Hitl M., Kladar N., Gavaric N., Bozin B. Rosmarinic Acid–Human Pharmacokinetics and Health Benefits. *Planta Medica*, 2021, **87**(4), P. 273–282.

[29] Petersen M., Abdullah Y., Benner J., Eberle D., Gehlen K., Hucherig S., Janiak V., Kim K.H., Sander M., Weitzel C., Wolters S. Evolution of rosmarinic acid biosynthesis. *Phytochemistry*, 2009, **70**, P. 1663–1679.

[30] Noor S., Mohammad T., Rub M.A., Raza A., Azum N., Yadav D.K., Hassan M.I., Asiri A.M. Biomedical features and therapeutic potential of rosmarinic acid. *Arch. Pharm. Res.*, 2022, **45**, P. 205–228.

[31] Habtemariam S. Anti-Inflammatory Therapeutic Mechanisms of Natural Products: Insight from Rosemary Diterpenes, Carnosic Acid and Carnosol. *Biomedicines*, 2023, **11**(2), P. 545.

[32] Bahri S., Jameleddine S., Shlyonsky V. Relevance of carnosic acid to the treatment of several health disorders: Molecular targets and mechanisms. *Biomed. & Pharmacother.*, 2016, **84**, P. 569–582.

[33] Asokan G.V., Ramadhan T., Ahmed E., Sanad H. WHO Global Priority Pathogens List: A Bibliometric Analysis of Medline-PubMed for Knowledge Mobilization to Infection Prevention and Control Practices in Bahrain. *Oman Med. J.*, 2019, **34**(3), P. 184–193.

[34] Mulani M.S., Kambale E.E., Kumkar S.N., Tawre M.S., Pardesi K.R. Emerging Strategies to Combat ESKAPE Pathogens in the Era of Antimicrobial Resistance: A Review. *Front. Microbiol.*, 2019, **10**, P. 539.

[35] Arunajatesan S., Krishna M., Sivan P., Kesavaram P., Paramasivam V., Ganapathy S.V. Antibacterial efficacy of *Mangifera indica* L. kernel and *Ocimum sanctum* L. leaves against *Enterococcus faecalis* dentinal biofilm. *J. Conserv. Dent.*, 2013, **16**(5), P. 454–457.

[36] Moradi M., Fazlyab M., Pourhajibagher M., Chiniforush N. Antimicrobial action of photodynamic therapy on *Enterococcus faecalis* biofilm using curing light, curcumin and riboflavin. *Aust. Endod. J.*, 2021, **48**(2), P. 274–282.

[37] Mazlan N.A., Azman S., Ghazali N.F., Yusri P.Z.S., Idi H.M., Ismail M., Sekar M. Synergistic antibacterial activity of mangiferin with antibiotics against *Staphylococcus aureus*. *Drug Invention Today*, 2019, **12**(1), P. 14–17.

[38] Hettiarachchi S.S., Perera Y., Dunuweera S.P., Dunuweera A.N., Rajapakse S., Rajapakse M.G. Comparison of Antibacterial Activity of Nanocurcumin with Bulk Curcumin. *ACS Omega*, 2022, **7** (50), P. 46494–46500.

[39] Sarker A., Amin N., Shimu I.J., Akhter Md.P., Alam Md.A., Rahman Md.M., Sultana H. Antimicrobial activity of methanolic extract of langra mango pulp. *J. Pharmacogn. Phytochem.*, 2017, **6**(6), P. 28–30.

[40] Sharahi J.Y., Ahovan Z.A., Maleki D.T., Rad Z.R., Rad Z.R., Goudarzi M., Shariati A., Bostanghadiri N., Abbasi E., Hashemi A. *In vitro* antibacterial activity of curcumin-meropenem combination against extensively drug-resistant (XDR) bacteria isolated from burn wound infections. *Avicenna J. Phytomed.*, 2020, **10**(1), P. 3–10.

[41] Vasudevan A., Kesavan D.K., Wu L., Su Z., Wang S., Ramasamy M.K., Hopper W., Xu H. *In Silico* and *In Vitro* Screening of Natural Compounds as Broad-Spectrum β-Lactamase Inhibitors against *Acinetobacter baumannii* New Delhi Metallo-β-lactamase-1 (NDM-1). *BioMed Res. Int.*, 2022, **2022**, P. 1–19.

[42] Kaur A., Sharma P., Capalash N. Curcumin alleviates persistence of *Acinetobacter baumannii* against colistin. *Sci. Rep.*, 2018, **8**, P. 11029.

[43] Nguyen H.T., Miyamoto A., Hoang H.T., Vu T.T.T., Pothinuch P., Nguyen H.T.T. Effects of Maturation on Antibacterial Properties of Vietnamese Mango (*Mangifera indica*) Leaves. *Molecules*, 2024, **29**(7), P. 1443.

[44] Gunes H., Gulen D., Mutlu R., Gumus A., Tas T., Topkaya A.E. Antibacterial effects of curcumin: An *in vitro* minimum inhibitory concentration study. *Toxicol. Ind. Health*, 2013, **32**(2), P. 246–250.

[45] Thambi P.A., John S., Lydia E., Iyer P., Monica S.J. Antimicrobial efficacy of mango peel powder and formulation of recipes using mango peel powder (*Mangifera indica* L.). *Int. J. Home Sci.*, 2016, **2**(2), P. 155–161.

[46] Kim M.K., Park J.C., Chong Y. Aromatic Hydroxyl Group Plays a Critical Role in Antibacterial Activity of the Curcumin Analogues. *Nat. Prod. Commun.*, 2012, **7**(1), P. 57–58.

[47] Zampini I.C., Arias M.E., Cudmani N., Ordonez R.M., Isla M.I., Moreno S. Antibacterial potential of non-volatile constituents of *Rosmarinus officinalis* against 37 clinical isolates of multidrug-resistant bacteria. *Bol. Latinoam. Caribe Plantas Med. Aromát.*, 2013, **12**(2), P. 201–208.

[48] Moreno S., Scheyer T., Romano C.S., Vojnov A.A. Antioxidant and antimicrobial activities of rosemary extracts linked to their polyphenol composition. *Free Radic. Res.*, 2006, **40**(2), P. 223–231.

[49] Tawfeeq A.A., Mahdi M.F., Abaas I.S., Alwan A.H. Phytochemical and antibacterial studies of leaves of *Rosmarinus officinalis* cultivated in Karbala, Iraq. *Al Mustansiriyah J. Pharm. Sci.*, 2017, **17**(2), P. 9.

[50] Amaral G.P., Mizdal C.R., Stefanello S.T., Mendez A.S.L., Puntel R.L., de Campos M.M.A., Soares F.A.A., Fachinetto R. Antibacterial and antioxidant effects of *Rosmarinus officinalis* L. extract and its fractions. *J. Tradit. Complement. Med.*, 2019, **9**(4), P. 383–392.

[51] Yazdi F.T., Behbahani B.A., Mortazavi A. Investigating the Minimum Inhibitory Concentration (MIC) and Minimum Bactericidal Concentration (MBC) of the *Lavandula stoechas* L. and *Rosmarinus officinalis* L. extracts on pathogen bacterias "*in vitro*". *J. Paramed. Sci.*, 2014, **5**(2), P. 91–101.

[52] Biharee A., Sharma A., Kumar A., Jaitak V. Antimicrobial flavonoids as a potential substitute for overcoming antimicrobial resistance. *Fitoterapia*, 2020, **146**, P. 104720.

[53] Parmanik A., Das S., Kar B., Bose A., Dwivedi G.R., Pandey M.P. Current Treatment Strategies Against Multidrug-Resistant Bacteria: A Review. *Curr. Microbiol.*, 2022, **79**(12), P. 388.

[54] Wei, Q.-Y., Xu, Y.-M., Lau, A.T.Y. Recent Progress of Nanocarrier-Based Therapy for Solid Malignancies. *Cancers*, 2020, **12**, P. 2783.

[55] Peng, S., Yuan, X., Li, H., Wei, Y., Zhou, B., Ding, G., & Bai, J. Recent progress in nanocarrier-based drug delivery systems for antitumour metastasis. *European journal of medicinal chemistry*, 2023, **252**, P. 115259.

[56] Morozkina S.N., Nhung Vu T.H., Generalova Y.E., Snetkov P.P., Uspenskaya M.V. Mangiferin as New Potential Anti-Cancer Agent and Mangiferin-Integrated Polymer Systems-A Novel Research Direction. *Biomolecules*, 2021, **11**(1), P. 79.

[57] Bansal S.S., Goel M., Aqil F., Vadhanam M.V., Gupta R.C. Advanced drug delivery systems of curcumin for cancer chemoprevention. *Cancer Prev. Res. (Phila)*, 2011, **4**(8), P. 1158–1171.

[58] Wu X., Yang Y. Research progress on drug delivery systems for curcumin in the treatment of gastrointestinal tumors. *World Journal of Gastrointestinal Oncology*, 2023, **15**(8), P. 1342–1348.

[59] Rahimi H.R., Nedaeinia R., Sepehri Shamloo A., Nikdoust S., Kazemi Oskuee R. Novel delivery system for natural products: Nano-curcumin formulations. *Avicenna J. Phytomed.*, 2016, **6**(4), P. 383–398.

[60] Kapustin M.A., Chubarova V.G., Tsyhankov V.P., Kurchenko V.P. Isolation of curcuminoids from the rhizome of curcuma longa L and the study of the composition of the resulting drug using chromatographic analysis methods. *Belarussian State University, seria Chemistry of natural and synthetic biologically active compounds*, 2016, **11**(2), P. 248–262.

[61] Aggarwal B.B., Sundaram C., Malani N., Ichikawa H. Curcumin: the indian solid gold in health and disease. *Advances in experimental medicine and biology*, 2007, **595**, P. 1–75.

[62] Wiggers H.J., et. Al. Curcumin, a multitarget phytochemical: challenges and perspectives. *Studies in Natural Products Chemistry*, 2017, **53**, P. 243–276.

[63] Priyadarsini K.I. The chemistry of curcumin: from extraction to therapeutic agent. *Molecules*, 2014, **19**(2), P. 20091–20112.

[64] Esatbeyoglu T. Curcumin – from molecule to biological function. *Angewandte Chemie (International Edition in English)*, 2012, **51**(22), P. 5308–5332.

[65] Noorafshan A., Soheil A.E. A Review of Therapeutic Effects of Curcumin. *Current Pharmaceutical Design*, 2013, **19**, P. 2032–2046.

[66] Chaitanya M.V.N.L., Ramanunny A.K., Babu M.R., Gulati M., Vishwas S., Singh T.G., Chellappan D.K., Adams J., Dua K., Singh S.K. Journey of Rosmarinic Acid as Biomedicine to Nano-Biomedicine for Treating Cancer: Current Strategies and Future Perspectives. *Pharmaceutics*, 2022, **14**(11), P. 2401.

[67] Xue X., Ricci M., Qu H., Lindstrom A., Zhang D., Wu H., Lin T.-Y., Li Y. Iron-crosslinked rososome with robust stability and high drug loading for synergistic cancer therapy. *J. Control. Release*, 2020, **329**, P. 794–804.

[68] Subongkot T., Ngawhirunpat T., Opanasopit P. Development of Ultradeformable Liposomes with Fatty Acids for Enhanced Dermal Rosmarinic Acid Delivery. *Pharmaceutics*, 2021, **13**(3), P. 404.

[69] Fuster M.G., Carissimi G., Montalbán M.G., Víllora G. Antitumor activity of rosmarinic acid-loaded silk fibroin nanoparticles on HeLa and MCF-7 cells. *Polymers*, 2021, **13**(18), P. 3169.

[70] Tabatabaeian K., Simayee M., Fallah S.A., Mashayekhi F. N-Doped Carbon Nanodots@UiO-66-NH(2) as Novel Nanoparticles for Releasing of the Bioactive Drug, Rosmarinic Acid and Fluorescence Imaging. *DARU J. Pharm. Sci.*, 2019, **27**(1), P. 307–315.

[71] Chung C.H., Jung W., Keum H., Kim T.W., Jon S. Nanoparticles derived from the natural antioxidant rosmarinic acid ameliorate acute inflammatory bowel disease. *ACS Nano*, 2020, **14**(6), P. 6887–6896.

[72] Campos D.A., Madureira A.R., Gomes A.M., Sarmento B., Pintado M.M. Optimization of the production of solid witepsol nanoparticles loaded with rosmarinic acid. *Colloids Surf. B Biointerfaces*, 2013, **115**, P. 109–117.

[73] Bhatt S., Vyas G., Paul P. Rosmarinic acid-capped silver nanoparticles for colorimetric detection of cn- and redox-modulated surface reaction-aided detection of Cr(VI) in water. *ACS Omega*, 2022, **7**(1), P. 1318–1328.

[74] Lian S., Lamprou D., Zhao M. Electrospinning technologies for the delivery of Biopharmaceuticals: Current status and future trends. *Int. J. Pharm.*, 2024, **651**, P. 123641.

[75] Vatankhah E. Rosmarinic acid-loaded electrospun nanofibers: *In vitro* release kinetic study and bioactivity assessment. *Eng. Life Sci.*, 2018, **18**(10), P. 732–742.

[76] Vaka S.R., Shivakumar H.N., Repka M.A., Murthy S.N. Formulation and evaluation of carnosic acid nanoparticulate system for upregulation of neurotrophins in the brain upon intranasal administration. *J. Drug Target.*, 2012, **21**(1), P. 44–53.

[77] Zheng H., Li J., Ning F., Wijaya W., Chen Y., Xiao J., Cao Y., Huang Q. Improving in vitro bioaccessibility and bioactivity of carnosic acid using a lecithin-based nanoemulsion system. *Food & Funct.*, 2020, **12** (4), P. 1558–1568.

[78] Khella K.F., Abd El Maksoud A.I., Hassan A., Abdel-Ghany S.E., Elsanhoty R.M., Aladhadh M.A., Abdel-Hakeem M.A. Carnosic Acid Encapsulated in Albumin Nanoparticles Induces Apoptosis in Breast and Colorectal Cancer Cells. *Molecules*, 2022, **27**(13), P. 4102.

Submitted 17 November 2024; revised 28 November 2024; accepted 29 November 2024

Information about the authors:

Vladislava I. Klimshina – ITMO University, Kronverkskiy pr., 49, bldg. A, St. Petersburg, 197101, Russia; ORCID 0000-0002-9979-3922

Roman O. Shaikenov – ITMO University, Kronverkskiy pr., 49, bldg. A, St. Petersburg, 197101, Russia; ORCID 0009-0005-1721-1044

Svetlana N. Morozkina – ITMO University, Kronverkskiy pr., 49, bldg. A, St. Petersburg, 197101, Russia; Kabardino-Balkarian State University, Chernyshevskogo 173, Nalchik, Russia; ORCID 0000-0003-0122-0251

Aleksey E. Romanov – ITMO University, Kronverkskiy pr., 49, bldg. A, St. Petersburg, 197101, Russia; ORCID 0000-0003-3738-408X

Petr P. Snetkov – ITMO University, Kronverkskiy pr., 49, bldg. A, St. Petersburg, 197101, Russia; ORCID 0000-0001-9949-5709; ppsnetkov@itmo.ru

Conflict of interest: the authors declare no conflict of interest.

NANOSYSTEMS:
PHYSICS, CHEMISTRY, MATHEMATICS

Kuznetsova T.A., et al. *Nanosystems: Phys. Chem. Math.*, 2024, **15** (6), 950–958.
http://nanojournal.ifmo.ru
DOI 10.17586/2220-8054-2024-15-6-950-958

Original article

Thermodynamics of gas mixtures in nanoporous materials: Extension to non-ideal systems at high pressures

Tatiana A. Kuznetsova[1,a], Eugene A. Ustinov[2,b]

[1]Chemistry Department, Lomonosov Moscow State University, Russian Federation
[2]Ioffe Institute, St. Petersburg, Russian Federation

[a]tchess54@mail.ru, [b]eustinov@mail.ioffe.ru

Corresponding author: E. A. Ustinov, eustinov@mail.ioffe.ru

ABSTRACT In this work, we developed a phenomenological approach to describe the equilibrium adsorption of nonideal gas mixtures in nanoporous adsorbents over a wide pressure range. The key point of the developed approach is an observation that the Gibbs free energy of a gas mixture is close to its ideal term. This feature, being more general than the empirical Raoult's law in the ideal adsorbed solution theory (IAST), was combined with the distribution of elements of the adsorption volume (EAV) of the porous material over potentials in the spirit of Polanyi's theory. We applied this approach to the adsorption of individual and binary gas mixtures of CO_2, CH_4, and N_2 on an activated carbon in a wide pressure range up to 13 MPa. The approach provides high accuracy in predicting the adsorption of gas mixtures based on individual adsorption isotherms and obeys the Gibbs-Duhem equation, which confirms its thermodynamic consistency.

KEYWORDS high-pressure adsorption, supercritical gases, nanoporous carbons, mixture adsorption, adsorbed phase thermodynamics, equation of state.

ACKNOWLEDGEMENTS The research was carried out within the framework of the state assignment on topic No. 121031300090-2 (TAK) and No. 0081-2022-0008 (EAU).

FOR CITATION Kuznetsova T.A., Ustinov E.A. Thermodynamics of gas mixtures in nanoporous materials: Extension to non-ideal systems at high pressures. *Nanosystems: Phys. Chem. Math.*, 2024, **15** (6), 950–958.

1. Introduction

Multicomponent adsorption of supercritical gas mixtures by nanoporous materials, in particular activated carbons, is widely used in gas separation and purification processes. In some cases, it is necessary to separate gases with similar physical properties, for example, nitrogen and methane, to reduce methane emissions into the environment or to purify natural gas from nitrogen during its liquefaction. In other cases, it is necessary to separate gases that have significantly different physical properties, such as carbon dioxide, methane, and nitrogen, which are part of the biogas. Biogas is a promising source of methane as a "green" fuel. Ensuring the efficiency of gas separation processes by adsorption requires reliable theoretical approaches for predicting multicomponent adsorption equilibrium. The theory of ideal adsorbed solution (IAST) of Myers and Prausnitz [1] has received the greatest application in describing multicomponent adsorption of gases. The ideality of the adsorbed solution essentially means the ideality of the bulk phase, which allowed the authors to resort to Raoult's law as an analog in relation to the adsorption system. This imposes obvious restrictions on the use of IAST when modeling the binary adsorption of CO_2–CH_4 or CO_2–N_2 mixtures by activated carbons at high pressures, reaching 1 [2], 2.5 [3, 4], 6 [5], and even 14 MPa in some studies [6–8]. It has been established [2] that the accuracy of the IAST prediction of phase diagrams at constant pressure in the gas phase increases with increasing pressure from 0.1 to 1 MPa, while the deviation between predicted and experimental values decreases from 30 to 5.5%. It was also observed [3] that IAST provides a good prediction of the CO_2–CH_4 mixture over a whole pressure range from 0 to 3 MPa. However, later, the same authors [4] pointed out that the same system is well described by IAST only in the range of 0–1.5 MPa. Additional contradictions arise due to the use of extensions of the Langmuir and Sipps equations for multicomponent adsorption [2, 5, 7, 8], although it is known that such extensions are thermodynamically valid only for the same limiting values of individual adsorption of mixture components [9]. This requirement is usually ignored. To overcome some shortcomings of the original IAST, some improvements were made to it. Thus, the heterogeneity of the adsorbent was introduced into the theory [10], suggesting that adsorption occurs independently on each surface area with the same energy. The authors called this modification HIAST. In a number of cases, this provided better agreement with experimental data. A more extended approach called the multispace adsorption model (MSAM) was presented by Jensen et al. [11]. The authors proceeded from the idea of the non-uniformity of the adsorption phase and introduced two spaces in the adsorption volume. In the first space, presumably near the pore walls, adsorption occurs independently, while in the second, the amount of the adsorbed mixture and its composition depend on those in the first space. As in the previous case, the IAST was used in combination with the energy distribution of elements of the adsorption volume, determined from individual adsorption isotherms. The authors successfully applied their approach to the adsorption of a methane-ethane mixture on an activated carbon at bulk pressures up to 30 bar. A similar idea was developed in the MPD (Myers-Prausnitz-Dubinin) model [12], where the Dubinin-Radushkevitch (DR) equation, extended to the supercritical region [13], was combined with the IAST. The authors applied their model to the adsorption of a CO_2–CH_4 mixture on a commercial activated carbon at constant pressures (0.1 and 1 MPa) and temperatures of 273 and 298 K and demonstrated excellent agreement between the calculated phase diagrams and experimental data. One more group of works rely on equations of state (EOS) extended to mixtures using arbitrary chosen combining rules for various parameters [6, 14–16]. This option requires reliable theoretical approaches for predicting multicomponent adsorption equilibrium.

Apparently, the most coherent approach is described in [17, 18], which is close to our model used in this study. The theoretical basis of the approach, called the Multicomponent Potential Theory of Adsorption (MPTA), follows from Polanyi's idea [19] of an adsorption potential distributed over the adsorption space, which contributes to the chemical potential in the adsorbed phase and, consequently, shifts the vapor-liquid equilibrium towards lower pressure values. The second assumption in the MPTA, taken from Polanyi's theory, was that a gas under the influence of an adsorption field behaves in accordance with its normal equation of state. The potential distribution, which can be obtained by analyzing adsorption isotherms of pure components, was used by the authors in the form of the DR equation extended to the supercritical region. The use of some additional assumptions to extend the equation of state to mixtures made it possible to describe with acceptable accuracy the adsorption of binary gas mixtures under high pressure on activated carbons and MOF.

This work is also based on Polanyi's idea of independent adsorption in elements of adsorption volume distributed over potential. We used this approach previously for determining the potential distribution function of an activated carbon [20] from the individual adsorption isotherms. Further, we extended this approach to the adsorption of gas mixtures using the Bender EOS and a set of combining rules for several EOS parameters [16]. Here we use a more general and rigorous thermodynamic method for extending EOS to gas mixtures, reminiscent of the idea behind IAST. In the present study, we apply the approach only to supercritical systems under high-pressure conditions, which poses a significant challenge for accurately describing mixture adsorption.

2. Model and thermodynamics

We rely on a simplified model of the elements of adsorption volume (EAV) [16, 20] distributed over the potential. Each element of the adsorption volume is not necessarily associated with a specific micro- or mesopore of the adsorbent. An element that is characterized by a certain potential, u, can simultaneously belong to several pores of different sizes or parts of them, if the potential inside them is not uniform. Thus, the distribution of EAVs of potential is an indirect characteristic of the porous structure of the adsorbent, not directly related to the pore size distribution. The absence of a specific physical image of the structure of active carbons in the proposed model is to some extent justified by their actual complexity, but nevertheless allows us to apply thermodynamics to a quantitative description of the relationship between the adsorption of individual components and their mixtures.

2.1. Individual adsorption

Let $f(u)$ be the distribution function of EAVs on the potential u, so that the integral of f is the pore volume of the adsorbent, W_0, i.e.,

$$W_0 = \int\limits_{u_{\min}}^{u_{\max}} f(u)du. \tag{1}$$

Then the amount adsorbed of an individual component is:

$$a = \int\limits_{u_{\min}}^{u_{\max}} \rho(T, \mu - \beta u) f(u)du. \tag{2}$$

Here ρ is the density of the adsorbed phase that depends on temperature, T and the intrinsic chemical potential $\mu' = \mu - \beta u$, where μ is the chemical potential in the bulk phase and β is the affinity coefficient of the component.

The density of the adsorbed phase can be determined using any equation of state. In this study we relied on Bender EOS for the pressure as a function of T and ρ [21]:

$$p = \rho RT + T\sum_{k=1}^{5} B_k\rho^{k+1} + T(B_6 + B_7\rho^2)\rho^3 \exp(-a_{20}\rho^2). \tag{3}$$

Here R is the gas constant; parameters B_k (k = 1,...,7) are functions of temperature. In total, twenty EOS constants a_k (k = 1,..., 20) have been determined for many gases. The chemical potential can easily be obtained in an analytical form by integration the relation $d\mu = \rho^{-1}dp$:

$$\mu = RT\ln\rho + \mu^r. \tag{4}$$

The first and second terms in the right side of Eq. (4) are the ideal and residual parts of the chemical potential, respectively. The standard chemical potential $\mu^\circ(T)$ is omitted because it cancels out in all balance ratios. For the residual chemical potential we have:

$$\mu^r = T\sum_{k=1}^{5} B_k \frac{k+1}{k}\rho^k + T\left[(B_6 + B_7\rho^2)\left(\rho^2 - \frac{1}{2a_{20}}\right) - B_7\frac{1}{2a_{20}^2}\right]\exp(-a_{20}\rho^2). \tag{5}$$

For a given chemical potential μ in the bulk phase, the density in the EAV with potential u is the root of the following equation:

$$RT\ln\rho + \mu^r(T,\rho) = \mu - \beta u. \tag{6}$$

Having an adsorption isotherm, it is possible to determine the distribution of EAVs over potential u for a specific adsorbent.

2.2. Binary mixture adsorption

As shown in [22], the entropy of mixing of a supercritical Ar-Kr mixture is very close to the ideal mixing entropy even at high pressures (at least up to 200 bar), when the densities of the gas components are comparable to the densities of liquid phases at subcritical temperatures, i.e., the supercritical individual gases were not ideal. It was also shown, that the enthalpy of mixing of the same Ar-Kr mixture is weakly convex function of composition and does not exceed 0.11 kJ/mol. This means that the Gibbs free energy of mixing is also close to the corresponding ideal value, i.e.,

$$G = n_1\mu_1 + n_2\mu_2 = n_1\mu_1^\circ + n_2\mu_2^\circ + RT\left(n_1\ln x_1 + n_2\ln x_2\right). \tag{7}$$

Here n_j, μ_j are number of molecules of the component j (j = 1,2) and its chemical potential at a given pressure p; μ_j° is the chemical potential of the individual component j at the same pressure p; x_1, x_2 are molar fractions of component 1 and 2, respectively. From Eq. (7) it follows that

$$\mu_j^\circ = \mu_j - RT\ln x_j, \quad j = 1,2. \tag{8}$$

Given the potential u in a particular EAV, Eqs. (8) can be rearranged to the following form:

$$\mu\text{'}_j^\circ = \mu_j - \beta_j u - RT\ln x_j, \quad j = 1,2. \tag{9}$$

Here the apostrophe means that the chemical potential is taken in the adsorbed phase (EAV) at the pressure Π not equal to the bulk pressure p. We also take into account the different affinity coefficients of the components relative to the potential u. The density ρ_j° of component j corresponds to the chemical potential $\mu\text{'}_j^\circ$ when this component is individual at the same temperature and pressure Π as in the mixture, while

$$\frac{\rho_1}{\rho_1^\circ} + \frac{\rho_2}{\rho_2^\circ} = 1. \tag{10}$$

It is important to note that Eq. (10) is a consequence of the Gibbs-Duhem equation and therefore has a general form regardless whether the system and individual components are ideal or not.

The system of Eqs. (8) and (10) is sufficient to determine the densities in EAV with the potential u. The algorithm is as follows.

(1) Having a pair of chemical potentials μ_1 and μ_2 in the bulk phase, eliminating x_1 and x_2 (= 1 – x_1) from Eqs. (9) leads to the following relationship:

$$\exp\left(\frac{\mu_1 - \beta_1 u - \mu\text{'}_1^\circ}{RT}\right) + \exp\left(\frac{\mu_2 - \beta_2 u - \mu\text{'}_2^\circ}{RT}\right) = 1. \tag{11}$$

The root of this equation is pressure Π, which immediately gives values of $\mu\text{'}_1^\circ$, $\mu\text{'}_2^\circ$, ρ_1°, and ρ_2°.

(2) Knowing $\mu\text{'}_1^\circ$, $\mu\text{'}_2^\circ$, the composition of the mixture can be determined using any of equations (9).

(3) Once the composition is known, the total density in the EAV is

$$\rho_1 + \rho_2 = 1/\left[x_1/\rho_1^\circ + x_2/\rho_2^\circ\right]. \tag{12}$$

The above equation follows from Eq. (10).

(4) Densities in the EAV are defined as

$$\rho_j = x_j(\rho_1 + \rho_2), \quad j = 1,2. \tag{13}$$

(5) Finally, the amount adsorbed of the component j is determined as

$$a_j = \int_{u_{\min}}^{u_{\max}} \rho_j(T,\mu_1,\mu_2,u)f(u)du, \quad j = 1,2. \tag{14}$$

2.3. The case of an ideal bulk phase

First, let us consider the case when adsorption occurs in a thin layer on a homogeneous surface. Then the composition of the adsorbed phase does not change over its volume at given chemical potentials μ_1 and μ_2, and the values μ_1°, μ_2° in Eqs. (8) correspond to chemical potential of individual gases in the bulk phase at the same pressure Π in the adsorption phase. If, in addition, the bulk phase is ideal, then from Eqs. (8) we have:

$$p_j = x_j p_j^\circ, \quad j = 1, 2. \tag{15}$$

This is Raoult's law adopted for the adsorbed phase in the ideal adsorbed solution theory (IAST) [1]. The values p_1°, p_2° are bulk pressures of individual components when the corresponding amounts adsorbed a_1°, a_1° are at the same pressure Π in the adsorption phase. Since the density of each component is uniformly distributed throughout the adsorbed phase, the following relationship can be written instead of Eq. (10):

$$\frac{a_1}{a_1^\circ} + \frac{a_2}{a_2^\circ} = 1. \tag{16}$$

Interestingly, Eq. (16) is very general and is also valid in the case of non-uniform adsorption phase, but values a_1°, a_1° are determined at the same average adsorbed phase pressure $\bar{\Pi}$ that can be easily calculated from individual adsorption isotherms.

Thus, IAST is a special case of a more general approach considered in this study. The advantage of IAST is that the use of EOS is not required. Instead, one can use a specific form of adsorption isotherm for each component, which is much simpler. On the other hand, the disadvantage is the limitation to the region of low pressures of the mixture, when the bulk phase is ideal.

2.4. Non-ideality of the adsorbed phase

In a more general case, it is reasonable to account for the non-ideality of the adsorption phase, which may be associated with the effect of the pore walls on the confined gas mixture. All existing equations for activity coefficients are derived under the condition of constant pressure. In the limiting case of very low pressures, the gas mixture must be ideal. For this reason, in this work we relied on the simplest Margules equation, which in our case is included in Eqs. (9) as follows:

$$\mu'^\circ_j = \mu_j - \beta_j u - RT\left[\ln x_j + \alpha\Pi(1 - x_j)^2\right], \quad j = 1, 2. \tag{17}$$

The only constant α can be determined by the least-squares fitting procedure.

3. Results and discussion

3.1. Individual isotherms

In this section, we consider the adsorption isotherms of pure gases by activated carbon by utilizing the model of elements of adsorption volume distributed by potential energy. A preliminary analysis of the results previously obtained in the framework of this model using the regularization method ([16, 20]) showed that of the EAV distribution is well approximated by the following simple function:

$$f(u) = b_1 \exp(-b_2 u + b_3 u^2). \tag{18}$$

It is assumed that this equation is written for the reference component (in our case CO_2) and the three coefficients are the same for any other gas, but its difference in the potential of interaction with EAV is taken into account by the affinity coefficient β. This means that describing of, for example, three isotherms of pure components requires the determination of five coefficients, including an additional two affinity coefficients for gases other than the reference. Joint processing of several adsorption isotherms reduces the total number of coefficients and, thereby, increases the reliability of determining the EAS distribution function by reducing their interrelation. An additional coefficient is the upper limit of the potential u_{max} for a specific activated carbon and the lower limit u_{min} can formally be taken equal to $-\infty$, since the exponential function decreases sharply with decreasing potential, starting from a certain value.

Figure 1a shows the isotherm of excess adsorption of CO_2, CH_4, and N_2 on activated carbon Filtrasorb-400 at 318.2 K from data published by M. Sudibandryo et.al. [6]. This activated carbon is manufactured by Calgon Carbon Corporation and is specified by the manufacturer to have an effective pore size distribution ranging from 0.55 to 0.75 nm (average 0.64 nm).

It is known that the adsorption excess can be directly determined by experiment, whereas absolute values of amount adsorbed require additional assumptions about the volume of the adsorbed phase. For this reason, we further compare theoretical results only with excess adsorption in the case of both individual and binary experimental adsorption data. The excess adsorption was calculated using the following equation:

$$a = \int_{u_{\min}}^{u_{\max}} \left[\rho(T, \mu - \beta u) - \rho(T, \mu)\right] f(u) du. \tag{19}$$

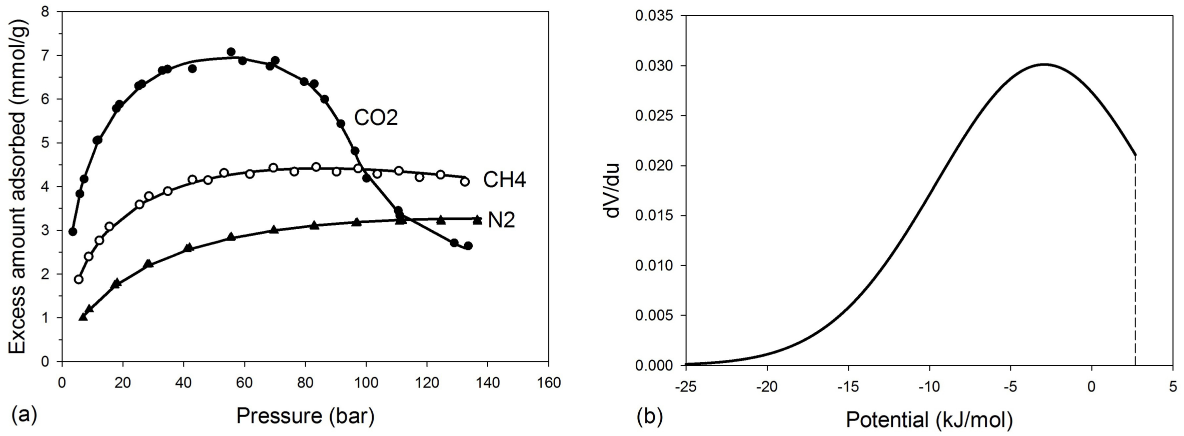

FIG. 1. (a) Calculated excess adsorption isotherms of CO_2, CH_4, and N_2 on activated carbon Filtrasorb-400 (lines) *vs* experimental data (symbols) [6] at 318.2 K. Lines are calculations using distribution (17) and the Bender's EOS. (b) Distribution of EAVs over the potential

The second term in square brackets is the gas density in the bulk phase. The lower limit u_{min} was taken to be -35 kJ/mol, when the function $f(u_{min})$ becomes negligible.

The least squares coefficients for the EAVs distribution function were 0.02734, 0.06620, and 0.01131 for b_1, b_2, and b_3, respectively. The resulting affinity coefficients β_2, β_3 were 0.9886, and 0.7694 for methane and nitrogen, respectively, under the assumption that $\beta_1 = 1$ for carbon dioxide. The upper limit u_{max} turned out to be 2.694 kJ/mol. The total pore volume W_0 calculated by Eq. (1) is 0.402 cm^3/g. The EAV distribution over the potential is shown in Fig. 1b. In fact, it is part of a Gaussian or normal function with a mean expectation u_0 of -2.925 kJ/mol and a standard deviation σ of 4.7 kJ/mol.

3.2. Binary isotherms

Binary excess adsorption isotherms are calculated according to the following algorithm.

(I) At a given temperature and bulk pressure p, individual chemical potentials μ_1°, μ_2° and densities ρ_1°, ρ_2° are determined with the EOS. Then, for known fractional composition y_1, $y_2 = 1 - y_1$ chemical potentials μ_1, μ_2 are determined using the following relationships:

$$\mu_j = \mu_j^\circ + RT\left[\ln y_j + \alpha p(1-y_j)^2\right], \quad j = 1, 2. \tag{20}$$

The actual densities ρ_1^b and ρ_2^b in the bulk phase can be further calculated using the equation, which is a combination of Eqs. (12) and (13):

$$\rho_j = y_j/[y_1/\rho_1^\circ + y_2/\rho_2^\circ], \quad j = 1, 2. \tag{21}$$

(II) For a given potential u in the selected EAV, the local chemical potentials are μ_1–$\beta_1 u$ and μ_2–$\beta_2 u$ for the first and second components, respectively. To determine the composition and pressure at given chemical potentials in the EAV, it is necessary to solve the following system:

$$\left.\begin{aligned} \mu\text{'}_1^\circ &= \mu_1 - \beta_1 u - RT\left[\ln x_1 + \alpha\Pi x_2^2\right], \\ \mu\text{'}_2^\circ &= \mu_2 - \beta_2 u - RT\left[\ln x_2 + \alpha\Pi x_1^2\right], \end{aligned}\right\} \tag{22}$$

where $\mu\text{'}_1^\circ$, $\mu\text{'}_2^\circ$ are functions of the same pressure Π for corresponding pure components.

The root of the system of equations (22) is Π and x_1 (or x_2, which does not matter). At the same time, this gives densities ρ_1°, ρ_2° of individual components corresponding to the pressure Π. The actual densities in the EAV can then be calculated with relations, similar to those in Eqs. (21):

$$\rho_j = x_j/\left[x_1/\rho_1^\circ + x_2/\rho_2^\circ\right], \quad j = 1, 2. \tag{23}$$

(III) At the final stage, the adsorbed amounts of the mixture components are determined by integration over all elements of adsorption volume, distributed over potential u:

$$a_j = \int\limits_{u_{\min}}^{u_{\max}} \left[\rho_j(T, \mu\text{'}_1, \mu\text{'}_2) - \rho_j^b(T, \mu_1, \mu_2)\right] f(u)du, \quad j = 1, 2. \tag{24}$$

Isotherms of carbon dioxide and methane on Filtrasorb-400 from CO_2–CH_4 mixture are presented in Fig. 2.

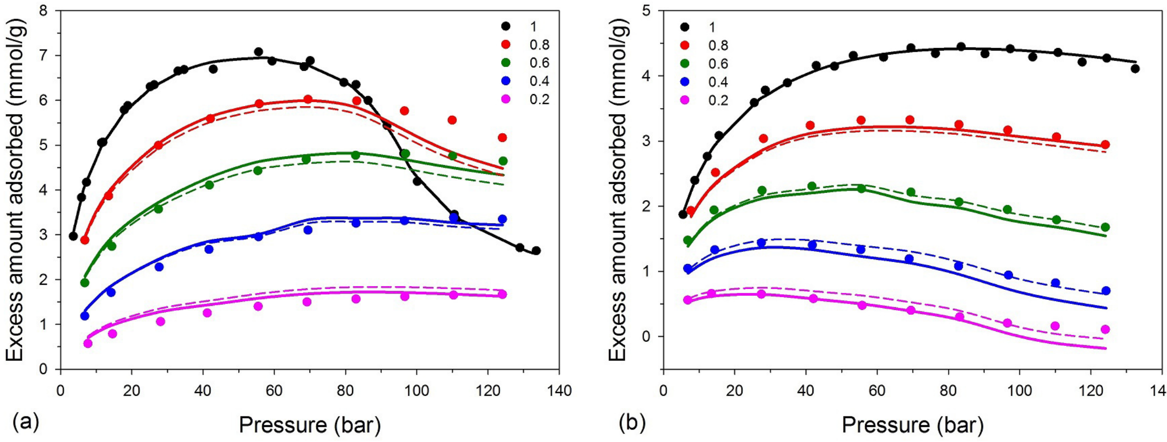

FIG. 2. Comparison of the calculated and experimental excess adsorption of CO_2 and CH_4 on activated carbon Filtrasorb-400 from a CO_2–CH_4 gas mixture at 318.2 K. The circles represent the experimental data from Ref. 6, and the lines represent calculations using the proposed method, accounting for the distribution (17) and a coefficient α of 0.000174 bar^{-1} in Eqs. (19) and (21). The dashed lines correspond to the ideal mixing Gibbs free energy at $\alpha = 0$. The numbers at the curves indicate the molar fraction of CO_2 (a) and CH_4 (b) in the gas phase, so the black circles and lines indicate adsorption of pure CO_2 (a) and CH_4 (b), respectively

As seen in Fig. 2, the agreement between experimental data and calculations is quite good despite we used the only adjusting parameter α. However, even with a zero value of α, i.e. in the absence of adjusting parameters, the description of experimental data remains acceptable.

In a similar way, experimental adsorption isotherms for binary systems CO_2–N_2 and CH_4–N_2 can be analyzed. Corresponding results are presented in Figs. 3,4.

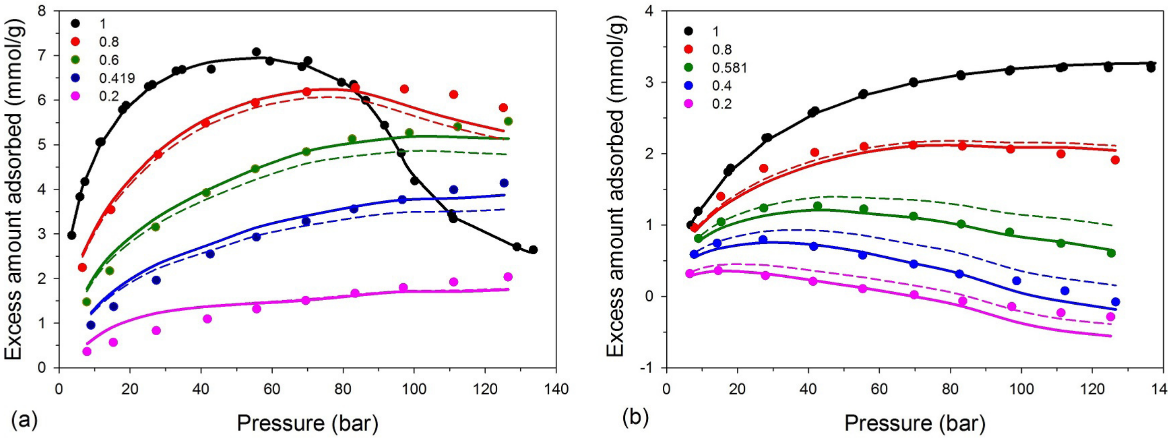

FIG. 3. Experimental [6] and calculated excess adsorption isotherms of CO_2 and N_2 on activated carbon Filtrasorb-400 from CO_2–N_2 mixture at 318.2 K. Coefficient α is 0.000469 bar^{-1} (solid lines) and 0 (dashed lines). The remaining conditions are the same as in Fig. 2

As can be seen from Figs. 2–4, in all examples of binary mixtures the concept works very reliably over a wide range of pressures in the bulk phase.

3.3. Adsorbed phase pressure

The pressure depends on the potential u in a specific element of the adsorbed phase and, for given chemical potentials of the components of a binary mixture, is the root of Eqs. (22) along with the fractional composition. The average pressure in the adsorption phase is determined by the following equation:

$$\bar{\Pi} = W_0^{-1} \int_{u_{\min}}^{u_{\max}} f(u)\Pi du. \tag{25}$$

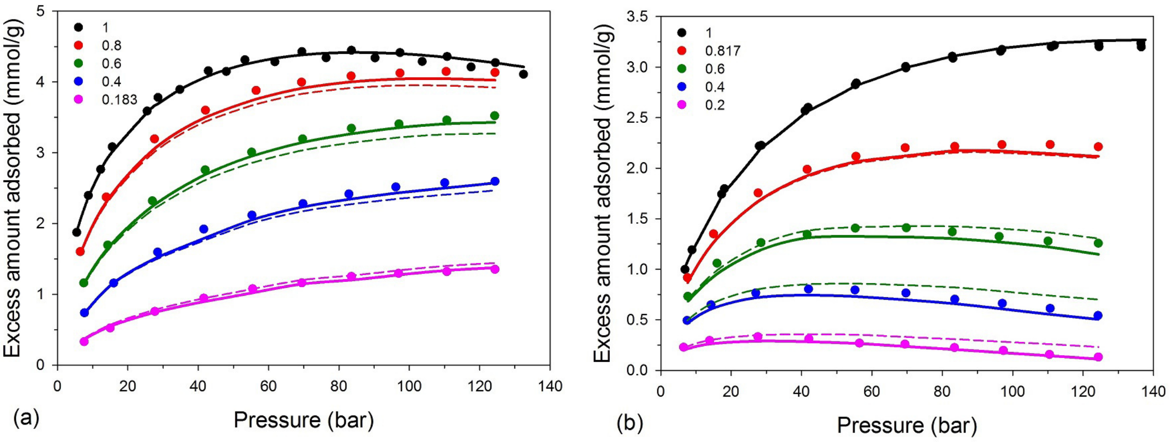

FIG. 4. Experimental [6] and calculated excess adsorption isotherms of CH_4 and N_2 on activated carbon Filtrasorb-400 from CH_4–N_2 mixture at 318.2 K. Coefficient α is 0.000292 bar^{-1} (solid lines) and 0 (dashed lines). The remaining conditions are the same as in Fig. 2

Fig. 5 presents the average pressure in the adsorption phase as a function of the bulk pressure for a CO_2–CH_4 mixture at various compositions in the bulk phase.

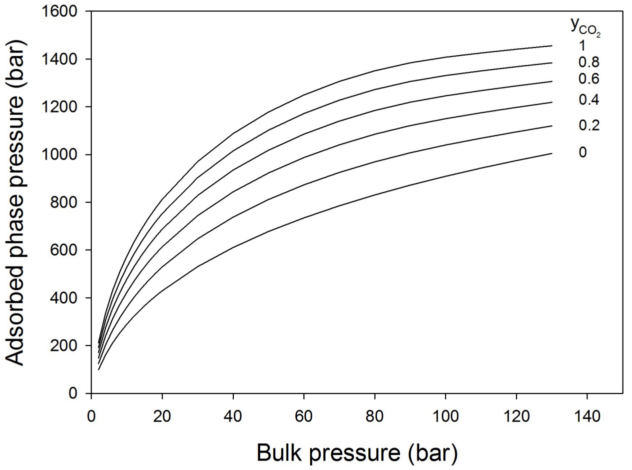

FIG. 5. Average pressure in the adsorbed CO_2–CH_4 mixture on activated carbon Filtrasorb-400 at 318.2 K. The numbers in the legend are mole fraction of carbon dioxide in the bulk phase

The average pressure reaches 1500 bar, which is an order of magnitude higher than the bulk pressure.

Taking into account the Gibbs-Duhem equation for a given potential u in the EAV,

$$d\Pi = \rho_1 d\mu_1 + \rho_2 d\mu_2, \tag{26}$$

we have:

$$W_0 d\bar{\Pi} = \int\limits_{u_{\min}}^{u_{\max}} f(u)\left[\rho_1 d\mu_1 + \rho_2 d\mu_2\right] du.$$

In equivalent form the above equation can be rewritten as

$$W_0 d\bar{\Pi} = a_1 d\mu_1 + a_2 d\mu_2. \tag{27}$$

This means that the Gibbs-Duhem equation in the form of Eq (27) is satisfied in the proposed method.

The Gibbs-Duhem equation can also be written for individual components, i.e.,

$$W_0 d\bar{\Pi} = a_j^\circ(\bar{\Pi}) d\mu_j, \quad j = 1, 2. \tag{28}$$

Combining Eqs. (27) and (28), we again obtain Eq. (16), where a_1°, a_2° are amounts of individual adsorption at the same average adsorbed phase pressure.

3.4. Thermodynamic consistency of experimental data

As mentioned earlier, excess quantities can only be obtained experimentally, so it is crucial to create an analog of the Gibbs-Duhem equation for excess functions. This can be done by subtracting from Eq. (27) a similar equation written for the bulk phase:

$$W_0 dp = W_0 \rho_1^b d\mu_1 + W_0 \rho_1^b d\mu_2.$$

This gives

$$W_0 d(\bar{\Pi} - p) = a_1^{ex} d\mu_1 + a_2^{ex} d\mu_2. \tag{29}$$

The variable $(\bar{\Pi} - p)$ can be called excess pressure $\bar{\Pi}^{ex}$, which at a given temperature can be considered as a function of chemical potentials μ_1 and μ_2. Since the chemical potential tends to $-\infty$ at zero density, it is more convenient to use $v_1 = \exp[\mu_1/(RT)]$ and $v_2 = \exp[\mu_2/(RT)]$ as independent parameters. Let the function $W_0\bar{\Pi}^{ex}$ be written as a polynomial:

$$W_0\bar{\Pi}^{ex} = \sum_{j=0}^{n}\sum_{k=0}^{n} b_{jk} v_1^j v_2^k \tag{30}$$

Then

$$\left.\begin{aligned} a_1^{ex} &= W_0\frac{\partial\bar{\Pi}^{ex}}{\partial\mu_1} = \frac{1}{RT}\sum_{j=0}^{n}\sum_{k=0}^{n} j b_{jk} v_1^j v_2^k, \\ a_2^{ex} &= W_0\frac{\partial\bar{\Pi}^{ex}}{\partial\mu_2} = \frac{1}{RT}\sum_{j=0}^{n}\sum_{k=0}^{n} k b_{jk} v_1^j v_2^k. \end{aligned}\right\} \tag{31}$$

The advantage of system (31) is that to calculate the excess amount of adsorbed both the first and second components, the same set of coefficients b_{jk} is used, and the thermodynamic consistency of calculations is guaranteed. The coefficients b_{jk} are determined by the standard least-squares technique using both mixture and individual experimental adsorption isotherms at a condition that the coefficient b_{00} is zero. The thermodynamic consistency of experimental data is assessed by small variations between the experimental values of excess adsorption and those calculated using equations (31).

Figure 6 presents the results of a regression analysis of experimental data on the adsorption of a CO_2–CH_4 mixture on Filtrasorb-400 activated carbon. The upper summation limits n in Eqs. (31) were taken to be 4.

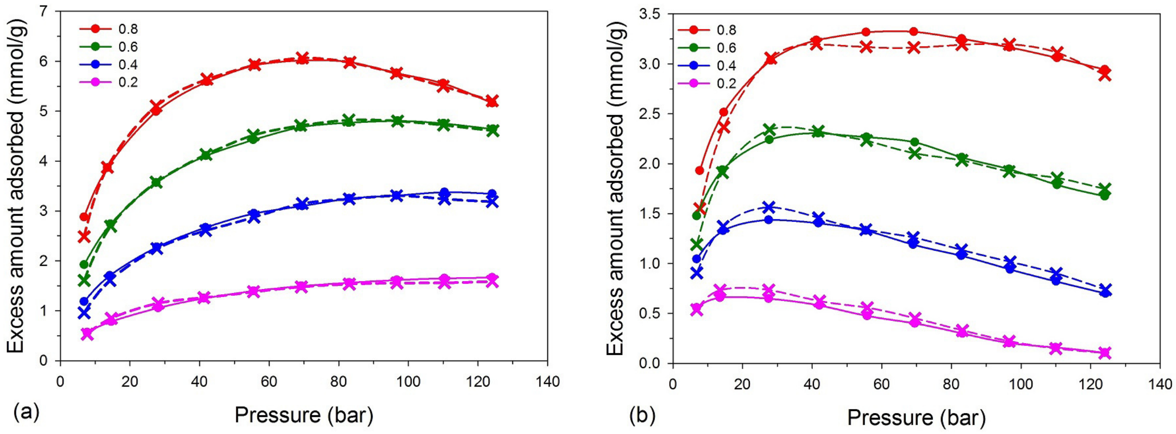

FIG. 6. Isotherms of excess adsorption of CO_2 (a) and CH_4 (b) from CO_2–CH_4 gas mixture on activated carbon Filtrasorb-400 [6] at 318.2 K. Circles are experimental data. Solid lines indicate the results of regression analysis using Eqs. (30). The numbers at the symbols represent the mole fractions of carbon dioxide and methane, respectively, in the feed gas

Lines in Fig. 6 show smoothed experimental adsorption excess values (circles) as required by the Gibbs-Duhem equation. Relatively small deviations between experimental and corrected amounts of adsorption confirm the thermodynamic consistency of experimental data. This is quite expected for supercritical fluid mixtures, but in case of adsorption of vapor mixtures it is not obvious, since equilibrium during the mixing process in the condensed liquid-like adsorbed phase occurs noticeably more slowly. In the latter case, the confirmation of thermodynamic consistency of experimental data should precede their further analysis.

4. Conclusion

An improved method for predicting the adsorption of a gas mixture using adsorption isotherms of pure gases is proposed. The idea behind the approach is that the Gibbs free energy of mixing is close to its ideal value. This can be formulated as the ideal mixing of non-ideal gases in the adsorbed phase, the elements of which are distributed over the potential. Using the equation of state of the individual components, this condition allows for the determination of the pressure and composition of the mixture in the adsorbed phase for given chemical potentials. We chose Bender's equation of state for this purpose, but any other suitable equation of state can be used as well. Therefore, the proposed approach is fundamentally different from the ideal adsorbed solution theory and does not rely on the Raoult's law in the adsorbed phase. The approach has been tested on a well-studied CO_2–CH_4- activated carbon system. All previous methods based on the IAST (see references 2-4, 8, and 12, for example) can more or less quantitatively describe the system under bulk pressures up to 1–1.3 MPa. Contrary to this, our approach exceeds the pressure range by at least one order of magnitude using directly measured excess experimental values as input, which has been validated by its application to experimental data from reference 6.The possibility of increasing the descriptive ability of the method is also provided by using an additional adjustable parameter.

A general method was also proposed for checking the thermodynamic consistency of experimental data on the adsorption of gas mixtures.

References

[1] Myers A.L., Prausnitz J.M. Thermodynamics of mixed-gas adsorption. *AIChE J.*, 1965, **11**, P. 121–127.

[2] Rios R.B., Stragliotto F.M., Peixoto H.S., Torres A.E.B., Bastos-Neto A.M., Azevedo D.C.S., Cavalcante C.L. Studies on the adsorption behavior of CO_2-CH_4 mixtures using activated carbon. *Braz. J. Chem. Eng.*, 2013, **30**, P. 939–951.

[3] Pino D., Plantier F., Bessieres D. Experimental determination of the adsorption isoterms in gas mixtures under extended pressure and temperature range. *J. Term. Anal. Calorim.*, 2014, **117**, P. 1469–1477.

[4] Pino D., Bessieres D. CH_4/CO_2 Mixture adsorption on a characterized activated carbon. *J. Chem. Eng. Data.*, 2017, **62**, P. 1475–1480.

[5] Dreisbach F., Staudt R., Keller J.U. High pressure adsorption data of methane, nitrogen, carbon dioxide and their binary and ternary mixture on activated carbon. *Adsorption*, 1999, **5**, P. 215–227.

[6] Sudibandriyo M., Pan Zh., Fitzgerald J.E., Robinson R.L., Gasem K.A.M. Adsorption of methane, nitrogen, carbon dioxide, and their binary mixtures on dry activated carbon at 318.2 K and pressures up to 13.6 MPa. *Langmuir*, 2003, **19**, P. 5323–5331.

[7] Rufford T.E., Watson G.C.Y., Saleman T.L., Hofman P.S. Adsorption equilibria and kinetics of methane + nitrogen mixtures on the activated carbon Norit RB3. *Ind. Chem. Eng. Res.*, 2013, **52**, P. 14270–14281.

[8] Fitzgerald J.E., Pan Z., Sudibandriyo M., Robinson R.L., Gasem K.A.M., Reeves S. Adsorption of methane, nitrogen, carbon dioxide and their mixtures on wet Tiffany coal. *Fuel*, 2005, **84**, P. 2351–2363.

[9] Vaart R. van der Huiskes C., Bosch H., Reith T. Single and mixed gas adsorption equilibria of carbon dioxide/methane on activate carbon. *Adsorption*, 2000, **6**, P. 311–323.

[10] Valenzuela D.P., Myers A.L., Talu O., Zwiebel I. Adsorption of gas mixtures: Effect of energetic heterogeneity. *AIChE J.*, 1988, **34**, P. 397–402.

[11] Jensen C.R.C., Seaton N.A., Gusev V., O'Brien J.A. Prediction of multicomponent adsorption equilibrium using a new model of adsorbed phase nonuniformity. *Langmuir*, 1997, **13**, P. 1205–1210.

[12] Goetz V., Pupier O., Guillot A. Carbon dioxide-methane mixture adsorption on activated carbon. *Adsorption*, 2006, **12**, P. 55–63.

[13] Dubinin M.M. Fundamentals of the theory of adsorption in micropores of carbon adsorbents: Characteristics of their adsorption properties and microporous structures. *Carbon*, 1989, **27**, P. 457–467.

[14] Hoory S.E., Prausnitz J.M. Monolayer adsorption of gas mixtures on homogeneous and heterogeneous solids. *Chem. Eng. Sci.*, 1967, **22**, P. 1025–1033.

[15] DeGance A.E. Multicomponent high-pressure adsorption equilibria on carbon substrates: Theory and data. *Fluid Phase Equilibria*, 1992, **78**, P. 99–137.

[16] Ustinov E.A., Do D.D., Herbst A., Staudt R., Harting P. Multicomponent adsorption on activated carbons under supercritical conditions. *J. Colloid Interface Sci.*, 2004, **275**, P. 376–385.

[17] Shapiro A.A., Stenby E.H. Potential theory of multicomponent adsorption. *J. Colloid Interface Sci.* 1998, **201**, P. 146–157.

[18] Dundar E., Zacharia R., Chahine R., Bénard, P. Potential theory for prediction of high-pressure gas-mixture adsorption on activate carbons and MOFs. *Sep. Purif. Technol.*, 2014, **135**, P. 229–242.

[19] Polanyi M. The potential theory of adsorption. *Science*, 1963, **141**, P. 1010–1013.

[20] Ustinov E.A., Do D.D., Herbst A., Staudt R., Harting P. Modeling of gas adsorption equilibrium over a wide range of pressure: A thermodynamic approach based on equation of state. *J. Colloid Interface Sci.*, 2002, **250**, P. 49–62.

[21] Platzer B., Maurer G. Application of a generalized Bender equation of state to the description of vapour-liquid equilibria in binary systems. *Fluid Phase Equilibria*, 1993, **84**, P. 79–110.

[22] Ustinov E.A. Thermodynamics of liquid and fluid mixtures from kinetic Monte Carlo viewpoint. *Phys. Chem. Chem. Phys.*, 2023, **25**, P. 27321–27330.

Submitted 7 August 2024; revised 12 November 2024; accepted 13 November 2024

Information about the authors:

Tatiana A. Kuznetsova – Chemistry Department, Lomonosov Moscow State University, GSP-1, Leninskie Gory, Moscow, 119991 Russian Federation; ORCID 0009-0002-1803-8464; tchess54@mail.ru

Eugene A. Ustinov – Ioffe Institute, 26 Polytechnicheskaya, St. Petersburg, 194021 Russian Federation; ORCID 0000-0003-4668-1326; eustinov@mail.ioffe.ru

Conflict of interest: the authors declare no conflict of interest.

NANOSYSTEMS:

PHYSICS, CHEMISTRY, MATHEMATICS

INFORMATION FOR AUTHORS

The journal publishes research articles and reviews, and also short scientific papers (letters) which are unpublished and have not been accepted for publication in other magazines. Articles should be submitted in English. All articles are reviewed, then if necessary come back to the author to completion.

The journal is indexed in Web of Science Core Collection (Emerging Sources Citation Index), Chemical Abstract Service of the American Chemical Society, Zentralblatt MATH and in Russian Scientific Citation Index.

Author should submit the following materials:

1. Article file in English, containing article title, the initials and the surname of the authors, Institute (University), postal address, the electronic address, the summary, keywords, MSC or PACS index, article text, the list of references.
2. Files with illustrations, files with tables.
3. The covering letter in English containing the article information (article name, MSC or PACS index, keywords, the summary, the literature) and about all authors (the surname, names, the full name of places of work, the mailing address with the postal code, contact phone number with a city code, the electronic address).
4. The expert judgement on possibility of publication of the article in open press (for authors from Russia).

Authors can submit a paper and the corresponding files to the following addresses: nanojournal.ifmo@gmail.com, popov1955@gmail.com.

Text requirements

Articles should be prepared with using of text editors MS Word or LaTex (preferable). It is necessary to submit source file (LaTex) and a pdf copy. In the name of files the English alphabet is used. The recommended size of short communications (letters) is 4-6 pages, research articles– 6-15 pages, reviews – 30 pages.

Recommendations for text in MS Word:

Formulas should be written using Math Type. Figures and tables with captions should be inserted in the text. Additionally, authors present separate files for all figures and Word files of tables.

Recommendations for text in LaTex:

Please, use standard LaTex without macros and additional style files. The list of references should be included in the main LaTex file. Source LaTex file of the paper with the corresponding pdf file and files of figures should be submitted.

References in the article text are given in square brackets. The list of references should be prepared in accordance with the following samples:

[1] Surname N. *Book Title*. Nauka Publishing House, Saint Petersburg, 2000, 281 pp.
[2] Surname N., Surname N. Paper title. *Journal Name*, 2010, **1** (5), P. 17-23.
[3] Surname N., Surname N. Lecture title. In: Abstracts/Proceedings of the Conference, Place and Date, 2000, P. 17-23.
[4] Surname N., Surname N. Paper title, 2000, URL: http://books.ifmo.ru/ntv.
[5] Surname N., Surname N. Patent Name. Patent No. 11111, 2010, Bul. No. 33, 5 pp.
[6] Surname N., Surname N. Thesis Title. Thesis for full doctor degree in math. and physics, Saint Petersburg, 2000, 105 pp.

Requirements to illustrations

Illustrations should be submitted as separate black-and-white files. Formats of files – jpeg, eps, tiff.

NANOSYSTEMS:

PHYSICS, CHEMISTRY, MATHEMATICS

Журнал зарегистрирован
Федеральной службой по надзору в сфере связи, информационных технологий и массовых коммуникаций
(свидетельство ПИ № ФС 77 - 49048 от 22.03.2012 г.)
ISSN 2220-8054

Учредитель: федеральное государственное автономное образовательное учреждение высшего образования
«Национальный исследовательский университет ИТМО»

Издатель: федеральное государственное автономное образовательное учреждение высшего образования
«Национальный исследовательский университет ИТМО»

Отпечатано в Учреждении «Университетские телекоммуникации»
Адрес: 197101, Санкт-Петербург, Кронверкский пр., 49

Подписка на журнал НФХМ
На первое полугодие 2025 года подписка осуществляется через
ОАО «АРЗИ», подписной индекс Э57385